13th International Conference on Heavy Ion Accelerator Technology

HIAT 2015

YOKOHAMA, JAPAN
September 7 - 11, 2015

PROCEEDINGS

Conference Venue: WORKPIA YOKOHAMA
Hosted by RIKEN Nishina Center
Conference Chair: Osamu Kamigaito

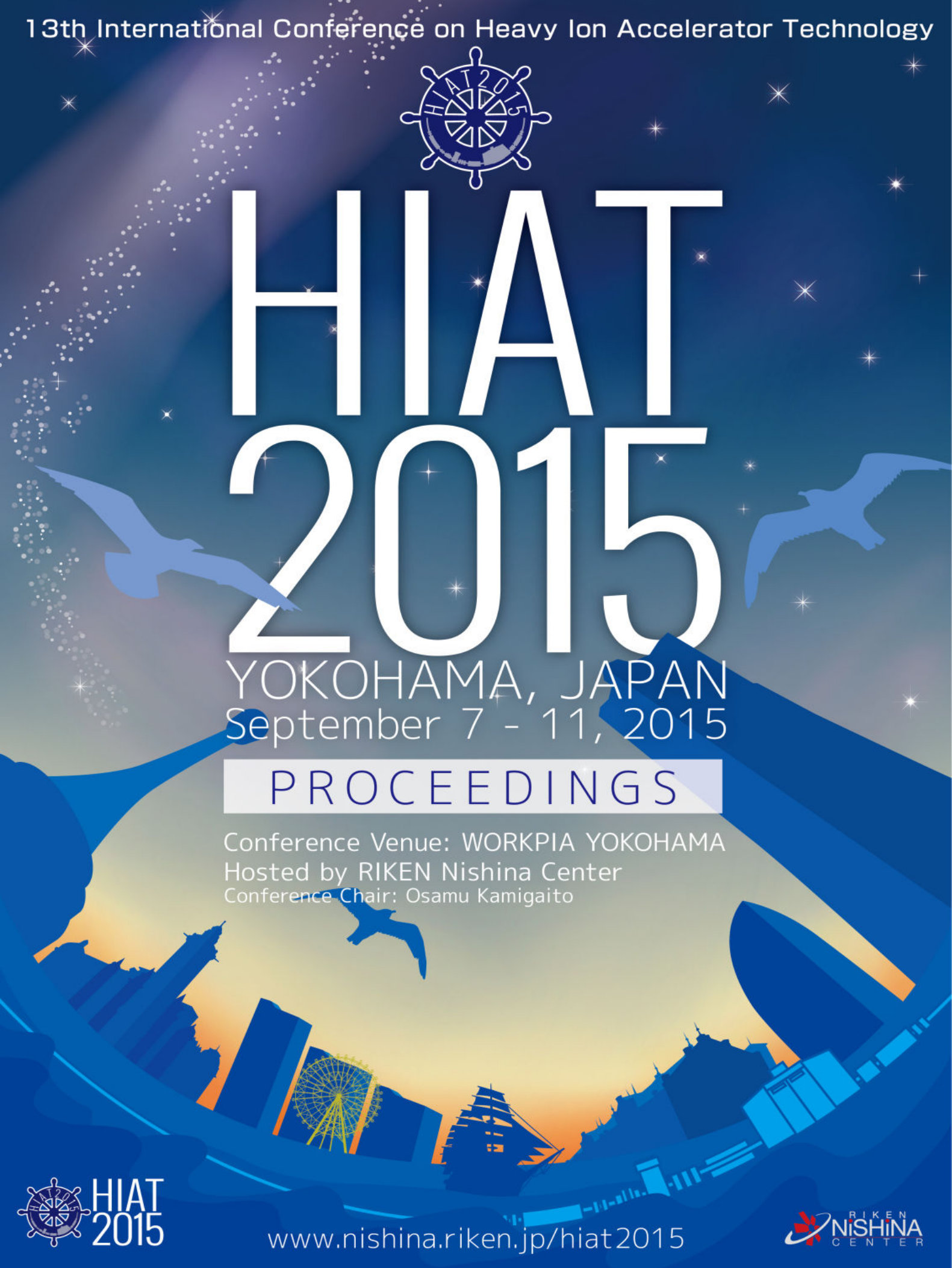

HIAT 2015

www.nishina.riken.jp/hiat2015

RIKEN NISHINA CENTER

Dear Colleagues,

Welcome to the HIAT2015 conference!

HIAT2015 is the 13th in a series of conferences, which is dedicated to the design, construction, development and operation of heavy-ion accelerators and their components. The conference series goes back to 1973 in Daresbury and followed by Strasbourg (1977), Oak Ridge (1981), Buenos Aires (1985), Strasbourg-Heidelberg (1989), Legnaro (1992), Canberra (1995), Argonne (1998), Delhi (2002), Brookhaven (2005), Venice (2009), and Chicago (2012). The present conference, held in Yokohama, is hosted by RIKEN Nishina Center, and co-hosted by Research Center of Nuclear Physics of Osaka University, National Institute of Radiological Sciences, The university of Tsukuba Tandem Accelerator Complex, and Takasaki Advanced Radiation Research Institute of Japan Atomic Energy Agency.

This HIAT conference is devoted to the accelerator teams of any institution, laboratory or university, running or developing heavy ion facilities or their components for studies in the basic research fields as well as the various applications of heavy ion beams in medicine, development and production of radionuclides, nuclear waste management, and so on. We believe this conference will devote to the further advancement and growth of heavy ion accelerator technology.

We gratefully acknowledge the financial assistance of Inoue foundation for Science, Foundation for High Energy Accelerator Science, Research Center for Nuclear Physics of Osaka University, and RIKEN. We are also deeply grateful to our Exhibitors and Sponsor companies for their financial support.

We hope you will enjoy this conference, and wish you a pleasant stay in Yokohama!

Sincerely,

Osamu Kamigaito

Chair, HIAT2015

Contents

International Advisory Committee

Ludwig Beck	LMU, Munich	Germany
Giovanni Bisoffi	INFN-LNL, Legnaro	Italy
Yuan He	IMP	China
Osamu Kamigaito	RIKEN	Japan
Dinakar Kanjilal	IUAC	India
Oliver Kester	GSI	Germany
Bernard Laune	Orsay	France
Robert Laxdal	TRIUMF	Canada
Daniela Leitner	MSU	USA
Nikolai Lobanov	Australian National Univ.	Australia
Francis Osswald	IPHC & SPIRAL2	France
Richard Pardo	ANL	USA
Zhaohua Peng	CIAE	China
Danilo Rifuggiato	INFN-LNS, Catania	Italy
Kimikazu Sasa	University of Tsukuba	Japan

Organizing Committee

Osamu Kamigaito	RIKEN (Conference Chair)

Advisory Board

Masayuki Kase	RIKEN (Board Chair)
Kichiji Hatanaka	RCNP, Osaka Univ.
Koji Noda	NIRS
Kimikazu Sasa	University of Tsukuba
Wataru Yokota	JAEA-Takasaki

Executive Board

Naruhiko Sakamoto	RIKEN (Board Chair)
Nobuhisa Fukinishi	RIKEN
Eiji Ikezawa	RIKEN
Misaki Komiyama	RIKEN
Narumasa Miyauchi	RIKEN
Hiroki Okuno	RIKEN
Karen Sakuma	RIKEN (Conference Secretary)
Tamaki Watanabe	RIKEN
Kazunari Yamada	RIKEN (Proceedings Editor)

PROGRESS ON THE HIE-ISOLDE FACILITY

Y. Kadi, M.J. Garcia Borge, W. Venturini Delsolaro, N. Delruelle, J.A. Ferreira, J.C. Gayde, G. Kautzmann, M. Martino, J.A. Rodriguez, E. Siesling, L. Valdarno, CERN, Geneva, Switzerland

Abstract

After 20 years of successful ISOLDE operation at the PS-Booster [1], a major upgrade of the facility, the HIE-ISOLDE (High Intensity and Energy ISOLDE) project was launched in 2010. It is divided into three parts; a staged upgrade of the REX post-accelerator to increase the beam energy from 3.3 MeV/u to 10 MeV/u using a super-conducting linac [2], an evaluation of the critical issues associated with an increase in proton-beam intensity and a machine design for an improvement in RIB quality. The latter two will be addressed within the HIE-ISOLDE Design Study [3]. This paper aims to provide an overview of the present status of the overall project by giving an insight to the infrastructure modifications, installation and tests of the HEBT lines as well as progress on the commissioning of the SC linac. Plans for the second phase of the project will be highlighted.

INTRODUCTION

The present schedule foresees to deliver beams up to 4.2 MeV/u for the heaviest species this autumn with a single high-beta cryomodule. A second cryomodule will be installed during the winter shutdown 2015/2016 bringing the energy to 5.5 MeV/u for all the radionuclides available at ISOLDE. This will complete phase 1, making Coulomb excitation studies possible up to A/q=4.5. A second phase will consist in adding two more high-beta cryomodules during the winter shutdown 2016/2017, thus doubling the available accelerating voltage. Finally, in phase 3, two low-beta cryomodules would be installed, replacing some normal conducting structures of the present REX-ISOLDE. This will allow varying continuously the energy between 0.45 and 10 MeV/u together with an improved beam quality. A detailed description of the optics and beam dynamics design choices for the linac can be found in [4].

As we write, installation of the HIE-ISOLDE technical infrastructure has been completed with minor disruptions to the parallel running of the Low-Energy physics programs at the ISOLDE facility. The SC linac as well as the HEBT lines have been installed and tested.

This paper offers a snapshot of the main activities as the commissioning of the HIE-ISOLDE linac with beam is in progress.

TECHNICAL INFRASTRUCTURE

The long shutdown of the CERN accelerators in 2013-2014 was used to upgrade the general infrastructure of the existing ISOLDE facility. All the services are by now fully operational.

The overhauled ALEPH compressor units/cold box together with the new cryogenic distribution line (Fig. 1) have been commissioned and supplying LHe at 4.5K since June 2015 [5].

Figure 1: Cryogenic distribution line feeding the SC linac with liquid He at 4.5K.

In the ISOLDE experimental hall, Controls, DC and RF cables with a total length of more than 65 kilometres have been installed and power supplies, beam instrumentation and vacuum equipment racks are in place and operational.

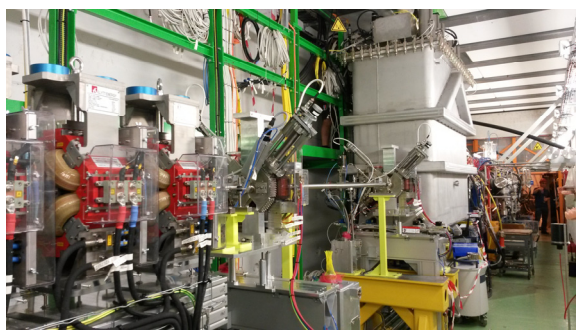

Figure 2: Cryomodule 1 and the first part of the straight section downstream of the superconducting (SC) linac inside the shielding tunnel.

The first high-beta cryomodule (CM1) was transported to the HIE-ISOLDE linac tunnel in May (Fig. 2) and after a dense installation campaign, CM1 was ready for cryogenic cool-down a month later. The installation and commissioning of the second high-beta cryomodule (CM2) is scheduled for the first quarter of 2016.

Subsystems such as cryogenic instrumentation, vacuum controls, RF interlocks, fire and oxygen deficiency alarms have all been tested.

Elements of the SC linac and the first two High-Energy Beam Transfer lines (XT01 and XT02) have all been installed (Fig. 3). The quadrupole, H/V corrector and dipole magnets and associated beam diagnostic boxes have all been tested and commissioned. The first two experiments (Miniball and the Scattering chamber) are being installed in view of the first physics run this coming Fall.

ISBN 978-3-95450-131-1

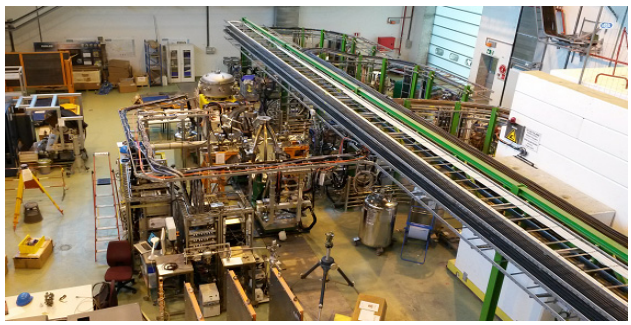

Figure 3: Top view of the SC linac tunnel (bottom right), the three HEBT lines (top right) and the two experiments: Miniball and the Scattering chamber (on the left).

The optics of the third beam line, for which the infrastructure has already been installed, will be added during the course of 2017.

COMMISSIONING THE ELECTRICAL CIRCUITS

49 circuits (HEBT and SC Linac) were commissioned, all complying with the dynamic performance specification. The circuits are grouped as in Table 1.

Table 1: Summary of HIE-ISOLDE commissioned circuits

Circuit Type	Nominal	Nominal Op
SC Solenoid	± 120 A	100 A
Corrector Magnet	± 50 A	± 45 A
Quadrupole Magnet	200 A	132 A
Quadrupole Magnet with Polarity Reversal	± 200 A	± 132 A
Dipole Magnet	± 500 A	± 423 A

Together with the verification that installed converters and all interfacing systems worked appropriately (magnet interlock, all layers of the control infrastructure, etc...), each converter was configured by an equipment specialist with the suitable operational parameters (minimum and maximum current, max allowable current rate). The digital regulation parameters were then set for optimal performance (according to individual circuit electrical resistance and inductance).

For the subsequent performance assessment of the installed converters, Noise Tests were carried out where the measured value of the current is sampled at 1 kS/s for both measurement channels during 8.192 seconds. This test concerns measurement of the noise and power ripple in the frequency range 0Hz-500Hz for both the HEBT and the SC Solenoid circuits and it is graphically illustrated in Fig. 4.

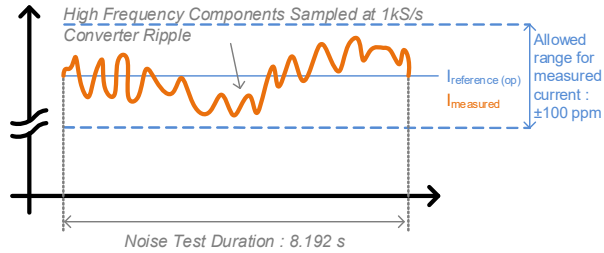

Figure 4: Noise or Ripple Test. The specification of ± 100 ppm (200 ppm pk-pk of the nominal current of the converter) holds strictly for Quadrupole, Dipole and SC Solenoid circuits.

MACHINE COMMISSIONING

The machine commissioning campaign covered the vacuum and cryogenics performance, monitoring and alignment adjustment of the active elements, conditioning and RF measurement of the superconducting cavities, power tests of the superconducting solenoid, and commissioning of the LLRF and of the tuning systems. Cold testing of the first cryomodule started in June 2015.

Vacuum Performance

Before the CM was transported from the assembly area to its final location a helium leak detection was carried out. It also included the pressurization of all the cryogenic circuits with He. To avoid the displacement of dust a slow pump-down procedure was applied [6]. The CM was monitored before and after transport, no abnormal increase of pressure was observed. As soon as the CM was installed the pressure monitoring was re-started while all the vacuum instrumentation (valves, pumps, connections) were installed and commissioned.

During the cool down the He background was continuously followed using one He leak detector. The base pressure of the CM at cold steady state conditions is approx. 5e-11 mbar (measured in the volume between the thermal shield and the vessel). During a period of 1 month the CM was isolated from its turbo-pumping. No pressure variation was observed during that period confirming the excellent tightness of the cryogenic circuits.

Figure 5 shows the pump down curve during cool down.

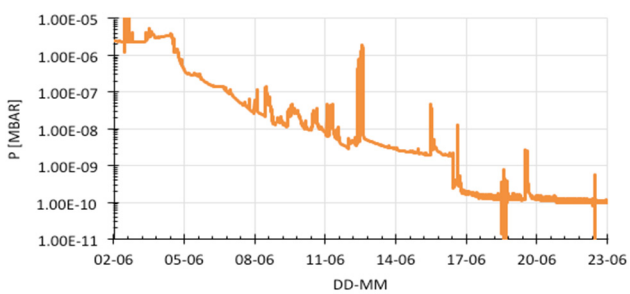

Figure 5: Vacuum monitoring of CM1 during cool-down (Spikes due to parallel RF conditioning of the cavities).

ISBN 978-3-95450-131-1

Cryogenics Performance

In the absence of precise calorimetric measurements on a dedicated test bench, first measurements of the static heat loads of CM1 were done during the commissioning in the HIE-ISOLDE linac. The heat loads to the 4.2 K level were estimated by measuring, via the built-in superconducting level gauges, the reduction in the liquid helium in the reservoir by boil-off at constant pressure.

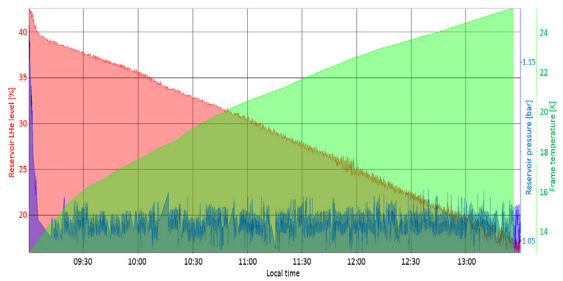

Figure 6: Liquid helium behaviour at constant pressure inside the reservoir during the test.

As illustrated in Fig. 6, at a constant pressure of 1.05 bar, the liquid helium level decreases by 20% during 4 hours of test, which corresponds to an average of 10 litres/h equivalent to a heat load of about 7W. During this time, the un-cooled frame accumulates thermal capacity due to the radiation heat loads from the thermal shield and to solid conduction through the frame supports, as measured by the temperature increases of about 12K. This increase in heat capacity is equivalent to a heat load of about 2.5 W. So, the overall measured static heat load at 4.5 K, in normal operation, amounts to ~9.5W, well below the design value [7].

Monitoring and Alignment System

The Monitoring and Alignment Tracking for Hie-IsoLDE (MATHILDE) system, as fully described in [8], allows reconstructing and monitoring of the positions of the active element beam port centers. Placed on metrological tables, HBCAM cameras are observing, through viewports, the 4 high index (~2) glass ball targets that are attached on each omega plate. The omega plates are supporting and guiding the active element beam ports, one per beam port [9].

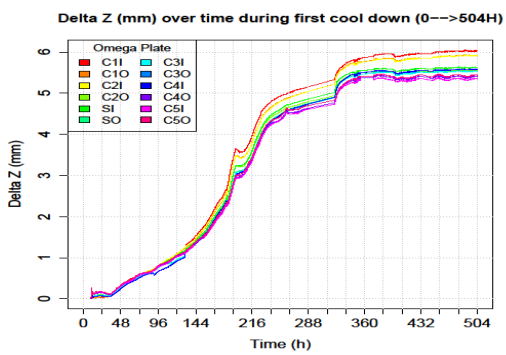

Figure 7: Vertical follow-up during the first cool down of the cavities (C%) and the solenoid (S), entry (I) and exit (O) omega plates.

For each omega plate, Fig. 7 illustrates the follow-up during the cool down of the target vertical movements with respect to measurements done at room temperature. The period plotted is from June 3rd to June 24th 2015, i.e. from room temperature to 4.5 K. The targets went up by 5.2 mm to 6 mm which is consistent with the expected vertical movement. Radially, the follow up with respect to the same original measurement shows that the omega plates moved by 0.3 mm to 0.4 mm to one side.

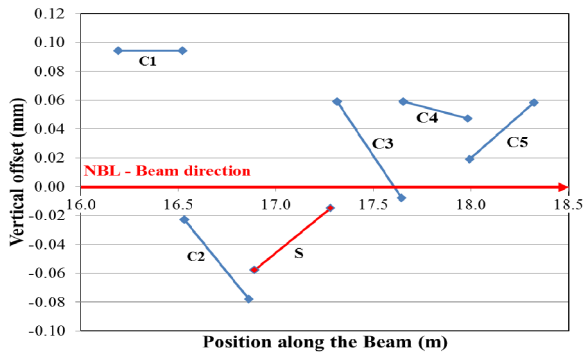

Figure 8: Vertical positions of the beam port centers after cold alignment.

The active element alignment on the nominal beam line is performed at cold. The frame supporting all the active elements inside the cryomodule is remotely moved vertically and horizontally by motors. The resulting alignment (see Fig. 8) was performed in an interval of ±0.1 mm in vertical for all the active elements with a precision level of 0.1 mm at one sigma. The relative precision between the points is about 0.05 mm (one sigma). The entry and exit beam port centers of each cavity and solenoid are plotted.

SC Linac – HIE

All 5 superconducting cavities (in CM1) were successfully RF conditioned at cold. The high field multipacting band around 1.5 MV/m was easily processed in 4/5 hours per cavity.

Extensive RF measurements were pursued, enabling to characterize fully the performance of the installed high-beta cryomodule. An important milestone was reached when all superconducting elements (cavities and solenoid) were successfully powered at nominal field at the same time.

The fully digital HIE ISOLDE low level RF system was deployed for the first time to control the first cryomodule. It was used to tune the SC QWRs very close to the target linac frequency of 101.28 MHz. A detailed status of the SRF systems at HIE-ISOLDE is given in [9].

NC Linac – REX

REX is the ISOLDE normal conducting linac post-accelerator. It is used to accelerate Rare Isotope Beams (RIB) produced at the ISOLDE targets after their charge state is boosted in the EBIS charge breeder. Alternatively, stable beam can be produced in the EBIS when residual gas is ionized [10].

ISBN 978-3-95450-131-1

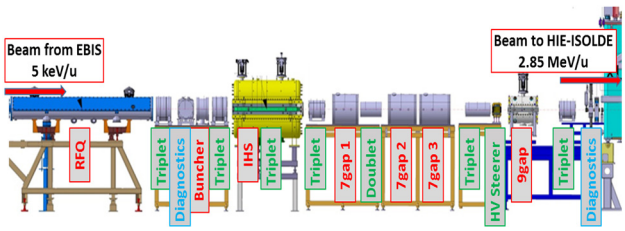

Figure 9: Layout of REX normal conducting post-accelerator.

Seven RF structures (Table 2) are used for longitudinally focussing and to accelerate the beam from 5 keV/u to 2.85 MeV/u. A total of nineteen quadrupoles grouped in triplets and doublets are used for transverse focusing. Two diagnostics boxes and a pair of beam steerers complete the main systems in the accelerator (Fig. 9).

Table 2: Main parameters of the linac post-accelerator normal conducting structures

RF structure	E_f [MeV/u] / β [%]	P [kW] for A/Q=4.0	A/Q acceptance
RFQ	0.3 / 2.5	29	< 5.5
Buncher	0.3 / 2.5	1.3	> 2.5
IHS	1.2 / 5.1	40	< 4.5
7gap1	1.55 / 5.7	60	> 2.5
7gap2	1.88 / 6.3	60	> 2.5
7gap3	2.2 / 6.8	60	> 2.5
9gap	2.85 / 7.8	71	> 2.5

Many components of REX have been replaced or refurbished during the last year. The power converters for the nineteen quadrupoles are new and have been commissioned. New thermal sensors have been retrofitted in several magnets and a high-resistance short in one of them has been repaired. Temperature rises and cooling water flow for many of them have been characterized. Two new fast Penning gauges are used to close a newly installed fast acting valve. Several faulty turbopumps and Penning gauges have been replaced and maintenance in all others has been completed. Maintenance of the RF amplifiers (cooling fans, DC power converters…) has been done. A new RF reference line is now operational. New water cooling circuits for magnets, cavities and amplifiers have been installed as well.

COMMISSIONING WITH BEAM

Beam produced in the EBIS charge breeder using residual gas with A/Q=4.0 (a mixture of $^{20}Ne^{5+}$, $^{16}O^{4+}$, $^{12}C^{3+}$ and $^{4}He^{+}$) and A/Q=3.0 ($^{12}C^{4+}$) has been used during the commissioning with beam.

A first beam accelerated to 0.3 MeV/u (output energy of the RFQ) was transported (all other RF structures were off) to the first HIE-ISOLDE diagnostics box and used to commission the Faraday cup, the silicon detector and the scanning slits.

Determining the Operational Settings of the RFQ

Several components in the LLRF of the amplifier for the RFQ were changed during its refurbishment making it necessary to redefine its operational settings. The beam transmission was measured for different power levels out of the amplifier (Fig. 10) and an amplitude in the 90-95% transmission plateau was chosen.

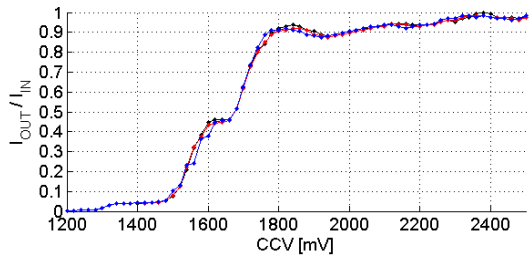

Figure 10: Beam transmission (A/Q=3.0) through the RFQ for different power levels.

First HIE-ISOLDE Diagnostics Box

The first HIE-ISOLDE diagnostics box is located at the end of the normal conducting linac right before the first cryomodule. It is equipped with a Faraday Cup, a scanning slit to measure the horizontal and vertical beam profiles, four circular collimators (20, 10, 5 and 3 mm diameter) and a silicon detector. Both the Faraday cup and the scanning slits have been tested during the commissioning with beam (Fig. 11) and they meet the design specifications [11].

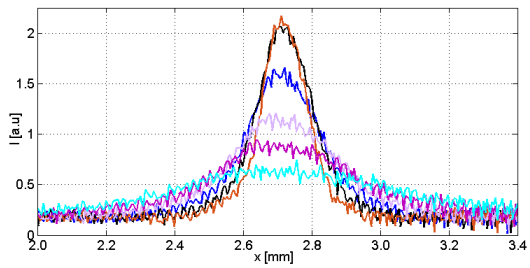

Figure 11: Beam profile for different focusing strengths in the last quadrupole before the cryomodule. Transverse profiles of beam with intensities as low as of a few epA have been measured.

The Si detector is used to measure the ions energy. It is able to detect single particles (Fig. 12) and can be used to measure properties of very low intensity beams.

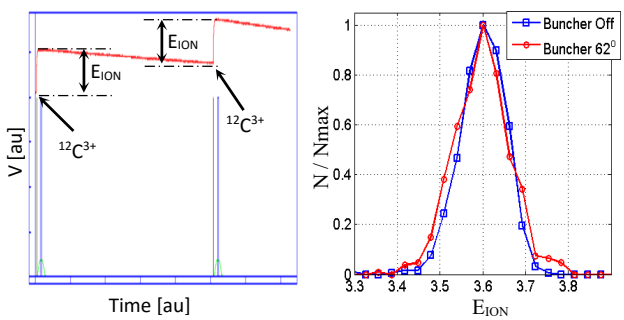

Figure 12: On the left in red: typical signal when ions hit the Si detector. The height of the signal is proportional to

ISBN 978-3-95450-131-1

the energy of the ion (E_{ION}). On the left in blue: train of ions counted by the data acquisition system. On the right: typical energy spectrum of a $^{12}C^{3+}$ beam with 0.3 MeV/u energy with the buncher off and with the buncher at its zero-crossing.

In the near future, the Si detectors will also be used to measure the time of flight (TOF) of the ions. However, this functionality has not been tested with beam yet.

Phasing of Accelerating Structures

One of the main applications of the Si detectors is to measure the changes in the energy of the beam when the RF cavities are operated at different phases. This type of measurements (Fig. 13) allows us to set the operational phase of the amplifier so that the synchronous particle gains the nominal energy when accelerated in the structure.

A large percentage of the time allocated to the commissioning with beam of REX has been spent conducting these measurements. The velocity (and the energy per nucleon since it is a non-relativistic beam) at the exit of each normal conducting cavity is the same for every ion. Therefore, the relative phases for the cavities will not change and it won't be necessary to re-phase the cavities frequently. It will only be necessary if there are changes in the RF reference line and/or the LLRF like the one conducted during the refurbishment REX.

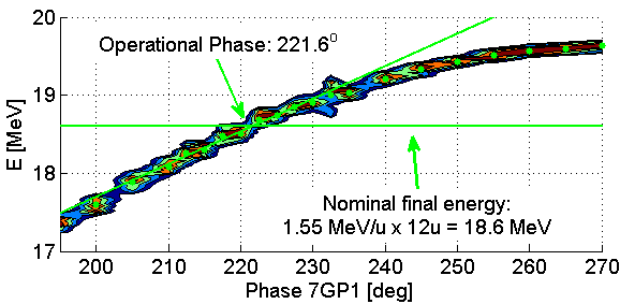

Figure 13: Phasing of the first 7gap RF structure using a silicon detector.

The Si detectors will also be used to phase the superconducting cavities. In this case, the relative phases of the cavities will often change during operations to allow higher final energies per nucleon for beams with lower A/Q.

CONCLUSION

Plenty of challenging physics is waiting for the startup of HIE-ISOLDE in Fall 2015. The physics cases approved expand over the wide range of post-accelerated beams available at ISOLDE with more than six hundred shifts approved for day one physics.

Considerable progress has been achieved:

- The HEBT hardware commissioning was completed;
- The cryomodule was installed, cooled-down and powered. A full test performance campaign was carried out;
- Beam commissioning of the NC Linac – REX is well advanced.

Beam commissioning of SC Linac is scheduled to start in September 2015.

ACKNOWLEDGMENT

We would like to express our warmest thanks to all the technical staff at CERN who is daily engaged in making the work progress and the CERN management for their support.

We acknowledge funding from the Belgian Big Science program of the FWO (Research Foundation Flanders) and the Research Council K.U. Leuven.

We acknowledge as well the receipt of fellowships from the CATHI Marie Curie Initial Training Network: EU-FP7-PEOPLE-2010-ITN Project number 264330.

REFERENCES

[1] A. Herlert, *The ISOLDE Facility*, Nuclear Physics News, Vol. 20/ No.4, 2010.

[2] M. Pasini et al., "A SC upgrade for the REX-ISOLDE accelerator at CERN", Proceedings of LINAC08, Victoria, BC, Canada (2008).

[3] R. Catherall et al., "An Overview of the HIE-ISOLDE Design Study", Nuclear Instruments and Methods in Physics Research B 317 (2013) 204-207.

[4] M. A. Fraser, "Beam Dynamics Studies of the ISOLDE Post Accelerator for High Intensity and Energy Upgrade", PhD thesis, ISBN 978-83-7814-008-5, Manchester University 2012.

[5] N. Delruelle et al., "Commissioning of the helium cryogenic system for the HIE-ISOLDE accelerator upgrade at CERN", Proceedings of CEC-ICMC15, Tucson, Arizona, USA (2015).

[6] Jose A. Ferreira, "Pumpdown and Venting of HIE-ISOLDE CryoModule", https://edms.cern.ch/document/1485142/1

[7] L. Valdarno et al., "Thermal Design and Performance results of the first High-Beta Cryo-module for HIE-ISOLDE at CERN", Proceedings of CEC-ICMC15, Tucson, Arizona, USA (2015).

[8] G. Kautzmann et al., "General presentation of MATHILDE", Proceedings of the 13th International Workshop on Accelerator Alignment, Shanghai, China (October 2014).

[9] W. Venturini et al., "Status of the SRF systems at HIE-ISOLDE", Proceedings of SRF-2015, Whistler, British Columbia, Canada (2015).

[10] REXEBIS. The Electron Beam Ion Source for the REX-ISOLDE Project. Design and Simulations. F. Wenander et al, CERN 1999

[11] The Status of Beam Diagnostics for the HIE-ISOLDE Linac at CERN, E.D. Cantero et al., IBIC2014.

ISBN 978-3-95450-131-1

FRIB ACCELERATOR: DESIGN AND CONSTRUCTION STATUS*

J. Wei#[1], H. Ao[1], N. Bultman[1], F. Casagrande[1], C. Compton[1], L. Dalesio[1], K. Davidson[1], K. Dixon[2], B. Durickovic[1], A. Facco[1,4], F. Feyzi[1], V. Ganni[2], A. Ganshyn[1], P. Gibson[1], T. Glasmacher[1], W. Hartung[1], L. Hodges[1], L. Hoff[1], K. Holland[1], H.-C. Hseuh[1,6], A. Hussain[1], M. Ikegami[1], S. Jones[1], M. Kelly[3], K. Kranz[1], R.E. Laxdal[1,5], S. Lidia[1], S. Lund[1], G. Machicoane[1], F. Marti[1], S. Miller[1], D. Morris[1], J. Nolen[1,3], P. Ostroumov[3], S. Peng[1], J. Popielarski[1], L. Popielarski[1], E. Pozdeyev[1], T. Russo[1], K. Saito[1], G. Shen[1], S. Stanley[1], M. Wiseman[2], T. Xu[1], Y. Yamazaki[1]

[1] Facility for Rare Isotope Beams, Michigan State University, East Lansing, MI 48824 USA
[2] Thomas Jefferson National Laboratory, Newport News, VA 23606 USA
[3] Physics Division, Argonne National Laboratory, Argonne, IL 60439 USA
[4] INFN - Laboratori Nazionali di Legnaro, Legnaro (Padova), Italy
[5] TRIUMF, Vancouver, Canada
[6] Brookhaven National Laboratory, Upton, NY 11973 USA

Abstract

With an average beam power approximately two to three orders of magnitude higher than operating heavy-ion facilities, the Facility for Rare Isotope Beams (FRIB) stands at the power frontier of the accelerator family. This report summarizes the current design and construction status.

INTRODUCTION

In August 2014, the Department of Energy's Office of Science approved Critical Decision-3b (CD-3b), Approve Start of Technical Construction, one year after approving CD-2 (Approve Performance Baseline) and CD-3a (Approve Start of Civil Construction and Long Lead Procurements) for the FRIB construction project (Fig. 1). The total project cost for FRIB is $730M, of which $635.5M is provided by DOE and $94.5M is provided by Michigan State University (MSU). The project will be completed by 2022. "When completed, FRIB will provide access to completely uncharted territory at the limits of nuclear stability, revolutionizing our understanding of the structure of nuclei as well as the origin of the elements and related astrophysical processes" [1].

FRIB will be a new national user facility for nuclear science. Under construction on campus and operated by MSU, FRIB will provide intense beams of rare isotopes (that is, short-lived nuclei not normally found on Earth). FRIB will enable scientists to make discoveries about the properties of these rare isotopes in order to better understand the physics of nuclei, nuclear astrophysics, fundamental interactions, and applications for society.

In creating this new one-of-a-kind facility, FRIB builds upon the expertise and achievements of the National Superconducting Cyclotron Laboratory (NSCL), a National Science Foundation (NSF) user facility at MSU. Since 2001, NSCL's coupled cyclotron facility, one of the world's most powerful rare isotope user facilities, has been conducting experiments on rare isotopes. Since 2014, the re-accelerator (ReA3), consisting of a radio-frequency quadrupole (RFQ) and a superconducting radio-frequency (SRF) linac, was constructed and commissioned to accelerate beams of rare isotopes. The FRIB project scope consists of a high-power driver accelerator, a high-power target, and fragment separators.

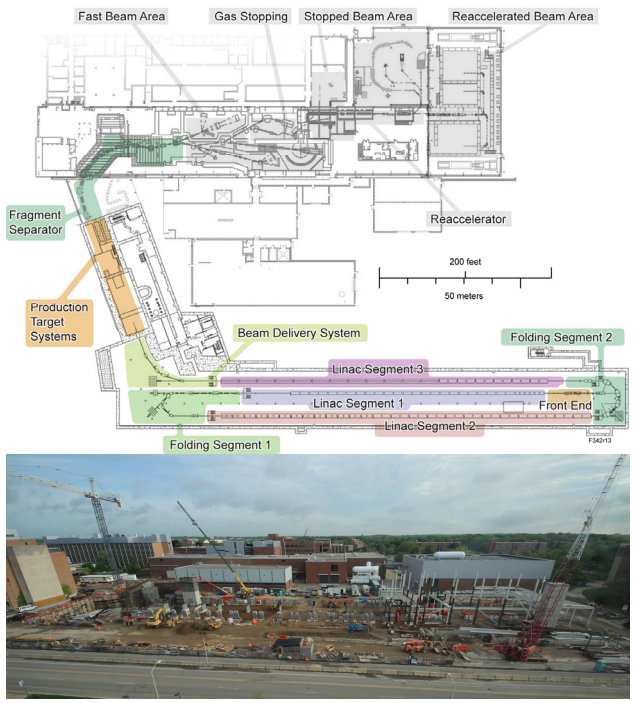

Figure 1: Layout of the FRIB driver accelerator, target and fragment separator (colored areas) and existing infrastructure (top); photograph showing FRIB civil construction (bottom).

The FRIB driver accelerator is designed to accelerate all stable ions to energies >200 MeV/u with beam power on the target up to 400 kW (Table 1). The driver accelerator consists of electron-cyclotron-resonance (ECR) ion sources; a low energy beam transport containing a pre-buncher and electrostatic deflectors for

*Work supported by the U.S. Department of Energy Office of Science under Cooperative Agreement DE-SC0000661 and the National Science Foundation under Cooperative Agreement PHY-1102511.
#wei@frib.msu.edu

ISBN 978-3-95450-131-1

machine protection; a radiofrequency quadrupole (RFQ) linac; Linac segment 1 with quarter-wave-resonators (QWR) of β_0=0.041 and 0.085, to accelerate the beam to 20 MeV/u, where the beam is stripped to higher charge states; Linac segments 2 and 3 with half-wave-resonators (HWR) of β_0=0.29 and 0.53, to accelerate the beam to >200 MeV/u; folding segments to confine the footprint and facilitate beam collimation; and a beam delivery system to transport to the target [2].

FRIB accelerator systems design and construction have been facilitated under work-for-others agreements with many DOE-SC national laboratories including ANL, BNL, FNAL, JLab, LANL, LBNL, ORNL, and SLAC, and in collaboration with institutes worldwide including BINP, KEK, IHEP, IMP, INFN, INR, RIKEN, TRIUMF, and Tsinghua University. The cryogenics system is developed in collaboration with the JLab cryogenics team. The recent experience gained from the JLab 12 GeV cryogenic system design is utilized for both the refrigerator cold box and the compression system designs. The liquid lithium charge stripping system is developed in collaboration with ANL. BNL collaborated on the development of the alternative helium gas stripper. The SRF development benefited greatly from the expertise of the low-β SRF community. FRIB is collaborating with ANL on RF coupler and tuner developments, assisted by JLAB for cryomodule design, and by FNAL and JLab on cavity treatments. FRIB is collaborating with LBNL on the development of VENUS type ECR ion source.

Table 1: FRIB Driver Accelerator Primary Parameters

Parameter	Value
Primary beam ion species	H to ^{238}U
Beam kinetic energy on target	> 200 MeV/u
Maximum beam power on target	400 kW
Macropulse duty factor	100%
Beam current on target (^{238}U)	0.7 emA
Beam radius on target (90%)	0.5 mm
Driver linac beam path length	517 m
Average uncontrolled beam loss	< 1 W/m

MAJOR TECHNOLOGY DEVELOPMENT

Major accelerator R&D and subsystem prototyping are completed. These systems include integrated cryogenics, "bottom-up" cryomodule, SRF technologies for low-β acceleration, charge stripping and machine protection for high-power, low-energy heavy ion beams.

Integrated Cryogenics

An integrated design of the cryogenic refrigeration, distribution, and cryomodule systems is key to efficient SRF operations [3, 4]. The FRIB refrigeration system adopts the floating pressure process Ganni Cycle [5] for efficient adaptation to the actual loads. Distribution lines are segmented and cryomodules are connected with U-tubes to facilitate staged commissioning and maintenance (Fig. 2). The 4-2 K heat exchangers are housed inside the cryomodules for enhanced efficiency. Figure 2 shows the FRIB prototype β_0=0.085 cryomodule developed at MSU and the prototype cryogenic distribution developed by JLab.

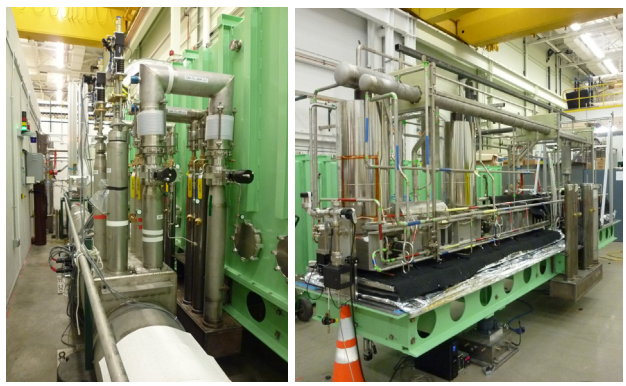

Figure 2: Left: test bunker with cryogenic distribution via U-tube connections. Right: prototype β_0=0.085 cryomodule housing 2 cavities and a solenoid.

Bottom-up Cryomodule Design

Low-β cryomodules built for MSU's 3 MeV/u Reaccelerator (ReA3) [6] use traditional "top-down" design, with the cavities and solenoids hanging from a "strong-back". To facilitate assembly efficiency, simplify alignment, and allow U-tube cryogenic connections for maintainability, FRIB adopted an innovative "bottom-up" cryomodule design (Fig. 3) with the resonators and solenoids supported from the bottom [7]. The cryogenic headers are suspended from the top for vibration isolation. In May 2015, the β_0=0.085 prototype cryomodule was cold tested (Fig. 2). It exceeded all FRIB design specifications, including mechanical stability, alignment accuracy, 2 K and 4 K cryogenic stability, RF bandwidth, phase and amplitude control (24-hour RF lock at full power), static and dynamic heat loads at full accelerating gradient, solenoid operation at full field, and susceptibility to ground noise and vibration. The local magnetic shielding design was validated, with remnant field controlled below 1.5 μT.

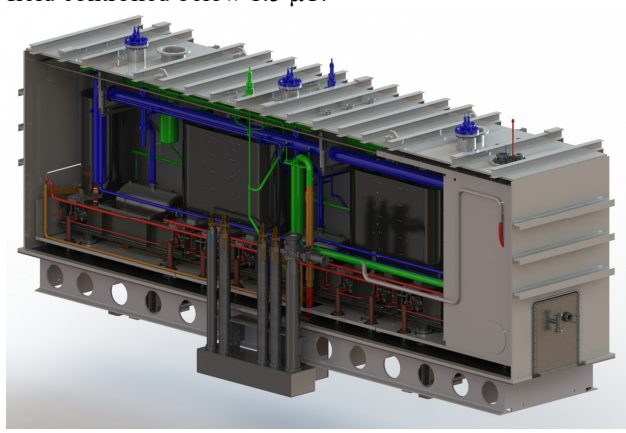

Figure 3: "Bottom-up" β_0=0.085 cryomodule design containing 8 cavities and 3 solenoids.

ISBN 978-3-95450-131-1

Low-β Superconducting RF Acceleration

The FRIB driver linac uses 330 low-β cavities. The cavity design is optimized for both optimum performance and low production cost. This requirement guided the choice of the cavity geometries, material, and mechanical solutions, avoiding complicated shapes, minimizing the amount of electron beam welds, eliminating bellows, and optimizing construction and surface treatment procedures. FRIB cavities operate in superfluid helium at 2 K. The increase in cavity Q_0 at the operating field more than compensates for the lower efficiency of the 2 K cryogenic system. This innovative choice for a low-β linac allows operation of the cavities in stable pressure conditions with a high safety margin on the maximum surface fields [8].

Designs are validated by vertical Dewar tests of individual cavities; by integrated tests of the cavity, power coupler, tuner, and ancillary systems (Fig. 4); and by assembled cryomodule testing in the bunker.

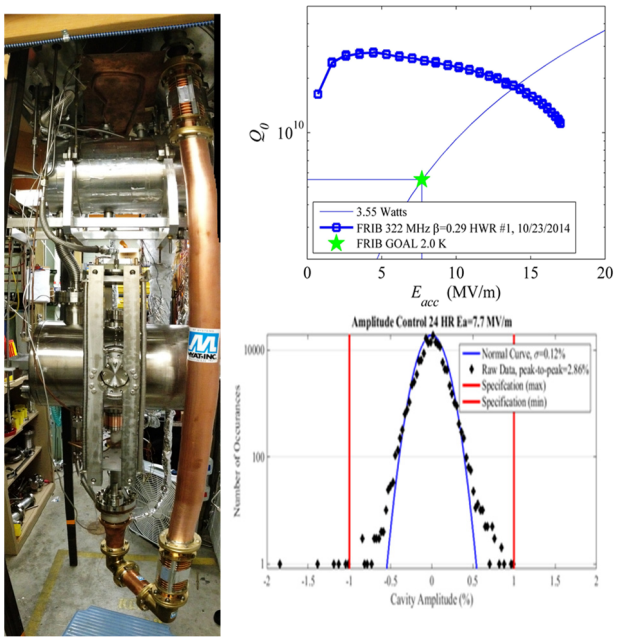

Figure 4: Preparation for 24-hour integrated test of β_0=0.29 cavity (left); Q_0 vs. E_{acc} performance measured at 2 K (top right); and measured RF amplitude control performance at 2 K (bottom right).

Liquid Lithium Charge Stripping

Intense heavy ions at low energies may cause severe damage to stripping material. FRIB uses a liquid lithium film moving at ~50 m/s speed. Tests with a proton beam produced by the LEDA source (Fig. 5) demonstrated that power depositions similar to the FRIB uranium beams could be achieved without destroying the film [9].

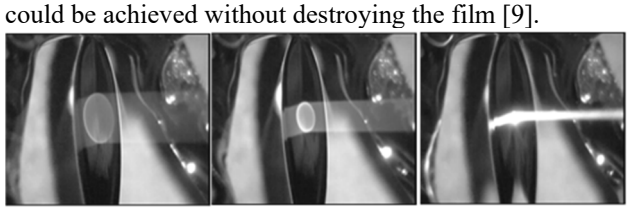

Figure 5: Liquid lithium film intercepting a proton beam of ~ 60 kV for a beam power survival test.

Multi-layered Machine Protection

Machine protection is challenging for intense low-energy heavy ion beams due to the low detection sensitivity and high power concentration/short range. Furthermore, due to the folded geometry of the driver linac, beam loss at high energy interferes with loss detection of low-energy beams [10]. Innovative techniques include the halo monitor ring [11] for high-sensitivity loss detection and current monitoring modules for critical magnet power supply inhibition. FRIB adopts multi-time scale, multi-layer approaches: the fast protection system (FPS) prevents damage from acute beam loss by quickly activating the beam inhibit device; the run permit system, RPS (1), continuously queries the machine state and provides permission to operate with beam; the even slower but highly sensitive RPS (2) prevent slow degradation of SRF system under low beam loss (Table 2).

Table 2: Machine Protection for the FRIB Driver Linac

Mode	Time	Detection	Mitigation
FPS	~35 μs	LLRF controller Dipole current monitor Differential BCM Ion chamber monitor Halo monitor ring Fast neutron detector Differential BPM	LEBT bend electro-static deflector
RPS (1)	~100 ms	Vacuum status Cryomodule status Non-dipole PS Quench signal	As above; ECR source HV
RPS (2)	>1 s	Thermo-sensor Cryo. heater power	As above

DESIGN STATUS

Major design reviews are conducted at the preliminary, intermediate, and final design stages. The preliminary design stage corresponds to the project baselining (CD-2) three years after the completion of the conceptual design (CD-1 in 2010). At the intermediate design stage, system requirements, specifications and interfaces are finalized and safety hazards identified and mitigated. At the final design stage, models and/or drawings are produced ready for procurement, the statement of work and acceptance criteria listing are developed, the procurement strategy is defined, and installation and commissioning plans are developed. Design maturity of each major subsystem is assessed according to the follow six questions:

- Are requirements and interfaces defined?
- Is appropriate prototyping completed?
- Do prototypes meet specifications?
- Is the detailed design completed?
- Has the design been reviewed?
- Does a procurement/fabrication plan exist?

Presently, all major technological developments and subcomponent prototyping have been successfully

ISBN 978-3-95450-131-1

completed, including cryogenic refrigeration and distribution [3], cryomodule and SRF subcomponents [6-8], RF [12], power supply [13], controls [14, 15], diagnostics [16], charge stripping [9], ion source [17], RFQ [18], and personnel and machine protection [10]. According to the measures defined by the FRIB Final Design Plan, the overall accelerator systems design is currently about 80% complete [19].

PRODUCTION INFRASTRUCTURE

To support the acceptance, processing, assembly and tests of production SRF subcomponents and cryomodules, a building is newly constructed with an area of 2500 m^2 as shown in Fig. 6. This "SRF Highbay" houses areas for material/subcomponent inspection, cavity coordinate measurement and alignment assessment, degassing furnace, parts cleaning and high pressure rinsing, chemical processing, power coupler conditioning, vertical test Dewars, cold mass assembly and tests, and cryomodule test bunkers. A 900 W cryoplant is dedicated to this building to supply liquid helium at 2 K. Once fully commissioned, this facility is expected to support the production throughput of testing five cavities per week and one cryomodule per month [20].

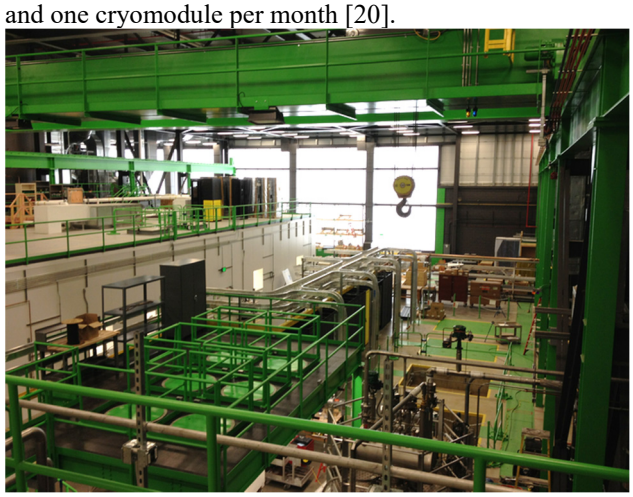

Figure 6: Newly constructed SRF Highbay at MSU.

CONSTRUCTION STATUS

FRIB construction officially started in 2013 upon the approval of CD-2 and CD-3a. Major accelerator long-lead procurements prepared prior to this date include the 4.5 K cryogenic refrigeration "cold box", the cryogenic distribution, the niobium material for SRF cavities, pre-production of the SRF cavities, the RFQ (Fig. 7), and the Electron Cyclotron Resonance ion source (ECR).

Full-scale technical construction started in 2014 upon the CD-3b approval. While critical processing and assembly are planned to be performed in house, fabrication of large quantities of components are planned through mass production by industrial providers. Approximately 35% of the accelerator scope is for in-house labor and 65% is for material, work-for-others efforts at partner laboratories, and procurements from industries.

Presently, about 65% of baselined major procurement funds have been either spent or committed. Both domestic and foreign industrial providers are engaged based on best-value practices. Intense vendor follow-up is in place to ensure timely execution of contracts.

Figure 7: First segment of the RFQ at the vendor site.

OUTLOOK

Figure 8 shows the high-level FRIB Integrated Master Schedule. The present critical path consists of linac tunnel construction, cryogenic area construction, cryogenic plant and distribution fabrication and assembly, cryomodule test and installation, and linac commissioning. Accelerator installation has started in parallel with the conventional facility construction.

Upon fabrication, installation, and integrated tests, early beam commissioning is expected to occur from 2017 to 2020, starting with the Front End. The facility is expected to meet key performance parameters and support routine user operations before June 2022 (CD-4). We plan to reach the full design capability within 4 years after beginning routine operations. Science driven upgrade options may be pursued at any stage.

ACKNOWLEDGMENTS

We thank the FRIB Accelerator Systems Advisory Committee chaired by S. Ozaki for their valuable guidance, colleagues who participated in FRIB accelerator peer reviews including A. Aleksandrov, G. Ambrosio, D. Arenius, W. Barletta, G. Bauer, G. Biallas, J. Bisognano, S. Bousson, S. Caspi, M. Champion, M. Crofford, D. Curry, R. Cutler, G. Decker, J. Delayen, J. Delong, N. Eddy, H. Edwards, J. Error, J. Fuerst, K. Kurukawa, J. Galambos, J. Galayda, G. Gassner, J. Gilpatrick, C. Ginsburg, S. Gourlay, M. Harrison, S. Hartman, S. Henderson, G. Hoffstaetter, J. Hogan, S. Holmes, M. Howell, R. Kersevan, N. Holtkamp, H. Horiike, C. Hovater, H. Imao, R. Janssens, R. Keller, J. Kelley, P. Kelley, J. Kerby, A. Klebaner, J. Knobloch, R. Lambiase, M. Lamm, Y. Li, C. LoCocq, C. Luongo, K. Mahoney, J. Mammosser, T. Mann, W. Meng, N. Mokhov, Y. Momozaki, G. Murdoch, W. Norum, H. Okuno, R. Pardo, S. Peggs, R. Petkus, T. Peterson, C. Piller, J. Power, T. Powers,

ISBN 978-3-95450-131-1

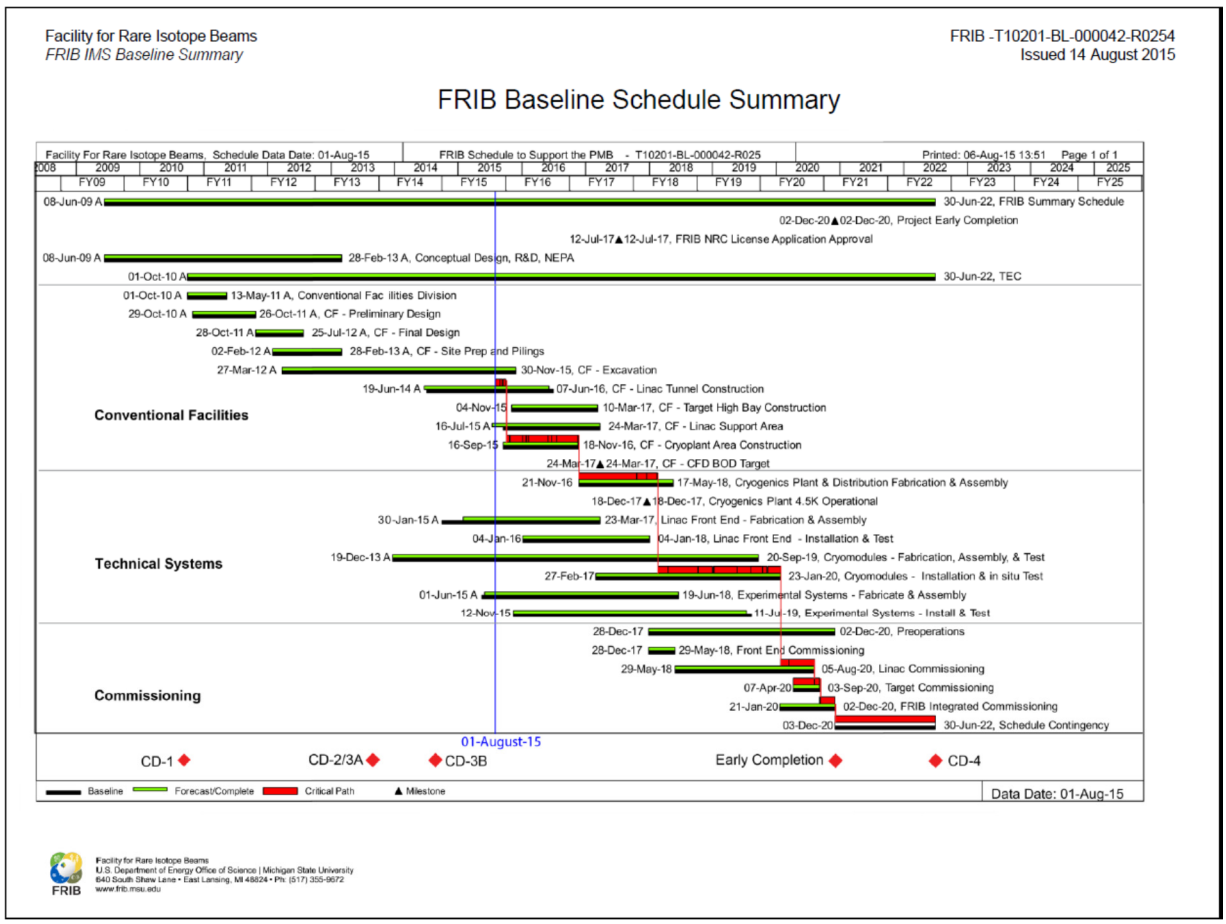

Figure 8: A snapshot of the FRIB Project Integrated Master Schedule showing the current critical path.

J. Preble, J. Price, D. Raparia, A. Ratti, T. Roser, M. Ross, R. Ruland, J. Sandberg, R. Schmidt, W.J. Schneider, D. Schrage, I. Silverman, K. Smith, J. Sondericker, W. Soyars, C. Spencer, R. Stanek, M. Stettler, W.C. Stone, J. Stovall, Y. Than, J. Theilacker, J. Tuozzolo, V. Verzilov, R. Vondrasek, P. Wanderer, P. Wright, H. Xu, L. Young, and A. Zaltsman, and colleagues who advised and collaborated with the FRIB team including A. Burrill, A.C. Crawford, K. Davis, X. Guan, P. He, Y. He, K. Hosoyama, A. Hutton, S.H. Kim, P. Kneisel, K. Macha, G. Maler, E.A. McEwen, S. Prestemon, J. Qiang, T. Reilly, R. Talman, J. Vincent, X.W. Wang, J. Xia, Q.Z. Xing. The FRIB accelerator design is executed by a dedicated team of the FRIB Accelerator Systems Division with close collaboration with the Experimental Systems Division headed by G. Bollen, the Conventional Facility Division headed by B. Bull, the Chief Engineer's team headed by D. Stout, and supported by the project controls, procurements, ES&H of the FRIB Project, by NSCL, and by MSU.

REFERENCES

[1] DOE statement Aug. 2013, http://www.frib.msu.edu/content/doe-office-science-approves-cd-2-and-cd-3a
[2] J. Wei et al, HIAT'12, Chicago, 8 (2012).
[3] F. Casagrande, IPAC'15, Richmond, THYB1 (2015).
[4] J. Wei, IPAC'14, Dresden, 17 (2014).
[5] V. Ganni et al, CEC-ICMC 59, 323 (2013).
[6] T. Xu et al, LINAC'14, Geneva, 155 (2014).
[7] S. Miller et al, SRF'15, Whistler, FRAA06 (2015).
[8] A. Facco et al, IPAC'12, New Orleans, 61 (2012).
[9] J. Nolen et al, FRIB Report FRIB-T30705-TD-000450 (2013).
[10] M. Ikegami, IPAC'15, Richmond, 2418 (2015).
[11] Z. Liu et al, Nucl. Instrum. Meth. A767, 262 (2014).
[12] S. Zhao et al, LLRF'13, Tahoe (2013).
[13] K. Holland, 3rd POCPA, Hamburg (2012).
[14] G. Shen et al, ICALEPCS'15, Melbourne, WEPGF113 (2015); M. Ikegami et al, IPAC'15, Richmond, 1201 (2015).
[15] K. Davidson, FRIB Report FRIB-M40103-TD-000500 (2014).
[16] S. Lidia, HB'14, East Lansing, 267 (2014).
[17] G. Machicoane, ICIS'15, New York, WEDM02 (2015).
[18] E. Pozdeyev et al, NA-PAC'13, 734 (2013); N. Bultman et al, IPAC'13, Shanghai, 2866 (2013).
[19] D. Stout, FRIB Report FRIB-T10500-BL-000040 (2012).
[20] L. Popielarski et al, LINAC'14, Geneva, 954 (2014).

ISBN 978-3-95450-131-1

REVIEW OF HEAVY-ION CYCLOTRONS

N. Fukunishi#, RIKEN Nishina Center, 2-1 Hirosawa, Wako, Saitama, Japan

Abstract

The basic features of heavy-ion cyclotrons are briefly summarized and various activities concerning heavy-ion cyclotron facilities worldwide are reviewed with an emphasis on important achievements and recent upgrades.

INTRODUCTION

Livingston reported that the 37-inch Berkeley cyclotron first accelerated a carbon beam up to 50 MeV in 1940 [1]. Seventy-five years have passed, and dramatic augmentations of beam energy, intensity, and ion species have been obtained for heavy-ion cyclotrons. Bending indices (K_B) for heavy-ion cyclotrons commissioned after 1980 and those commissioned before 1980 but currently working are plotted in Fig. 1 by year of commissioning. The bending limit of cyclotron energy is given by $E/A = K_B \times (q/A)^2$, where E, q, and A are the total kinetic energy, charge state, and mass number, respectively. These data are based on the "List of Cyclotrons" compiled in 2005 [2] and include newly commissioned cyclotrons and recent developments reported at subsequent international cyclotron conferences.

Many heavy-ion cyclotrons were commissioned from 1980 to 2000. Two major trends are innovation in compact superconducting (SC) cyclotrons and the introduction of separate-sector (SS) cyclotrons for heavy ions. Conventional Thomas-type cyclotrons have also been continuously commissioned. Most of the cyclotrons shown in Fig. 1 have undergone upgrades since their commissioning. In this review, these heavy-ion cyclotrons are classified into three groups according to their type. Their basic features are briefly summarized and important achievements so far and recent (up to 2013 or 2014) upgrades are described. Note that some important activities such as those related to heavy-ion cyclotrons dedicated to medical uses, innovative design studies, and novel applications are not included in order to remain within the paper's space limitations and the author's area of expertise.

COMPACT CYCLOTRONS

More than 20 compact cyclotrons are currently in operation, some of which are listed in Table 1. All of them are Thomas-type cyclotrons [3]. The bending indices (K_B) of the compact cyclotrons shown in Fig. 1 range from 10 to 625 MeV, but cyclotrons with K_B of 100–200 MeV are widely used for stand-alone operations. The isochronous magnetic field is formed by a set of magnet poles with an azimuthally varying gap and a set of main and trim coils. Conventional dee electrodes are used for acceleration with typical voltages ranging from 50 to 100 kV. These cyclotrons are now equipped with electron cyclotron resonance (ECR) ion sources and beams are axially injected. Beam extraction is performed by the electrostatic deflector (ESD) or charge-stripping technique.

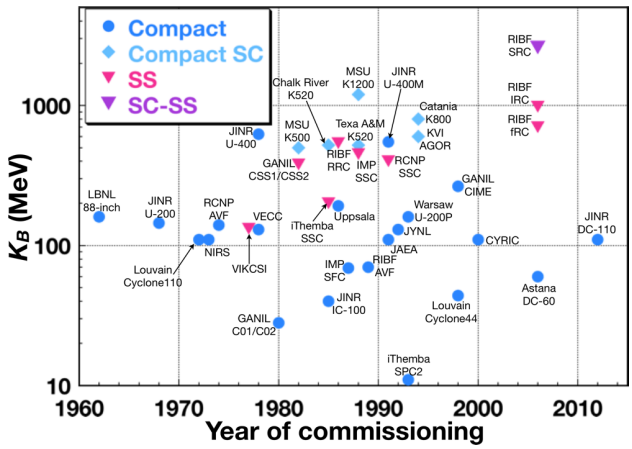

Figure 1: Heavy-ion cyclotrons.

University of Jyväskylä (JYFL)

The main accelerator at JYFL is the K130 cyclotron [4] constructed by Scanditronix. Since its commissioning in 1992, the cyclotron has been used for both nuclear physics and applications. The latter includes testing space electronics and producing medical isotopes and nano-filters. The annual use of K130 has exceeded 6000 h for more than 15 years [5]. To meet increasing demands, a new compact cyclotron (MCC30/15) producing high-intensity 30-MeV H^- and 15-MeV D^- beams was introduced in 2009 [6], and the building facilities were expanded. JYFL has demonstrated that a medium-scale isochronous cyclotron combined with original and sophisticated experimental techniques can make important contributions to nuclear physics studies.

Lawrence Berkeley National Laboratory (LBNL)

The historically famous 88-inch cyclotron at LBNL commissioned in 1962 serves highly charged ions like Xe^{43+} for microchip testing and medium-charge-state high-intensity beams (^{48}Ca) for nuclear physics experiments [7] thanks to its powerful ECR ion sources, AECR-U and VENUS. Super-heavy element research demands higher-intensity ^{48}Ca beams, so the low-energy part of the facility was modified to reduce the space charge effect. Specifically, the extraction voltage of the AECR-U ion source was increased from 14 to 25 kV, which is comparable to that of VENUS. The axial injection line was also modified to manage 25-kV

#fukunisi@ribf.riken.jp

ISBN 978-3-95450-131-1

extraction. A new spiral inflector dedicated to high-intensity medium-heavy ions was also introduced [8]. As a result, a 250-MeV ^{48}Ca beam with a peak intensity of 2 pμA was obtained. The high-intensity ^{48}Ca beam was delivered to an 8-week-long experiment. The average intensity ranged from 1.1 to 1.5 pμA and the consumption rate of ^{48}Ca at the source was 0.27 mg/h on average.

FLNR JINR (Dubna)

FLNR has operated two big cyclotrons (U-400 and U-400M) for nuclear physics and two smaller cyclotrons (U-200 and IC-100) for application uses [9]. These cyclotrons are all of the four-sector type with two or four dee electrodes. The charge-stripping extraction technique is widely used [10]. U-400 was commissioned in 1978 and upgraded in 1996 [11]. The upgrade, aimed at stable operations with low material consumption at the source, replaced the old internal PIG source with an ECR ion source. An axial beam injection system was also introduced. U-400 has contributed greatly to super-heavy-element research [9] and its modernization to U-400R is ongoing [12]. U-400M is used to produce light exotic nuclei. In the Dubna Radioactive Isotope Beams (DRIBs) project, U-400 and U-400M are used as a driver and a post-accelerator. Furthermore, construction of a new cyclotron DC-280 has started to greatly enhance the present beam intensity of 250–270 MeV ^{48}Ca (1.4 pμA) [13]. 10-pμA ^{48}Ca beams are planned at DC-280 [14].

Industrial applications such as production of nuclear track membranes are also being actively pursued at FLNR. IC-100 (DC-40) was modernized in 2004, when an SC-ECRIS and an ESD were introduced [15]. In addition, a new cyclotron DC-110 dedicated to industrial applications was commissioned in 2012. It successfully produced beams exceeding 10 μA for 2.5A-MeV Ar, Kr, and Xe beams [16].

Post-accelerators

Acceleration of radioactive isotope (RI) beams requires a wide-energy-range, large-acceptance, high-mass-resolution machine. Suitably designed cyclotrons fulfill these requirements. A good example is CIME [17] at the GANIL-SPIRAL facility. CIME was designed to accelerate RIs up to adjustable final energies ranging from 1.7A MeV to 25A MeV. Two central-region geometries covered a wide RF harmonic ranging from 2 to 5. The harmonic range was later increased to 6 to obtain lower-energy beams. The acceptance was designed as 80π mm-mrad, a good vacuum (5×10^{-6} Pa) was achieved, and silicon and scintillation detectors were equipped to diagnose faint RI beams. As a result, many gaseous elements have been accelerated by CIME [18]. The mass resolution obtained was at the 10^{-4} level [19].

Cyclone 110 and Cyclone 44 at Université catholique de Louvain were also engaged in post-acceleration. The latter was dedicated to low-energy RI beams for astrophysical interests [20].

Table 1: Specifications of various compact heavy-ion cyclotrons. Compiled data [2] are used, but data noted as (1) and (2) are from individual reports [21] and [22], respectively.

Facility & machine	K_B (MeV)	No. of sectors	Spiral angle (deg.)	Gap hill/valley (cm)	No. of dees	V_{gap} (kV)	Frequency (MHz)	Beam extraction
Jyäskylä K130	130	3	58	17.4 / 33.0	2	50	10–21	ESD / CS
JAEA-Takasaki AVF	110	4	53	16.6 / 40.5	2	60	10.6–22	ESD
CYRIC K110	110	4	53	16.6 / 40.5	2	60	10.6–22	ESD / CS
LBNL 88-inch	160	3	55	19.0 / 30.0	1	50	5.5–16	ESD
Warsaw U-200P	160	4	0	2.6 / 15.0	2	70	12–18(1)	CS
FLNR JINR U-400	625(2)	4	0	4.2 / 30.0	2	100(2)	5.5–12(2)	CS
FLNR JINR U-400M	550(2)	4	43(2)	10.0 / 50.0	4	170(2)	11.5–24(2)	CS
VECC K130	130	3	~55	19.0 / 30.0	1	60	5.5–15.5	ESD
GANIL CIME	265	4	0	12.0 / 30.0	2	100	9.6–14.5	ESD
TSL Gustaf Werner	192	3	55	20.0 / 38.0	2	50	12.3–24.0	ESD

COMPACT SC CYCLOTRONS

Compact SC cyclotrons were pioneered by the Chalk River [23] and MSU [24] groups. The aim was to accelerate all the ion species from proton (or H_2^+) to uranium up to much higher energies than previously obtained with moderate construction costs. Table 2 summarizes the specifications of the compact SC cyclotrons already commissioned. Important features of these cyclotrons have been reviewed in detail by several experts, especially by Blosser et al. [25]. Some basic features are recalled here.

These compact SC cyclotrons adopt room-temperature (RT) magnet poles, liquid-helium-cooled SC main coils and RT trim coils or trim rods (Chalk River) for isochronous magnetic fields, conventional dee electrodes for acceleration, and ESDs for beam extraction. A set of iron poles produces azimuthally varying magnetic fields essential for vertical focusing of the ion's betatron motion. Iron poles are fully saturated on the whole operating diagram. An SC main coil is divided vertically into two individually excitable coils, namely, the inner (near the median plane) and outer coils. The inner and outer coils both produce azimuthally symmetric fields but their radial

ISBN 978-3-95450-131-1

profiles differ. Excitation currents of the inner and outer coils are adjusted so as to obtain coarse isochronism for a wide variety of mass-to-charge ratios and beam energies to realize modest power consumption of the trim coils used for fine isochronism.

Betatron tunes of the ion in the cyclotron vary according to the ion's energy during acceleration. In addition, betatron tunes in the compact SC cyclotron depend strongly on the excitation level of the magnet, because the magnetic-field profile changes according to excitation currents in the SC main coils, which produce azimuthally symmetric magnetic fields, but with the flutter magnetic field of the iron poles unchanged. This behavior of tunes, together with tight resonance conditions especially imposed on three-sector machines, requires a delicate magnet design. For example, $\nu_r = 2\nu_z$ and $\nu_z = 1$ resonances are usually crossed in these cyclotrons. In addition, $\nu_r = 1$ resonance is also crossed just before beam extraction, by which a radial betatron oscillation is induced and the turn separation is widened for efficient beam extraction (precessional extraction). Another difficulty in beam extraction is variation of orbit geometry caused by variation of the magnetic-field profile.

Pioneering researchers finally solved these difficulties, providing many valuable lessons. These compact SC cyclotrons demonstrated their capabilities covering a wide working region [26–29]. MSU K1200 fully covered its operating diagram in its stand-alone operation mode [26]. KVI-AGOR accelerated not only heavy ions with energies ranging from 10*A* to 85*A* MeV, but also 190-MeV protons [27]. The maximum energy obtained by LNS-SC (K800) of INFN-LNS was limited due to insufficient deflector performance in 2001 [28], but later increased to 80*A* MeV [30].

Table 2: Basic parameters of compact superconducting cyclotrons. Compiled data in [2] are used except for Chalk River K520 [31] and VECC K500 [32].

Facility & machine	K_B (MeV)	K_F (MeV)	R_{ext} (m)	Gap hill/valley (cm)	No. of sectors and dees	B_0 (T)	Frequency (MHz)	Stored energy (MJ)
Chalk River K520	520	100	0.65	3.7 / 65.0	4	2.4–5.0	31–62	22
INFN-LNS LNS-SC	800	200	0.87	8.6 / 91.6	3	2.2–4.8	15–48	45
KVI AGOR	600	220	0.9	7.0 / 168	3	1.7–4.1	24–62	56
NSCL-MSU K500	500	160	0.66	6.35 / 91.4	3	3.0–5.0	11–27	18
NSCL-MSU K1200	1200	400	1.0	7.6 / 91.4	3	3.0–5.3	9–27	60
Texas A&M K500	520	160	0.67	6.35 / 91.4	3	3.1–4.9	9–28	16.9
VECC K500	520	160	0.67	6.35 / 91.4	3	3.1–4.9	9–27	22

High-intensity Operations

To meet increasing demands for rare isotope beams, these compact SC cyclotrons have upgraded their beam intensities. At INFN-LNS, construction of an ISOL-type facility started in 1995 (the EXCYT program). Its original acceleration scheme used the 15-MV Tandem as an injector and the K800 cyclotron as an energy booster. In the EXCYT program the K800, equipped with ECRISs and an axial injection system, serves as a driver and the 15-MV Tandem as a post-accelerator. For light ions, 1-pμA primary beams were envisaged [33]. A further intensity upgrade, aiming at 20-kW light ion beams using charge-stripping extraction, was also proposed at INFN-LNS [28]. NSCL at MSU proposed the Coupled Cyclotron Facility (CCF) using its two existing compact SC cyclotrons K500 and K1200 in order to realize a thousand-fold increase in the yield of rare isotope beams produced by its fragment separator. In the CCF, high-intensity beams extracted from ECRISs are axially injected into K500 and the extracted beams from K500 are injected radially into K1200 via charge stripping [34]. In 2003, KVI started its TRIμP program, in which violation of time-reversal symmetry was tested by RI beams. One-kilowatt beams were required for Ne and Pb [35].

To fulfill these requirements, high-performance ECR ion sources were introduced, new axial injection lines and central regions were constructed at INFN-LNS [36] and NSCL [37], the extraction systems were improved, beam loss was carefully controlled [35], and other measures were taken. As a result of these upgrades, the CCF now delivers high-energy (approx. 150*A* MeV) heavy-ion beams with beam powers exceeding 1 kW [38]. Almost 900 RI beams have been used in experiments there [39]. AGOR also achieved 1-kW light ion beams [40].

Texas A&M started a RI beam program based on the ion guide technique. Its old 88-inch cyclotron was re-commissioned as a driver cyclotron and K500 will be used as a post-accelerator [41]. VECC obtained its first internal beam at K500 in 2009 [42].

Separate-orbit Cyclotron Prototype (Tritron)

Trinks proposed an SC version of the separate-orbit cyclotron (SOC) [43]. The SC-SOC consists mainly of SC magnetic channels and SC acceleration cavities. The former define a spiral-shaped orbit along which ions are accelerated. The latter produce sufficient turn separations required by the geometry of SC magnetic channels. SC magnetic channels covering the same azimuthal region form a sector, in which channels are radially separated from each other and enclosed by a set of steel frames.

ISBN 978-3-95450-131-1

Each SC channel produces a magnetic flux inside its small aperture, and the magnetic flux is immediately returned in the adjacent part of the steel frames. Voluminous return yoke is not necessary. Each SC channel has essentially no effect on neighboring turns and transverse and longitudinal focusing properties can be designed more freely than in conventional cyclotrons. AG focusing in the transverse directions and phase stability in the longitudinal direction are available. Trinks and collaborators constructed a prototype SC-SOC Tritron [44] and demonstrated the validity of the concept by accelerating $^{32}S^{14+}$ ions up to 72 MeV [45].

SEPARATE-SECTOR CYCLOTRONS

The separate-sector (SS) cyclotron, proposed by Willax [46], is also widely used for heavy ions. Table 3 summarizes the heavy-ion SS cyclotrons currently in operation. The introduction of open (magnet-less) valleys between sector magnets produces high-flutter isochronous magnetic fields and sufficient spaces for high-acceleration-voltage cavities to be installed. High-flutter magnetic fields induce sufficient vertical focusing for 100A-MeV ions, so the SS cyclotrons in Table 3 are all of the radial sector type except for RCNP Ring Cyclotron, which is designed to accelerate proton beams up to 400 MeV. The high-voltage acceleration cavities produce a larger turn separation at beam extraction than compact cyclotrons do, which is beneficial for safe extraction of high-power beams. On the other hand, the SS cyclotron is much larger and its construction cost is much higher in comparison with a compact SC cyclotron with comparable bending power.

Table 3: Specification of heavy-ion separate-sector cyclotrons. Compiled data in [2] are used except for the acceleration voltages of HIRFL [47] and GANIL [19]. RIBF fRC, IRC, and SRC use single gap cavities.

Facility & machine	K_B (MeV)	No. of sectors	Spiral angle (deg.)	Hill gap (cm)	No. of dees	V_{gap} (kV)	Frequency (MHz)	Injector
HIRFL SSC	450	4	0	10.0	2	200	6.5–14	SFC
GANIL CSS1	380	4	0	10.0	2	160	7–13.45	C01 / C02
GANIL CSS2	380	4	0	10.0	2	250	7–13.45	CSS1
RCNP Ring	400	6	30	6.0	3	375	30–52	RCNP-AVF
HZB K130	132	4	0	6.0	2	140	10–20	Tandetron
iThemba LABS SSC	200	4	0	6.6	2	230	6–26	SPC1 / SPC2
RIBF RRC	540	4	0	8.0	2	270	18–40	AVF/RILAC/RILAC2
RIBF fRC	700	4	0	5.0	2	450	54.75	RRC
RIBF IRC	980	4	0	8.0	2	700	18–38	RRC / fRC
RIBF SRC	2600	6	0	70.0	4	650	18–38	IRC

GANIL

GANIL has operated a high-power cyclotron complex since 1982 [48]. Either of the two compact injectors C01 and C02 (K_B = 28 MeV) serves as an injector of the second-stage cyclotron CSS1. Extracted beams from CSS1 are charge-stripped before being injected into the final-stage cyclotron CSS2. In this scheme, light ions are accelerated up to 95A MeV. 10^{12}-pps light ion beams were obtained just after commissioning and a series of upgrade programs (OAE [49], OAI [50], THI [51]) was conducted to obtain higher energies for heavy ions, higher intensities, and so on. The ECR ion source serving beams to C01 is installed on a high-voltage platform. Its maximum extraction voltage is 100 kV in total. The axial injection line to C01 and its central region are designed to accept large emittance (60π mm-mrad) beams and to fulfill 6D phase-space matching [52, 53]. Turn separations at C01 and C02 are sufficiently large. Relatively low-charge-stage ions are accelerated up to CSS1 and the ions are charge stripped only once before CSS2 at higher energies. All these contribute to the high-intensity beams obtained by GANIL. The beam power obtained is 5 kW [54].

HIRFL IMP (Lanzhou), RCNP, iThemba LABS

A unique feature of the HIRFL cyclotron complex comprising the SFC (K_B = 69 MeV) and SSC [55] is that these cyclotrons are used as injectors to a cooler-storage ring complex, CSRm and CSRe [56]. Light ions accelerated by SFC can be injected directly into CSRm via charge stripping or multiple multi-turn injection schemes. Heavy ions obtained by SSC coupled with SFC are also injected into CSRm. Nearly 10^{10} ppp ions are injected, accumulated, cooled, and accelerated up to 600A MeV in CSRm. The accelerated ions are fast extracted and then used to produce RI beams at the fragment separator RIBLL2. The RI beams injected into CSRe are used for precise mass measurements of exotic nuclei and so on. A new linac injector to SSC is now under construction to further upgrade the intensity at SSC [57].

The RCNP cyclotron cascade consists of an AVF (K_B = 140 MeV) cyclotron and the Ring cyclotron. It has been providing ultra-high-quality light ion beams. The cascade was upgraded to increase beam currents and ion variety. A flat-top acceleration cavity was introduced into the AVF cyclotron, and a 18-GHz SC ion source was also introduced [58]. RCNP have been developing magnets utilizing high-temperature superconducting wires [59].

ISBN 978-3-95450-131-1

iThemba LABS has proposed constructing a RI beam facility where its SPC2 and K200 cyclotron complex is used as a post-acceleration system [60].

RI Beam Factory (RIBF)

RIBF consists of two injector linacs (RILAC [61] and RILAC2 [62]), an injector AVF cyclotron (K_B = 70 MeV) [63], three conventional SS cyclotrons (RRC [64], fRC [65] and IRC [66]), and the world's first superconducting SS cyclotron SRC [67]. RILAC2, fRC, IRC, and SRC were newly constructed in the RIBF project, which started in 1997. The remaining accelerators have been used for over 25 years. Very light ions can be accelerated up to 400A MeV with a combination of AVF + RRC + SRC. Light and medium-heavy ions are also accelerated to 400A MeV using RILAC, RRC, IRC, and SRC in series (variable energy mode). Very heavy ions such as xenon and uranium are accelerated in a fixed-energy mode where RILAC2, RRC, fRC IRC, and SRC are used in series. The beam energy is fixed to 345A MeV in this mode, because RILAC2 and fRC are fixed-frequency machines. Beam intensities obtained for light ions are 1 pμA, limited by current radiation safety regulations. For medium-heavy ions, 0.53- and 0.49-pμA beams were obtained for 345A-MeV ^{48}Ca and ^{78}Kr, respectively. The beam power of ^{78}Kr reaches 13 kW. Performance of the fixed energy mode has steadily improved. The present intensity of a 345A-MeV ^{238}U beam is 40 pnA. Beam availability, defined as the ratio of actual beam service time to scheduled beam service time, exceeded 90% in these two years.

The present performance of RIBF does not fully utilize the potential of the newly constructed cyclotron cascade, in that these cyclotrons are operated far below their space charge limits, especially for very heavy ions. One reason is that RIBF adopts a two-stage charge-stripping scheme when accelerating beams up to 345A MeV. The total charge-stripping efficiency for uranium ions is only 5.5%. In the case of ^{48}Ca, ions are charge-stripped twice, with the first stripping performed at 2.7A MeV, much lower than NSCL-CCF and GANIL. If we apply the fixed energy mode to medium-heavy ions, we can skip the first-stage charge stripping thanks to the 28-GHz SC ECRIS [68]. We thus successfully obtained a 13-kW ^{78}Kr beam, but its beam quality was worse than that obtained in the variable energy mode. Elaborate tuning of the accelerator complex and a more reliable beam interlock system are essential for the 30-kW operations envisaged for the near future.

SUMMARY AND FUTURE

Worldwide activities concerning heavy-ion cyclotrons now cover energy ranges up to 345A MeV for all ion species, despite construction of new heavy-ion cyclotrons slowing and nonnegligible activities related to accelerating heavy ions being phased out or significantly reduced at several facilities. Examples of the beam intensity obtained so far are 10 pμA for very low-energy beams ($E \leq 1A$ MeV) or very light ions such as lithium, at the level of 1 pμA (0.5–2 pμA) for light and medium-heavy ions with energies up to 345A MeV, and less than 0.1 pμA for high-energy very-heavy ions such as uranium. DC-280 of FLNR JINR plans to extend the 10-pμA region up to 5A–6A MeV for medium-heavy ions, which is a good example of a future high-performance heavy-ion cyclotron dedicated to specific applications.

Many facilities are making efforts at improving the efficiency of injection into cyclotrons and understanding beam behaviors more precisely in low-energy regions. Further intensity upgrades are possible if heavy-ion cyclotrons fully utilize the recent high performance obtained in so-called third-generation ECRISs that can produce beams of hundreds of micro-amperes with intrinsic emittance areas exceeding 150π mm-mrad.

Cyclotrons have long been the energy-frontier accelerator operated in CW mode. Realizing a cyclotron accelerating heavy ions up to 0.7A–1A GeV is a rational challenge, although isochronous cyclotrons of the existing types will seriously suffer from difficulties in both vertical focusing and turn separation at beam extraction under highly relativistic conditions as $E > 1A$ GeV.

Finally, the large-scale SC linac complexes [69, 70] plan to cover in the near future nearly the whole operating region (as defined by ion species and beam energy) of existing heavy-ion cyclotrons with higher beam intensities. However, this does not mean that these SC linacs can cover all the present activities of existing heavy-ion cyclotrons. Good synergetic effects from these SC heavy-ion linacs are expected.

REFERENCES

ICCA means "International Conference on Cyclotrons and their Applications" hereafter.

[1] R.S. Livingston, 5th Int. Cyclotron Conf., Oxford, UK (1969) p. 423.
[2] In proceeding of ICCA 2004, Tokyo, Japan (2004), edited by A. Goto and Y. Yano.
[3] L.H. Thomas, Phys. Rev. **54** (1938) p. 580.
[4] E. Liukkonen, 13th ICCA, Vancouver, BC, Canada (1992) p. 22.
[5] P. Heikkinen, ICCA 2013, Vancouver, BC, Canada (2013) p. 43.
[6] P. Heikkinen, ICCA 2010, Lanzhou, China (2010) p. 295.
[7] D.S. Todd et al., ICCA 2013, Vancouver, BC, Canada (2013) p. 19.
[8] K. Yoshiki Franzen et al., ICCA 2013, Vancouver, BC, Canada (2013) p. 186.
[9] G. Gulbekyan et al., ICCA 2010, Lanzhou, China (2010) p. 33.
[10] G.G. Gulbekyan et al., ICCA 2007, Giardini Naxos, Italy (2007) p. 308.
[11] B. Gikal et al., 15th ICCA, Caen, France (1998) p. 587.
[12] G. Gulbekyan et al., IPAC2011, San Sebastían, Spain (2011) p. 2700.

ISBN 978-3-95450-131-1

[13] B.N. Gikal et al., ICCA 2004, Tokyo, Japan (2004) p. 100.
[14] G.G. Gulbekian et al., RuPAC2014. Obninsk, Russia (2014) p. 333.
[15] B. Gikal et al., ICCA 2007, Giardini Naxos, Italy (2007) p. 27.
[16] B.N. Gikal et al., RuPAC2014. Obninsk, Russia (2014) p. 146.
[17] M. Lieuvin and the SPIRAL group, 14th ICCA, Cape Town, South Africa (1995) p. 651.
[18] F. Chautard et al., ICCA 2007, Giadrini Naxos, Italy (2007) p. 99.
[19] B. Jacquot et al., ICCA 2004, Tokyo, Japan (2004) p. 57.
[20] M. Loiselet et al., 15th ICCA, Caen, France (1998) p. 305.
[21] O. Steczkiewicz et al., RuPAC2014, Obninsk, Russia (2014) p. 453.
[22] B. Gikal et al., RuPAC2008, Zvengorod, Russia (2008) TUCAU02.
[23] C.B. Bigham, J.S. Fraser and H.R. Schneider, Report AECL-4654 (1973).
[24] H. Blosser et al., 7th ICCA, Zürich, Switzerland (1975) p. 584.
[25] H. Blosser et al., 14th ICCA, Cape Town, South Africa (1995) p. 674.
[26] F. Marti et al., ICCA 2001, East Lansing, MI, USA (2001) p. 64.
[27] S. Brandenburg et al., ICCA 2001, East Lansing, MI, USA (2001) p. 99.
[28] L. Calabretta and D. Rifuggiato, ICCA 2001, East Lansing, MI, USA (2001) p. 79.
[29] H.W. Schreuder, PAC95, Dallas, Texas, USA (1995) p. 317.
[30] D. Rifuggiato et al., ICCA 2013, Vancouver, BC, Canada (2013) p. 52.
[31] In proceeding of 13th ICCA, Vancouver, BC, Canada (1992) edited by C. Dutto and M.K. Craddock.
[32] VECC staff, presented by R.K. Bhandari, 15th ICCA, Caen, France (1998) p. 692, R.K. Bhandari for VECC staff, ICCA 2004, Tokyo, Japan (2004) p. 183.
[33] D. Rifuggiato et al., 15th ICCA, Caen, France (1998) p. 599.
[34] R.C. York et al., 15th ICCA, Caen, France (1998) p. 687.
[35] S. Brandenburg et al., ICCA 2007, Giardini Naxos, Italy (2007) p. 493.
[36] D. Rifuggiato et al., 15th ICCA, Caen, France (1998) p. 599.
[37] S.L. Snyder and F. Marti, PAC95, Dallas, Texas, USA (1995) p. 375.
[38] J. Stetson et al., ICCA 2010, Lanzhou, China (2010) p. 27.
[39] A. Stolz et al., ICCA 2013, Vancouver, BC, Canada (2013) p. 7.
[40] M.A. Hofstee et al., ICCA 2010, Lanzhou, China (2010) p. 21.
[41] D.P. May et al., ICCA 2007, Giardini Naxos, Italy (2007) p. 505.
[42] Chaturanan Mallik et al., ICCA 2010, Lanzhou, China (2010) p. 292.
[43] U. Trinks, Nucl. Instr. and Meth. **A244** (1986) 273.
[44] U. Trinks, 14th ICCA, Cape Town, South Africa (1995) p. 20.
[45] A. Cazan, P. Schütz, U. Trinks, EPAC98, Stockholm, Sweden (1998) p. 556.
[46] H.A. Willax, Proc. 3rd Int. Conf. on Sector-Focused Cyclotrons, Geneva (1963) p. 386.
[47] H.W. Zhao et al., ICCA 2004, Tokyo, Japan (2004) p. 121.
[48] J. Fermé et al., 9th ICCA, Caen, France (1981) p. 3.
[49] J. Fermé et al., 11th ICCA, Tokyo, Japan (1986) p. 24.
[50] Ch. Ricaud et al., 13th ICCA, Vancouver, BC, Canada (1992) p. 446.
[51] E. Baron et al., 14th ICCA, Cape Town, South Africa (1995) p. 39.
[52] Ch. Ricaud et al., 12th ICCA, Berlin, Germany (1989) p. 372.
[53] A.R. Beck et al., 12th ICCA, Berlin, Germany (1989) p. 432.
[54] F. Chautard, Bd Henri Becquerel, ICCA 2010, Lanzhou China (2010) p. 16.
[55] Wei Bao-Wen, 12th ICCA, Berlin, Germany (1989) p. 9.
[56] W.L. Zhan et al., ICCA 2001, East Lansing, MI, USA, (2001) p. 175.
[57] X. Yin et al., Proc. IPAC2014, Dresden, Germany (2014) p. 3277.
[58] K. Hatanaka et al., ICCA 2007, Giardini Naxos, Italy (2007) p. 125.
[59] K. Hatanaka et al., ICCA 2013, Vancouver, BC, Canada (2013) p. 242.
[60] J.L. Conradie et al., ICCA 2013, Vancouver, BC, Canada (2013) p. 94.
[61] M. Odera et al., Nucl. Instrum. Methods **A227** (1984) p. 187.
[62] K. Yamada et al., IPAC2012, New Orleans, Louisiana, USA (2012) p. 1071.
[63] A. Goto et al., 12th ICCA, Berlin, Germany (1989) p. 51.
[64] Y. Yano, Proc. 12th ICCA, Berlin, Germany (1989) p. 12.
[65] T. Mitsumoto et al., ICCA 2004, Tokyo, Japan (2004) p. 384.
[66] J. Ohnishi et al., ICCA 2004, Tokyo, Japan (2004) p. 197.
[67] H. Okuno et al., IEEE Trans. Appl. Supercond., **17**, (2007) p. 1063.
[68] T. Nakagawa et al., Rev. Sci. Instrum. **81** (2010) 02A320.
[69] J. Wei et al., PAC2013, Pasadena, CA, USA (2013) p. 1453.
[70] Dong-O Jeon et al., LINAC2014, Geneva, Switzerland, (2014) p. 775.

ISBN 978-3-95450-131-1

HISTORY OF SOLID DISK IMPROVEMENT FOR ROTATING CHARGE STRIPPER

H. Hasebe, H. Okuno, H. Kuboki, H. Imao, N. Fukunishi, M. Kase, and O.Kamigaito
Nishina Center for Accelerator-Based Science, RIKEN
2-1 Hirosawa, Wako, Saitama 351-0198, Japan

Abstract

In 2007, we installed a rotating disk stripper device in the final charge stripper section for acceleration of U beam. At first, we selected a carbon disk stripper. However, the quality of the beam after it passed through the stripper was unusable because of the non-uniform thickness and unexpected low density of the stripper. In 2012, the rotating stripper using a Be-disk successfully realized the stable U beam operation. However, the thermal load of the increasing beam intensity caused deformation of the Be-disk even after a short irradiation period. In 2015, highly oriented graphite sheets of high density were used as the disk stripper, which had the longest lifetime. The graphite sheet exhibited improved stripping and transmission efficiencies.

INTRODUCTION

A charge stripper is an essential device used to strip U beams to produce the high-charge state of U^{86+} at 50 MeV/nucleon before acceleration by a subsequent cyclotron at the RIKEN RI Beam Factory (RIBF). A 17-mg·cm^{-2} thick static-type carbon foil (C-foil) was used as the stripper at the RIBF because of its high melting point. As the intensity of the U beam was expected to increase, a rotating carbon disk (C-disk) stripper device was constructed in 2006[1]. A C-disk of diameter 120 mm was installed and tested in 2007. However, the C-disk could not be used as the stripper because of its non-uniform thickness and unexpected low density. Other C-disks, which were commercially available or originally fabricated, were tested, but none met our requirements. Therefore, until 2011, the only alternative was to use polycrystalline graphite foils fabricated by Arizona Company[2]. These foils were used as the static-type C-foil stripper and needed to be replaced every time their lifetime was over in order to accomplish the U beam time. However, the lifetime of these static C-foils decreased to 9 h as the beam intensity increased. Hence, providing stable U beams was difficult.

BERYLLIUM DISK STRIPPER

In October 2012, other materials were tested as alternatives to C-disks: low-density C [2], Ti [3], and Be [3]. Each disk had a thickness of 19 mg·cm^{-2}. A U^{64+} beam at 50 MeV/nucleon was irradiated on the C/Ti/Be disk at rotating speeds ranging from 300 to 1000 rpm. The charge states at the peak were 82+ and 86+ for the Ti- and Be-disk, respectively. The charge distribution of Be was almost the same as that obtained for the static C-foil. Therefore, Be-disk could be used instead of the C-foil stripper. The charge distribution of the C-disk could not be obtained because of non-uniformity in its thickness.

The Be-disk was used during the beam-time operation from November to December, 2012. We successfully delivered a stable U beam during the long-term operation. Totally 1.18×10^{18} U particles were irradiated on the Be-disk over a period of 37 days[4]. The number of irradiated particles and the disk conditions are summarized in Table 1 along with other disks described below. The first Be-disk is denoted as Disk 1 in Table 1. For Disk 1, the emittance of the beam increased after the stripper exceeded the accepted levels for subsequent cyclotrons because of the non-flatness of the disk. To obtain flatter disks, we fabricated a Be-disk that was subjected to diamond polishing (Disk 2) in March 2013[5]. In addition, the disk thickness was reduced from 0.1 mm (19 mg·cm^{-2}) to 0.085 mm (16 mg·cm^{-2}), which was suited for the injection energy of the subsequent cyclotron. Therefore, transmission efficiencies of the downstream cyclotrons were improved. The Be-disk seemed still usable after irradiation with 9.29×10^{17} U particles during the 30-day beam-time operation[6]. Therefore, the Disk 2 was used again for the U beam-time operation in March 2014. Although the disk was already distorted, it survived for 21 days more. During the beam time of 51 days (including the 30 days in 2013) as mentioned in Table 1, a total of 1.68×10^{18} U particles was irradiated on the disk. Figure 1 shows the photographs of the Be-disks before (left) and after usage (right). As shown in Figure 1 (Disk 2), many cracks were observed along the beam irradiation traces, and the beam transmission efficiency decreased as well, thus, indicating that the lifetime of the disk was over. The Be-disk was replaced with a new disk (Disk 3), which was identical to Disk 2 (0.085-mm-thick, diamond polished), for the remaining beam time. In addition, a total of 8.83×10^{17} U particles was irradiated on the new Be-disk over a period of 17 days. The beam transmission efficiency was improved owing to the diamond polish. However, as the upstream beam intensity increased, the thermal load increased from 90 W to 230 W, resulting in deformation of the disk. In October 2014, we introduced a Be-disk with a special design (Disk 4) to reduce the thermal deformation. Because of this improvement, Disk 4 survived even after the 20-day U beam time with radiation of approximately 9×10^{17} U particles. The main changes were as follows. 1) The outer diameter of the disk was changed from 120 mm to 110 mm; 2) Small cuts

ISBN 978-3-95450-131-1

were made at 12 positions around the circumference of the disk; 3) The disk holder was made of copper (changed from aluminum) with an outer diameter of 65 mm; 4) Twelve holes of 2-mm diameter were made around the holder. Beam availability was improved because the beam fluctuation was suppressed by reducing the deformation. Disk 4 is still usable without any degradation[7].

The lifetime of Be-Disk is approximately 140 times longer than that of the static type C-foil.

Table 1: Summary of the Four Be-disks

	Irradiation current Total beam particle	Days	State
Be Disk 1 Not polish 0.1-mm thick	4 - 5 eμA 1.18×10^{18}	37	Many cracks Still usable Slight beam fluctuation
Be Disk 2 Diamond polish 0.085-mm thick	4 - 12 eμA 1.68×10^{18}	51 30+21	Distortion and Many cracks Not usable Slight beam fluctuation
Be Disk 3 Diamond polish 0.085-mm thick	12 eμA 8.83×10^{17}	17	Distortion, Slightly cracked Still usable No beam fluctuation
Be Disk 4 Diamond polish 0.085-mm thick φ110 mm Special processing	8 eμA 9×10^{17}	20	Slightly Distorted No crack Still usable No beam fluctuation

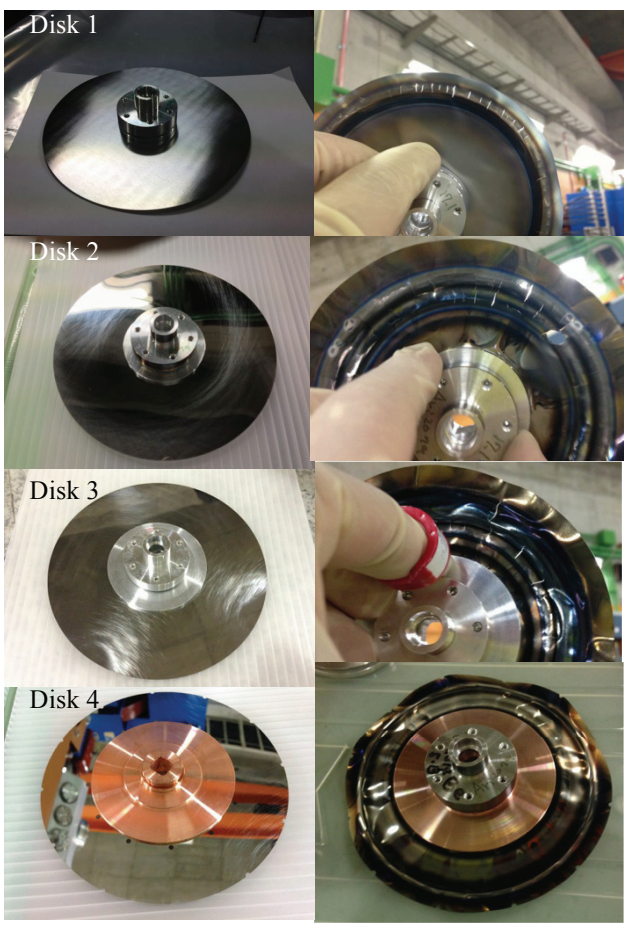

Figure 1: The four Be-disks: before usage (left) and after usage (right).

GLASSY CARBON DISK STRIPPER

In the autumn of 2014, we tried to polish a glassy carbon (GC) disk by using the polishing technology applied for the Be-disk. The main characteristics of GC are good heat resistance, high mechanical strength, and fine-grained structure. The model number of GC was F-22, and the density was 1.93 $g\cdot cm^{-3}$. This GC-disk was fabricated from a 1-mm thick disk. Both sides of the disk were processed using diamond polishing, and the thickness was reduced up to 0.085 mm. The material manufacturer was Tanken Seal Seiko Co. LTD[8], and machining was carried out by Crystal Optics Inc.[9] The fabricated GC-disk had uniform thickness. In Figure 2, the disk at the upper left is the new GC-disk.

GRAPHITE SHEET DISK STRIPPER

In the autumn of 2014, a 0.035-mm (7.1-$mg\cdot cm^{-2}$) thick sample of highly oriented graphite sheet (GS) having high density was tested by Kaneka Corporation[10] as a stripper material. This GS was made from a polymer sheet under the high-temperature and high-pressure condition. The characteristics of GS are listed in Table 2. A prominent feature of the GS is the very high thermal conductivity of 1500 W/mK in the plane direction. In addition, GS has a higher thermal diffusivity than copper or aluminum. Therefore, the rise in temperature at the beam spot position is suppressed. The other features include high density and uniform thickness. The fluctuation in thickness for the GS is approximately half of that for the Be-disk. In addition, the GS is mechanically strong and can be handled easily by using scissors or a cutter knife. The disk at the lower right side in Figure 2 is the new GS-disk. The GS-disk has two layers roughly cut to have an outer diameter of 110 mm.

Table 2: Characteristic of Kaneka GS

		Units	Typical values
Thermal conductivity	In plane (XY axis)	W/mK	**1500**
	Thru plane (Z axis)		5
Thermal diffusivity		cm^2/s	9.0
Density		g/cm^3	**2.0**
Tensile strength		MPa	40
Bending		Cycles	>10000
Electrical conductivity		S/cm	13000

BEAM TESTS OF GC AND GS DISK

In October 2014, the two new carbon disks were tested with U beam. Figure 3 shows the results of the charge distribution for the Be-, GC-, and GS-disks. Blue, red, and green plots indicate the distribution of the Be-, GC-, and GS-disks, respectively. It was observed that the charge distributions of the GC- and GS-disk were similar to that of the Be-disk. Moreover, as observed from the profile data measured at the downstream of the charge

ISBN 978-3-95450-131-1

stripping section, the thickness uniformities of the GC- and GS-disk were similar to that of the Be-disk.

Figure 2: New GC-disk (upper left) and new GS-disk (lower right).

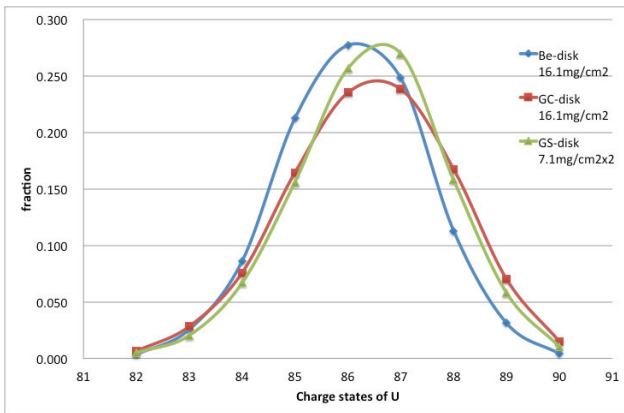

Figure 3: Charge distributions of Be-, GC-, and GS- disks.

GS DISK IN BEAM TIME

We successfully obtained two types of C-disks, and the GS-disk was used during the U beam time from March to May, 2015. A total of 1.4×10^{18} U particles with an intensity of 15 eμA, which corresponds to a thermal load of 205 W, was irradiated on the GS-disk. A total of 1.4×10^{18} U particles corresponds to the amount irradiated during the Be-disk lifetime. However, the GS-disk was still usable. Figure 4 shows the photograph of the GS-disk after usage. No change in the appearance of the new GS-disk was observed except for a slight color change. The lifetime measurement of the GS-disk is still in progress. The maximum temperature of the GS-disk was estimated to be about 600K according to the ANSYS[11] calculation. It was also observed that the thickness uniformity of the two-layer GS-disk is equivalent to that of the single-layer GS-disk. Hence, thickness can be tuned by combining multiple sheets of different thickness.

CONCLUSION

The U beam intensity has been increasing continually. We have developed foil and disk strippers with very long lifetime (the lifetime of the GC-disk has not been measured yet.). Moreover, the cost for the stripper materials has decreased because of the use of C-disks. The performance of the GS-disk as the stripper is excellent and it has the longest lifetime. The GS is also applicable for constructing multilayer disks with variable thickness for acceleration of other ion beams. The three-layer GS-disk was used for the krypton beam operation after the U beam time, and it successfully provided high-intensity beam with good stability. Thus, the problem related to the final stripping section was solved.

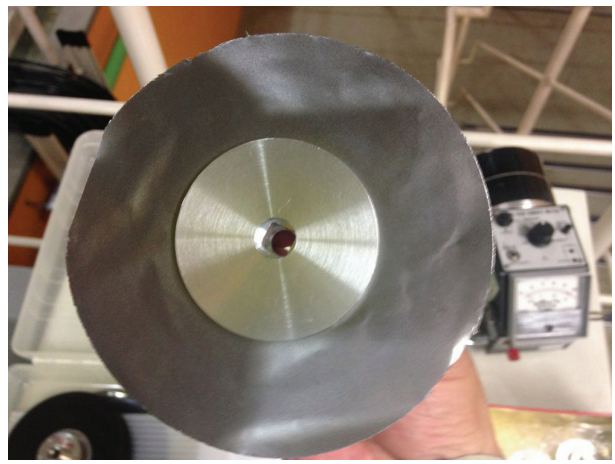

Figure 4: GS-disk after usage.

REFERENCES

[1] H. Ryuto et al., Nucl. Instr. Meth. A **569**, 697 (2008).
[2] ACF-Metals Arizona Carbon Foil Co. Inc., http://www.techexpo.com/firms/acf-metl.html
[3] Goodfellow Cambridge Ltd. http://www.goodfellow.com/
[4] H. Hasebe et al., RIKEN Accel. Prog. Rep. **46**, 133 (2013).
[5] PASCAL CO., LTD. http://www.pascal-co-ltd.co.jp/home.html
[6] H. Hasebe et al., RIKEN Accel. Prog. Rep. **47**, 144 (2014).
[7] H. Hasebe et al., RIKEN Accel. Prog. Rep. **48**, in press.
[8] TANKEN SEAL SEIKO Co.,LTD. http://www.tankenseal.co.jp/other/english.html
[9] Crystal Optics Inc. http://www.crystal-opt.co.jp/global/
[10] Kaneka Corporation http://www.elecdiv.kaneka.co.jp/english/index.html
[11] ANSYS Inc. http://www.ansys.com/

ISBN 978-3-95450-131-1

GANIL OPERATION STATUS AND NEW RANGE OF POST-ACCELERATED EXOTIC BEAMS

O. Kamalou[1)], J. Angot[2)], O. Bajeat[1)], F. Chautard[1)], P. Delahaye[1)], M. Dubois[1)], T. Lamy[2)], L. Maunoury[1)], G. Normand[1)], A. Savalle[1)]
1) GANIL, Grand Accélérateur National d'Ions Lourds, CEA-DSM/CNRS-IN2P3, Bvd H. Becquerel, BP 55027 14076 Caen cedex 5, France
2) LPSC - Université Grenoble Alpes - CNRS/IN2P3, 53 rue des Martyrs, F-38026 Grenoble cedex, France

Abstract

The GANIL facility (Grand Accélérateur National d'Ions Lourds) at Caen produces and accelerates stable ion beams since 1982 for nuclear physics, atomic physics, radiobiology and material irradiation. The range of stable beam intensity available at GANIL extends from very low intensity (< 109 pps) to high beam intensity (~2.1013 pps). The review of the operation from 2001 to 2015 is presented. One of the methods to produce exotic beam at GANIL, is the Isotope Separation On-Line method with SPIRAL1 facility. It is running since 2001, producing and post-accelerating radioactive ion beams mainly from gaseous elements. Due to the physicists demands for new radioactive nuclei, the facility is being improved in the framework of the project "Upgrade SPIRAL1". The goal of the project is to extend the mass range of post-accelerated as well as low energy exotic beams using devoted 1+ Target Ion Source System associated with a charge breeder. The latest results of the charge breeder tests and the status of the upgrade will be presented.

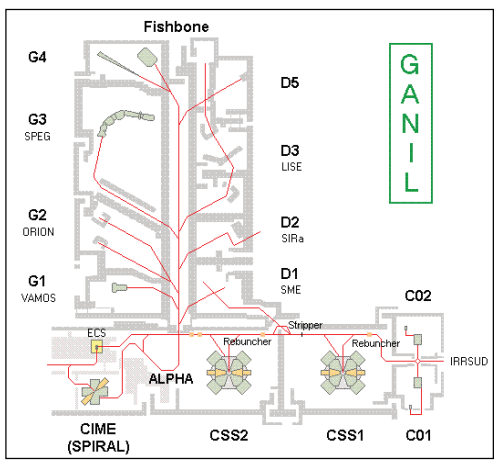

Figure 1: GANIL layout.

OPERATION REVIEW

Multi-beam delivery is routinely done at GANIL using its 5 existing cyclotrons. Up to five experiments can be run simultaneously in different rooms with stable beams (Fig. 1):

1. Beams from C01 or C02 are sent to an irradiation beam line IRRSUD (<1MeV/u).
2. A charge state of the ion distribution after the ion stripping foil downstream CSS1 is sent to atomic physics, biology and solid states physics line D1 (4-13MeV/u).
3. A high-energy beam out of CSS2 is transported to experimental areas (<95MeV/u), for nuclear physics and previous applications.
4. An auxiliary experiments may share the previous CSS2 beam (10% of the pilot experiment time)
5. Finally, stable beams from SPIRAL1 source can be sent to LIRAT (<10 keV/q) or post-accelerated by CIME and used for testing detector for example.

During radioactive beam production with SPIRAL1, the combinations are reduced to the four first (cases 1, 2, 3, 4) and radioactive beam is sent to the experimental areas.

2001-2015 GANIL OPERATION STATUS

Since 2001 (Fig. 2), more than 71400 hours of beam time has been delivered by GANIL to physics, which correspond to 88.6 % of scheduled experiments.

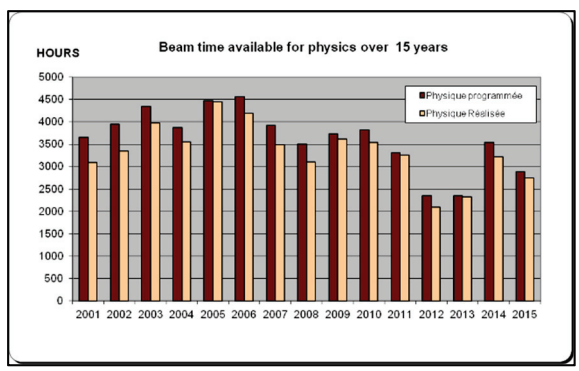

Figure 2: Beam time available for physics over 15 years.

In average, the number of beams delivered per year has increased until 2010. Owing to the construction and assembly of the new SPIRAL2 accelerator, the running time has been shrinked to devote more human ressources to the project, in particulier in 2012 and 2013 with only 2000 hours of running time (instead of 3500 hours per years).

Figure 3 shows the statistic running of the machine over 14 years. As we can see, 67 % of beam time is dedicated to Physics and 12.5% for machine tuning.

ISBN 978-3-95450-131-1

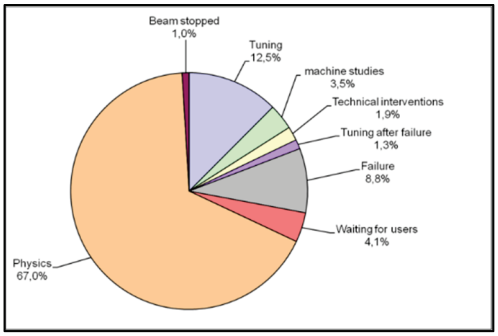

Figure 3: Statistic running of the machine between 2001 and 2015.

SPIRAL1 UPGRADE

The first Isotope Separator On Line System installed at GANIL, named SPIRAL1, has delivered radioactive ions for 13 years. Radioactive atoms produced by fragmentation of swift heavy ions (up to 95 MeV/u) on a carbon target are ionized in an ECR multi-charged ion source before being post-accelerated in a cyclotron. Due to the design of the target ion source system (TISS), mainly gaseous ions are produced. To satisfy the request of physics community for extending the choice of ions to those made from condensable elements, with masses up to Xe, an upgrade of SPIRAL1 has been undertaken [1]. Beams and technical options considered during the prospective phase have been sorted out. A schematic of the ongoing upgrade is presented in Fig. 4. Surface ionization, FEBIAD (Forced Electron Beam Induced Arc Discharge) or ECR (Electron Cyclotron Resonance) ion sources [2, 3] will be installed in the production cave after its modification to provide 1+ beam of condensable elements. Out of the cave and after mass separation, a Phoenix charge breeder will be installed on the present low energy beam line to increase the charge of the radioactive ions from 1+ to N+ for post-acceleration to get energy up to 25 MeV/A using CIME accelerator [4].

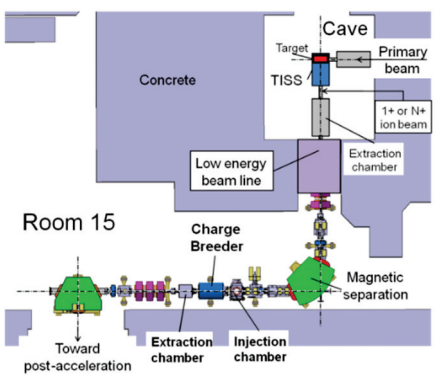

Figure 4: Schematic of the SPIRAL1 upgrade.

NEW BEAMS VERSUS NEW TISS

New elements will be mainly produced by fragmentation of the primary beam ions on a graphite target. Thus most of the masses and atomic numbers will generally not be higher than those of the primary beams available at GANIL. The elements to be produced can be divided in three groups:

1- Alkali elements and alkaline earth elements (Li, Mg, Na, Al, Ca, K, Rb and Sr). The elements could be ionized in an existing TISS, already tested and optimized on line at GANIL on a test bench.

2- Metallic ions (Sc, Cr, Mn, Co, Ni, Cu, Zn, Ga, Ge, As and Se). They will be produced by association of a carbon target with a FEBIAD of VADIS (Versatile Arc Discharge Ion Source) type developed at CERN (Fig. 5). This association indicates good performances for the TISS and yields have been measured favorably for Mg, Al, Cl, K, Mn, Cu and even Fe ions [5].

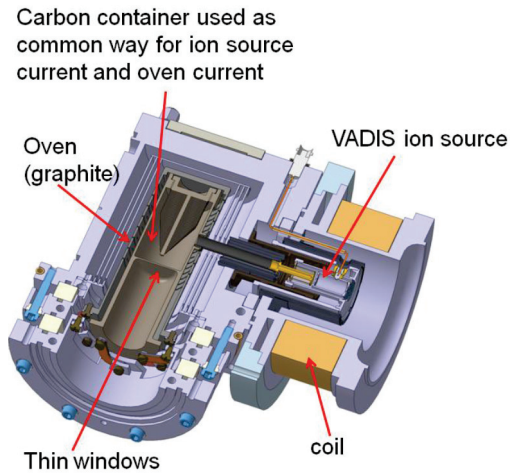

Figure 5: TISS made by association of a graphite target with a VADIS FEBIAD ion source.

3- Non-metallic ions, halogen and rare gas ions (He, Ne, Ar, Kr, O, C, P, Cl and Br). Multi-charged ions from rare gases, C and O are currently produced using the ECR ion source of SPIRAL1 upgraded to enhance the ionization efficiencies.

Because of the length of the singly-charged ion sources is shorter than the present NANOGAN III ECRIS along the low energy beam line axis, a chamber containing optical elements will be installed to transport and adapt the 1+ beam to charge breeder.

CHARGE BREEDER MODIFICATION

Figure 4 shows the connection of the charge breeder in the beam line. Generally, a double Einzel lens is used to focus the 1+ beam into a charge breeder, in order to give more flexibility on the optical tuning, it has been replaced by an electrostatic quadrupole triplet. A movable puller and Einzel lens are mounted in the extraction box; the puller is made of stainless steel. The charge breeder is based on the Phoenix Booster developed at LPSC Grenoble and used at ISOLDE to determine its characteristics with radioactive

ISBN 978-3-95450-131-1

ions [6]. The major features have been described in the reference [7].

EXPERIMENTAL RESULTS

The following procedure was done before each optimization – measurement of charge breeding efficiency or time. Charge breeder OFF (RF OFF), the 1+ incoming is maximized on the faraday cup located (FC1+) before the quadrupole triplet and on the faraday cup (FCn+) placed downstream the charge breeder after the mass over charge separation provided by a 120° dipole. Thereafter, charge breeder ON (RF ON), the charge breeder is tuned so as to get the highest <Z> possible for the buffer gaz charge state distribution (CSD). The charge breeding efficiency and time are measured by pulsing the incoming 1+ beam using and electrostatic steerer and measuring the n+ response on FCn+. The n+ signal is maximized thanks to all available parameters of the charge breeder (RF power, magnetic field, buffer gas) as those of the beam line (voltages on Einzel lenses, voltages on the quadrupole triplet electrodes, position of deceleration grounded tube, etc…). The acceleration voltage of the 1+ ion beam was set at 20 kV, the charge breeder voltage being accurately tunable around this value (20 kV± ΔV. The RF power was always around 350 - 400W and the total current from high voltage supply was in the range 0.5 – 0.8 mA.

The charge breeder had to be tested with condensable elements: alkali elements which are easy to ionize using pellets from the HeatWaveLabs [8] have been chosen for this purpose. Na^{1+}, K^{1+} and Rb^{1+} beams were successively produced and injected into the charge breeder; typical intensities were in the range from 200 to 400 nA. Charge state distributions obtained by the breeding process in different situations are presented in the Figure 6.

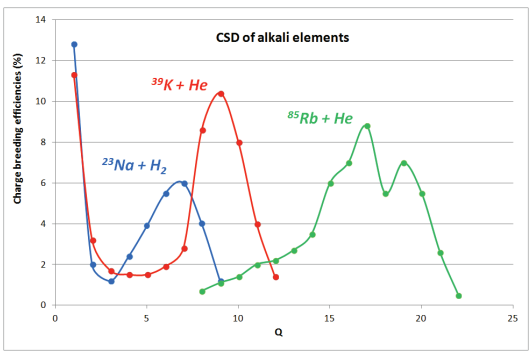

Figure 6: Charge state distributions of alkali elements with He or H2 as buffer gas.

Focused on the ^{39}K case, the Figure 7 displays a graph on the evolution of the ^{39}K CSD with the buffer gas. Lighter is the buffer gas, higher is the charge breeding efficiency of the $^{39}K^{9+}$ and narrower is the CSD. It is an important parameter for the future accelerated beams after CIME. Increasing the charge Q of the ion proportionally increases the final energy. In the case of a $^{39}K^{10+}$ beam, the buffer gas should be He contrary to $^{39}K^{9+}$ where it should be H_2. The effects of the ΔV value and of the buffer gas on the charge breeding process are described in much more details in [9].

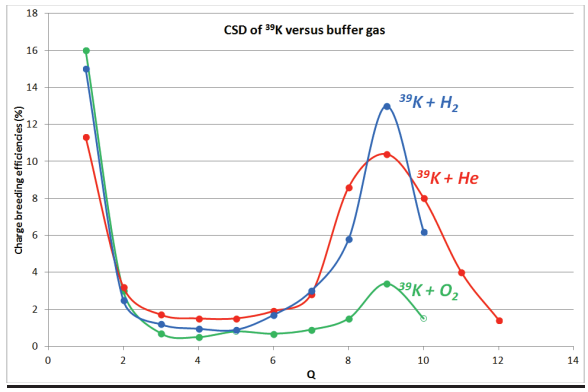

Figure 7: Evolution of the Kn+ charge state distributions versus buffer gas.

REFERENCES

[1] P. Jardin et al., Rev. Sci. Instrum. 83, 02A911(2012)
[2] S. Sundell et al., Nucl. Instrum. Method. B 70 (1992) 160-164.
[3] R. Vondrasek et al., Rev. Sci. Instrum. 83, 02A913(2012)
[4] C. Tamburella. Thesis, ISN Grenoble (1996).
[5] O. Bajeat et al., Nucl. Instr and Meth. in Phys. Res (2013)
[6] P. Delahaye et al, Review of Scientific Instruments. 77, 03B105 (2006)
[7] P. Delahaye et al., Nuclear Instruments and Methods in Physics Research A. 693, 104 (2012)
[8] T. Lamy et al., Proceedings of the 21st International Workshop on ECR Ion Sources, Nizhny Novgorod, Russia, 24th -28th August 2014
[9] L. Maunoury et al., submitted to Rev. sci. Instr. For publication in the proceedings of the 16th International Conference on Ion Sources, New-York, August 23-28, 2015.

ISBN 978-3-95450-131-1

PROPOSAL TO INCREASE THE EXTRACTED BEAM POWER FROM THE LNS-INFN SUPERCONDUCTING CYCLOTRON

A. Calanna[1], L. Calabretta[1], D. Rifuggiato[1], G. Cuttone[1], G. D'Agostino[1], A.D. Russo[1], A. Radovinsky[2]
1) INFN-LNS, Catania, Italy 2) PSFC T&ED MIT, Cambridge, MA 02139, USA

Abstract

The LNS Superconducting Cyclotron, CS, is an isochronous 3-sector compact machine with a wide mass-energy range of heavy ions: beams from protons to lead from 10 to 80 AMeV have been delivered for the past 20 years. However, the extracted current density does not exceed the tenth of enA, corresponding to a beam power of 100 W. Recently, the demand to increase the beam intensity of light ion of a factor 10 to 100 was posed by nuclear physicists. A feasibility study proved a new mode of extraction by stripping would allow for an extraction efficiency of 99% and consequently a high intensity provided by the cyclotron. Here the design of the actual central region as well as the feasibility study of the new extraction for this range of ions is presented. It emerges that the present cryostat is not compatible with the new extraction geometry; therefore, a new cryostat has to replace the present one.

INTRODUCTION

The goal of the study presented is to investigate the possible gain on the extracted beam power from the CS.

Two approaches were chosen. At first, we studied the feasibility of a new mode of extraction from the cyclotron that could radically improve the beam power on target. Today, two electrostatic deflectors and a set of magnetic channels perform the beam extraction. The extraction efficiency is low since almost the 50% of the accelerated beam is lost on the first electrostatic deflector. When a beam power of 100 watt is extracted, the same power is dissipated in the electrostatic deflector septum. Going beyond this value produces serious instabilities in the voltage holding. Extraction by stripping for light ions, with A<20, within the range of 15-70 MeV/amu should guarantee an extraction efficiency of 99% or more because the probability to have q=Z after the stripper foil is >99% for this range of ions and energies [1]. This can increase the maximum beam intensities up to a factor 10-100, to reach beam power values of few kW.

Furthermore, a parallel study started to design a new dedicated central region optimized for these ions and energies. The new central region will be operated with the RF cavity voltages higher of a factor two respect to the present one. Like the existing central region, it will be working in the so-called constant orbit mode, which means the cavity voltage to accelerate the beam scales with the beam energy. Now, a 3D model of the actual central region has been created and the first tracking orbits have been performed thanks to the peculiarity of OPERA 3D, which allows the combination of magneto-static and modulated electric fields. A sketch of the CS actual central region is shown in Fig. 1.

The NUMEN experiment, which proposes to measure the element of nuclear matrix using double charge exchange reactions [2, 3], is the main reason to increase the beam power. However, many other experiments, currently accomplished at LNS, will take advantage from this upgrade. These experiments make use of radioactive ions beam produced with fragmentation in-flight technique at FRIBS@LNS [4]. Production of radioisotopes of medical interest can be considered too.

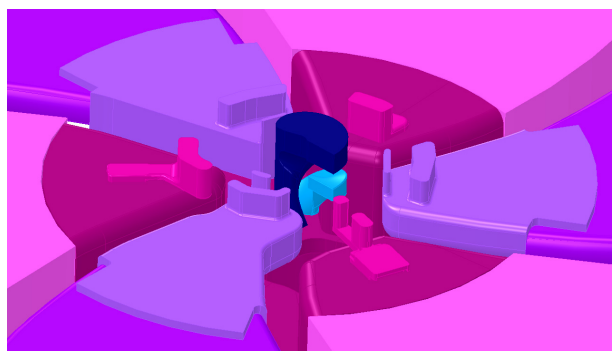

Figure 1: Drawing of the CS actual central region.

The present extraction mode will be maintained, which means the CS will provide all the beams accelerated up to date since there is a huge demand for these beams. For this reason, after the upgrade, the beams will be extracted from the CS with both extraction modes: extraction by stripping and extraction by electrostatic deflectors.

RESULTS OF THE FEASIBILITY STUDY FOR THE STRIPPING EXTRACTION

Since the CS is an operating cyclotron, measured maps are available. From them, we created 3D maps of the field in the gap between the poles solving the Maxwell's equations. Then we imported them on the Post- Processor module of OPERA 3D to have the field on the whole gap and to track particle trajectories. In this way, on one hand we created a new modern tool to reproduce all beam dynamics features that have been computed during the past 20 years with two old codes developed initially at MSU by Gordon [5], GENSPE and ESTRAZ. On the other hand, this new tool allows to easily visualize single

ISBN 978-3-95450-131-1

particle trajectories and envelopes and, moreover, it overcomes some limitations of the ESTRAZ code. That means we have now all the instruments to compute stripping extraction for every ion and energy whatever the charge state of the accelerating particle is.

Details on the technical approach can be found on [6]. For each ion and energy, the last closed orbit was tracked for the reference particle. Then the best azimuthal position for the stripping foil was chosen tracking the extraction trajectory of the particle after the stripping foil with the limitation that the reference particle had to stay at least 7 cm away from the centre of the cyclotron to avoid interference with the central region components. We computed axial and radial envelopes assuming a normalized emittance of 1 π mm mrad at the stripping foil, which is a conservative value since it is almost twice what we measured from the source. Moreover, since the stripping extraction is a multi-turn extraction [6], we took into account also the energy spread introduced by this process[7]. The conditions to fulfil to accept the trajectories were related to mechanical constraints on the extraction channel of the cyclotron. We accepted axial envelopes less than +/-1.5 cm inside the acceleration gap and less then +/- 3 cm in the gap between the coils and in the extraction channel through the yoke.

An example of an extraction trajectory in the cyclotron median plane is shown on Fig. 2 in dark blue. In red there are the dees boundaries, in cyan the coils and the striped area represents the yoke. The yoke is full of penetrations since there are two electrostatic deflectors that need 5 and 4 arms respectively to slightly change the deflector position to adapt to the accelerated particle and 9 penetrations for the correcting magnetic channels, dignostic devices, and the radial probe. In Fig. 3 radial and axial envelopes related to Fig. 2 are shown.

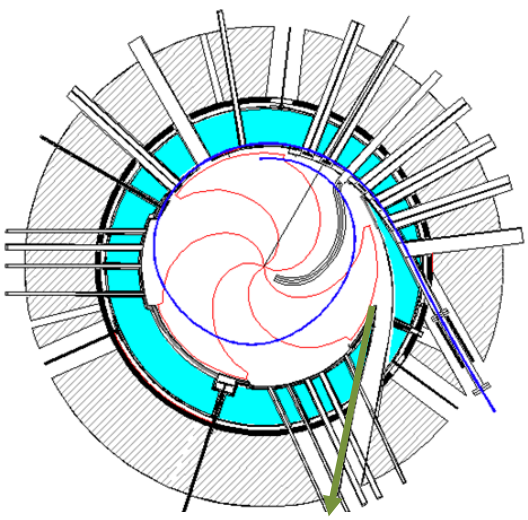

Figure 2: Example of extraction trajectory of ^{18}O at 70A MeV. 7 MC have to be considered on.

After the pole radius, it is possible to insert some magnetic channels providing small changes to the magnetic field to focus and slightly steer the beam along the extraction channel. For the case shown in Fig. 2 and Fig. 3, 8 magnetic channels are necessary to maintain the beam dimensions and direction within the specifications.

The maximum field correction we accepted in the magnetic channels is 0.2 T and the maximum gradient is 0.2 T/cm. A preliminary study on the shape of these magnetic channels has been accomplished.

The green arrow in Fig. 2 indicates a penetration that does not exist yet. Indeed, during the computation process, we discovered that a lot more ions can be extracted with fewer corrections when considering a new penetration rotated of about 30 deg.

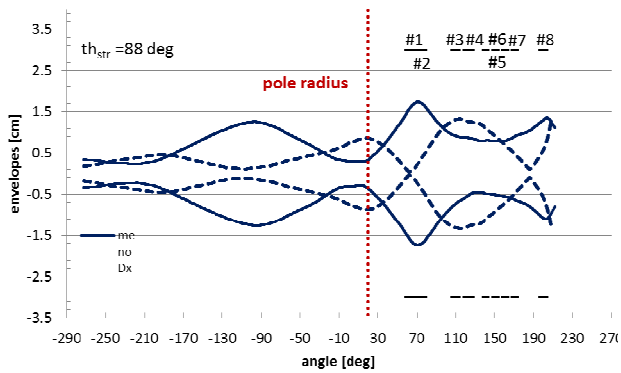

Figure 3: Radial and axial beam envelope along the extraction trajectory of ^{18}O at 70A MeV. The energy spread considered is 0.5 %, which is overestimated.

This new penetration is the one indicated with the green arrow in Fig. 2. An example of extraction path along the new extraction hole is shown in Fig. 4. In Fig. 5 radial and axial envelopes associated with Fig. 4 are shown.

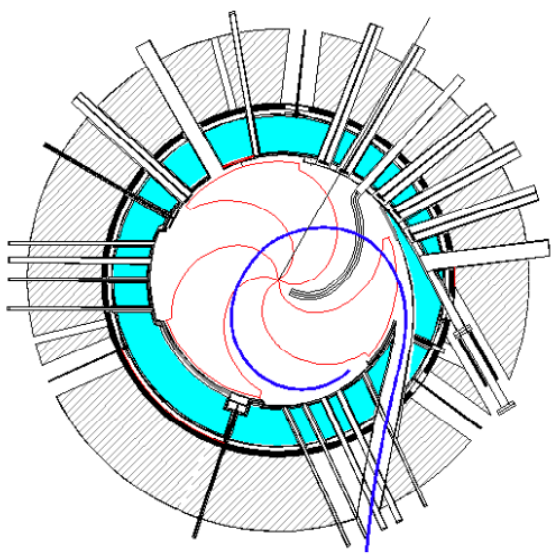

Figure 4: Example of extraction trajectory of ^{18}O at 45.5A MeV. 3 MC have to be considered on.

ISBN 978-3-95450-131-1

In this case, the radial and axial envelopes are smaller and smoother. Moreover, only 3 magnetic channels are necessary and the field and gradient needed are smaller. A full table of the ions and energy calculated through the new magnetic channel, together with another example and the intensities of the field and the requested gradients are reported on [6]. In ref. [6] there is also an overview of all the beams and energies extracted by stripping through the existing extraction channel.

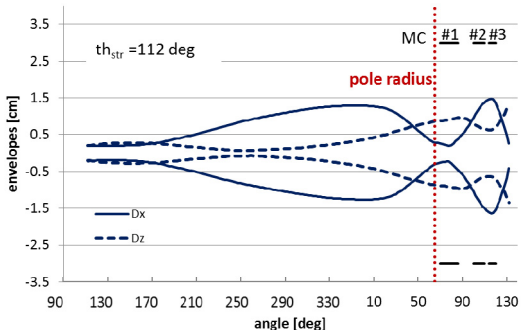

Figure 5: Radial and axial beam envelope along extraction trajectory of ^{18}O at 45.5 A MeV. The energy spread considered is 0.5 %, which is overestimated.

FURTHER CONSIDERATIONS

Although the computations seem to show the necessity of the new extraction channel, there are other considerations to be done.

As Fig. 2 and Fig. 4 show, there are lot of penetrations in the yoke, which lead to lot of sub-systems. The introduction of a new extraction channel has to be carefully studied. In fact, the cross-section of the new channel has to be wider of the existing one, which in vertical is only +/- 12 mm, to have a beam of 5-10 kW extracted. Quite probably, a cooling system for the two channels is mandatory. As a consequence of the modifications described, a new cryostat is necessary, including a new set of superconducting coils. In particular, a stress analysis of the cryostat structure has to be evaluated.

The Plasma Science and Fusion Centre of MIT (Cambridge, MA) [8] prepared a study report for the "New superconducting magnet for the LNS Cyclotron". Some details of the report are in [6]. The specifications we asked for were:

• the form factors of the new coils must be very similar to the previous coils with differences below 0.05% because we all the beams within the present operating diagram must be guaranteed;

• the new cryostat must have the same outer size of the previous cryostat, but the distance of the first coil from the median plan has to be increased to allow a possible clearance of +/- 3cm for the beam to pass;

• hoop stresses in the self-supporting coils and the influence of broadened extraction channel has to be conservative;

• the expected liquid helium and nitrogen consumption had to be reduced respect to the actual ones.

The PSFC main conclusion was that such a cryostat is feasible with the present state-of-art of superconducting cable. The main difference with the present coil is the design of the cold mass. The existing coils consist of a set of double pancakes wound with pretension [9]. This solution is very cryostable and it has worked very well. In the new coil design the maximum overall current density is 54 A/mm^2 instead of 35 A/mm^2 in the old design. Moreover, the new coils epoxy according to their suggestion will be impregnated (potted) using helium pooled cooling scheme. This choice is supported by the worldwide experience, for the construction of this kind of coil.

The PSFC provided even an estimation of costs, in these days at LNS we are evaluating more in detail each part of their calculation to write down a full technical design report, which will include all the modifications to the cyclotron. Indeed, we plan to change all the trim coils and to replace the liner to increase as much as possible the accelerating gap. Other minor changes are also planned to guarantee better reliability. Figure 6 shows a first design of the new beam line out the cyclotron connecting the new extraction channel to the existing beam line.

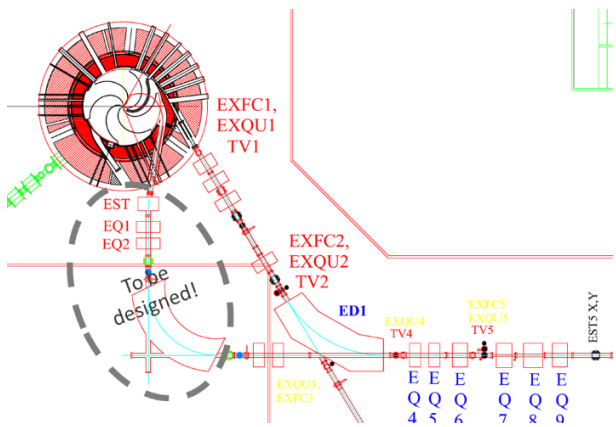

Figure 6: First design of the new beam line connecting the new extraction channel with the existing beam lines.

CONCLUSIONS

The present study demonstrates that it is possible to achieve a extracted beam power 100 times bigger out of the CS. The focusing strength requests to the magnetic channels are higher than for the existing channels, but it seems feasible thank to the larger sizes of the new extraction channels. The optical property of the beam extracted by stripper are similar to the previous and satisfies the requirement of NUMEN and other new experiments.

ISBN 978-3-95450-131-1

REFERENCES

[1] Atomic Data and Nuclear Data Tables, Vol. 51, No. 2, July 1992, Table 2 pp.187.
[2] M. Cavallaro et al., INFN-LNS activity report 2013-14.
[3] C. Agodi et al., INFN-LNS activity report 2013-2014.
[4] Raciti G. et al., Nucl. Phys. Sec. A, Vol. 834, Issue 1-4, March, 2010, pp.780c-783c.
[5] Gordon, Particle Accelerators 1984, Vol.16, pp.39-62.
[6] Calanna et al., "Upgrade of the LNS superconducting cyclotron", IPAC2015, Richmond, VA, USA, May 2015, paper THPF037.
[7] S.S.Tomic, E. V. Samsonov, Phys. Rev. E, Vol. 65, 036504.
[8] A. Radovinsky et al. TBP Magnet Technology 2015.
[9] E. Acerbi et al., www.jacow.org, Cyclotrons 1981, p. 169.

ISBN 978-3-95450-131-1

DESIGN OF A SECTOR MAGNET FOR HIGH TEMPERATURE SUPERCONDUCTING INJECTOR CYCLOTRON

Keita Kamakura*, K. Hatanaka, M. Fukuda, T. Yorita, H. Ueda, K. Shimada,
S. Morinobu, T. Saito, K. Nagayama, H. Tamura, Y. Yasuda, RCNP, Osaka University
10-1, Mihogaoka, Ibaraki, Osaka, Japan

Abstract

We propose a separated sector cyclotron (SSC) using high temperature superconducting (HTS) magnet for a next generation cyclotron. From its stability and low operating cost, HTS cyclotrons are expected to apply for accelerator-driven subcritical reactors or beam cancer treatment systems. On the other hand, we still have a variety of issues and challenges to implement them. As a first step, we are planning to develop an HTS cyclotron as an injector for K400 ring cyclotron at RCNP. It will be the first attempt in the world. This plan will improve beam intensity in our facility and also contribute to component developments for the next generation cyclotron. The most serious issues are development of large-size HTS magnets that can be used in SSC. One-meter-size HTS dipole magnet is made for testing. Now we are going to exam the magnet and evaluate the characteristics of large HTS magnets. The result of the test will be incorporated with the sector magnet design. Moreover, we have been working on conceptual design of the new injector, developed magnetic field and orbit analysis programs. In this session, the current status of designing HTS injector cyclotron at RCNP will be discussed.

CURRENT STATUS OF RCNP

At RCNP, K140 AVF cyclotron and K400 ring cyclotron are used to accelerate various ion species from proton to Xe (Figure 1). Those beams are used for nuclear physics experiments, neutron irradiation, isotope production, etc.

One of the most important features of our facility is the precise nuclear measurement with high energy resolution beam and Grand Raiden Spectrometer. It makes us possible to achieve resolution shown in formula (1).

$$\frac{\Delta E}{E} \sim \frac{12.8\ \text{keV}}{295\ \text{MeV}} \sim 4.3 \times 10^{-5} \quad (1)$$

Beam intensity of the precise beam is about few nA.

For secondary beam production, intensity limit of primary proton beam is 1.1 μA which is not that high.

NEW INJECTOR PROJECT

Currently, we are planning to upgrade our facility by increasing the beam current up to 10 times of present values. One crucial factor of our problem is the low transmission of AVF injector cyclotron. So we decided to implement a new separated sector cyclotron as injector, as shown in Figure 2.

Conceptual Design

Considering requirements from the K400 ring cyclotron downstream, we finished a conceptual design on the new injector cyclotron [1].

For heavier ion acceleration, K value is raised up to 200 MeV. Maximum magnetic field is 1.7 T. It can be generated by normal conductor, but we decided to apply HTS coils for technological development.

Motivations for HTS Cyclotron

High temperature superconductors have several advantages over normal conductors and low temperature superconductors, which are:

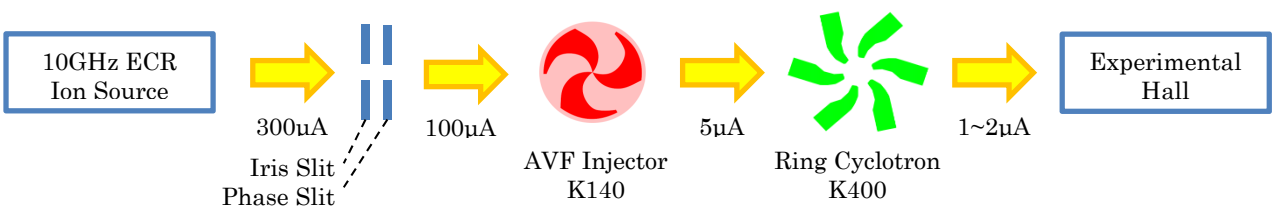

Figure 1: One example of proton acceleration in current RCNP cyclotron cascade.

Figure 2: One example of proton acceleration in current RCNP cyclotron cascade.

* keita@rcnp.osaka-u.ac.jp

ISBN 978-3-95450-131-1

- Magnets can be compact, and can generate higher magnetic field.
- Low power consumption.
- Critical temperature is higher than 100 K, no liquid helium is needed for cooling.
- When the operation temperature is set around 10 K, large margin against quenching.

However, large scale HTS coil used for cyclotron is not yet available. Development of such coil will be the challenging part in the project.

Main Coil and Trim Coils

Based on the conceptual design, I designed 3D model of the sector magnet. On one pole, it has 1 set of HTS main coil, and 36 sets of trim coils of normal conductor which will be reduced later to moderate number, as shown in Figure 3.

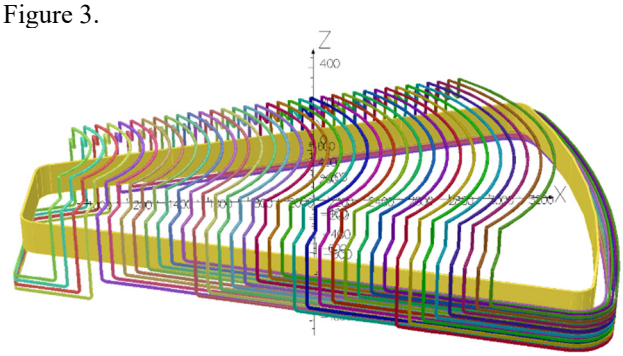

Figure 3: HTS main coil and 36 trim coils on one pole of sector magnet. Main coil size is 2.8 m along X axis.

Isochronous Field

Isochronous field should be maintained on the median plane as shown in (2). I developed a design assistant program to determine currents in the trim coils [2][3].

$$\bar{B}(R) = \gamma(R)\overline{B_0} = \overline{B_0}\sqrt{\frac{M^2}{M^2 - (Q\overline{B_0}Rc)^2}} \qquad (2)$$

To control the average field ($\bar{B}$) on average radius (R), we have to know the shape of equilibrium orbits. I used finite element method analysis to obtain main coil field, and did an orbit simulation using Runge-Kutta method to get equilibrium orbit for each radius. Now we know the relationship between average field $\bar{B}(R)$ and field $B(r)$ on X axis; formula (3), also the average radius R and the position r on X axis; formula (4).

$$K_B = B(r)/\bar{B}(R) \qquad (3)$$

$$K_r = r/R \qquad (4)$$

Now, we can use K_B and K_r to convert the isochronous formula (2), and get isochronous field on X axis; (5).

$$\bar{B}(R) = K_B\overline{B_0}\sqrt{\frac{M^2}{M^2 - (Q\overline{B_0}rc/K_r)^2}} \qquad (5)$$

We have to fit formula (5), which is also shown in Figure 4, by magnetic field of main coil (Figure 4) and trim coil contributions (Figure 5).

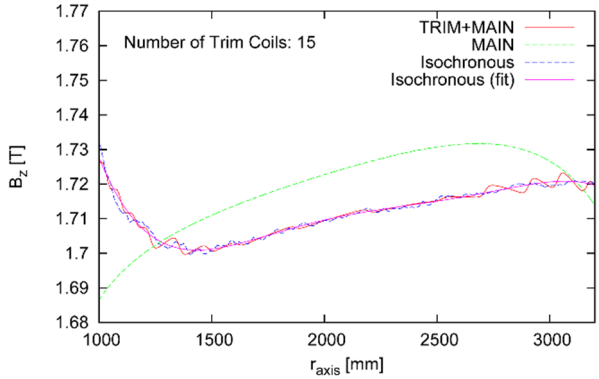

Figure 4: Vertical field B_z along X axis (see Figure 3). TRIM+MAIN: Field generated by main coil and trim coils by optimized parameters. MAIN: Field generated by main coil alone. Isochronous: Isochronous field shown in Formula using raw K_B, K_r. Isochronous (fit): Isochronous field using K_B, K_r fit by quintic curves.

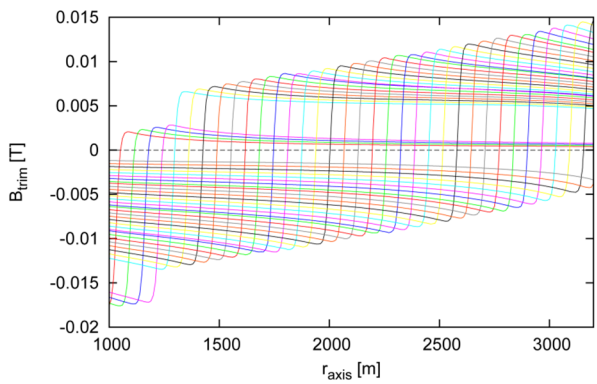

Figure 5: Contributions on vertical field by 36 trim coils excited to 504 A. Trim coils are exited one by one on main field and subtracted main coil contribution.

I used least square method for fitting. ΔB_z: shown in Figure 6 is the subtraction of isochronous field and main coil field.

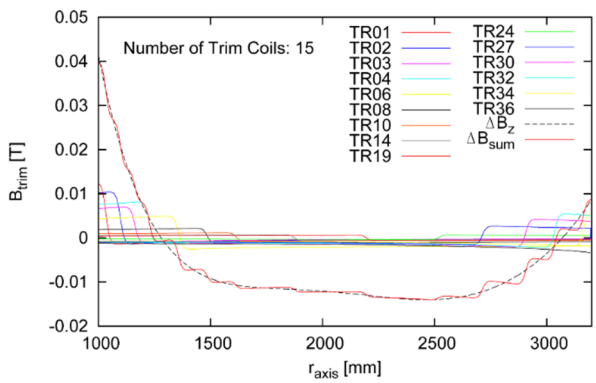

Figure 6: Excitation level of 15 trim coils to fit ΔB_z.

Around r=2000 mm, ΔB_z is very flat so we don't need many trim coils to fit it. So I reduced trim coils mainly from that region down to 15 coils.

ISBN 978-3-95450-131-1

The isochronous field generated by those currents is shown in Figure 6. I did the orbit simulation including impulse acceleration at RF cavities to evaluate the isochronous field. $^{12}C^{4+}$ beam is successfully accelerated up to extraction energy (Figure 7). It confirmed the field generated by 15 trim coils.

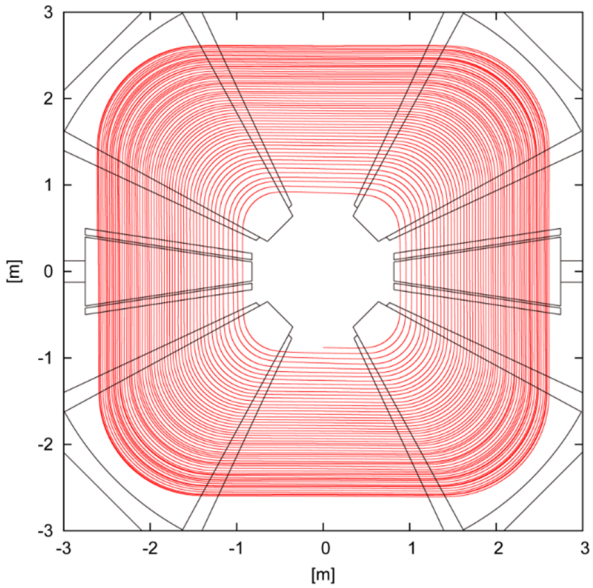

Figure 7: Orbit simulation on isochronous field.

DEVELOPMENT OF HTS MAGNETS

A lot of HTS magnets have been developed in RCNP. [4] Two of them are shown in Figure 8. These experiments are important steps for large scale HTS magnet improvements.

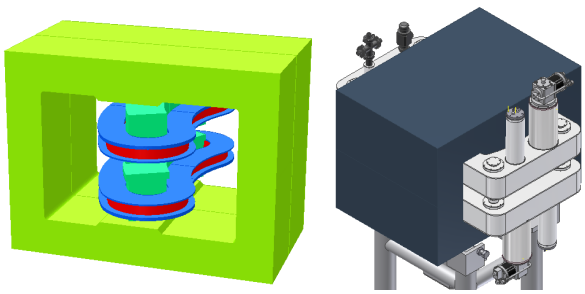

Figure 8: 40 cm toy model magnet (left), and 1 m switching magnet (right).

Half-meter-size HTS Magnet

The left drawing in Figure 8 is a half-meter-size bending magnet model with DI-BSCCO. It has 60 degrees of bending angle and 40 cm radius of curvature. This magnet is made for preliminary research. We did thermal and magnetic field measurements during ramping operation.

One-meter-size HTS Magnet

The left drawing in Figure 8 is a one-meter-size switching magnet for time sharing between two experimental halls. It is developed with BSCCO-2223. Now this magnet is being tested at RCNP. One of the results is shown in Figure 9. It shows coil temperature stays in the operating temperature during switching operation. The result confirmed the thermal design.

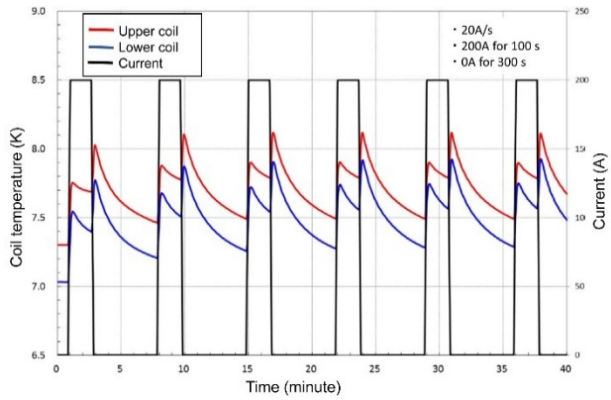

Figure 9: Coil temperature during ramping operation. Ramping rate is 20 A/s.

Perspective for Next Generation Cyclotron

We have been developed half-meter toy magnet, one-meter switching magnet with weak field operation (1.5 T). Next we are going to build three-meter sector magnet with weak field operation (1.7 T).

This HTS cyclotron is an important step for the next generation compact and high field cyclotron.

CONCLUSION

At RCNP, upgrading cyclotron facility has been planned to increase beam currents up to 10 times of present value. HTS cyclotron is proposed for the new injector. Design of sector magnet is completed, and confirmed by magnetic field and orbit simulations. Now 1-meter-size HTS magnet is being tested. The HTS injector cyclotron will be the first step to the next generation cyclotrons.

REFERENCES

[1] K. Kamakura, et al., “Design of Sector Magnets for Next Generation High Temperature Superconducting Cyclotron”, Proceedings of the 11th Annual Meeting of Particle Accelerator Society of Japan, (August, 2015, Tsuruga, Japan).

[2] M. Barre, et al., “Main Results of the SSC’s Magnetic Field Mapping at GANIL”, Proceedings of the 9th Intl. Conf. on Cyclotrons and their Applications, (September, 1981, Caen, France).

[3] A. Goto, et al., “Isochronous Fields for RIKEN Cyclotron”, Proceedings of the 11th Intl. Conf. on Cyclotrons and their Applications, (October, 1986, Tokyo, Japan).

[4] K. Hatanaka, et al., “Development of HTS Magnets”, Proceedings of the 6th Intl. Particle Accelerator Conf., (May, 2015, Richmond, USA).

ISBN 978-3-95450-131-1

INJECTION AND ACCELERATION OF INTENSE HEAVY ION BEAMS IN JINR NEW CYCLOTRON DC280

G. Gulbekian, I. Ivanenko, N. Kazarinov, E. Samsonov, JINR, Dubna, 141980, Russia

Abstract

At the present time the activities on creation of the new heavy-ion isochronous cyclotron DC280 are carried out at Joint Institute for Nuclear Research. The isochronous cyclotron DC-280 will produce accelerated beam of ions with A/Z= 4 - 7 to energy W= 4 – 8 MeV/n and intensity up to 10 pμA (for 48Ca). The goal for DC-280 accelerator complex is more then 40 % beam transfer efficiency. To achieve high-intensity ion beam, the cyclotron is equipped with high-voltage, up to 80 kV, injection line and independent Flat-Top RF system. To decrease the aperture losses at centre region the electrostatic quadruple lens will be installed between inflector and first accelerating gap. The paper presents the results of simulation of beam injection and acceleration.

INTRODUCTION

One of the basic scientific programs which are carried out in the FLNR JINR is synthesis of new elements which requires intensive beams of heavy ions. At present time the isochronous cyclotron U-400, which is in operation since 1978, is capable of providing long term experiments on 48Ca beams with an intensity of 1 pμA. Its operation time is more than 6000 hours per year. To enhance the efficiency of experiments it is necessary to obtain accelerated ion beams with the following parameters:

Ion energy 4÷8 MeV/n
Ion masses 10÷238
Beam intensity (up to A=50) 10 pμA
Beam emittance less 30 π mm mrad

These parameters formed the base for the new isochronous cyclotron DC-280 [1]. The basic technical solutions to realize new project are shown in Table 1.

Table 1: DC-280 Cyclotron - Basic Technical Solutions

Parameter DC280	Goals
1. High injecting beam energy (up to 100 keV/Z)	Decreasing space charge factor. Decreasing beam emittance.
2. High gap in the centre	Space for a long spiral inflector
3. Low magnetic field	Large starting radius. Good orbit separation. Low deflector voltage
4. High acceleration rate	Good orbit separation.
5. Flat-top system	High capture. Beam quality.

The new cyclotron complex provides an opportunity of carrying out physical and chemical research using radioactive targets, such as U, Pu, Am, Cm, Bk. The layout of the cyclotron assembling is shown in Figure 1.

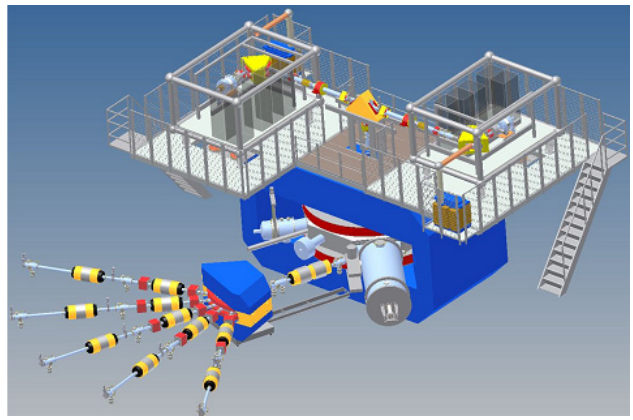

Figure 1: The layout of the DC-280 cyclotron.

Now the most of new cyclotron complex elements have been manufactured and the project is at the stage of laboratory building construction.

THE AXIAL INJECTION SYSTEM

The DC-280 injection system has to provide ion transition from the ECR-ion source to the cyclotron centre and capturing into acceleration more than 70 % of ions with the atomic mass to charge ratio of A/Z=4÷8 [2]. The experience in operation of FLNR cyclotrons demonstrates that at ion energies of 15 keV/Z the injection efficiency essentially depends on the ion beam current. At the ion beam currents of 80÷150 eμA the efficiency of capture into acceleration reaches 30÷35 %, but for the ion currents less than 10 eμA increasing of the efficiency to 50÷60 % has been observed. The reason of it may be the decreasing of the ion beam space charge effect and decreasing the beam emittance, especially at low level of the microwave power in the ECR source. To improve the injection efficiency we will increase the injection energy up to 100 keV/Z, since the emittance and the space charge effects have to be decreased.

The high-voltage axial injection of the DC-280 will consist of two high voltage platforms, HVP. The maximal voltage on the HVP will be 75 kV. Every HVP will be equipped with an ECR ion source with injection voltage 25 kV, a focusing elements and a magnet for ion separation and analyzing. The high voltage accelerating tube will be installed at the edge of the HVP to increase the ion energy.

Two types of ECR ion sources will be used: the DECRIS-PM source with permanent magnets and the DECRIS-SC superconducting one. The first ECR ion source has to produce high intensities (15÷20 pμA) of ions with medium masses (for example, $^{48}Ca^{7+,8+}$), the

ISBN 978-3-95450-131-1

second one has to produce the high charged heavy ions, such as $^{238}U^{39+,40+}$.

The numerical calculations have shown that the acceleration in high voltage accelerating tube allows us to decrease the ion beam emittance in about 1.5 times. The calculated efficiency of the ion transport from the ECR to the DC-280 median plane is equal to 100 %.

To increase the accelerating efficiency the poly-harmonic buncher will be installed in the vertical part of the channel at the distance of 388 cm from the cyclotron median plane. The buncher uses 1, 2 and 3 harmonics of cyclotron RF voltage. The numerical simulation has shown that efficiency of beam grouping in range 20° of RF phase will be up to 80 %. The estimated beam losses at the grids are about 8-10 %.

DC280 MAGNET

To produce an isochronous field, DC280 magnet is equipped with four pairs of sectors. The aperture between the sectors is 208 mm and enough to place Flat-Top dees and 4 pairs of harmonic correcting coils, see Figure 2. The wide range of the magnetic field levels 0.64 – 1.32 T allows making a smooth variation of the beam energy in a range 4 – 8 Mev/nucl. For operational optimization of the magnetic field the 11 radial correcting coils are used. The beam phase divergence along acceleration not more than ±2° for 48Ca, Figure 3, and about ±15° for edge operation modes.

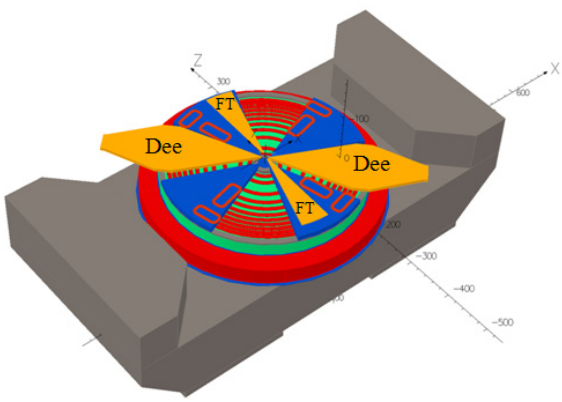

Figure 2: The model of DC-280 magnetic system.

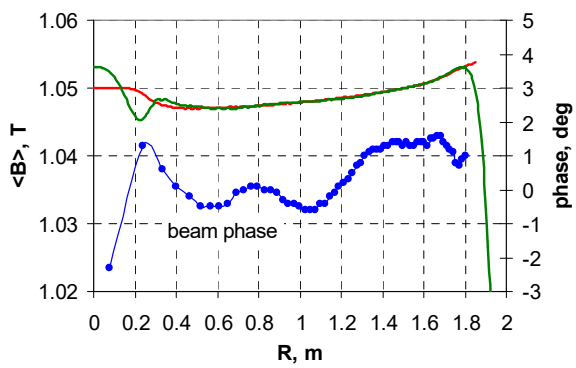

Figure 3: 48Ca8+ beam phase along acceleration, isochronous and formed magnetic field.

DC280 CENTRAL REGION

Because of a wide range of operation modes the DC-280 cyclotron uses electrostatic spiral inflector with different magnetic radiuses Rm = 7.5 and 9.2 cm. With the two interchangeable inflectors it is possible to maintain a high level of injection voltage in the range 50 to 85 kV. In this case a 100 % transmission of the injected beams through the axial injection system can be achieved.

The electric radii of both inflectors are the same and equal to Ae=6 см. To avoid the sparking between the electrodes the inflector voltage is not greater than ±16 kV. Inflector is placed at cyclotron centre by means of radial evacuating system. Because of two different starting radii the double puller of the first dee is used, Figure 4.

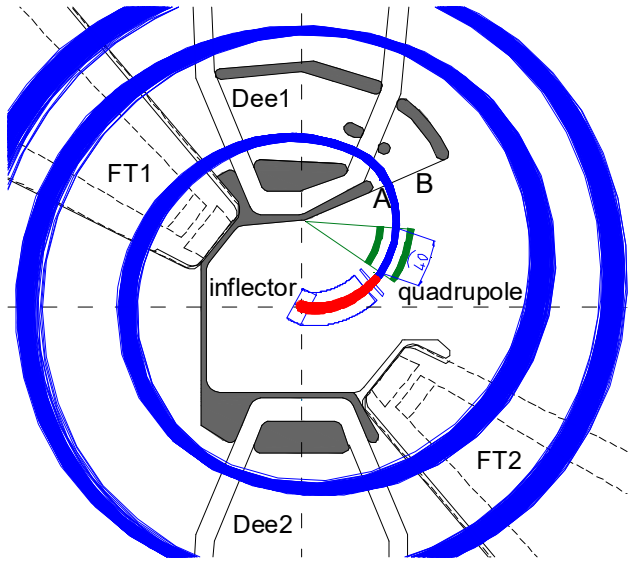

Figure 4: The central region of DC280 cyclotron. Inflector of 7.5 cm magnetic radius is placed.

The disadvantage of spiral inflector is vertical divergence of the beam at the exit. For DC280 it leads to about 25 % of aperture losses along the acceleration, especially at the first orbits. To avoid that losses an electrostatic quadrupole lens is placed between inflector and first accelerating gap, Figure 5.

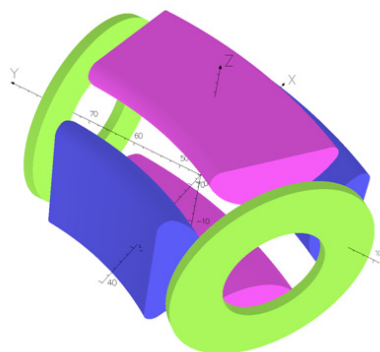

Figure 5: Quadrupole lens provides vertical focusing of the beam before first accelerating gap.

Quadrupole lens with aperture of 22 mm and length of 40 mm has a potential at electrodes 3 kV and provide

ISBN 978-3-95450-131-1

vertical focusing of the injected beam before first accelerating gap. It decreases aperture losses along acceleration down to 2 %.

MAIN AND FLAT-TOP RF SYSTEMS

The cyclotron main accelerating system consist of two dees with 45° angular size and works at h_o=3 harmonic RF. The main resonator provides RF voltage in the range of 7.32-10.38 MHz and amplitude U_o up to 130 kV. The high voltage provides the high rate of acceleration and orbit separation, especially at the last orbits.

To achieve high-intensity ion beams, the cyclotron is equipped with Flat-Top system [3]. The scheme of two additional Flat-Top dees, worked at h_{ft}=3h_o=9 harmonic RF, was chosen. The Flat-Top dees are placed between the sectors in a gap of 208mm, at the angle 51.5° to the main dees and have angular size δ_{ft} = 20°. The Flat-Top RF voltage is 0.1 of the main dee voltage.

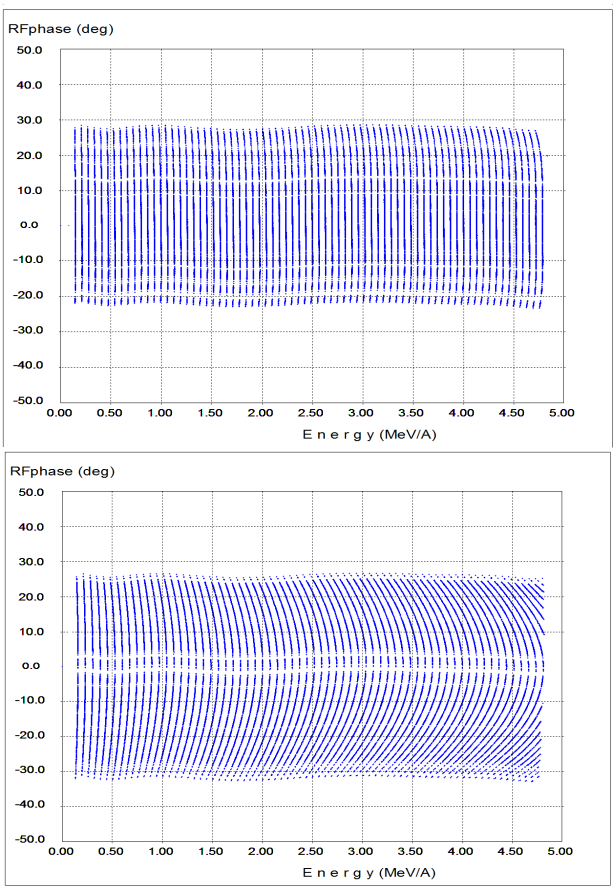

Figure 6. The energy – phase distribution of 48Ca beam along acceleration with and without Flat-Top system.

Figure 6 demonstrates the efficiency of Flat-Top system for 48Ca beam acceleration. The calculations have shown that the extracted beam has a good orbit separation before deflector and energy spread of about 0.5 %. The transition efficiency of acceleration from centre to deflector falls in a range 85 – 98 % and can be optimized by changing the phase and voltage of Flat-Top system.

BEAM EXTRACTION

The extraction system consists of electrostatic deflector and magnetic channel, Figure 7. Deflector is placed at radius 178 cm. Electric field 60 kV/cm deflect the beam and direct it to the benchmark of extracted beam line. The calculation has shown the losses at septum and inside deflector are about 8 % and 31 % respectively. For DC280 extraction system the total transmission factor is expected 60-70 %.

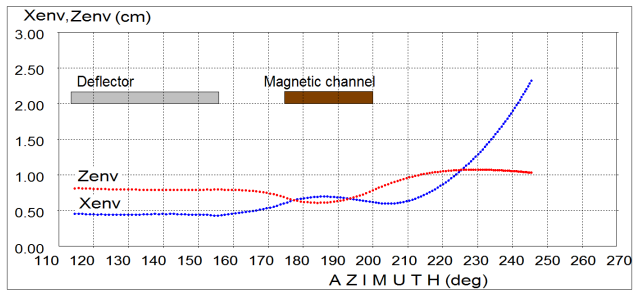

Figure 7: The 48Ca beam transverse dimension from last orbit to the benchmark of extracted beam line.

CONCLUSION

One of the main goals of SHE cyclotron complex DC-280 is an attainment of high intensity of 48Ca beam on a target. Table 2 presents our expectation of cyclotron transition factor range and a beam intensity from ECR, corresponded to 10 pmcA of 48Ca8+ on a target.

Table 2: DC-280 Cyclotron Transition Factor

	min	max
injection	70 %	80 %
acceleration	85 %	98 %
extraction	60 %	70 %
total	36 %	56 %
beam intensity from ECR	220 mcA	140 mcA

The results of calculations show that the designed parameters of DC280 cyclotron complex are achievable and can give a wide possibility to further upgrades.

REFERENCES

[1] G.Gulbekian et al., "Status of DC-280 cyclotron project", In: Proceedings of RuPAC-14, October 2014, Obninsk, Russia.

[2] G.Gulbekian et al., "The project of HV axial injection for DC280 cyclotron at FLNR JINR", In: Proceedings of RuPAC-14, October 2014, Obninsk, Russia.

[3] G.Gulbekian et al., "Flat-Top system of DC280 cyclotron", Particles and Nuclei, Letters, 2013, Volume 10 4(181), JINR, Dubna.

ISBN 978-3-95450-131-1

STATUS OF THE ACCULINNA-2 RIB FRAGMENT SEPARATOR

W. Beeckman, S. Antoine, P. Bocher, M. Cavellier, O. Cosson, F. Forest, N. Huttin, P. Jehanno, P. Jivkov, C. Kellener, A. Kreiss, J.L. Lancelot, M.J. Leray, X. Milpied, R. Riedinger, O. Tasset, SIGMAPHI, Vannes, France
A.S. Fomichev, L.V. Grigorenko, V.I. Kazacha, S.A. Krupko, S.V. Stepantsov, G.M. Ter-Akopian on behalf of the ACCULINNA-2 collaboration, Flerov Laboratory of Nuclear Reactions, JINR, RU-141980 Dubna, Russia

Abstract

Operated since 1996, the ACCULINNA RIB fragment separator has provided scientific results recognized by the nuclear physics community. In 2008 it was decided to build a new separator, ACCULINNA-2 which should deliver RIBs produced with 35-60 A MeV primary heavy-ion beams with $3 \leq Z \leq 36$. It is optimized for large RIB intensities and high precision studies of direct reactions populating nuclear systems near and beyond the drip lines through sophisticated correlation experiments [1].

Late 2011, SIGMAPHI got a global contract for optics check, design, fabrication, installation and alignment of the complete ACCULINNA-2. It includes magnets, vacuum and PS for about 40 magnets, from small correctors to 1-6 tons quads, 14 tons dipoles and 6- and 8-poles. We describe the evolution of the project, from functional needs to working system. Thanks to the early involvement of the industrial partner, the collaborative spirit and the freedom of tradeoff between magnet, PS and vacuum chamber, the final product meets all and even exceeds most requirements while meeting industrial needs for standardization.

The next step of the upgrade, a zero-angle spectrometer is also reported.

INTRODUCTION

FLNR JINR ACCULINNA-2 does not compete with large RIB facilities but rather complement them in a **cost effective** solution, delivering **high intensity RIBs** in the **lowest energy range** accessible to in-flight separators shown in Table 1.

Table 1: Characteristics of in-flight separators. $\Delta\Omega$ and $\Delta p/p$ are angular and momentum acceptances, $Rp/\Delta p$ is the first-order momentum resolution for 1mm size object.

	ACC / ACC-2 FLNR JINR	RIPS / BigRIPS RIKEN	A1900 MSU	FRS / SuperFRS GSI	LISE3 GANIL
$\Delta\Omega$ [msr]	0.9 / 5.8	5.0 / 8.0	8	0.32 / 5.0	1
$\Delta p/p$ [%]	±2.5 / ±3.0	±3.0 / 6.0	±5.5	±2.0 / 5.0	±5.0
$Rp/\Delta p$	1000 / 2000	1500 / 3300	2915	8600 / 3050	2200
$B\rho$ [Tm]	3.2 / 3.9	5.76 / 9.0	6	18 / 18	3.2 – 4.3
Length [m]	21 / 38	27 / 77	35	74 / 140	19 (42)
E [AmeV]	10÷40 / 6÷60	50÷90 / 350	110÷160	220÷1000 / 1500	40÷80
Additional RIB Filter	No / RF-kicker	RF-kicker / S-form	S-form & RF-kicker	S-form / Preseparator	Wien filter

As shown in Fig. 1, its structure is very comparable to that of RIPS in RIKEN [2] with a separation accomplished by means of dipole-wedge-dipole selection. High intensity, DC mode primary beam of U-400M cyclotron hits the solid beryllium, rotated liquid-cooled production target. Normal conducting magnets including 6- and 8-poles are used. The low intensity secondary part of separator is placed outside the accelerator closed area providing good background conditions in the experimental area.

The reader is referred to [3] for the expected beams, sources, instrumentation and planned experimental program and [4] for further reading on the facility.

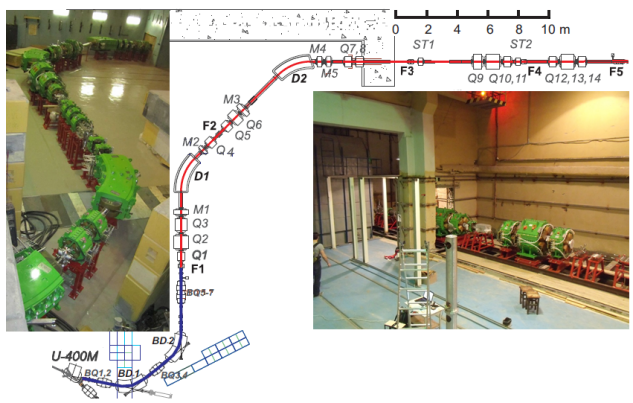

Figure 1: General layout and Room1 magnets, from primary line (blue) dipole BD1 to secondary line (red) quad Q8 (left) and Room2 Q10 to Q14 (right).

OPTIMIZATION

The scope of responsibility for SIGMAPHI was:

1. Optics check and « challenging »
2. All magnets – full electromagnetic calculations, mechanical design and fabrication
3. All power supplies, choice and fabrication
4. All vacuum, pressure calculations, layout, fabrication
5. Installation of all hardware
6. Alignment

Being in control of the 4 first items gives full freedom for an **optimized design** leading to an **energetically efficient** and **cost effective** facility, a too rare, although very interesting opportunity.

Indeed, the usual practice for labs is to have separate contracts for magnets, PS and vacuum, on the basis of *technical* specifications rather than *functional* ones. Every individual supplier is given very little room for change or improvement and must manage to achieve the cost goal

ISBN 978-3-95450-131-1

decided in the offer, itself a result of downward pressure on prices from competition.

In the present situation, the overall contract based on functional needs for all subsystems, with room for proposal from mastering root calculations like optics, allows the search for a system that is optimal for customer and supplier, both working as a unique team, a win-win situation that is itself an optimum in human relationships.

The main candidates for optimizing the system are listed below in arbitrary order. The process being iterative in essence, a given candidate may be revisited many times or changed backwards if this provides a better solution.

- Shaping chambers to reduce bores
- Trading gradient for length
- Standardizing magnets (within limits)
- Trading current for turns
- Trading voltage for copper
- Using standard power supplies

The figures of merit are:

- Global power consumption in operation, a figure that will influence the system during its whole life.
- Global costs i.e. design, material and fabrication costs; they are a "one of" and must be optimized as a whole.
- Standardization which not only drives the costs downwards but also highly simplify maintenance.

Of course, at any step of the process, preserving the functional needs is of paramount importance.

Shaping Chambers to Reduce Bore

Figure 2 shows examples of reducing the quadrupole size.

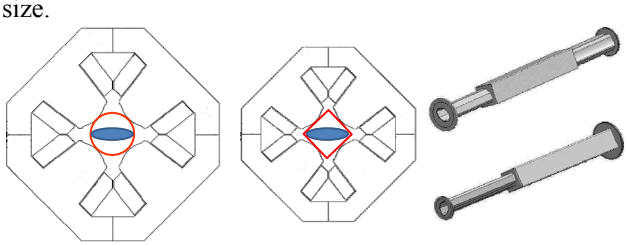

Figure 2: Using square chambers instead of round ones may help reducing the quadrupole size, weight and consumption. Two examples of tailored-to-the beam chambers in Acculinna-2 are presented on the right.

Trading Coils for PS and Gradient for Length

It is very important for the sake of standardization as well as it is for costs, to work with existing PS as the cost of redesign would be a huge part of the total, especially if every single object must be tailored to needs.

The field in gap of an electromagnet depends on the product of the current in one turn of the coil, times the number of turns, i.e. a parameter of the PS only and a parameter of the coil only. Trading turns for current can then bring the current into the proper range for the PS.

For static fields there is no inductive voltage and Ohm's law applies, with the resistance being proportional to the conductor length and inversely proportional to the conductor section. To bring the voltage down one must thus increase the conductor section.

The net effect of these 2 trades is an increase in the coil size and weight and the optimum is reached when the global extra cost – not only in money but also in time, loss of standardization …- of this increase is balanced by the decrease in cost of the PS.

Another possible trade that influences the magnet is the exchange of gradient and magnetic length. To first order, the beam is only sensitive to integrated gradient and, if optics and available space permit, the length can be, within limits, increased to lower the required gradient.

Standardization and Grouping

Standardization groups objects with similar properties. Its advantages are a huge reduction in cost for design, tooling and fabrication and an improved exchangeability and servicing. It has the drawbacks of leading to slightly sub-optimal individual designs and higher material costs. Partial standardization might already help keeping most of the advantages while taming drawbacks.

The 14 secondary quadrupoles offer a good example of partial standardization. The 14 cores are built out of only 3 laminations. Because of very special characteristics, Q1 is unique in its category while the remaining 13 magnets share 2 types of laminations and 2 different lengths, coils and designs for each lamination type as shown in the following Table 2.

Table 2: Grouping the 14 Secondary Quadrupoles

Type	Qty	Quad name	Core	Coil	Design
QM11	1	Q1	A	1	1
QM21	1	Q2	B	1	1
QM22	7	Q4,Q5,Q7,Q8,Q11,Q12,Q14	B	1	1
QM31	1	Q3	C	1	1
QM32	4	Q6,Q9,Q10,Q13	C	1	1
5	14		3	5	5

The success of the complete optimization process is demonstrated by a 41% reduction of the total power wrt initial specification, of secondary quadrupoles (Fig. 3).

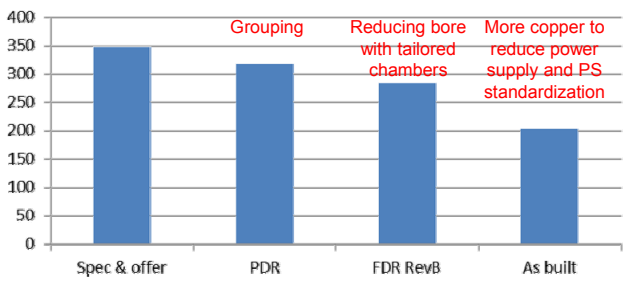

Figure 3: Result of optimization on power consumption of secondary quadrupoles at 4 stages of the process. The main driving term in is indicated on top of each step bar but is not the sole responsible for the achieved result.

ISBN 978-3-95450-131-1

INSTALLATION AND ALIGNMENT

Figure 4: UL Primary beamline, UR 2 quads, 2 6-poles and 1 8-pole in secondary beamline, LL Installation of D1 secondary dipole on its stand, LR End of primary and secondary beamlines with vacuum elements assembled.

In room 2, the existing floor has a maximum resistance of 1 t/m² and must be reinforced to accommodate the local forces exerted by the 2 groups of large quads, as shown in Fig. 5. Figure 4 shows different magnets in rooms 1 and Fig. 6, shows the power supplies.

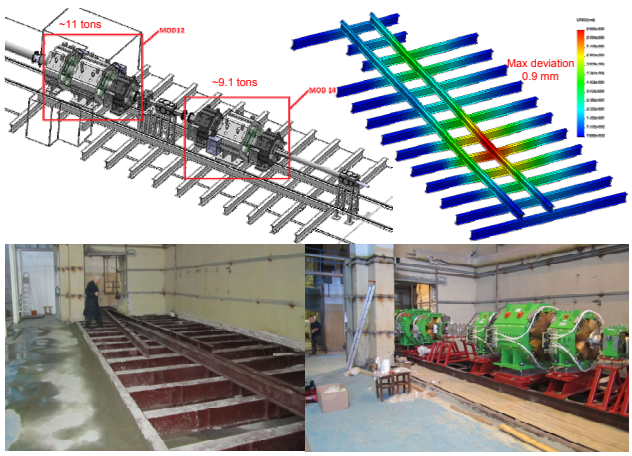

Figure 5: UP beam structure and deformation DOWN floor reinforcement and installed magnets.

Figure 6: The power supply cabinets.

Alignment is performed with a Leica AT401 laser tracker. An accuracy of ±0.1 mm is achieved (see Fig. 7).

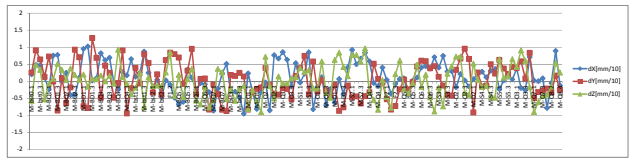

Figure 7: Positioning error (tenths of mm, ±2 full scale) in the 3 coordinates for all objects of Acculinna-2.

ZERO DEGREE DIPOLE

Heavy decay products of the studied exotic nuclei -and decay protons emitted by proton-unstable nuclei- are bent by the well mapped magnetic field. The hit positions of RIB nuclei at F5 are known with 1mm accuracy and one should measure the transverse coordinates passed by the searched heavy decay products and protons after they exit the dipole in at least two planes: 0.5m and 1~2 m from the dipole exit. The nuclei (and protons) are detected by some position-sensitive detectors like MWPC. A TOF detector installed 1~2 m away from the dipole exit provides velocity measurement and, from the measured momentum known from the path in dipole, mass number estimate (Fig. 8).

For neutron-unstable exotic nuclei, the dipole only bends heavy decay products. Neutrons go straight on, passing through the open space allowed by the vacuum chamber and are detected by a plastic-scintillation array installed 2~3 m away from F5.

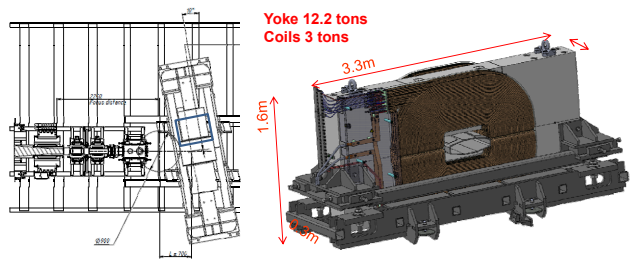

Figure 8: 0° dipole location and mechanical design.

CONCLUSIONS

ACCULINNA-2 is fully installed and commissioned, on time and on budget. First runs should start by end 2015

A global contract for all hardware has opened the possibility for thorough optimization and drastic improvements of the long term operation costs.

The zero-angle dipole is currently under study and production should start soon.

REFERENCES

[1] L.V. Grigorenko, A.S. Fomichev and G.M. Ter-Akopian, Light Exotic Nuclei at JINR: ACCULINNA and ACCULINNA-2, Nucl Phys News, 24(4) 2014, 22.

[2] T. Kubo, In-flight RI beam separator BigRIPS at RIKEN and elsewhere in Japan, Nucl. Instr. and Meth. in Phys. Res. B 204 (2003) 97–113.

[3] S.A. Krupko et al., The status of new fragment separator ACCULINNA-2 project and the first day experiments, EPJ Web of Conferences 66 11021 (2014). aculina.jinr.ru/pdf/epjconf_inpc2013_11021.pdf

[4] Webpage of Acculinna2; aculina.jinr.ru/acc-2.php

ISBN 978-3-95450-131-1

BEAM ALIGNMENT PROCEDURE FOR SCANNED ION-BEAM THERAPY

Y. Saraya#[1], E. Takeshita[2], T. Furukawa[1], Y. Hara[1], K. Mizushima[1], N. Saotome[1], R. Tansho[1], T. Shirai[1] and K. Noda[1]
[1]National Institute of Radiological Sciences, 4-9-1 Anagawa, Inage-ku, Chiba 263-8555, Japan
[2]Kanagawa Cancer Center Hospital, 2-3-2 Nakao, Asahi-ku, Yokohama 241-8515, Japan

Abstract

It's important to control the beam position for the 3D pencil-beam scanning because the position accuracy of the beam has a serious matter on the alignment of the irradiation field. In order to suppress this matter, we have been developed a simple procedure for the beamline tuning. The fluctuation of the beam position is tuned with the steering magnets and bending magnets with monitoring the beam positions using the fluorescent screen monitors. After the tuning, the beam position at the isocenter is checked on the verification system which is consists of the screen monitor and the acrylic phantom. These adjustments are iterated until the deviation for all energies of the beam are within 0.5 mm. We had been performed the beam commissioning using our procedure in Kanagawa Cancer Center.

INTRODUCTION

Heavy-ion beams such as carbon-ion beams are superior in terms of high dose localization and biological effect around the Bragg peak. Three-dimensional (3D) pencil-beam scanning is an ideal irradiation technique to use these fundamental advantages [1]. In 3D pencil-beam scanning, extremely precise dose distribution could be deliver to the tumour since beams interact only with a low material budget in the beamline. Misalignment of the beam position at the patient position causes discrepancy between irradiated dose distribution and prescribed dose distribution. The difference of dose distribution increases unwanted dose to normal tissue. Thus, beam adjustment is important, periodically check of beam position is necessary. We have been developed a simple procedure for beam adjustment.

Adjustment of the beam transfer line is performed by steering beam position to the central orbit. There is difference between central orbit and the reference axis in the treatment room. The reference axis is defined with the acrylic phantom that steel sphere is embedded. The reference axis is called isocenter. Coordinate axes of the CT image and X-ray image are adjusted to the isocenter as well as beam position. All devices concerning patient setup have to be adjusted against the isocenter in order to deliver accurate dose distribution to the tumour. In this paper, we report our beam alignment procedure which we applied to beam transfer line in Kanagawa Cancer Center.

A compact dissemination treatment system of carbon-ion therapy had been constructed at Kanagawa Cancer Center. The carbon-ion scanning system which is designed by National Institute of Radiological Sciences had been installed. We are undertaking the commissioning to start treatment in December this year.

#y_saraya@nirs.go.jp

BEAM ALIGNMENT METHOD

A layout of high energy beam transfer line in Kanagawa Cancer Center is shown in Fig.1. Carbon-ion beams extracted from the synchrotron are transported to four treatment rooms. Two treatment rooms have a horizontal beamline, other two rooms have horizontal and vertical beamlines. In the beam transfer line, some fluorescent screen monitors (SCN) are installed for monitoring beam position and profile. Center of a beam profile is moved to central position at each screen monitor.

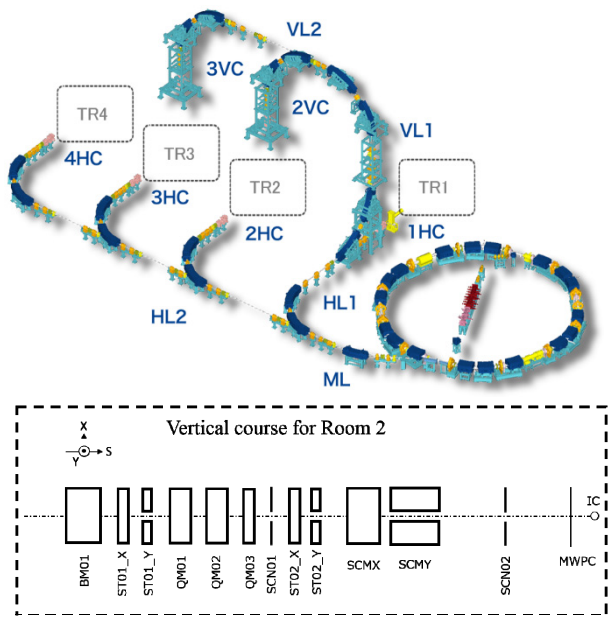

Figure 1: A layout of high energy beam transfer line in Kanagawa Cancer Center. The beamlines are composed of the horizontal and vertical beamlines. A figure surrounded with dotted line is configuration of magnets and SCN on the vertical beamline for Room 2.

In our beam alignment method, we basically steer the beam position using steering magnets. If deflection angle of steering magnet is large, beam position is steered with bending magnet. Since beam duct aperture is most narrow at the bending magnet for deflecting the beam toward upstairs or downstairs, beam adjustment of vertical beam line is performed before the adjustment of horizontal beam line. If the beam position is tuned at upstream SCN,

ISBN 978-3-95450-131-1

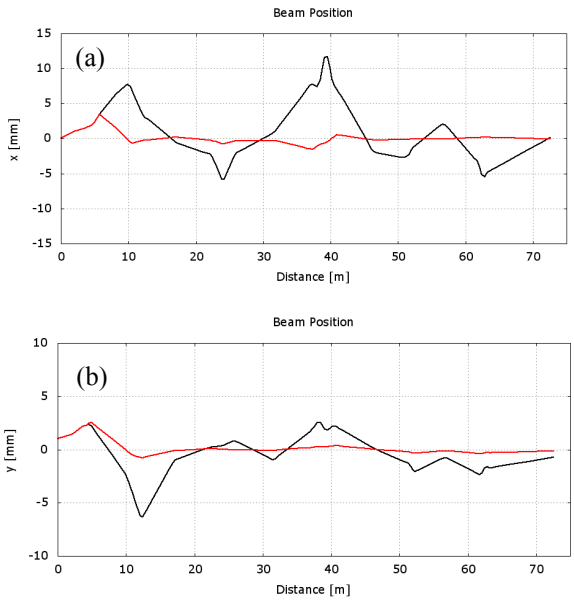

Figure 2: Simulation results of beamline tuning of vertical course for Room2. Horizontal (a) and vertical (b) beam's trajectories are shown. The beam's trajectories before the beamline tuning (Black) and after the beamline tuning (Red) are shown.

we tune the beam position at downstream SCN using a pair of steering magnets which are placed behind of upstream SCN. This rule is to converge beam's trajectory to central orbit. If this rule is applied for tuning, it is required that the distance between downstream SCN and steering magnet is shorter than the distance between upstream steering magnet and SCN [2].

Excitation current of steering magnet for beam adjustment could be calculated if we know strength of the quadrupole magnet and distance of drift space and length of magnet. In Fig. 1, an illustration surrounded with a dotted line represents configuration of magnets and SCNs on the downstream of the vertical beamline. A pair of steering magnets are placed at downstream of the bending magnet. One of the SCN (SCN01) is placed at downstream of the triplet quadrupole magnets. Another pair of steering magnets (ST01) are placed behind of SCN01. Another SCN (SCN02) is placed at downstream of scanning magnets. Multi wire proportional chamber (MWPC) is placed just upstream from isocenter. In this beamline, transfer matrix equation from ST01 to SCN01 is as follows:

$$\begin{bmatrix} \Delta x_{SCN01} \\ \Delta x'_{SCN01} \end{bmatrix} = \begin{bmatrix} m_{11} & m_{12} \\ m_{21} & m_{22} \end{bmatrix} \begin{bmatrix} x_{ST01} \\ \Delta x'_{ST01} \end{bmatrix}$$

where $\Delta x'_{ST01}$ is deflection angle of ST01, Δx_{SCN01} is the measured beam position at SCN01, m_{11}~m_{22} are the transfer matrix elements. The deflection angle ($\Delta x'_{ST01}$) generates deviation of beam position at SCN01 (Δx_{SCN01}). Required deflection angle of ST01 is calculated from measured beam position at SCN01 using the following expression:

$$\Delta x'_{ST01} = -\Delta x_{SCN01} / m_{12} .$$

The last steering magnets (ST02) are tuned by deviation of beam position at SCN02 and $\Delta x'_{ST01}$ in a similar way. Moreover, ST02 are also tuned by deviation of beam position at MWPC. These deflection angles of steering magnets are converted to electric current with measured coefficient.

Figure 2 shows the simulation results when this procedure is applied for beamline tuning. The beam's trajectory could be converged to the central orbit. In this simulation, error incident angles to the transfer line ($\sim$0.1 mrad) and error deflection angles ($\sim 10^{-3}$%) of bending magnets were assigned. In the vertical axis, error of incident position (1 mm) was assigned.

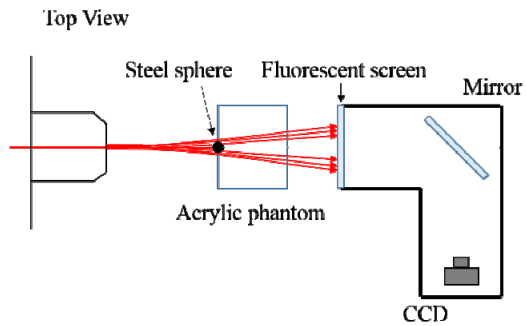

Figure 3: Configuration of the verification system. Light emissions are detected by CCD camera via 45 degree rotated mirror.

Eleven energies (430~140 MeV/u) could be provided due to multiple synchrotron operation. Beamline tuning is carried out for eleven energies, respectively.

Beam position is fluctuated by several factors such as fluctuation of extracted angle from a synchrotron and fluctuation of the excitation current of bending magnet. For every days tuning, it is important to know the magnitude of fluctuation of the beam position. Especially, fluctuation of beam position at MWPC is important. If the magnitude of fluctuation of the beam position is small, every days tuning will be performed only with most downstream steering magnets.

VERIFICATION OF BEAM ALIGNMENT

The measurement for verification of isocentric beam alignment is carried out after the beamline tuning. Figure 3 shows the setup of isocentric beam alignment verification. Verification system consists of acrylic phantom and fluorescent screen monitor which is located behind of the acrylic phantom [3]. Screen monitor is consists of fluorescent screen with terbium-doped gadolinium oxysulfide (Gd2O2S2:Tb) and high-speed 8-bit CCD camera (Type XG-H035M, KEYENCE, JAPAN). Mirror is placed at 45 degree to the beam direction for protecting the camera from radiation damage. The spatial resolution of screen monitor is about 0.2 mm/pixels.

ISBN 978-3-95450-131-1

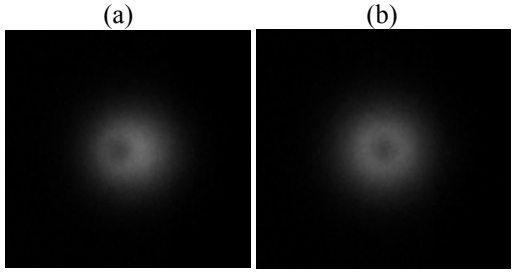

Figure 4: Beam spot images before the beamline tuning (a) and after the beamline tuning (b).

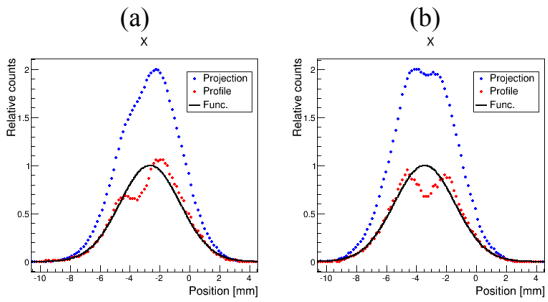

Figure 5: The beam profile before the tuning (a) and after the tuning (b). The red points show normalised line profile. The blue points show normalized projected image. The black line shows the 2D Gaussian distribution.

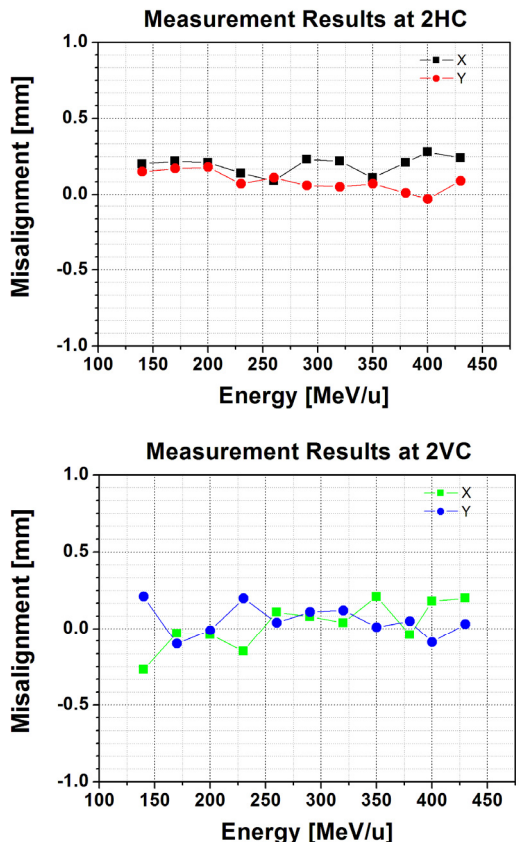

Figure 6: Measurement results of the beam misalignment.

A steel sphere (Ø=2.0 mm) is embedded in the surface of this phantom, and its position is on the reference axis.

Density of steel sphere is larger than that of acrylic. Beams which passed through the steel sphere are more scattered than beams which passed through the acrylic [4]. Thus, the difference of fluence generates a shadow at downstream of steel sphere as shown Fig. 4. Misalignment can be measured as a position difference between centroid of the beam spot and the center of the shadow. The center of the shadow is derived as a centroid of different map between original image and 2D Gaussian distribution. Standard deviations of horizontal and vertical projected image are used as sigma of 2D Gaussian distribution. In the Fig. 5, line profile of beam spot image and 2D Gaussian distribution are represented. The projected image is also represented. These profiles are normalized with maximum value of 2D Gaussian distribution. Excitation currents of steering magnets which are placed most downstream are calculated using measured deviation between the beam spot and shadow. Figure 4 (a) shows the beam spot image before the beamline tuning. The deviation between the beam spot and the shadow is observed. Figure 4 (b) shows the beam spot image after the tuning. The position difference between beam spot and shadow is smaller than that before beamline tuning. If the deviation is over the tolerance of 0.5 mm, beamline tuning is performed again. These adjustments are iterated until deviations for all energies are within 0.5 mm. Figure 6 shows measurement results of beam misalignment at horizontal and vertical course after the tuning. Finally, it was confirmed that misalignments are within $\pm$0.5 mm for all energies.

CONCLUSION

We applied our adjustment procedure to beam transfer line in Kanagawa Cancer Center. Beam positions were tuned at each screen monitor until the deviations are within 0.5 mm. After the beamline tuning, isocentric beam alignment was verified with an acrylic phantom and screen monitor. It was confirmed that misalignments are within $\pm$0.5 mm for eleven energies.

ACKNOWLEDGMENT

The authors would like to express gratitude to staff at the Kanagawa Cancer Center for the skilful operation of the accelerator complex. The authors are grateful to members of the Medical Physics Research Group at NIRS for their warm support and useful discussions.

REFERENCES

[1] T. Furukawa et al., Phys Med Biol. 34 (2007) 1185.
[2] M. Torikoshi et al., in: Proceedings of 1999 Particle Accelerator Conference, New York, 1999, p.1309.
[3] K. Mizushima et al., in: Proceedings of IBIC2012, Tsukuba, Japan, 2012, paper MOPB78, p.256.
[4] J. Barkhof et al., Med. Phys. 26, 2429-2437 (1999).

ISBN 978-3-95450-131-1

A NOVEL METHOD OF BEAM SCANNING OVER A LARGE SAMPLE AREA AT PLF, MUMBAI

C. Rozario, S. Pal*, J.N. Karande,
Pelletron Linac Facility, TIFR, Mumbai, India- 400005
V. Nanal, R.G. Pillay
Dept. of Nuclear and Atomic Physics, TIFR, Mumbai, India - 400005

Abstract

Many applications require uniform irradiation with heavy ion beams and special electric/magnetic devices are employed to scan the beam over the desired target area. We report a novel method of beam scanning using a magnetic steerer in the beam line. Indigenously developed magnetic steerers, comprising a pair of coils with sine-cosine winding, are installed in beam lines at PLF (Mumbai) for correcting the X-Y position of beam. This steerer is adapted to work as a scanner by employing a microcontroller and an interface unit for constant current bipolar power supply. A triangular waveform is applied to control the excitation current for scanning the beam simultaneously in both horizontal (X) and vertical (Y) planes. A programme generates a raster pattern governed by a pre-settable number of X sweeps for each Y sweep. The dwell time at each of X-Y position was adjusted considering the time constant arising due to the inductance of the steerer. Multiple raster scans were used to produce uniform irradiation over the sample. The scanner has been successfully employed for uniform irradiation of GaAs substrate for photoconductive THz applications using ^{12}C beam.

INTRODUCTION

The Pelletron LINAC Facility (PLF), Mumbai is a major centre for heavy ion accelerator based research in India. The Pelletron (14MV) was commissioned in 1989 and the superconducting LINAC booster employing Pb plated QWRs was added in 2007 [1, 2]. Several experimental facilities have been established at this centre to pursue research in nuclear, atomic, condensed matter physics, interdisciplinary areas and applications. For R&D in materials for science applications, the uniform irradiation of high-energy, intense ion beams over a large area is required. It is therefore, desirable to design and develop a relatively simple and inexpensive beam scanner. There are various methods for making uniform irradiation with a well focused pencil like narrow beam over a large area. Some of them involve simply broadening the spatial profile of the beam by defocusing, or scattering, while others employ special electric/magnetic devices for moving the beam over desired sample area. The defocusing method, although simple, can not yield a uniform irradiation over a large area and lacks good reproducibility of dose distribution. The scattering method using double scattering foils and occluding ring [3, 4] results in loss of particle energy and in beam intensity due to the scattering foils. Raster scanning with electromagnetic device is very useful for heavy ions as it does not involve scattering or energy loss. The present paper describes a novel method of beam scanning using a magnetic steerer in the beam line.

SCANNING SYSTEM

The beam scanning system is required to provide beam deflection in both horizontal (X) and vertical (Y) direction. The magnets in the scanning system must have sufficient rigidity to generate the required deflection at the target and should have fast ramping speed to ensure uniform intensity in desired area even for small doses. Moreover, the accuracy and reproducibility are highly essential for preparation of multiple samples. Indigenously developed magnetic steerers, are installed in beam lines for correcting the X-Y position of beam. This steerer is adapted to work as a scanner by employing a microcontroller and an interface unit for constant current bipolar power supply. The steerer consists of standard 36 slotted motor-stator housing with two independent pairs of sine and cosine windings, which produces a homogeneous field in the X and Y directions over a large volume. The vacuum chamber is cylindrical in shape with ~10 cm diameter and ~15 cm long. The sine-cosine winding pairs are connected in parallel to reduce the effective coil inductance. The field is found to be homogeneous (better than 1 %) in central region of 50 mm radius over an effective length of ~ 9 cm. Each doublet coil can take a maximum current of 10 A, which gives a B_{max} = 0.5 T along the axis of the steerer. The inductance of the coil is 50 μH and time constant is 15 μsec. Figure 1 shows a photograph of steerer magnet and schematic of the beam scanning system.

*sanjoy.pal@tifr.res.in

ISBN 978-3-95450-131-1

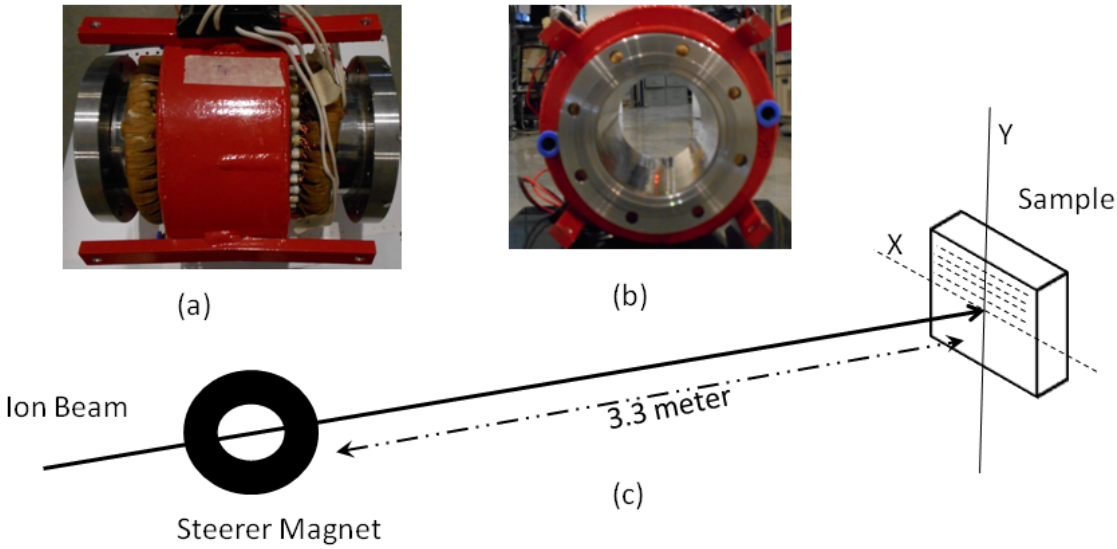

Figure 1: Steerer magnet showing (a) side view and (b) front view; and (c) schematic diagram of the beam scanner.

MAGNET CONTROL SYSTEM

The inductive load is best driven by the voltage controller with constant current drive. A pair of bipolar constant current power supplies 35V, ±15A, is used to energize the steerer. Two banks of complementary emitter follower transistors in Push-Pull configuration are used for a smooth transition from positive to negative current. For given voltage setting, the power supply provides a constant current (±0.03%) irrespective of the load resistance, within the compliance limit.

Figure 2 shows a block diagram of the scanner control system. The scanner is developed using a Silicon Lab C8051F020 microcontroller, which is a package containing a 8051 microcontroller (with 20 MHz clock), 64K bytes of flash memory, 4K RAM and a set of peripherals like 12-bit ADC, 12-bit DAC and digital I/Os. The DAC is used to control the current and the voltage of the power supply, while the ADC is used to sense the voltage and current from the power supply. In addition, the digital I/Os are used to operate the power supplies (on/off), enable the scan mode and provide the status display through a LED indicator. The control/sense signals of the power supply are not directly compatible with the microcontroller. Therefore, an interface card is developed for gain adjustment and level shifting for suitable conversion of the power supply signals. Programming of the 8051 is achieved using an open source Small Device C Compiler (SDCC). The SDCC 8051 tools are integrated into the Silicon Lab IDE (Integrated Development Environment). The IDE provides an efficient development environment with compose, edit, build, download, and debug operations integrated into the same program.

A triangular waveform is applied to control the excitation current for scanning the beam simultaneously in both X and Y planes. A programme generates a raster pattern governed by a pre-settable number of X sweeps for each Y sweep. The dwell time at each of X-Y position was adjusted considering the time constant arising due to the inductance of the steerer.

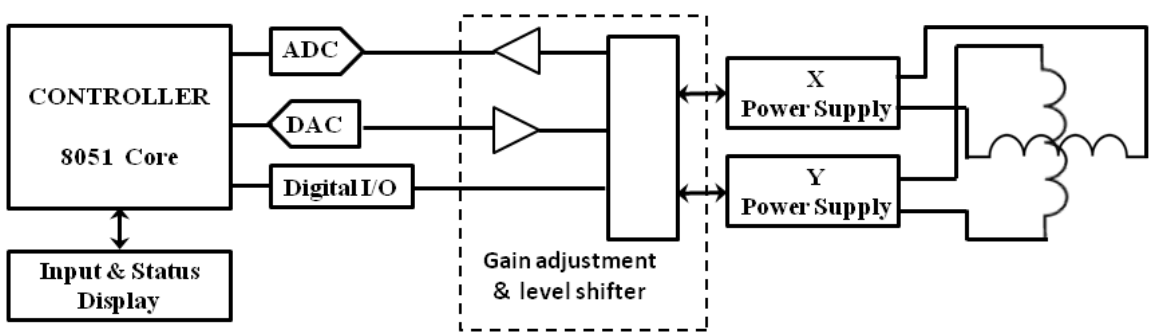

Figure 2: Block diagram of the beam scanner controller.

ISBN 978-3-95450-131-1

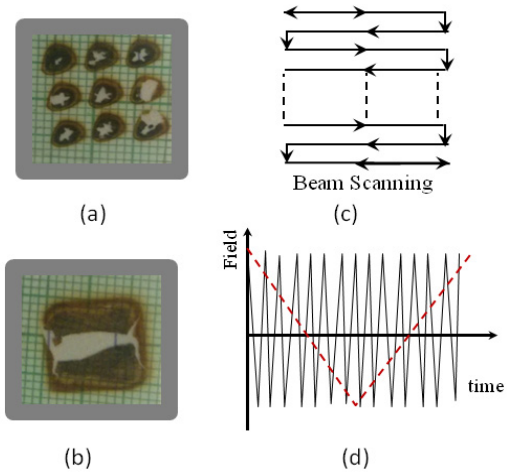

Figure 3: Picture of beam spots obtained on graph paper at target position with ^{12}C beam, corresponding to (a) different steerer current settings and (b) complete scan. (c) Scanning pattern and (d) the magnetic field amplitude as a function of time for X deflection (black solid line) and Y deflection (red dotted line).

Multiple raster scans were used to produce uniform irradiation over the sample.The scanned area on the target is controlled by adjusting the maximum current in the coil. Figure 3 shows a typical beam spot on graph paper at target position with ^{12}C beam (E = 33.5 MeV), different positions correspond to different steerer current settings. The scanning was done with horizontal frequency of 80 Hz and the vertical frequency of 0.2 Hz. In the present setup, the maximum area of 15 x 15 mm^2 can be scanned on a sample.

CONCLUSION

We have developed a simple method of beam scanning using a X-Y magnetic steerer in the beam line. A triangular waveform is applied to control the excitation current in the steerer for scanning the beam simultaneously in both horizontal (X) and vertical (Y) planes. A programme generates a raster pattern governed by a presettable number of X sweeps for each Y sweep. The scan area, step-size and scanning speed are adjustable parameters. The dwell time at each of X-Y position was adjusted considering the time constant arising due to the inductance of the steerer. Typically, a beam scan on a ~10 x 10 mm^2 is achieved in ~5 sec. The scanner has been successfully employed for uniform irradiation of GaAs substrate for photoconductive THz applications using ^{12}C beam [5, 6].

ACKNOWLEDGMENT

The authors would like to thank Mr. A.A. Shinde, Mr. S.P. Singh, Ms. P.A. Dhumal, Mr. M.E. Sawant, Mr. M.S. Pose and other PLF members for assistance during the assembly and testing of the beam scanner system; and Prof. S.S. Prabhu for his support.

REFERENCES

[1] V. Nanal et al., "Operational experience of superconducting Linac booster at Mumbai", http://accelconf.web.cern.ch/AccelConf/HIAT2009/papers/th-07.pdf; HIAT09, Venice (Italy) 2009.

[2] V. Nanal et al., "Extension of superconducting linac operation to lighter beams", http://accelconf.web.cern.ch/AccelConf//HIAT2012/papers/po06.pdf; HIAT12, Chicago, (IL USA) 2012.

[3] Y. Takada, "Dual-ring double scattering method for proton beam spreading," Japan J. Appl. Phys., 33, 353-359 (1994).

[4] E. Grusell, A. Montelius, A. Brahme, et al., "A general solution to charged particle beam flattening using an optimized dual-scattering-foil technique, with application to proton therapy beams," Phys. Med. Biol., 39, 2201-2216 (1994).

[5] Abhishek Singh, Sanjoy Pal, Harshad Surdi, S. S. Prabhu, Vandana Nanal and R. G. Pillay "Highly Efficient and Electrically Robust Carbon Irradiated Semi-Insulating GaAs Based Photoconductive THz Emitters" Appl. Phys. Lett. 104, 063501 (2014); doi:10.1063/1.4864623.

[6] Abhishek Singh, Sanjoy Pal, Harshad Surdi, S. S. Prabhu, S. Mathimalar, Vandana Nanal, R. G. Pillay, and G.H. Döhler "Carbon Irradiated Semi-Insulating GaAs For Photoconductive Terahertz Pulse Detection" Optics Express 23(5), 6656 (2015); doi:10.1364/OE.23.006656.

ISBN 978-3-95450-131-1

NEW HIGH-ENERGY BEAM TRANSPORT LINE DEDICATED TO BIOLOGICAL APPLICATIONS IN RIKEN RI BEAM FACTORY

N. Fukunishi#, M. Fujimaki, M. Komiyama, K. Kumagai, T. Maie, Y. Watanabe, T. Hirano, T.Abe
Nishina Center for Accelerator-based Science, RIKEN, 2-1 Hirosawa, Wako, Saitama, Japan

Abstract

The existing beam transport system of the RIKEN RI Beam Factory has been extended to deliver higher energy beams to the existing irradiation port for biological applications in order to breed seaweed using an ion-beam breeding technique widely used for flowers and crops. The maximum magnetic rigidity of the new branch beam line is 4.4 T-m. As a result, a 160-MeV/nucleon argon beam is available for seaweed breeding experiments. The new beam line was commissioned in January 2015 and we confirm that the design specifications have been met.

INTRODUCTION

Heavy-ion beams are widely used for biological applications thanks to their high biological effectiveness. The RIKEN Nishina Center has used energetic heavy ions as an effective tool inducing mutations of flowers, crops, and microbes [1]. Selective breeding is conducted from irradiated samples and many commercially useful plants have been produced. The beams used in these experiments are 135-MeV/nucleon carbon, nitrogen and neon beams, a 95-MeV/nucleon argon beam and a 90-MeV/nucleon iron beam. These are obtained from the RIKEN Ring Cyclotron commissioned in 1986 [2]. Linear Energy Transfer (LET) is proportional to the second power of the ion's charge for the ions having the same velocity. Hence we can control damage to the sample by changing ion species. The LET dependence of biological effects has been demonstrated by modern genetic analysis in which the pattern of gene deletion was shown to differ among ion species [3].

The difference between our method and cancer therapy is that the Bragg peak region is not used because too much damage leads to a low survival rate of irradiated samples and would be less effective for obtaining useful new breeds. Using the Bragg peak region would also create a further difficulty. In these breeding experiments, the LET-dependence of the mutation effectiveness should be precisely determined to develop a database, essential for efficient breeding. But an ion's LET changes greatly within the sample irradiated if we use the Bragg peak region of the ion. The only exception is the irradiation of very thin samples, but these are not always available.

The effectiveness of ion-beam breeding has been established for a wide variety of plants. Based on this success, a new project has started, in which ion-beam breeding is applied to seaweeds, such as wakame (*Undaria pinnatifida*) and kombu (*Saccharina japonica*). Wakame is a special product of the Tohoku region in Japan, which was seriously damaged by a big earthquake in 2011. In applying this technique to seaweed, heavier ions, such as argon and iron, were expected to be more effective than lighter ions; but these ions do not have sufficient energies to form nearly flat LET distributions. To solve this problem, we decided to use a higher-energy cyclotron: the Intermediate-stage Ring Cyclotron (IRC) [4]. The bending limit of the IRC is 980 MeV, much higher than that of the RRC (540 MeV). The maximum beam energy of the IRC for medium-heavy ions is 160 MeV/nucleon, also much higher than the 95 MeV/nucleon of the RRC. This energy upgrade results in a nearly 3-fold increase of the ion range in the assumed experiments with argon ions. However, the existing beam delivery system of the RIBF cannot deliver a beam extracted from the IRC to the existing irradiation port where a fully automated irradiation system is installed [1]. Hence, the existing beam delivery system has been extended to meet this demand.

HIGH-ENERGY BEAM LINE

Beam Line Description

The relevant part of the RIBF beam delivery system is shown in Fig. 1. A beam extracted from the IRC is deflected by the DAKR dipole magnet in order to separate the beam from the existing SRC-injection line. The SRC (Superconducting Ring Cyclotron) is the final-stage accelerator of the RIBF. The section from IRC extraction to DMR2 makes the dispersive IRC beam doubly achromatic. The beam is bent up by DMR3 and bent down by DMR4 to shift the beam vertically by 3 m to compensate for the floor level difference. Here, the beam is doubly achromatic in the vertical direction. The section from DMR5 to DMR6 forms an achromatic bending system of 90°. The section from DMR7 and DMR8 is also doubly achromatic. After that, the beam line is joined to the existing beam delivery fishbone at the DMA1. The section from just after the DMR2 to DMR6 is not newly constructed but uses the existing IRC bypassing beam line in reverse. The IRC bypassing beam line was constructed to inject a beam accelerated by the RRC directly into the SRC, skipping the IRC, in order to perform light-ion experiments, especially polarized deuteron experiments. Faraday cups are added to the IRC bypassing beam line to adapt it for the present purpose.

The ion optical design was made by using TRANSPORT code. The maximum magnetic rigidity was 4.4 T-m, slightly smaller than the maximum magnetic rigidity of the IRC (4.57 T-m). The beam envelopes

#fukunisi@ribf.riken.jp

ISBN 978-3-95450-131-1

obtained are shown in Fig. 2. No special ion-optical requirements are necessary for the section from IRC extraction to the confluent point DMA1 because the beams are used for irradiation experiments and a system dedicated to producing a uniform irradiation field of 10 cm in diameter already exists. However, to make beam tuning easier, point-to-point and waist-to-waist imaging is imposed from the point just after the IRC to the final irradiation point.

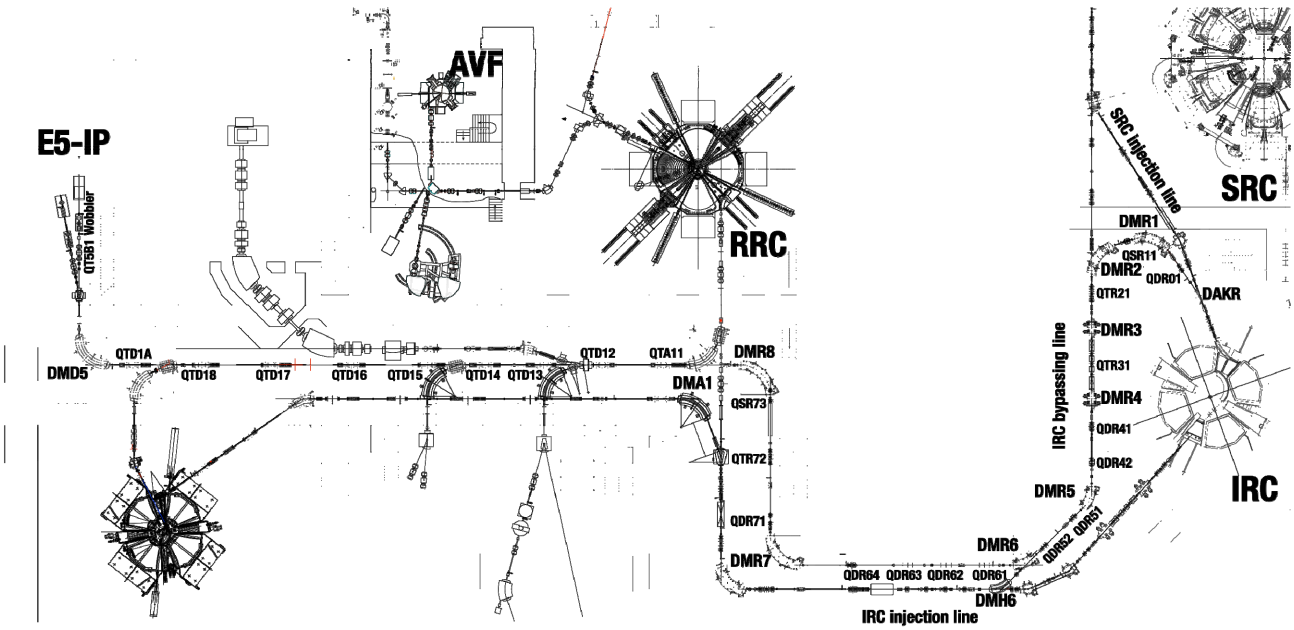

Figure 1: Layout of the RIBF beam transport system. Beams extracted from the IRC are transported to DMA1 via a new beam line and the existing IRC bypassing line. Beams are then transported to the existing irradiation port (E5-IP) through the existing beam delivery fishbone.

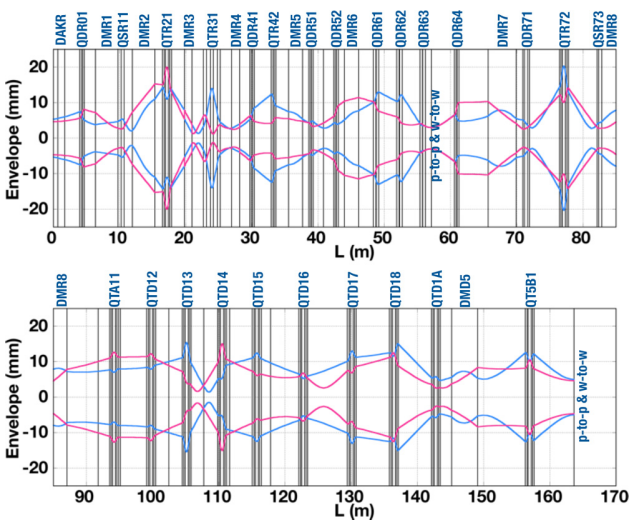

Figure 2: Beam envelopes of the high-energy beam line. Blue and magenta lines indicate horizontal and vertical beam envelopes, respectively, for a beam with $\varepsilon_{H,V} = 5\pi$ mm-mrad.

Subsystem

The specifications of the magnets are summarized in Tables 1 and 2. All of them are conventional normal conducting magnets. To reduce costs, old magnets are reused here as much as possible. In addition, some quadrupole and steering (correction) magnets are temporarily moved from one of the neighboring beam lines. The power supplies exciting the magnets used in the new beam line are not newly fabricated because we can use the sufficient number of existing power supplies that are free from exciting the magnets used in the new beam line. Beam vacuum is obtained using turbo molecular pumps with a pumping speed of 220 L/s, supplemented by rotary pumps. The beam monitors are Faraday cups for beam intensity measurements and wire scanners for beam profile measurements. These monitors are newly designed taking cost reduction and maintainability into account. Two kinds of vacuum chamber have been newly designed for vacuum pumping and beam monitoring. These devices are all controlled remotely and the control system of the new beam line was integrated into the existing EPICS-based RIBF control system.

Table 1: Specifications of dipole magnets used in the high-energy beam line.

Magnet	Bending radius (m)	Bending angle (deg.)	Gap (cm)	B_{max} (T)	Edge angle (deg.)
DAKR	4.0	15	6	1.5	7.5
DMR1, 2	2.7	72.5	6	1.65	25
DMR3, 4	2.7	25	6	1.64	12.5
DMR5, 6	2.7	45	6	1.64	15
DMR7, 8	2.7	90	6	1.65	25
DMD5	2.5	90	6	1.78	26.5

ISBN 978-3-95450-131-1

Table 2: Specifications of Quadrupole Magnets

Magnet type	Length (cm)	Bore diameter (mm)	Field Gradient (T/m)
Q220	22	70	16
Q420	42	70	16
2.5-inch Q	36	63.5	15

BEAM COMMISSIONING

Beam commissioning was on January 24 and 25, 2015. A 160-MeV/nucleon-argon beam was obtained using a non-orthodox three-stage acceleration mode in which energy degradation between the RRC and the IRC was necessary because such a beam was not part of the original RIBF design. The injector is the AVF cyclotron [5], which accelerates argon beams up to 4 MeV/nucleon. The beam extracted from the AVF is charge-stripped there and injected into the RRC. After the RRC, a thick carbon disk induces additional charge stripping and energy degradation. The efficiency of this process is 100%, although there is sizable emittance growth. However, this is not important because the irradiation experiments use faint beams and we can select as small a part of the emittance as we like.

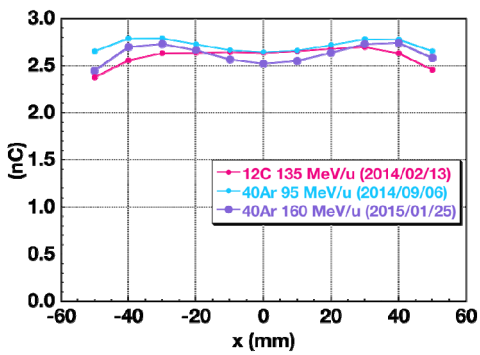

Figure 3: Uniformity of irradiation field for a 160-MeV/nucleon argon beam. X=0 corresponds to the center of the irradiation field.

After extracting a 160-MeV/nucleon argon beam from the IRC, the commissioning of the beam line was begun. Pre-determined magnet excitation currents worked well and the beam was transported to the confluent point (DMA1) within 30 min. Beam tuning improved the transmission efficiency from IRC extraction to the irradiation port to 100%. After that, we formed a uniform irradiation field using two wobbler magnets and a beam scatterer made of a gold film. Figure 3 shows the uniform irradiation field obtained in comparison with two widely used beams. The depth-dose curve of the 160-MeV argon ions was obtained using a calibrated ionization chamber with various beam energies degraded by a set of aluminum plates with various thicknesses that are used for the routine dose calibration. The results are shown in Fig. 4 compared with the result of the PHITS [6] simulation. The measured ion range in the aluminum degrader is slightly shorter than the PHITS simulation. This difference cannot be explained by the estimated uncertainty in the beam energy (~1%) of the IRC and a direct energy measurement is necessary to fix this small discrepancy.

In conclusion, we have successfully transferred the high-energy argon beam to the existing irradiation port as expected and, just after commissioning, wakame and kombu samples were irradiated with the high-energy argon beams.

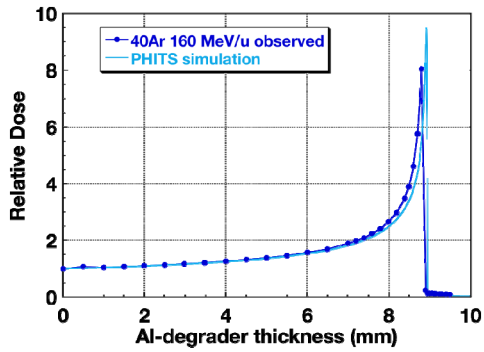

Figure 4: Depth-dose curves for a 160-MeV/nucleon argon beam.

ACKNOWLEDGEMENTS

We would like to thank the accelerator operators of SHI Accelerator Service Ltd. for their dedication in installing many beam line components. A part of the present work was supported by the Tohoku Marine Science Center project from MEXT.

REFERENCES

[1] T. Abe, H. Ryuto and N. Fukunishi, “Ion beam radiation mutagenesis”, Plant Mutation Breeding and Biotechnology, edited by Q.Y. Shu, the Joint FAO/IAEA Programme, pp. 95 – 102. (2010).

[2] Y. Yano, Proc. 12th Int. Conf. Cyclotrons and their Applications, Berlin, Germany (1989) p. 13.

[3] T. Hirano et al., “Molecular nature of mutations induced by high-LET irradiation with argon and carbon ions in *Arabidopsis thaliana*”, Mut. Res. **735**, 19-31 (2012).

[4] J. Ohnishi et al., Proc. 17th Int. Conf. on Cyclotrons and Their Applications, Tokyo, Japan (2004) p. 197.

[5] A. Goto et al., Proc. 12th Int. Conf. Cyclotron and their Applications, Berlin, Germany (1989) p. 51.

[6] T. Sato, K. Niita, N. Matsuda, S. Hashimoto, Y. Iwamoto, S. Noda, T. Ogawa, H. Iwase, H. Nakashima, T. Fukahori, K. Okumura, T. Kai, S. Chiba, T. Furuta and L. Sihver, Particle and Heavy Ion Transport Code System PHITS, Version 2.52, J. Nucl. Sci. Technol. **50**:9, 913-923 (2013).

ISBN 978-3-95450-131-1

PROPOSAL FOR A HIGH POWER DEUTERON CYCLOTRON AT RISP

A. Adelmann[1], J.R. Alonso[2], L. Calabretta[3],A. Calanna[3], D. Campo[4], J. Yang[5], J.W. Kim[6], S. Jeong[6]
[1]PSI, Villigen, Switzerland, [2]MIT, USA
[3]INFN-LNS, Catania, Italy, [4]INFN-LNL, Legnaro, Italy
[5]CIAE, Beijing, China, [6]RISP, Daejeon, Korea

Abstract

We are proposing a compact isochronous cyclotron able to accelerate a high intensity beam with q/A 0.5 up to the final energy of 60 MeV/A. When accelerating H_2^+, it can be used as a driver for a high-intensity anti-neutrino source, as in the IsoDAR experiment. We believe that this type of cyclotron source placed near a neutrino detector, like Reno_50 or KamLAND would give impressive sensitivity to sterile neutrino searches and to electroweak measurements using neutrino-electron scattering. Here we present the idea of a modified IsoDAR cyclotron as the primary accelerator to drive the ISOL system of Rare Isotope Science Project (RISP) at Daejeon (Korea). The IsoDAR cyclotron is able to accelerate any ion with charge to mass ratio q/A=0.5 so deuterons or fully stripped light ions can be accelerated with high beam current and delivered to the production target for radioactive ions of RISP.

INTRODUCTION

The IsoDAR neutrino source [1] consists of a (q/A=0.5) cyclotron delivering 60 MeV protons to a ^{9}Be target. IsoDAR can use the same cyclotron design as the injector cyclotron for the two-cyclotron system for the 800 MeV DAEδALUS experiment [1, 2].

This paper describes a design study of the IsoDAR cyclotron [3], the features of this accelerator and the possible uses in other research fields. In particular, we are exploring the use of the IsoDAR cyclotron to accelerate a deuteron beam up to an energy of 40 MeV/A to fulfill the requests of RISP (the Rare Isotope Science Project) in Daejon, Korea. In particular, RISP is evaluating the advantage of using a high power deuteron beam to strike a target converter producing an intense neutron flux to irradiate a target of ^{238}U. The rare isotopes produced by the neutron-induced fission are then analyzed and reaccelerated. A modified IsoDAR cyclotron could not only deliver a proton beam through the acceleration of the H_2^+, but also fully-stripped light ions like carbon and oxygen. These different projectiles allow the use of the most convenient target-beam combination to produce different radioactive species. Here we focus on how the IsoDAR cyclotron can satisfy the needs of RISP.

ISODAR CYCLOTRON FEATURES

The cyclotron designed for the IsoDAR experiment is very similar to the one designed for DAEδALUS injector. It is a 4 sector normal conducting machine able to provide H_2^+ beams, and more generally, beams with q/A=0.5 up to an energy of 60 MeV/A. Several reasons have convinced the IsoDAR collaboration that H_2^+ was the right ion to accelerate.

The binding energy of the electron in H_2^+ is 2.75 eV, this eliminates the Lorentz stripping problem. The acceleration of a molecular beam like H_2^+ needs a better vacuum, of the order of 10^{-5} Pa, to minimize the interaction with the residual gas. This vacuum level is within the range of existing machines.

Furthermore, H_2^+ acceleration reduces space-charge effects. A simple way to see this is to note that for every two protons injected at the center, there is only +1 electric charge. Thus, we have 5 mA of H_2^+ while we provide 10 mA of protons to the target.

Table 1: Details of the IsoDAR Cyclotron Design

Design element	Design value	Design element	Design value
E_{max}	60 MeV/A	E_{inj}	35A keV
R_{ext}	1.99m	R_{inj}	55 mm
<B> @R_{ext}	1.16 T	<B> @R_{inj}	0.97 T
Sectors	4	Hill width	25.5° - 36.5°
Valley gap	1.8 m	Pole gap	80-100 mm
Outer diameter	6.2 m	Full height	2.7 m
Cavities	4	Cavity type	λ/2 double gap
Harmonic	4th	frequency	32.8 MHz
Acc. Voltage	70 – 240 kV	Power /cavity	310 kW
ΔE/turn	1.7 MeV	Turns	95
ΔE/turn @R_{ext}	<20 mm	ΔR/turn @R_{inj}	>56 mm
Coil size	200x250 mm^2	Current density	3.617 A/mm^2
Iron weight	450 tons	Vacuum	<10^{-7} mbar
Beam Injection	By spiral inflector	Beam Extraction	electrostatic deflector

A measure of the space charge effect is the generalized perveance K [4]:

$$K = \frac{qI}{2\pi\epsilon_0 m\gamma^3\beta^3}$$

where: q and m are the charge and mass of the particle, β and γ are the usual relativistic parameters, ε_0 is the vacuum permittivity, and I is the beam current.

ISBN 978-3-95450-131-1

The K value of a 5 mA H^{2+} beam injected at 70 keV (35 keV/amu) is quite similar to that of 2 mA of protons (or H-) injected at 30 keV. As this H- performance has been demonstrated in commercial cyclotrons today, we expect that the required H2+ current should be achievable.

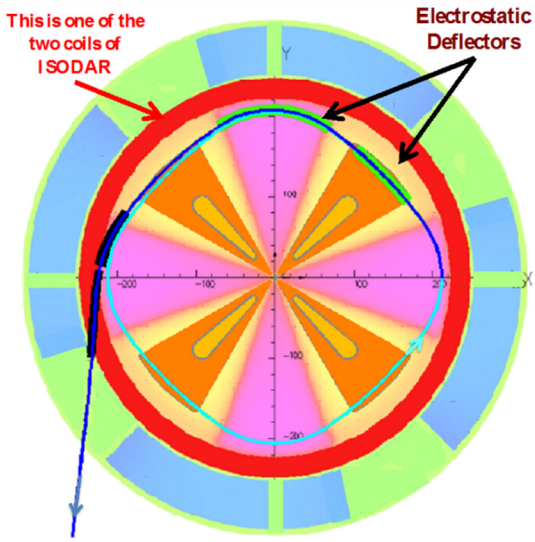

Figure 1: Sketch of IsoDAR cyclotron median plane.

On the other hand, high intensity ion sources of H_2^+ are still under development. A summary of the machine parameters is reported on Table 1.

Figure 1 shows a schematic cut at the median plane. In particular, the coils are in red, the hills in pink, the return yoke in blue and the RF cavities in orange.

Also shown is the last closed orbit in cyan and the extracted one in blue. Two electrostatic deflectors (ED) give a radial kick to the beam to reach the extraction channel. In black are sketched the two magnetic channels, whose function is to focus and slightly steer the beam locally correcting the magnetic field.

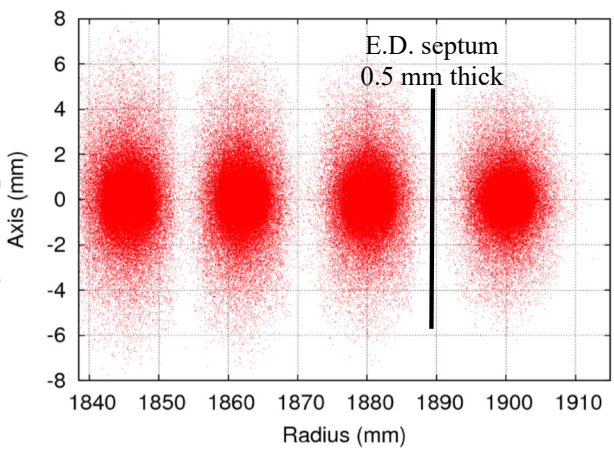

Figure 2: Snapshot of the last 4 accelerated turns of a 60 MeV/A IsoDAR cyclotron in front the E.D. entrance. The separation between the turns increases from 14 mm up to 20 mm.

The key point of a high current cyclotron is the extraction efficiency of the beam that must be about 99.98%. In Fig. 2 shows the particle distribution on the last 4 orbits accelerated in the IsoDAR cyclotron. This simulation was performed using the OPAL code [5] and takes into account of the space charge effects.

Although the beam halo size is of about 15 mm the inter-turn separation between the last two turns is 20 mm. So it is expected that the septum of the electrostatic deflector placed at R=1890 mm and having thickness of 0.5 mm should intercept only 0.02% of the beam particle that correspond to a beam power of 120 W for a 5 mA of H_2^+ at 60 MeV/A. The large inter-turn separation is due to the high energy-gain at the end of acceleration, about 1.9 MeV/turn, that gives about 14 mm of separation. The additional 6 mm produced by the orbit precession induced by a slow crossing of the ν_r=1 resonance, see fig. 3. This is achieved by a careful design of the cyclotron pole boundary, see Fig.3.

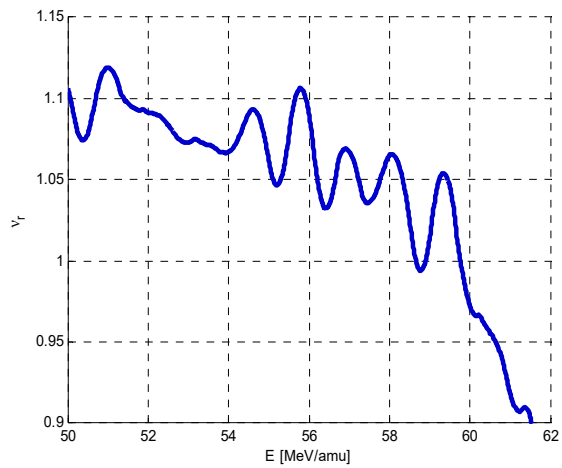

Figure 3: Plot of ν_r vs E showing the crossing of the resonance ν_r =1 around 60 MeV/A.

HOW ISODAR CYCLOTRON SUITS RISP NECESSITIES

The use of the IsoDAR cyclotron to accelerate and deliver a 1 mA D^+ beam is quite straightforward and much easier than the acceleration of the 5 mA of H_2^+. Indeed the space charge effects are smaller, ion sources able to produce a deuteron beam in excess of 10 mA already exist and last but not least, the acceleration of a bare nucleus like the D^+ instead of the molecular beam as the H_2^+ allows operation at a relaxed vacuum level. The expected beam power losses for 1 mA of H_2^+ beam along the acceleration path from 0.5 MeV/A up to 40 MeV/A will be below 30 W, see Fig.4, if the working vacuum stays around $5*10^{-6}$ Pa and the cyclotron is equipped with 4 RF cavities. The cavity voltage used in the simulation is assumed to be equal to the average value of 140 kV, a pessimistic value compared to the expected real voltage profile that should

ISBN 978-3-95450-131-1

rise from 70 kV at inner radii up to 240 kV at the extraction radius of R=1.9 m. The beam power losses are about 30 W and 60 W, respectively at 40 and 60 A MeV. The corresponding beam intensity losses are respectively 1.4 μA and 1.6 μA.

It is important to emphasize that when comparing IsoDAR to RISP, several parameters are relaxed and that makes the extraction easier. Firstly, at 40 MeV/A the turn separation is naturally larger for the same voltage versus radius profile. Secondly, the maximum accelerating voltage can be reduced to 200 kV instead of the 240 kV used for IsoDAR. Moreover, the same number of microamps lost on the septum translates into less power. This has even more impact due to the fact the beam current is less (1 mA vs 5 mA).

In the case of the acceleration of the bare deuteron the expected working vacuum pressure can be relaxed to (0.5- 1)*10^{-4} Pa. The interaction of the beam with the residual gas is the main source of the beam losses. The ED's are the other source of beam loss. From the previous considerations, if we scale the beam power intercepted by the septum of the ED at of 1 mA a deuteron beam at 40 MeV/A, the expected power lost should be in the order of 16 W.

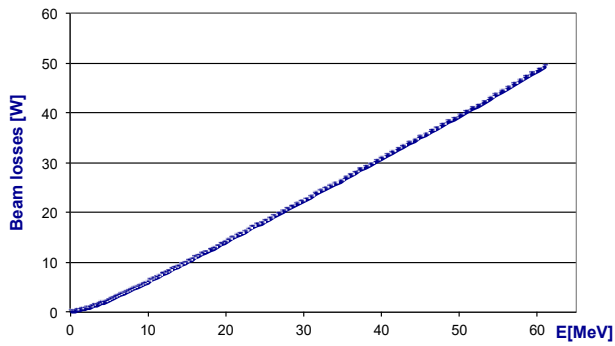

Figure 4: Beam losses of H_2^+ along the acceleration up to 60 MeV/A. The gas pressure is 5*10^{-6} Pa and the energy gain-per-turn about 1.4 MeV.

The radial size of an IsoDAR-like cyclotron to deliver the deuteron beam for the RISP at 40 MeV/A will be 15% smaller than IsoDAR cyclotron. The extraction radius will be reduced to 1.63 m. The acceleration of a deuteron nucleus avoids any problem of electromagnetic dissociation due to the high magnetic field and also reduces the interaction with the residual gas. Assuming a working vacuum of 10^{-4}-10^{-5} Pa the expected amount of particle losses is about 30 W for a 1 mA deuteron beam at 40 MeV/A.

Despite the fact that the expected beam full power losses will stay below 50 W, the flux of neutrons produced will still be quite high. For this reason, it is desirable to find solutions to mitigate the activation of the machine. In particular, the dees of the cavities made of copper, can be a major source of activation. To mitigate this problem the dees of the cavities could be made out of aluminum, or alternatively, a 5 mm thick layer of aluminum could cover the surfaces of the dees in the vicinity of the median plane.

CONCLUSIONS

The study performed for the IsoDar cyclotron is very useful to evaluate the possibility of a smaller version dedicated mainly to the acceleration of a deuteron beam at 40 MeV/A, with a beam current of 1 mA. Existing ion sources [6,7] are able to produce sufficient beam current of deuteron or of H_2^+ to satisfy the required beam current of RISP. If one wished to achieve currents of about 50 particle μAmp (pμA) for light ions it is mandatory to start with a new-generation ECR ion source that could produce beam currents of about 50-100 pμA for fully stripped light ions such as C^{6+} and O^{8+}. However, the typical injection efficiency into a Cyclotron is about 10% of the continuous beam, which could be increased up to 30% using a well-designed Buncher. The injection efficiency could be further increased up to 80-90% using an RFQ pre-accelerator to couple the ion source to the cyclotron. The RFQ could be installed in the injection central hole of the cyclotron. A interesting investigation of this option has been presented recently [8].

Contacts are in progress with the main cyclotron-building companies to determine the interest and costs to build this cyclotron.

REFERENCES

[1] J.M. Conrad and M.H. Shaevitz, Phys.Rev.Lett. 104,141802 (2010).
[2] A. Bungau, et al, Phys. Rev. Lett. 109, 141802 (2012).
[3] D. Campo et al., "A Compact High Intensity Cyclotron Injector for DAEδALUS Experiment", IPAC New Orleans 2012, MOPPD026.
[4] M. Reiser, Theory and design of charged Particle Beams, Wiley series in Beam Phys. And Acc. Tech.
[5] J.J. Yang et al., "Beam dynamics simulation for the high intensity DAEδALUS cyclotrons", Nucl. Ins. and Meth. in Physics Research A704(2013)84–91.
[6] J. Alonso et al., Int. Cycl. Conf. App., Vancouver 2013.
[7] L. Celona et al., IPAC 2015, p. 2563
[8] D. Winklehner et al., IPAC 2015, p. 3384

ISBN 978-3-95450-131-1

PROGRESS ON THE UPGRADE FOR TRT AT NIRS CYCLOTRON FACILITY

S. Hojo#, T. Wakui, K. Katagiri, K. Nagatsu, H. Suzuki, M. Nakao,A. Sugiura, and A. Noda
NIRS, Anagawa 4-9-1, Inage, Chiba, JAPAN

Abstract

The cyclotron facility at National Institute of Radiological Sciences (NIRS) includes two cyclotrons, a NIRS-930 cyclotron (Thomson-CSF, Kb=110 MeV and Kf=90 MeV) and a small cyclotron HM-18 (Sumitomo-Heavy-Industry) [1]. The NIRS-930 cyclotron has been used for radionuclide production, nuclear physics, detector development and so on, since the first beam in 1973. The HM-18 has been used for radionuclide production for PET since 1994.

In recent years, the production of radionuclides for Targeted Radionuclide Therapy (TRT) by using NIRS-930 has been one of the most important activities in NIRS. Since demand of radionuclide users on beam intensity is growing, we have launched to upgrade the cyclotron facility, such as installation of multi-harmonic beam buncher in NIRS-930 and a reinforcement of nuclear ventilation system in a cave.

Progress on the upgrade for TRT at the cyclotron facility and status of the NIRS cyclotrons are to be presented in this report.

INTRODUCTION

The NIRS-930 cyclotron has been mainly operated to produce radionuclides. The system layout of NIRS-930 facility is shown in Fig. 1. This facility has 10 beam ports, and 4 beam ports of them are exclusively used for radionuclide production. The C-1 and C-2 beam port are used for production of radionuclides for PET. The C-4 beam port is used for production of metal radionuclides such as ^{62}Zn/^{62}Cu for SPECT. The C-9 beam port is used for production of radionuclides with a low-melting-point solid target such as ^{124}I and ^{76}Br [2]. In addition to these 4 beam ports, renewal of the C-3 beam port is in progress for radionuclides production. This beam line has wobbler magnets for avoiding heat concentration on a target [3]. Radionuclide production using this beam port will be started in January, 2015.

The ratio of operation times of NIRS-930 in fiscal year 2014 is shown in Fig. 2. The radionuclide production account for 49% of the operation times, and its related operation, namely beam tuning and machine studies to make a suitable beam, was 21%. Thus, almost 70% of whole operation time was shared for the purpose of radionuclides production.

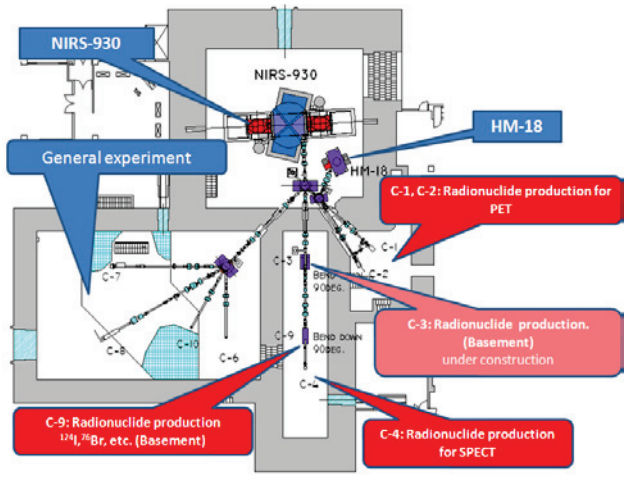

Figure 1: The system layout of the NIRS-930 facility.

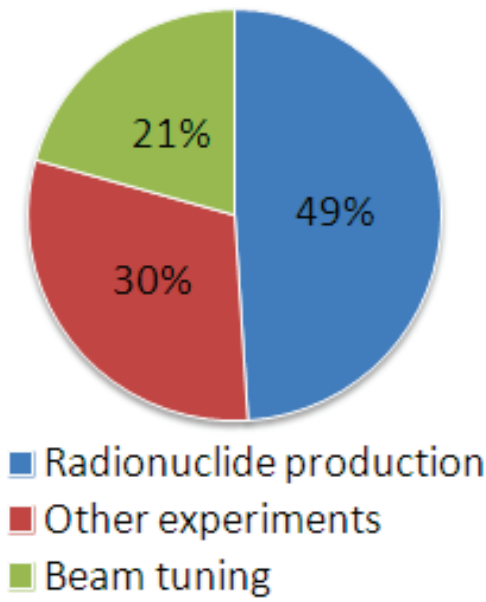

Figure 2: The ratio of operation times of NIRS-930 in fiscal year 2014.

CURRENT STATE OF RADIONUCLIDE PRODUCTION USING NIRS-930

In the past, radionuclide produced using NIRS-930 was mainly used for molecular imaging such as PET and SPECT. In recent years, production techniques of radionuclides such as ^{211}At, ^{186}Re, ^{64}Cu, and ^{67}Cu have been developed and applied for studies of TRT at NIRS.

A list of radionuclide produced NIRS-930 is shown in Table 1 with reactions and beams. The highest beam power is 600 W at 30 MeV proton 20 eμA.

s_hojo@nirs.go.jp

ISBN 978-3-95450-131-1

The proton beams of 12-60 MeV are mainly used for the production of radionuclides such as ^{64}Cu, ^{67}Cu, ^{89}Zr, ^{62}Zn/^{62}Cu, and ^{124}I. The Helium beams of 30-75 MeV are used for production of ^{155}Tb, ^{211}At, and ^{28}Mg. The deuteron beams of 20 MeV are used for production of ^{177}Lu and ^{186}Re.

In radionuclide production with low energy protons such as ^{64}Cu and ^{124}I, the beam intensity is insufficient to produce required yield. It is difficult to increase the beam intensity because of the space charge effect at beam injection. Therefore, H_2^+ beam has been used instead of proton beam.

Table 1: List of Radionuclide Production Using NIRS930

Radionuclide	Reaction	Beam
^{89}Zr	^{89}Y(p, n) ^{89}Zr	15 MeV proton 10 eμA
^{11}C	^{14}N(p, α) ^{11}C	18 MeV proton 20 eμA
^{62}Zn/^{62}Cu	^{nat}Cu(p, 2n) ^{62}Zn	30 MeV proton 20 eμA
^{68}Ge	^{nat}Ga(p, x) ^{68}Ge	30 MeV proton 20 eμA
^{67}Cu	^{68}Zn(p, 2p) ^{67}Cu	60 MeV proton 5 eμA
	^{64}Ni(α, p) ^{67}Cu	40 MeV He 15 eμA
^{64}Cu	^{64}Ni(p, n) ^{64}Cu	12 MeV proton (H_2^+ 24 MeV) 10 eμA
^{124}I	^{124}Te(p, n) ^{124}I	13.5 MeV proton (H_2^+ 27 MeV) 10 eμA
^{177}Lu	$^{nat(176)}$Yb(d, n) ^{177}Lu	20 MeV deuteron 10 eμA
^{43}Sc	$^{nat(40)}$Ca(α, x) ^{43}Sc	34 MeV He 10 eμA
^{47}Sc	^{44}Ca(α, p) ^{47}Sc	34 MeV He 10 eμA

INCREASED OF BEAM INTENSITY 34 MEV HELIUM

A demand on higher beam intensity for 34 MeV He^{2+} is growing in radionuclide production for TRT. Therefore beam intensity was increased by adjusting operation parameter. Progress of extracted beam intensity and extraction efficiency is shown on Fig. 3. In beam tuning, operation parameters such as deflector voltage, current of magnetic channel, harmonic coil and so on were adjusted. In Fig. 3 marks "A" and "C" shows adjustment of trim coil field with beam phase [4]. The beam phase is shown on Fig. 4. The ordinate axis is beam phase (the ideal acceleration phase =0) and the abscissa axis is phase probe number. The beam phase excursion was reduced to ±5 degree. In Fig. 3 mark "B" shows adjustment of injection energy and magnetic field at central region.

Tables 2 and 3 show the results of beam tuning in beam intensity and efficiency. The beam current at inflector is stopped beam by change a connection inflector electrode to current meter from inflector voltage power supply. The R=920 mm is extraction radius and entrance of electric deflector. The extracted beam intensity was measured at the first faraday cup at NIRS-930 beam line. The extraction efficiency is defined by the ratio of the extracted beam intensity to the beam intensity at R=920 mm, and it was 92%. The extracted beam current was 24.5 eμA. Then, the beam intensity at the target for radionuclide production was 20 eμA.

Figure 5 shows the dependence of the extracted beam intensity on the extraction efficiency. The beam intensity increases with the extraction efficiency.

Further improvement in the beam intensity is demanded. The desired beam intensity at the target is 30 eμA. Thus, we are planning to increase the beam intensity by improvement of beam buncher to multi harmonic type and optimization of the injection beam line including ion source.

Table 2: The Beam Intensity of 34 MeV He^{2+}

Inflector [eμA]	R=920 mm [eμA]	Extracted [eμA]
53.2	26.6	24.5

Table 3: The Beam Efficiency of 34 MeV He^{2+}

R=920 mm /Inflector	Extracted /R=920 mm	Extracted /Inflector
50%	92%	46%

ISBN 978-3-95450-131-1

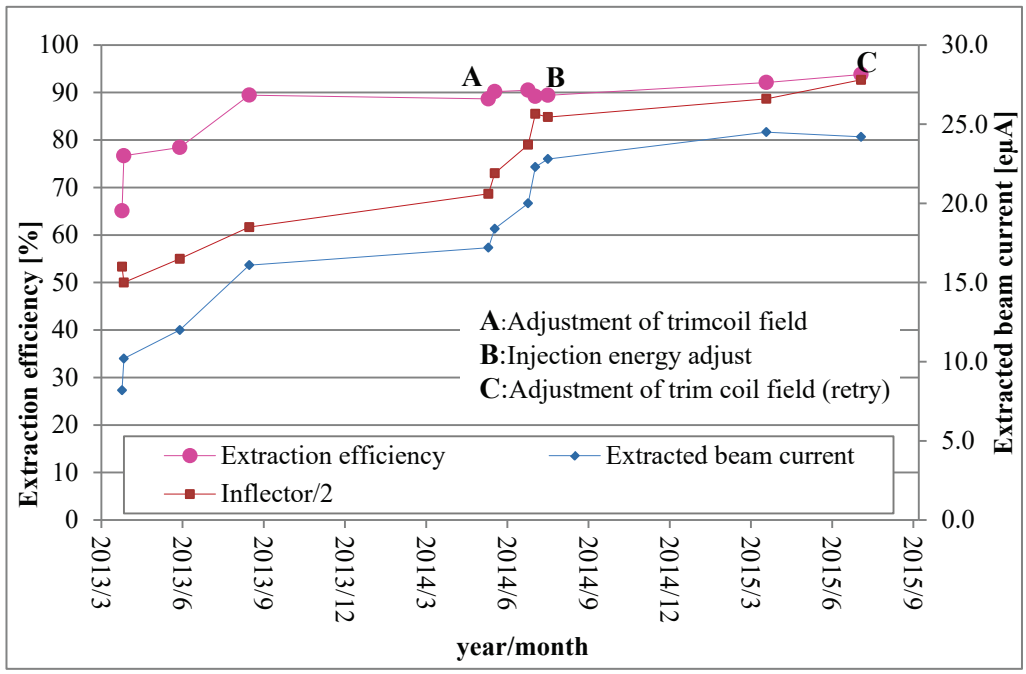

Figure 3: Progress of extraction efficiency and extracted beam intensity by the operation for beam tuning.

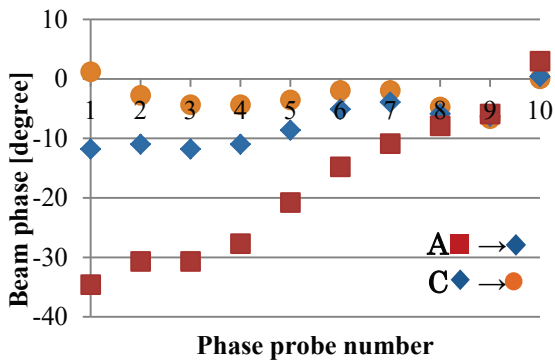

Figure 4: The excursion of beam phase when the operation for beam tuning.

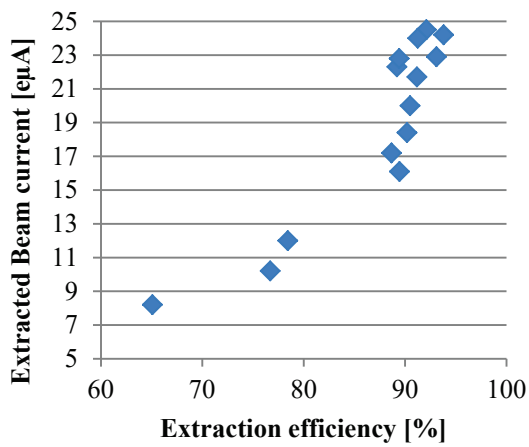

Figure 5: Extraction efficiency and extracted beam intensity.

REFERENCES

[1] S. Hojo et al., Proceedings of the 20th International Conference on Cyclotrons and their Applications, Vancouver, BC, Canada, MOPPT008, (2013).

[2] K. Nagatsu et al., "Fully automated production of iodine-124 using a vertical beam", Applied Radiation and Isotopes 69 (2011) 146–157.

[3] K. Katagiri et al., Proceedings of IPAC2014, Dresden, Germany, WEPRO088, (2014) 2162-2164.

[4] S. Hojo et al., Proceedings of IPAC2014, Dresden, Germany, MOPRI080, (2014) 794-796.

ISBN 978-3-95450-131-1

THE MULTI PARTICLE SIMULATION FOR THE CYCLOTRON NIRS-930

M. Nakao#, S. Hojo, K. Katagiri, A. Noda, K. Noda, A. Sugiura, T. Wakui, NIRS, Chiba, Japan
V. Smirnov, S. Vorozhtsov, JINR, Dubna, Moscow, Russia
A. Goto, Yamagata University, Yamagata, Japan

Abstract

Simulation for the cyclotron NIRS-930 of many particles considering space charge effect has been performed and results are compared with experiment. NIRS-930 is used for producing radionuclide used as nuclear medicine and for providing beam for physical and biological experiment. To increase the yield of radionuclides, they need to increase beam intensity of cyclotron. For such a purpose, computer simulation using a code SNOP has been performed. The simulation of proton with 30 MeV of extraction energy with harmonic number of 1 was already performed and well simulated RF phase and extraction efficiency. Then we tried to apply SNOP to 18 MeV protons with harmonic 2. The bunch length of injection beam changes injection and extraction efficiency. This indicates optimizing buncher improves the efficiency. We optimized electric deflector and magnetic channel in order to maximize extraction efficiency. We show the phase space plot to visualize the improvement of efficiency. We intend to apply the parameters suggested by the simulation to actual cyclotron operation to improve beam intensity and quality.

INTRODUCTION

Simulation studies about the cyclotron NIRS-930 [1] (Thomson-CSF, K_b=110 MeV, K_f=90 MeV) have been carried out aiming to understand the beam behavior for increasing beam intensity. If we assume negative ion injection, beam intensity could become more than double. But it needs large scale upgrade of target and shielding. So we hope to improve the injection, acceleration and extraction efficiency to increase beam intensity.

We need to know what causes the beam loss though we can detect the lost beam current only at the probe experimentally. Therefore beam simulation study of the purpose of identifying the beam loss point and find parameters of cyclotron elements which can realize high efficiency.

SIMULATION METHOD

Simulation Program SNOP

Simulation program SNOP [2,3] simulates particle orbit from beam injection to extraction with the electric fields of the inflector, the Dee electrodes and the deflector; the magnetic fields of the main coils, the trim coils and the harmonic coils and the magnetic channel which were calculated by OPERA-3d [4]. The particle orbit was derived continuously from the beginnig point to the lost point (or successfully extracted), dividing to the regions of injection (inflector), acceleration, and extraction internally of the program. The particle orbit was solved by the fourth order Runge-Kutta method. The space charge effect was taken into account both by particle to particle method and by particle in cell (PIC) method using FFT and Poisson boundary. Results of both methods are compared and parameters such as time and space division are determined considering the consistency of the both methods.

Modeling of NIRS-930

Figure 1 shows the calculation model of the NIRS-930. The beam from the ion source sit on the cyclotron yoke is guided by a bending magnet and comes into the central part of cyclotron. The inflector injects the beam with the use of static electric field. NIRS-930 has 4 spiral sectors. Main coil, 12 pairs of trim coils, 4 injection harmonic coils and 4 extraction harmonic coils are utilized to form magnetic field of accelerating region. The beam is accelerated by the RF electric field by the dee electrode whose central angle is 86°. The extraction radius is 920 mm and there are an electrostatic deflector, a magnetic channel and a gradient corrector for beam extraction.

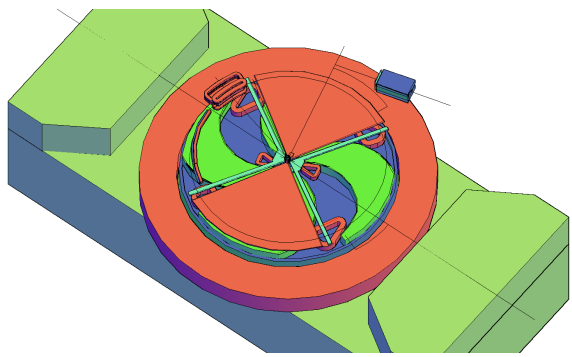

Figure 1: The half cut model of the cyclotron NIRS-930.

INJECTION AND EXTRACTION EFFICIENCY DEPENDENCE ON BUNCH LENGTH

Changing the RF phase difference of buncher and dee electrodes, the efficiency of injection and extraction depends on particle amount in phase acceptance varies. The experimental result is shown in Fig. 2. Injected beam intensity was measured by main probe inserted to the position of the radius of 10 cm and extracted beam intensity was measured by faraday cup at beam line just after extraction form cyclotron. The maximum extraction efficiency was 28 % and which was more than twice higher

ISBN 978-3-95450-131-1

than efficiency of 11 % of without buncher. Figure 2 indicates that the width of the peak is 1σ=66.3±3.0° at injection and 1σ=55.2±0.3° at extraction. This value is determined by the phase acceptance of the cyclotron and injected bunch length.

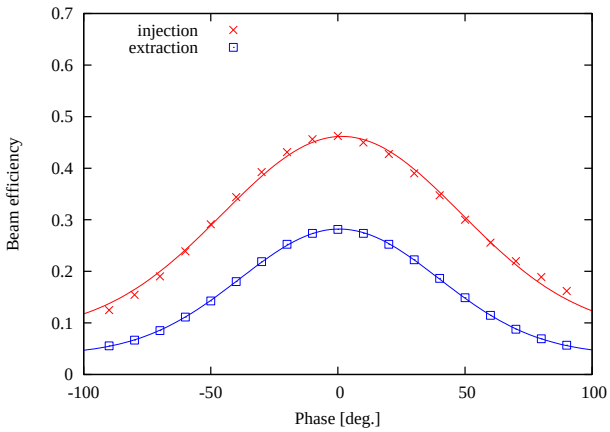

Figure 2: Experimental results of injection and extraction efficiency changing RF phase difference. Each width of the peak is 1σ=66.3±3.0° at injection and 1σ=55.2±0.3° at extraction.

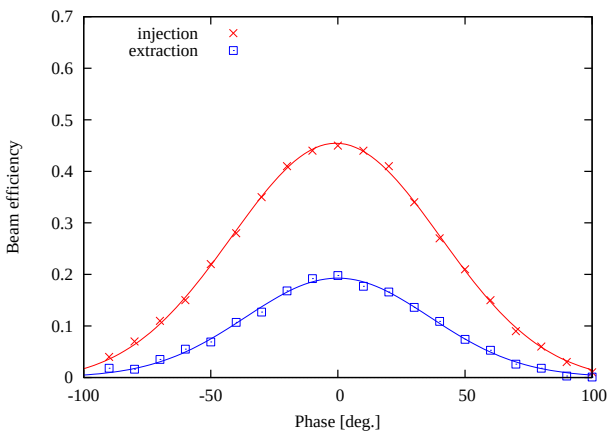

Figure 3: Simulation results of injection and extraction efficiency with a long (60°) bunch. Each width of the peak is 1σ=56.5±2.2° at injection and 1σ=57.0±4.7° at extraction.

Simulation result whose bunch length was 60° of RF period is shown in Fig. 3. The widths of the peaks of beam efficiency in Fig. 2 and Fig. 3 are almost consistent. The origin of Fig. 3 has pedestal is as follows: The particles in bunch distributes only in 60° region in simulation. By contrast, some particles still exist outside of the bunch in actual experiment.

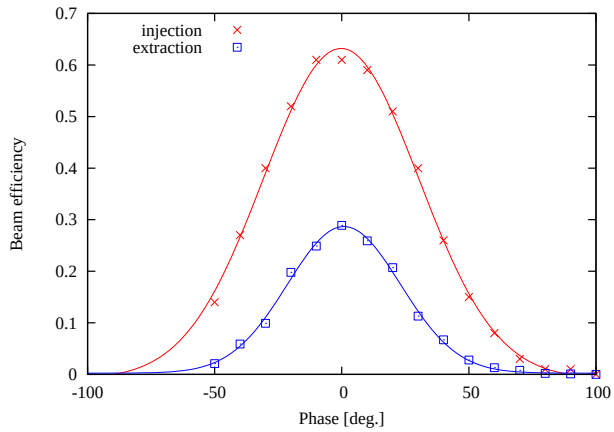

Figure 4: Simulation results of injection and extraction efficiency with a short (30°) bunch. Each width of the peak is 1σ=43.2±0.8° at injection and 1σ=31.4±0.7° at extraction.

Figure 4 shows the simulation result of bunch length of 30°. Figure 4 shows the peak injection and extraction efficiency is higher than that of Figure 3. This indicates shorter injection bunch can achieve more beam efficiency. If we add buncher RF wave form, which is a sine wave presently, to higher harmonics properly, the width of injection bunch will be shorter, and then injection and extraction efficiency can be increased.

ADJUSTMENT OF DEFLECTOR AND MAGNETIC CHANNEL

Figure 5 is a phase space plot just before deflector, showing a place where each particle will lose. The loss points are classified to magnetic channel, deflector electrode and deflector septum. For example, a particle passing rather outside and going outwards is shown in the upper right position of Fig. 5. Such particle will lose at deflector electrode. There is a long and narrow region in the center of Fig. 5, where the particles are lost at deflector septum. In left of that region, particles are going through the inside of deflector and they go around another turn. Such particles are expected to be accelerated by dee electrodes, which increases revolution radius.

Figure 6 shows the simulated single beam bunch of the same turn number overwriting to Fig. 5. Each bunch is ±10° wide, one (×; 0°) is at maximum extraction efficiency and the other (-; 20°) is 20° earlier than that. The expressed particles in Fig. 6 are in a certain time of one bunch. And particles pass before deflector next turn is not shown. Extraction efficiency of two bunches are 59% and 38%, respectively. Although radial spread of 0° bunch is larger than that of 20°, they can be extracted in multiple turns. On the other hand, spread of beam direction of 0° is smaller than that of 20°, which make the extraction efficiency better.

ISBN 978-3-95450-131-1

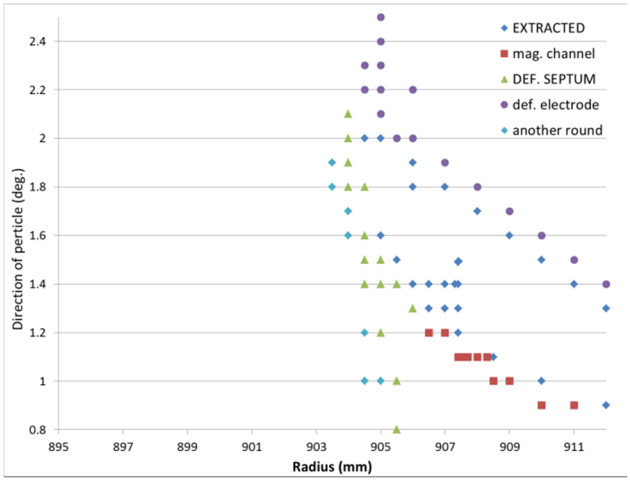

Figure 5: Phase space plot just before deflector, showing a place where each particle will lose.

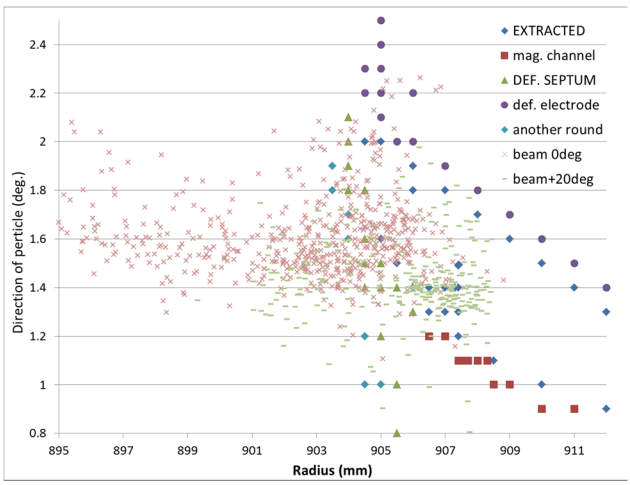

Figure 6: Phase space plot just before deflector, showing a place where each particle will lose. There is also plotted bunch (×) at maximum extraction efficiency and bunch (-) 20° earlier than it.

Calculating tracks of the particles which are lost at magnetic channel, it was found they collided to the slit of right side at the entrance of the magnetic channel. To pass such particles, magnetic channel was shifted inside 5 mm to radial direction. Then each point of Fig. 5 changed to be shown in Fig. 7. It shows the particles lost at magnetic channel in initial situation made to extract. Such an improvement is also possible to the parameters of deflector position and applied voltage in similar way.

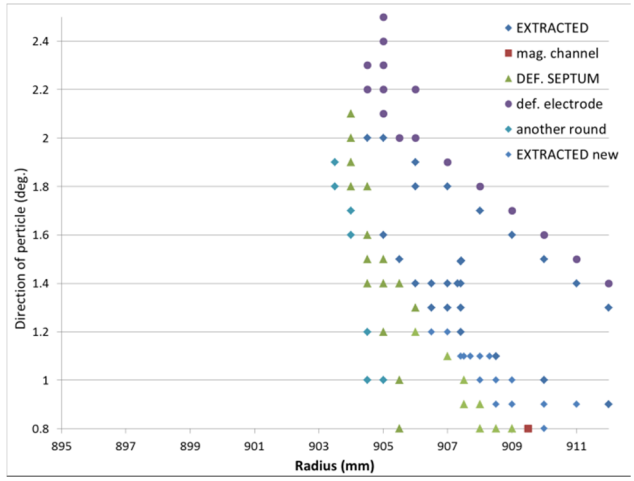

Figure 7: Phase space plot just before deflector showing a place where each particle will lose. Magnetic channel was shifted 5 mm radially outward from the positon of Fig. 5.

CONCLUSION

Simulation study of beam in the cyclotron NIRS-930 was carried out by the use of simulation program SNOP. The simulation suggested if the buncher could collect to the particle in a shorter bunch, the injection efficiency would increase. What is more, it was confirmed and graphically-demonstrated that the beam bunch had to be adjusted to the inside of extraction acceptance in the phase space.

REFERENCES

[1] S. Hojo, et al. "Progress on the upgrade for TRT at NIRS cyclotron facility" In these proceedings HIAT2015 MOPA07 (2015).
[2] V.L. Smirnov, S.B. Vorozhtsov, Proc. of RUPAC2012 TUPPB008 325 (2012).
[3] V.L. Smirnov et al., Proc. of IPAC2012 292 (2012).
[4] OPERA-3D, Cobham plc http://www.cobham.com/

ISBN 978-3-95450-131-1

RIKEN RING CYCLOTRON (RRC)

Yutaka Watanabe, Masayuki Kase, Masaki Fujimaki, Nobuhisa Fukunishi, Eiji Ikezawa,
Osamu Kamigaito, Keiko Kumagai, Takeshi Maie, Jun-ichi Ohnishi, Kazutaka Ohzeki,
Hiroki Okuno, Naruhiko Sakamoto, Kenji Suda, Shu Watanabe, Kazunari Yamada
RIKEN Nishina Center, Wako, Saitama, Japan
Seiji Fukuzawa, Makoto Hamanaka, Shigeru Ishikawa, Kiyoshi Kobayashi,
Ryo Koyama, Takeshi Nakamura, Minoru Nishida, Makoto Nishimura,
Junsho Shibata, Noritoshi Tsukiori, Kazuyoshi Yadomi
SHI Accelerator Service Ltd., Tokyo, Japan

Abstract

The RIKEN Ring Cyclotron (RRC) has operated stably for over 28 years and has supplied many types of heavy-ion beams for various experiments. The RRC has three types of injectors: the azimuthal varying field (AVF) cyclotron for comparatively light ions, the variable-frequency RIKEN heavy-ion linac (RILAC), and the RIKEN heavy-ion linac 2 (RILAC2) for high intensities of very heavy ions, such as those of U and Xe. Many accelerator combinations are possible, although the RRC should act as the first energy booster in any acceleration mode. The total operation time of the RRC is usually more than 3000 h/year. Recently, however, frequent malfunctions caused by age-related deterioration and beam loss, such as a layer short of main coils and vacuum leaks at feed-through, cooling water pipes, extraction devices, a bellows and so on, have been occurring at the RRC. The present status of the RRC is presented in this paper.

INTRODUCTION

Although the RIKEN Ring Cyclotron (RRC) began operation in 1986, it still plays an essential role as the first energy booster in the Radioactive Isotope Beam Factory (RIBF) accelerator complex. The RIBF was built by 2007 to expand the scope of research on heavier nuclei, thus building upon previous work on light unstable nuclei. The RIBF uses a combination of three injectors, RRC, three new cyclotrons (fRC, fixed-frequency Ring Cyclotron; IRC, Intermediate-stage Ring Cyclotron; and SRC, Superconducting Ring Cyclotron), and the RIKEN projectile fragment separator [1]. Using the RIBF, we aim to produce the most intense radioactive isotope beams in the world, with intensities of up to 1 pμA and including isotopes of all atomic masses. Stable operation of highly intense beams has been gradually realized at the RIBF. However, frequent malfunctions have recently occurred at the RRC due to age-related deterioration and beam loss. Some components have been repaired, and others have been replaced, but these issues remain serious and have not yet been solved. The operation of and problems with the RRC are as follows.

Table 1: RIBF Operating Statistics from August 2014 to July 2015.

Beam particle	Energy (MeV/u)	Acceleration mode	Actual beam current (pnA)	Beam tuning time (h)	Actual beam time (h)	Availability (%)
12C	70	AVF-RRC	350.0	28.4	36.0	100.0
12C	135		393.2	149.5	47.0	100.0
40Ar	95		76.5	169.5	32.0	100.0
56Fe	90		6.3	108.8	21.0	100.0
84Kr	70		5.6	72.8	121.0	100.0
86Kr	36	RILAC-RRC	8.8	41.3	12.0	100.0
48Ca	63		235.3	39.5	104.3	95.4
136Xe	10.75	RILAC2-RRC	405.0	90.3	106.0	109.4
238U	10.75		2500.0	110.2	48.0	100.0
40Ar	160	AVF-RRC-IRC	1.6	136.7	48.0	100.0
pol.d	190	AVF-RRC-SRC	290.0	77.1	123.9	105.6
48Ca	345	RILAC-RRC -IRC-SRC	530.0	175.6	492.2	96.3
78Kr	345	RILAC2-RRC -fRC-IRC-SRC	486.1	143.5	732.0	90.1
238U(1st)	345		27.9	261.8	532.1	94.2
238U(2nd)	345		31.4	214.6	553.0	91.5
238U(3rd)	345		39.5	87.2	252.0	99.5
			Total	1907	3260	

RRC OPERATION

The operation of the RRC from August 2014 to July 2015, including that of the fRC, IRC, and SRC, was published previously [2]. A list of the beams accelerated by these cyclotrons during this period is presented in Table 1. As shown, seven acceleration modes have employed the RRC, including an AVF-RRC-IRC mode for biological experiments that was first used in the winter of 2015. The actual beam service time during which the RRC was used, excluding beam tuning time, was 3260 h in the past year. The beam availability [1], defined as the ratio of actual beam service time to scheduled beam service time, was more than 90 %. Although there was downtime due to hardware trouble in 2011, this beam availability has recently increased each year [1-3]. The total yearly operation time of the RRC, including beam

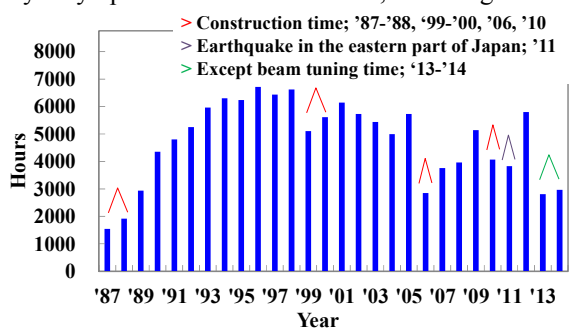

Figure 1: Total yearly operation time of RRC.

ynabe@riken.jp

ISBN 978-3-95450-131-1

tuning time, was more than 3000 h/year during the past year, as shown in Figure 1, and recently, the RRC has operated stably without significant downtime. Furthermore, the transmission efficiency and stability of the beams have recently been improved, and a 345 MeV/nucleon ^{238}U beam with a maximum intensity of 39.5 pnA at FC-G01 (the exit of the SRC) was obtained in May 2015.

PROBLEMS

Main Coils

Two main coils of sector magnets exhibited signs of layer shorts, and an epoxy resin and glass fiber tape were carbonized throughout each layer short. Therefore, these main coils were both replaced [4-6]. In May 2011, a layer short that was causing the RRC magnetic field to fluctuate by as much as ± 20 ppm was found in the upper main coil of the RRC-E sector magnet. We found that it would be nearly impossible to repair the coil and therefore decided to fabricate a new RRC main coil, which replaced the old one in the summer of 2012. Because the RRC main coil had never before been replaced, the task was scheduled to be performed over a period of three weeks. In June 2012, the lower main coil of the RRC-W sector magnet also exhibited signs of a layer short. This layer short in the RRC-W sector magnet was identical to the short identified and repaired in 1999. We attempted to repair it using the same method that had been used in 1999, but the fluctuations of the coil voltage and magnetic fields were not fully corrected. Thus, we decided to replace the damaged lower main coil and the deteriorated upper main coil of the RRC-W sector magnet with new main coils; these were replaced in the summer of 2013. The task was scheduled to be performed over a period of eight weeks because we had never before replaced the lower main coil of the RRC during the entire 26 years of operation. Though the magnetic field of the RRC-W sector magnet before the replacement had been fluctuating over a wide range of ± 5 ppm, the field of the new magnet is stable and exhibits no fluctuation, as shown in Figure 2.

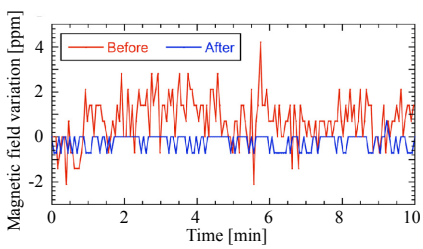

Figure 2: Fluctuation of magnetic field before and after replacement of W-sector main coils.

Vacuum Leak

The numerous vacuum leaks at the RRC have been the most serious problems in recent years. Almost all of these leaks have been caused by age-related deterioration and have been easily repaired, but the repair of a few leaks has not yet been scheduled, as the means of mending them remains unclear.

In April 2012, a vacuum leak occurred in the electric power feeder of RF resonator No. 2. This vacuum leak was attributed to a crack in the insulator and to the partial melting of the aluminium gasket. Therefore, the insulator and gasket were replaced with new ones. In the spring of 2013, a vacuum leak occurred in the inner copper cooling-water pipe for the lower dee electrode in the resonator No. 2 cavity. So, the cavity was opened in July, and the inside of the inner conductor was investigated carefully. The water leak occurred at a connection in the inner copper cooling-water pipe, as shown in Figure 3 (a), but it was impossible to repair the leak point due to the narrowness of the space surrounding the pipe. Therefore, because a new bypass line was made for the lower dee electrode, this pipe line was cut at some spot and connected with a new pipe using a sleeve and a silver braze. In October 2013, a vacuum leak occurred in a lower feed-through trim coil in the E-sector sub-chamber [2-3]. So, the E–S valley cavity, which is located next to these lower feed-through trim coils, was opened to perform these repairs in the summer of 2014. Three O-rings and plastic blocks for the feed-through had been melted, as shown in Figure 3 (b). The feed-through was cut at each melted location because there was no coupling to enable desorption of the O-rings and plastic blocks. The melted O-rings and plastic blocks were replaced with new ones, and the feed-through was again connected with coupling.

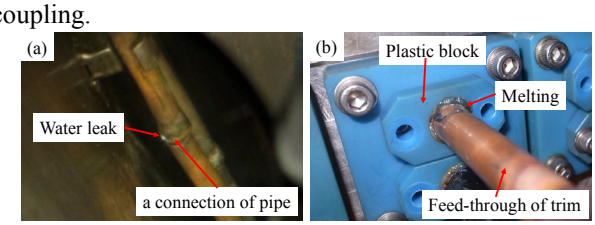

Figure 3: RRC vacuum leaks: (a) connection of the inner copper cooling-water pipe, (b) O-rings and plastic blocks for feed-through.

An investigation of the vacuum in August 2014 revealed several vacuum leaks [2]. First, a vacuum leak at a coupling of the upper copper cooling-water pipe for the dee electrode in the resonator No. 2 cavity was identified. The coupling was located at a shallow spot and was tightened, so the vacuum was improved slightly. Next, two vacuum leaks in the outer cooling-water pipe for the lower stem in the resonator No. 1 cavity were found. However, this lower stem is located in the interior and cannot be observed directly, so this vacuum leak was not investigated in detail and was not repaired. Finally, a vacuum leak occurred at a stainless bellows between the resonator No. 2 cavity and a main chamber of the S-sector magnet. This vacuum leak also was not investigated in detail, for the same reason that the lower stem leak was not further examined. Furthermore, as this bellows is long and is welded to a side-wall of the cavity, substantial work time and cost would be required to replace it.

ISBN 978-3-95450-131-1

Though a vacuum of about 2×10^{-5} Pa is currently present in the two resonator cavities, beam loss is increasing more than before. Figure 4 shows the circulating beam currents of ^{78}Kr and ^{238}U that were measured by a radial probe (RP) in a 1.6×10^{-5} Pa vacuum in the winter of 2015 [2]. The RP position is defined as the distance from the center of the circulating orbit. Though the ^{78}Kr beam current only decreases by about 9 %, that of the ^{238}U decreases substantially, by more than 30 %. This ^{238}U beam current loss is six times greater than 5 % that measured in 2012, so it is necessary to repair the remaining leaks.

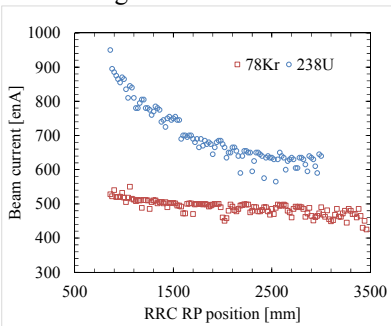

Figure 4: Circulating beam currents of ^{78}Kr and ^{238}U.

Coil Power Supplies

The capacitors of the main and trim coil magnet power supplies had exceeded their service lives, and cooling water had been leaking from pinholes in the thyristor cooling blocks. Therefore, we removed the old power supplies and installed a new main coil power supply and six trim coil power supplies in the winter of 2014 [7].

Magnetic Deflection Channels 1 and 2

Recently, a vacuum leak occurred in the RRC due to beam loss damage to its extraction device, magnetic deflection channel (MDC) 2. Though this vacuum leak is not hazardous, MDC 1 and 2 both also exhibited age-related deterioration. Therefore, we designed and produced two new MDCs in 2013 and 2014, which are usable with high-intensity heavy-ion beams, such as those of U and Xe.

Electrostatic Deflection Channel

During the U-beam service time in November 2012, a septum electrode of an electrostatic deflection channel (EDC), which deflects the circulating beam to the extraction orbit, was seriously damaged on the injection side by significant beam loss, as shown in Figure 5 [3]. After this issue arose, a beam interlock system was installed to monitor the temperature of the EDC septum electrode of the RRC and to reduce the heat load. Furthermore, a new EDC septum electrode structure was designed, in which the septum electrode forms a V-shape pointing towards the injection side.

Upgrades and Installations Around the RRC

In 2012, a new gas charge stripper system [8] with large differential pumping was installed for U-beam acceleration just after the RRC installation, and a new high-power beam dump [9] was also installed by inserting in two dipole magnets (DAA1 and DMA1) just after the gas charge stripper system. These systems were installed because the charge states of beam particles accelerated by the RRC must be multiplied before they are injected into the fRC and because the various charge states of a stripped beam must be separated. The vacuum level of the high-energy beam transport line between the RILAC2 and the RRC was also enhanced in FY2011 by mounting additional vacuum pumps, and some of the vacuum chambers in the section were modified in FY2013 to enable the use of additional beam diagnosis devices [10]. In the winter of 2012, some magnets in the injection beam transport line were rearranged, and some magnets and ducts were modified in the Magnetic Inflection Channel No. 2, Extraction Bending Magnet, and Bending Magnet of the fRC [1]. The return beam transport line from the IRC to the E5 room was installed between FY2012 and FY2014 to enable biological experiments to be conducted that require higher-energy beams of relatively heavy ions, such as Ar [2].

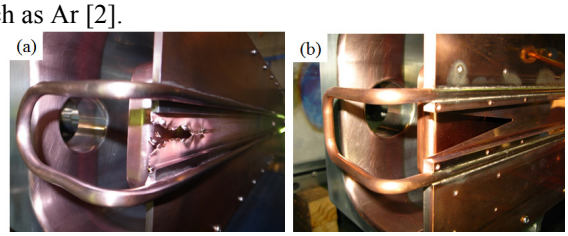

Figure 5: EDC: (a) septum electrode damaged by beam loss, (b) new V-shaped septum electrode.

REFERENCES

[1] N. Fukunishi et al., "Acceleration of Intense Heavy Ion Beams in RIBF Cascaded-cyclotrons", Prof. of Cyclotrons '13 (20th Int. Conf. on Cyclotrons and their Applications), MO1PB01, Vancouver, Canada, September 2013.

[2] M. Nishida et al., "Status Report of the Operation of the RIBF Ring Cyclotron", FSP003, Proc. of PASJ12, Tsuruga, Fukui, August 2015, in press.

[3] S. Fukuzawa et al., "Status Report of the Operation of the RIBF Ring Cyclotron", FSP024, Proc. of PASJ12, Aomori, Aomori, August 2014, 401.

[4] Y. Watanabe et al., "Present Status of RIKEN Ring Cyclotron", MOPPD030, Proc. of IPAC 2012, New Orleans, USA, May 2012, 433 (2012).

[5] Y. Watanabe et al., "Replacement of main coil of RRC-E sector magnet", RIKEN Accelerator Progress Report 46, 130 (2013).

[6] Y. Watanabe et al., "Replacement of main coils of RRC-W sector magnet", RIKEN Accelerator Progress Report 47, 150 (2014).

[7] K. Kumagai et al., "Replacement of the RIKEN ring cyclotron (RRC) power supplies", RIKEN Accelerator Progress Report 47, 151 (2014).

ISBN 978-3-95450-131-1

[8] H. Imao et al., "Recirculating He-gas stripper for high-intensity uranium beam", RIKEN Accelerator Progress Report 46, iv (2013).
[9] K. Yamada et al., "New high-power beam dump for charge stripper at RRC", RIKEN Accelerator Progress Report 46, 131 (2013).
[10] K. Yamada et al., "Modification of beam diagnosis chambers in RILAC2 high-energy beam transport", RIKEN Accelerator Progress Report 47, 156 (2014).

ISBN 978-3-95450-131-1

DEVELOPMENT OF LOW-ENERGY HEAVY-ION BEAMS BY THE RIKEN AVF CYCLOTRON AND HYPER ECR ION SOURCE OF CNS

Y. Kotaka#, Y. Ohshiro, S. Watanabe, H. Yamaguchi, N. Imai,
S. Shimoura, Center for Nuclear Study, University of Tokyo, Wako, Saitama, Japan
M. Kase, S. Kubono, Riken Nishina Center, RIKEN, Wako, Saitama, Japan
K. Hatanaka, Research Center for Nuclear Physics, Osaka University, Ibaraki, Osaka, Japan
A. Goto, Yamagata University, Yamagata, Yamagata, Japan
H. Muto, Center of General Education, Tokyo University of Science, Chino, Nagano, Japan

Abstract

The first of three categories of the upgrade of RIKEN AVF cyclotron is to expand a variety of metal ion beams using Hyper ECR ion source. The non-axial rod method, multi-hole micro-oven method and plasma spectroscopy was developed. The second is to increase acceleration energy. By the beam simulation, the center region was renovated and $^{4}He^{2+}$ 12.5 MeV/u ion beam can be available. The third is to increase beam intensity. For injection, a pepper-pot emittance monitor is developed for the purpose of measuring a four-dimensional phase space distribution. For extraction, flat top system was developed. Using a faraday cup installed at the exit of deflector, the extraction efficiency is improved. For the transmission efficiency from AVF cyclotron to CNS RI Beam separator, the redesign of beam transport system is planned.

INTRODUCTION

RIKEN AVF cyclotron was built in 1989. This original design is the following. RF frequency range is 12-24 MHz. The acceleration harmonics is 2. Maximal RF voltage is 50 kV. Average magnetic field range at the extraction is 0.5-1.76 T. K-value is 70.

The upgrade of AVF cyclotron has been conducted since 2000 by a collaboration of the Center for Nuclear Study (CNS) of the University of Tokyo and RIKEN Nishina Center to meet the request of CNS RI Beam separator (CRIB) which can produce the low energy RI beam to study nuclear astrophysics [1].

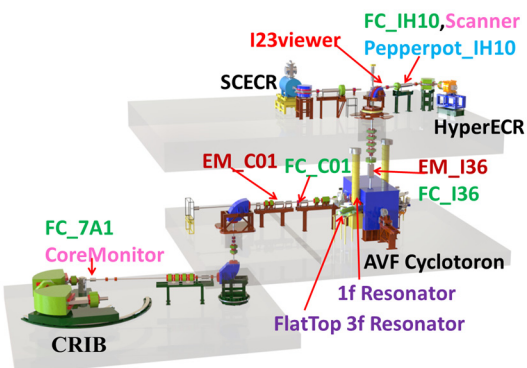

Figure 1: The schematic view of Hyper ECRIS, AVF cyclotron and CRIB with beam transport line.

We have three categories of the upgrades. One is to expand a variety of ion species. Two is to expand the region of available acceleration energy. Three is to increase beam intensity. Each will be in the following.

Besides, nondestructive beam monitors, Scanner [2] and Core Monitor [3], were developed to see stability.

Figure 1 shows the location of AVF cyclotron, Hyper ECR ion source (ECRIS), CRIB and the several diagnostics.

EXPAND ION SPECIES

We have developed two methods for feeding vapor of solid materials into the plasma by ECRIS in order to expand the ion species as well as increasing the beam intensity stably [4]. One is the non-axial rod method applied for CaO, SiO_2 and FeO, operating up to 2600 degrees. Since the tip of the material rod is placed near the wall of plasma chamber, the constant vapor rate of material is obtained. Two is the multi-hole micro-oven method applied for P_2O_5, Li, and S, operating up to 800 degrees. We can control the vapor rate with the number of holes of crucible. The beam intensities extracted from the ECRIS are listed in Table 1 together with melting point.

Table 1: Solid Ion Species Ionized by Hyper ECRIS

Ion Species	Beam Intensities (eμA)	Charged Material	m.p. (°C)
$^{6,7}Li^{2+}$	200→280	Li pure metal (Oven)	180
$^{6,7}Li^{3+}$	34→75	Li pure metal (Oven)	180
$^{10}B^{4+}$	50	$B_{10}H_{14}$ (^{10}B-99.9,MIVOC)	99
$^{11}B^{4+}$	50	$B_{10}H_{14}$ (MIVOC)	99
$^{24}Mg^{8+}$	30→45	Mg pure metal (Oven)	650
$^{28}Si^{9+}$	32→35	SiO_2 (Rod)	1500
$^{31}P^{9+}$	29	P_2O_5 (Oven)	563
$^{32}S^{9+}$	47	S grain (Oven)	119
$^{40}Ca^{12+}$	25	CaO (Rod)	2572
$^{56}Fe^{15+}$	7→15	FeO (Rod)	1420
$^{58}Ni^{15+}$	13	$C_{10}H_{10}Ni$ (MIVOC)	173
$^{59}Co^{15+}$	7→20	Co pure metal (Rod)	1493
$^{87}Rb^{20+}$	1.2	RbCl (Oven)	682

Plasma spectroscopy has been developed in order to separate the desired ion species from the same m/q ion species in the plasma. The method is to observe the light intensity of the desired ion species by a grating monochromator. We confirmed the relation between the light intensity of an optical line spectrum of $^{6}Li^{3+}$ and its beam intensity measured by the faraday cup (FC) located at the exit of AVF cyclotron. Therefore, we can apply the light intensity to the beam intensity [5]. By this method, the tuning efficiency of ECRIS has been improved.

#kotaka@cns.s.u-tokyo.ac.jp

ISBN 978-3-95450-131-1

EXPAND ENERGY REGION

For the request of $^{15}N^{5+}$ 9 MeV/u ion beam, K-value and RF voltage needs 81 and 56 kV, respectively. At first, we improved the maximum output current of main and some trim coils power supply so that K-value was increased to 78 and $^{15}N^{5+}$ 8.67 MeV/u ion beam was available [6]. However, this has not been realized yet because the cooling capacity of main coil is not enough and the wideband amplifier of RF is unimproved.

$^{16}O^{7+}$ and $^{6}Li^{3+}$ 12 MeV/u ion beams were also requested with the high intensity beam. Due to the original design of AVF cyclotron, the maximal energy of $^{6}Li^{3+}$ and $^{16}O^{7+}$ ion beams had been respectively up to 9.7 MeV/u and 9.0 MeV/u at that time.

To meet the request, we focused on the beam dynamics simulation using the computed 3D electromagnetic fields [7] [8] [9]. The result indicated that it was possible to expand the region of available acceleration energy as well as improving injection efficiency by modifying the central region geometry [10] [11].

The renovation of the center region was carried out in august 2009. The energy of $^{16}O^{7+}$ and $^{6}Li^{3+}$ has been up to 11.2 MeV/u by now. Moreover, we succeeded $^{4}He^{2+}$ 12.5 MeV/u ion beam, whose intensity is 10.7 eμA, is available. This injection efficiency is successfully 0.26, which is close to the average injection efficiency 0.31.

INCREASE BEAM INTENSITY

Improve Injection Efficiency

Injection efficiency goes down as the ECRIS beam intensity increases and scatters widely (Fig.2). In order to improve this, we began to study the beam emittance.

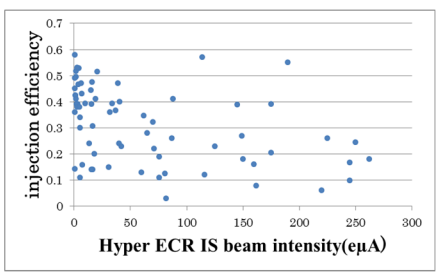

Figure 2: The relationship between injection efficiency and ECRIS beam intensity.

Since some solenoid coils exist in injection beam line, horizontal (x) and vertical (y) beam elements can be coupled. Considering it was important, we focused a four-dimensional phase space (x, x', y, y'). At first, we studied the beam simulation of ECRIS. Then, we started a pepper-pot emittance measurement [12].

The measurement principle is indicated in the left of Fig.3. A pepper-pot which is a plate with holes arranged in a square lattice shape is set perpendicular to beam axis. The beam passing through the holes reaches Detector set at the back. Each beam-spot measured by Detector can have a certain corresponding hole of pepper-pot like (x1, y1) and (x2, y2). Using the distance (L) between pepper-pot and Detector, the angle can be calculated.

We have developed a pepper-pot emittance monitor (the right of Fig.3). The diameter of hole is 0.3 mm. Each distance of adjacent hole is 3 mm.

Since we selected the viewer plate coated by KBr phosphor as Detector, the beam image can be recorded by digital camera. We assume the beam intensity would be proportional to pixel size of digital image. Viewer plate is inclined at 45 degrees against beam axis because the beam image is seen through the view port. L is 55 mm.

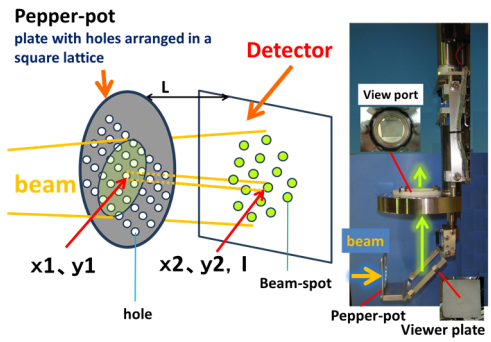

Figure 3: The schematic view of pepper-pot emittance measurement (left) and developed monitor (right).

To see the performance, we irradiated this monitor, installed at Pepperpot_IH10 (Fig.1), with $^{4}He^{2+}$ 20 keV ion beam of 51 eμA from ECRIS. The red frame of Fig.4 indicates the recorded image. Using this image and the positions of pepper-pot holes, we calculated the four-dimensional phase space distribution.

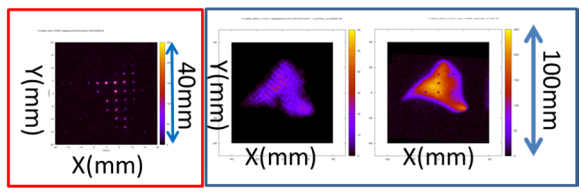

Figure 4: The beam image of pepperpot_IH10 (red frame). The image transported to the point of I23viewer from pepperpot_IH10 (the left of blue frame) and the beam image of I23viewer (the right of blue frame).

In order to see the performance, we transported this distribution to the two points of the beam line where I23viwer and EM_I36 are indicated in the Fig.1.

At first, we show the (x, y) distribution transported to I23viewer in the left of blue frame of Fig.4 and the beam image of I23viewer in the right. The transported (x, y) distribution is close to the I23viewer beam image.

ISBN 978-3-95450-131-1

Second, Fig.5 indicates the following. The left column shows the calculated emittances of the distribution transported to the point of EM_I36. The right column shows the measured emittances by the slit type emittance monitor installed at EM_I36. The (u, w) coordinate system is rotated 45 degrees with respect to (x, y).

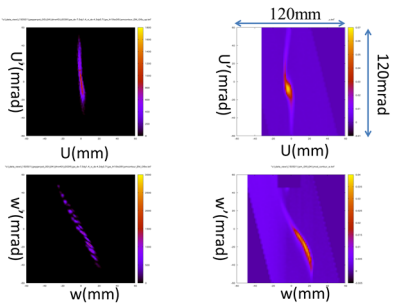

Figure 5: Left and right column show respectively the calculated emittances and measured emittances of EM_I36. Upper row is (u, u') and lower row is (w, w').

The calculated emittances have some disappeared parts compared with the measured emittance. We guess the reason why the sensitivity is zero for low intensity beam. Allowing for the guess, the calculated emittance is close to the measured emittance.

Improve Extraction Efficiency

Extraction efficiency is defined as beam transmission ratio through the deflector, magnetic-channel (MC) and gradient-collector (GC). In order to improve extraction efficiency, we developed flat top system (FT) [13].

FT was found to be effective. However, the discharge frequently occurred in the RF amplifier due to FT. We attempted to constrain the discharge so that the main and FT voltage were stably able to generate at 45 kV and 5 kV respectively when RF frequency was 16.3 MHz [14]. At the moment, we refrained from using FT in order to provide the stable beam to user.

In order to measure the beam intensity of the exit of deflector, we installed FC there in January 2010. Using it, we researched the beam loss and found that GC had to be corrected. As a result, the extraction efficiency after 2010 is improved compared with the one of 2006-2007 (Fig.6).

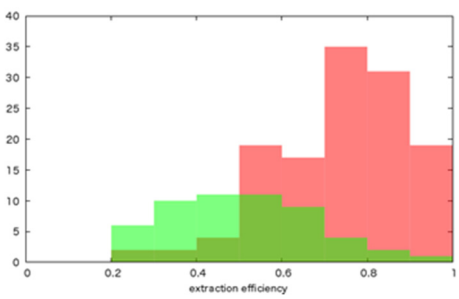

Figure 6: The distribution of extraction efficiency in 2010-2015(red box) and 2006-2007(green box).

Improve Transmission Efficiency to CRIB

The average transmission efficiency from AVF cyclotron to CRIB is 70 %. The loss must be recovered.

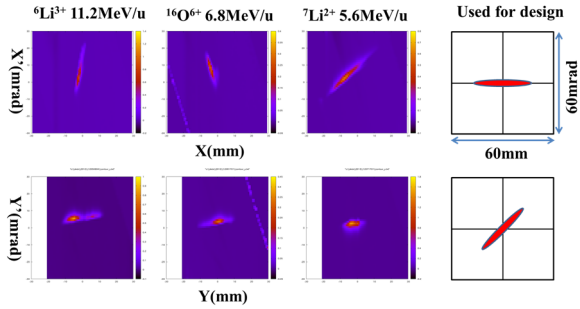

Figure 7: Columns from 1st to 3rd are the measured emittances. 4th column is the emittance used for design. Upper and lower rows indicate respectively a horizontal emittance and a vertical emittance.

We have measured the emittance by the slit type emittance monitor installed at EM_C01 (Fig.1) since 2012. We found the measured emittances differ from the emittance used for designing the beam transport system from AVF cyclotron to CRIB (Fig.7). Considering the difference is one reason for the low transmission efficiency, we will redesign the beam transport system.

SUMMARY AND CONCLUSION

We have supplied CRIB since 2000 with ion beams indicated in the Table 2, which also shows the beam time and RI beam produced by CRIB. Total beam time is 10283.2 hours. The average transmission efficiency from Hyper ECRIS to CRIB has been 0.065 since 2012. In order to improve this, we currently concentrate on the improvement of injection efficiency and transmission efficiency from AVF cyclotron to CRIB.

Table 2: Ion Beams and Beam Times Supplied to CRIB

ion species	energy(MeV/u)	beam time(hr)	RI beam produced by CRIB
$^{6}Li^{3+}$	9.5, 11.2	482.2	^{8}B
$^{7}Li^{3+,2+}$	3.4, 3.5, 5.0, 5.5, 5.6. 8.6, 8.8	1230.4	^{7}Be, ^{8}Li
$^{10}B^{4+}$	7.8, 8.5	497.1	^{10}C, ^{11}C, ^{12}N
$^{11}B^{3+}$	4.6, 5.0	521.5	^{10}Be, ^{11}C
$^{13}C^{4+}$	6	124.8	^{13}N
$^{14}N^{6+,5+}$	6.4, 7.0, 8.2, 8.4	1112.9	^{11}C, ^{14}O, commissioning, test
$^{15}N^{5+,4+}$	5.0, 5.5, 7.0	552.3	^{15}O, ^{16}N
$^{16}O^{7+,6+}$	6.3, 6.8, 10,3, 11	810.2	^{17}F, ^{17}Ne, ^{18}Ne
$^{18}O^{6+}$	3.9, 4.0, 4.5, 5.9,6.1, 7.0	1214.6	^{14}C, ^{17}N, ^{17}O, ^{18}N, ^{18}O, ^{18}F, ^{18}Ne
$^{20}Ne^{8+,7+,6+}$	6.0, 6.2, 6.3, 6.5, 8.2	1118.7	^{21}Na, ^{22}Mg
$^{22}Ne^{7+}$	6.1	364.7	^{22}Nai
$^{24}Mg^{8+}$	7.5	975.2	^{23}Mg, ^{25}Al, ^{26}S
$^{28}Si^{10+,9+}$	4.8, 6.9, 7.4, 7.5	519.1	^{30}P, ^{30}S
$^{31}P^{9+}$	6	37.4	^{30}P
$^{36}Ar^{10+}$	3.6	379.1	^{46}Ti, ^{46}Cr
$^{40}Ar^{11+}$	4.5	174.8	^{39}Ar, ^{49}V
$^{40}Ca^{12+}$	5.5, 5.6	67.1	^{46}Cr, ^{49}Cr
$^{42}Ca^{12+}$	5.9	101.1	^{44}Ti

REFFERNCE

[1] Y.Yanagisawa et al., Nucl. Instr. and Meth. Phys. Res., **A539** (2005) 74

[2] S.Watanabe et al., CNS Annual Report 2011 (2013) 82

ISBN 978-3-95450-131-1

[3] S.Watanabe et al., Nucl. Instrum. and Meth. **A633** (2011) 8
[4] Y.Oshiro et al., Rev. Sci. Instr. 85, 02A912 (2014)
[5] H. Muto et al., Rev. Sci. Instr. 85 (2014) 02A905
[6] S.Watanabe et al., CNS Annual Report 2005 (2006) 55
[7] A.S.Vorozhtsov et al., RIKEN-NC-AC-2
[8] E.E.Perepelkin et al., RuPAC 2008 (2008) p40
[9] S.B. Vorozhtsov et al., RuPAC 2008 (2008) p51
[10] S.B. Vorozhtsov et al., Proc. Particle Accelerator Society Meeting 2009 p240
[11] A.Goto et al. RIKEN Accel. Prog. Rep. 43 (2010) 127
[12] T.Hoffmann et al., Proc. 9th BIW 2000, Cambridge, USA, PP.432-439
[13] S.Kohara et al., Nucl. Instrum. and Meth. **A526** (2004) 230
[14] S.Kohara et al. RIKEN Accel. Prog. Rep. 39 2005(2006) 23

ISBN 978-3-95450-131-1

PHASE BUNCHING IN THE CENTRAL REGION OF THE JAEA AVF CYCLOTRON FOR HEAVY-ION ACCELERATION IN THE THIRD-HARMONIC MODE

N. Miyawaki#, S. Kurashima, H. Kashiwagi, S. Okumura, JAEA, Gunma, Japan
M. Fukuda, Osaka University, Osaka, Japan

Abstract

Phase bunching realized in the central region of the JAEA AVF cyclotron for heavy ion acceleration in the third-harmonic mode (h = 3) was evaluated using both calculations with a simplified geometric trajectory model and measurements of internal beam phase distributions. The phase bunching effect for h = 3 was compared with that for h = 2, where the geometric condition of the central region differs from that for the former. Both of the measurements of internal beam phase distributions without the buncher and the calculations with the model have shown that the phase bunching effect for h = 3 was equivalent to that for h = 2 when a beam buncher was not used before the acceleration. In the measurement using the buncher, the phase width in the case of h = 3 was larger than that of h = 2. In order to enhance of the phase bunching for h = 3, it is necessary to modify the geometric condition of the central region and to increase the ratio of a peak dee-voltage to an extraction voltage of an ion source, which is one of the parameters determining the phase bunching performance, with a suitable injected beam distribution in the radial phase space.

INTRODUCTION

The azimuthally varying field (AVF) cyclotron with a K number of 110 MeV at the Japan Atomic Energy Agency (JAEA) is widely utilized for research in radiochemistry, biotechnology and materials science as well as nuclear physics and the production of radioisotopes [1]. In order to produce a variety of heavy ion beams in a wide range of energy, the cyclotron is operated with three acceleration harmonic modes of h = 1, 2 and 3, which is defined as f_{rf} / $f_{particle}$, a ratio of the rf frequency to the orbital one. Heavy ions up to osmium ions are produced by four normal conducting electron cyclotron resonance (ECR) ion sources.

Recently, the cyclotron was upgraded for the advanced ion beam applications using a microbeam [2] and a single-pulse beam [3]. In the microbeam formation, an energy spread of the order of 10−4 is required to reduce the influence of chromatic aberrations caused in the focusing lenses. A flat-top acceleration system was developed to minimize energy spread of an ion beam [4], and the central region of the cyclotron was remodelled to minimize the beam phase width [5]. For production of the single-pulse beam, specific techniques to optimize the acceleration phase [6] and to stabilize the magnetic field [7] are needed to enhance the controllability of the beam pules number extracted from the cyclotron [3].

#miyawaki.nobumasa@jaea.go.jp

ISBN 978-3-95450-131-1

The remodelled central region generates the phase bunching effects in the acceleration harmonic mode of h = 2 and 3. Phase bunching originates in energy-gain modulation produced in a rising-slope region of an acceleration-voltage waveform at the first acceleration gap, and minimizes the beam phase width at the second acceleration gap. We elucidated the mechanism of phase bunching by a simplified geometric trajectory model [8]. The beam phase correlations between the first and the second acceleration gap obtained by the geometric trajectory model for three acceleration harmonics in the JAEA AVF cyclotron were consistent with the correlations between the initial beam phase and the beam phase at 100 turns analysed by the orbit simulation [9]. Moreover, the phase bunching performance in the central region of the cyclotron was evaluated by measurement of the beam phase distributions. The correlations between the buncher phase and the measured internal phase distribution for h = 1 and 2 were consistent with the calculated results obtained by the geometric trajectory model [10]. However, the phase bunching effect for h = 3 in the central region, where the geometric condition of h = 2 is different, was not evaluated yet.

In this paper, we described the calculation and the measurement of the phase bunching for h = 3 in the JAEA AVF cyclotron, and the comparison of the phase bunching effect for h = 3 with that for h = 2.

CALCULATION OF PHASE BUNCHING BY GEOMETRIC TRAJECTORY MODEL

The phase bunching performance was evaluated with the correlation between the initial phase difference $\Delta\phi$ and the phase difference $\Delta\phi$S at the second acceleration gap by the geometric trajectory model in homogeneous magnetic field, as indicated by the following equation,

$$\Delta\phi_S = \Delta\phi + h\left(\theta_E + \Delta r'\right) + h\cdot\sin^{-1}\left[\begin{array}{l}\dfrac{\sqrt{1-V_R\sin\phi_P}+\Delta r}{\sqrt{1-V_R\sin\left(\phi_P+\Delta\phi\right)}}\sin\theta_P \\ -\sin\left(\theta_E+\Delta r'+\theta_P\right)\end{array}\right], \quad (1)$$

where θ_P is a span angle from the first to the second acceleration gap, θ_E is the angle between the straight line of the acceleration gap passing through the cyclotron center and the line perpendicular to the particle emitting direction, V_R is the ratio of a peak dee-voltage to an extraction voltage of an ion source in units of MV, Δr and Δr' are the position difference and emission angle difference from the reference particle, respectively and ϕ_P

is the initial RF phase of the reference particle at the first acceleration gap. When the reference particle passes through the center of the dee electrode, the RF phase ϕ_P is defined to be 0, and ϕ_P is indicated by the following equation,

$$\phi_P = -h\left(\theta_P - \frac{\theta_{Dee}}{2}\right) \quad (2),$$

where θ_{Dee} is a span angle of a dee electrode. When both Δr and $\Delta r'$ are 0, the phase bunching performance mainly depends on the combination of the four key parameters; θ_P, θ_{Dee}, h and V_R [8]. The phase difference $\Delta\phi_S$ is susceptible to higher h as shown in the third term of Eq. (1). The higher harmonic mode is typically needed to accelerate the heavier ion within upper limit of the magnetic field in a cyclotron. Therefore, the phase bunching effect is easily obtainable in the acceleration condition of heavy ions.

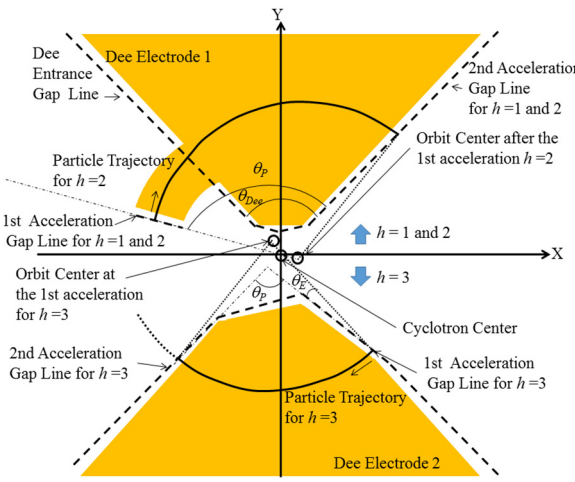

Figure 1: Layout of the geometric trajectory analysis model for the remodelled central region in the JAEA AVF cyclotron.

The geometric trajectory model was applied to the remodelled central region the JAEA AVF cyclotron with two dee electrodes of $\theta_{Dee} = 86°$, as shown in Fig. 1. In h = 1 and 2, the span angle θ_P is equal to 118° since the first acceleration gap is located in front of the puller electrode of the dee electrode 1. The initial phase width of 40 RF degrees for reference particle centered at ϕ_P was reduced to 7.8 RF degrees for h = 2. The span angle θ_P for h = 3 is equal to 78° since a tip of the dee electrode 2 is deformed. The angle difference θ_E from θ_{Dee} is equal to 17°. Then, the phase offset $h\theta_E$ of 51 RF degrees at the second acceleration gap results from the second term of Eq. (1). Moreover, the optimum initial phase, at which the phase bunching effect is maximized, is changed by the phase offset in the third term. The initial phase width of 40 RF degrees for reference particle centered at the initial phase of −22 RF degrees was minimized to 7.8 RF degrees. The phase bunching performance of h = 3 was equal to h = 2.

MEASURMENT OF BEAM PHASE DISTRIBUTION IN THE CYCLOTRON

The beam phase distributions were measured to compare the effect of phase bunching on the beam phase width between the acceleration modes in the JAEA AVF cyclotron. The measurement of the beam phase without the buncher was carried out by the radial probe with a plastic scintillator (BC400, Saint-Gobain) in the cyclotron since the buncher restricts the initial beam phase. In order to enhance the accuracy of the measurement, the deviation from an isochronous field was decreased within ±3 RF degrees and a phase shift from the top of the sinusoidal dee-voltage waveform was reduced within 3 RF degrees by changing the currents of the trim coils. The measured beam phase distributions for a 107 MeV $^4He^{2+}$ beam of h = 1 (black), a 260 MeV $^{20}Ne^{7+}$ beam of h = 2 (red) and a 120 MeV $^{20}Ne^{6+}$ beam of h = 3 (blue) are shown in Fig. 2. The beam phase distributions of h = 2 and 3 were narrower than that of h = 1 because of phase bunching. There is little difference on the beam phase width between h = 2 and 3 after phase bunching. These results were consistent with the calculation results. The phase offset had no effect on phase bunching, because the beam phase after phase bunching was adjusted to the top of the waveform by changing the currents of the trim coils.

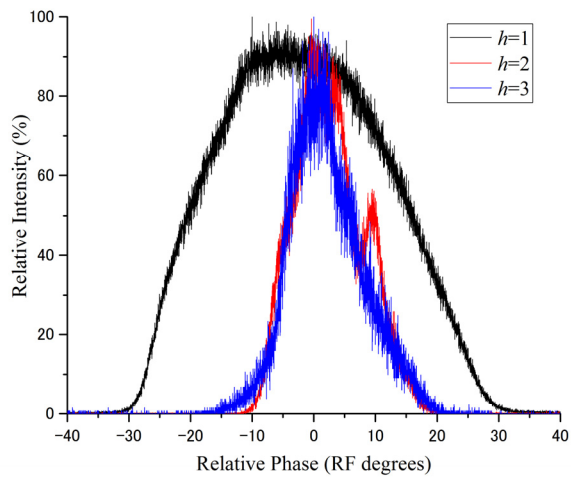

Figure 2: Measured phase distributions by the radial probe without the buncher for a 107 MeV $^4He^{2+}$ beam of h = 1, a 260 MeV $^{20}Ne^{7+}$ beam of h = 2 and a 120 MeV $^{20}Ne^{6+}$ beam of h = 3 in the JAEA AVF cyclotron.

The effect of the initial phase on phase bunching was investigated by the measurement of the beam phase distribution with changing the buncher phase. The initial phase at the first acceleration gap can be relatively determined by adjusting the buncher phase with a resolution of less than 0.367 RF degrees. The measurement results for a 260 MeV $^{20}Ne^{7+}$ beam of h = 2 and a 120 MeV $^{20}Ne^{6+}$ beam of h = 3 are shown in Fig. 3 and 4, respectively. These contour maps (black line) were formed by merging larger than 50% regions of particle density distributions measured in 1% relative buncher phase

ISBN 978-3-95450-131-1

increments from −8% to 8%, which correspond to the initial RF phase region from −29.4 to 29.4 RF degrees. Moreover, in order to investigate the shape of the measured contour map, the phase correlations for h = 2 and 3 calculated by the model with Δr and $\Delta r'$ were also shown in Fig. 3 and 4, respectively. The calculation was carried out for 9 particles with different initial conditions: Δr = −2 (red), 0 (green), 2 mm (blue), and $\Delta r'$ = −20 (broken line), 0 (solid line), 20 mrad (dotted line). We assumed that the center of the initial phase of distributions in the measured contour map corresponded to the initial phase in the calculated correlations which the slope at the center of the distributions in the measured contour map is consistent with the slope of the calculated correlation.

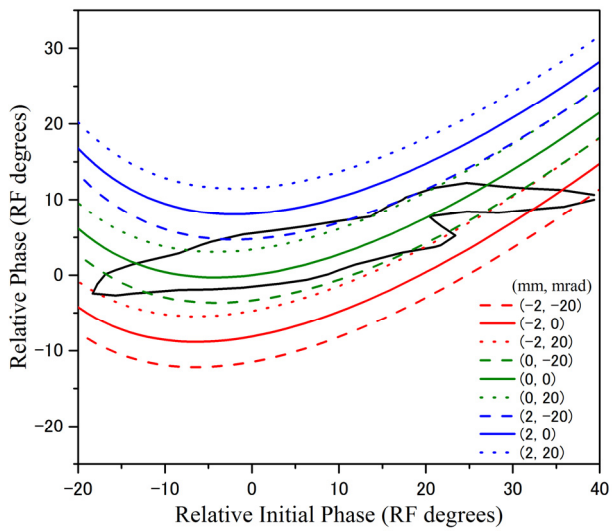

Figure 3: Contour map formed by merging larger than 50% regions in measured particle density distribution for a 260 MeV $^{20}Ne^{7+}$ beam and the calculation result for h = 2.

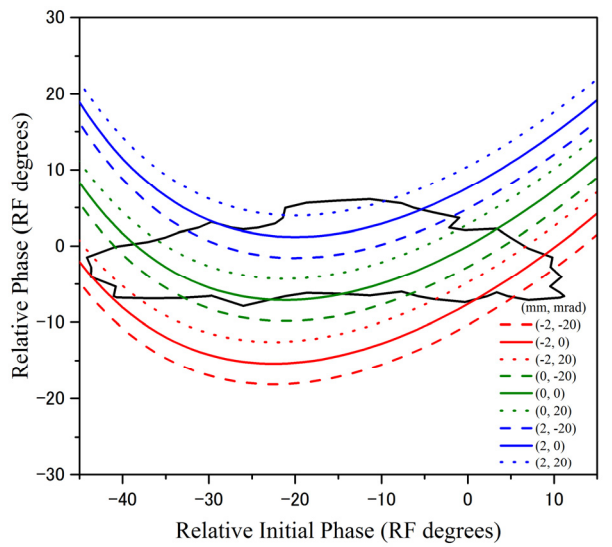

Figure 4: Contour map formed by merging larger than 50% regions in measured particle density distribution for a 120 MeV $^{20}Ne^{6+}$ beam and the calculation result for h = 3.

Both distributions in the contour maps clearly show the phase bunching effect; the initial phase difference larger than 55 RF degrees was compressed to the measured phase difference less than 15 RF degrees. The measured total phase width for the whole initial phase of h = 2 was nearly equal to that of h = 3. However, the measured local phase width of h = 2 for each initial phase was the smaller than that of h = 3.

The center of the initial phase in the measured contour map for h = 2 and 3 were estimated at 11 and −16 RF degrees, respectively. The difference of the center of the initial phase between h = 2 and 3 was consistent with the initial phase difference caused by the phase offset. The distribution in the contour maps depends on the phase offset in the geometric condition. On the other hand, the calculation indicated that the interval between the correlation lines narrowed in an upward-sloping region of the lagged initial phase. The interval between the correlation lines depended on V_R which is one of the parameters determining the phase bunching performance. Moreover, the interval between the correlation lines also depended on the particle distribution in radial phase space, because the calculated correlations with (Δr, $\Delta r'$) = (0, -20) and (0, 20) were proximate to (-2, 20) and (2, -20), respectively. The distribution in the measured contour map for h = 2 overlapped with the upward-sloping region, but the distribution for h = 3 was away from the region. Therefore, the local beam phase width for h = 2 was narrower than that for h = 3.

Enhancement of the phase bunching effect for h = 3 needs to modify the geometric condition with a decrease in θ_E and to optimum V_R with a suitable injected beam distribution in the radial phase space. Further empirical studies are needed to obtain optimum conditions in radial phase space for enhancement of the phase bunching effect.

REFERENCES

[1] K. Arakawa et al., in: Proceedings of the 13th International Conference on Cyclotrons and their Applications, Vancouver, Canada, 1992, p. 119.
[2] M. Oikawa et al., Nucl. Instr. and Meth. B 260 (2007) 85.
[3] S. Kurashima et al., Rev. Sci. Instrum. 86 (2015) 073311.
[4] M. Fukuda et al., Rev. Sci. Instrum. 74 (2003) 2293.
[5] N. Miyawaki et al., Nucl. Instr. Meth. A 636 (2011) 41.
[6] S. Kurashima et al., Rev. Sci. Instrum. 81 (2010) 033306.
[7] S. Okumura et al., Rev. Sci. Instrum. 76 (2005) 033301.
[8] N. Miyawaki et al., Nucl. Instr. Meth. A 715 (2013) 126.
[9] N. Miyawaki et al., in: Proceedings of the 20th International Conference on Cyclotrons and their Applications, Vancouver, Canada, 2013, p. 350.
[10] N. Miyawaki et al., Nucl. Instr. Meth. A 767 (2014) 372.

ISBN 978-3-95450-131-1

STATUS REPORT OF THE OPERATION OF THE RIKEN AVF CYCLOTRON

K. Suda*, M. Fujimaki, N. Fukunishi, T. Kageyama, O. Kamigaito, M. Kase, M. Komiyama, K. Kumagai, T. Maie, M. Nagase, T. Nagatomo, T. Nakagawa, H. Okuno, N. Sakamoto, A. Uchiyama, T. Watanabe, Y. Watanabe, K. Yamada,
RIKEN Nishina Center for Accelerator-Based Science, Wako, Saitama, Japan
T. Nakamura, S. Fukuzawa, M. Hamanaka, S. Ishikawa, K. Kobayashi, R. Koyama, M. Nishida, M. Nishimura, J. Shibata, N. Tsukiori, K. Yadomi,
SHI Accelerator Service Ltd., Shinagawa, Tokyo, Japan
Y. Kotaka, Y. Ohshiro, S. Yamaka,
Center for Nuclear Study, University of Tokyo, Wako, Saitama, Japan

Abstract

The RIKEN AVF cyclotron has been operating 26 years as an injector for the RIKEN ring cyclotron. The AVF cyclotron also provides low energy ion beams for the CNS Radio-Isotope Beam separator (CRIB) of the Center for Nuclear Study (CNS), the University of Tokyo, as well as to produce RIs for commercial use. The operating time is more than 2,000 hours per year.

INTRODUCTION

The RIKEN AVF cyclotron (AVF, K=70 MeV) [1] was constructed as an injector for the RIKEN Ring Cyclotron (RRC, K=540 MeV) [2]. In the AVF-RRC acceleration mode, ions from H^{2+} to ^{87}Rb are accelerated by AVF up to 3.78 to 7 MeV/u, and are further accelerated by RRC up to 65 to 135 MeV/u. They are provided to experimental course of RIKEN Accelerator Research Facility (RARF).

Since 1991, it was started to provide low energy heavy ion beams as a stand alone accelerator (AVF standalone mode). In the AVF standalone mode, various ions from proton (A/Q=1) to ^{42}Ca (A/Q=3.5) are accelerated up to 3.41 to 12.5 MeV/u (14 MeV for proton). The beams are provided for experiments of nuclear physics with CRIB (E7A course) [3], for student experiments (E7B course) and for production of Radioactive Isotopes (C03 course), as shown in Fig 1.

Since 2009, the AVF was started to be used as an injector of light ions for the RI-Beam Factory (RIBF) [4, 5]. In the light-ion mode of RIBF, the AVF Cyclotron has provided polarized deuteron, ^{14}N, ^{18}O, etc., so far. The beams further accelerated by RRC and Superconducting Ring Cyclotron (SRC, K=2600 MeV) [6] are provided for experiments of RIBF.

Three external ion sources (HYPER-ECR, SC-ECR, and Polarized deuteron) are available. One of the ion sources are selected to be used depending on the requirement of nuclear species (metal, gas). The beam time schedule is decided by considering the development and preparing time of ion sources, so that the nuclear species can be changed in a short time as much as possible.

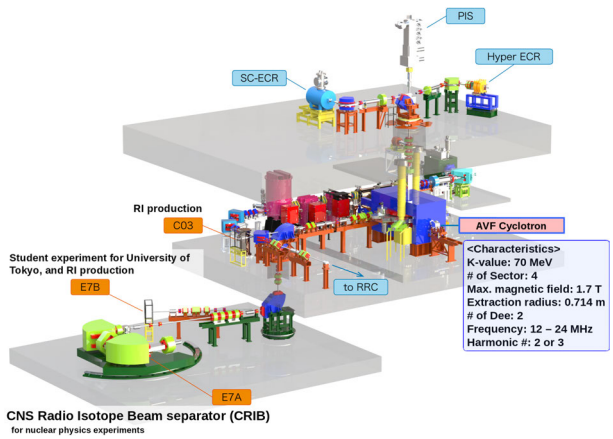

Figure 1: Overall view of the RIKEN AVF cyclotron with ion sources, and beam courses of the AVF standalone operation.

We will report the operating status of AVF (beam energies and species, operation statistics, troubles, and maintenance work) for the period from August 2014 to July 2015.

ACCELERATED BEAMS

Figure 2 shows energy per nucleon versus mass number for all kinds of beams accelerated by the AVF cyclotron. The species accelerated before August 2014 are shown by open solid circles. In this period, in the AVF standalone mode, two kinds of beams ($^4He^{2+}$ at 7.5 and 10.0 MeV/u) were extracted for the first time (red solid circles). The other eight beams in this mode are shown by red open circles. In the AVF-RRC mode, $^{40}Ar^{11+}$ accelerated up to 3.78 MeV/u was extracted for the first time (blue solid circles). The other six beams in this mode are shown by blue open circles. In the RIBF mode, polarized deuteron at 3.97 MeV/u was extracted (a green open circle). Accelerated beams in this period for these acceleration modes are summarized in Table 1.

* ksuda@ribf.riken.jp

ISBN 978-3-95450-131-1

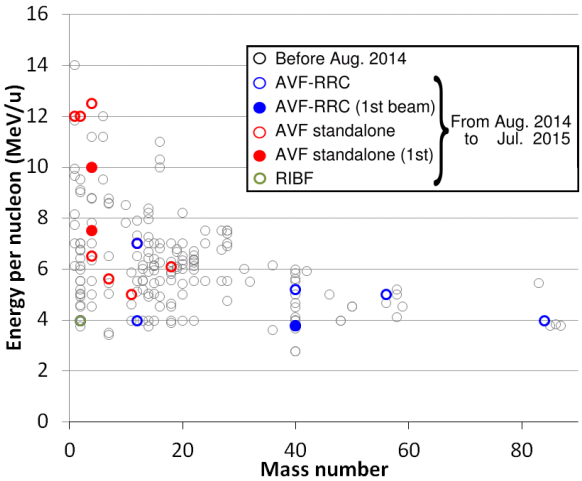

Figure 2: Energy per nucleon versus mass number of ions extracted from the AVF cyclotron.

Table 1: Beams Extracted from the AVF in this Period

Mode	Ions	Energy [MeV/u]
AVF standalone	$^{1}H^{+}$	12
	$^{2}H^{+}$	12
	$^{4}He^{2+}$	6.5, 7.5*, 10.0*, 12.5
	$^{7}Li^{2+}$	5.6
	$^{11}B^{3+}$	5.0
	$^{12}C^{4+}$	7.0
	$^{18}O^{6+}$	6.07
AVF-RRC	$^{2}H^{+}$	12
	$^{12}C^{4+}$	3.97, 7.0
	$^{40}Ar^{11+}$	3.78*, 5.2
	$^{56}Fe^{15+}$	5.0
	$^{84}Kr^{20+}$	3.97
RIBF	Polarized $^{2}H^{+}$	3.97

*First beam

OPERATING STATISTICS

Figures 3 and 4 show the operation time for the AVF standalone mode, and the AVF-RRC and RIBF modes, respectively. The tuning time is a sum of periods from a start

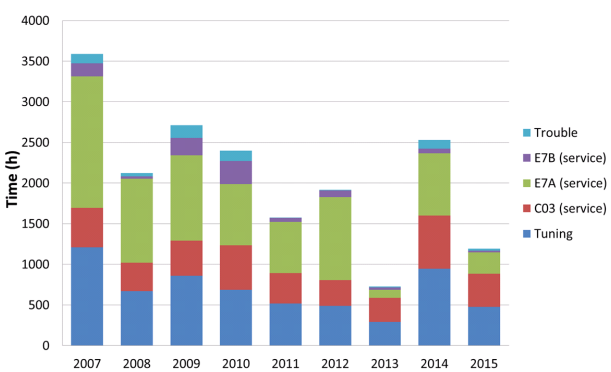

Figure 3: Operation time for AVF standalone mode.

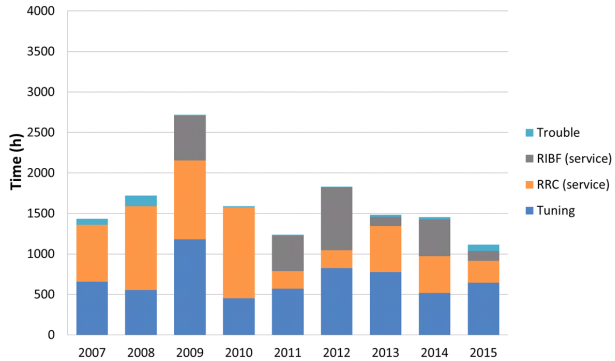

Figure 4: Aeration time for AVF-RRC and RIBF modes.

of the cycling of AVF main magnet to a finish of the spot tuning on a target. In the case of the AVF-RRC and RIBF modes, the tuning time for accelerators other than AVF is also included. The beam service time for each course (C03, E7A, E7B, RRC, RIBF) is defined as a sum of the period from the finish of spot tuning to the end of the experiment. The statistics for each year from August 2006 to July 2015 are presented.

In the latest period (2015), for the AVF standalone mode, beam service time for C03, E7A, and E7B were 478, 261, and 22 h, respectively. The total operation time was 1169 h, which was decreased by 52% from 2423 h in the previous period. Most troubles occurred during beam tuning at a magnetic channel, and they were fixed during that time. The total failure time was 26 h. All the beam service scheduled was completed.

For the AVF-RRC and RIBF modes, total operation time was 1036 h, which was decreased by 27% from 1426 h. This was because the operation time of other injectors RILAC [7] and RILAC2 [8] was increased. There was almost no trouble for the AVF cyclotron, however, the total failure time including RRC was 79 h, which was increased by 52 h compared with the previous period.

TROUBLES

Major troubles occurred at a magnetic channel (one of beam extraction devices), which was used since 2007 (Fig. 5). In September 2014, during beam tuning of the AVF, a leakage of cooling water occurred at one of hollow conductors due to a pinhole (Fig. 6). We closed the hole with paste. In July 2015, during a startup of the AVF, no electric current was observed in coils of the magnetic channel. The coils became open circuited because fixing bolts of electrodes which connects two hollow-conductors were loosened and melted (Fig 7). The bolts and electrodes were replaced with spare parts.

NEW MAGNETIC CHANNEL

To improve reliability, we replaced the old magnetic channel with a newly fabricated one in this summer (Fig. 8). The exchange operation was started at the end of July 2015, and finished in August 2015. Beam test was successfully performed on the middle of August.

ISBN 978-3-95450-131-1

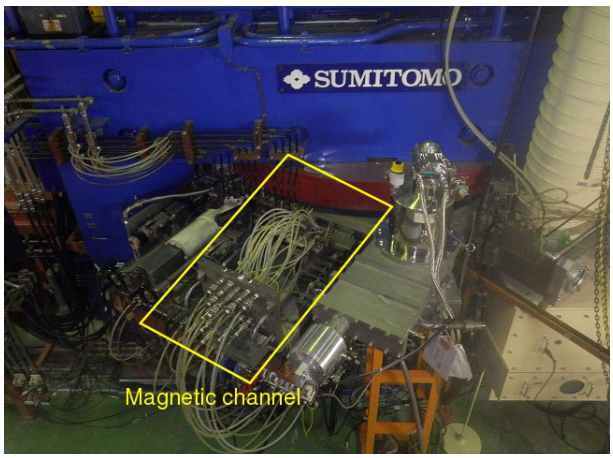

Figure 5: Magnetic channel of the AVF cyclotron.

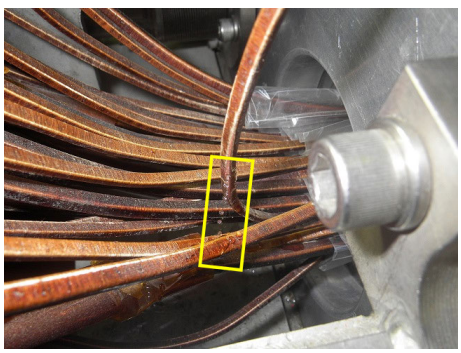

Figure 6: A leakage of cooling water at a hollow conductor of the magnetic channel.

Figure 7: Normal connection between two hollow-conductors with electrodes (left), and damaged electrodes (right).

Figure 8: A new magnetic channel.

REFERENCES

[1] A. Goto et al., Proceedings of 12th International Conference on Cyclotrons and their Applications, Berlin, Germany (1989) 51.

[2] Y. Yano, Proceedings of 13th International Cyclotron Conference (1992) 102.

[3] Y. Yanagisawa et al., Nucl. Instrum. and Methods A 539 (2005) 74–83.

[4] Y. Yano, The RIKEN RI beam factory project: A status report, Nucl. Instrum. and Methods B 261 (2007) 1009–1013.

[5] K. Ozeki et al., Status Report on the Operation of the RIBF Ring Cyclotrons, WEPB01, in this proceedings.

[6] H. Okuno et al., IEEE Trans. Appl. Supercond., 17, (2007) 1063.

[7] M. Odera et al., Variable frequency heavy-ion linac, RILAC: I. Design, construction and operation of its accelerating structure, Nucl. Instrum. and Methods 227 (1984) 187–195.

[8] K. Yamada et al., Beam commissioning and operation of new linac injector for RIKEN RI beam factory, IPAC12, New Orleans, TUOBA02 (2012) 1071–1073.

ISBN 978-3-95450-131-1

IMPROVEMENT OF MASS-TO-CHARGE RATIO RESOLUTION OF THE JAEA AVF CYCLOTRON USING A BEAM CHOPPING SYSTEM

S. Kurashima#, N. Miyawaki, H. Kashiwagi, JAEA, Gunma, Japan
M. Fukuda, Osaka University, Osaka, Japan

Abstract

A mass-to-charge ratio (M/Q) resolution of the JAEA cyclotron is about 3,300 and this high-resolution enables us to quickly change the ion species by a cocktail beam acceleration technique. To further improve the M/Q resolution, a new technique is being developed by combining the cocktail beam acceleration and beam chopping techniques. The beam chopping system consists of a pre-beam kicker installed in the beam injection line and a post-beam kicker downstream of the cyclotron. This new technique is able to separate beam bunches from a pulse train of the ion beam including impurity ion species. As a result, we succeeded to completely separate the 125 MeV $^{20}Ne^{5+}$ and the 100 MeV $^{16}O^{4+}$ beams, that was quite difficult using previous techniques. The M/Q resolution of the cyclotron has been significantly improved to 25,000 at present.

INTRODUCTION

An AVF cyclotron with a K-value of 110 MeV was constructed at TIARA (Takasaki Ion accelerators for Advanced Radiation Application) facility of the Japan Atomic Energy Agency (JAEA) to provide high-energy ion beams mainly for research in biotechnology and materials science [1]. Various kinds of beam irradiation techniques such as a heavy-ion microbeam formation and a large-area uniform irradiation were developed for beam users.

A cocktail beam acceleration technique [2,3] was also developed for quick change of the ion species extracted from the cyclotron. In this technique, a cocktail of ions having almost identical mass-to-charge ratio (M/Q), produced in an ion source, is injected into the cyclotron. The cyclotron can separate an ion species from others since the cyclotron has another aspect as a high-performance mass spectrometer. Change of the ion species completes within about ten minutes by adjusting an acceleration frequency and changing a feeding gas of the ion source if necessary. However, the cocktail of ions such as $^{16}O^{4+}$ and $^{20}Ne^{5+}$ was not available since the M/Q resolution of the cyclotron was inadequate to separate them. To improve the M/Q resolution, a new technique has been developed by combining the cocktail beam acceleration and a beam chopping techniques.

In this paper, we briefly describe theories of the cocktail beam acceleration and the unique method to improve the M/Q resolution, and show some experimental results.

E-mail: kurashima.satoshi@jaea.go.jp

COCKTAIL BEAM ACCELERATION

A radio frequency f_{RF} of an acceleration voltage generated on a pair of dee electrode is expressed as

$$f_{RF} = hf_{ion} = \frac{h}{2\pi}\frac{eQ}{uM}B\,, \qquad (1)$$

where h is an acceleration harmonics defined by the ratio of f_{RF} to the orbital frequency of the ion f_{ion}, e elementary electric charge, Q charge state of the ion, u atomic mass unit, M mass of the ion in u, B magnetic field for isochronism. A beam bunch of the ion is repeatedly accelerated at a fixed phase of the rf voltage under good isochronous field, and is extracted from the cyclotron through an electrostatic deflector and a magnetic channel. When other ion species with a slight difference of the mass-to-charge ratio $\Delta(M/Q)$ is injected into the cyclotron, shift of the acceleration phase $\Delta\phi$ after N revolutions is given by

$$\Delta\phi = 2\pi hN\frac{\Delta(M/Q)}{(M/Q)}\,. \qquad (2)$$

Table 1 shows a list of ion species with the $M/Q \approx 4$, and here, we assume that $^{12}C^{3+}$, $^{16}O^{4+}$ and $^{20}Ne^{5+}$ beams are simultaneously injected into the cyclotron tuned to accelerate them up to 6.25 MeV/u. When the acceleration frequency f_{RF} is adjusted for $^{16}O^{4+}$ beam the acceleration phase of $^{20}Ne^{5+}$ advances and that of $^{12}C^{3+}$ lags gradually. The $\Delta\phi$ of $^{12}C^{3+}$ is much larger since the M/Q difference from $^{16}O^{4+}$ is about 5 times as large as that of $^{20}Ne^{5+}$, as shown in Fig. 1. The design values of the total number of revolutions are 550, 265 and 210 for the acceleration harmonics h = 1, 2 and 3, respectively. The impurity ion species cannot be extracted from the cyclotron when the energy gain of the beam bunch reaches deceleration region or decreases considerably after hundreds of revolutions. As a result, only one ion species is extracted. The ion species can be changed quickly by adjusting f_{RF} corresponding to the M/Q difference. This is the principle

Table 1: List of ion species with the $M/Q \approx 4$. Beam energy is 6.25 MeV/u for all ion species (h = 2).

Ion	M/Q	$\Delta(M/Q)/(M/Q)$	f_{RF} (MHz)
$^{4}He^{1+}$	4.00205		11.9079
		6.501×10^{-4}	
$^{12}C^{3+}$	3.99945		11.9156
		3.176×10^{-4}	
$^{16}O^{4+}$	3.99818		11.9194
		6.003×10^{-5}	
$^{20}Ne^{5+}$	3.99794		11.9201
		5.230×10^{-4}	
$^{36}Ar^{9+}$	3.99585		11.9264
		4.004×10^{-5}	
$^{40}Ar^{10+}$	3.99569		11.9268

ISBN 978-3-95450-131-1

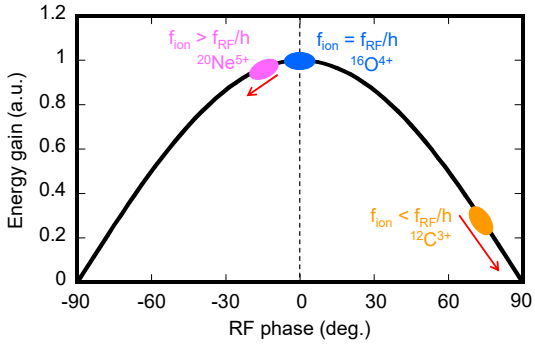

Figure 1: Correlation of the rf phase and the beam bunch for the ion species with the M/Q ≈ 4. The acceleration frequency f_{RF} is optimized for $^{16}O^{4+}$.

of the cocktail beam acceleration.

The M/Q resolution R is defined by

$$R = \left| \frac{(M/Q)}{\Delta(M/Q)} \right|, \qquad (3)$$

and the value of the cyclotron is about 3,300 [3]. Although cocktail beams such as the $M/Q \approx 2$ (26.7 MeV/u) and 5 (3.75 MeV/u) are available, the M/Q resolution is inadequate to separate the cocktail of ions such as $^{16}O^{4+}$ and $^{20}Ne^{5+}$, or $^{36}Ar^{9+}$ and $^{40}Ar^{10+}$, shown in Table 1. To separate them completely, a unique technique described in next section is being studied.

IMPROVEMENT OF M/Q RESOLUTION USING A CHOPPING SYSTEM

A beam chopping system, consisting of two types of high voltage kickers, is used to drastically increase the interval between beam pulses [4]. The first kicker (chopper 1) is installed in the beam injection line and injects a short beam pulse with repetition periods greater than 4.2 μs. The other kicker (chopper 2) downstream of the cyclotron thins out unwanted beam pulses caused by multi-turn extraction. As a result, a single-pulse of the ion beam with a repetition period over micro seconds is formed [5]. A variety of single-pulse beams are used for experiments such as pulse radiolysis and time-of-flight measurement of secondary particles.

A kicker voltage of the chopper 2 is originally sinusoidal waveform ranging from 1 to 3 MHz, and 40 kV at a maximum. The chopper 2 was temporarily modified to a pulse voltage beam kicker as shown in Fig. 2 for this study. The modified chopper 2 using a fast pulse generator (PVX-4110, Directed Energy Incorporated) is able to cut the beam bunches over a long duration compared to the original sinusoidal waveform one.

In the case of cocktail beam acceleration, as shown in Fig. 1, the energy gain of the impurity ion species gradually decreases every revolution, while the beam bunch of $^{16}O^{4+}$ whose f_{ion} equals f_{RF}/h is accelerated at a fixed rf phase. This means that more number of revolutions compared to the $^{16}O^{4+}$ is needed to reach the extraction radius for the impurity ion species. In other

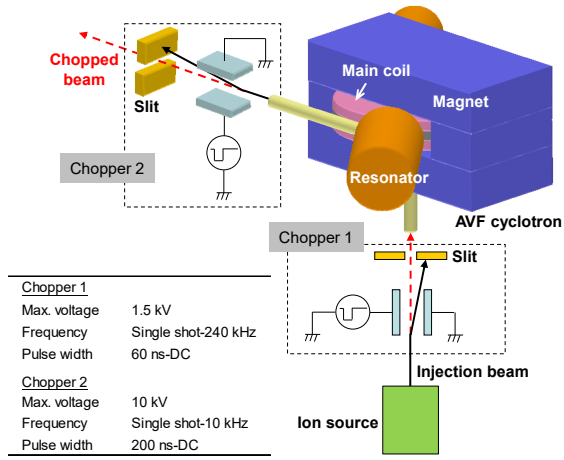

Figure 2: Layout of the cyclotron and the beam chopping system consisting of two beam kickers, installed in the beam injection line and downstream of the cyclotron, respectively.

words, the impurity ion species are extracted with delay if the cyclotron cannot remove them completely. When the chopper 1 injects a short beam pulse with about 1 cycle length (= $1/f_{RF}$), the beam pulses appear out of the cyclotron in the order of $^{16}O^{4+}$ and $^{20}Ne^{5+}$. A tiny amount of the $^{12}C^{3+}$ beam might be observed at last since the M/Q resolution of the cyclotron is close to the M/Q difference between $^{16}O^{4+}$ and $^{12}C^{3+}$. If the chopper 2 can remove the impurity ion beams by kicking them out fast, only the $^{16}O^{4+}$ beam is separated and transported to a user's target. This is the principle for improving the M/Q resolution by combining the cocktail beam acceleration and the beam chopping techniques. To realise this technique, it is indispensable to accelerate the objective ion species on the top of cosine wave where the energy gain is maximum; a method to measure and control the acceleration phase of the beam bunch is described in Ref. 6, in detail [6].

EXPERIMENTAL RESULTS

Cocktail ions listed in Table 1, excluding $^{4}He^{1+}$, were used for the experiment. The 100 MeV $^{16}O^{4+}$ (6.25 MeV/u, $h = 2$) was selected as a standard beam, and the magnetic field for isochronism and the acceleration phase were optimized using the beam. The number of revolutions was increased from the design value of 265 to about 290 by reducing the dee voltage to enlarge the phase shift $\Delta\phi$ of the impurity ion species. Only oxygen gas was fed into an electron cyclotron resonance (ECR) ion source, first.

Figure 3 shows an energy spectrum of the 100 MeV $^{16}O^{4+}$ beam measured by a solid-state detector (SSD) and a multi-channel analyser (MCA). Peaks of the 75 MeV $^{12}C^{3+}$ and the 125 MeV $^{20}Ne^{5+}$ were observed other than the main peak of 100 MeV $^{16}O^{4+}$. The amounts of contamination were estimated to be 0.06% for $^{12}C^{3+}$ and 0.2% for $^{20}Ne^{5+}$, respectively. The tiny amount of contamination was caused by residual gases in the ECR

ISBN 978-3-95450-131-1

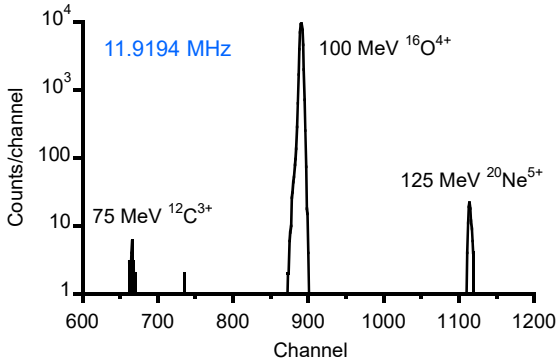

Figure 3: Energy spectrum of the 100 MeV $^{16}O^{4+}$ beam measured by using the SSD and MCA. Only oxygen gas was fed to the ECR ion source.

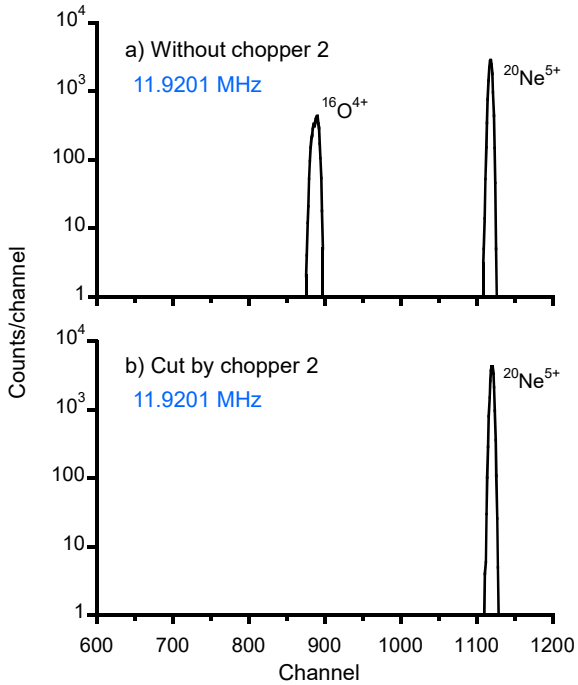

Figure 4: Energy spectra of the 125 MeV $^{20}Ne^{5+}$ beam. Only Ne gas was fed to the ion source just after generation of the $^{16}O^{4+}$ beam. a) The chopper 1 was used alone, and b) both the choppers were used to remove the 100 MeV $^{16}O^{4+}$.

ion source. Next, the feeding gas of the ion source was changed to neon. The acceleration frequency was also changed from 11.9194 to 11.9201 MHz, and the energy spectrum was immediately measured by the SSD using the chopper 1 alone for short pulse injection, as shown in Fig. 4 a). The amount of contamination by the $^{16}O^{4+}$ was estimated to be about 20%. Figure 5 shows a pulse train of the 125 MeV $^{20}Ne^{5+}$ beam, contaminated by the 100 MeV $^{16}O^{4+}$, measured by a plastic scintillator and a picosecond time analyser (9308, Ortec). The pulse train consists of the first main pulse and the other small sub-pulses. The beam bunches after the second pulse were cut

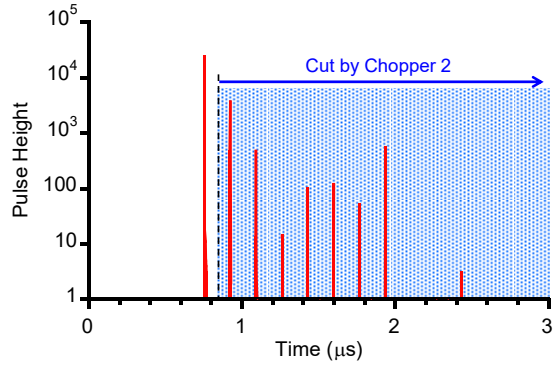

Figure 5: Pulse train of the 125 MeV $^{20}Ne^{5+}$ beam measured by a plastic scintillator. Condition of the beam tuning corresponds with that of Fig. 4 (a). The beam bunches covered by blue box were removed by the chopper 2 later, as described in the text.

by carefully adjusting the chopper 2, and the energy spectrum was measured again. The 125 MeV $^{20}Ne^{5+}$ and the 100 MeV $^{16}O^{4+}$ were completely separated as shown in Fig. 4 b). On the other hand, the $^{16}O^{4+}$ beam could not be removed for the case of bam cutting after the third pulse shown in Fig. 5. After that, the ion beam was changed to $^{16}O^{4+}$ again, and the $^{20}Ne^{5+}$ and $^{12}C^{3+}$ beams were successfully removed by the chopping system.

Finally, we tried to separate a 250 MeV $^{40}Ar^{10+}$ and a 225 MeV $^{36}Ar^{9+}$ beams. The M/Q difference of them is the smallest among the ion species shown in Table 1. The impurity $^{36}Ar^{9+}$ beam, however, could not be removed even when sub-pulses other than a first main pulse were cut by the chopper 2. In order to adequately enlarge the energy gain difference between the $^{40}Ar^{10+}$ and $^{36}Ar^{9+}$, the acceleration phase was lagged by about 25 degrees from the top of cosine wave. As a result, only the 250 MeV $^{40}Ar^{10+}$ beam was extracted by using the chopping system. The M/Q resolution of the cyclotron has been significantly improved, and is estimated to be about 25,000. The resolution will be further improved by precise control of the acceleration phase and restriction of the beam phase width.

REFERENCES

[1] K. Arakawa, et al., Proc. 13th Int. Conf. on Cyclotrons and their Applications, Vancouver, Canada, 1992, p. 119.
[2] M.A. McMahan, et al., Nucl. Instrum. and Meth. A 253 (1986) 1.
[3] M. Fukuda, et al., Proc. 1999 Particle Accelerator Conference, New York, USA, 1999, p. 2259.
[4] W. Yokota, et al., Rev. Sci. Instrum. 68 (1997) 1714.
[5] S. Kurashima, et al., Rev. Sci. Instrum. 86 (2015) 073311.
[6] S. Kurashima, et al., Rev. Sci. Instrum. 81 (2010) 033306.

ISBN 978-3-95450-131-1

ELECTROSTATIC DEFLECTOR OF THE CYCLOTRON DC-280 AXIAL INJECTION CHANNEL

N.Kazarinov#, I.Ivanenko, FLNR, JINR, Dubna, Russia

Abstract

The spherical electrostatic deflector will be used in the axial injection channel of the DC-280 cyclotron for rotation of the ion beam onto vertical axis. The results of the simulation of beam dynamics in the deflector based on 3D electrical field map are discussed in this report. The results of simulation of the ion beam transport in the axial injection beam line of the cyclotron are presented also.

INTRODUCTION

The isochronous heavy-ion cyclotron DC-280 is a basic part of the Super Heavy Element Facility – the new accelerator complex of Joint Institute for Nuclear Research [1,2]. The DC-280 cyclotron will produce high-intensity beam of accelerated ions in the range from helium to uranium. The maximum design value of a current of ion beams will be 10 pmcA and the maximum kinetic energy will be 8 MeV/u.

In this report the design of the spherical electrostatic deflector of high voltage injection system [2, 3] of DC-280 cyclotron is presented. Using the electrostatic deflector is explained both weight reduction and lower power of the power supply system in comparison with the bending magnet. The design is based on three-dimensional calculation of the electric field carried out by using OPERA 3D program code [4].

The 3D macro-particle beam dynamic simulation in the deflector was done in the curvilinear coordinates system connected with reference orbit, defined for computational field map. This simulation was carried out by using MCIB04 program code [5].

3D PHYSICAL MODEL OF DEFLECTOR

3D physical model of electrostatic deflector is shown in Fig. 1.

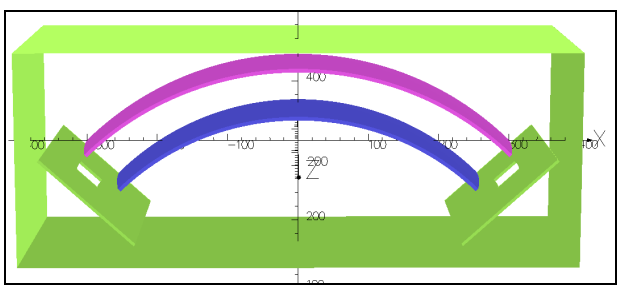

Figure 1: Physical model of deflector.

Bender consists of two electrodes under the potentials U_1 (blue colour), U_2 (red colour) and three ground electrodes (green colour). The design bending radius R=40 cm, the gap between the electrodes d = 6 cm, the horizontal width of the electrodes h = 16 cm. The electric field map consists of two distributions $\Phi_{1,2}(\vec{r})$ corresponding to the following combinations of voltages at the electrodes (U_1=-10kV,U_2=0) and (U_1=0,U_2=10kV). The resulting field map of the deflector $\Phi(\vec{r})$ is a superposition of these distributions:

$$\Phi(\vec{r}) = \left[U_2\Phi_2(\vec{r}) - U_1\Phi_1(\vec{r})\right]\times 10^{-4} \qquad (1)$$

The distributions of the components $E_{X,Y}$ of the electric field along the designed orbit of the deflector are shown in Fig.2.

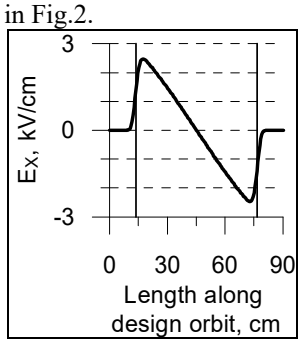

Figure 2a: E_X component of electric field.

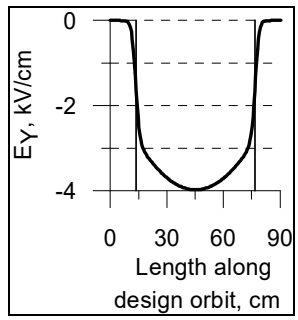

Figure 2b: E_Y component of electric field.

CALCULATED EQUILIBRIUM ORBIT

The calculated equilibrium (solid line) and design (dashed line) orbits are shown in Fig.3a. Deviation Δ between calculated and designed orbits is shown in Fig.3b. In the non-relativistic approximation, the equilibrium orbit in the deflector does not depend on the mass-to-charge ratio A/Z of the ion.

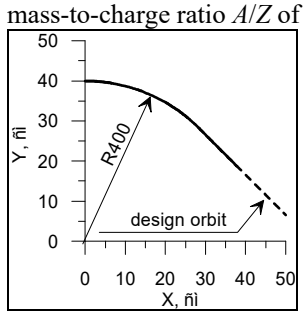

Figure 3a: Deflector orbits.

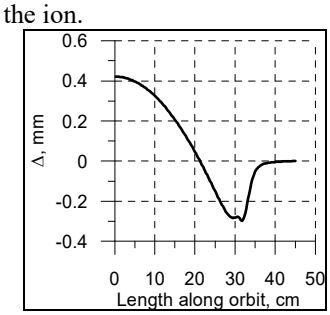

Figure 3b: Deviation Δ.

The particle motion at the equilibrium orbit of the deflector is completely determined by two functions – the curvature of the orbit $K_0(s)$ and "friction coefficient" $\Lambda_0(s)$:

#nyk@lnr.jinr.ru

ISBN 978-3-95450-131-1

$$K_0(s) = -\frac{E_n(s)}{(B\rho\beta)_0};\ \Lambda_0(s) = \frac{E_t(s)}{(B\rho\beta)_0} \qquad (2)$$

Where s – is the distance along the equilibrium orbit; $E_{n,t}(s)$ – are normal and tangent components of the electric field at the equilibrium orbit; $B\rho_0$ and β_0 – are magnetic rigidity and relativistic velocity of the reference particle, respectively.

BEAM FOCUSING IN THE DEFLECTOR

The simulation of the dynamics of the ions in the deflector is convenient to carry out in the natural system of the coordinate (x,z,s) associated with calculated equilibrium orbit. The equation for the radius of the particle $\vec{r}$ in this coordinate system has a form (prime denotes the differentiation with respect to s):

$$\vec{r}'' = \left(\frac{V'}{V} - \frac{V_0'}{V_0}\right)\vec{r}' + \frac{1}{B\rho\beta}\left[\left(\frac{V}{V_0}\right)^2 \vec{E} - \left(\vec{r}'\vec{E}\right)\vec{r}'\right]$$
$$(B\rho\beta)' = [2 - \beta_0^2 (V/V_0^2)](\vec{r}'\vec{E}) \qquad (3)$$
$$\frac{V}{V_0} = \sqrt{(1+K_0 x)^2 + x'^2 + z'^2}$$

The linear approximation of the equations of motion (3) determines the focusing properties of the deflector:

$$x'' = -\Lambda_0 x' - (3-\beta_0^2)K_0^2 x + \frac{1}{(B\rho\beta)_0}\frac{\partial E_n}{\partial x}x +$$
$$+ 2\frac{\Delta M}{M_0}K_0\ ;\ z'' = -\Lambda_0 z' + \frac{1}{(B\rho\beta)_0}\frac{\partial E_z}{\partial z}z \qquad (4)$$
$$(\Delta M / M_0)(B\rho\beta)_0 = const$$

The derivatives of components of the electric field in equation (4) should be evaluated at the equilibrium orbit with the help of the field map. The variable $\Delta M / M_0$ connects with momentum deviation $\Delta p / p_0$ of the ion:

$$\Delta M / M_0 = \Delta p / p_0 + K_0 x \qquad (5)$$

Let us consider the focusing property of the commonly used spherical and cylindrical deflectors.

Spherical Deflector

In the case of ideal spherical deflector we have:

$$K_0 = \frac{1}{R};\ \Lambda_0 = 0;\ \frac{\partial E_n}{\partial x} = -2\frac{E_n}{R};\ \frac{\partial E_z}{\partial z} = \frac{E_n}{R}$$
$$x'' = -\frac{1-\beta_0^2}{R^2}x + \frac{2}{R}\frac{\Delta M}{M_0};\ z'' = -\frac{1}{R^2}z;\ \frac{\Delta M}{M_0} = \left(\frac{\Delta p}{p_0}\right)_{in} \qquad (6)$$

Here $(\Delta p / p_0)_{in}$ – is the momentum spread at the entrance of the deflector. In accordance with equations (6) the focusing terms are approximately the same both for x- and z- motions.

Cylindrical Deflector

In the case of ideal cylindrical deflector we have:

$$K_0 = \frac{1}{R};\ \Lambda_0 = 0;\ \frac{\partial E_n}{\partial x} = -\frac{E_n}{R};\ \frac{\partial E_z}{\partial z} = 0$$
$$x'' = -\frac{2-\beta_0^2}{R^2}x + \frac{2}{R}\frac{\Delta M}{M_0};\ z'' = 0;\ \frac{\Delta M}{M_0} = \left(\frac{\Delta p}{p_0}\right)_{in} \qquad (7)$$

The focusing term is absent for z- motion.

Edge Field

The simulation of the beam focusing in the field map of the spherical deflector by using the linear equations (4) shows the significant asymmetry of the beam envelopes at the exit of the deflector. This asymmetry is caused by edge field and may be minimized by shifting the equilibrium orbit towards the inner electrode of the deflector. The entrance and the exit points of the orbit do not changed during this shifting.

In this regime the magnitude of the voltage at the electrodes are U_1 ≅-16 kV and U_2 ≅10 kV in the case of maximum injection voltage U_{inj} = 80 kV. The maximum deviation of the calculated equilibrium orbits from the design one is about 8 mm. The difference between x- and z-envelopes at the exit of deflector is less than 1mm.

Beam Transport through Deflector

The macro particle simulation of the ion beam transport through the deflector by using equation of motion (3) verified the possibility of the correction of the beam focusing asymmetry. The beam envelopes and the beam emittance during transportation are shown in Fig.4.

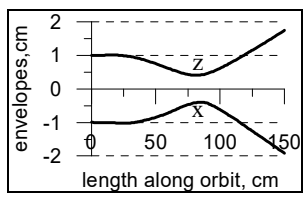

Figure 4a: Beam envelopes.

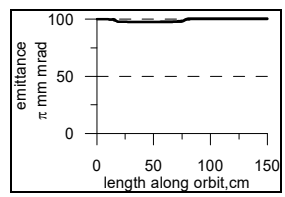

Figure 4b: Beam emittance.

The ion distributions at various phase planes in the final point of transportation are shown in Fig.5.

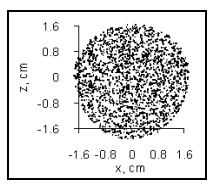

Figure 5a: Plane (x,z).

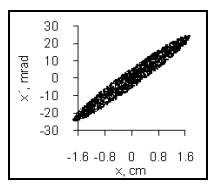

Figure 5b: Plane (x,x′).

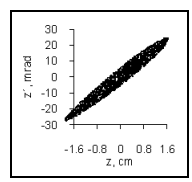

Figure 5c: Plane (z,z′).

ISBN 978-3-95450-131-1

As may be seen from Fig.5 in the "shifted orbit" regime the beam is almost axial symmetric. The influence of the nonlinearity of the electric field is negligibly small.

DC-280 AXIAL INJECTION CHANNEL

The scheme of the high voltage axial injection beam line of DC-280 cyclotron is shown in Fig.6.

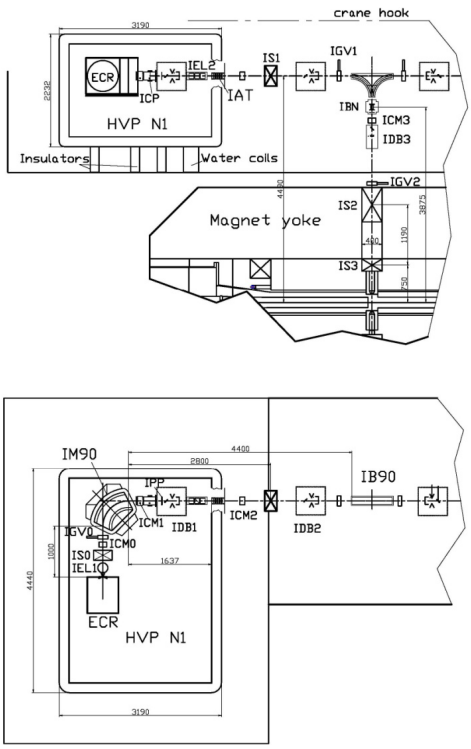

Figure 6: Scheme of axial injection channel. HVP – High Voltage Platform; ECR – ECR ion source; IS0-3 – focusing solenoids; IM90 – analyzing magnet; IEL1,2 electrostatic lenses; IAT – acceleration tube; IBD90 – spherical electrostatic deflector.

The ion beam is extracted from ECR ion source with energy 25 keV/Z. After analyzing and separation in the IM90 magnet the beam is accelerated in IAT tube. The kinetic beam energy may be increased by acceleration up to 80 keV/Z. All these equipment is placed at High Voltage Platform HVP. The electrostatic deflector IB90 rotates the beam onto vertical axis and two solenoids IS2,3 match the beam emittance with acceptance of the cyclotron inflector.

In the numerical simulation of the ion beam dynamics in the axial injection beam line 3D field maps of analyzing magnet IM90 [6], solenoids IS0-3, acceleration tube IAT and spherical electrostatic deflector IB90 are used.

The transport of $^{48}Ca^{8+}$ ion beam with kinetic energy of 75 keV/Z was considered. The dependence of the beam envelopes on length along the channel are shown in Fig.7.

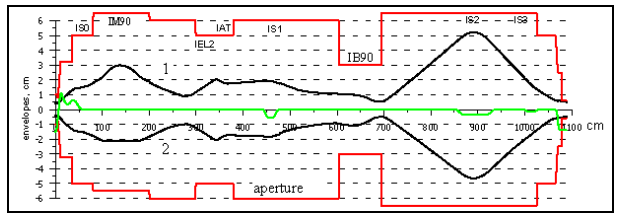

Figure 7: Horizontal (curve 1) and vertical (curve 2) $^{48}Ca^{8+}$ ion beam envelopes.

The horizontal (red curve) and vertical (blue curve) beam emittances are shown in Fig.8. The decreasing of the beam emittance is explained by increasing of kinetic energy in the acceleration tube IAT.

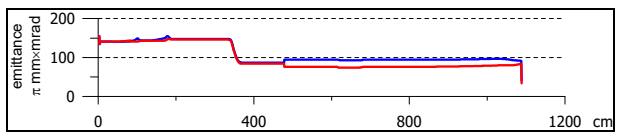

Figure 8: $^{48}Ca^{8+}$ ion beam emittances.

The efficiency of the beam transport is equal to 100%.

REFERENCES

[1] G.Gulbekyan, B.Gikal, I.Kalagin, N.Kazarinov. "Status Report and Future Development FLNR JINR Heavy Ions Accelerators Complex", Proceedings of 11-th International Conference on Heavy Ion Accelerators Technology, HIAT09, 8-12 June 2009, Venezia, Italy, p.p. 59-63.

[2] I.Ivanenko, G.Gulbekyan, N.Kazarinov, E.Samsonov, "Injection and Acceleration of Intense Heavy Ion Beams in JINR New Cyclotron DC280", MOA1C02, these proceedings, HIAT 2015, Yokohama, Japan (2015).

[3] G.G. Gulbekyan, V. Bekhterev, S.L. Bogomolov, A.A. Efremov, B. Gikal, I.A. Ivanenko, I.V. Kalagin, N.Yu. Kazarinov, M.V. Khabarov, V.N. Melnikov, N.F. Osipov, S.V. Prokhorov, A. Tikhomirov, "The Project of the HV Axial Injection for the DC-280 Cyclotron at the FLNR JINR", Proceedings of XXIV Russian Accelerator Conference, RuPAC'2014, Obninsk, Russia (2014), p.p. 333-335.

[4] OPERA-3D Reference Manual, Oxford OX5 1JE, England, October 2012

[5] V.Alexandrov, N.Kazarinov, V.Shevtsov, "Multi-Component Ion Beam code – MCIB04". Proceeding of XIX-th Russian Particle Accelerator Conference, RUPAC2004, 4-9 October, Dubna, Russia, p.p.201-203.

[6] N.Yu.Kazarinov, I.A.Ivanenko, "Magnets of Injection and Extraction Systems of Cyclotron DC280". Proceedings of XXIV Russian Accelerator Conference, RuPAC'2014, Obninsk, Russia (2014), p.p. 339-341.

ISBN 978-3-95450-131-1

COOLING STACKING INJECTION IN NICA BOOSTER

E. Syresin, Joint Institute for Nuclear Research, Russia

Abstract

The multi cycling injection from the linear accelerator to the NICA booster is planned to use for storage of Au^{31+} ions at energy 3.1 MeV/u. The intensity of the stored ions is increased by 3-5 times at injection intensity of $5\cdot10^8$-10^9 ppp. The intensity of the stored beam is higher by one order of magnitude comparing with injection intensity of 10^8 ppp. The maximal intensity is restricted by the incoherent diffusion heating of the stack and the ion life time. The simulations of the cooling stacking injection were performed by BETACOL code. The coherent instability can be developed at a high ion intensity in presence of the electron cooling. The increment of instability essentially depends on the choice of the working point.

INTRODUCTION

The Nuclotron-based Ion Collider fAcility (NICA) [1] is a new accelerator complex is under construction at Joint Institute of Nuclear Research aimed to provide collider experiments with heavy ions up to gold at maximum energy at center of mass of $\sqrt{s} \sim 11$ GeV/u.

The complex NICA consists of three superconducting accelerators: booster, acting synchrotron-Nuclotron and collider which provides average luminosity of $10^{27}cm^{-2}s^{-1}$.

The collider NICA is proposed for study of baryon interaction in the hot and dense quark-gluon matter and search of mixed phase of that matter. The planed experiments will realize in colliding ion-ion beams.

The main goals of booster are connected with of $4\cdot10^9$ ppp gold ions Au^{31+} and its acceleration up energy of 600 MeV/u which is required for stripping of ion charge state Au^{79+}. Booster synchrotron has maximum magnetic rigidity of 25 Tm and the circumference of about 215 m. The Booster is equipped with an electron cooling system that allows to provide cooling of the ion beam in the energy range from the injection energy up to 100 MeV/u.

The multi cycling cooling stacking injection is planned to increase the stored ion intensity in booster NICA at injection energy of 3.1 MeV/u. The injection from the electron linac is repeated with frequency of 10 Hz. The intensity of gold ion beam at linac exit is equal to 10^8-10^9 ppp. The vacuum pressure in booster is $5\cdot10^{-11}$ mbar that corresponds to the ion life time of 3-5 sec at injection energy of 3.1 MeV/u. The average ion flax is the key booster characteristic, it is equal to $R=N/\tau$, where N is number of stored ions, τ is time duration of booster cycle. Average ion flax is equal to $R=2\cdot10^8$ sec^{-1} at number of stored ions $N=10^9$ ppp and time duration of booster cycle of $\tau=5$ sec.

The rms beam emittance $\varepsilon_{x,y}=\sigma_{x,y}^2/\beta_{x,y}$ at exit of the linear accelerator is equal to $\varepsilon_x/\varepsilon_y=3$ π·mm·mrad, here $\sigma_{x,y}$ – rms transverse beam size, $\beta_{x,y}$ is the beta function in injection area. The horizontal acceptance for stored stack ions is equal to $\varepsilon_{ac}=10$ π·mm·mrad. The equilibrium stack orbit is displaced relatively to the septum on a distance $(\beta_{inj}\varepsilon_{ac})^{1/2}$, where β_{inj} is the horizontal beta function in injection area. The bump of equilibrium orbit is displaced at single turn injection on a distance $2\sigma_x=2(\beta_{inj}\varepsilon_x)^{1/2}$. The angle spread of injected beam is equal to $(\varepsilon_x/\beta_{inj})^{1/2}$. The initial horizontal beam emittance corresponds to $\varepsilon_{inj\text{-}x}=2\varepsilon_x+(\varepsilon_x\varepsilon_{ac})^{1/2}=11{,}5$ π·mm·mrad in the booster.

The simulation of multi cycling cooling stacking injection were performed by the BETACOOL code [2] for gold ions Au^{31+}. The electron beam current is equal to 0.1 A, the beam has uniform density at radius less than 2 cm. The length of electron cooling section is equal to 1,94 m.

The efficiency of electron cooling is equal to ratio of amplitude of second injection pulse to amplitude of first injection pulse (Fig.1). The efficiency of electron cooling is equal to 40% at injection repetition frequency of 10 Hz. The maximal ion stored intensity corresponds to $4.6\cdot10^9$ ppp at injection intensity of 10^9 ppp and ion life time of 4.4 sec.

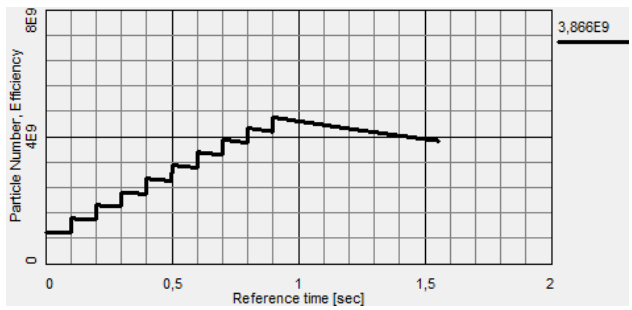

Figure 1: Dependence of stored ion intensity on time at 10 cycle injection.

The average ion flax is equal to $R=7.6\cdot10^8$ sec^{-1} at an number of stored ions of $N=4.6\cdot10^9$ ppp and time duration of booster cycle of $\tau=6$ sec. Cooling stacking injection increases by 3.8 times the average flax in comparison with single turn one cycle injection.

The maximal stack ion intensity is restricted by several effects: the incoherent stack noise, the instability of cooled ion stack and the ion life time at interaction ions with residual gas atoms and molecules.

The emittance of cooled ion stack is defined by number of stored ions N_{st} and betatron tune shift ΔQ

$$\varepsilon_v=(r_pZ^2N)/(4\pi A\beta^2\gamma^3\Delta Q),$$

ISBN 978-3-95450-131-1

where Z is the nuclear charge, A is the atomic number, β and γ - are the relativistic factors, r_p is the proton radius. The equilibrium between sack noise incoherent heating and electron cooling determinates the ion stack emittance. The incoherent stack heating reduces the electron cooling efficiency and finally it became to reduction of stored ion intensity. The emittance rate at diffusion heating is proportional to number of the stack ions N normalized on number of the injected ions N_{inj}: $d\varepsilon/dt=kN/N_{inj}$ [3]. The maximal stack intensity corresponds to $N=5{,}5\cdot10^9$ ppp at time duration of cooling stacking injection of 2 sec and emittance heating rate $d\varepsilon_h/dt=d\varepsilon_v/dt= 0.3N/N_{inj}$ sec^{-1} for 20-cycle injection with repetition frequency of 10 Hz.

Coherent instability or "electron heating" is developed at storage of the high intensive ion beams in presence of the electron cooling [4]. To avoid stack instability the hollow electron beam is formed in the electron cooling system [5]. The hollow beam with low density in central region is used for stack cooling; the high density for the boundary electrons is applied for cooling of new injected ions with the large betatron amplitudes. The increment of beam instability can be essentially reduced in case of hollow electron beam and ion stack life time can be increased.

The internal radius with the low electron density $n=5\cdot10^6$ cm^{-3} is equal to 0.5 cm. The electron density in boundary region corresponds to $n=2\cdot10^7$ cm^{-3}, the electron beam current is equal to 0,095A. The hollow electron beam provides similar stack intensity as uniform electron beam when the ion life time is same for both cases. However for hollow beam electron heating is weak and ion life time is larger than for uniform electron beam. Finally it became to increase of the stack intensity.

The stack intensity is defined by incoherent emittance rate at electron heating. The presence of diffusion heating with emittance rate $d\varepsilon_h/dt=d\varepsilon_v/dt=0.1N/N_{inj}$ became to reduction of stack intensity from $6.3\cdot10^9$ ppp to $5.7\cdot10^9$ ppp. An increase of emittance heating rate up $d\varepsilon_h/dt=d\varepsilon_v/dt=0.3N/N_{inj}$ sec^{-1} leads to reduction of stack intensity from $6.3\cdot10^9$ ppp to $4.1\cdot10^9$ ppp (Fig.2).

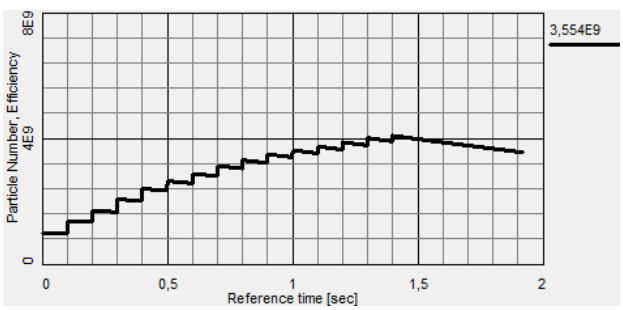

Figure 2: Dependence of stored ion intensity at 15-cycle injection on time for hollow beam at presence of incoherent stack heating.

The equilibrium emittance is defined by internal radius of hollow beam at a high incoherent emittance heating rate. Therefore the cooling stacking injection provides by 4-5 times increase of stored stack intensity in comparison with one cycle single turn injection.

The stored ion intensity depends on the ion life time. The ion life time is defined by its interaction with residual gas atoms and molecules. The ion life time depends on two parameters: the pressure and the charge-mass spectrum of residual gas [6,7].

Dependence of stored ion intensity on the ion life time is given in Fig.3 for parameters presented in Fig.2. The ion life time reduction from 4.4 sec to 0.65 sec became to ion intensity reduction from $4.1\cdot10^9$ ppp to $2.2\cdot10^9$ ppp.

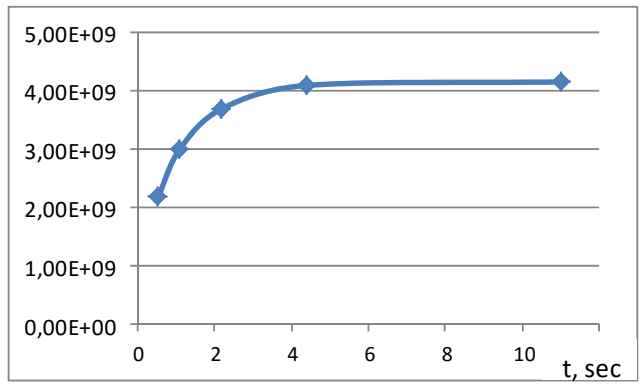

Figure 3: Dependence of stored ion intensity on ion life time at injection repetition frequency of 10 Hz.

The intensity of stored ion beams Au^{31+} can increased by 10-15 times at low injected ion intensity of 10^8 ppp during 50 cycles with repetition frequency of 5-10 Hz (Fig.4).

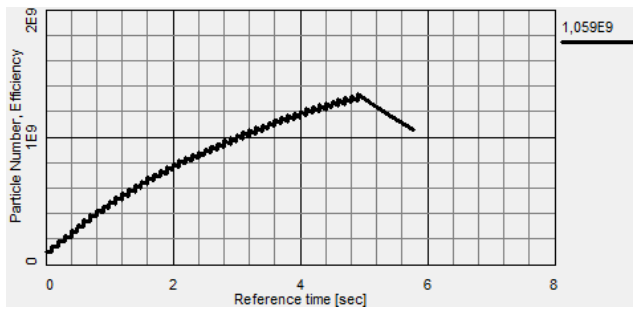

Figure 4: Dependence of the stored ion intensity on time at 50-cycle injection with repetition frequency of 10 Hz.

Reduction of the repetition frequency from 10Hz to 5Hz leads to decrease of the ion intensity from $1.3\cdot10^9$ ppp to 10^9 ppp caused by short ion life time of 4.4 sec.

INSTABILITY OF ION BEAM AND CHOICE OF WORKING POINT

Coherent instability or so called "electron heating" [5] is developed for high intensive ion beam in presence of electron cooling. The ion losses are rapidly increased when the ion intensity reaches the critical value. The space charges of electron and ion beams together with solenoid magnetic field in cooling section provide

ISBN 978-3-95450-131-1

connection between horizontal and vertical coherent oscillations. The transverse motion of the ion and the electron beam center gravities are given by following equations [4]:

$$d^2z/dt^2+i\omega_c dz/dt+\omega_i^2 z=\omega_i^2 z_e, \qquad dz_e/dt+i\omega_d z_e=i\omega_d z,$$

at initial conditions $z(0)=z_0$, $dz_{(0)}/dt=(dz/dt)_0$, $z_e(0)=0$, $dz_e(0)/dt=0$, where $\omega_c=ZeB/\gamma m_i$ is the ion cyclotron frequency, $\omega_i^2=Ze^2n_e/2\varepsilon_0\gamma m_i$ is the ion plasma frequency in the electron beam field, $\omega_d=\omega_e^2/\omega_{ce}$ is the drift electron frequency, $\omega_e^2=Ze^2n_i/2\varepsilon_0\gamma^3 m_e$ is the electron plasma frequency, $\omega_{ce}=eB/\gamma m_e$ is the electron cyclotron frequency, B is the magnetic field of solenoid, n_e and n_i are electron and ion densities, correspondently. Centre gravity motion can represented in matrix form $X=M_{cool}X_0$ [5], where M_{cool} is 4×4 matrix of cooling section. Matrix M_{cool} corresponds to unstable motion caused by $\det M_{cool} \neq 1$ [4]. Ion motion outside of cooling section is characterized by Twiss matrix. Single turn booster matrix M_{ring} with electron cooling is equal $M_{ring}=L_{dr}\cdot R_{Twiss}\cdot L_{dr}\cdot M_{sol}^{-1}\cdot M_{cool}\cdot M_{sol}$ [4], where L_{dr} is matrix of drift cooling section with negative length $-L/2$ and M_{sol} is solenoid matrix. The peculiarity of booster matrix M_{ring} is related to that module of its Eigen values do not equal to 1: $\Delta\lambda_{1,2,3,4}=|\lambda_{1,2,3,4}|-1\neq 0$ [4]. At small value the $\Delta\lambda$ characterizes the increment of instability $\gamma_{ins}=|\lambda|-1$ in number of booster turns. Two dipole modes are exited with increment γ_1, and other two modes with decrement γ_2. The dipole modes have resonance character at $Q_x-Q_y=0$. The values γ_1 and γ_2 change the signs at transition through the resonance $Q_x-Q_y=0$.

The unstable modes are exited before resonance. The damp mode are exited after transition through resonance. Therefore there are exited modes all time in the system. The increment is asymmetric in relation to difference resonance $Q_x-Q_y=0$ and sum resonance $Q_x+Q_y=9$. Increment has maximum at difference resonance and it has minimal value around sum resonance [7]. The dependence of increment and decrement on the vertical betatron tune is given in Fig.5 at fixed value of horizontal betatron tune $Q_x=4.8$ for hollow electron beam with density in central area of $n_e=5\cdot10^6$ cm^{-3} and number of stored ions Au^{31+} of $3\cdot10^9$ ppp.

The hollow electron beam is planned to use for reduction of increment. The density in central region is by 4 time smaller in comparison with boundary electron density. However for hollow electron beam is possible development of instability at high ion intensity. The instability increment essentially depends on choice of working point [7].

The booster working point $Q_x/Q_y=4.8/4.85$ is close to difference resonance $Q_x-Q_y=0$ and it corresponds to increment closed to maximal value. The horizontal betatron tune will fixed in booster and vertical tune will changed at variation of current in quadrupole lenses. The choice of the working point in area closed to sum resonance permits to reduce the increment of the instability. New working point $Q_x/Q_y=4.8/4.15$ is displaced from sum resonance $Q_x+Q_y=9$ and high orders resonances $2Q_y+Q_x=13$ и $4Q_x=19$. The simulated increment for working point $Q_x/Q_y=4.8/4.15$ is by several times smaller than increment for booster working point $Q_x/Q_y=4.8/4.85$.

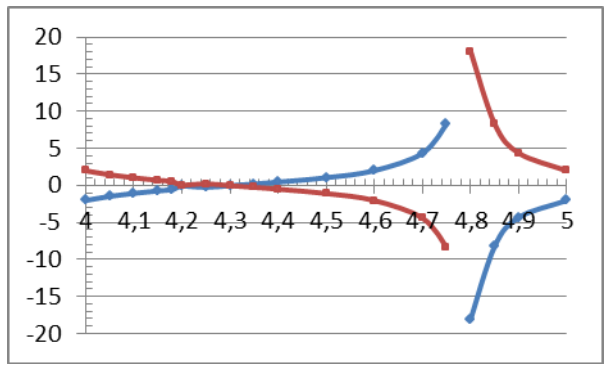

Figure 5: Dependence of increment and decrement of instability on vertical betatron tune at horizontal betatron tune of $Q_x=4.8$.

REFERENCES

[1] Design and Construction of Nuclotron-based Ion Collider facility NICA, Conceptual design, Dubna (2008).

[2] A. Sidorin et al, BETACOOL Program for simulation of Beam Dynamic in Storage Rings. Nucl. Instr. Meth. A., v.558, p.325-328 (2006).

[3] E.M. Syresin, Incoherent Vertical Ion Losses during Multiturn Stacking Cooling Injection, Physics of Particles and Nuclei Letters, v. 11, No. 4, p. 497–501 (2014).

[4] V.V. Parkhomchuk, V.B. Reva Coherent interaction of ion and electron beams in systems with electron JETPh. v.118, №5, p.1125-1133 (2000).

[5] V. Parkhomchuk Comparison of the hollow electron beam devices and electron heating. Proceedings of COOL 07, p.64-67 (2007).

[6] S. Baird et al, Recent results on lead-ion accumulation in LEAR for the LHC, Nucl. Instr. Meth. A. v.391, p.17-23 (1997).

[7] T. Uesugi et al, Cool-Stacking Injection and Damping of a Transverse Ion-Beam Instability at the HIMAC Synchrotron Nucl. Instr. Meth. A. v.545, p.43-56 (2005).

ISBN 978-3-95450-131-1

COHERENT SYNCHRO-BETA COUPLING IN THE KEK DIGITAL ACCELERATOR

T. Monma[A,B], K. Takayama[A,B,C,D], T. Yoshimoto[A,B], Liu Xigguang[A,B]
[A]Tokyo Institute of Technology, Nagatsuda, Kanagawa, Japan
[B]High Energy Accelerator Research Organization (KEK), Tsukuba, Ibaraki, Japan
[C]The Graduate University for Advanced Studies (SOKENDAI), Hayama, Kanagawa, Japan
[D]Tokyo City University, Tamadsutsumi, Tokyo, Japan

Abstract

The KEK Digital Accelerator is a small-scale fast cycling induction synchrotron, where induction pulse voltages discretely accelerate heavy ion beam. Its voltage height V_{out} is constant due to a technical restriction and does not correspond to the required acceleration voltage per turn $V_n=\rho C_0[dB/dt]$ at the n-th turn. The induction acceleration system is triggered when $\Sigma V_n - \delta\Sigma V_{out} > V_{out}$ (δ=1 when acceleration voltage is supplied. δ=0 when acceleration voltage is not supplied). Consequently, a perturbation on the betatron oscillation induced by a discrete change of the equilibrium orbit becomes notably large. A size of this perturbation is quantitatively estimated by means of numerical simulation and is compared with the experimental result.

INTRODUCTION

The KEK Digital Accelerator (DA) [1,2] is a small-scale fast-cycling induction synchrotron that does not require a high-energy injector (see Fig. 1). The induction acceleration system shown in Fig. 2 was developed to demonstrate the induction synchrotron concept in 2006 using the KEK 12-GeV proton synchrotron [3], which is a typical slow-cycling synchrotron. There are two basic technical issues for induction acceleration in the KEK-DA.

1. An induction cell is employed as the acceleration device, which is simply a one-to-one pulse transformer energized by a switching power supply (SPS) generating pulse voltage pulses. The SPS is connected to the DC voltage power supply. The output voltage height for acceleration, V_{acc}, is necessarily determined by the setting voltage of the DC power supply, which is fixed to a constant value in the range from 0.3 kV to 2.0 kV per cell within the acceleration cycle.
2. The KEK-DA ring does not have dispersion-free regions. The induction acceleration cells are placed at the region where the size of the momentum dispersion function is 1.4 m.

Since the guiding magnetic fields of the KEK-DA are excited sinusoidally, an ideal profile of V_{acc} is of half sine shape as shown in Fig. 3. The ideal profile of V_{acc} is not realized because of the technical reason 1.

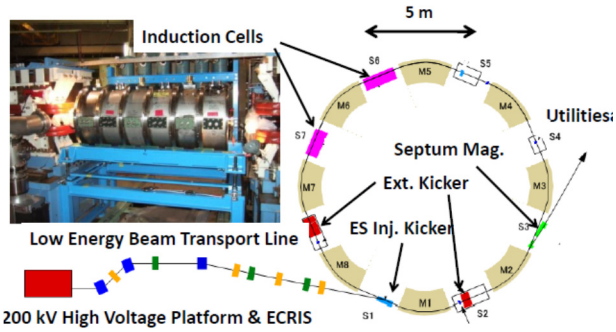

Figure 1: Schematic view of the KEK-DA.

In the early and late stages of acceleration, the required acceleration voltage is lower than the fixed output voltage of the induction cell. Thus, the pulse density of the acceleration voltage must be controlled. This is actually carried out in the following way. Gate trigger of the solid-state switching elements employed in the SPS is generated when the integrated required acceleration voltage V_{req} reaches V_{acc} of the induction cell, resulting in the production of V_{acc} at the induction cell. This method has been called "pulse density control" since its proposal [4].

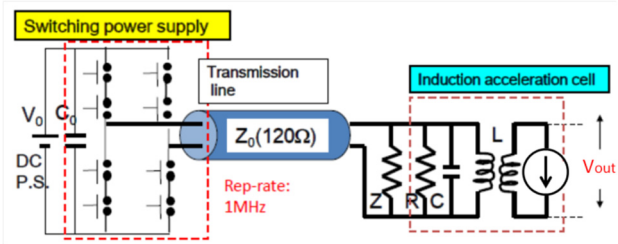

Figure 2: Equivalent circuit for the induction acceleration system, where the induction cell with a matching resistor is connected to the SPS through a 120 Ω transmission line.

The individual equilibrium orbit $D(s)\Delta p/p$ of particles changes gradually associated with ramping of the guiding magnet until the acceleration voltage is generated. The equilibrium orbit of an assumed particle located at the bunch center should return to position zero after acceleration voltage generation. The oscillation amplitude and phase of the betatron motion of an individual particle, however, simultaneously change, because the actual orbit $x(s)=x_\beta(s)+D(s)\Delta p/p$, which is a deviation from the ideal orbit, never changes at the acceleration gap position. If momentum dispersion function vector ($D(s)$, $D'(s)$) at the

ISBN 978-3-95450-131-1

acceleration gap position, where $\Delta p/p$ changes discretely with acceleration voltage generation, is zero, the oscillation amplitude and phase of the betatron motion never change. The beam is completely free from crucial issues discussed here. The present KEK-DA is not the case because of the technical reason 2.

TYPICAL INDUCTION ACCELERRATION UNDER VOLTAGE PULSE DENSITY CONTROL

An typical example of induction acceleration under the pulse density control is shown in this section, where the following machine parameters of the KEK-DA are assumed,

Table1: Machine Parameters of the KEK-DA

Circumference of the beam orbit	C_0=37.7 m
Bending raius	ρ=3.3 m
Repetition rate	f=10 Hz
Maximum bending flux density	B_{max}=0.84 T.

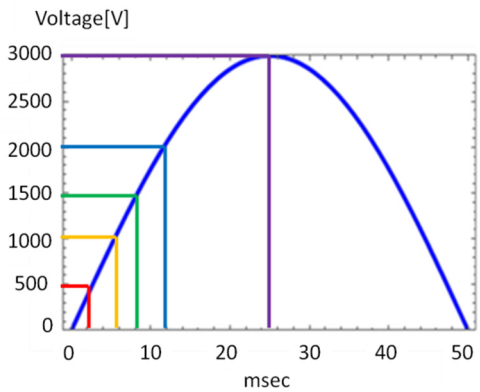

Figure 3: Required acceleration voltage per turn.

The required acceleration voltage V_{req} is shown in Fig. 3, Fig. 4 shows the timing to generate actually V_{acc} at the area to generate V_{acc}=0.5 kV, which the area which 500 V from zero in Fig. 3.

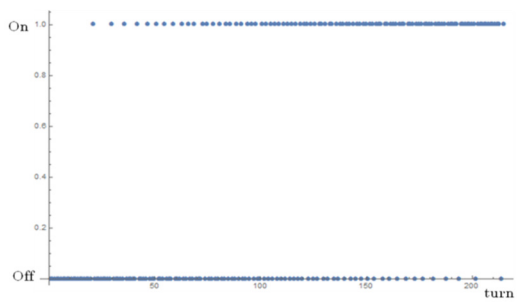

Figure 4: Timing to generate the induction voltage pulse.

5 of V_{acc}, which is 0.5 kV, 1.0 kV, 1.5 kV, 2.0 kV and 3.0 kV, is generated in this acceleration simulation (see Fig. 5). Barrier voltage V_{bb} is always 1.0 kV.

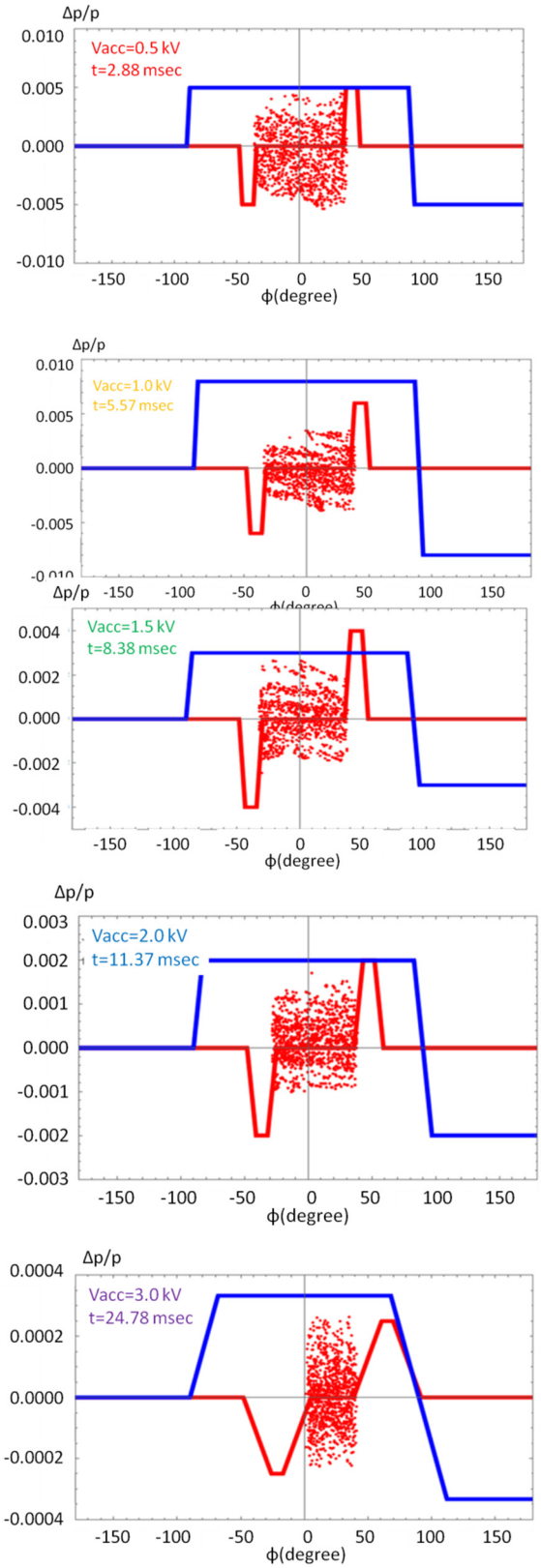

Figure 5: Discrete acceleration (Red and blue lines V_{bb} and V_{acc}, respectively).

ISBN 978-3-95450-131-1

BETATRON MOTION AND DISCRETE CHANGE IN THE EQUILIBRIUM ORBIT

The Poincare plane to observe the betatron motion at the acceleration cell position is shown together with tracks of two particles sharing the same equilibrium orbit denoted by O before getting the acceleration voltage in Fig. 6. In the other word, the two particles have the same momentum deviation $\Delta p/p$. The origin O' indicates the position of the ideal particle. For simplicity it is assumed that two particles have the same betatron amplitude but betatron phase different by π. The equilibrium orbit $D(s)\Delta p/p$ moves gradually from O' to O since the previous acceleration, because the acceleration voltage pulse is not triggered until the next trigger timing in the pulse density control scenario. The averaged orbit of the two particles places at O during the time interval between the previous acceleration and the next acceleration. The equilibrium orbit returns to O' just after the next acceleration. At this moment, the amplitude and phase of the betatron motion of the two particles vary as shown in Fig. 6. This is caused by a fact that the actual orbit $x(s)=x_\beta(s)+D(s)\Delta p/p$ does not change. As a result, the averaged orbit of the two particles never stay at the same position but should oscillate with a gradual drift toward the left side. We can say that some coherent betatron oscillation is induced.

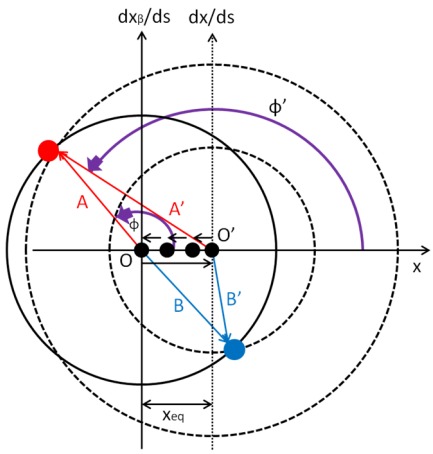

Figure 6: Betatron motions in the phase space.

In order to understand more realistic behaviors of the bunch of particles, macro-particle simulations have been extensively carried out, where 5000 macro-particles uniformly distributed in the horizontal phase space at beginning are assumed and the position of the bunch centroid is evaluated every turn. The beam centroid is shown as a function of turn number in Fig. 7. Two different acceleration voltage Plan A and B have been considered. In Plan A the voltage profile is divided into three stages, in which V_{acc}=0.2 kV (1~300 turns), 0.7 kV (301~800 turns), and 1.2 kV (801~1000 turns). In Plan B V_{acc} is always 1.2 kV (1~1000 turns). It is clear that in both cases of Plan A and B the oscillation amplitudes of the beam centroid increase with turn coherently. Even so, it is observed that its increasing is suppressed in Plan A employing the small step-size change in the acceleration voltage.

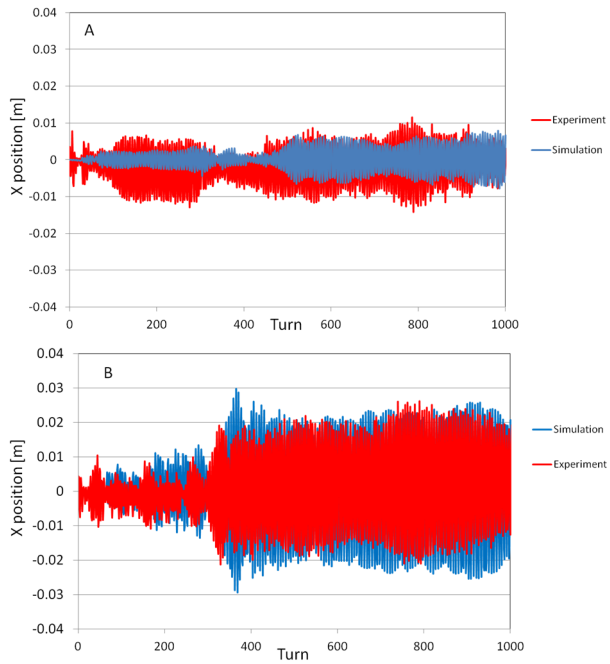

Figure 7: Simulation (blue) and experimental (red) results of temporal evolution of the beam centroid for Plan A and Plan B.

COMPARISON WITH EXPERIMENTAL RESULTS

In the experiments, the beam centroid was observed at the location of $D(s)=1.4\ m$ and $D'(s)=0$ by the position monitor, which is located at S4 in Fig. 1. The experimental results are shown in red lines [2]. It may be concluded that the simulation result reproduces the experimental result at a sufficient level.

CONCLUSION

It has been confirmed from both of the experiment and simulation that the discrete acceleration under the pulse density control scenario induces the coherent oscillation of the beam centroid. It has become clear that this coherent oscillation is suppressed by changing the acceleration voltage in a small step. The present result suggests what must be taken in a future ideal induction synchrotrons [5].

REFERENCES

[1] T. Iwashita, K.Takayama *et al.*, Phys. Rev. ST-AB 14, 071301 (2011).
[2] K.Takayama, T.Yoshimoto, Liu Xingguang *et al.*, Phys. Rev. ST-AB **17**, 010101 1-6 (2014).
[3] K.Takayama *et al.*, Phys. Rev. Lett. 98, 054801 (2007).
[4] T.Dixit, T.Iwashita, and K.Takayama, Nucl. Inst. Meth. A 602, 326-336 (2009).
[5] Leo, Kwee Wah, T. Adachi, T.Kwakubo, T.Monma, T.Dixit, and K. Takayama, submitted to Phys. Rev. ST-AB (2015) and Leo Kwee Wah *et al.*, in this conference

ISBN 978-3-95450-131-1

SUPER-BUNCH INDUCTION ACCELERATION SCHEME IN THE KEK DIGITAL ACCELERATOR

T.Yoshimoto[#,1,2], X. Liu[1,2] T. Adachi[2,4],T.Kawakubo[2], H. Kobayashi[2,3], S.Takano[2], E.Kadokura[2], K.Okamura[2], and K.Takayama[1,2,3,4]
[1]Tokyo Institute of Technology, Nagatsuta, Kanagawa, Japan
[2]High Energy Accelerator Research Organization (KEK), Tsukuba, Ibaraki, Japan
[3]Tokyo City University, Todoroki, Tokyo, Japan
[4]The Graduate University for Advanced Studies, Hayama, Kanagawa, Japan

Abstract

KEK Digital Accelerator (KEK-DA) [1] is a fast cycling induction synchrotron with induction cells driven by switching power supplies (SPS). The rectangular pulse voltages are precisely controlled by a field-programmable gate array (FPGA). One of our next missions for the KEK-DA is to demonstrate super-bunch (very long beam) acceleration technique in which the beam occupies over half of the ring at injection [2]. For that, power supplies for the SPS have to be upgraded from fixed voltage to time-varying voltage to provide beam-required acceleration. This is effective to suppress the blow-up of the longitudinal emittance and ensures the super-bunch acceleration stably.

INTRODUCTION

The concept of induction synchrotron was originally invented by Takayama and Kishiro in 2000 [2] and then a super-bunch hadron collider was proposed in 2002 [3]. The proof-of-principle experiment for induction synchrotron was successfully performed in the KEK 12GeV PS synchrotron in 2007 [4]. After that, the same group developed the KEK-DA, a small prototype of fast cycling induction synchrotron, which was converted from the old PS 500MeV booster ring. With this machine, the wide-band acceleration as a novel scheme of induction synchrotron was demonstrated [5], in which the revolution frequency can be increased by a factor of more than 10 in one acceleration cycle.

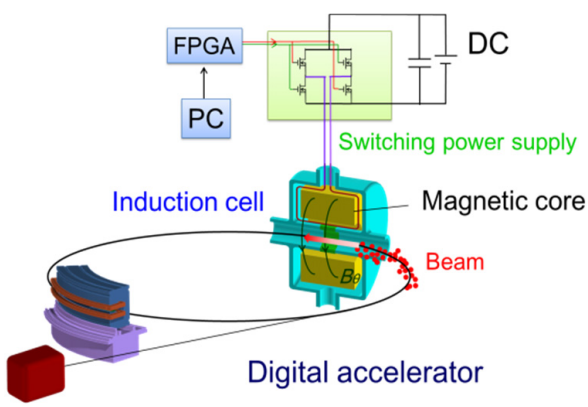

Figure 1: The Overview of the KEK-DA.

The schematic view of the KEK-DA is shown in Fig. 1. Heavy ion beams are produced in the electron cyclotron resonance ion source (ECRIS) and accelerated by the extraction voltage of 200 kV. Then, they are directly injected into the ring by the electrostatic injection kicker. The timings of the acceleration pulses are precisely controlled by a FPGA. The optimization of the timing is made following the ramping magnetic flux density of the bending magnets $B(t)$ [6].

In the current setup of the KEK-DA, fixed DC power supplies provide acceleration voltages for induction cells as shown in Fig. 1. It is difficult to give the acceleration voltages precisely following the required acceleration voltage per turn $V(t)$ ($= \rho C_0 dB(t)/dt$) that is necessary for the curvature radius of the ion in the bending magnet ρ and the circumference of the beam orbit C_0. In order to avoid the discrepancy, the acceleration voltage has to be generated intermittently as they correspond with the required acceleration voltage equivalently. The detailed discussion was already reported in other places [5, 7]. Although the present scheme can achieve the wide-band acceleration, it generates some synchro-beta coupling in horizontal direction and longitudinal emittance blow-up at the initial acceleration stage. In such a way to reduce both effects, an upgrade plan with time-varying DC power supply is considered in the next section. Furthermore, this plan can be adapted to super-bunch acceleration scheme.

ACCELERATION SCHEME

In induction acceleration, confinement and acceleration voltage can be generated independently as shown in Fig. 2. Two sets of confinement voltages produce a beam bucket with the length of one third of a beam revolution period at every turn. The height and width of the positive pulse are the same as the negative pulse. On the other hand, the required acceleration voltage changes continuously in the whole acceleration period. The positive pulse height is the half of the negative one, whereas the positive width is twice of the negative one to prevent magnetic cores of induction cells from saturation. This means that the acceleration pulse is asymmetric different from other existing accelerators.

#yoshimo@post.kek.jp

ISBN 978-3-95450-131-1

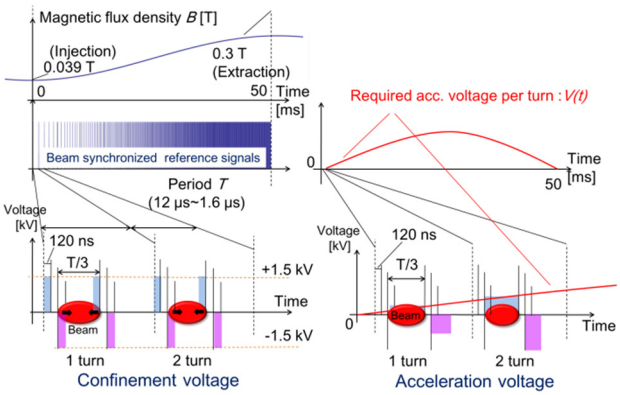

Figure 2: The proposed acceleration scheme for super-bunch acceleration at the KEK-DA.

PARTICLE TRACKING

In this simulation, a heavy ion beam with injection energy of 200 keV and mass to charge ratio of 4 is accelerated under the condition that the ramping magnetic flux density of the ring increases from 0.039 T to 0.3 T in 50 ms. The beam revolution frequency also increases from 82 kHz to 628 kHz correspondingly. The number of macro particle is 5000 with the momentum spread of 0.17 % as one sigma of Gaussian distribution and the length of 4 μs at the injection. The height of the confinement voltage is 1.5 kV with the rising and falling time of 80 ns. The longitudinal beam motions at the initial stage were shown in Fig. 3.The detail parameter set of this simulation is written in Ref. [7].

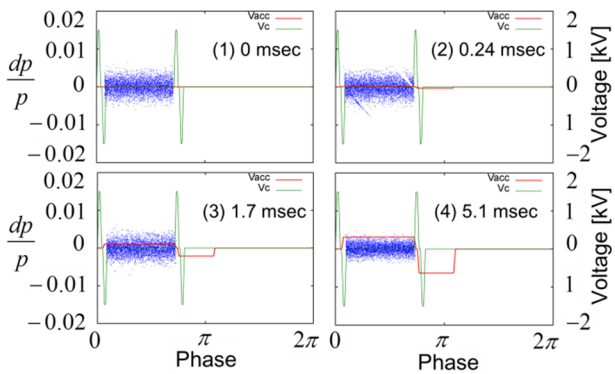

Figure 3: The longitudinal beam motion in the initial acceleration stage under the time-varying induction acceleration (simulation).

The longitudinal emittance decreases by the adiabatic dumping in Fig. 3. Ideal confinement and acceleration waveforms are shown in green and red line, respectively.

The horizontal oscillation caused by the synch-beta coupling is negligible small as shown in Fig. 4 because the acceleration voltage gradually changes in one acceleration cycle.

From the data set, the mountain plot is generated in the 3D space where the horizontal axis, vertical axis, and third axis denote the revolution time per turn, the time from injection, and the beam intensity, respectively. Its

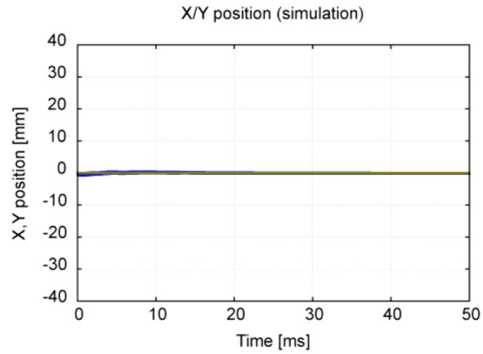

Figure 4: Horizontal (blue) and vertical (yellow) beam position in super-bunch acceleration at the KEK-DA.

projection on the x–y plane is shown in Fig. 5 (a). The beam is confined uniformly in the whole acceleration. With the same axes, Fig.5 (b) and (c) are the time-turn plane view of confinement waveform with the height of ± 1.5 kV and acceleration waveform, respectively. The positive acceleration height is the half of the negative one and gradually changes as it follows the required acceleration voltage. The time width of positive pulse is twice of the negative one at every turn.

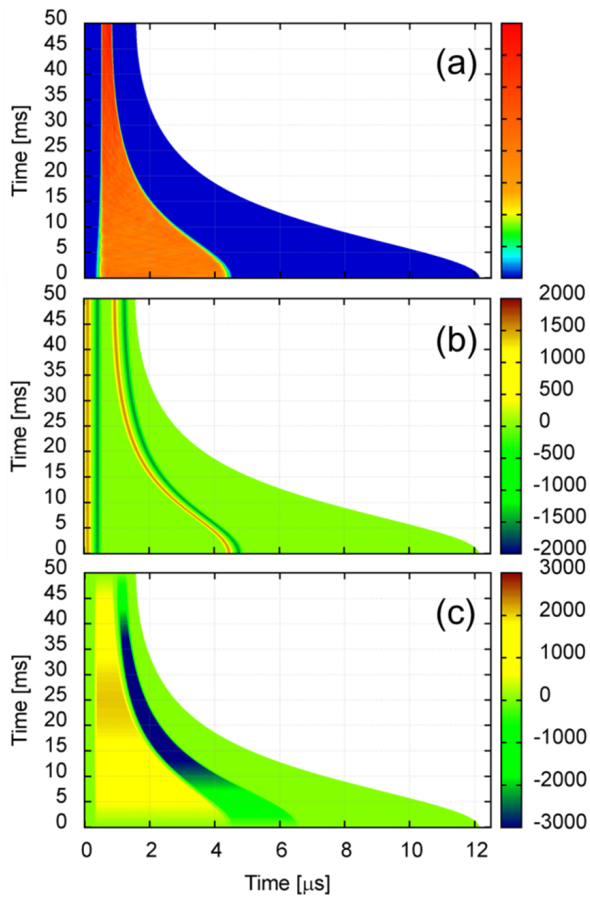

Figure 5: (a) Longitudinal beam motion in the initial acceleration stage under the time-varying induction acceleration (simulation), (b) Time-turn plane view of confinement voltage where positive set pulse and negative

ISBN 978-3-95450-131-1

reset pulse are in red and blue (simulation), (c) Time-turn plane view of acceleration voltage where set pulse and reset pulse are in yellow and blue (simulation).

HARDWARE SYSTEM

To realize above acceleration voltage with the existing equipment of the KEK-DA, the smart acceleration system is contrived as shown in Fig. 6. The two DC-DC converters are connected to the switching power supply to provide time-variable asymmetric acceleration waveform which has positive and negative acceleration pulses with different heights.

Figure 7 shows the LT-spice model of the circuit in Fig. 6. The height of positive acceleration voltage corresponds to the required sinusoidal acceleration voltage throughout the entire acceleration cycle. The power supply voltage to the SPS follows the reference sinusoidal waveform through the single feedback system. In addition, a voltage drop circuit is embedded so that the height of the acceleration voltage can follow the required one smoothly.

The negative acceleration pulse has the same system.

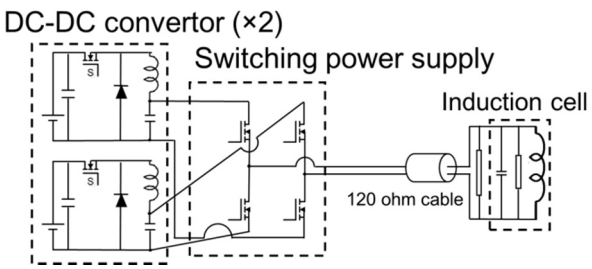

Figure 6: Induction acceleration system with two DC-DC convertors in order to generate asymmetric and time-variable acceleration pulse.

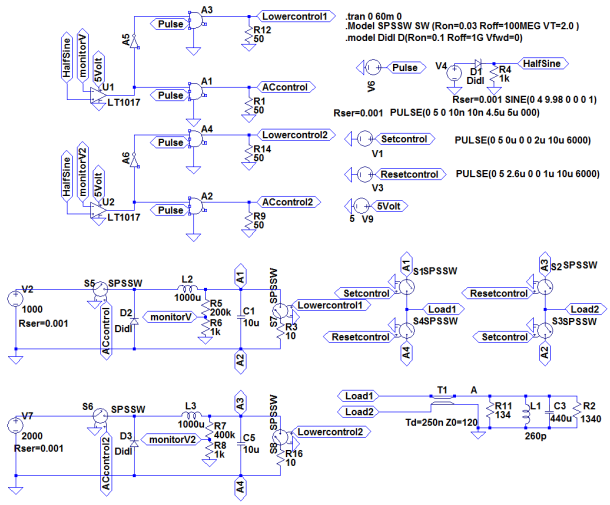

Figure 7: LT-spice model in order to generate asymmetric and time-variable acceleration pulse.

The acceleration waveform at the induction cell in one acceleration cycle is shown in Fig. 8 (a). The positive envelope is a sinusoidal waveform corresponding to the required acceleration voltage and the half of the negative envelope. The expansion view around 10 ms from the injection time is shown in Fig. 8 (b). The non-uniform spikes of the waveforms of Fig. 8 (a) and (b) originate from the calculation accuracy.

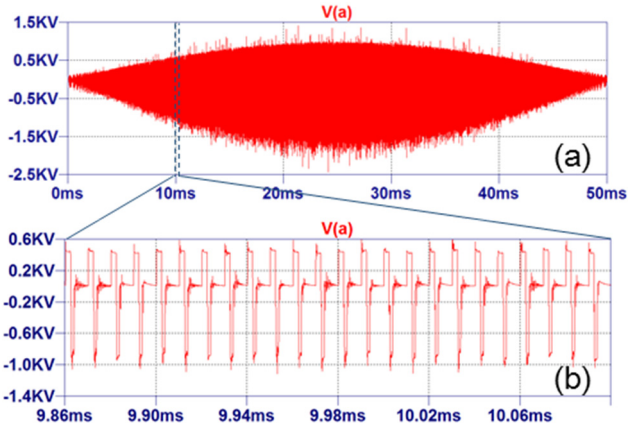

Figure 8: (a) Acceleration waveform with the proposed induction acceleration system. (b) Expansion view around the 10 msec from the injection time.

This calculation with LT-spice shows that it is possible to develop an induction acceleration system which generates asymmetric and time-variable acceleration pulse in principle.

CONCLUSION

The super-bunch acceleration scheme of induction synchrotron and its hardware system are discussed with simulation. These results suggest that super-bunch acceleration is feasible on condition that its beam loading effect is ignored.

REFERENCES

[1] T.Iwashita et al., "KEK digital accelerator", Phys. Rev. ST-AB 14, 071301(2011).

[2] K.Takayama and J.Kishiro, "Induction Synchrotron", Nucl. Inst. Meth. A 451, 304 (2000).

[3] K.Takayama et al., "Superbunch Hadron Colliders", Phys. Rev. Lett. 88, 144801 (2002).

[4] K.Takayama et al., "Experimental Demonstration of the Induction Synchrotron", Phys. Rev. Lett. 98, 054801 (2007).

[5] K.Takayama et al., "Induction acceleration of heavy ions in the KEK digital accelerator: Demonstration of a fast-cycling induction synchrotron", Phys. Rev. ST-AB 17, 010101(2014).

[6] T.Yoshimoto et al., "Heavy ion beam acceleration in the KEK digital accelerator: induction acceleration from 200 keV to a few tens of MeV", Nucl. Inst. Meth. Phys. Res. A 733 141-146 (2014).

[7] T.Yoshimoto et al., "Wideband induction acceleration and its intrinsic nature in the KEK digital accelerator", Nucl. Inst. Meth. Phys. Res. A 797 191-195 (2015).

ISBN 978-3-95450-131-1

A RACETRACK-SHAPE FIXED FIELD INDUCTION ACCELERATOR FOR GIANT CLUSTER IONS

K. Takayama[1,2,3,4)], A. Adachi[1,3)], M. Wake[1)], K. Okamura[1,3)], and Y. Iwata[5)]

[1)]High Energy Accelerator Research Organization (KEK), Tsukuba, Ibaraki, Japan
[2)]Tokyo Institute of Technology, Nagatsuda, Kanagawa, Japan
[3)]The Graduate University for Advanced Studies, Hayama, Kanagawa, Japan
[4)]Tokyo City University, Tamadsutsumi, Tokyo, Japan
[5)]National Institute of Advanced Industrial Science and Technology (AIST), Tsukuba, Ibarali, Japan

Abstract

Recently the racetrack-shape fixed field induction accelerator (RAFFIA) has been proposed as a unique driver to obtain high energy giant cluster ions [1]. Its essential properties are introduced here. The first realistic model under designing is described.

INTRODUCTION

Since the first proposal of the RAFFIA it has attracted interests of the related society developing applications of giant cluster ions such as C-60. So far a single-end electrostatic accelerator has been the typical diver for giant cluster ions. Achievable energy there is limited to around 50 keV/nucleon. A synchrotron or cyclotron may be suitable to obtain higher energy. However, the restriction on the frequency band-width of acceleration RFs requires an expensive and extremely large scale injector. It is a better choice to employ induction acceleration [2] instead of RF acceleration in order to avoid this restriction. As a matter of fact, the synchrotron employing induction acceleration has been demonstrated both in a slow-cycling mode [3] and fast-cycling mode [4] at KEK.

The racetrack-shape fixed field induction accelerator given in Reference 1, which looks like a microtron, seems to be much suitable to accelerate giant cluster ions with an extremely large mass to charge ratio, *A/Q,* to high energy in a limited site space for the accelerator, because a large magnetic rigidity is expected with the 90 degrees bending magnet.

Not only C-60 but also another attractive giant cluster atom with super lattice structure such as Si-108 [5] is available now. High charge–state ion sources for C-60 or Si-108 are under development. Integrating these cluster ion sources with the RAFFIA, we can realize a unique giant cluster ion driver.

ESSENTIAL PROPERIES OF THE RAFFIA

The schematic layout of the RAFFIA is shown in Fig. 1. The ring consists of 4 bending magnets of 90 degrees and 8 pairs of doublet Q magnet occupying the two long straight sections. The injection device and extraction region are placed in the upper straight section. The former is a 20 kV electrostatic injection kicker, which is the same as that being operated in the KEK digital accelerator [4]. There are several choices for the latter. A conventional extraction system consisting of extraction kickers and septum magnets is among them. Meanwhile, the lower straight section is occupied by the induction acceleration cells.

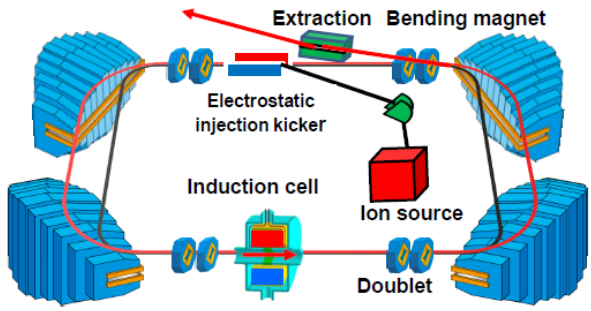

Figure 1: Layout of the RAFFIA with initial orbit (black) and the last orbit just (red).

Energy gain per nucleon in the RAFFIA is rather small, less than (*Q/A)*x50 keV. This means a large number of revolution in the machine. Orbit stability in the transverse direction is mostly crucial. In Reference 1 the reverse field strip in the open front of the bending magnet and negative gradient on the median plane are introduced to improve the vertical focusing(see Fig. 2). It turns out that the introduced focusing effects leads to the sufficient stability for both directions with a help of optimized time-

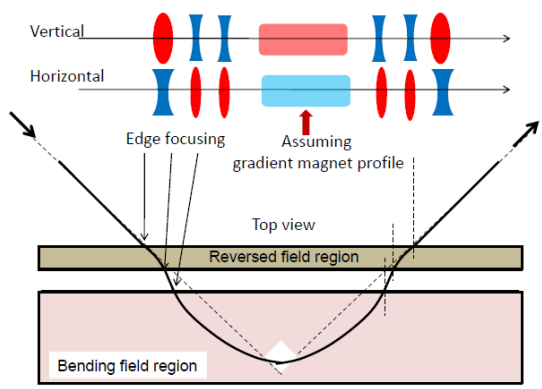

Figure 2: Properties of focusing/defocusing on the median plane.

ISBN 978-3-95450-131-1

varying doublet fields.

Preliminary beam dynamic study [1] has delineated the following properties of the RAFFIA.

(1) Lattice function is achieved by an appropriate configuration of the lattice magnets.
(2) Betatron tunes may swiftly cross resonance lines on the way to extraction.
(3) Long stay of the cluster ions in the accelerator ring requires extremely a good vacuum pressure of order of 10^{-7} Pascal, because the large cross-section of electron capture is quite large at the low energy.

For the induction acceleration, there seems to be no crucial issues. However, our experience from the existing induction synchrotrons [3,4] still suggests several improvements in the induction acceleration system shown in Fig. 3.

(1) DC voltage should vary in a desired pattern in the same acceleration cycle.
(2) A number of solid-state switching elements in the switching power supply (SPS) should be reduced to be as small as possible for the simplicity of gate control.

It is possible to realize a circuit architecture to meet (1). For the latter purpose, a SPS employing original SiC package devices with a larger withstand voltage is under development [6].

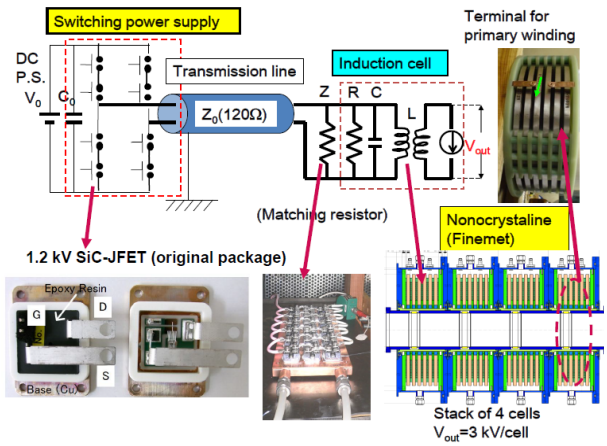

Figure 3: Assumed induction acceleration system.

The beam bunch trapped in a barrier bucket shown in Fig.4 is handled in a desired manner without any delicate control of the circulating path length in an electron microtron so as to always satisfy phase matching with the RF frequency.

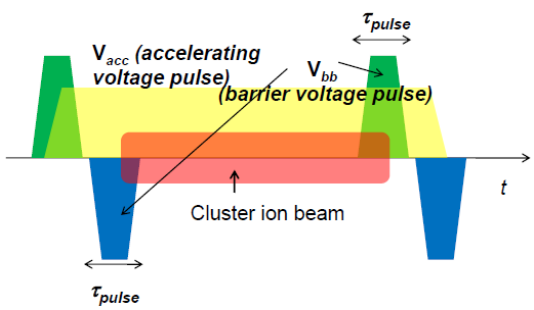

Figure 4: Induction acceleration/confinement scenario.

THE FIRST MODEL UNDER CONSIDERATION

A medium size RAFFIA is being seriously considered, which will be constructed in the KEK site if its construction budget is accepted by the financial agency. The construction space is limited and the existing floor condition eventually restricts on a maximum weight of the bending magnet. The candidate site for the construction is shown in Fig. 5.

It is practically important how big magnets for the

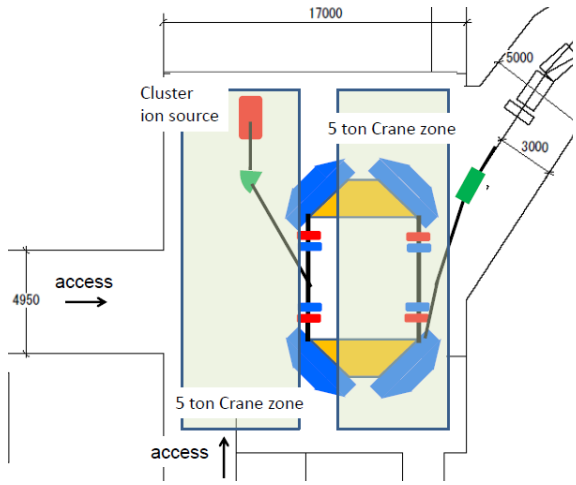

Figure 5: Possible construction site, where the KEK-DA is being operated now.

RAFFIA are constructed under the given condition. From the practical point of view, we have assumed that the maximum weight of the bending magnet is around 80 ton. It will be segmented into 20 blocks at a manufacturer. The components will be carried in the accelerator tunnel though the access path and assembled into 1 magnet.

This restriction suggests us parameters of a possible RAFFIA, which are listed in Table1.

Table 1: Beam and Machine Parameters

Ion	C-60
A	720
Q	10
energy per nucleon	0.2 MeV
Bending magnet	
length, Z_{max}	5.5 m
maximum pole face widt	1.35m
flux density, B_{max}	1.5 T
Gradient, dB/dX	0.3 T/m
Doublet	
K_F	0.80→ 0.91 /m^2
K_D	-1.025→ -1.3 /m^2
Long straight section, L_s	10 m
Lattice function at symmetric point	
β_y	95 m → 30 m
β_y	110 m -> 10 m
Betatron tune, Q_x/Q_y	(0.8 →1.0) / (0.6 →0.52)

The 2D field distribution of the bending magnet is shown in Fig. 6.

ISBN 978-3-95450-131-1

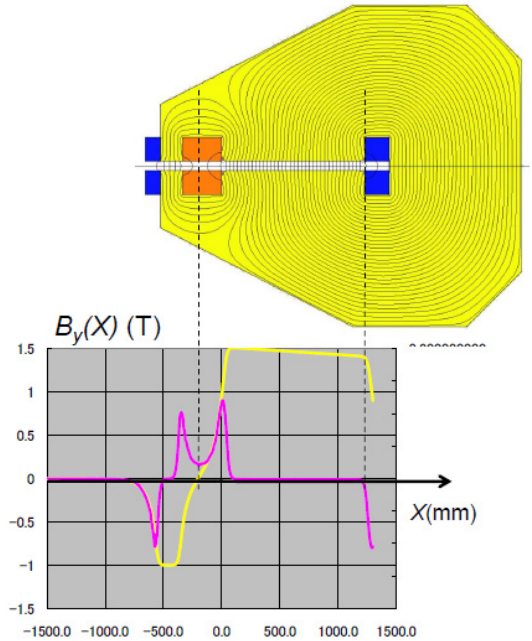

Figure 6: $B_y(X)$ (yellow) and dB_y/dX (red) of the bending magnet with the reverse field strip on the open front.

Assuming the above guiding fields, orbit tracking from the injection to the last stage of acceleration has been carried out by the newly developed 4th-order Runge-Kutta orbit tracking code taking account of the 3D magnetic field extended from the calculated 2 D field distribution. In the present example, the magnet is ramped at the early stage (1-100 turn) so as to provide the orbit stability. Beyond that, its flux density is kept to be 1.5 Tesla. In this sense, the example is a kind of hybrid type among the induction synchrotron and pure RAFFIA.

The central orbit through the acceleration is shown in Fig. 7, where the effect of the reversed field is visible at the lower energy.

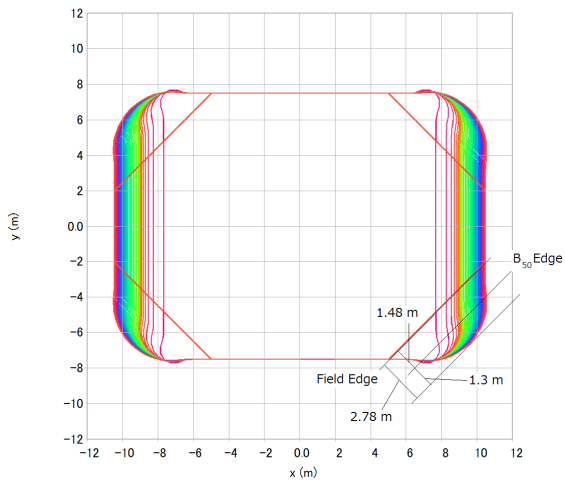

Figure 7: Continuous central orbit from injection to the end of acceleration and shown every 8 turns.

Many issues such as betatron tunes closed to half-integer and integer are left unsolved.

IMPACT ON APPLICATIONS

The most attractive feature of the cluster ion is the stopping power that materials have when the ion is introduced in them. It in principle exceeds the case of C by a factor of 60 and even the case of U ion. In addition, nonlinear effects, called cluster effects, in the electromagnetic interaction between the projectile ion and electrons surrounding material atoms are expected. Rough estimations suggest that the stopping power may be amplified by a factor of 10.

This features are strongly expected to induce unknown and nonequilibrium states of the matters [7,8]. Creation of extremely strong micro-size shock waves in water and an ion-track formed in gold or ceramic are among them. The stopping powers are shown in water and some solid-state material in Fig. 8.

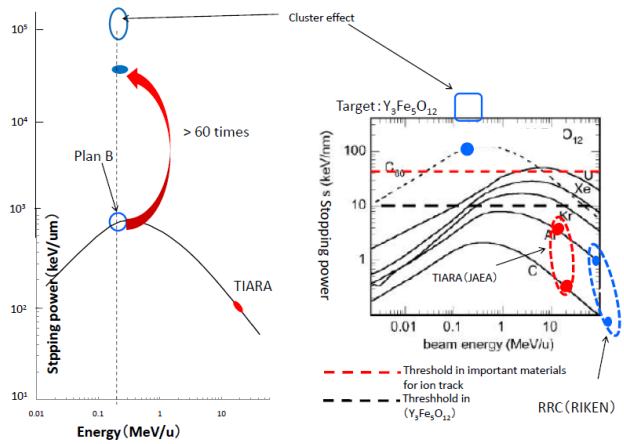

Figure 8: Stopping power of water and $Y_3Fe_5O_{12}$ for C-60 as a function of energy.

SUMMARY

The concept of the RAFFIA has been briefly reviewed and its essential properties are described. An example of practical RAFFIA for the first demonstration is shown here, although a lot of optimization must be done. If our proposal is successfully accepted by the financial agency, we will start to construct this machine and 3 years later cluster ions with an attractive energy will be delivered for various applications.

REFERENCES

[1] K.Takayama, T.Adachi, M.Wake,a nd K.Okamura, *Phys. Rev. ST-AB* **18**, 050101 (2011).
[2] K.Takayama and R.J.Briggs, Induction Accelerators (Springer, Heidelberg, 2011).
[3] K.Takayama *et al.*, *Phys. Rev. Lett.* **98**, 054801 (2007).
[4] K.Takayama, *et al.*, *Phys. Rev. ST-AB* **17**, 010101 1-6 (2014).
[5] Y.Iwata *et al.*, *Crystal Growth & Design* **15**, 2119 (2015).
[6] K.Okamura *et al.*, 5th Euro-Asian Pulsed Power Conference, OB1-1, Kumamoto , Sep. 8-12 (2014)
[7] private communications with K.Narumi and Y.Hase (JAEA-Takasaki) (2015).
[8] private communications with H.Amekura (NIMS) (2015).

ISBN 978-3-95450-131-1

NUCLOTRON AT JINR: OPERATION EXPERIENCE AND RECENT DEVELOPMENT

N. Agapov, O. Brovko, A. Butenko, E.E. Donets, E.D. Donets, A. Eliseev, V. Fimushkin, A. Govorov, E. Ivanov, V. Karpinsky, V. Kekelidze, H. Khodzhibagiyan, A. Kovalenko, V. Mikhailov, V. Monchinsky, S. Romanov, V.Slepnev, A.Sidorin, A. Smirnov, E. Syresin, G. Trubnikov, V. Volkov

JINR, Dubna, Moscow Region, Russia

Abstract

The results of 20 years of operation and development of the first superconducting synchrotron based on 2T cold iron fast cycling SC-magnets are presented. The Nuclotron technology of superconducting magnetic system for the NICA facility at JINR and for FAIR project will be used.

INTRODUCTION

The Nuclotron accelerator complex at Laboratory for High Energy Physics is the basic facility of JINR for generation of proton, polarized deuteron (also neutron/proton) and multicharged ion (nuclear) beams in energy range up to 6 GeV/amu. The Nuclotron was built during 1987-92. This accelerator based on the unique technology of superconducting magnetic system [1]. All design, tests and assembling works were carried out at the LHEP. Production of the structural cryomagnetic elements was done by the JINR workshops.

The Nuclotron accelerator complex (Fig. 1) consists of

- set of ion sources,
- Linac LU-20,
- 45 T·m SC synchrotron Nuclotron,
- 1000 m^2 experimental hall,
- beam transport lines,
- liquid He plant.

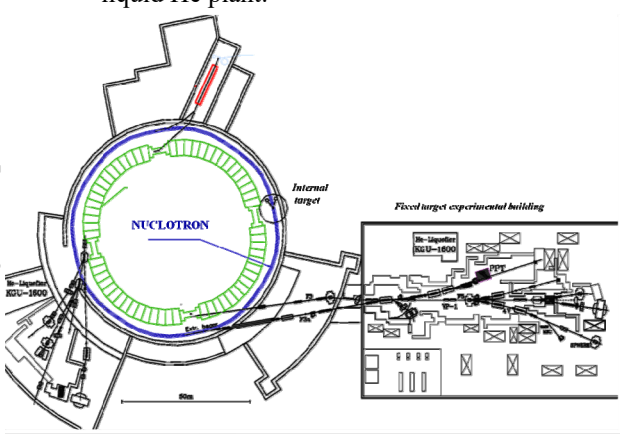

Figure 1: The Nuclotron accelerator complex.

The complex used presently for fixed target experiments on extracted beams and experiments with internal target. The program includes experimental studies on relativistic nuclear physics, spin physics in few body nuclear systems (with polarized deuterons) and physics of flavours. At the same time, the Nuclotron beams are used for research in radiobiology and applied research.

In the nearest future the Nuclotron technology of superconducting magnetic system will be used for new accelerators of the NICA facility under creation at JINR [2].

OPERATION

51 runs of the Nuclotron operation were performed since March 1993. Main result of the Nuclotron development during this period is stable and reliable operation of all the systems proving beam quality required for users. The operational time is about 2000 hours per year optimized in accordance with the JINR topical plans accounting the plan of the NICA construction. For more efficient usage of the beam time, the regime with two parallel users is realized routinely: experiment with internal target at the first plateau and beam extraction at the second one. Different types of the ion beams are delivered for the experiments (Table 1).

Table 1: Nuclotron and Beam Parameters

Nuclotron parameter	Project	Status (2015)
Max. main. field, T	2	2 (1.85 routine)
B-field ramp, T/s	1	0.8
Accelerated particles	p–U, d↑	p, d-Xe
Max. energy, GeV/u	12 (p), 5.9 (d) 4.5(^{197}Au^{79+})	5.9 (d, ^{12}C), 1.5 (^{124}Xe^{42+}, ^{40}Ar^{16+})
Intensity, ions/cycle	10^{11} (p,d) 10^9 (A> 100)	d 2-5·10^{10} ^{124}Xe^{24+} 1·10^4 ^{12}C 2·10^9 ^{40}Ar^{18+} 2·10^5 ^{7}Li^{3+} 3·10^9

Increase of the beam intensity and widening of the ion species are related with construction of three new ion sources: SPI (Source of Polarized Ions), LIS (Laser Ion Source), Krion-6T (ESIS type heavy ion source). New powerful Nd-YAG laser was tested for the carbon beam generation during the run #48. For the first time Krion-6T

ISBN 978-3-95450-131-1

was operated at the Nuclotron during the run #50. Test of the SPI is in progress at a test bench [3].

Development of slow extraction system resulted in realization of acceptable quality of the extracted beam in the interval of the spill duration from 60 ms up to 20 s and for the beam intensity from 10^{11} down to 10^5 ions per cycle (Fig. 2).

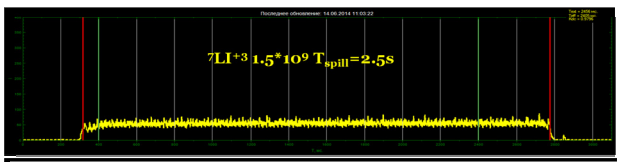

Figure 2: Example of the slow extraction beam spill.

NUCLOTRON AS TESTBENCH FOR NICA

In addition to the implementation of the current physics program the Nuclotron having the same magnetic rigidity as the future NICA collider [2] and based on the same type of the magnetic system is the best facility for testing of the collider equipment and operational regimes. Development works for NICA performed during recent Nuclotron runs include the testing of elements and prototypes for the MPD (Multy Purpose Detector which will be operated at the collider) using extracted deuteron beams; tests of the automatic control system based on the Tango platform, which has been chosen for the NICA facility; tests of diagnostic equipment for the Booster – small superconducting synchrotron constructing in the frames of the NICA project to improve the Nuclotron performance.

Simulation of the collider magnetic system operational conditions was performed at the Nuclotron during runs #45-47 (in years 2012-2013). This presumed test of the Nuclotron systems in the operational mode with long plateau of the magnetic field. In the run #45 the circulation of accelerated up to 3.5 GeV/u deuteron beam during 1000 seconds was demonstrated. During the runs #46 and #47 such a regime was used for test of stochastic cooling at the Nuclotron, which is an important phase of the NICA collider cooling system design.

During 2011-2013 the elements of the stochastic cooling chain for test at the Nuclotron were designed, constructed and installed at the ring. Main parameters of the system are the following: bandwidth 2-4 GHz, optimal beam kinetic energy 3.5 GeV/u, system (and notch filter) delay accuracy 1 ps, N_{ion}~10^9. In March 2013 (run #47) the effect of the longitudinal stochastic cooling using notch-filter method had been demonstrated at the Nuclotron for the first time (Fig. 3). Experimentally obtained characteristic cooling time is in good agreement with simulation results [4].

The next step of the stochastic cooling experiments was dedicated to test of a bunched beam cooling (such a regime corresponds to luminosity preservation during collider experiment). Partial modernization of the Nuclotron RF accelerating system permitted to prolong the RF pulse duration up to about 25 s. Thereafter during the run #48 (December 2013) the stochastic cooling effect had been successfully demonstrated in both for coasting and bunched carbon beams. In the last case the bunching factor (ratio between peak and mean current) was about 5.

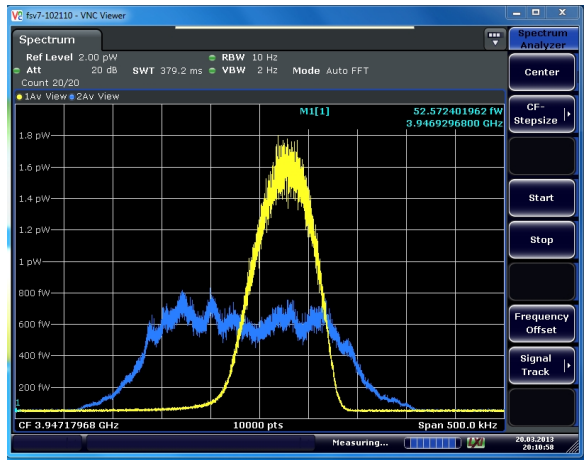

Figure 3: A longitudinal Schottky spectrum of the 3 GeV/u deuteron beam at 3500th harmonics of the revolution frequency, showing the initial spectrum (blue curve) and after 8 minutes of cooling (yellow curve). The beam intensity is $2 \cdot 10^9$ ions.

The experimental investigation of stochastic cooling was a complex test of machine performance. During the experiment, the cryogenic and magnetic systems, power supply, cycle control and diagnostic equipment were operated stably in a mode in which the circulation time of the accelerated beam at the flat-top of the magnetic field was gradually increased from a few tens of seconds up to eight minutes.

NICA facility will consists of two linacs, two synchrotrons, collider rings equipped with two detectors and a few beam transport lines. To operate this equipment a modern automatic control system is necessary. The concept of the NICA control system based on Tango platform in 2012 was developed. The Tango control system is a free open source device oriented controls toolkit for controlling any kind of hardware or software and building SCADA systems. It is used for controlling synchrotrons, lasers and physics experiments in over 20 sites. It is being actively developed by a consortium of research institutes. Addition argument for the Tango usage is that this system has been chosen as a basis for the control system of the FAIR facility, which is developed in very close co-operation with NICA.

Minimum set of equipment was prepared to the run #46 (December 2012) and since this period the new control system is under active development. Several subsystems (beam injection control, beam slow extraction control and so on) have been converted to the Tango-based structure [5].

To implement the Tango control system as a control system of the NICA accelerator complex the 4 main tasks there were performed:

1) The control equipment database was designed and created.

ISBN 978-3-95450-131-1

2) The web-tool for using and managing of the control equipment database was developed.
3) Servers were purchased and configured.
4) The necessary toolbox for development, storing, documenting and using of Tango-based software was set up.

DEVELOPMENT OF SC MAGNET TECHNOLOGY

The Nuclotron-type design based on a window frame iron yoke and a saddle-shaped superconducting winding has been chosen for the NICA booster and collider magnetic system as well as for the SIS100 synchrotron (FAIR project). Nuclotron-type magnets include a cold (4.5K) window frame iron yoke and a superconducting winding made of a hollow NbTi composite superconducting cable cooled with a two-phase helium flow.

The building construction of the new test facility for simultaneous cryogenic testing of the SC magnets on 6 benches is completed at the Laboratory of High Energy Physics [6]. More than 430 magnets will be tested at the facility during the next 4 years. Premises with an area of 2600 m^2 were prepared to install the equipment. The 15 kA, 25 V pulse power supply, three helium satellite refrigerators with capacity of 3 x 100 W were commissioned (Fig. 4).

Figure 4: First bench of the SC magnet test facility.

The equipment for cable production allows producing a Nuclotron -type hollow composite superconducting cable with the capacity of up to 50 m/h. The diameter of the cooling channel of the cable can vary from 3 to 5 mm. The number of SC wires in the cable may be up to 32. The wire diameter may be up to 1 mm. Hall for manufacturing of SC coils is equipped with a rotating table and tooling for winding of various types of SC coils as well as a furnace for heat treatment of coils with the length up to 3.5 m. The place for the assembling of the magnets is equipped with a few tables and tooling for rotating the magnet round the longitudinal axis to ease welding and brazing the cooling channels, devises for electrical insulation test, resistance and inductance measurement, hydraulic of cooling channels test and adjustment. The place for "warm" (room temperature) magnetic measurements is equipped with magnetic measurement system, pulsed linear regulated power converter with the current up to 100 A and DAQ based on National Instruments PXI measuring electronics and LabVIEW software.

The first magnets for the NICA Booster and collider have successfully passed cryogenic test on the bench. Three pre-serial dipole magnets for the NICA booster were tested in 2014 (Fig. 5). These tests include measurements of the magnetic field quality.

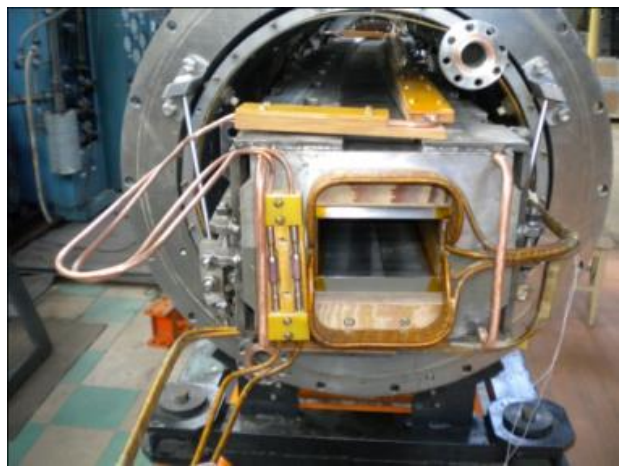

Figure 5: Pre-serial dipole magnet of the NICA Booster.

CONCLUSION

Nuclotron technology of superconducting magnetic system has been tested during more than 20 year of safety and stable operation of the ring. The results obtained can be useful under design of a modern fast cycling superconducting synchrotrons of different applications.

REFERENCES

[1] A.M.Baldin et al., «Cryogenic System of the Nuclotron - a New Superconducting Synchrotron», Advances in Cryogenic Engineering, v.39, p.501-508, New York, 1994.
[2] G. Trubnikov et al., "Heavy ion collider facility NICA at JINR (Dubna): status and development", Proc. ICHEP'12, Melbourne, Australia.
[3] A.V.Butenko et al, "Development of NICA injection complex", Proceedings of IPAC2014, Dresden, Germany.
[4] N.Shurkhno et al., Study for stochastic cooling at Nuclotron, JINR, Proceedings of COOL13, Murren, Switzerland
[5] E.Gorbachev et al., Upgrade of the Nuclotron injection control and diagnostic system, Proceedings of ICALEPCS2013, San Francisco, CA, USA
[6] S. Kostromin, Facility for Assembling and Testing of SC Magnets for NICA and FAIR projects, Proceedings of RuPAC 2014, Obninsk, Russia.

ISBN 978-3-95450-131-1

PARTICLE TRACKING SIMULATION WITH SPACE CHARGE EFFECTS FOR AN INDUCTION SYNCHROTRON AND PRELIMINARY APPLICATION TO THE KEK DIGITAL ACCELERATOR

X. Liu#
Tokyo Institute of Technology, Nagatsuda, Kanagawa, Japan
High Energy Accelerator Research Organization (KEK), Tsukuba, Ibaraki, Japan

Abstract

In order to study the beam behaviour of the induction synchrotron which features low energy injection, a dedicated particle tracking simulation code with a 2.5D space charge field solver, which takes into account of the boundary condition, has been developed. The beam dynamics included in this code are discussed and simulation results assuming parameters of the KEK Digital Accelerator are presented. This code will help to understand the various features of the beam behaviour in the present beam commissioning and serve as a tool for the design of the future induction synchrotrons.

INTRODUCTION

The concept of induction synchrotron has been raised around 2000 by K. Takayama and J. Kishiro [1]. This concept has been experimentally confirmed in 2006 with the former KEK Proton Synchrotron (PS) [2]. After that, the booster for the KEK-PS has been modified to the present KEK Digital Accelerator [3]. The beam commissioning has been started since the middle of 2011 and the recent experimental studies can be seen in [4] and [5]. Though the longitudinal motion has been discussed in [6] and the longitudinal space charge field has been studied with simulation in [7], the 3D particle tracking simulation with the space charge has not been done yet.

In this paper, a 2.5D "slice-by-slice" scheme and the space charge solver with a boundary matrix method will be discussed. The justification of this solver is also described. Preliminary results of its application to the KEK-DA will be briefly shown.

SCHEME DESIGN

The following vector is chosen to represent the information of a macro particle in the simulation:

$$\vec{x} = (x, xp, y, yp, z, dpp) \tag{1}$$

where (x, xp) and (y, yp) are the positions in the horizontal and vertical phase space respectively, and $(z, \Delta p/p)$ is the longitudinal phase space. Here $z = s - \beta_0 c \cdot dt$ ($\beta_0 = v_0 / c$, v_0 is the velocity of the reference particle and c is the light speed) is the particle's longitudinal distance and $\Delta p/p$ is the momentum deviation from the referential particle.

For particle tracking without the space charge from s_0 to s_1 along the beam orbit of the referential particle, the change of particle information defined in Eq. (1) is given by,

$$\vec{x}_{s_1} = M_{s_0 \to s_1} . \vec{x}_{s_0} \tag{2}$$

where M is a 6×6 transfer matrix from s_0 to s_1. In order to include the space charge and keep the simplicity of Eq. (2), the single kick approximation is used [8],

$$x(s) \xrightarrow{K_{sc}} x(s)' \xrightarrow{M} x(s + \Delta s) \tag{3}$$

where K_{sc} is the kick due to space charge forces and $\Delta s = s_2 - s_1$. K_{sc} can be expressed with the space charge induced field [9]

$$\vec{x}_{sc} = (0, \frac{\Delta s \cdot Qe}{\gamma_0^2 p_0 \beta_0 c} E_x, 0, \frac{\Delta s \cdot Qe}{\gamma_0^2 p_0 \beta_0 c} E_y, 0, \frac{\Delta s \cdot Qe}{\beta_0^2 E_{total}} E_z) \tag{4}$$

Here we assume that during a very small step size of Δs, the change of the space charge field caused from a change of the beam distribution is ignorable. In Eq.(4), (E_x, E_y, E_z) is the electric field in the beam frame, Q is the charge state of the particle, e is the unit electron charge, $\gamma_0 = 1/\sqrt{1-\beta_0^2}$, p_0 is the momentum and E_{total} is the total energy of the reference particle. The magnetic field due to moving beam is considered by including $1/\gamma_0^2$.

2.5D SPACE CHARGE SOLVER

A "slice-by-slice" scheme is chosen to solve the space charge field induced by the beam. In this scheme, the particle distribution will be longitudinally divided into k slices as seen in Fig. 1. Each slice will be meshed into $m \times n$ grids. Thus, there will be $m \times n \times k$ boxes in the 3D space.

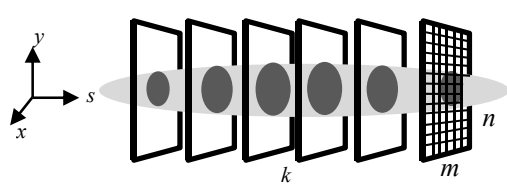

Figure 1: 2.5D slice-by-slice scheme.

The charge of the macro particles will be assigned to closest grid points (eight points for each macro particle) with the Particle-In-Cell (PIC) method, in which the

#liuxg@post.kek.jp

ISBN 978-3-95450-131-1

distances from the particle's position to the grid points are treated as weighting coefficients.

Then for each slice the transverse electric potential will be solved in a 2D manner. The transverse electric field is obtained from the potential. The longitudinal electric field is directly derived from the potential difference between adjacent slices.

Finite Method to Solve Poisson's Equation

Poisson's equation is,

$$\nabla\phi = -\frac{\rho}{\varepsilon_0} \tag{5}$$

where ϕ is the potential induced by the particle distribution, ρ is the charge density and ε_0 is the electric constant in vaccum.

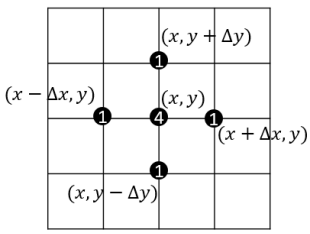

Figure 2: Finite method for Poisson's equation.

A finite method to solve this equation numerically is shown in Fig. 2, where the space is meshed into small tiles. In the case of $\Delta x = \Delta y = \Delta$, Eq. (5) in 2D case can be expressed as,

$$\phi(\Delta + x, y) + \phi(x, \Delta + y) - 4\phi(x, y) + \phi(x - \Delta, y) + \phi(x, y - \Delta) = -\frac{\rho(x, y)}{\varepsilon_0}\Delta^2 \tag{6}$$

Boundary Matrix Method

If the equations similar to Eq. (6) are written down for all points on the mesh, these equations will form a linear system with the left hand side (l.h.s) to be the potential on each grid point and the right hand side (r.h.s) to be the charge density, as shown below,

$$\begin{pmatrix} -4 & 1 & & & 1 & & & & & & & \\ 1 & -4 & 1 & & & 1 & & & & & & \\ & 1 & -4 & 1 & & & 1 & & & & & \\ & & 1 & -4 & & & & 1 & & & & \\ \vdots & & & & \ddots & & & & \vdots & & & \\ & & & & & & & -4 & 1 & & & \\ & & & & & & & 1 & -4 & 1 & & \\ \cdots & & & & \cdots & & & & 1 & -4 & 1 & \\ & & & & & & & & & 1 & -4 & \end{pmatrix} \begin{pmatrix} \phi_1 \\ \phi_2 \\ \\ \\ \vdots \\ \\ \\ \phi_{n-1} \\ \phi_n \end{pmatrix} = \begin{pmatrix} \rho_1 & \rho_2 & \cdots & \rho_n \end{pmatrix}^T \cdot \frac{\Delta^2}{\varepsilon_0} \tag{7}$$

Once the distribution is determined, the electrical potential can be obtained directly by solving Eq.(7), which can be easily solved with available numerical libraries such as Intel MKL[10] used in this simulation code.

The advantages of this method are obvious: (1) the boundary matrix determined only by the boundary shape, which allows any shape just by setting the potential of the grid points outside or on the boundary to be zero; (2) the number of boundary shape for accelerator is not so large, these boundary shapes can be prepared at the beginning and repeatedly used later.

Justification

In order to justify the method described in the previous subsection, two ideal distributions that the space charge potential and electric field can be obtained analytically have been considered.

The case of a round beam with current I_b in a cylindrical vacuum chamber is assumed as in Fig. 3. In the transverse direction, the beam is uniformly distributed within the beam radius a. The radius of the vacuum chamber is b.

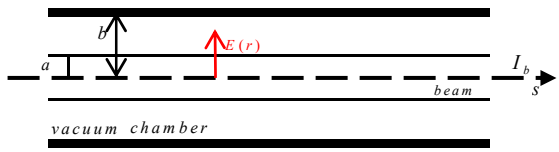

Figure 3: Round beam in cylindrical vacuum chamber.

The potential in the transverse direction with a distance r from the center of the beam can be obtained as,

$$E[r] = \begin{cases} \dfrac{\lambda}{2\pi\varepsilon_0}\dfrac{r}{a^2}, 0 \le r \le a \\ \dfrac{\lambda}{2\pi\varepsilon_0}\dfrac{1}{r}, a \le r \le b \end{cases} \tag{8}$$

where λ is the charge line density, related to the beam current I_b as,

$$\lambda = \frac{I_b}{\beta c} \tag{9}$$

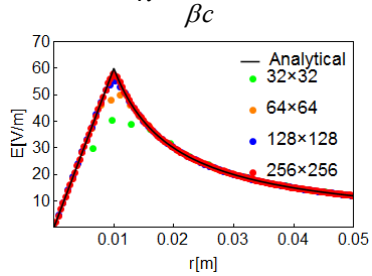

Figure 4: Simulation results compared with analytical solution.

Figure 4 shows the comparison between the simulation results and the analytical solution given by Eq. (8) where I_b =100 μA, a = 1 cm, b = 10 cm and β =0.01. In the simulation 10^4 number of macro particles are generated uniformly within the radius of a. In order to minimize the error for the field calculation, a large mesh size is often preferred, as shown in this figure.

ISBN 978-3-95450-131-1

In the case of a Gaussian distribution which has no sharp edge in the beam distribution, the electric field is given by

$$E[r] = \frac{1 - e^{-r^2/(2\sigma^2)}}{2\pi r \varepsilon_0} \lambda \qquad (10)$$

where σ is the standard deviation for normal distribution. Similarly, the comparison between the simulation results and the analytical solution given by Eq. (10) is shown in Fig. 5 ($\sigma = a$), from which one can see that the result of 64×64 is better than that in Fig. 4 due to smooth beam distribution.

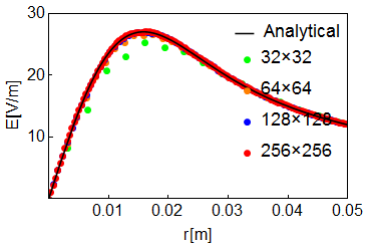

Figure 5: Simulation results for normal distribution.

PRELIMINARY APPLICATION TO THE KEK-DA

Lattice Calculation

With the guiding magnet components in the KEK-DA ring, the lattice functions can be calculated with this simulation code as shown in Fig. 6.

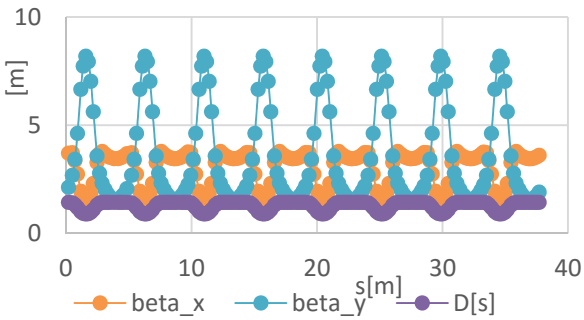

Figure 6: Lattice calculated for the KEK-DA ring.

Simulation Parameters Optimization

To minimize the error induced in the tracking simulation, the step size Δs has to be optimized. Figure 7 shows the rms emittance of a beam with transverse normal distribution is tracked one turn in the KEK-DA ring with different step size. It indicates that Δs should be less than 0.3m in this case.

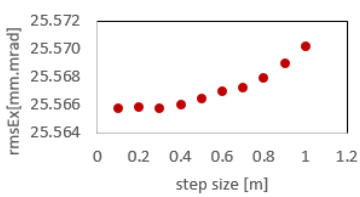

Figure 7: Step size optimization.

Static Magnetic Tracking Results

With the optimized step size, the beam can be tracked through the KEK-DA ring repeatedly to study the beam evolution due to the space charge force. For example, Fig. 8 shows transverse phase space of mismatched beam injection. In this simulation, the beam has the normal distribution in the transverse direction. The result shows that the beam tends to match the lattice and the evolution on the phase space due the space charge force.

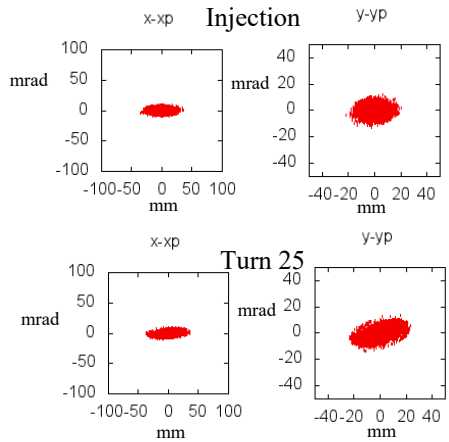

Figure 8: Phase space evolution of a mismatched beam.

CONCLUSION

A general simulation code considering the space charge with boundary conditions has been developed for the induction synchrotron. A 2.5D "slice-by-slice" scheme has been used and the boundary matrix method used as space charge solver has been well justified. Preliminary application to the KEK-DA, which is a fast cycling induction synchrotron, has been presented. Further study with the simulation to understand the beam behaviour in the KEK-DA ring will be continued and this simulation code can also be applied to the design and study of the future induction synchrotrons.

REFERENCES

[1] K. Takayama & J. Kishiro, Nucl. Instruments Methods Phys. Res. Sect. A. 451 (2000) 304–317.
[2] K. Takayama, et al., Phys. Rev. Lett. 98 (2007) 8–11.
[3] T. Iwashita, et al. , Phys. Rev. Spec. Top. - Accel. Beams. 14 (2011).
[4] X. Liu, et al., Laser Part. Beams. 33 (2015) 237–243.
[5] T. Yoshimoto, et al., Nucl. Instruments Methods Phys. Res. Sect. A 733 (2014) 141–146.
[6] T.S. Dixit, Nucl. Instruments Methods Phys. Res. Sect. A. 602 (2009) 326–336.
[7] X. Liu, et al. Proc. HIAT 2012. (2012) 83–88.
[8] A. Bazzani, et al., Cern Report (1994) 1–234.
[9] G. Franchetti, et al. Nucl. Instruments Methods Phys. Res. Sect. A. 415 (1998) 450–454.
[10] Intel, Intel ® Math Kernel Library, MKL 11.2, n.d.

ISBN 978-3-95450-131-1

BEAM CONFINEMENT DYNAMICS IN A BARRIER BUCKET

*Masatake Hirose [A,B], Ken Takayama [A,B,C,D], Takashi Yoshimoto [B,C], Liu Xiggung [B,C]
[A]Tokyo City University, Tamatsutsumi, Setagaya, Tokyo, Japan
[B]High Energy Accelerator Research Organization (KEK), Tsukua, Ibaraki, Japan
[C]Tokyo Institute of Technology, Nagatsuda, Yokohama, Kanagawa, Japan
[D]The Graduate University for Advanced Studies (SOKENDAI), Hayama, Kanagawa, Japan

Abstract

In an induction synchrotron such as the KEK digital accelerator, the barrier voltage pulse with almost rectangular shape is generated in an induction cell of a 1-to-1 pulse transformer driven by the switching power supply. Its peak amplitude and pulse length are flexibly changed but the rising/falling time is uniquely determined by a combination of the circuit parameters including characteristics of the employed solid-state switching element. Behavior of particles captured in the barrier bucket is quite various, depending on the barrier voltage shape. This paper systematically discuss about the phenomenology of beam dynamics for the barrier bucket and compare numerical simulations with the experimental results obtained in the KEK digital accelerator.

INTRODUCTION

Beam handling using the barrier bucket has been initiated by Jim Griffin of Fermilab in 1983, where the barrier voltage was obtained by superimposing multiple harmonic RFs[1]. The stability region in the phase space that the barrier voltage made came to be called an isolated bucket, However, it is hard to realize almost square pulse in a high-Q cavity, because, a large number of harmonics are needed. This technique has evolved since then [2]. The barrier voltage was realized in the low-Q cavity where necessary number of harmonic waves for square pulse formation is reduced. By feeding the harmonic waves amplified by a semiconductor amplifier to the cavity, the beam handling using the barrier bucket was demonstrated [3].

On the other hand, in an induction synchrotron such as the KEK digital accelerator, the barrier voltage pulse with an almost rectangular shape is generated in an induction cell of a 1-to-1 pulse transformer driven by a switching power supply (SPS). Such an induction acceleration technique is equivalent to the RF acceleration. The induction acceleration has been successfully demonstrated in the slow-cycling and fast-cycling synchrotrons in KEK [4, 5]. The KEK digital accelerator is a fast-cycling induction synchrotron, which is shown in Fig. 1. The experiment of beam handling by the barrier bucket has been extensively conducted in the KEK digital accelerator.

The barrier voltage shown in Fig. 2 is generated by the induction acceleration system shown in Fig. 3. Pulse height V_{bb} of the barrier voltage is uniquely determined by setting the voltage of the DC power supply. Pulse length t_f and barrier pulse duration T are determined by setting of timings *(t1, t2, t3, t4)*, which manages the On/Off operation of the switching elements of the SPS. It is controlled by a program installed in Fields Programmed Gate Array (FPGA). Rising and falling times of the voltage pulse, t_{rise} and t_{off}, are determined by the intrinsic nature of the switching power supply including the circuit parameters and characteristics of the solid-state switching device. It is about 30 nsec in this case.

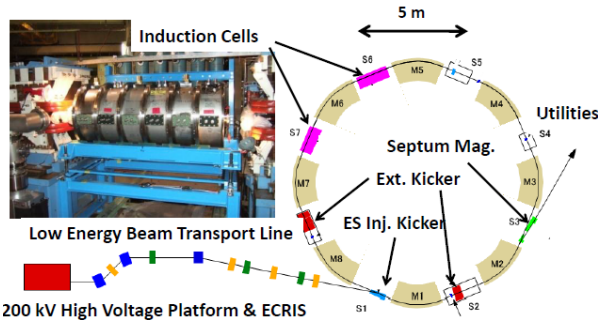

Figure 1: Schematic view of the KEK Digital Accelerator.

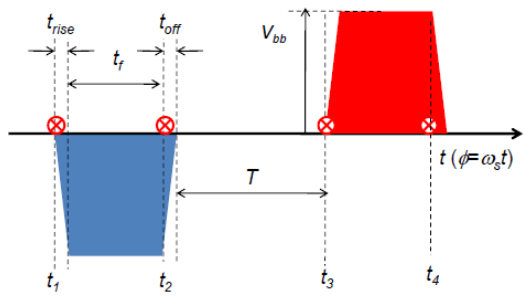

Figure 2: Barrier voltage pulses.

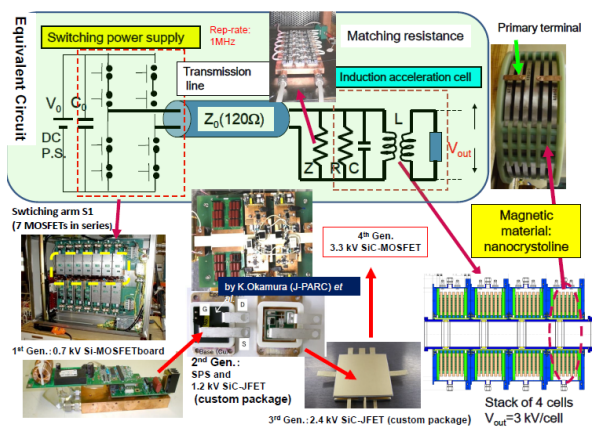

Figure 3: Equivalent circuit for the induction acceleration system.

masatake@post.kek.jp

ISBN 978-3-95450-131-1

CALCULATION OF PHASE SPACE ORBIT AND EMITTANCE

Longitudinal motion of the particles trapped in the barrier bucket is described by its energy E and phase ϕ.whose evolutions for each turn are given by a recurrence formula, as shown in Equation (1). Since the applied voltage to the induction acceleration cell is time-dependent, the voltage seen by a particle is given by $V(\phi_n)$.

$$\begin{cases} E_{n+1} = E_n + QeV(\phi_n) \\ \phi_{n+1} = \left\{ \phi_n + 2\pi\eta \cdot \left(\frac{\Delta p}{p} \right) \right\}_{\mathrm{mod}\ 2\pi} \end{cases} \quad (1)$$

$$\frac{\Delta p}{p} = \frac{\Delta E_n}{\beta_s^2 E_s} = \frac{E_n - E_s}{\beta_s^2 E_s} \quad (2)$$

$$\eta = \frac{1}{\gamma_T^2} - \frac{1}{\gamma_s^2} \quad (<0) \quad (3)$$

Where η is the momentum slippage factor and γ_T is the transition γ. Here, the parameters with suffix s are those of synchronous particle.

The longitudinal emittance is evaluated in terms of the following formula. The emittance defines it as the surface to include 95% of the particles.

$$\begin{aligned} \overline{s^2} &= \frac{1}{N}\sum_{i=1}^{N} s_i^2, \\ \overline{(\mathrm{E}+\Delta E)^2} &= \frac{1}{N}\sum_{i=1}^{N} (\mathrm{E}+\Delta \mathrm{E})_i^2, \\ \overline{\mathrm{s}\cdot(\mathrm{E}+\Delta E)} &= \frac{1}{N}\sum_{i=1}^{N} \mathrm{s}\cdot(\mathrm{E}+\Delta \mathrm{E})_i \end{aligned} \quad (4)$$

where s is distance from ideal particles and N is the number of particles.

$$\varepsilon = 4\sqrt{\overline{s^2}\cdot\overline{(\mathrm{E}+\Delta E)^2} - \left(\overline{\mathrm{s}\cdot(\mathrm{E}+\Delta E)}\right)^2} \quad (6)$$

COMPARISON BETWEEN EXPERIMENTS AND SIMULATIONS

The beam handling experiment has been conducted for the various amplitude and phase of the barrier voltage. The initial distribution in the phase space (ϕ, E) is shown in Fig. 4, where the uniform distribution is assumed in both directions with the maximum momentum error $(\Delta p/p)_{\max}$ of 0.25 %.

Typical five cases of the barrier voltage have been experimentally studied, which are shown in the first row of Fig. 5. Each case is distinguished by the height V_{bb} and pulse length t_f of the barrier voltage pulse. It is noted that the actual voltage profile includes the main pulse with the rectangular shape, their reflections, and some overshoot components. It is known later that these undesired voltage profiles induce asymmetric particle distributions.

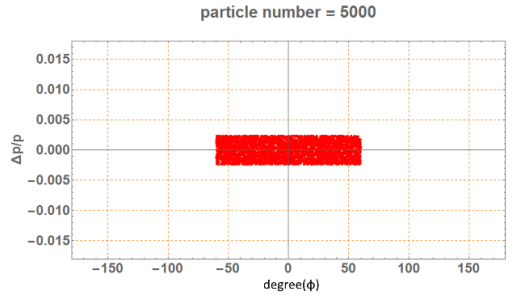

Figure 4: Initial distribution in the phase space (ϕ, $\Delta p/p$).

Table 1: Each Parameters of Barrier Voltage

Case	V_{bb} (V)	t_f (ns)
A	1.200	200
B	1.000	1,200
C	1.200	1,000
D	5	4,000
E	50	4,000

The 2nd row of Fig. 5 represents the phase pace structure of the individual case, which has been obtained by numerical tracking of test particles assumed in the phase space. The barrier bucket structures are clear. However, some of them are not symmetric due to a combination of asymmetric barrier voltage pulses. In addition, some of the buckets have their sub-structures. This means that a fraction of particles is trapped in such a substructure island.

The 3rd row denotes temporal evolutions of the macro particles of 5000, where the initial distribution is same among five cases and shown in Fig.4. The line density is projected on the 2D time space, time within a single revolution (horizontal) and time from injection (vertical).

The 4th row shows temporal evolutions of the beam bunch trapped in the barrier bucket, where the bunch signal obtained by the bunch monitor is projected on the 2D time space mentioned above. We can say that the simulation results are in a good agreement with the experimental results when the 3rd and 4th rows are compared.

The 5th row represents the change in time of the emittance defined by Eq. 6 for each case. Macroscopic oscillation is visible in Case B, C, and D. It is reasonable to understand that these phenomena are caused by mismatching of the injected bunch shape in the phase space to the waiting barrier bucket and a finite number of macro particles. Gradual increasing of the emittance is notable for Case A, B, and C, where the large barrier voltage is assumed. It has been known that the large barrier voltage reflects a particle entering the barrier region with a finite time step with an additional momentum. This is not found in Case D and E, where a lower barrier voltage is assumed.

ISBN 978-3-95450-131-1

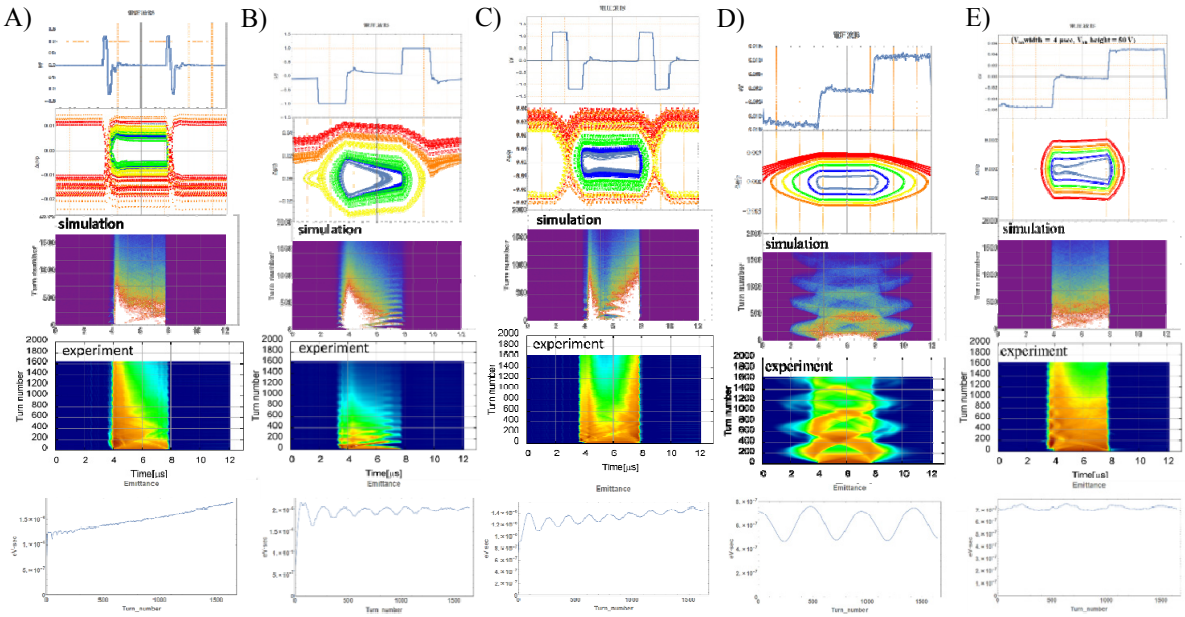

Figure5: Barrier voltage profile with reflections, phase space structure, bunch evolution in turn (simulation), bunch evolution in turn (experiment), and evolution of the emittance in turn. The parameters are shown in the Table 1.

In order to investigate the barrier voltage height dependence of emittance increasing in a more systematic way, the following simulation has been conducted. Assuming a typical waveform with t_f of 500 ns shown in Fig. 6 that has been actually realized in the experiment, the temporal evolution of the .emittance has been calculated for the different heights. In the early stage of confinement, that is, the first few tenth turns, the emittances abruptly increase and then gradual increasing is observed for the voltage height exceeding 1 kV shown in the Fig. 7.

CONCLUSION

Dynamics for beam confinement has been manifested by means of the actual experiment in the KEK-DA and the numerical simulation. Its turns out that both results are fairly in good agreement with each other. The present studies suggest that it is quite important to optimize the barrier voltage profile including its height to avoid undesired emittance increasing.

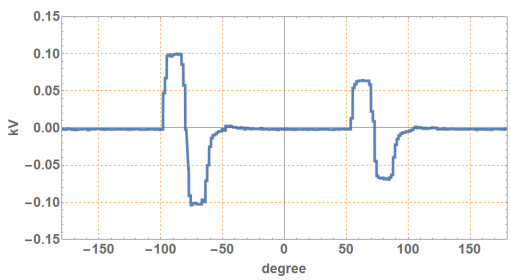

Figure6: Typical waveform of the barrier voltage.

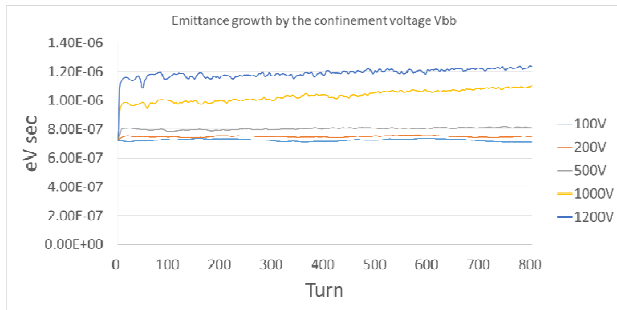

Figure7: Temporal evolution of emittance.

REFERENCES

[1] J. Griffin, C. Ankenbrandt, J. MacLachlan, and A. Moretti, “Isolated Bucket RF Systems in the Fermilab Antiproton Facility”, IEEE Trans. Nucl. Sci. NS-30, 3502 (1983).

[2] M. Blaskiewicz and J. Brennan, “A Barrier Bucket Experiment for Accumulating De-bunched Beam in the AGS”, Proc. of EPAC1996, 2373 (1996).

[3] C.M. Bhat, “Applications of Barrier Bucket RF Systems at FERMILAB”, Proc. of Int. Workshop on Recent Progress in Induction Accelerators, Tsukuba, **45** (2006).

[4] K. Takayama et al., “Experimental Demonstration of the Induction Synchrotron”, Phys. Rev. Lett. **98**, 054801 (2007).

[5] K. Takayama, T. Yoshimoto, Liu Xingguang et al., “Induction Acceleration of Heavy Ions in the KEK Digital Accelerator: Demonstration of a Fast-Cycling Induction Synchrotron”, Phys. Rev. ST-AB **17**, 010101 1-6 (2014).

ISBN 978-3-95450-131-1

PERFORMANCE OF A FAST KICKER MAGNET FOR RARE-RI RING

H. Miura[A], Y. Abe[B], Z. Ge[B], K. Hiraishi[C], Y. Ichikawa[C], I. Kato[A],
T. Moriguchi[C], D. Nagae[B], S. Naimi[B], T. Nishimura[A], S. Omika[A], A. Ozawa[C],
F. Suzaki[A,B], S. Suzuki[A], T.Suzuki[B], N.Tadano[A], Y. Tajiri[C], Y. Takeuchi[A],
T. Uesaka[B], M. Wakasugi[B], T. Yamaguchi[A], and Y. Yamaguchi[B]
[A]Saitama University, [B]RIKEN Nishina Center, [C]University of Tsukuba

Abstract

To inject rare isotopes individually into the storage ring, Rare-RI Ring, recently constructed at RIBF, a fast kicker magnet was developed. The developed kicker magnet is distributed constant twin type. The shape of magnetic field is essential for the individual injection, and the timing property is given by the inductance and capacitance components of the kicker. Based on detailed simulations of the equivalent electronic circuit of the kicker, we optimized the electrodes and ferrite cores of the kicker. In June 2015, we carried out the first commissioning of Rare-RI Ring using $^{78}Kr^{36+}$ beam with an energy of 168 MeV/nucleon. We succeeded in injection and ejection particle-by-particle by using the developed kicker system.

INTORODUCTION

The Rare-RI Ring is an isochronous storage ring developed to measure the masses of rare isotopes with a precision in the order of 10^{-6} [1]. The rare isotopes are randomly produced as secondary beams by in-flight fission or fragmentation of an intense DC beam from the RIBF accelerator complex, and their yields are as small as 1 events/day. Therefore, we apply the individual injection method to perform mass measurements of rare RI efficiently.

The individual injection method consists of fast kicker magnet with the RI beam self-trigger system [2]. The trigger pulse for the kicker is generated by a particle detector installed upstream of the beam line at F3, and is sent to the kicker system by a fast coaxial cable (see Fig. 1). The most important is that magnetic field is quickly excited before rare RI of interest arrives at the ring. The kicker should have a fast rising time and also a fast falling time for injected rare RI to be stored in the central orbit of the ring.

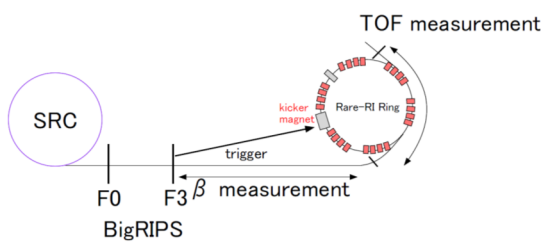

Figure 1: Schematic of the beam line of the Rare-RI ring facility.

DEVELOPMENT OF KICKER MAGNET

The developed kicker magnet is distributed constant twin type. The kicker magnet is equivalent to an electronic circuit that is π type *LC* circuit. To achieve the impedance $Z = 12.5\ \Omega$, the parameters of inductance $L = 70$ nH and capacitance $C = 230$ pF were designed. The inductance is given by the shape of ferrite cores, and the capacitance is given by the distance between high-voltage and ground electrode of the kicker. Figure 2 shows a photograph of the prototype kicker magnet.

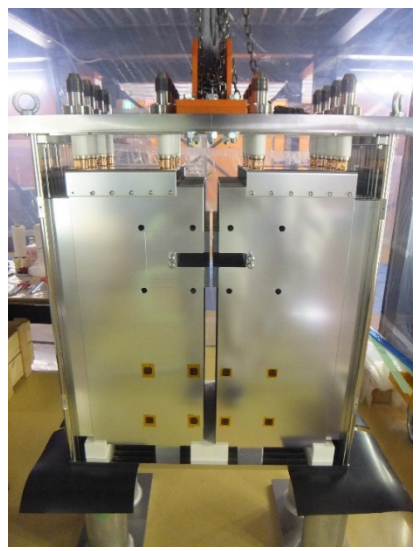

Figure 2: Prototype kicker magnet.

First, we optimized the parameter for one side of the kicker magnet (left or right electrode shown in Fig. 2). As the result, the parameter are $L = 120$ nH and $C = 280$ pF. Figure 3 shows a comparison of the simulation result and experimental data. The agreement is satisfactory.

However, the current pulse shape of the both side kicker magnet (full system) was different from that of one side kicker magnet, because of mutual inductance between both ferrite, as shown in Fig. 4. Based on the result of one side kicker magnet and the simulations, the mutual inductance was estimated to be $M = 30$ nH. The result was well reproduced by the simulation, as shown in Fig. 4. However, a tail component around 800 ns in the pulse shape still remains as shown in Fig. 4. The tail component of magnetic field disturbs the trajectory of particle stored in the ring.

ISBN 978-3-95450-131-1

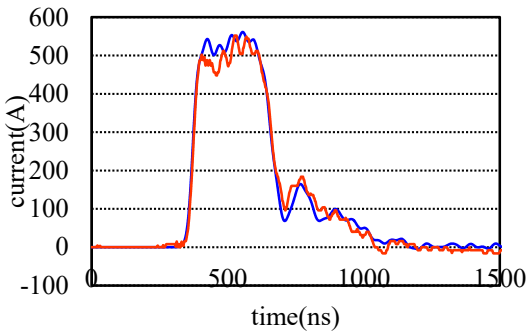

Figure 3: Typical current pulse shape (one side kicker) as a function of time. Blue and red lines are simulation and experiment data, respectively.

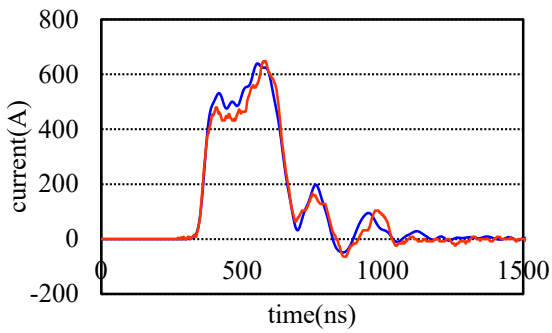

Figure 4: Typical current pulse shape (full kicker system) as a function of time. Blue and red lines are simulation and experiment data, respectively.

We use these simulation results to develop a new kicker magnet. The new kicker magnet parameters are designed to be L = 100 nH and C = 350 pF to improve impedance matching. Therefore, additional capacitance of 2600 pF was attached to the entrance of kicker magnet to prevent reflection. The current pulse shape of improved kicker magnet is shown in Fig. 5.

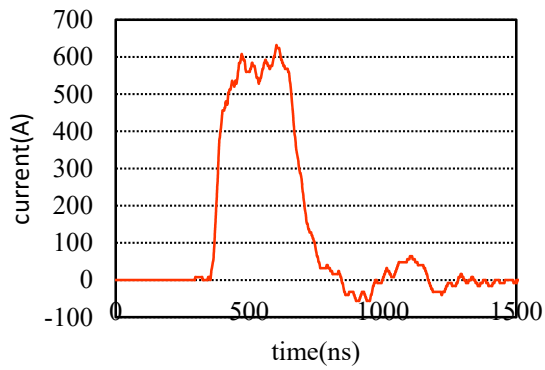

Figure 5: Typical current pulse shape of a new kicker magnet.

We apply the search coil method to measure magnetic field. The magnetic field (magnetic flux ϕ) is determined from raw voltage signals V of the search coil (turn number N) using the equation,

$$\phi = -\frac{1}{N}\int V dt \qquad (1)$$

The result of magnetic field of the new kicker magnet is shown in Fig. 6, where the magnetic field has a flat top with a width of about 100 ns.

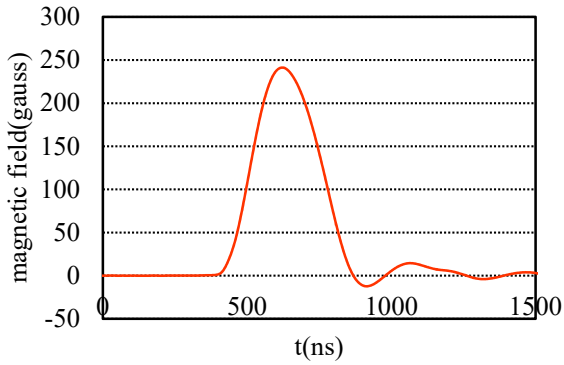

Figure 6: Typical magnetic field of a new kicker magnet.

RESULT OF COMMISIONING

In June 2015, we carried out the first commissioning of Rare-RI Ring using $^{78}Kr^{36+}$ beam with an energy of 168 MeV/nucleon. The kick angle of 11.4 mrad is required to inject into the Rare-RI Ring. The relation between the kick angle θ and necessary magnetic field is described as

$$B = \frac{B\rho}{L}\theta \ , \qquad (2)$$

where L is the kicker magnet length (369 mm) and $B\rho$ is magnetic rigidity, 4.21 Tm. For the present beam condition, a magnetic field of 434 G is required. Thus, kicker power supply should be charged up to 26.6 kV.

Result of Injection

We tested individual injection method using the new kicker magnet. To confirm injection of the beam, a plastic scintillation counter was placed in the central orbit after one sector. When the beam is kicked correctly, it is counted by the plastic scintillation counter. We measured the number of counts by changing injection timing and charging voltage, as shown in Fig. 7. The change of the number of counts by the plastic scintillator is consistent with the shape of magnetic field. Also, the charging voltage giving the maximum is consistent with the estimated value. The present results show that the individual injection method was successfully performed.

Result of Ejection

We tested the ejection of stored beam using the same kicker magnet after 700 μs storage. A plastic scintillation counter was placed at the exit of the ring. We measured the number of events counted by the plastic scintillator by changing the ejection timing. The result is shown in Fig. 8. The maximum number of events was observed around 350 ns, which is consistent with the revolution period in the ring. The stored beam was successfully ejected from the ring.

ISBN 978-3-95450-131-1

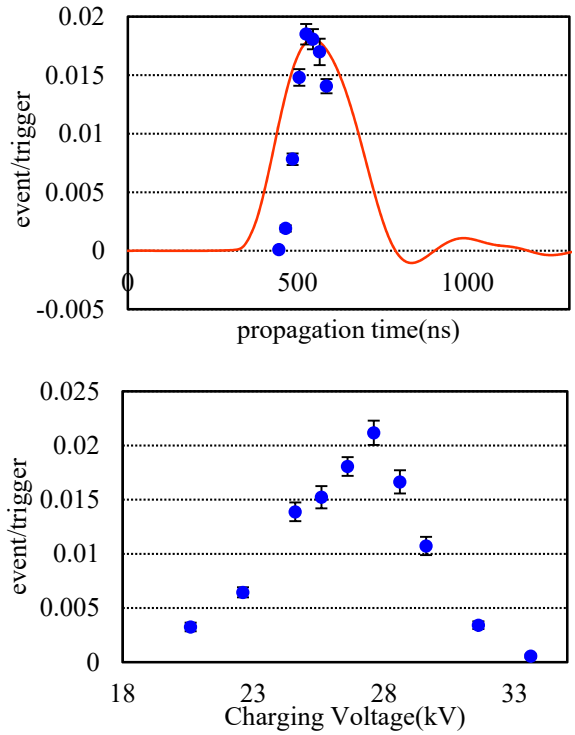

Figure 7: Up: The number of events counted by the plastic scintillation detector as a function of kicker timing. Down: The same as a function of the charging voltage of kicker magnet. Blue points are experimental data and the red line is the magnetic field for comparison.

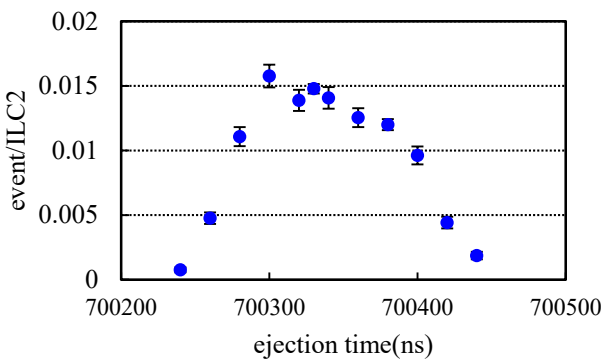

Figure 8: The number of events counted by the plastic scintillation detector at the exit of the storage ring as a function of ejection delay timing.

CONCLUSION

Rare-RI Ring is a storage ring developed to measure the masses of unstable nuclei with a precision in the order of 10^{-6}. To inject rare isotopes individually into the ring, we developed the fast kicker magnet with a fast rising and falling time. Based on the offline test of the kicker magnet and detailed simulations of equivalent kicker circuit, we improved the kicker magnet with better impedance matching. The resultant magnetic field shape is satisfactory for the individual injection. In June 2015, we carried out the commissioning of Rare-RI Ring using $^{78}Kr^{36+}$ beam with an energy of 168 MeV/nucleon. We succeeded in injecting and ejecting Kr ions particle-by-particle by using the present kicker system.

REFERENCES

[1] A. Ozawa et al., Prog. Theor. Exp. Phys. 2012 (2012) 03C009.
[2] I. Meshkov et al., Proceedings of EPAC 2004, Lucerne, Switzerland.

ISBN 978-3-95450-131-1

PERFORMANCE OF A RESONANT SCHOTTKY PICK-UP IN THE COMMISSIONING OF RARE-RI RING

F. Suzaki*, Y. Abe, Z. Ge, D. Nagae, S. Naimi, T. Uesaka, T. Watanabe, M. Wakasugi, K. Yamada, Y. Yamaguchi, J. Zenihiro, Y. Yano, RIKEN, Wako, Japan
I. Kato, H. Miura, T. Nishimura, S. Omika, T. Suzuki, N. Tadano, Y. Takeuchi, T. Yamaguchi, Saitama University, Saitama, Japan
K. Hiraishi, Y. Ichikawa, T. Moriguchi, A. Ozawa, S. Suzuki, Y. Tajiri, University of Tsukuba, Tsukuba, Japan

Abstract

Rare-RI Ring was constructed at RIKEN RIBF for precise isochronous mass spectrometry of unstable nuclei. In June 2015, we performed the first commissioning of the ring using ^{78}Kr beam with the energy of 168 MeV/nucleon. We successfully carried out the individual injection which is one of the characteristics of the ring, and also we succeeded in the storage of ^{78}Kr ions for a few seconds.

We evaluated the performance of the resonant Schottky pick-up which was installed in the Rare-RI Ring. The purpose of the resonant Schottky pick-up is a monitor for tuning of the isochronous field in the ring. The resonant Schottky pick-up detected single ^{78}Kr ions, where the frequency resolution was 1.29×10^{-6} (FWHM). The resolution is in the same order of the required isochronicity. The sensitivity and resolution of the resonant Schottky pick-up are sufficient for the tuning of isochronous optics.

INTRODUCTION

Determining masses of extremely neutron-rich nuclei is important for study of nuclear structure and nucleosynthesis. Such unstable nuclei which locate far from β-stability line are short lived and rare, so here we call such nuclei rare RIs. In order to measure masses of rare RIs precisely, Rare-RI Ring was constructed at RIBF [1, 2]. Because rare RIs are randomly produced by nuclear reactions with intense primary beam from the cyclotron complex, only one rare RI is injected into the ring by using the individual injection with the fast kicker system.

We employ the isochronous mass spectrometry method. For high precision of the masses ($\Delta m/m \sim 10^{-6}$), we require to tune the isochronous field in the order of 10^{-6}. As a monitor for the tuning, we adopt a resonant Schottky pick-up. The resonant Schottky pick-up was designed by the systematic 3D electromagnetic simulations with Micro Wave Studio [3], and was tested offline before installation in the ring [4]. From Schottky spectra, we obtain the revolution frequency information of circulating ions. The momentum change of a stored ion causes the frequency change in the Schottky spectrum, so the isochronicity indicates no change in frequency, despite momentum change of the stored ion. The resonant Schottky pick-up is required to have high sensitivity such that it can detect a single ion with sufficient resolution. In the present study, we evaluated the performance of the resonant Schottky pick-up in the commissioning.

* suzaki@ribf.riken.jp

RESONANT SCHOTTKY PICK-UP

The resonant Schottky pick-up consists of a pillbox-type resonant cavity and ceramic gap. The resonant cavity is made of aluminum with outer diameter, length, and inner diameter of 750, 200, and 320 mm, respectively. Figure 1 is the photographs of the resonant Schottky pick-up. When the beam pass through the resonant Schottky pick-up, an electromagnetic field is induced in the cavity. The change of magnetic flux in the induced electromagnetic field is detected by a pick-up loop. The coupling factor of the pick-up loop was optimized to be one. By adjusting the position of two tuners, the resonance frequency is changed in the range of 173 ± 1.5 MHz.

We performed an offline test of the resonant Schottky pick-up with a network analyzer. We determined the shunt impedance R_{sh} with the bead method. As the result, we acquired basic quantities of the resonant cavity: the resonance frequency f_{res} = 171.43 MHz, R_{sh} = 161 $k\Omega$ and unloaded quality factor Q_0 = 1880.

ONLINE RESULT AT COMMISSIONING

The first commissioning of Rare-RI Ring using ^{78}Kr beam with the energy of 168 MeV/nucleon was carried out

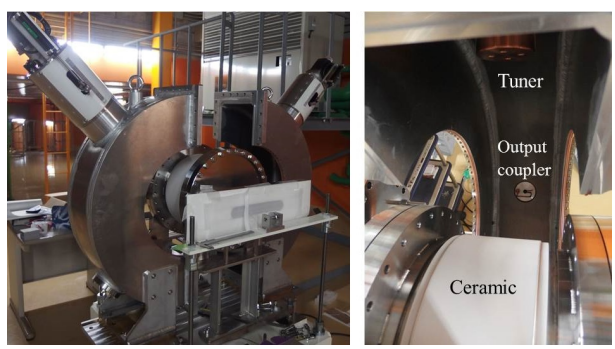

Figure 1: (Left): The resonant Schottky pick-up divided in half. The Schottky pick-up has a pillbox-type resonant cavity. (Right): Inside of the resonant cavity. In the upper part, a tuner for fine tuning the resonance frequency is shown. In the lower part, a pick-up loop for detecting the induced magnetic flux is shown.

ISBN 978-3-95450-131-1

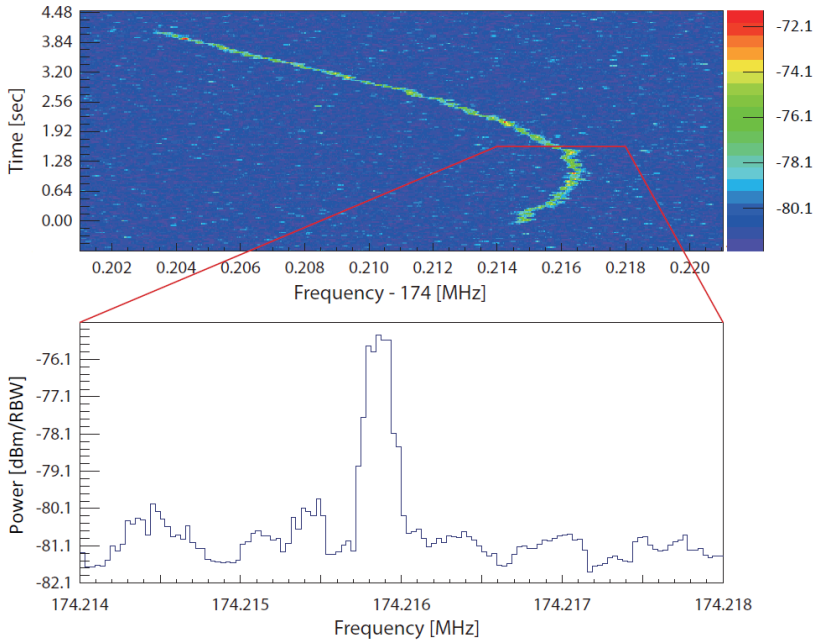

Figure 2: The upper part is a spectrogram of a single ^{78}Kr ion. The ^{78}Kr ion was stored for 4 s. The lower part is a zoomed FFT spectrum in a frame of 32 ms. The output signal power is $P = -65.8$ dBm which is obtained by integrating the peak after subtracting the thermal noise. The frequency width is 224 Hz in FWHM.

in June 2015. We succeeded in injecting ^{78}Kr ions into the ring, by using the individual injection method with the fast-response kicker system. At first, the storage of ^{78}Kr ions was confirmed by a thin TOF detector installed in the ring [5]. The periodic pulses from the TOF detector were observed for approximately 25 μs, which corresponded to 60 turns in the ring. From this measurement, the revolution time of ^{78}Kr ions was obtained, and then resonance frequency was adjusted to be approximately 174.2 MHz, by moving the tuner position, where the 66th harmonics was taken. The first order correction of isochronicity was applied by adjusting the trim coils installed in the dipole magnets. After a storage of 700 μs, typical measurement time of mass spectrometry, the ^{78}Kr ions were successfully extracted by the same kicker magnet [6, 7].

Then, the operation mode of the ring was switched to the storage mode for the performance evaluation of the resonant Schottky pick-up. In the storage mode, the ^{78}Kr ions were stored for approximately 5 s. We successfully observed the signals of single ^{78}Kr ions in the Schottky spectrum, as shown in Fig. 2. The upper part of Fig. 2 is a spectrogram of ^{78}Kr. In this plot, the horizontal and vertical axis are the resonance frequency and time after injection, respectively. The lower part of Fig. 2 is a zoomed FFT spectrum in a frame of 32 ms. The vertical axis represents the induced power in dBm/Resolution Band Width (RBW). The frequency width was 224 Hz in FWHM, so here the frequency resolution was 1.29×10^{-6}. The measured signal power was $P = -65.8$ dBm, where P was obtained by integrating the peak in the Schottky spectrum after subtracting thermal noise background. For comparison, we calculated the expected signal power $P_{\rm cal}$. $P_{\rm cal}$ was calculated using the following equation which represents the signal power of single ion with charge q [8, 9],

$$P_{\rm cal} = \frac{1}{8}(qef)^2 R_{\rm load}, \quad (1)$$

where e is an elementary charge, f is a revolution frequency, and $R_{\rm load}$ is calculated from the equation; $R_{\rm load} = R_{\rm sh}/Q_0 \times Q_{\rm load}$. For ^{78}Kr beam with the energy of 168 MeV/nucleon, $P_{\rm cal}$ = -145.1 dBm. Actually, the pick-up signals were amplified by two low-noise amplifiers with the gain of 81 dB, and were sent to the counting room by a 30 m cable. Take into account the gains of the amplifiers and transmission losses of -2 dB, the expected signal power is obtained to be $P_{\rm cal}$ = -66.1 dBm. The observed Schottky signal power P is in good agreement with the expected $P_{\rm cal}$.

If the isochronous field is perfectly fulfilled, the frequency peak observed in the spectrogram of Fig. 2 should not change even though the momentum of the stored ion changes. This means that observed curve in Fig. 2 should be a straight line. However we found a frequency shift which is considered to be caused by the momentum change due to the interactions with residual gas in the ring. The vacuum was still in the order of 10^{-5} Pa without the baking procedure.

Figure 3 shows the revolution time of ^{78}Kr ions as a function of momentum, where the revolution time was measured by the plastic scintillation counters placed at the entrance and exit of the ring, and the momentum was obtained from the position of ^{78}Kr ion at the dispersive focal plane in the injection beam line. The data was well reproduced by the fitted curve of the 2nd order polynomial, as shown by

ISBN 978-3-95450-131-1

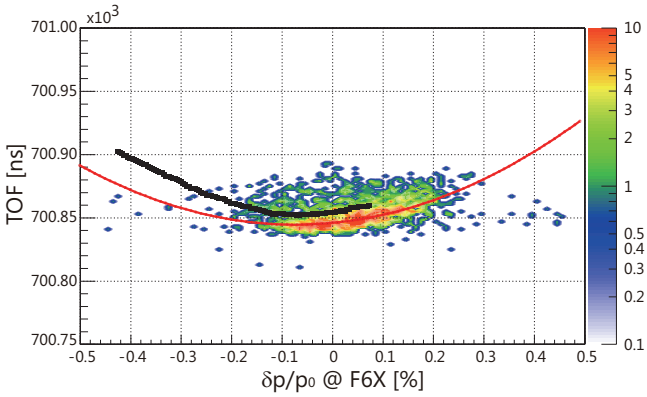

Figure 3: Revolution time as a function of the momentum of ^{78}Kr ions. Red curve is a fitted curve of the 2nd order polynomial. Black curve was obtained from the Schottky data after the conversion of the resonance frequency into the revolution time and the time after injection into the momentum based on the energy loss calculations in residual gas in the ring.

red curve. This indicates that the first order correction of isochronicity was properly applied. The black curve represents the converted data from the resonant Schottky pick-up as shown in Fig. 2. The revolution time was calculated from the resonance frequency taking into account the harmonics number. The momentum was calculated from the time after injection, by assuming that the ^{78}Kr ion loses kinetic energy in residual gas in the ring. The black curve is consistent with the red one. The injected ^{78}Kr ion with nearly central momentum moved along this curve. Thus, behavior of ^{78}Kr ion in the ring is suggested so that the ion lost kinetic energy gradually during storage of 4 s due to the energy loss process in residual gas.

CONCLUSION AND PROSPECT

First commissioning of the Rare-RI Ring using ^{78}Kr beam was performed successfully in June 2015. We confirmed injection into the ring and storage of single ^{78}Kr ions for a few seconds. The resonant Schottky pick-up detected single ^{78}Kr successfully. Based on the Schottky spectrum, the observed signal power is almost same as the expected signal power. The frequency resolution of $\sim 1.29 \times 10^{-6}$ was calculated from the width of the Schottky spectrum. The performance of the resonant Schottky-pick up is sufficient in terms of sensitivity and resolution. In addition, we will be able to evaluate the long term stability of the Rare-RI Ring operation based on the results of analysis which is in progress.

ACKNOWLEDGMENTS

F. S. is grateful for the RIKEN Junior Research Associate Program. This work has been partially supported by Competitive Program for Creative Science and Technology Pioneering Projects, RIKEN and JSPS KAKENHI Grant no. 26287036.

REFERENCES

[1] Y. Yamaguchi et al., "Construction of rare-RI ring at RIKEN RI Beam Factory", Nucl. Instr. Meth. B 317, 629 (2013).

[2] A. Ozawa et al., "The rare-RIring", Prog. Theor. Exp. Phys, 03C009 (2012).

[3] F. Suzaki et al., "Design Study of a Resonant Schottky Pick-up for Rare-RI Ring Project", Nucl. Instr. Meth. B 317, 636 (2013).

[4] F. Suzaki et al., "Performance of a resonant Schottky pick-up for the Rare-RI Ring project", JPS Conf. Proc. 6, 030119 (2015).

[5] Y. Abe et al., "Developments of time-of-flight detectors for Rare-RI Ring", JPS Conf. Proc. 1, 013059 (2014).

[6] Y. Yamaguchi et al., "The Rare-RI Ring at RIKEN RI Beam Factory", presented at HIAT2015, Yokohama, Japan, paper TUM1C03, these proceedings.

[7] H. Miura et al., "Performance of a Fast Kicker magnet for Rare-RI Ring", presented at HIAT2015, Yokohama, Japan, paper MOPA23, these proceedings.

[8] F. Nolden et al., "A fast and sensitive resonant Schottky pick-up for heavy ion storage rings", Nucl. instr. Meth. A 659, 69 (2013).

[9] F. Suzaki et al., "A resonant Schottky pick-up for Rare-RI Ring at RIKEN", Proc. of STORI'14, Sankt Goar, Germany (2014).

ISBN 978-3-95450-131-1

SI-THYRISTOR MATRIX ARRAY DRIVEN ELECTROSTATIC INJECTION KICKER FOR THE KEK DIGITAL ACCELERATOR AND BEAM DYNAMICS ANALYSIS OF INJECTION

H. Kobayashi[#1,2], X. Liu[2,3], T. Kawakubo[2], and T. Adachi[2,4]

[1]Tokyo City University, Setagaya, Tokyo, Japan
[2]High Energy Accelerator Research Organization/Accelerator Laboratory (KEK), Tsukuba, Japan
[3]Tokyo Institute of Technology, Nagatsuda, Japan
[4]The Graduate University for Advanced Studies (SOKENDAI), Hayama, Kanagawa, Japan

Abstract

The electrostatic (ES) kicker is used for heavy ion beam injection [1] into the KEK digital accelerator (DA) ring [2]. A voltage of 20 kV, which must be immediately turned off after injection, is put across the electrostatic electrodes before injection so as to deflect the injected beam on the ring orbit. The SI-Thyristor Matrix Array (SI-Thy MA) as a turning off switching device has been developed to replace the conventional thyratron [3]. The long ringing in the turn-off voltage affects on longitudinal motions of the injected beam bunch. Its careful analysis is discussed here.

INTRODUCTION

Voltage ringing continues for about 3.5 μs after switching on of the SI-Thy MA as shown in Fig. 1. It is apparently longer than that of the thyratron. This is caused by intrinsic natures of the SI-Thy MA. Details of the newly developed SI-Thy MA were reported in Reference 3. Fortunately, such relatively longer ringing time duration does not become any actual problem even in the case of hydrogen ion of A/Q=1, because its revolution time of 6 μs is much longer than the ringing time duration . The ringing in voltage vibrates in time with damping. The oscillation period is about 550 ns.

Since its operation we have noticed interesting phenomena related to this voltage ringing. Creation and annihilation of micro-bunches as seen in Fig. 2 are among them. In order to investigate such ringing effects on the beam dynamics, extensive injection experiments were conducted. From the experiment adjusting the kicker discharge timing, the ringing was known to be responsible for perturbations on the circulating beam bunch. As a result, it turned out that the residual electric fields generated at an entrance and the exit of the ES-kicker, originating from the ringing voltage affects on the longitudinal beam dynamics. In addition, it has been observed that the creation of microstructure strongly depends on a beam intensity.

The physics model that explains the direct ringing effect is shown in Fig. 3. The ES-kicker region is 1 m long, and the transit time (τ) necessary for a particle to pass the region is about 330 ns. It is clear that the net effect of the residual voltage remains in the energy gain of a particle during passing the injection kicker.

For the purpose to fully understand the longitudinal beam dynamics in the early stage just after injection, the simulation program has been developed, which takes account of the longitudinal space charge effect and wake fields in an isolated impedance with the oscillation frequency close to the microstructure. The observation point is shown in Fig. 3. φ and E in the Figure denote the phase and the energy of the macro-particles at the observed point.

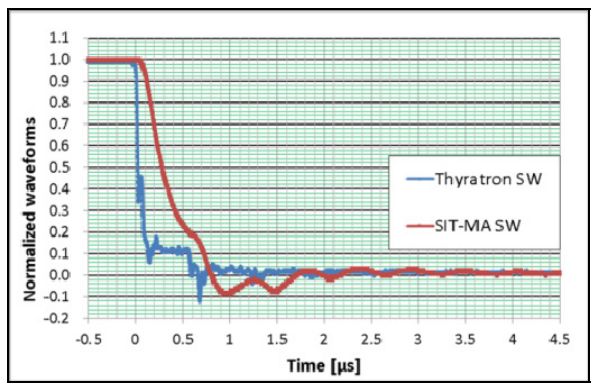

Figure 1: ES-Kicker voltage waveforms for both switches.

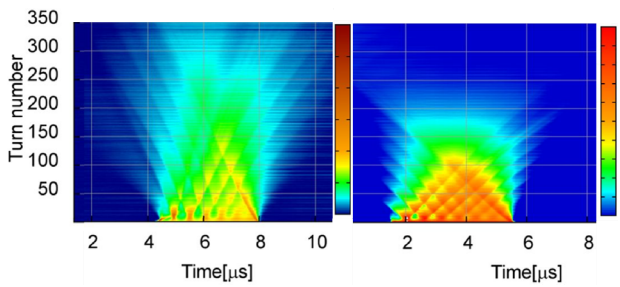

Figure 2: Temporal evolution of the injected bunch for 40 μA (experiment: left) and 100 μA (experiment: right), the line density is projected on the 2D time space, the time within a single revolution (the horizontal direction) and time from the injection (the vertical direction).

#khiroshi@post.kek.jp

ISBN 978-3-95450-131-1

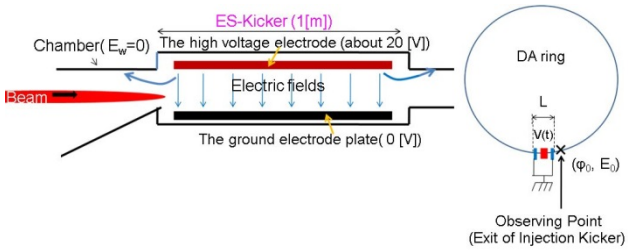

Figure 3: Analytical model for the injection kicker and Analytic model for interaction, where the dynamical parameters (φ, E) of macro-particles are picked up at the observing point.

NUMERICAL SIMULATION

The initial condition for the distribution of the macro-particles of 10^4 is assumed so as to mimics the actual situation as shown in Fig. 4, where the maximum momentum deviation $(\Delta p/p)_{max}$ is 0.2 % and its width in phase is 120 degrees corresponding to the injected beam bunch of 4 μs.

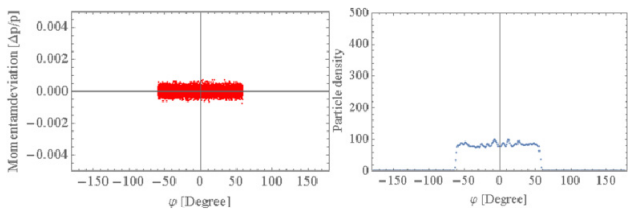

Figure 4: Phase plot and line density of macro-particles at injection timing.

Residual voltage V is assumed by a dumped Sin function. The energy gain by macro-particles is written by

$$\Delta E = Qe\left[V(t+\tau) - V(t)\right] \quad (1)$$

where τ is transit time and Q is the charge state of ion. At 1 turn after injection, thus, the particle distribution changes as shown in Fig. 5, where there is a large modulation in the momentum direction, meanwhile, the line density is almost same as in Fig. 4. In the situation that any external forces do not act on, the macro particles distribution evolves following the step equation for the phase keeping the same $\Delta p/p$,

$$\varphi_{n+1} = \left\{\varphi_n + 2\pi\eta \cdot \frac{\Delta p}{p}\right\} \quad (\eta < 0) \quad (2)$$

where n is the turn number. The simulation result is shown in Fig. 6. Creation and its drift and annihilation of the micro structure in the bunch are clear.

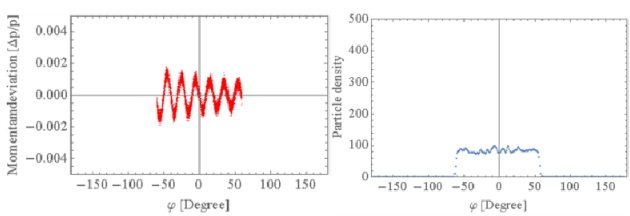

Figure 5: Phase plot and line density of the macro-particles just after passing the ES-kicker region.

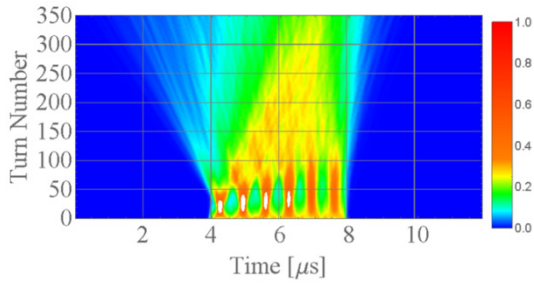

Figure 6: Projection of the line density on time axes (revolution time and turn number) for 100 μA.

The microstructure formation is reproduced. It turns out that the modulation in the momentum due to the residual voltage is a source causing the micorstructure. However, the drift speed on the 2D time space seems to be different from the experimental result. From the observed drift speed, the maximum momentum deviation is evaluated as follows,

$$\left|\left(\frac{\Delta p}{p}\right)\right|_{max} = \begin{cases} 0.1\ \%\ \text{for}\ 40\ [\mu\text{A}] \\ 0.2\ \%\ \text{for}\ 100\ [\mu\text{A}] \end{cases}$$

This difference is apparently attributed to the discrepancy in the beam current.

The longitudinal space charge effects and wake fields effects may be possible candidates that can explain this difference. The longitudinal space charge effects and wake fields effects are known to be written by the following equations.

$$E_S = -\frac{g_0}{4\pi\varepsilon_0\gamma^2}\cdot\frac{d\lambda}{ds} \quad (3)$$

where g_0 is the average geometric coefficient of the vacuum chamber, ε_0 is the dielectric constant of vacuum, γ is the relativistic gamma (approximately one), λ is a line density,

$$V_{int} = \frac{\omega_{rf}}{TTF}\left(\frac{R_{shunt}}{Q}\right)\int_{\varphi_{head}}^{\varphi}\exp\left(-\frac{\omega_\lambda(\varphi-\varphi')}{2Q\omega_{rf}}\right)\times\sin\left(\frac{\omega'_\lambda}{\omega_{rf}}(\varphi'-\varphi)\right)\frac{\partial\lambda(\varphi')}{\partial\varphi'}d\varphi' \quad (4)$$

[4] where ω_{rf} is the revolution frequency, TTF is the transit-time factor of the resonant impedance structure (assumed 1 for simplicity), R_{shunt} is the shunt impedance, Q is quality factor (~10). ω_λ is ringing frequency and $\omega'_\lambda \approx \omega_\lambda$.

It is a custom to include the space charge effects and wake fields effects as a delta function-like kick in the beam tracking simulation, under an assumption that the member change in phase by 1 turn is small, as shown in the following step equation,

$$E_{n+1} = E_n + Qe(C_0 \cdot E_S + V_{int}) \quad (5)$$

where C_0 is the orbit circumference (37.7 m).

ISBN 978-3-95450-131-1

SIMULATION RESULTS WITH OTHER EFFCTS

Table 1 shows beam parameters in the experiments and numerical simulations.

Table 1: Beam Parameters at Injection

Beam Current	40,100 μA
Beam length	4 μs
A/Q	4
v/c	0.01

Simulation results with the space charge effects are shown in Fig. 7 and 8.

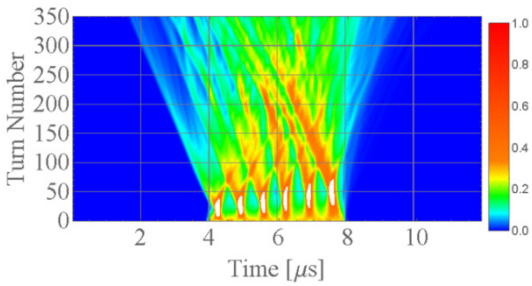

Figure 7: Temporal evolution of the injected bunch for 40 μA.

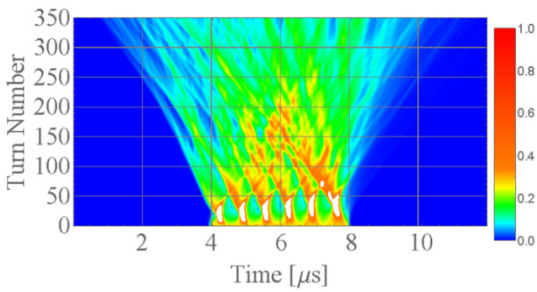

Figure 8: Temporal evolution of the injected bunch for 100 μA.

The diffusion speed seems to be still lower than the experimental results for both cases of 40 μA and 100 μA. This fact tells us that the space-charge effects are not enough to quantitatively explain increasing of the momentum deviation to result in the diffusion on the 2D time space. At last we arrive at wake field effects. Honestly speaking, we have no information about the impedance of the beam pipe, especially in the range of MHz. Unknown parameters except the resonance frequency ω_λ, such as the Quality factor Q and shunt impedance R_{shunt}, are assumed to be free-parameters in the simulation. Simulation results taking account of both of the space charge effects and wake fields effects are shown in Fig. 9 and 10, where Q=5 and R_{shunt}=1 Ω are assume .

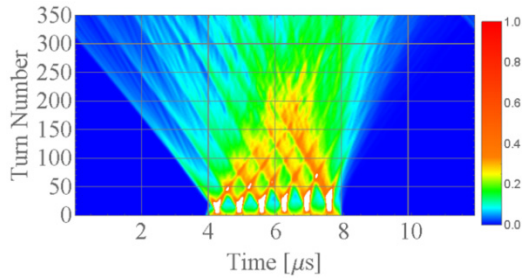

Figure 9: Temporal evolution of the injected bunch for 40 μA (simulation with space-charge effects and wake fields effects).

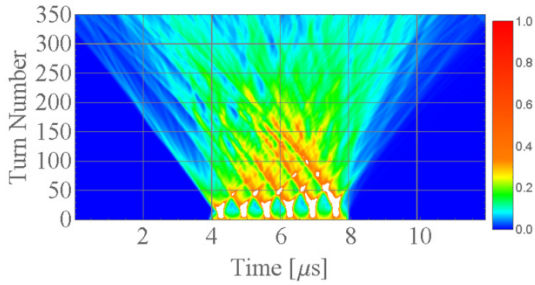

Figure 10: Temporal evolution of the injected bunch for 100 μA.

The simulation results seem to be in good agreement with the experimental result.

CONCLUSION

The influence of the longitudinal space charge effect was evaluated during the circulation of the low energy ion beam in the KEK-DA. The numerical simulation has suggested that the experimental results are not explained without the effects of wake fields. The topics is rather academic; the replacement of the Thyratron by the SI-Thy MA happened to give a good chance to study the microstructure created in the beam bunch that is visible in the distinct way.

REFERENCES

[1] T. Iwashita et al., "KEK Digital Accelerator", Phys. Rev. ST-AB 14, 071301 (2011).
[2] T. Adachi and T. Kawakubo, "Electrostatic Injection Kicker for KEK-DA", Phys. Rev. ST-AB 16, 053501 (2013).
[3] H. Kobayashi, T. Kawakubo, and A. Tokuchi, 5th Euro-Asian Pulsed Power Conference, Kumamoto, Japan OB1-2 (2014).
[4] K. Takayama et al., "Microwave Instability at Transition Crossing: Experiments and a Proton-Klystron Model", Phys Rev. Lett. **78**, (1996).

ISBN 978-3-95450-131-1

RECENT UPDATES ON THE RIKEN RI BEAM FACTORY CONTROL SYSTEM

M. Komiyama, M. Fujimaki, N. Fukunishi, K. Kumagai, A. Uchiyama,
RIKEN Nishina Center, Wako, Saitama, Japan
T. Nakamura, SHI Accelerator Service, Ltd., Shinagawa, Tokyo, Japan

Abstract

RIKEN Radioactive Isotope Beam Factory (RIBF) is a cyclotron-based heavy-ion accelerator facility for producing unstable nuclei and studying their properties. Following the first beam extraction from a superconducting ring cyclotron, the final-stage accelerator of RIBF, in 2006, several types of extensions and updates have been performed in the RIBF control system as well as the accelerators and their components. In this paper, we will present two latest updates of the RIBF control system. One is the upgrade of the existing beam interlock system in order to adapt to the increase in the types of experiments performed in RIBF recently. The other is the development of two types of successors that are designed to be compatible with the existing controllers for magnet power supplies.

INTRODUCTION

Overview of RIBF Accelerator Complex

RIKEN Radioactive Isotope Beam Factory (RIBF) is a multistage accelerator complex, which consists of two heavy-ion linacs and five heavy-ion cyclotrons including the world's first superconducting ring cyclotron (SRC); several acceleration modes can be made available by selecting a combination of the accelerators depending on the purpose of the experiment [1]. The RIBF accelerator research facility consists of the old facility, which was commissioned in 1986, and the newly constructed one (new facility), which was commissioned in 2006. At the old facility, various types of experiments such as biological irradiation are performed using the RIKEN ring cyclotron (RRC) [2]. The new facility was constructed in the downstream of the old facility and has added new dimensions to the facility's capability. Three new cyclotrons were constructed in the downstream of the RRC to accelerate beams with energies of several hundreds of MeV/nucleon over the entire range of atomic masses. In May 2015, a 345-MeV/nucleon ^{238}U beam of 39.5 pnA was successfully extracted from the SRC. A high-power heavy-ion beam extracted from the SRC is transported to the superconducting radioactive isotope beam separator, BigRIPS [3]. At the BigRIPS, various types of RI beams are produced, separated, and identified in an event-by-event mode. The tagged RI beams are delivered to experimental setups placed downstream of the BigRIPS.

* misaki@riken.jp

Overview of the RIBF Control System

Figure1 shows the overview of the RIBF control system. The components of the RIBF accelerator complex, such as magnet power supplies, beam diagnostic devices, and vacuum systems, are controlled using the experimental physics and industrial control system (EPICS) [4]. In addition, there are several control systems, such as a system for radio frequency (RF) and ion source, that are not integrated into the EPICS-based system. The RIBF accelerator complex is operated under the control of the EPICS-based and the non-EPICS-based control systems [5].

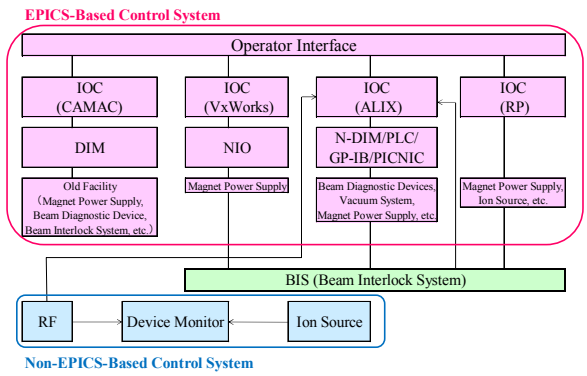

Figure 1: Overview of RIBF Control System.

There are two kinds of interlock systems in the RIBF facility, which are independent of the above-mentioned control systems. One is a radiation safety interlock system for human protection, HIS [6], and the other is a beam interlock system (BIS) to protect the hardware of the RIBF accelerator complex from significant beam losses for high-power heavy-ion beams [7]. The BIS stops a beam within 10-15 ms after detection of any interlock signal. For realizing the specification, after the BIS detects an interlock signal, it sends the signal to a beam chopper placed at the exit of the ion source. In addition, the BIS sends a signal to the closest Faraday cup located upstream of the trouble point to be set into a beam transport line. Although in the latter process, approximately 1 s is required to complete the movement of the Faraday cup, which is determined by mechanical limitations, this function is effective to ensure redundancy of the safety mechanism. At present, the BIS stops a beam within 10-15 ms in average. Many interlock signals such as failure signals are transported to the BIS sent from RF systems used in cyclotrons, magnet power supplies, vacuum gate valves in the beam transport lines, and beam

ISBN 978-3-95450-131-1

spill monitors installed in the cyclotrons. Since there are several acceleration modes in the RIBF, parameter files defining the interlock signals relevant to each acceleration mode are prepared and one of them is registered to the BIS before performing an experiment.

Two sets of BIS are in operation: one at the old facility (RRC-BIS) and the other at the new facility (RIBF-BIS). Both the BIS have the same components and the systems are exactly the same. The hardware constitution of the BIS is shown in Fig. 2. Each BIS has approximately 320 digital input signals, 80 analog input signals, and 30 digital output signals. All of the interlock signals are connected to the I/O modules of the programmable logic controllers (PLCs) manufactured by Mitsubishi Electric Corporation (hereafter, Melsec PLCs). Since the components issuing the interlock signals are distributed over a wide area in the facility and fulfill the requirement of the response time, the BIS is constructed using five Melsec PLCs and a dedicated PC for setting and monitoring the interlock signals. The Melsec PLCs are connected to each other through the MELSECNET/H network system, an optical loop system. All signal information is summarized in one of the five PLCs, which has an Ethernet module, and we monitor and control the signal at the dedicated PC using SoftGOT [8] through the Ethernet. We have started their operation since 2006.

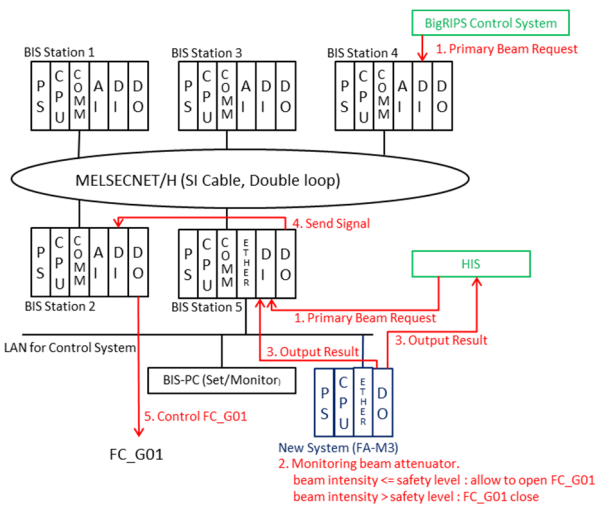

Figure 2: Hardware constitution of the Beam Interlock System. Blue module and colored logic have been added in 2014.

UPGRADE OF BEAM INTERLOCK SYSTEM

During the past 10 years, the intensity of a 345-MeV/nucleon ^{238}U beam extracted from the SRC has increased ~100 times by implementing various improvements. As the performance of the accelerators has improved, the variation in the experiments performed at RIBF has also increased. Especially, an experiment has been performed using a primary beam extracted from the SRC with the experimental instruments placed at the downstream of the BigRIPS, which are designed to perform experiments using faint RI beams produced by the BigRIPS (hereafter, a secondary beam), and the maximum beam intensity there is limited to 10^7 pps. While transporting the primary beam directly to the downstream of the BigRIPS, the beam intensity may exceed the safety limits set by the radiation safety regulation. Although the HIS secures radiation safety of the whole facility, the BIS is required to protect the experimental setups more reliably from accidental irradiation with high-intensity primary beams. Therefore, we upgraded the BIS in 2014 to have a function that allows transportation of the primary beam to the downstream of the BigRIPS only when the intensity of the primary beam is lower than the safety limit. In other words, when the intensity of the primary beam exceeds the safety limit, the BIS has to stop the beam immediately.

In order to achieve the above-mentioned functions, the BIS has to constantly monitor the beam intensity of the primary beam extracted from the SRC. However, the existing BIS has no information about the beam current, and there is no non-destructive beam current monitor for this purpose in the RIBF beam transport line because we usually obtain the data of beam intensity at the beam transport line by stopping a beam by Faraday cups. Therefore, we decided to monitor the insertion status of the beam attenuators in the beam transport line. Since the beam intensity at the ion source is frequently checked, it is possible to evaluate the maximum beam intensity by knowing the attenuation of the beam. There are many beam attenuators in the low-energy region of the RIBF accelerator complex controlled by EPICS. Therefore, we additionally installed a dedicated small PLC system manufactured by Yokogawa Electric Corporation (hereafter, FA-M3) in the EPICS-based control system to achieve the following three tasks.

- To evaluate the attenuation of the beam continuously.
- To send the signal to the RIBF-BIS so as to prohibit the injection of the primary beam to the BigRIPS when the attenuation of the beam does not satisfy the safety level.
- To send the signal to the HIS so as to update the result.

Usually, the beam is stopped by the Faraday cup at the exit of the SRC, denoted as FC_G01, during accelerator tuning before it is injected into BigRIPS. Before the experimental instruments start using the primary beam, the BigRIPS control system, which is independent from the RIBF control system, sends a start signal to the RIBF-BIS. Therefore, when the attenuation of the beam satisfies the safety level, we can set out the FC_G01 from the beam transport line and can transport the beam to the BigRIPS. After that, when the insertion status of the attenuators is changed and it does not satisfy the safety level, the RIBF-BIS stops the beam immediately by the beam chopper and FC_G01. After this improvement of the BIS, we can perform the experiments of BigRIPS more safely and efficiently because the high-intensity

ISBN 978-3-95450-131-1

primary beam is no longer transported to the downstream of the BigRIPS in the event of misoperation.

DEVELOPMENT OF SUCCESSORS FOR MAGNET CONTROL

The second topic is the update of the Network I/O (NIO) system, which is used to control many magnet power supplies in the new facility and a part of the old facility. The NIO is a commercially available control system manufactured by Hitachi Zosen Corporation, and the NIO system consists of three types of controllers: the NIO-S board, NIO-C board, and branch board. The NIO-S board is a slave board attached directly to the magnet power supply and controls it according to a signal sent from an upper-level control system through the NIO-C board. The NIO-C board works as a master board of the NIO-S boards and is designed to operate in the Versa Module European (VME) computing machines. The NIO-C and NIO-S boards are connected using an optical fiber cable through a branch board. Since one NIO-S board can control only one magnet power supply, there are about 500 NIO-S boards in the RIBF accelerator complex, and this corresponds to 60% of the total magnet power supplies used in the RIBF accelerator complex. The major part of the remaining power supplies are used in the old facility. We are gradually updating the old power supplies to a new power supply controlled by the NIO system. The existing NIO system has been working stably, but production of the present NIO-S board was terminated because some parts used for communication are currently not available. Therefore, in 2014, we developed a successor of the existing NIO-S board. This successor was designed to be compatible with the existing NIO-S board. Communication is the most significant feature of the successor; the high level data link control procedure (HDLC) transmission method, which is performed using an adaptor chip used for serial communication in the existing NIO-S, is replaced by using the IP in the field-programmable gate array (FPGA) in the successor. As another improvement in the successor, we increased the number of digital inputs from 32 to 48 in consideration of future expandability. We tested the successor by attaching it to one of the existing power supply and confirmed that the successor successfully controlled the power supply as the existing NIO-S.

Production of the NIO-C has also been terminated for the same reason as the NIO-S. Hence, we should also develop a successor of the present NIO-C, and its research and development began in 2014. The specifications required for the new board are essentially the same as for the existing one, but we decided to design the new board to run in a control system constructed by PLC modules instead of the VME computing environment currently used, in order to achieve cost reduction and functional scalability. The NIO-C successor is based on FA-M3, according to recent trends in the control systems of RIBF accelerators. One of the advantages of adopting FA-M3 is that we can set up a simple control system because a Linux-based PLC-CPU (F3RP61 [9]), on which EPICS programs are executed, is chosen and F3RP61 works not only as a device controller but also as an input/output controller (IOC). This means that additional hardware to serve as an EPCIS IOC is not required for F3RP61 [10]. The major features of the NIO-C successor are summarized in Table 1. Software development is in progress in 2015, where some new features will be added while maintaining full compatibility with the existing NIO-C.

Table 1: Specifications of the NIO-C Successor

CPU	NIOS2 Processor 32 MHz
ROM	EPCS16 16 Mbit
DRAM	16 M*16
DPRAM	16 Kbyte (in FPGA)
SCA	TD-HDLCip
FPGA	Cyclone4 EP4CE22
Bus Controller	A6374LG (Yokogawa)
Serial interface	RS-485 *1 (2 Mbps(max), HDLC)
Debug Port	RS-232C *1
External Dimensions	1 slot
Supply Voltage	5 V DC. 2 A (max)

REFERENCES

[1] O. Kamigaito et al., MOPRI082, IPAC2014, Dresden, Germany, http://jacow.org
[2] Y. Yano, in Proc. of the 13th Int. Cyclo. Conf., Vancouver, BC, Canada, (1992).
[3] T. Kubo, et al., IEEE Trans. Appl. Supercond. 17, 1069 (2007).
[4] http://www.aps.anl.gov/epics/
[5] M. Komiyama, et al., MOPPC103 , ICALEPCS2013, San Francisco, USA, http://jacow.org
[6] H. Sakamoto et al., RIKEN Accel. Prog. Rep. 37, 281 (2004).
[7] M. Komiyama et al., RIKEN Accel. Prog. Rep. 39, 239 (2006).
[8] http://www.mitsubishielectric.com/fa/products/hmi/got/items/sgt
[9] http://www.yokogawa.co.jp/rtos/Products/rtos-prdcpu9-ja.htm
[10] A. Uchiyama et al., WEX03, PCaPAC08, Ljubljana, Slovenia, http://jacow.org

ISBN 978-3-95450-131-1

A FAST, COMPACT PARTICLE DETECTOR FOR TUNING RADIOACTIVE BEAMS AT ATLAS*

C.A. Dickerson#, B. DiGiovine, C. Hoffman, L. Y. Lin, R.C. Pardo, K.E. Rehm, G. Savard
ANL, Argonne, IL 60439, USA
C. Deibel, J. Lai, D. Santiago-Gonzalez, LSU, Baton Rouge, LA 70803, USA

Abstract

Radioactive ion beams (RIB) at the Argonne Tandem Linear Accelerator System (ATLAS) are produced either from the in-flight method at 5-15 MeV/u for A < 30, or via reacceleration of fission fragments from the CAlifornium Rare Isotope Breeder Upgrade (CARIBU) at 4-10 MeV/u for 80 < A < 160. These RIB are typically accompanied by contaminant beams >100x more intense. The goal of this work is to develop a fast (>10^5 pps), compact (retractable from the beam line) particle detector capable of A and Z identification to enable accelerator optimization on the exact species of interest. The detector should have an energy resolution of ≤5% and be resistant to radiation damage. A gas ionization chamber supplemented with an inorganic scintillator was chosen as the basic conceptual design. GSO:Ce was chosen as the primary candidate scintillator due to a demonstrated energy resolution of ~3% for 15 MeV/u He and less irradiation induced performance degradation than other candidate materials.

INTRODUCTION

At the Argonne Tandem Linear Accelerator System (ATLAS) we are developing a fast, compact particle detector to aid the tuning of low intensity beam constituents with relatively high intensity (>100x) contaminants. These conditions are regularly encountered during radioactive ion beam production via the in-flight method, or when charge breeding fission fragments from the CAlifornium Rare Isotope Breeder Upgrade (CARIBU). Presently silicon barrier detectors (SBD) are used for mass identification via total energy measurements. However, the total acceptable SBD rate is limited to ~1000 pps, so the signal rate from any minority constituents 100x less intense is typically much too slow to enable meaningful accelerator optimization. In addition, SBDs can tolerate a very limited integrated flux before their performance deteriorates.

The in-flight method of RIB production at ATLAS generally produces beams of interest with energies 5–15 MeV/u and masses less than 30 AMU, while reaccelerated fission fragments from CARIBU, 80 < A < 160, are typically accelerated to energies of 4–10 MeV/u. Our goal is to achieve ~5% energy resolution at a total rate of 10^5 pps over these energy and mass ranges without significant performance degradation after extended use.

*Work supported by U.S. Department of Energy, Office of Nuclear Physics, under contract DE-AC02-06CH11357
#cdickerson@anl.gov

The detector will combine a gas ionization chamber with an inorganic scintillator to generate ΔE and residual E signals and enable the identification of both the Z and the A of the beam constituents. This configuration allows the needed compactness to retract the assembly from the beam path. The conceptual design of the detector and considerations for the selection of the scintillator, photoelectric device, and counting gas are presented in this paper.

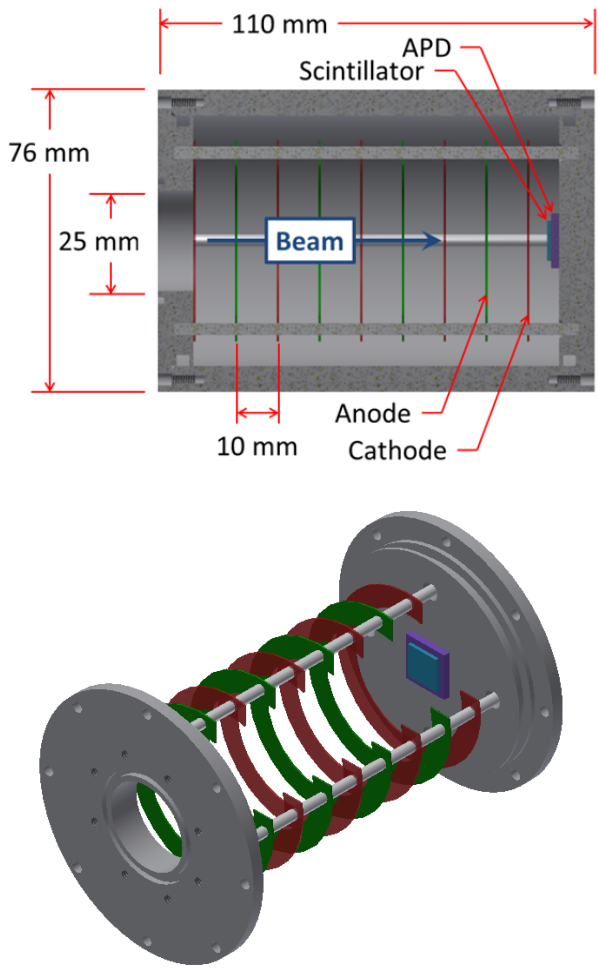

Figure 1: (Upper) A cross section showing the general layout and dimensions of the detector configuration. (Lower) A view of the detector with the vacuum tube removed and the electrodes cut away for clarity.

DESIGN

A hybrid of a gas ionization chamber (IC) supplemented with a scintillator was the chosen conceptual design, shown in Fig. 1. Both the gas and scintillator are fast,

ISBN 978-3-95450-131-1

resistant to radiation damage, and have appropriate resolutions. Silicon detectors cannot maintain their performance at high integrated flux and diamond detectors are not widely available. The ionization chamber will follow the designs of Kimura and Chae [1, 2], whose Tilted Electrode Gas Ionization Chambers (TEGIC) have operated at rates >1x10^5 ions/sec with energy resolution <5%.

The nominal operating pressure of the detector is 1.5 atm or 1100 Torr. The use of the scintillator will eliminate the need to completely stop the ions within the gas and the significant design considerations to operate at higher pressures with thick windows. Even high stopping power gases alone (iC_4H_{10} or CF_4) at 25 C and 1100 Torr do not have enough density to stop the light (A<10) high energy (15 MeV/u) particles in less than ~350 mm, and the use of thick degrader materials could impart significant energy and angular scatter. The target length for a compact design was nominally ~100 mm, and the anticipated window material is Kapton which is available in a variety of thicknesses.

The ATLAS detector electrodes will be spaced closer than either of the two reference TEGIC designs but the smaller electrode area will ultimately result in lower cathode-anode capacitance which is an advantage for higher rates and lower electronic noise. The electrodes will be built from narrow gauge, ø17.5 μm, wire which will sacrifice ~1% transmission per electrode to avoid the additional angular scattering from using metalized mylar foils. The initial detector design will not use tilted electrodes for compactness and simplicity, but the detector response vs. rate will be studied to determine if recombination becomes a significant factor.

The scintillator will give a residual energy signal for particles not stopped in the gas, and enables the flexibility to tune the gas density for the best signal while largely ignoring the gas stopping power. Operating with RIB from CARIBU should be straight forward. The high Z ions will easily stop in the gas, and the good beam quality, <0.2π μm full normalized, will be easily controlled. Light, high energy RIB from in-flight production can have >10x worse quality due to the reaction kinematics and will be more challenging. With appropriate focussing and collimation a clean signal should be achievable given the large restricting aperture diameters (25 mm for the entrance window and 38 mm for the inner diameter of the electrode wire mesh mounting).

SCINTILLATOR SELECTION

The primary criteria for the scintillator selection were the ability of accepting rates >10^5 pps, an energy resolution ≤5%, high radiation hardness, and non-hygroscopicity. Table 1 shows the relevant properties for a number of candidate materials. Organic scintillators were not considered due to higher energy resolution, susceptibility to radiation damage, lower light yield, and non-linearity for heavy charged particles

GSO:Ce was ultimately selected for this detector application. GSO:Ce has good energy resolution (~3% for 15MeV/u ^{3}He [3]), has relatively high light output, is non-hygroscopic, can tolerate rates >10^6 pps, and has the best radiation hardness of any well characterized scintillator by 2-3 orders of magnitude. While the radiation hardness values listed in Table 1 are for low energy γ rays, Kobayashi also studied proton irradiated GSO:Ce [4] and found the onset of performance degradation occurred at ~1.6x106 rad. As an example, for a ø4 mm beam spot at 10^5 pps it would take 12 days and 4 days to accumulate an equivalent dose for 15 MeV/u ^{9}Be and 10 MeV/u ^{12}C, respectively. These estimates ignore the differences between proton and heavy ion radiation damage kinematics, but indicate GSO:Ce can be a robust ion detector.

PHOTOELECTRIC DEVICE

Three photoelectric devices were investigated for this application: a photo multiplier tube (PMT), a PIN photodiode, and an avalanche photodiode (APD). Table 2 highlights the performance of these devices for configurations relevant for this application. The PMT is generally the fastest option with by far the highest gains, but the overall size of the PMT is a big drawback considering the goal of a compact detector system. The typically low quantum efficiencies are also disadvantages which eliminated the PMT as the first choice. Compactness, insensitivity to magnetic fields, and lower complexity are general photodiode features that make these devices better suited for this application. Ultimately an APD was selected, Hamamatsu S8664-1010, due to the device's higher gain (better sensitivity to low light intensities), and typically better radiation hardness.

Table 1: Properties of Candidate Scintillators

Quantity	GSO:Ce	NaI:Tl	BGO	BaF	CsI:Tl	CeF_3
Density (g/cm^3)	6.71	3.67	7.13	4.89	4.51	6.16
Decay constant (ns)	30-60	230	300	0.6/320	980	30
Peak emission (nm)	440	415	480	220/310	530	375
Light yield (relative)	20	100	7–10	5/16	45	4–5
Hygroscopicity	No	Yes	No	Yes	Yes	No
Radiation Hardness (rad) [4]	10^9	10^3	10$^{4-5}$	10$^{6-7}$	10$^{4-5}$	10^6

ISBN 978-3-95450-131-1

Table 2: Approximate Characteristics for Relevant Photoelectric Devices

Quantity	APD	PMT	PIN diode
Gain	10-100	$>10^5$	1
Quantum efficiency*	75%	25%	85%
Thickness (mm)	~3	>50	~3
Active area (mm^2)	1–100	100–5000	1–1000

*for 440 nm emission peak of GSO:Ce

GAS CONSIDERATIONS

CF_4 will be the primary counting gas due to its fast electron drift velocity, ~13 cm/ms at 3 V/(cm-Torr) [5]. The detector will be designed to operate up to 1100 Torr, but at this pressure and nominal electrode spacing, 1 cm, >3 kV is necessary to achieve the fastest counting. To obviate these higher voltages and comfortably avoid the proportional counting regime up to 90% Ar can be mixed with CF_4 to realize the same high velocity but at ~1 V/(cm-Torr). The addition of Ar can also improve the resolution due argon's lower ion pair production threshold, 26 eV vs. 54 eV for CF_4, and, with the scintillator able to provide a residual energy signal, the stopping power of the gas can be largely disregarded.

DEVICE TESTING

Initially testing of the scintillator and APD will be conducted independently of the gas IC to investigate the radiation hardness of the scintillator for heavy ions and optimize the output signal of the APD with respect to energy resolution and signal to noise ratio. For simplicity these initial tests will use a scintillator with an area equivalent to the active area of the APD, 10x10 mm^2. This scintillator – APD configuration will also be the first used in the full detector assembly with the gas IC. In operation, fully intercepting larger emittance secondary RIBs from in-flight production may become problematic due to this relatively small size. In these cases collimators may be used to constrain the beam size into the gas portion of the detector, or in the future a larger scintillator may be installed. A larger scintillator will in turn require a light guide or a larger photoelectric device in which case a PIN photodiode would likely be used. Once a production model of the IC is finalized it will be fabricated and assembled to test as well. The IC will initially be tested in a fixed position while the insertion mechanism and vacuum chambers are developed.

SUMMARY

Optimizing ATLAS for the delivery of radioactive ion beams requires a detector capable of distinguishing a low intensity species of interest from a high intensity background. The combination of a gas ionization chamber and scintillator will enable incident ion rates of $>10^5$ ions per second, will be compact, will have energy resolutions <5%, will identify species by both A and Z, and will have the flexibility to operate with wide mass and energy ranges. GSO:Ce was selected as the best scintillator candidate material largely due to its high radiation hardness, fast response time, good resolution, and high light yield. The scintillator will be coupled to an APD, but the relatively small size of the APD may limit the overall detector performance. The high electron drift velocity in CF_4 make it the best counting gas candidate, but Ar may be added to maintain this high velocity at lower pressure normalized electric fields.

REFERENCES

[1] Kimura et al., "High-rate Particle Identification of High-energy Heavy Ions Using a Tilted Electrode Gas Ionization Chamber", NIM A 538, 608-614 (2005).

[2] Chae et al., "Construction of a Fast Ionization Chamber for High-rate Particle Identification", NIM A 751, 6-10 (2014).

[3] Avdeichikov et al., "Light Output and Energy Resolution of CSI, YAG, GSO, BGO, and LSO Scintillators for Light Ions", NIM A 349, 216-224 (1994).

[4] Kobayashi et al., "Radiation Hardness of Cerium-doped Gadolinium Silicate GD_2SiO_3:Ce Against High Energy Protons, Fast and Thermal Neutrons", NIM A 330, 115-120 (1993).

[5] Christophorou et al., "Fast Gas Mixtures for Gas-filled Particle Detectors", NIM 163, 141-149 (1979).

ISBN 978-3-95450-131-1

STATUS AND UPGRADES OF HIRFL*

Y.J. Yuan#, L.T. Sun, J.C. Yang, X.J. Yin, L.J. Mao, J.X. Wu, X.W. Ma, X.H. Zhang, D.Q. Gao, R.S. Mao, Z. Xu, W. Zhang, J. Meng, L.Z. Ma, P. Li, J.W. Xia, H.W. Zhao IMP/CAS, Lanzhou, China
Y.R. Lu, K. Zhu, G. Liu, State Key Laboratory of Nuclear Physics and Technology, Peking University, Beijing, China
S. Litvinov, Y. Litvinov, M. Steck, F. Nolden, GSI, Darmstadt, Germany
V. Parkhomchuk, BINP SB RAS, Russia

Abstract

The Heavy Ion Research Facility at Lanzhou (HIRFL) is the only one large scale heavy ion accelerator complex that uses cyclotron (SFC and SSC) as injector, synchrotron (CSRm) for accumulation and post acceleration, storage ring (CSRe) for in-ring experiments in Asia. To reach the increasing requirements from nuclear physics, atomic physics, interdisciplinary science and their applications, many upgrading plans were launched or scheduled. The present status and recent upgrading plans of HIRFL will be introduced in this paper. For the upgrading plans, the development of new linac injector for HIRFL and the plans to improve the performance of experiments will be discussed in detail.

INTRODUCTION

HIRFL is the only one large scale heavy ion accelerator complex that uses cyclotron (SFC and SSC) as injector, synchrotron (CSRm) for accumulation and post acceleration, storage ring (CSRe) for in-ring experiments in Asia[1-5]. The layout of HIRFL is shown in Fig.1. For CSRm, both multi-turn injection and charge exchange injection methods are used with strong support from cross-section-variable electron cooling during beam accumulation; and both fast and slow extracted[6] beams are available for experiments and transmission to CSRe.

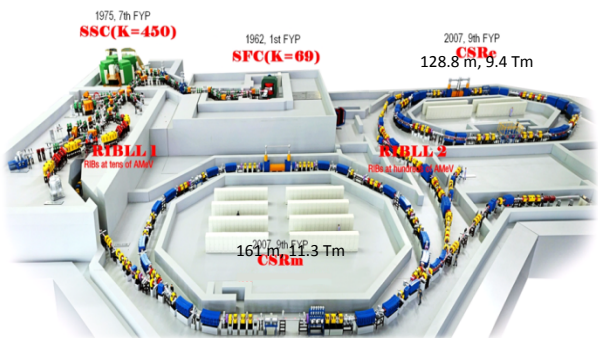

Figure 1: Layout of HIRFL

The operation time is 7,272 h in 2014, while beam time for experiments counts 5,199.5 h. The distribution of operation time is shown in Fig.2. The distribution of experiment time among researches is shown in Fig.3.

In 2014, about 25 kinds of ions, with different charge states and energies, were provided by HIRFL accelerator complex (See Table 1). Among them about 10 beams were provided for the 1st time (green background), 6 beams (marked by *) were supplies for ring experiments.

Table 1: Typical Beams Supplied in 2014

No.	SFC			SSC	
	Ion	Energy MeV/u	Current eμA	Energy MeV/u	Current eμA
1*	$^{78}Kr^{19+/28+}$	4	4.2		
2	H_2^+	10	4		
3	$^{40}Ar^{11+}$	4.8	3.2		
4*	$^{16}O^{6+}$	7	8.5		
5	$^{12}C^{4+/6+}$	7	2.3	80.55	0.17
6	$^{40}Ar^{12+/17+}$	6.17	5	70	0.45
7	$^{16}O^{6+/8+}$	6.17	5.9	70	0.45
8	$^{12}C^{4+/6+}$	5.361	2.8	60	0.24
9	$^{209}Bi^{31+}$	0.911	0.6	9.5	0.04
10	$^{58}Ni^{19+/25+}$	6.17	1.2	70	0.07
11	$^{32}S^{9+}$	3.9	1.7		
12	$^{40}Ar^{9+/15+}$	2.794	3	30	0.05
13	$^{20}Ne^{7+}$	6.17	3.8		
14	$^{16}O^{6+}$	7.5	2		
15	$^{22}Ne^{8+}$	7.5	2.2		
16	$^{86}Kr^{17+/26+}$	2.345	4.5	25	0.13
17	$^{12}C^{4+/6+}$	4.906	5	54.5	0.35
18*	$^{36}Ar^{15+}$	8.5	1.9		
19	$^{14}N^{4+}$	4.5	2.8		
20	$^{40}Ca^{12+}$	5	2		
21*	$^{12}C^{3+}$	4.2	5		
22*	$^{12}C^{4+}$	7	10		
23	$^{40}Ca^{12+}$	4.825	2		
24	$^{209}Bi^{31+}$	0.911	0.3	9.5	0.01
25*	$^{58}Ni^{19+}$	6.3	1.2		

*For ring experiments

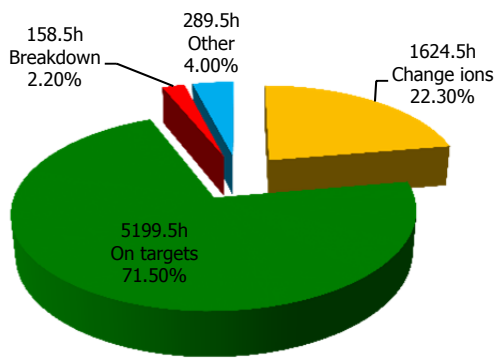

Figure 2: Distribution of operation time

*Work supported by NSFC(Contract No. 11575265, NSFC-Creative research groups (Contract No. 11221064) and National key basic research and development plan (Contract No. 2014CB845500)
#yuanyj@impcas.ac.cn

ISBN 978-3-95450-131-1

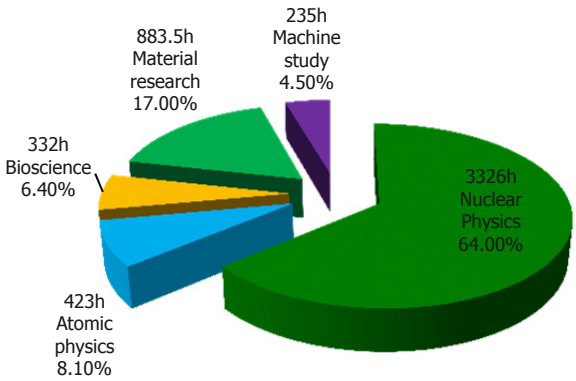

Figure 3: Distribution of experiment time

ACTIVITIES OF UPGRADING

To keep the high level performance of HIRFL, continuous upgrading is necessary. The upgrading of HIRFL includes following aspects: New high intensity heavy ion injectors, various heavy ion cooling methods, new setups for experiments and improvement of the dynamic vacuum condition of rings.

New Injectors for CSRm

The cyclotron injectors were not built on the requirements of HIRFL-CSR project, especially for heavier ions, beam energy and intensity is rather lower for sufficient lifetime in the ring for accumulation. New high intensity heavy ion linac's are planned to be constructed instead of cyclotrons to provide better injection beam and increase the beam time by a large scale. Figure 4 shows the new layout of HIRFL with new injectors.

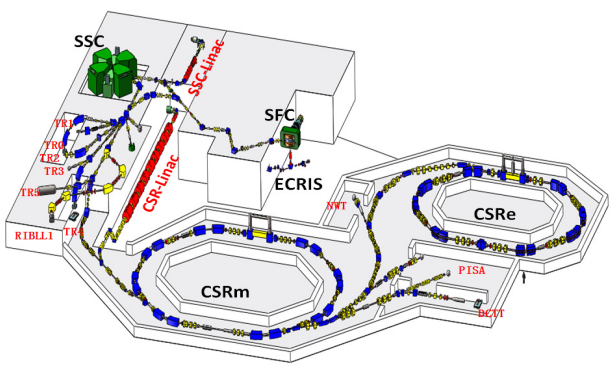

Figure 4: Layout of HRFL with new injectors.

The low energy linac injector for SSC, SSC-Linac, is designed and being constructed (Fig.5) [7-12]. The frequency of RFQ cavity is designed to 53.667 MHz. Due to the matching condition of SSC, the designed energy is fixed to 0.58 and 1.025 MeV/u (6.0 and 10.7 MeV/u after SSC, respectively). The ECR to RFQ section is commissioned in 2014 with good performance (Fig.6)[13]. A new evaporation cooling non-superconducting high magnetic field ECR source has been developed for beam testing. During beam testing transverse coupling due to solenoid field and hollow beam formation (right-down of Fig.6) due to space charge effects are investigated [14], the LEBT is redesigned and rebuilt.

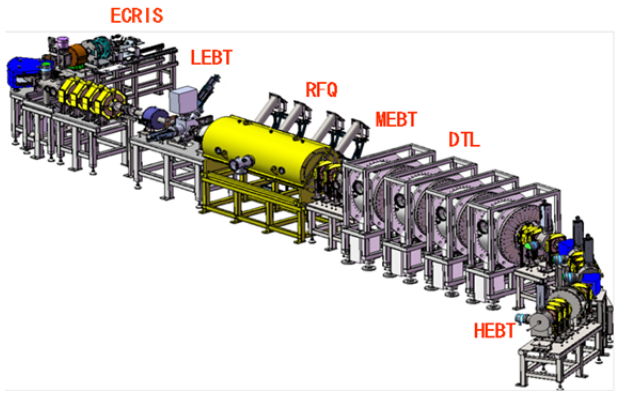

Figure 5: Layout of SSC-Linac.

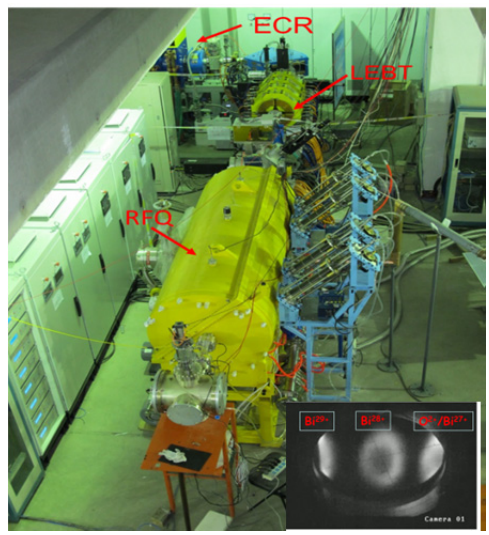

Figure 6: SSC-Linac testing platform.

The heavy ion linac injector for CSRm[15], CSR-Linac is being designed, which will provide >3.5 MeV/u pulsed high intensity heavy ion beams directly.

Heavy Ion Beam Cooling Technology

Electron cooling is used in HIRFL[16-19] for both CSRm and CSRe. The cross-sections of electron beams are variable for optimization the cooling efficiency. In addition to routine operation for beam accumulation and preparation for experiments, the electron cooler of CSRm is also used as internal target for atomic physics research. Recently, according to the requirement of nuclear physics research of short lived isotopes, new local injection orbit of CSRe is investigated to enable electron cooling on right after single turn injection.

For the purpose of cooling of large momentum spread secondary beam in CSRe, stochastic cooling is being developed at HIRFL [20-21]. The setup of stochastic cooling at CSRe and some of the hardware is shown in Fig.7. Most of the hardware will be ready by the end of 2015. It's expected to reduce cooling time of high energy

ISBN 978-3-95450-131-1

secondary beam in SMS (Schottky Mass Spectrometry) experiments.

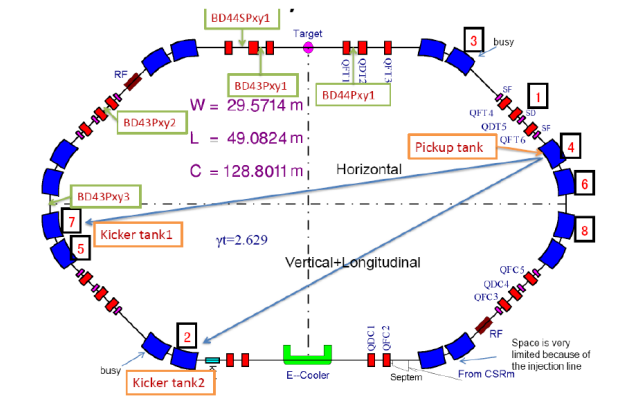

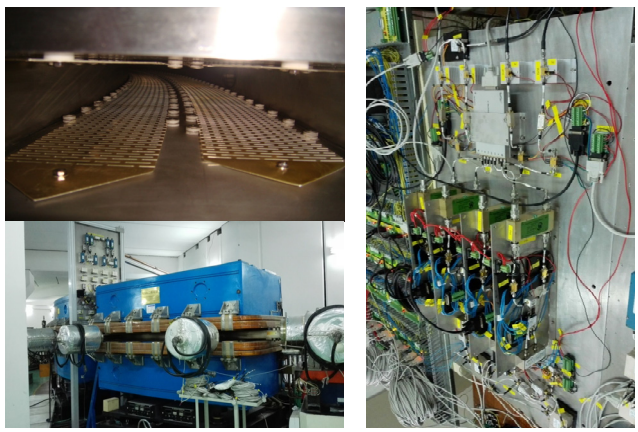

Figure 7: Layout of stochastic cooling at CSRe and some components.

Another cooling method – the laser cooling is being investigated at CSRe (Fig.8). Cooling of 122 MeV/u $^{12}C^{3+}$ beam is focused on at present. Some preparation experiments were committed [22-24], the multi-harmonic RF buncher, UV-sensitive Channeltron and Resonant Schottky were tested. The investigation of laser cooling at CSRe will be helpful for future ring projects at cooling of relativistic ion beam.

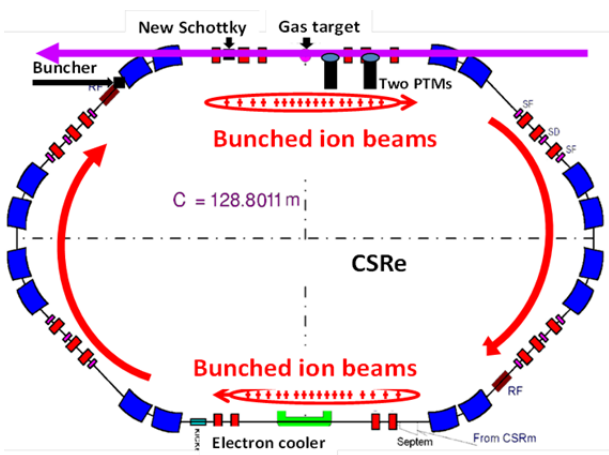

Figure 8: Layout of laser cooling at CSRe.

Mass Spectrometry at CSRe

At CSRe, in addition to normal storage ring mode and internal target mode, isochronous mode mass spectrometry (IMS) is designed and operated for precise atomic mass measurement successfully [25-31]. With relative high momentum acceptance (0.6%) of CSRe-ISO mode, the overall mass resolution power can reach about 300,000 based on the high intrinsic resolution (30 ps) of TOF detector and new charge resolution method. The online data processing software is very important for optimization of ISO mode of CSRe and experiment setup. It will be improved by high performance GPU computing technology to realize online pulse by pulse data analyses. Recently, new velocity resolved double-TOF IMS is installed and tested. The layout of TOFs at CSRe is shown in Fig.9. New isochronous mode is designed to reduce the dispersion at locations of TOFs. The SMS is expected to be realized at CSRe when the stochastic cooling is ready.

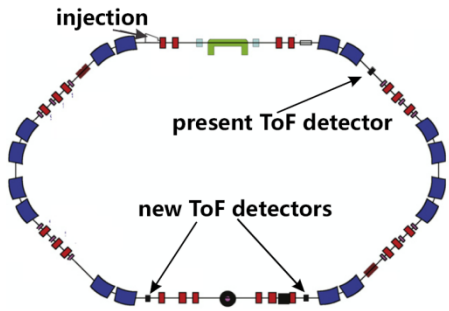

Figure 9: Layout of TOFs at CSRe.

Beam Collimation

To maintain extra-low and stable vacuum pressure at heavy ion synchrotrons and storage rings, the vacuum collimation of beam loss is necessary. It's considered in the design of FAIR project at Darmstadt, Germany [32-35]. For the research and application at HIRFL and newly approved HIAF project, a new simulation program is developed independently at IMP[36]. Test experiments will be committed at CSRm. One of the simulation results of beam loss distribution and collimation efficiency study at CSRm is shown in Fig. 10. The collimation efficiency at present layout and design of CSRm can only reach 60%. Higher efficiency is expected for HIAF project, if it's considered during lattice design.

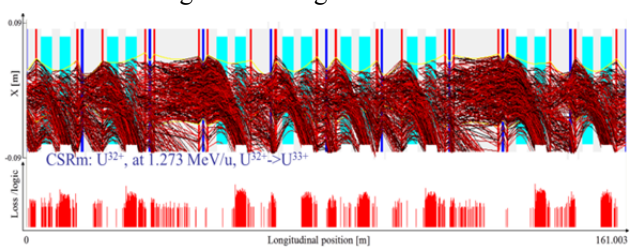

Figure 10: One of the simulation results of dynamic vacuum collimation.

ISBN 978-3-95450-131-1

NEW PROJECT – HIAF

To further enhance the basic research ability in heavy ion science of China, one of the national critical infrastructure facilities - High Intensity Heavy Ion Accelerator (HIAF) is planned [37-39]. Layout and some parameters of HIAF are shown in Figure 11. Based on present HIRFL facility, HIAF will significantly improve the intensity and energy of heavy ion beams for front edge nuclear physics and interdisciplinary science researches. A post phase project is also planned.

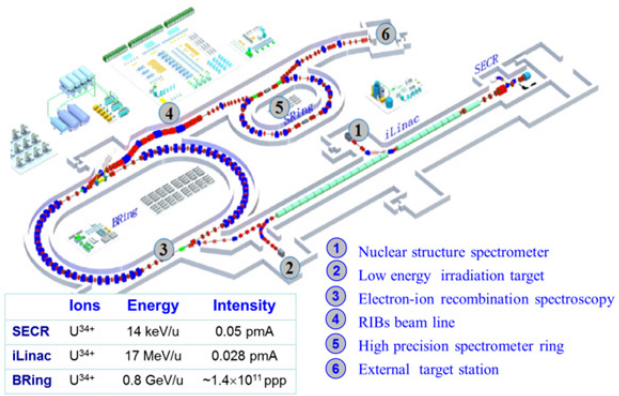

	Ions	Energy	Intensity
SECR	U^{34+}	14 keV/u	0.05 pmA
iLinac	U^{34+}	17 MeV/u	0.028 pmA
BRing	U^{34+}	0.8 GeV/u	~1.4×10^{11} ppp

Figure 11: Layout and major parameters of HIAF project.

ACKNOWLEDGMENT

The author would like to thank colleagues from HIRFL accelerator division and friends from GSI, BINP, CERN and other institutions for their efforts to improve the performance of HIRFL. The author also feels grateful for the organizers of HIAT'2015.

REFERENCES

[1] Y.J. Yuan, J.C. Yang et al., Status of the HIRFL–CSR complex, NIMB, Vol.317, pp 214-217(2013)
[2] Y.J. Yuan, J.W. Xia, Present status of storage rings at HIRFL, STORI'11, Frascati (Rome), Oct. 2011
[3] Y.J. Yuan et al, HIRFL-CSR facility status and development, CYCLOTRONS'2010, Lanzhou, China, Oct. 2010
[4] Zhan, W. L. et al., Progress in HIRFL-CSR, Nuclear Physics A, 834(1-4), pp 694C-700C(2010)
[5] Xia Jia-Wen et al., HIRFL-CSR complex, Chinese Physics C, 33(9), pp 804-810(2009)
[6] J. Shi et al., Feedback of slow extraction in CSRm, NIMA, Vol.714, pp 105-109(2013)
[7] G. Liu el al, Design of a CW high charge state heavy ion RFQ for SSC-LINAC, NIMA, Vol.701, pp 186-193(2013)
[8] Du Xiao-Nan et al., Optimization of the three-dimensional electric field in IH-DTL, Chinese Physics C, 36(5), pp 452-455(2012)
[9] C. Xiao et al., A particle-in-cell mode beam dynamics simulation of medium energy beam transport for the SSC-Linac, Chinese Physics C, 36(1), pp 84-90(2012)
[10] Xiao Chen et al., Numerical optimization and multi-particle dynamics simulation of the radial matching section of the RFQ, Chinese Physics C, 35(10), pp 964-968, 2011/10.
[11] Xiaoni Li et al., The study of acceptance and the transmission efficiency of separated sector cyclotron, Nuclear Technology & Radiation Protection, 30(1), pp 18-22, 2015/3.
[12] Li Xiao-Ni et al., Beam dynamics simulation of HEBT for the SSC-linac injector, Chinese Physics C, 36(11), pp 1126-1131, 2012/11.
[13] K. Zhu el al., The beam commissioning of a CW high charge state heavy ion RFQ, NIMA, Vol.794, pp 113-121(2015)
[14] Y. Yang el al., Transverse coupling property of beam from ECR ion sources, Review of Scientific Instruments, 85(11), 2014.
[15] Xiao-Hu Zhang el al., Conceptional design of a heavy ion linac injector for HIRFL-CSRm, Chinese Physics C, 38(10), 2014/10.
[16] XiaoDong Yang et al., Electron cooling experiments in CSR, Science China Physics, Mechanics & Astronomy, Vol.54, pp S274-S278, 2011/12.
[17] Xiao-Dong Yang et al., Commissioning of electron cooling in CSRe, Chinese Physics C, 34(7), pp 998-1004, 2010/7.
[18] L.J. Mao et al, Cooling Force Measurements with Variable Profile Electron Beam at HIRFL-CSR, COOL'09, Lanzhou, China, Aug. 2009
[19] Xiao-Dong Yang et al., Commissioning of electron cooling in CSRm, Chinese Physics C, Vol.33, pp 18-21, 2009/6.
[20] J.X. Wu et al., Design of Stochastic Cooling System at HIRFL-CSRe, COOL'09, Lanzhou, China, 2009.
[21] Xue-Jing Hu et al., Particle tracking simulation in the CSRe stochastic cooling system, Chinese Physics C, 39(8), 2015/8.
[22] W.Q. Wen et al., Longitudinal dynamics of RF-bunched and electron-cooled ion beam at the CSRe, NIMA, Vol.736, pp 75-80, 2014/2/1.
[23] Wei-Qiang Wen et al., Longitudinal Schottky spectra of a bunched Ne10+ ion beam at the CSRe, Chinese Physics C, 37(10), 2013.
[24] Weiqiang Wen et al., Preparation of laser cooling experiment at the CSRe, Physica Scripta, T15(2013)
[25] HuShan Xu et al., First mass measurement of short-lived nuclides at HIRFL-CSR, Chinese Science Bulletin, 54(24), pp 4749-4752, 2009/12.
[26] Xiao-Lin Tu et al., A pilot experiment for mass measurement at CSRe, Chinese Physics C, 33(7), pp 516-520, 2009/7.
[27] X. L. Tu et al., Precision isochronous mass measurements at the storage ring CSRe in Lanzhou, NIMA, 654(1), pp 213-218, 2011/10/21.
[28] X. L. Tu et al., Direct Mass Measurements of Short-Lived A=2Z-1 Nuclides Ge-63, As-65, Se-67, and Kr-71 and Their Impact on Nucleosynthesis in the rp Process, Physical Review Letters, 106(11), 2011/3/16.

ISBN 978-3-95450-131-1

[29] Y. H. Zhang et al., Mass Measurements of Proton-rich Nuclides at the Cooler Storage Ring at IMP, the 4th international conference on proton emitting nuclei and related topics, Bordeaux, 2011.
[30] Bo Mei et al., A high performance Time-of-Flight detector applied to isochronous mass measurement at CSRe, NIMA, 624(1), pp 109-113, 2010/12/1.
[31] P. Shuai et al., Charge and frequency resolved isochronous mass spectrometry and the mass of 51Co, Physics Letters B, Vol.735, pp 327-331, 2014/7/30.
[32] P. Spiller et al ., in Proceedings of 33rd ICFA Advanced Beam Dynamics Workshop on High Intensity and High Brightness Hadron Beams, Bensheim, Germany, 2004 (AIP, Bensheim, 2004), pp. 40–44.
[33] C. Omet et al., New J. Phys. 8, 284 (2006).
[34] P. Puppel et al., in Proceedings of the International Particle Accelerator Conference, Kyoto, Japan, 2010 (ICR, Kyoto, 2010), pp. 594–596.
[35] L. Bozyk et al., in Proceedings of the International Particle Accelerator Conference, New Orleans, Louisiana ,USA, 2012 (IEEE, Piscataway, NJ, 2012), pp. 3237–3239.
[36] P. Li et al., Beam loss distribution calculation and collimation efficiency simulation of a cooler storage ring in a heavy ion research facility, Physical Review Special Topics - Accelerators and Beams, 17(8), 2014/8/28.
[37] J.C. Yang et al., this conference.
[38] J.C. Yang et al., High Intensity heavy ion Accelerator Facility (HIAF) in China, NIMB, 731(B), pp 263-265, 2013/12/15.
[39] J.C. Yang et al., High Intensity heavy ion Accelerator Facility (HIAF) in China, NIMB, Vol.317, pp 263-265, 2013/12/15.

ISBN 978-3-95450-131-1

BEAM LOSS IN THE LOW ENERGY ION RING (LEIR) IN THE LIGHT OF THE LHC INJECTOR UPGRADE FOR IONS (LIU-IONS)

M. Bodendorfer, M.E. Angoletta, J. Axensalva, D. Manglunki, S. Pasinelli
CERN, Geneva, Switzerland

Abstract

For the LHC injector upgrade for Ions (LIU Ions), the Low Energy Ion Ring (LEIR) is requested to deliver twice the intensity per extraction compared to the last Pb^{54+} ion run in 2013 [1]. As the number of injected ions has been increased into LEIR, a fast loss is observed during the RF-capture of the electron cooled ion beam, and this loss today leads to an effective saturation of the available ion intensity at extraction.

Based on chromaticity measurements with Pb^{54+} beam in LEIR with bunched beam and during acceleration in February 2013 [2], we suspected the chromaticity of the LEIR machine to be wrong in the vertical plane. To investigate the stationary behavior of the LEIR machine, we have developed a new method to measure the machine chromaticity on the low energy flat bottom of LEIR during a single cycle, where the ion beam is un-bunched and coasting. The new method controls the ion beam momentum by the LEIR electron cooler beam rather than the LEIR RF-system. The new method uses the LEIR Schottky system to measure the applied momentum change rather than the radial beam position offset in dispersive regions. The existing tune measurement system is used to measure the tune in the same way as in the classic way involving the RF-system and bunched ion beam. The new method allows a single-cycle-chromaticity measurement of coasting and un-bunched beam with high accuracy and no dependency of cycle-to-cycle machine variation.

INTRODUCTION

LEIR has accumulated, cooled and stacked ion beams of Oxygen (O^{4+}), Lead (Pb^{54+}) and Argon (Ar^{11+}). For LIU, LEIR is requested to deliver $1.6x10^9$ ions in 2 bunches, which is 50% more intensity compared to the last Pb^{54+} ion run in 2013. The number of injected lead ions into LEIR has been increased during several machine development studies (MDs) in late 2012 and early 2013. Total intensities of up to $1.8x10^9$ lead ions have been observed during the coasting beam phase before RF capture. An ion beam loss is then observed during and after the RF-capture. Today, this loss leads to an effective saturation of the available ion intensity at extraction. Fig.1 shows a typical Pb^{54+} NOMINAL cycle as it is used for LHC injections. Fig.2 shows that with two bunches per extraction up to $5.9x10^8$ ions per bunch have been measured.

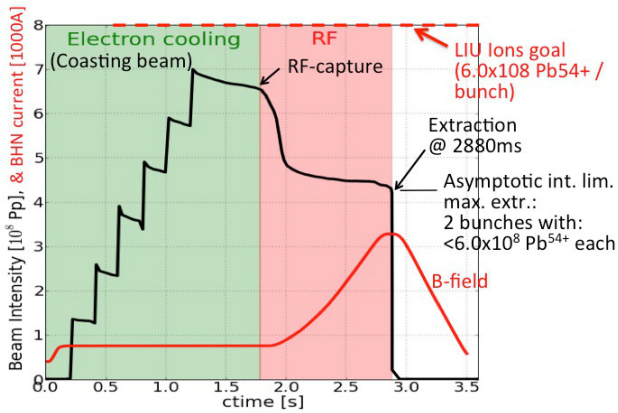

Figure 1: A typical LEIR NOMINAL cycle, 3.6s in length with main magnet current, proportional to particle momentum in red and ion beam intensity in black versus cycle time.

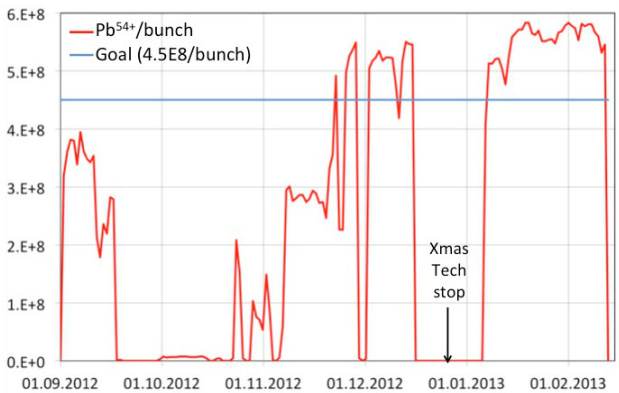

Figure 2: Extracted ions per bunch from LEIR from September 1st 2012 until February 1st 2013. The intensity goal of the LHC ion run for LEIR was $4.5x10^8$ ions per bunch, which was achieved in January 2013.

However, with respect to the LIU Ions beam parameter goals, the extracted beam intensity, which was achieved during the last ion run in early 2013, is not sufficient. In fact, $8x10^8$ ions per bunch are required for LIU Ions [1].

BEAM LOSS SYMPTOMS IN 2013

The LEIR Pb^{54+} low energy beam loss has been analysed in the past [2, 3]. The chromaticity of LEIR with Pb^{54+} was measured to be positive in the vertical plane (Fig.3) in February 2013, and as such, was found to be inconsistent with the machine design [4] and beam stability needs, both requiring at first order negative chromaticity for the horizontal plane and for the vertical plane.

ISBN 978-3-95450-131-1

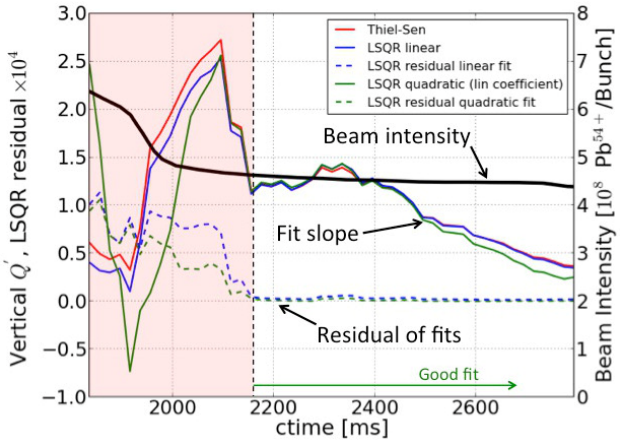

Figure 3: Fitted slopes to measured [2] chromaticity (Thiel-Sen fit in red, linear LSQR fit in blue and quadratic LSQR fit in green), residuals of described fits and beam intensity versus cycle time.

However, advancing the RF-capture in the magnetic cycle by 200 ms before the magnetic ramp, positioning it on the flat bottom has shown that the critical beam loss is advancing together with the RF-capture. This revealed that the low energy beam loss occurs with the machine optics of the flat bottom (see Fig.4) and that the machine optics has to be analysed in more detail, especially with respect to its chromatic behaviour.

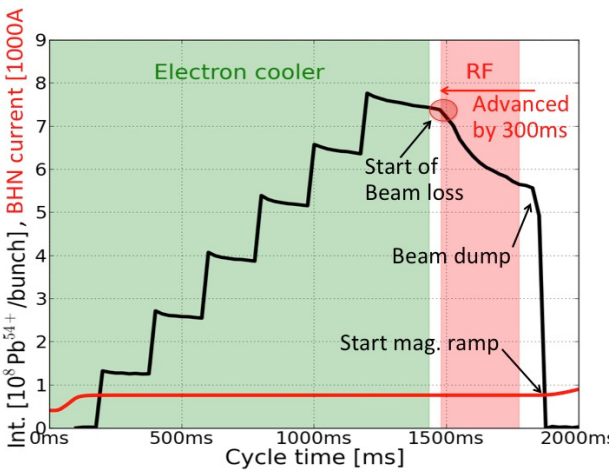

Figure 4: LEIR ion beam intensity with advanced RF-capture and main bending magnet current versus cycle time.

However at low energy, the ion beam is coasting. This denies access to chromatic information via the LEIR RF-system, which would produce bunched beam, but also would introduce transient effect during the bunching itself making the measurement not possible. Hence, another method, not relying on an RF-captured ion beam, is required to analyse the chromatic behaviour of LEIR.

A NEW METHOD

The Classic Chromaticity Measurement

So far, the chromaticity in the LEIR machine was determined by correlating a tune change due to a controlled energy change imposed by the RF-system on the already bunched beam. A radial beam offset was programmed in one of the two dispersive regions in the LEIR machine. The LEIR RF-system would then accelerate or decelerate the ion beam in order to meet the desired radial beam offset. The resulting change in beam momentum induces a tune change, and thus reveals the chromatic behaviour of the machine. Furthermore, it requires a large number of LEIR cycles to span the desired interval of momentum offsets.

Electron Cooling in the LEIR Machine

In LEIR, un-bunched ion beam is injected by Linac3 with a $\Delta p/p = 4x10^{-3}$ momentum ramp (see ref [4] for the details of the injection process). The ion beam remains on a flat and low energy plateau for up to 1.6s for electron cooling and for further multi-turn injections before it is bunched and accelerated. During the beam-cooling phase, the LEIR electron cooler is used to shrink the 6D-phase space emittance and to increase the phase space density of the coasting ion beam without significant beam loss.

The electron beam of the LEIR electron cooler also has the ability to drag the ion beam in momentum space. This feature is used to park the ion beam on a low momentum orbit and makes room for up to 7 additional 70 turn (multi-turn) injections. This way LEIR can stack up to 8 multi-turn injections in a 3.6 second NOMINAL cycle. Fig.5 shows the most common cycle setup with 7 multi-turn injections, with momentum dragging to a cooled stack and the momentum dragging to the RF-capture at the end of the diagram.

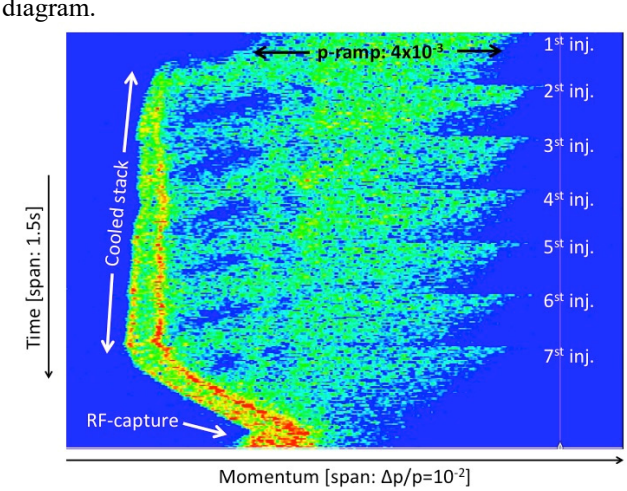

Figure 5: Schottky spectrum in momentum space of the Pb^{54+} ion beam in LEIR in a waterfall diagram (time versus beam momentum).

ISBN 978-3-95450-131-1

Measurement of the Chromaticity by the Electron Cooling Velocity Shift Method

Due to its beam cooling and momentum shifting capabilities, the LEIR electron cooler, in conjunction with the LEIR Schottky-system, can be used to precisely move and measure the coasting beam in momentum space (see Fig.6).

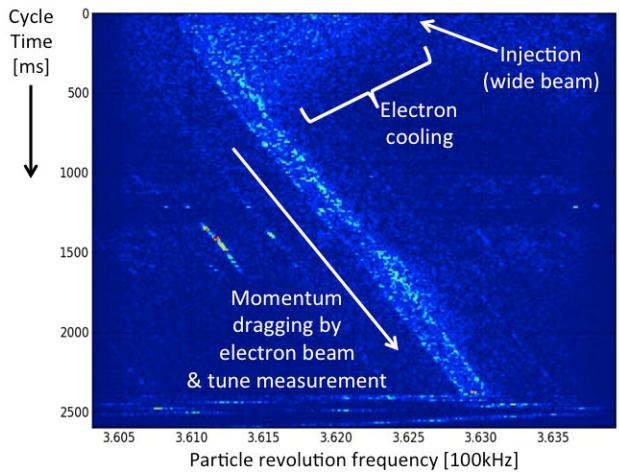

Figure 6: Schottky spectrum of the Ar^{11+} beam as it is used for the new method of chromatic measurement.

At the same time, the LEIR tune measurement system can determine the machine tune thanks to a Base-Band Q (BBQ) Measurement with Direct Diode Detection [5], which does not need a fully bunched beam to identify betatronic oscillations. We then correlate the measured tune with the measured momentum offset, apply linear least square fits and, then infer the machine chromaticity (see Fig.7).

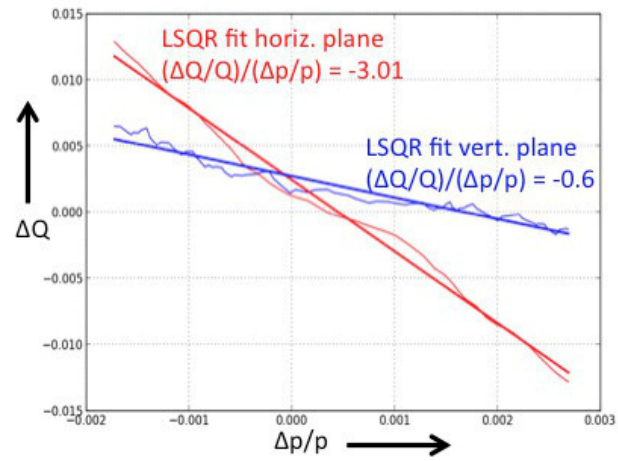

Figure 7: Measured machine tune deviation versus measured ion beam momentum deviation

The new method leads to a measured horizontal chromaticity of -3.01 and a vertical chromaticity of -0.6 with the Ar^{11+} ion beam. It has done so in a single cycle with a length of 4.8s, or 4 basic periods of the LHC injector chain timing system. The time resolution of the tune acquisition system was limited to 40ms and the one of the Schottky system was capable of a time resolution of 12.7ms.

To produce this measurement, we have injected into LEIR ion beam from Linac3 with a momentum ramp of $\Delta p/p = 4x10^{-3}$ across a ramp duration of 200µs. The LEIR electron cooler then cools the ion beam within 400ms to $\Delta p/p = 4x10^{-4}$. The velocity of the electron beam is then linearly changed during a period of 1800ms, momentum-dragging the ion beam accordingly. The dragging of the ion beam covers half the momentum acceptance of LEIR, which is $\Delta p/p = 10^{-2}$.

The measurement accuracy is limited by the extent of the longitudinal momentum distribution of the ion beam. This extent is determined by the effectiveness of the longitudinal electron cooling and is currently limited at $\Delta p/p = 4x10^{-4}$.

CONCLUSION

The new method made accessible the horizontal and the vertical chromaticity of the LEIR machine on the low energy plateau with coasting Ar^{11+} beam. Earlier measurements with Pb^{54+} ion beam in February 2013 have revealed a positive vertical chromaticity during a noisy beam loss period after RF-capture and at the beginning of the momentum ramp.

This electron cooler method requires a sufficiently long plateau of constant magnetic field, where the LEIR electron cooler has sufficient time to shrink to a sufficiently small extension the longitudinal momentum distribution of the coasting ion beam before the chromaticity measurement can start. Due to the single cycle required for the measurement, it is immune to the large cycle-to-cycle variations, which we observe in LEIR. This makes it a very useful new tool in better understanding the low energy beam loss in LEIR.

ACKNOWLEDGMENT

Our special thanks go to S.Gilardoni, R. Scrivens and G.Tranquille for their constructive support during the MD session. Without their help in organizing MD time, improving the electron cooler performance and countless conversations and new ideas, this new development would not have been possible.

REFERENCES

[1] D.Manglunki, "Performance of the LHC ion injectors after LS1", Review of LHC and injectors Upgrade Plans Workshop (RLIUPW), October 2013, Archamps, France.

[2] M.Bodendorfer, "Chromaticity in LEIR performance", CERN-ACC-NOTE-2013-0032, CERN, November 11th 2013, Geneva, Switzerland.

[3] M.Bodendorfer, "Is Pb^{54+} in LEIR limited by space charge?" Space Charge Collaboration Meeting, CERN, May 20th 2014, Geneva, Switzerland.

[4] LHC design report , "LEIR", Vol. III, Part 4, Chap. 35

[5] M.Gasior, "High sensitivity tune measurement by direct diode detection", CERN-AB-2005-060, CERN 2005, Geneva, Switzerland.

ISBN 978-3-95450-131-1

THE CRYOGENIC STORAGE RING CSR

M. Grieser, A. Becker, K. Blaum, C. Breitenfeldt, F. Fellenberger, S. George, J. Göck, F. Grussie, R. von Hahn, P. Herwig, J. Karthein, C. Krantz, H. Kreckel, S. Kumar, J. Lion, S. Lohmann, C. Meyer, P. M. Mishra, O. Novotný, A. P. O'Connor, R. Repnow, S. Saurabh, C. D. Schröter, D. Schwalm, S. Vogel, A. Wolf
MPI für Kernphysik, Heidelberg, Germany
S. Schippers, K. Spruck, Institut für Atom- und Molekülphysik, Universität Gießen, Germany
D. Zajfman, Weizmann Institute of Science, Rehovot, Israel

Abstract

The CSR is a cryogenic electrostatic storage ring located at MPI for Nuclear Physics in Heidelberg. The CSR is designed to perform experiments on ions stored in a low thermal radiation field (≈ 10 K) and in ultra high vacuum conditions. The experimental vacuum system of the CSR, together with all ion optical elements, is entirely housed in a cryostat. On March 17, 2014 a 50 keV Ar^+-beam, delivered from the new electrostatic ion accelerator platform was successfully injected and stored in the CSR at room temperature. The ion beam storage was an important mile stone in verifying the optical design and high-voltage stability. In spring 2015, the complete CSR was cooled to an average temperature below 10 K and first experiments with stored atomic and molecular ions have been successfully performed. We discuss the layout and first operation with a focus on ion beam diagnostics.

Figure 1: The cryogenic storage ring CSR with 35 m circumference.

INTRODUCTION

The CSR shown on Fig. 1, is a fully electrostatic storage ring used to store atomic, molecular and cluster ion beams [1] in the energy range of q·(20-300) keV, where q is the charge state of the ions. The whole storage ring can be cooled down to temperatures of only a few Kelvin where the stored molecular ion beams reach their lowest quantum states. This very low temperature also creates an extremely high vacuum. In fact, observations in the first cryogenic operation indicate residual gas densities below 20 molecules/cm^3. Cooling all ion optics and the vacuum enclosure to 10 K also provides the benefit of a uniquely low level of blackbody radiation in studies with molecular ion beams. In March 2014, to demonstrate the functionality of the CSR, a 50 keV $^{40}Ar^+$ beam was stored for hundred of turns in the ring under room temperature conditions. The complete storage ring was not yet cooled or baked-out at this time, a vacuum in the 10^{-7} mbar range was obtained, limiting the storage life times for singly charged ions to the order of a few milliseconds. In 2015, the storage ring was cooled down to an average temperature below 10 K. At this temperature lifetimes for singly charged ions up to 2500 s have been achieved. A detailed report of the first cryogenic operation of the storage ring will be given in an upcoming publication.

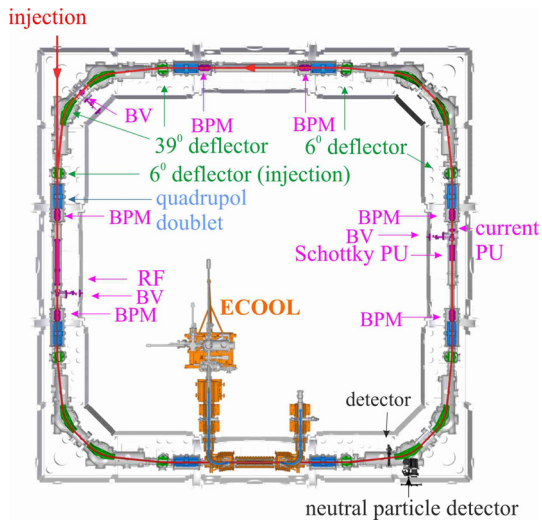

Figure 2: Layout of the cryogenic storage ring CSR. The diagnostics are marked in purple color, it means: BPM-horizontal and vertical beam position monitor, BV-beam viewer, PU- pick-up, RF-rf-system.

LAYOUT

The circumference of the storage ring is approximately 35 m. The beam optical elements consist of two quadrupole families, 6° deflectors to separate the ion beam from neutral reaction products and 39° deflectors (Fig. 2). In the current configuration it is possible to merge the ion beam with laser beams. The remaining experimental straight sections will contain an electron cooler and a reaction microscope for reaction dynamics investigations, respectively. The last remaining linear section is uniquely reserved for beam diagnostics, which contains a beam viewer for the first turn

ISBN 978-3-95450-131-1

diagnosis, a Schottky pick-up and a current monitor to measure the intensity of bunched ion beams (see Fig. 2).

CRYOGENICS

The CSR consists of 16 cryostat chambers with a cross section of about 1 m by 1 m [1], three at each corner and one for each straight section. The outer chambers provide the insulation vacuum of 10^{-6} mbar to ensure thermal insulation of the inner vacuum chamber containing the storage ring ion optical elements (Fig. 3). The inner vacuum chamber is surrounded by two radiation shields, where the inner radiation shield is held by titanium supports to the inner vacuum chamber. The lower part of the 40 K shield is carried by a specially designed support structure made from corrugated titanium sheet mounted inside the outer chamber. The rectangular 80 K sheets is suspended from the 40 K base plate by inconel wires. Thirty layers of multi-layer insulation around the 80 K shield are used to reduce the heat load from the outer chamber walls. For baking of the inner vacuum chambers, which is important for room temperature operation, the 80 K shield is equipped with copper tubes for water cooling to prevent destruction of the outer multi-layer insulation at temperatures above 100 °C. The supply lines for liquid helium to the cryogenic chambers are mounted inside the 40 K shield.

Figure 3: View along the ion beam path into a cryogenic quadrupole unit of the CSR. The electrodes in the center are surrounded by the cryogenic vacuum chamber, refrigerant tubes, and two radiation shields with the inner one serving as a mechanical chassis held at 40 K.

ION BEAM DIAGNOSTICS

The ion currents envisaged for operation of the CSR lie in the approximate range from 1 nA - 1 μA. The resulting low signal strengths on the beam position pickups, current monitors and Schottky monitor require strong demands for the diagnostic tools. For the first turn diagnostics in the CSR, three destructive low intensity beam viewers are used to detect a low intensity injected ion beam [2, 3]. The beam viewers consist of an aluminum plate on which secondary electrons are produced when hit by ion beams. Using a grid the electrons are extracted and accelerated towards a 40 mm MCP/phosphorous screen combination. The image of the beam is recorded via a CCD camera. Two rotary feedthroughs are used to move the aluminum plate. For monitoring of stored beams during the first few turns, a pulse length less than the revolution time must be injected into the ring. The dc current from the ion source is pulsed via a chopper before the beam injection. In combination with the switching of the first 6° deflector,seen by the ions when entering the storage ring, pulses of desired temporal length can be injected and stored. With our current pick-up, a 3.5 cm long tube, we are able to measure the number of injected and stored singly charged ions down to $\approx 10^6$. Every time the circulating ion pulse passes the pick-up a voltage signal, discussed in [4], is induced. The measured pick-up signal for a stored $^{40}Ar^+$ (E=60 keV) ion beam is shown in Fig. 4. An absolute measurement of the stored ion number is possible by integration of one measured ion pulse. From the measurement shown in Fig. 4 an injected ion number of $8.5 \cdot 10^7$ is derived. The current monitor can be used

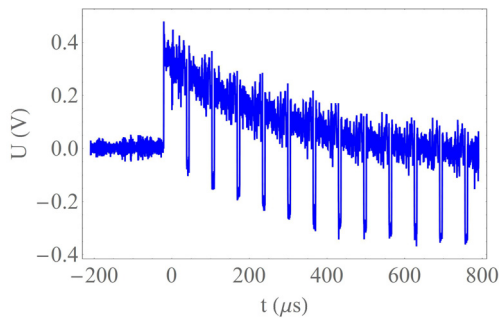

Figure 4: Measured current pick-up signal as a function of time for $^{40}Ar^+$ ions (E=60 keV).

for beam detection until the injected ion beam pulse loses its time structure due to the momentum spread. With the Schottky pick-up it is possible to detect a coasting beam by measuring the Schottky noise of the stored ion beam. Fig. 5 shows the measured Schottky power of a stored Co_2^- ion beam at different times after injection. The Schottky spectra were recorded at the 20th harmonic of the revolution frequency. As the noise power scales with the particle number, Schottky noise analysis can be used to measure the beam life time. From the spectra shown in Fig. 5 a life time of 660 s can be calculated for the stored 60 keV Co_2^- ion beam. A Gaussian fit to the spectra enables the determination of the momentum spread of the stored ion beam. Directly after injection a sigma value of $1.1 \cdot 10^{-3}$ for the momentum spread $\Delta p/p$ was found. A sensitive method for the detection of weak stored ion beams is to bunch the beam. For ion beam bunching a rf system, essentially a 35 cm long drift tube, is installed in the CSR storage ring. More details of the rf system are given elsewhere [3]. The closed orbit of the bunched ion beam can be measured with six beam position monitors (BPM), each consisting of a horizontal and verti-

ISBN 978-3-95450-131-1

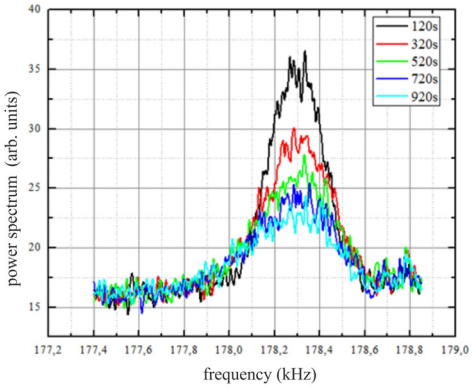

Figure 5: Measured Schottky spectra at different times after injection of a Co_2^- ions (E=60 keV). The injected ion number was about 10^8.

cal position pick-up [5]. These pick-ups are of the diagonal slotted linear pick-up type with a circular aperture. The overall beam position monitor length is approximately 29 cm and the diameter of the electrodes is 10 cm. The pick-up shielding tube is electrically isolated from the experimental vacuum chamber. Beam position measurements were made to measure the closed orbit of the stored ion beam, as well as to determine the dispersion of the storage ring at the pick-up positions. In these measurement an Ar^+ ion beam was injected into the CSR and the closed orbit was changed via variation of all electrostatic potentials by $\Delta U/U$. With $D_x = -2\frac{\Delta x}{\Delta U/U}$, where Δx is the change of the closed orbit, the dispersion at the location of the BPMs can be determined. Due to the symmetry of the storage ring, the dispersion at the six pick-up positions should be identical. The measurements yielded an average dispersion of $\overline{D}_x = 2.17$ m, where the 6 measured values for the dispersion were in the range of 2.09 m to 2.23 m. Calculations using the G4beamline code [6], where ions were tracked through the real fields of the storage ring lead to a dispersion of D_x=2.14 m, which is close to the measured value. Furthermore, one plate of the pick-up system was used to determine the horizontal and vertical tune of the storage ring when an Ar^+ 60 keV ion beam was injected with an horizontal and vertical offset to the central orbit. Due to the betatron oscillations of the whole beam, in both the horizontal and vertical direction, betatron side bands are generated in the pick-up frequency spectrum located at frequencies: $f_{x,y} = f_0(n \pm q_{x,y})$, where f_0 is the revolution frequency, n is an integer number and $q_{x,y}$ is the non-integer part of the horizontal and vertical tune. A measured pick-up spectrum of a horizontal pick-up plate is displayed in Fig. 6. The highest three peaks in the spectra belong to an integer number of the revolution frequency, whereas the small peaks marked with f_x are the betatron side bands. From this measurements a horizontal tune of $Q_x = 2.84$ can be derived, where the integer part of the tune is determined from simulations.The measured horizontal and vertical tunes were used to determine the effective lengths of the two quadrupole families by comparing the measured tunes with the calculated tunes. This comparison

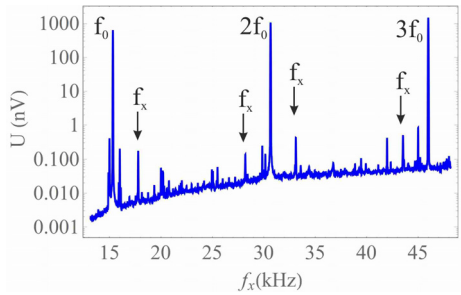

Figure 6: Spectrum of a pick-up signal induced on a horizontal plate.

leads to an effective length of 0.208 m for quadrupole family 1 and 0.209 m for family 2, respectively, which are very close to the effective length $l_{eff} = 0.212$ m obtained from finite element calculations.

CONCLUSIONS AND OUTLOOK

Beam lifetimes greater than 1000 s, as anticipated, could be reached from storing ion beams at cryogenic temperatures below 10 K. These temperatures offer an an environment of uniquely low radiation , which enables vibrational and even rotational relaxation of molecular ions during their storage in the CSR. An electron cooler for phase space cooling is currently under construction. The completion the electron cooler will allow measuring the profile of stored ion beams with the help of the dissociative recombination process between the positive single charged molecules and the free electrons of the electron cooler. The neutral fragments from this process are detected via a position sensitive detector located at the straight ahead position of the cooler. The center of mass of the neutral fragments reveals the transverse electron cooling process [7] and its distribution can be used to calculate the ion beam profile in the electron cooler. At CSR, fragment detectors based on microchannel plates were already set up and tested at cryogenic temperatures [8].

REFERENCES

[1] R. von Hahn et al. "The cryogenic storage ring project at Heidelberg- mechanical concept and realization" NIMB 269 (2011) p. 2871.

[2] T. Sieber et al. "Beam Diagnostics Development for the Cryogenic Storage Ring CSR" DIPAC07, Mestre, May 2007, p. 283.

[3] M. Grieser et al. "The Status of the Diagnostic System at the cryogenic Storage Ring CSR" IPAC2014, Dresden, Germany, June 2014, p. 3521.

[4] M. Grieser et al. "Beam Current Measurements at the TSR Heidelberg" IPAC2011, San Sebastian, Spain, September 2011, p. 1195.

[5] F. Laux et al. "Position Pickups for the Cryogenic Storage Ring" DIPAC 09 Proceedings, Basel, May 2009, p. 288.

[6] G4beamline: http://g4beamline.muonsinc.com

[7] A. Wolf et al., NIMA 532 (2004) p. 69.

[8] K. Spruck et al., Rev. Sci. Instrum. 86 (2015) 023303.

ISBN 978-3-95450-131-1

THE RARE-RI RING AT RIKEN RI BEAM FACTORY

Y. Yamaguchi*, Y. Abe and Rare-RI Ring Collaborators, RIKEN Nishina Center, Wako, Japan

Abstract

The Rare-RI Ring is an isochronous storage ring to measure masses of short-lived rare nuclei by using relative TOF measurement method. The expected precision of the measured mass is of the order of ppm.

We examined the basic performance of the devices, i.e. injection line, septum magnets, dipole magnets with trim-coils, and fast-kicker system by using α-source in 2014. We demonstrated that trim-coils, which are fixed on the dipole magnets of the ring, can adjust the isochronous condition of the ring. An α-particle was injected into the ring individually by using self-trigger mechanism and was extracted from the ring several turns after the injection.

In June 2015, a commissioning run using a ^{78}Kr beam was performed and basic performances of the Rare-RI Ring were verified. We succeeded in injecting a particle, which was randomly produced from a DC beam using cyclotrons, into the ring individually with the fast-kicker system, and in extracting the particle from the ring less than 1 ms after the injection with same kicker system. We measured time-of-flight (TOF) of the ^{78}Kr particles between the entrance and the exit of the ring to check the isochronism. Through the first-order adjustment with trim-coils, the isochronism on the 10-ppm order was achieved for the momentum spread of ±0.2%. Higher-order adjustment employed in future will lead us to the isochronism on the order of ppm. In addition, we confirmed that a resonant Schottky pick-up successfully acquired the frequency information of one particle in storage mode.

In this paper, the technical aspects of the Rare-RI Ring and the preliminary results of the beam commissioning will be described.

INTRODUCTION

Systematic mass measurements, especially for neutron-rich exotic nuclei very far from the stability, are essential for solving the *r*-process path. However, nuclei in such regions have very short half-lives and have a very low production rate even with the powerful accelerator complex in RI Beam Factory, therefore, very fast and sensitive apparatus is needed. To this end, we have proposed a unique apparatus, the so called "Rare-RI Ring" about 10 years ago [1], to precisely measure masses of such rare-RIs.

Figure 1 shows the conceptual design of mass measurement by using the Rare-RI Ring. When a produced secondary particle passes through the timing detector at F3 of the BigRIPS separator [2], a trigger signal is generated. The trigger signal is transmitted to a fast-kicker system via a high speed coaxial tube. Kicker magnets are then immediately excited by thyratrons. In the meanwhile, the particle

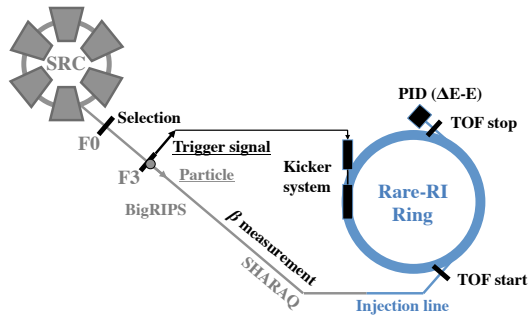

Figure 1: Conceptual design of mass measurement with the Rare-RI Ring located after the SHARAQ spectrometer.

goes through the BigRIPS separator, the SHARAQ spectrometer [3], and an injection line. The particle that arrives at the entrance of the ring is injected into an equilibrium orbit of the ring using septum and kicker magnets. After the particle revolves in the ring about 700 μs, it is extracted using another septum and the same kicker magnets to measure TOF. In addition, it is identified by ΔE-E detectors after extraction. The revolution time of the particle is measured with an precision of better than 10^{-6} under the precise isochronous condition. The β measurement is necessary to correct a revolution time of non-isochronous condition particles. In addition to the short measurement time, this method enables us to measure the mass of even one particle which is suited to measure masses in the *r*-process region. The mass measurement principle details can be found in Ref. [4].

THE RARE-RI RING

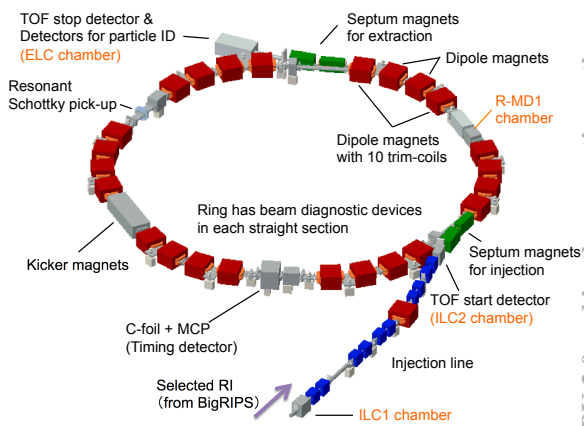

Figure 2: Components of Rare-RI Ring.

Figure 2 shows the components of the Rare-RI Ring. Injection line consists of five quadrupole doublets and one

* yamaguch@ribf.riken.jp

ISBN 978-3-95450-131-1

dipole. TOF start detector is located in the ILC2 chamber (see Fig. 2), in addition to two septa for injecting the particles. The ring consists of six magnetic sectors, each consisting of four dipoles. There is no quadrupole for the ring. This dipole is a rectangular magnet with a radially homogeneous magnetic field. The circumference of the ring is about 60.35 m, and the length of a straight section is about 4.02 m. Kicker magnets are located in the position of the phase advance $3\pi/2$ from the injection septa, and the extraction septa are located in the position of the phase advance $3\pi/2$ from the kicker magnets. In order to ensure an isochronism of the ring by making a gradient magnetic field, the two outer dipoles of each magnetic sector were equipped each by ten trim-coils. The ring has beam diagnostic devices in each straight section. Plastic scintillation counters located in all straight sections to check the injection trajectory. Resonant Schottky pick-up [5] and MCP [6] devices are used to measure the frequency of the revolving particle. Figure 3 shows the bird's-eye view photograph of the Rare-RI Ring.

Figure 3: Bird's-eye view photograph of Rare-RI Ring.

Technical Challenges

The individual injection method, which has been proposed in Ref. [7], is a crucial technique for injecting a rare particle into the ring. In order to realize the individual injection, kicker magnets must be excited before the particle arrives at the kicker magnets. For this purpose we constructed a high speed coaxial tube to transmit the trigger signal from F3 of the BigRIPS separator to the kicker system as fast as possible and a fast-response mechanism with thyratron switch to excite the kicker magnets as soon as possible. In addition, fast recharge is necessary to extract a particle from the ring in 700 μs by using same kicker magnets. Therefore, we developed a fast-recharging mechanism, the so called "hybrid charging system", which has main and sub part. Main part provides 90% of the charging voltage, and the remaining 10% is supplied by sub part of the system. Sub part works to maintain a constant charging voltage level within the range of fluctuation of less than ±1%. The time of recharge by this system is achieved in 200 μs. The details of the fast-kicker system can be found in Ref. [8].

Second challenge concerns the isochronous adjustment using trim-coils. We recently performed the isochronous adjustment of the ring with α-particles by using trim-coils. The α-source (^{241}Am) was installed on the central orbit of the ring in the R-MD1 chamber (see Fig. 2). Two detectors were installed just before/after the α-source to measure the TOF of one turn. Then, we checked the condition of the isochronism based on the TOF width. Figure 4 shows the results of the TOF width as a function of the first-order trim field ($(dB/dr)/B_0$). The minimum value of the TOF width is obtained with $(dB/dr)/B_0 = 0.205$. This is consistent with the results calculated by using the α-source energies, which confirmes that the trim-coils play the role of adjusting the isochronism. The details of the study by using the α-source can be found in Ref. [9].

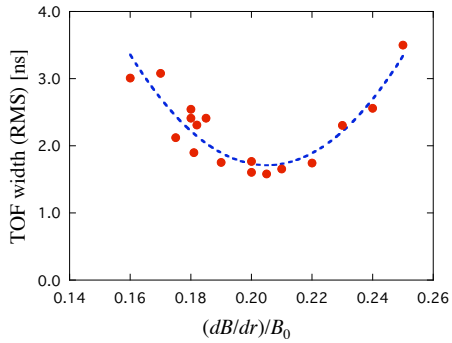

Figure 4: TOF width of one turn of α-particles as a function of the first-order trim field $(dB/dr)/B_0$.

BEAM COMMISSIONING

In June 2015, we performed a beam commissioning using ^{78}Kr with 168 MeV/u, the energy of which matches to the individual injection. Specifications of the ring for this commissioning are given in Table 1.

Table 1: Specifications of the Ring for This Commissioning

Transition γ_{tr}	1.18
Betatron tune	$\nu_x = 1.18$, $\nu_y = 0.93$
Beta function	$\beta_x = 8.4$ m, $\beta_y = 11.9$ m
Dispersion	7.0 m
Kick angle	11 mrad

First, we transported the beam to the ring with a dispersion matching at the center of kicker magnets in accordance with the optical calculations. After that, we injected ^{78}Kr particles individually on the equilibrium orbit of the ring using the fast-kicker system. We confirmed the periodic signals of the circulating particles with the MCP, which is located on the closed orbit of the ring. The particle cannot be stored for long time and it's lost after 25 μs due to the penetration efficiency at the MCP material. After removing the MCP from the closed orbit, we succeeded in extracting the circulating particles from the ring after 700 μs.

Isochronism

Figure 5 shows the TOF of ^{78}Kr particles as a function of the momentum spread with different values of the

ISBN 978-3-95450-131-1

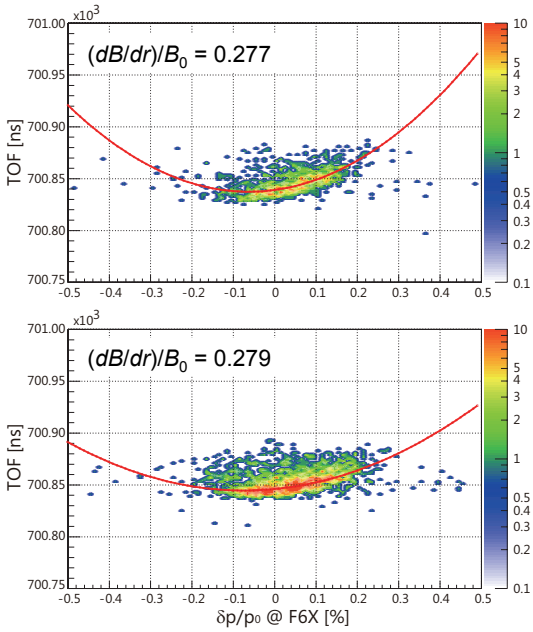

Figure 5: TOF spectra as a function of the momentum spread with different value of $(dB/dr)/B_0$. Red lines shows the quadratic fitting curve of TOF spectra.

$(dB/dr)/B_0$. We understand from this figure that the extractable momentum spread is about ±0.2 %. The TOF width of $(dB/dr)/B_0 = 0.279$ is about 25 ns in FWHM as a result of fitting in the projection on the vertical axis. Therefore, the degree of isochronism is about 3.5×10^{-5} for the momentum spread of ±0.2 %.

The value of $(dB/dr)/B_0 = 0.279$ is an optimum value by using a numerical analysis. However, the experimental optimum value of it may be a little bigger since the quadratic curve is still not symmetry. We haven't enough time to tune the first-order trim field any further, but we were able to achieve a 10-ppm isochronism by adjusting the first-order trim field.

Resonant Schottky Pick-up

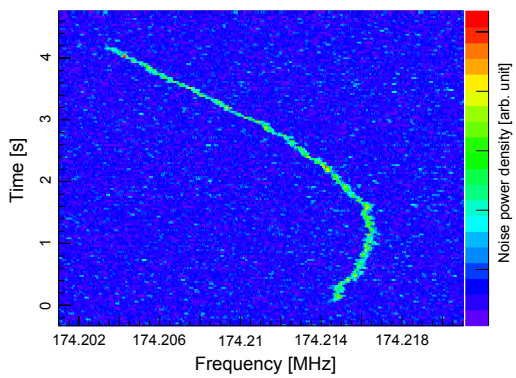

Figure 6: Frequency information of one ^{78}Kr particle from resonant Schottky pick-up.

We verified that a resonant Schottky pick-up successfully acquired the frequency information of one ^{78}Kr particle in a storage mode with a high frequency resolution of 1.29×10^{-6} in FWHM [10] by using a real-time spectrum analyzer. The particle was stored in the ring about 4 seconds while changing its frequency, as shown in Fig. 6. The change in frequency is due to the poor degree of vacuum in the ring, and the shape of curve is influenced by the isochronism for each momentum. We try to understand this interesting phenomena coupled with the results of TOF spectra [10].

PROSPECTS

^{78}Kr beam commissioning run was finished successfully and the off-line analysis is in progress. To achieve higher isochronism, we will perform second-order adjustment with trim-coils by using the frequency information from the resonant Schottky pick-up during the forthcoming high-precision mass measurement experiments.

We are planning the next commissioning using the secondary beams in order to verify the principle of mass measurement in December 2015. The mass measurement experiments will start from 2016.

ACKNOWLEDGMENT

Beam commissioning was performed at RI Beam Factory operated by RIKEN Nishina Center and CNS, University of Tokyo. This work was partially supported by JSPS KAKENHI no. 26287036.

REFERENCES

[1] Y. Yamaguchi, et al., "Rare-RI ring project at RIKEN RI beam factory", Nucl. Instrum. and Methods, B266, 4575 (2008).

[2] T. Kubo, "In-flight RI beam separator BigRIPS at RIKEN and elsewhere in Japan", Nucl. Instrum. and Methods, B204, 97 (2003).

[3] T. Uesaka, et al., "The SHARAQ spectrometer", Prog. Theor. Exp. Phys, 03C007 (2012).

[4] A. Ozawa, et al., "The rare-RI ring", Prog. Theor. Exp. Phys, 03C009 (2012).

[5] F. Suzaki, et al., "Performance of a resonant Schottky pick- up for Rare-RI Ring project", JPS Conf. Proc. 6, 030119 (2015).

[6] Y. Abe, et al.,"Developments of time-of-flight detectors for Rare-RI Ring", JPS Conf. Proc. 1, 013059 (2014).

[7] I. Meshkov, et al., "Individual rare radioactive ion injection, cooling and storage in a ring", Nucl. Instrum. and Methods, A523, 262 (2004).

[8] Y. Yamaguchi, et al., "Fast-kicker system for rare-RI ring", Proc. of STORI'14, Sankt Goar, Germany (2014).

[9] Y. Abe, et al., "Isochronous field study of the Rare-RI Ring", Proc. of STORI'14, Sankt Goar, Germany (2014).

[10] F. Suzaki, et al., "Performance of a resonant Schottky pick-up in the commissioning of Rare-RI Ring", in this proceedings.

ISBN 978-3-95450-131-1

JINR SUPERCONDUCTING SYNCHROTRON FOR HADRON THERAPY

E.M. Syresin, V.A. Mihailov, N.A. Morozov, A.V. Tuzikov
Joint Institute for Nuclear Research, Dubna, Russia

Abstract

The medical carbon synchrotron at maximal ion energy of 400 MeV/u was developed in JINR. The project goal is accumulation of the superconducting technology at construction of the carbon synchrotron with a circumference of 69.6 m on basis of the Nuclotron type magnet elements. For injection of the carbon ions it is proposed to use IH linac of C4+ at energy 4 MeV/n. The superconducting gantry is developed for patient treatment. The gantry consists of two 67.5° and one 900 bending sections, each including two similar dipole magnets of a low aperture (about 120 mm). Such gantries are intended for multiple raster scanning with a wide carbon beam and the technique of layer wise irradiation with a spread out Bragg peak of several mm.

INTRODUCTION

Hadron therapy with beams of heavy nuclear particles (protons and carbon ions) is the most efficient radiation oncology treatment. Hadron therapy in Russia can offer substantial advantages for treatment to 50000 patients per year. Carbon ion therapy is particularly efficient for patients with radioresistant tumors. A project of the medical superconducting synchrotron dedicated for the carbon therapy has been designed in JINR (Fig.1).

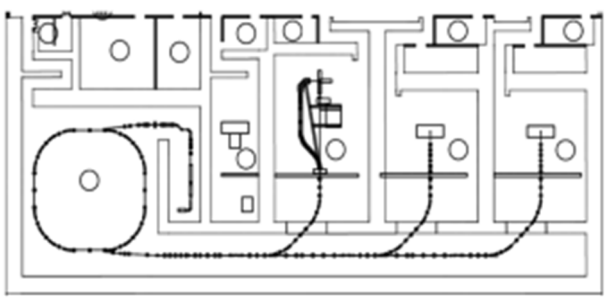

Figure 1: Layout of JINR accelerating equipment based on superconducting synchrotron for center of ion therapy.

The perimeter of the superconducting synchrotron in this complex is 70 m. The magnetic system of the synchrotron consists of four superperiods. The distribution of carbon ions with energy from140 MeV/u to 400 MeV/u from synchrotron into three medical booths is implemented in the transport channel.

The basis of this medical accelerator is the superconducting JINR synchrotron – Nuclotron [1,2]. The Nuclotron type straight dipole magnets [2] were adopted for the optic of the medical synchrotron and beam delivery system. The superconducting magnets permit to reduce the accelerator electrical consumption, the size and weight of the accelerator. Especially the superconducting technology is important at design of the carbon gantry. A superconducting gantry was developed for tumor treatment.

INJECTION

The superconducting electron string ion source [3] is planed to use for $^{12}C^{4+}$ injection in the carbon linac. The compact IH linac [4] will apply as synchrotron injector.

The injection channel consists from two sections: the discharge section, where accelerated in IH linac ions C^{4+} are discharged to ions C^{6+}, and the section of injection of ions C^{6+} in the synchrotron.

CARBON SYNCHROTRON

The basic parameters of the carbon synchrotron [5] are given in Table 1. The FODO structure (Fig.2) is more preferable for injection and extraction schemes and corrections of the closed orbit distortions. The synchrotron magnetic system (Table 2) consists of 4 superperiods, which involves 8 straight dipole magnets, 8 quadrupole lenses and multipole correctors. The maximum magnetic field in dipole magnets corresponds to 1.8 T. The beam and the synchrotron structure dynamic characteristics are given in Table 3.

Table 1: Basic Parameters of Carbon Synchrotron

Injection/maximal energy	4/400 MeV/u
Injection magnetic rigidity/ maximal	0.59/ 6.36T·m
Circumference	69.6 м
Column limit of intensity at injection	10^{10} p/cycle
Betatron tune shift	0.03
Revolution time at injection	2.37 μs
Number of turns at injection	20
Injection efficiency	50 %
Time of synchrotron acceleration	0.5 s
Slow extraction time	(0.5 -10) s
Energy of extracted beam	(140 – 400) MeV/u
Extraction efficiency	96%
Critical energy	3.1 GeV/u

ISBN 978-3-95450-131-1

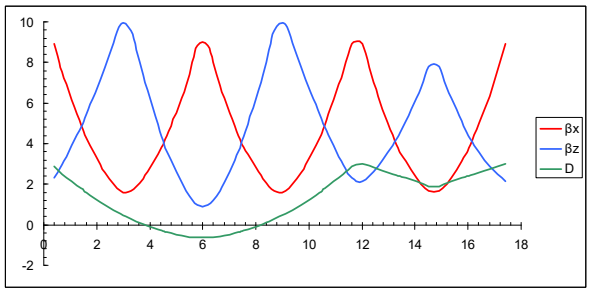

Figure 2: Synchrotron super period characteristics.

The multiturn injection is realized at fulfilling of the horizontal acceptance during 20 ion turns. The stored beam intensity is equal to 1010 ions C6+ per pulse. The working point corresponds to betatron tunes Qx,z ≈3.25. Nonlinear 3 order resonance 3Qx=10 is used for slow beam extraction. The extraction time is varied from 0.5 s to 10 s. The intensity of extracted beam is equal to 109 pps.

Table 2: Structure and Magnetic Elements

Number of superperiods/FODO periods	4/12
Number of dipole magnets/ quadrupole lenses	32/24
Magnetic field at injection/maximal field	0.17/1.8 T
Rate of magnetic field	3.26 T/s
Maximal/injection gradients in F lenses	8.5/0.8 T/m
Maximal/injection gradients in D lenses	–7.5/–0.7 T/m
Curvature radius in dipole magnets	3.53 m
Sagitta in dipole magnets	8.7 mm

Table 3: Beam and Synchrotron Structure Dynamic Characteristics

Betatron tunes	3.25
Chromaticity $\Delta Q_x/(\Delta p/p)$	-3.1
$\Delta Q_z/(\Delta p/p)$	-3.2
Parameter of orbit compaction	0.053
COD, mm	3
Horizontal/Vertical acceptance, π·mm·mrad	180/70
Emittance of injected beam, π·mm·mrad	10
Emittances of accelerated beam $\varepsilon_x/\varepsilon_z$, π·mm·mrad	20/1.5
Emittance of extracted beam $\varepsilon_x/\varepsilon_z$, π·mm·mrad	0.5/1.5
Relative momentum spread	$\pm 10^{-3}$

BEAM DELIVERY SYSTEM

The beam delivery system (Fig.3) consists of following sections: the extraction section; the foil section provided equal beam emittances in both transverse planes; the accommodation section; the section for beam delivery in the cabin; the section of beam transportation between the medical cabins; the isocentric gantry; the channel with fixed beam position cabin. The beam delivery system should provide the fixed transverse beam sizes in the gantry isocenter. These sizes do not depend on the gantry rotation angle, the extracted ion energy, emittance of the extracted carbon ion beam.

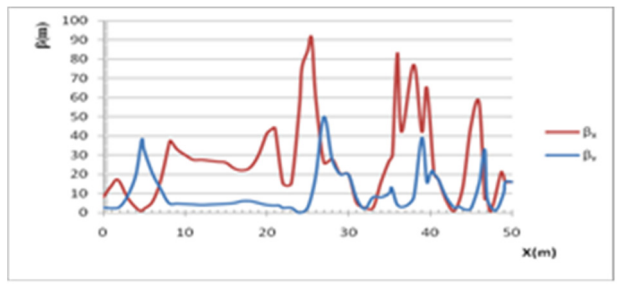

Figure 3: Beta-functions of beam delivery system.

The extracted carbon beam has non symmetric horizontal and vertical emittances, the vertical emittance is few times larger horizontal one. A special scattering foil is installed in the beam delivery system to provide both equal horizontal and vertical beam emittances. The accommodation section is used to provide same optical beam characteristic in the vertical and horizontal directions at exit. It accommodates the beam optic to the gantry for any its rotation angles. The section for beam delivery in cabin consists of the chopper, the achromatic bend and 2 triplets. The chopper involves 4 dipole magnets. The beam is pick-upped by an absorber trap, when dipoles switch off. The beam is transported in the channel when magnets switch on. The section of beam transportation between cabins has the horizontal betatron phase shift 2π and vertical one π. The optic of the isocentric gantry is achromatic at beam transportation to the tumor target. The gantry optic provides equal horizontal and vertical beta functions and zero alpha-function on the tumor target. The parameters of gantry optic are adjusted to obtain the equal vertical and horizontal beta and alpha functions at the gantry entrance at variation of extracted beam emittances and sizes.

SUPERCONDUCTING CARBON GANTRY

The superconducting magnets of low aperture (about 120 mm) are used in the gantry [6]. The gantry consists of two 67.5° and one 90^0 bending sections (Fig.4), each including similar dipole magnets with bending angle 22.5^0.

The total gantry size corresponds to 10.5×6.5 м. Two duplets of quadruple lenses (Q1-Q2), (Q3-Q4) are placed between dipole magnets. The quadruple lenses have the effective length of 2 m and gradients Q1-Q2 – 9.5 T/m, Q3-Q4 – 10.5 - 13.5 T/m.

Two scan magnets are placed at the end of gantry magnetic system with scanning area ±10cm at isocenter. The horizontal scanning magnet (SM-HOR) is situated on a distance of 2.7m from isocenter, the magnet length corresponds to 0.3m, the maximal magnetic field is equal to 0.8T. The vertical scanning magnet (SM-VER) is placed

ISBN 978-3-95450-131-1

on a distance of 2.1 m from isocenter, its maximal field is equal to 0.8 T and length is of 0.4 m.

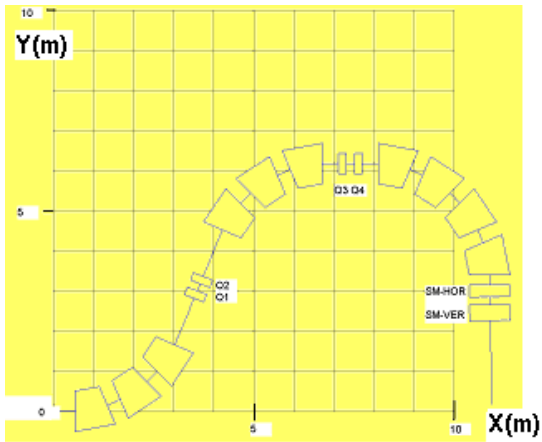

Figure 4: Layout of the JINR superconducting carbon ion gantry.

The beam has following parameters at gantry entrance: carbon ion energy 400 MeV/u, vertical and horizontal sizes of 4 mm, ion energy spread 0.1–1 %. Dipole magnets with working aperture of ± 3cm provide beam transportation at ion energy spread of 1%.

After the last magnet, the system of beam formation is installed. It includes a vertically scanning magnet, comb filter, wedge like filter of variable thickness, and a monitor of beam position. As a result, the distance from isocenter to output edge of the last dipole magnet is about 3.5 m.

Such gantries are intended for multiple raster scanning with a wide carbon beam and the technique of layer wise irradiation with a spread out Bragg peak of several mm. The efficiency of beam formation for such gantry is about 40%. The advantage of this gantry system is a simpler technology of manufacturing of superconducting dipole magnets with a small aperture and weight. The weight of all dipole magnets is about 10–15 t. The limitations of the system are a large diameter of gantry truss and 40% efficiency of beam.

The parameters of gantry dipole magnet are given in Table 4. Superconducting dipole magnets are cooled by circulated He gas high impurity through Sumitomo cryocooler head. The maximum magnetic field corresponds to 3.2T. The iron yoke weight is equal to 500 kg, and weight of cooled mass is about 650 kg. Two cryogenic coolers are installed at each dipole magnet.

Homogeneity of magnetic field 2×10-4 is performed in the magnet aperture of R~10 mm. Tthe errors of magnetic field $\delta B/B \cong 2\times10\text{-}4$ lead to 10% beam position displacement at dipole magnet exit. Relative deviation of the magnetic field integral is equal to ±1.4 10-4 at transverse aperture of $\Delta X = \pm 3$ cm.

Table 4: Parameters of Superconducting Dipole Magnets of Gantry

Magnet parameters	Value
Number of dipole magnets	8
Magnet type, current distribution	cosψ
Number of winding sectors	10
Total number of turns (per pole)	2841
Operating current, A	220
Magnetic field, T	3.2
Magnetic field rigidity, T m	6.63
Turning radius, m	2.07
Turning angle, °	22.5
Horizontal homogeneity of magnetic field, mm	±16
Homogeneity of magnetic field	$\pm2.2\times10^{-4}$
Homogeneities of field integral	10^{-3}
Internal and external radii of winding, mm	61/72
Internal and external radii of yoke, mm	78/178
Diameter of internal warm vacuum chamber of beam, mm	40
Radius of external vacuum chamber of magnet, mm	258/273

REFERENCES

[1] A.D. Kovalenko UPhN, v.177, №8, p. 914 (2007).
[2] A.A. Smirnov, A.D. Kovalenko, Nuclear Particle Letters, v.1, №6, p.11 (2004).
[3] E.D. Donets et al., Review of Scientific Instruments, v71, N2, part II, p.896 (2000).
[4] K. Noda et al., Radiation Res. 48 suppll. A43 (2007).
[5] E.M. Syresin et al, Particle and Nuclei Letters, v.8, No4, p.202 (2012).
[6] E. Syresin, N. Morozov, D. Shvidkiy, IPAC14, Dresden, Germany, WEPRO092, p.2174 (2014).

ISBN 978-3-95450-131-1

FIRST SIMULATION RESULTS OF HEAVY-ION ACCELERATION IN THE RCS OF J-PARC

P.K. Saha*, H. Harada, M. Kinsho, M. Yamamoto and H. Sako
J-PARC Center, KEK & JAEA, Tokai-mura, Naka-gun, Ibaraki-ken, Japan

Abstract

We present first space charge simulation results of heavy-ion (HI) acceleration in the 3-GeV Rapid Cycling Synchrotron (RCS) of Japan Proton Accelerator Research Complex (J-PARC). RCS is 1 MW proton beam power source for the Material and Life Science Experimental Facility (MLF) as well as an injector for the Main Ring (MR). Recently, importance of heavy-ion (HI) physics program in J-PARC are being intensively discussed for studying so-called QCD phase structures at high baryon density by using slowly extracted HI beam of 1-20 AGeV in the MR. Although detail accelerator scheme to adapt HI has not yet been fixed, in this work we studied possibilities of U^{86+} acceleration in the RCS by using ORBIT 3-D simulation code. The simulation results show that a more than 1×10^{11} of U^{86+} ions per pulse can be accelerated in the RCS without any significant beam losses. That gives a total of 4×10^{11} ions for each MR cycle and sufficiently meets experimental requirements concerning primary beam intensity.

INTRODUCTION

Japan Proton Accelerator Research Complex (J-PARC) has 3 proton accelerators and several experimental facilities that make use of high intensity proton beams [1]. The accelerator facility comprises a 400 MeV H^- Linac, a 3-GeV Rapid Cycling Synchrotron (RCS) and a 50-GeV (30-GeV at present) Main Ring synchrotron (MR) [2]. Major experimental facilities are Material and Life Science Experimental Facility (MLF), Hadron Experimental Facility (HD), Neutrino Experimental Facility (NU) and also an Accelerator Driven Transmutation Experimental Facility (TEF).

The importance of heavy-ion (HI) physics program in J-PARC is being intensively discussed recently, which consists of low and high energy programs [3]. The high energy program aims to explore QCD phase structures at nearly one order higher baryon density as compared to the normal nuclear density (ρ_0). The aim is to use slowly extracted HI beam from the MR with kinetic energy 1~20 AGeV. In order to reach baryon density as high as possible, the U+U system is considered by bombarding more than 1×10^{10} U ions per cycle (a few sec) on a fixed U target. On the other hand, advantages of studying strangeness physics produced by HI collisions are also being discussed. The J-PARC energy gives maximum hypenuclear production due to coalescence of high density baryons [4].

However, there exist many issues and challenges to adapt a new HI accelerator scheme in the specifically designed and already running high intensity proton machines. Other than space and budget one big issue is not to interfere any existing or planned programs that make use of proton beams.

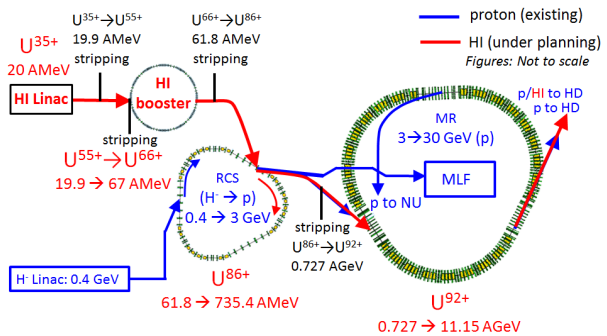

Figure 1: A preliminary scheme for HI acceleration (yet unofficial) to adapt in the existing J-PARC proton facilities.

Figure 1 shows a preliminary HI accelerator scheme (guided by red arrows), added to the existing J-PARC proton accelerators and facilities (guided by blue arrows). The first approach is to use existing RCS and also the MR, where a HI Linac followed by a smaller HI booster ring have to be constructed. There exist many advantages if RCS and the MR can be successfully utilized for accelerating HI to the required energy. Proton beam powers in both machines are approaching to the design goal, while RCS has already demonstrated 1-MW equivalent beam acceleration in early 2015 [5]. The measured beam losses were as low as less than 0.2% and were mostly due to the foil-beam interaction during more than 300 turns H^- change-exchange injection. The beam dynamics issues are well understood, resulting a well beam loss mitigation even at 1 MW, which can be successfully applied for discussing HI beam dynamics issues and realistic measures.

While HI accelerator scheme and how it can be connected to J-PARC facility are under planning, we have investigated the possibilities of HI acceleration in the RCS. The numerical simulation results are presented in this paper.

HI SCHEME IN THE RCS

Figure 2 shows a layout of the RCS. The proton beam energy at injection and extraction are 0.4 and 3 GeV, respectively. The extracted beam is simultaneously delivered to the MLF and MR at a repetition rate of 25 Hz. A new HI injection system is considered to be added at the end of RCS extraction straight section. The uranium ions having 86+ charge states (U^{86+}) will be injected for a single turn from the upstream new HI booster. The injection system can be thus very simple and straightforward, which may not require a large space. However, injection energy of HI has to be

* E-mail address: saha.pranab@j-parc.jp

ISBN 978-3-95450-131-1

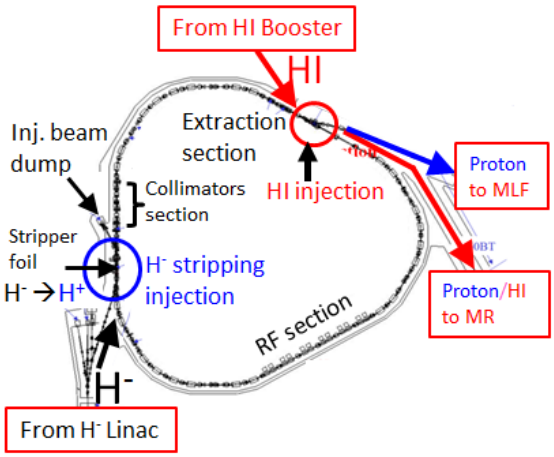

Figure 2: Layout of J-PARC 3-GeV RCS. The HI injection system can be added at the end of extraction straight section.

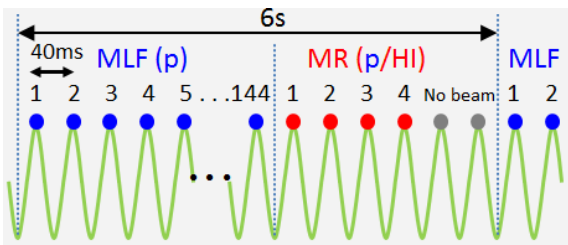

Figure 3: RCS beam delivery pattern to the MLF and MR when MR operates for HD experiments (6s cycle). If HI scheme is added in the RCS, either proton or HI can be accelerated in the RCS for MR cycle depending on MR operation.

matched with B field at bottom set for the 0.4 GeV proton. A higher charge state is necessary in order to avoid any changing of charge state during acceleration due to RCS pressure level ($\sim 10^{-6}$ Pa) is significantly higher than required for a lower charge state injection. One can also gain on the extraction energy through a higher charge state injection, which is useful to achieve maximum yield for the highest charge state at final stripping before injecting into the MR.

Figure 3 shows the pattern of RCS beam delivery cycle to the MLF and MR when MR operates at slow extraction (6s cycle) for the HD users. RCS can inject HI in the MR cycle instead of proton, only when MR operates with HI for the HD users. Unless otherwise MR operates for HI, the whole accelerator complex runs for proton as of now.

SIMULATION RESULTS OF U^{86+} ACCELERATION IN THE RCS

The present simulation is done by using ORBIT code [6], which is recently upgraded successfully for realistic beam simulations with space charge including impedances in synchrotrons [7]. In the simulation, the bending, quadruple and also the sextuple magnets are kept same as optimized for 1 MW proton beam acceleration. The ramping energy, the betatron tunes and the degree of chromaticity correction are then automatically determined and unchangeable. The injection energy of U^{86+} ions are set to be 0.0618 GeV/nucleon (AGeV), which can be accelerated up to 0.735 AGeV. The horizontal and vertical betatron tunes at injection are set to be 6.45 and 6.42, respectively. Figure 4 (top) shows typical rf voltage patterns for U^{86+} (red lines), which are found to be similar to those for proton and can be changed between cycles. However, rf system has to be made capable of changing rf resonant frequency between cycles and/or independent compensation with beam in each cycle. Similar to proton, the 2nd harmonic rf voltage is also applied for the present case in order to reduce the space charge effect at lower energy. The sinusoidal B field and the corresponding successful acceleration of a single particle U^{86+} ion up to the expected 0.735 AGeV is shown in the bottom plot in Fig. 4.

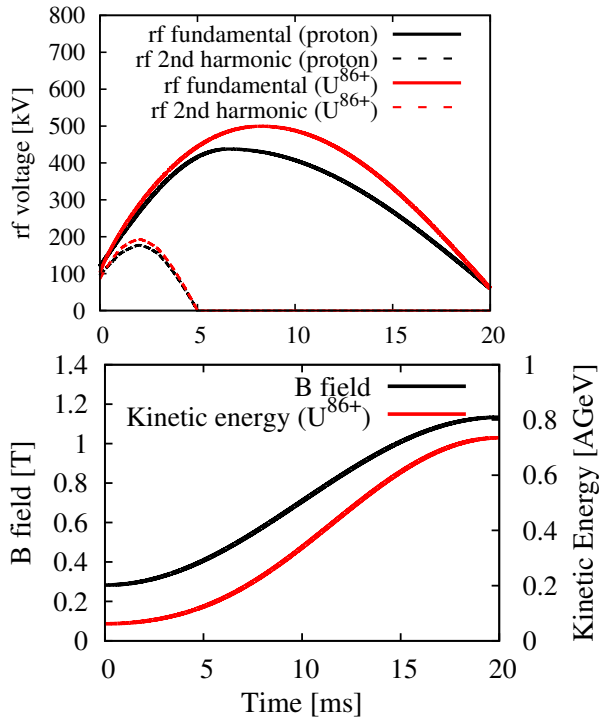

Figure 4: (Top) RCS rf voltage patterns for U^{86+} acceleration are found to be almost similar to those for protons. (Bottom) B field and the corresponding acceleration of U^{86+}.

Next, we performed multi-particles simulations for different intensities up to 1.1×10^{11} U^{86+} ions with a single turn injection from the HI booster in one of the two RCS rf bucket. The space charge limit for U^{86+} ion beam intensity can be roughly obtained by estimating Laslett tune shift (ΔQ) [8] at injection and comparing the value with 1 MW proton case (8.33×10^{13} particles in 2 bunches). Due to lower beam energy ($\frac{1}{\beta^2\gamma^3}$ term) and charge state ($\frac{q^2}{A}$ term), ΔQ for U^{86+} at 0.0618 AGeV is calculated to be more than 300 times higher as compared to that for 0.4 GeV proton. Here, β and γ are relativistic parameters, q and A are the charge and mass of the ion, respectively. An injection of 1.1×10^{11} U^{86+} ions (with a transverse emittance of 100π mm mrad and bunching factor of 0.3) gives a same ΔQ of -0.34 as obtained for the proton at 1 MW.

ISBN 978-3-95450-131-1

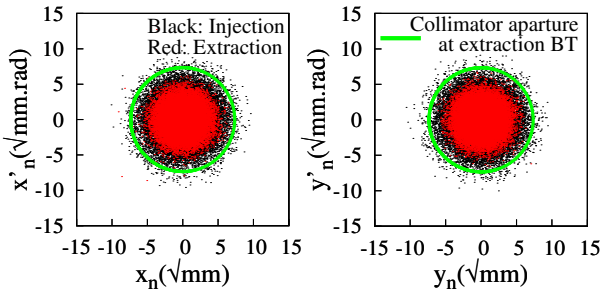

Figure 5: Normalized transverse phase space (black) of a single turn injected U^{86+} beam and the accelerated one at the top energy (red). A more than 99.9% particles at extraction are obtained to be within the 3-50BT collimator aperture as shown by the green circle.

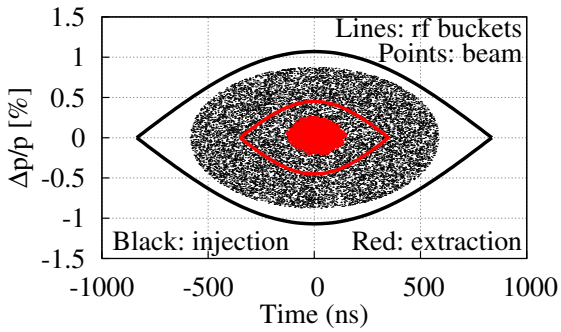

Figure 6: Longitudinal distributions of the U^{86+} at injection and extraction energies.

As detail parameters upstream HI booster are not fixed yet, the transverse and longitudinal beam distributions for RCS injection are considered to be similar to those for protons obtained at the end of injection painting. Figure 5 shows normalized transverse phase space distributions at injection (black) and extraction (red) for both horizontal (left) and vertical planes (right). The maximum emittance at injection was nearly 100π mm mrad, where more than 99.9% particles at extraction energy are obtained to be within the collimator aperture (54π mm mrad) at the beam transport from RCS to the MR (3-50 BT), as shown by the green circle. Due to relatively smaller aperture and limited capacity of the 3-50 BT collimator, it is very important to have the extracted beam with less halo. Figure 6 shows longitudinal beam distribution along with rf buckets. In order to reduce space charge effect at lower energy, injected beam is considered to cover nearly 80% of the rf bucket.

Figure 7 shows the beam survival studied for 3 different intensities. A more than 99.95% beam survival can be obtained even for injecting 1.1×10^{11} U^{86+} ions in the RCS. Differing from the multi-turn H^- charge-exchange injection, there is no foil-beam interaction in the RCS for the HI case in the present proposed plan, resulting a negligible beam losses only caused by the space charge effect. The lower the beam intensity, the lower the space charge effect and hence there is practically no beam losses for 2.0×10^{10} U^{86+} ions injection (green).

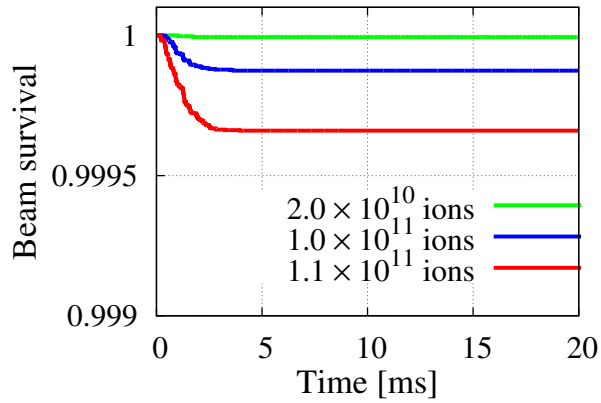

Figure 7: Beam survival as a function of acceleration time for 3 different intensities of U^{86+} ions. An injection of even 1.1×10^{11} ions gives a more than 99.95% beam survival.

The extracted 1.1×10^{11} U^{86+} ions of 0.735 AGeV from the RCS will be fully stripped to U^{92+} in the 3-50BT before injecting into the MR. A total of 4 RCS cycles can be injected in one MR cycle (see Fig. 3. By considering a typical stripping efficiency of 80%, a total of nearly 4×10^{11} U^{92+} ions can be obtained in the MR, which is sufficiently enough concerning the primary beam intensity required for the proposed experiments.

SUMMARY

In order to include HI physics program in J-PARC, a new HI accelerator scheme to adapt in the present J-PARC proton accelerators are in consideration. The RCS and the MR have to be utilized not only to reduce budget and space but also to take advantage of understanding beam dynamics issues learned with protons up to the design beam intensities. The possibilities of U^{86+} ions acceleration in the RCS are studied in this work. The preliminary simulation results show that a maximum of 1.1×10^{11} U^{86+} ions can be accelerated without any significant beam losses. Extracted U^{86+} ions from the RCS will be fully stripped to U^{92+} before injecting 4 RCS cycles into the MR. The expected intensity in the MR is thus nearly 4×10^{11} U^{92+} ions for each 6s MR cycle and sufficiently meets the experimental requirements. However, for further realistic discussions, detail studies are necessary by using realistic injection parameters fixed by the upstream new HI booster.

REFERENCES

[1] "J-PARC official website", http://j-parc.jp
[2] "Accelerator Technical Design Report for J-PARC", JAERI-Tech 2003-044 and KEK Report 2002-13.
[3] H. Sako et al., Nucl. Phys. A 931, 1158 (2014).
[4] A. Andronic et al., Phys. Lett. B 697, 203 (2011).
[5] H. Hotchi et al., Proceedings of IPAC'15, 1346 (2015).
[6] J.A. Holmes et al., Proceedings of EPAC'02, 1022 (2002).
[7] P.K. Saha et al., Proceedings of IPAC'14, 1683 (2014).
[8] L.J. Lasslet, BNL Report 7534, 325 (1963).

ISBN 978-3-95450-131-1

COMMISSIONING OF HEAVY-ION TREATMENT FACILITY I-ROCK IN KANAGAWA

E. Takeshita #, S. Minohara, Y. Kusano, S. Yamada
Kanagawa Cancer Center, Kanagawa, Japan
T. Furukawa, K. Mizushima, Y. Hara, N. Saotome, R. Tansho, Y. Saraya, K. Noda
National Institute of Radiological Sciences, Chiba, Japan

Abstract

As part of the Kanagawa "Challenge-10-years strategy to cancer" it was decided in March 2005 to establish a carbon-ion therapy system at the Kanagawa Cancer Center (KCC). From around 2009, the basic design and the foundational planning of the facility were considered and in January 2012 a contract was made with the Toshiba Corp. In December of the same year, the construction of the main building for the acceleration and treatment devices was started and completed in October 2014. Currently, the KCC is in a commissioning phase with the aim to start treatment in December of this year. Various treatments for cancer, which include the present photon LINAC for the radiation therapy, will be provided to patients in cooperation with our cancer center hospital. In addition, we will combine a compact dissemination treatment system of carbon-ion therapy to the pencil beam 3D scanning technique designed by the National Institute of Radiological Sciences (NIRS). The treatment experience with the carbon-ion scanning technique will be the second in the country following NIRS. In this paper, we report on the progress of the beam commissioning at KCC.

INTRODUCTION

The carbon-ion therapy facility of the KCC, which is called "Ion-beam Radiation Oncology Center in Kanagawa (i-ROCK)", has been introduced with concepts for cancer treatment as described below. At first, we aim to provide the most suitable treatment, which includes the existing photon LINAC for the radiation therapy, to any patient in cooperation with our hospital organization. The facility for carbon therapy has been constructed, focusing the cancer treatment on "Quality of Life (QOL)".

The general layout and schedule of the i-ROCK project was considered with its original specifications from around 2009. In January 2012, an agreement with the Toshiba Corp. was made to introduce and install the carbon-ion therapy system. The construction of the facility building was started from December 2010 by the Kajima Corp. and was completed in October 2014. The equipment of the treatment system was delivered from May 2014. At present, various commissionings have been performed to start first treatment in December 2015.

SPECIFICATIONS

The original specifications of the facility used for the treatment follow that of the compact dissemination treatment system of carbon-ion therapy [1] designed and developed by the NIRS. This system was already used for the cancer treatment in Gunma University and SAGA HIMAT achieving good results while each facility vendor was different. One of the main features in i-ROCK is the combined installation with a 3D pencil beam scanning system [2] developed by NIRS and the compact dissemination treatment system of carbon-ion therapy. The main specifications are indicated in Table 1.

Table1: Specifications of i-ROCK

Item	Basic specifications
Ion	C^{6+}
Energy	140～400 MeV/u (variable)
max. Field	20×20 cm^2
max. Dose rate	2 Gy/min
Beam intensity	~1.2×10^9 pps (variable)
Irradiation type	Scanning Extended scanning
Treatment room	Horizontal: 2 rooms Horizontal/Vertical: 2rooms

In order to use efficiently use the pencil beam delivered from the synchrotron accelerator, the treatment room set up contains 4 (Horizontal/Vertical x 2 rooms, Horizontal x 2 rooms, 6 ports for total of 4 rooms). Generally, more than one treatment room per accelerator was set up in the present facility because during treatment time more than 80 % is spent on the positioning of the patient by the X-ray imaging system. However for our facility, it is a little bit different. We considered with the ration of the treated tumor in Kanagawa and the treatment protocol for the carbon therapy to fix the number of the treatment room. With these considerations, our facility can accept 880

#takeshita.e@kcch.jp

ISBN 978-3-95450-131-1

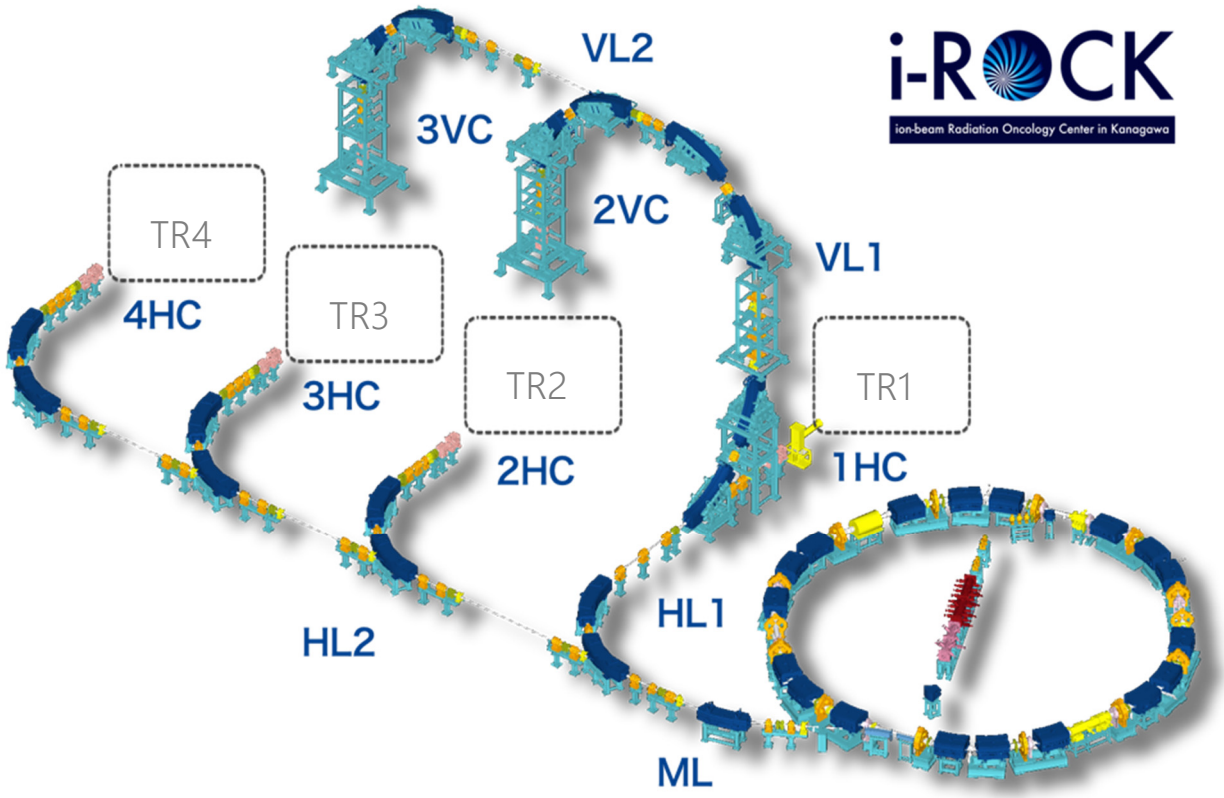

Figure 1: Configuration of the accelerator system.

patients per year when our center will be operated at full capacity.

ACCELERATOR SYSTEM

The accelerator system consists of the injector, the synchrotron accelerator, and the high energy beam transport line. Figure 1 shows the configuration of the accelerator system. The most important role of the accelerator system for the treatment is to deliver the beam with tolerable stability and certainty. To achieve the required stability of the pencil beam during the scanning irradiation, several functions were added to the conventional treatment system.

The operation mode of the synchrotron accelerator was improved to achieve efficient respiration gated irradiation for the treatment of moving organ, such as lung and liver. The synchrotron control system is capable of flexible flattop extension, called the "extended FT operation," which can decrease the dead time, as schematically shown in Fig. 2. Since a few synchrotron acceleration cycles can deliver a sufficient number of carbon ions for one fractional irradiation, the dead time of the synchrotron will be almost negligible owing to this extended FT operation.

In addition, more flexible operation of the synchrotron, as an alternative to the energy degrader, i.e. range shifter, is also be realized. This operation mode is called "multiple-energy operation", which is developed and already routinely used in NIRS [3,4]. This operation uses synchrotron operation patterns having a stepwise flattops. Cooperating with extended flattop operation, carbon ions with various energies can be provided in a single synchrotron cycle. Since the extraction energy can be quickly changed by the accelerator, no energy degrader is required to control the Bragg-peak position in the patient's body.

Accelerator system can deliver the beam automatically as required from the irradiation system without manual operation. So small number of the operators can control every system.

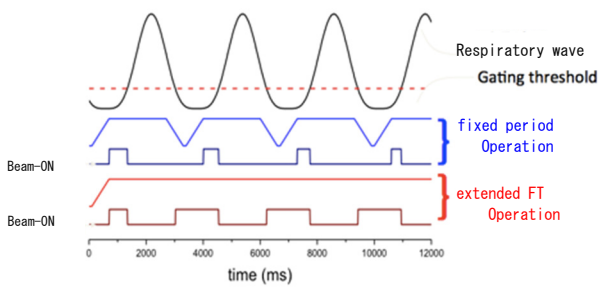

Figure 2: Schematic picture of an extended flat-top operation.

ISBN 978-3-95450-131-1

COMISSIONING

Performance Test of Non-Scanned Beam

Since the beam stability is directly affects the delivered dose to the patient, i.e. treatment quality, the beam from the synchrotron should be highly stabilized in terms of intensity, position and size. Figure 3 shows the typical result of intensity check. In this test, 11 energies (430, 400, 380, 350, 320, 290, 260, 230, 200, 170 and 140 MeV/u) are delivered within single synchrotron cycle. As a result, it was verified that the constancy of the intensity and the ripples are suppressed within 20%.

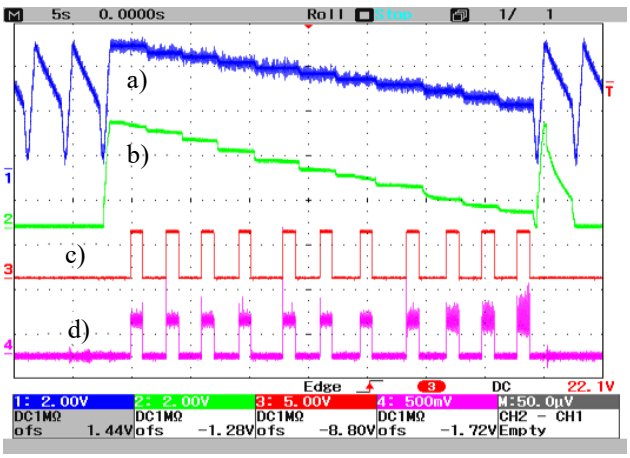

Figure 3: Spill in one cycle with the flat-top extension operation (all 11 energy). a) BM current, b) DCCT, c) Enable signal of extraction and d) Dose monitor.

The position and the size of the beam were measured using the ISO-SCN [5] (fluorescence film + CCD camera). The results of the beam position and size in the respective energy are shown in Figure 4. The measurement time was set to about 10 seconds for each energy. As a result, it was verified that the beam position and size are highly stabilized within ±0.5 mm during 10 seconds extraction. The beam size for each energy was adjusted to a symmetric profile because for the clinical requirement. Furthermore, it was adjusted so that the beam size becomes fixed to keep the compatibility for all irradiation ports (1HC, 2HC, 2VC, 3HC, 3VC and 4HC). The results are indicated in Figure 5.

Performance Test of Scanned Beam

The evaluation points for the performance test of the scanned beam are as following:

1) Verification of the scanned beam position,
2) Reliability confirmation of the dose monitor,
3) Reliability confirmation of the position monitor, and
4) Overall verification for the irradiation system.

We confirmed these points based on the protocol developed by NIRS [6].

For point 1), using the measurement of the spot irradiation, the precision of the scanned beam position was verified within ± 0.5 mm. For point 2), we verified the linearity and the position dependence of the dose monitor to accurately check the dose control. For point 3), the performance of the position monitor, which was used to

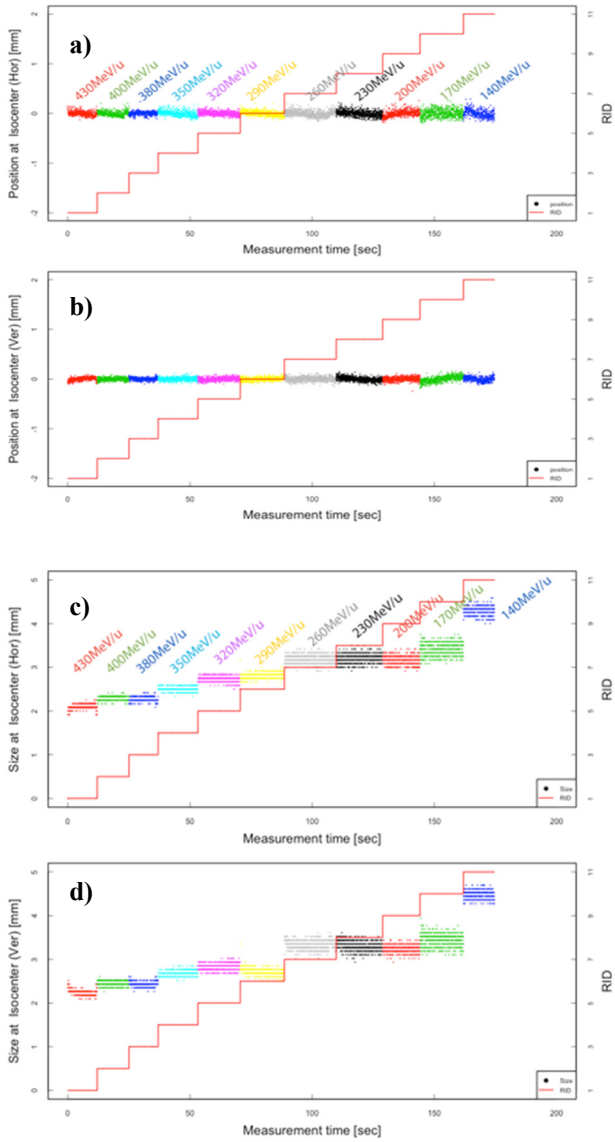

Figure 4: Beam position and size stability at 2VC. a) Beam position X, b) Beam position Y, c) Beam size X, d) Beam size Y and color differences represent the data for each energy.

survey the beam position during the irradiation, was evaluated to provide the stability of the irradiation field. The distributions of the uniform irradiation filed were measured by a screen monitor for QA (QA-SCN) [7] to estimate the position dependence of the dose monitor as shown in Fig. 6. A flatness of the field within 3 % was deduced. Finally, the overall irradiation system was checked using the QA pattern [8] in point 4), as shown in Fig. 7.

ISBN 978-3-95450-131-1

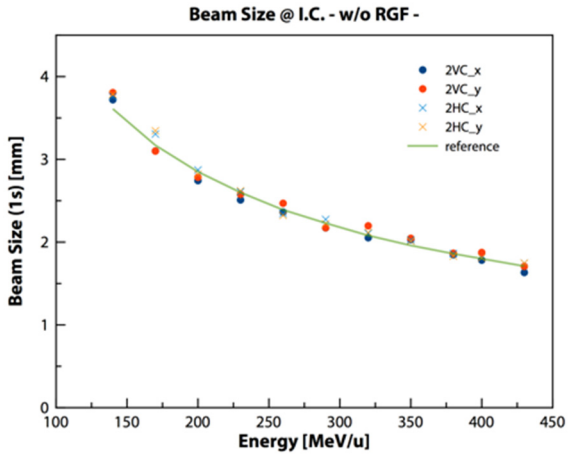

Figure 5: Beam size for each energy of 2HC and 2VC in the isocenter. Each point shows the measured data and the lines indicate the reference value for the adjustment.

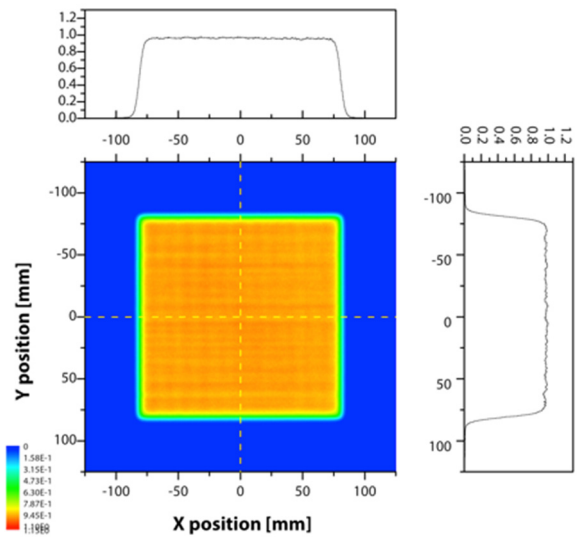

Figure 6: Measured distribution of the uniform field (150 x150 mm^2, 2 mm pitch, 290 MeV/u).

FUTURE PLAN

In June 2015, the pharmaceutical affairs in Japan was applied to prepare for the first treatment in December 2015. During summer 2015, the combination tests between each system were finished assuming several work-flows of specific protocols for the treatment. We are planning to start the preparation of the treatment with all personal (doctor, therapist, engineer, nurse and medical physicist) around this September 2015, with training of the treatment planning system, the patient positioning system and the irradiation system. We plan to provide the first treatment in December 2015.

ACKNOWLEDGMENT

We would like to express our thanks to the members of the Physics Research Group at NIRS for their support and useful discussion. We also thank the members of Toshiba Corp., Sumitomo Heavy Industries Co., Ltd., Hayakawa Industries Co., Ltd., Toshiba Electric Service Corp., Shibaura Eletec Corp., and Accelerator Engineering Corp., for their technical support during the tuning and testing of the beam commissioning in our center.

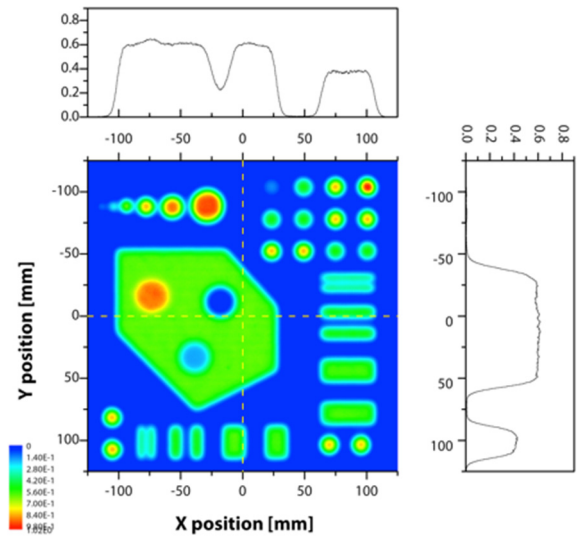

Figure 7: Measurement result with the comprehensive pattern (2 mm pitch, 290 MeV/u).

REFERENCES

[1] K. Noda, et al., Proc. of PAC04 (2004) 552.
[2] T. Furukawa, et al., Med. Phys. 37 (2010) 5672.
[3] T. Furukawa, et al., Med. Phys. 34 (2007) 1085.
[4] Y. Iwata, et al., Nucl. Instr. and Meth. A 572 (2007) 1007.
[5] K. Mizushima, et al., Proc. of IBIC2012 (2012) 256.
[6] Internal reports of the QA section meeting at NIRS (2011).
[7] E. Takeshita, et al., Nucl. Instr. Meth. B 269 (2011) 2936.
[8] J. Flanz, "Quality assurance, accelerator and beam delivery", PTCOG49, 2010.

ISBN 978-3-95450-131-1

DEVELOPMENT OF A LIQUID LITHIUM CHARGE STRIPPER FOR FRIB*

F. Marti#, P. Guetschow, FRIB, East Lansing, MI, USA
Y. Momozaki, J. A. Nolen, C. B. Reed, ANL, Argonne, IL 60439, USA

Abstract

The Facility for Rare Isotope Beams (FRIB) being built at Michigan State University for the US Department of Energy (DOE) will deliver heavy ion beams with beam power of 400 kW. SRF cavities accelerate the ions to energies above 200 MeV/u. At energies of 16-20 MeV/u a charge stripper increases the charge state just before the first bend in the linac (a second bend is located downstream). Due to the high power deposition on the stripping media and radiation damage solid strippers are not practical. The baseline design selected a liquid lithium film stripper. This stripper has been developed in collaboration with Argonne National Laboratory (ANL). A stripper module is being built at MSU with an estimated completion date of December 2015. We plan to operate the stripper outside the FRIB tunnel for 18 months to learn the reliability and stability issues before final installation in the accelerator.

INTRODUCTION

Michigan State University was charged by the Office of Science of the DOE of the US to design and build the Facility for Rare Isotope Beams (FRIB) at the end of 2008. The facility is funded by the Office of Nuclear Physics with contributions and cost share from Michigan State University. The goal of the facility is the production of rare isotopes produced by the in-flight separation method. This method provides fast development time for any isotope and allows short lived isotopes of any element to be available.

One of the main components of the facility is a driver linac capable of producing beams of ions from the low mass region up to U at energies above 200 MeV/u and with a total beam power on target of 400 kW [1, 2]. The linac is folded in three segments running parallel to each other with two 180 degree bends in between. After the first linac segment and before the first bend a charge stripper is located to increase the Q/A of heavy ions by more than a factor two.

This paper describes the design and construction of the liquid lithium charge stripper and the extensive experimental work done up to now.

WHY LITHIUM?

As described previously [3], liquid lithium was selected as the baseline design for the FRIB charge stripper because traditional solid carbon strippers have very limited lifetime under heavy ion bombardment [4]. There is no solid lattice that can be damaged by the high energy deposition and the flowing liquid takes away the heat deposited by the beam on the stripping media. The use of lithium was initially proposed by the ANL group at the time of the Rare Isotope Accelerator (RIA) R&D [5]. Lithium has several properties that make it the preferred liquid metal for this application.

The vapour pressure of lithium at its melting temperature (186 C) is quite low (~ 10^{-7} Pa). If we compare with Hg for example, mercury has a vapour pressure of ~ 10^{-1} Pa at room temperature and when heated by the beam it will be even higher.

The heat capacity of lithium is quite high (~ 4.2 J/g/C at 200 C) meaning that it will have a limited temperature increase when exposed to the beam, and its boiling point (1336 C at 1 bar) is much higher than the melting point.

The major drawback of lithium is its pyrophoricity. [6] It will burn in oxygen and nitrogen producing caustic fumes (oxide and nitride). Contact of molten alkali metal with concrete will cause spalling of the concrete and spattering of the metal. Special precautions must be taken to avoid any contact of the lithium with water or humid air.

EXPERIMENTAL WORK

Production of the Lithium Film

The film thickness required to achieve near equilibrium charge state is of the order of 10 µm. We need the film to move fast through the beam to take the heat away. Speeds of close to 50 m/s are necessary. The initial ANL experiments [7] created a high velocity jet of liquid lithium by pressurizing a tank with argon gas that contained the liquid and pushing the lithium through a small diameter nozzle. This high velocity jet impinged on a flat plate that created the thin film, about 9 mm wide as illustrated in Fig. 1.

The original experiments proved the feasibility of creating the lithium film using pressurized liquid at temperatures around 200 C.

Stability and Thickness Measurements

In 2009 a collaboration was established between FRIB and ANL to continue the experimental work at ANL with the objective of measuring the thickness and stability of the lithium film.

A limitation on these experiments was that the flow of lithium could be maintained for less than 30 minutes because the liquid would flow from the supply tank to the

*Work supported by the U.S. Department of Energy Office of Science under Cooperative Agreement DE-SC0000661
#marti@frib.msu.edu

ISBN 978-3-95450-131-1

receiving tank and the flow had then to be reverted and start over.

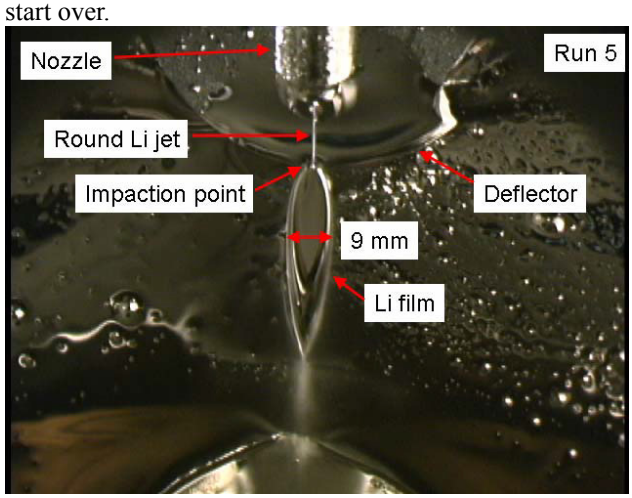

Figure 1: Formation of the liquid lithium film in the ANL test stand. The high speed jet from the nozzle hits the deflector plate forming the thin film.

The stability of the film is a major concern because variations in its thickness would create variations in the energy loss of the beam and consequently probable losses downstream from the charge stripper. The linac lattice has been designed accepting a stripper thickness variation of +/- 20%.

With the goal of measuring the film thickness the ANL group used an electron gun beam following a technique developed at GSI [8]. It utilizes an electron beam (~ 20 keV) to traverse the film under study. The electrons are scattered by the film and the fraction intercepted by a Faraday cup downstream depends on the film thickness. The process is calibrated with standard carbon foils, allowing a real time measurement of the lithium film thickness, see Fig. 2. [9]

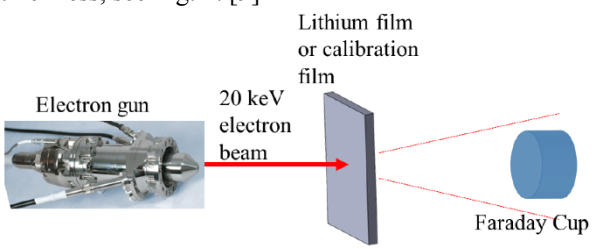

Figure 2: Monitoring the liquid film thickness in real time is possible by measuring the scattering of an electron beam, see text for details.

The experiments showed that a stable film with the correct thickness (~ 10 µm) could be established. [10]

Proton Beam on Film Experiment

A proton beam of 65 keV was used to demonstrate that the lithium film could survive the power deposited by the FRIB beam. The Low Energy Demonstration Accelerator (LEDA) ion source from the Los Alamos National Laboratory (LANL) [11] was utilized in the experiment. The source was modified with a new beamline at FRIB with the goal of later matching it to the lithium loop at ANL. The new beamline produced a 3 mm diameter beam at the location where the lithium film would later be located at ANL. The restriction of not having water cooled elements near the lithium loop was satisfied by utilizing an electrostatic einzel lens with a positive voltage of ~ 30 kV. An additional safety measure was to focus the beam through a 4 mm diameter aperture at an intermediate image.

The modified source and beamline were installed at ANL and connected to the lithium vacuum chamber used in the previous experiments. An isolated beam dump located downstream of the lithium film recorded the proton current that traversed the film. More details of the experiment can be found in [12]. It is important to note that to avoid any water in the area of the lithium loop the beam dump was air cooled, limiting the time the beam could be on the dump.

The einzel lens was used to focus the proton beam on the film until a small spot was achieved, see Fig. 3. The concern was that increasing the power density could induce the formation of bubbles in the film or disrupt it. In that case we would detect current on the Faraday cup behind the film.

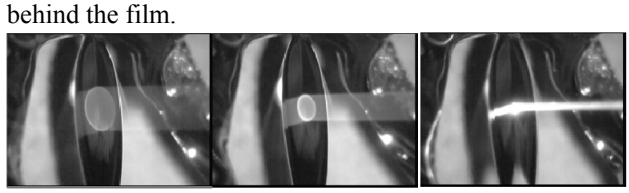

Figure 3: Photos of the proton beam (coming from the right) on the liquid lithium film. The einzel lens voltage increases from the left photo to the right photo. The film is seen to break up at the maximum power but below the interaction point with the beam.

Table 1 shows the estimated beam parameters in the experiment compared to the FRIB conditions. Due to the much shallower penetration of the low energy (65 keV) protons, the whole energy is deposited in the first 1.5 µm, giving a higher power density in the experiment than in the FRIB condition.

Figure 3 shows three photos of the lithium film with different focusing of the proton beam. The photo on the right shows the highest power density and the splitting of the film below the impact point. Even when this splitting was occurring no proton current was detected on the beam dump, indicating that the film was intact at the impact point.

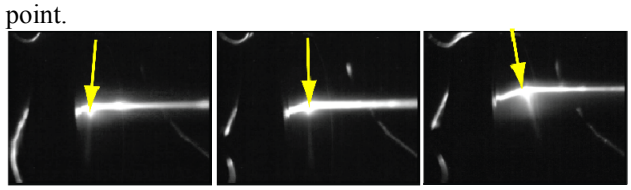

Figure 4: The beam spot is displaced from the left to the right of the lithium film showing the heat trails, visualizing the flow lines of the heated liquid.

ISBN 978-3-95450-131-1

The photos of Fig. 4 visualize the flow lines of the heated lithium. The proton beam impact point was moved in the direction transverse to the liquid flow. The flow lines seem to converge to the impact point of the lithium jet on the deflector plate, see Fig. 1.

Table 1: Comparison of the beam parameters in the FRIB case and in the proton beam experiment.

	FRIB	Exp.	Ratio
Beam power (W)	700	299	0.43
Beam size σ (mm)	0.62	0.7	1.17
Beam penetration (μm)	10	1.5	0.15
Power density (kW/mm^3)	58	129	2.2

CHARGE STRIPPER MODULE DESCRIPTION

The charge stripper consists basically of a main vacuum chamber where the lithium film is formed, an electromagnetic pump that produces the pressure to form the liquid jet, the auxiliary equipment in the lithium loop and a secondary containment steel vessel that encloses them.

Main Vacuum Chamber

The vacuum chamber that contains the nozzle and deflector is shown in Figures 5 and 6. The position of the flange where the deflector plate is mounted determines the location of the chamber in the beamline. The nozzle has to be accurately positioned with respect to the deflector and an adjustable mount is being constructed that will allow precise positioning of the impact point of the lithium jet. Two ports in the chamber connect the stripper to the beam line upstream and downstream. One other port is used for the electron beam dump (Faraday cup). Other ports in the chamber are used for observation, illumination and vacuum pumping.

The chamber is mounted on a table that can be moved in the plane transverse to the beam path. The objective is to tune the beam along the axis of the beam line and then adjust the position of the vacuum chamber to place the center of the lithium film on the beam path.

Several heater cartridges are wrapped around the chamber to maintain it at temperatures above the melting point of lithium and avoid condensation on the chamber walls.

The ports connected to the chamber as well as the tubing connecting the different components are wrapped with heating tape to be able to systematically heat and cool down the system in an ordered fashion. The goal is to start the heating from the open surfaces of the solid lithium and progress toward the center of the loop (the E&M pump). The cooling order is the opposite.

A large vacuum manifold connects the chamber to a couple of cryo-pumps that are located outside the secondary steel vessel. The pump compressors will be located outside the tunnel in the final configuration. Special care has been taken to eliminate all copper gaskets from the system because the extreme damage that lithium produces on copper products. No aluminum is present in the system either.

The viewer ports are covered with shutters unless they are in use to minimize the possible coating of them with lithium.

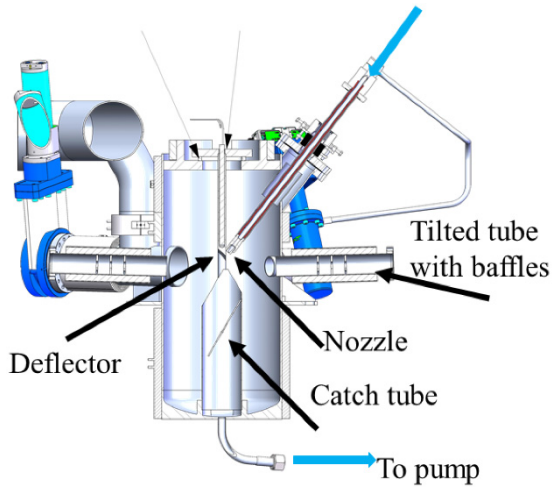

Figure 5: Main vacuum chamber showing the incoming lithium on the upper right and the exit to the pump in the lower right.

The catch tube shown in Fig. 5 has been included to minimize the splashing of the lithium on the chamber walls. The liquid film enters the tube through a narrow slit and is captured inside.

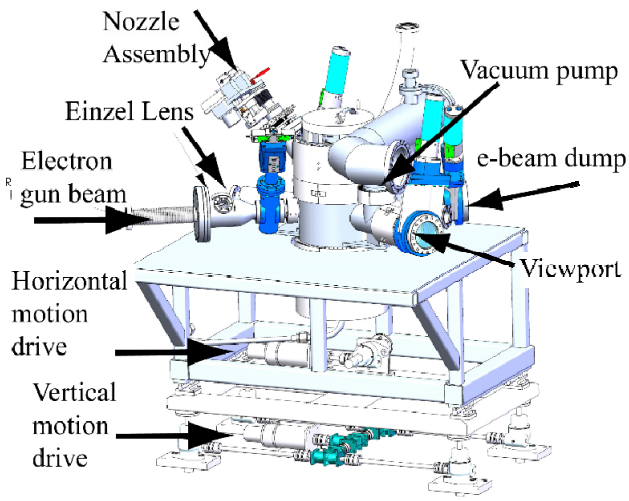

Figure 6: Description of some of the ports on the main vacuum chamber shown in the previous figure.

Secondary Containment Vessel

The secondary containment vessel has multiple purposes. It acts as a radiation shield to limit the exposure from the activated components in the main vacuum chamber. It also serves as a containment for the argon gas used to blanket a possible lithium leak from the air components (oxygen, nitrogen and water vapour).

ISBN 978-3-95450-131-1

The vessel is shown in Fig. 7 located in the test area of FRIB where it will be commissioned until installed in the FRIB tunnel in about 18 months. It is built from 25 mm thick steel plate.

Figure 7: Photo of the secondary containment vessel installed in the test area of FRIB. The vessel is 2 m long.

The panels visible in the photo will be used to mount the multiple feedthroughs. More than 100 thermal sensors will be used to monitor with redundancy the temperatures of the various zones in the internal lithium loop. About 27 heaters will be used to maintain the temperatures in the different areas. Other panels will be used to bring the power to the electromagnetic pump described below. Two large removable doors allow the insertion of the components. For normal operation the panels on top of the vessel will be removed.

Electromagnetic Pump

The helium flow is established by a permanent magnet DC electromagnetic pump. The most common liquid metal pumps utilize an AC supply but the requirement of a very constant pressure to maintain the film thickness constant rules out such pumps. We have built a high temperature version of a DC pump developed by R. Smithers [13].

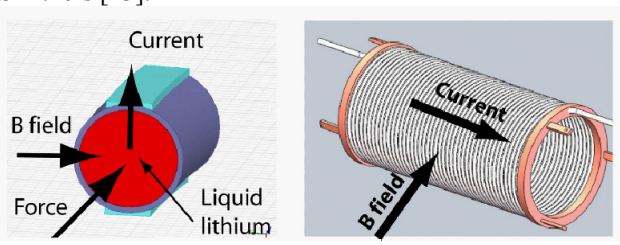

Figure 8: Principle of operation of the lithium electromagnetic pump. The DC current flows on the helical tube from turn to turn, parallel to the helix axis. The magnetic field produce by permanent magnets is radially oriented.

The lithium flows in a helical stainless steel tube subjected to a radial magnetic field generated by rings of SmCo permanent magnets and a DC current that moves from turn to turn in a direction parallel to the axis of the helical tube (see Fig. 8). The force in the lithium is then in the azimuthal direction propelling it along the helix. The permanent magnets produce a radial field of approximately 0.7 T. We estimate that the current required to achieve a pressure of 15 bars is below 2000 A. If the tests show that a lower pressure is achieved due to friction, turbulence or other effects, more rings with permanent magnets (see Fig. 9) can be added to the pump and a longer helical tube used.

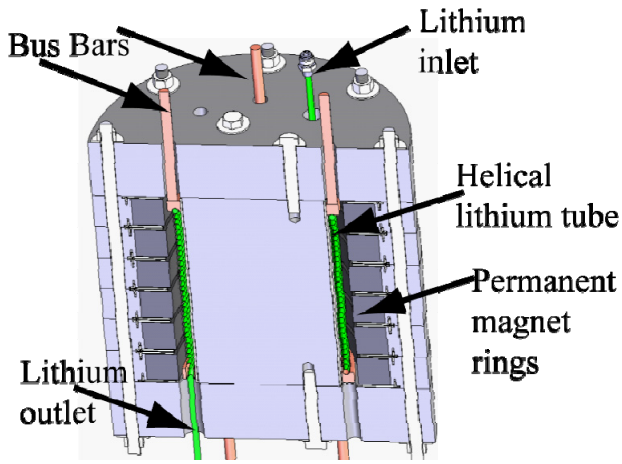

Figure 9: Basic elements of the DC electromagnetic pump. Four bus bars introduce the current into the helical tube. Six rings of permanent magnets produce the radial magnetic field. The magnet is completed by an inner core, two end caps and a return yoke.

The radial magnetic field has been measured and agrees quite well with the simulations, see Fig. 10.

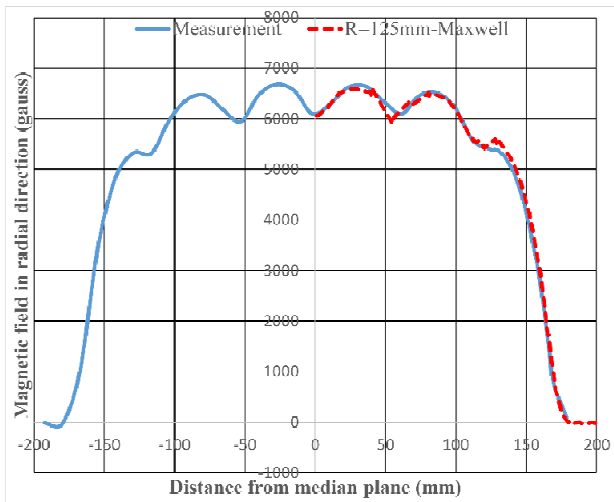

Figure 10: Measured (blue) and calculated (red) radial magnetic field in gauss vs. mm.

We are in the process of manufacturing the helical tube and we will next test the pump by itself to measure the pressure. The pump magnet during assembly is shown in Fig. 11. Five of the six permanent magnet rings are

ISBN 978-3-95450-131-1

visible as well as two of the four hydraulic cylinders used to control the motion of the components during assembly.

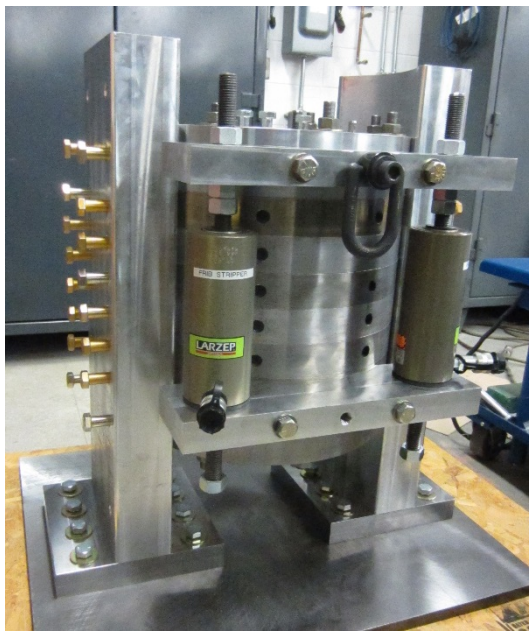

Figure 11: Liquid lithium pump during assembly. The hydraulic cylinders (only two are shown) are removed after final assembly.

HAZARD MITIGATION

Multiple precautions have been taken to minimize the possibility of a fire of the lithium in the stripper module. We have minimized the amount of liquid in the system and expect to load it with approximately five liters of liquid. We mitigate the danger in case of a leak from the lithium loop into the secondary containment vessel by maintaining it filled with argon (slightly above atmosphere) during operation. When doing maintenance through the panels on top of the containment vessel the lithium will be solid at room temperature and we will keep the argon in the vessel.

If a loss of vacuum is detected in the main chamber, we will isolate the gate valves that connect the stripper to the rest of the accelerator, turn off the electromagnetic pump and introduce argon into the stripper chamber. At the same time we will start the cool down of the system.

The multiple heaters will be controlled by a PLC that will open and close the relays feeding the AC to the heaters. Each circuit has two relays in series, with one of them permanently closed and the other relay cycling. In case that we detect that a relay stayed closed after receiving the order to open, the redundant relay will be ordered to open and interrupt the current.

CONCLUSION

The design and construction of the liquid lithium charge stripper is proceeding on schedule at FRIB. It follows a series of experimental developments and tests in a collaboration between FRIB and ANL. No show-stoppers have been found but extensive tests are planned before the stripper module is installed in the FRIB tunnel in mid-2017. During the testing period we will monitor the reliability and stability of the lithium film over long periods (~ two weeks) matching the expected duration of a FRIB experiment.

ACKNOWLEDGMENT

We would like to acknowledge the following collaborators that contributed to the work presented here: J. Specht (ANL), J. Sherman (retired LANL), N. Bultman, N. Joseph, D. Knight, R. Ronningen, M. Kostin (FRIB), I. Silverman (Soreq, Israel).

REFERENCES

[1] J. Wei et al., "FRIB accelerator status and challenges", LINAC2012, Tel Aviv, Israel, p. 417: http://accelconf.web.cern.ch/AccelConf/LINAC2012/papers/tu1a04.pdf

[2] J. Wei et al., "Status of the FRIB Project", HIAT2015, Yokohama, Japan, paper MOM1I02, these proceedings.

[3] F. Marti et al., "Charge stripper development for FRIB", IPAC 2015, p. 1339 (2015): http://accelconf.web.cern.ch/AccelConf/IPAC2015/papers/tubb1.pdf

[4] J. A. Nolen and F. Marti, "Charge Strippers of Heavy Ions for High Intensity Accelerators," Rev. Acc. Sc. and Tech. 6 (2013) 221.

[5] Thin-film liquid-lithium stripper for the RIA driver linac. DOE RIA R&D proposal (2003).

[6] DOE Handbook, "Primer on spontaneous heating and pyrophoricity", DOE-HDBK-1081-94, 1994.

[7] Y. Momozaki et al., "Development of a liquid lithium thin film for use as a heavy ion beam stripper", J. Inst. 4, p. 04005, doi:10.1088/1748-0221/4/04/P04005.

[8] R. Mann et al., "On-line Target Control", GSI Scientific Report 2003: https://www-alt.gsi.de/informationen/wti/library/scientificreport2003/files/196.pdf

[9] S. Kondrashev et al., "Upgrade of the FRIB Prototype Injector for Liquid Lithium Film Testing," PAC09, May 2009, Vancouver, BC, Canada, p. 1656: http://accelconf.web.cern.ch/AccelConf/PAC2009/papers/tu6rfp048.pdf

[10] C. B. Reed et al., (2011) "FRIB lithium stripper thickness and stability measurements", ANL report: ANL/NE-11/01 (2011).

[11] J. Sherman et al., "Status report on a DC 130 mA, 75 keV proton injector. Rev. Sci. Instrum. (1998) doi:10.1063/1.1148706.

[12] Y. Momozaki et al., "Proton beam-on-liquid lithium stripper film experiment", J. Radioanal. Nucl. Chem. 305, p. 843 (2015). DOI 10.1007/s10967-015-4074-9.

[13] R. Smither, "Summary of the operating characteristics of the ANL liquid metal pump after its latest modification (AGP-III-M), 9-20-95.

ISBN 978-3-95450-131-1

UPGRADE OF THE UNILAC FOR FAIR

L. Groening[1], S. Mickat[1], A. Adonin[1], W. Barth[1,3], X. Du[1], Ch.E. Düllmann[1,3,4], H. Hähnel[2], R. Hollinger[1], E. Jäger[1], M.S. Kaiser[1], U. Ratzinger[2], A. Rubin[1], P. Scharrer[1,3,4], B. Schlitt[1], G. Schreiber[1], A. Seibel[1,2], R. Tiede[2], H. Vormann[1], C. Xiao[1], C. Zhang[1]
[1]GSI, D-64291 Darmstadt, Germany
[2]Goethe University of Frankfurt, D-60438 Frankfurt, Germany
[3]Helmholtz Institute Mainz, Mainz, Germany
[4]Johannes Gutenberg-University, Mainz, Germany

Abstract

The UNIversal Linear Accelerator (UNILAC) at GSI serves as injector for all ion species from protons to uranium since four decades. Its 108 MHz Alvarez type DTL providing acceleration from 1.4 MeV/u to 11.4 MeV/u has suffered from material fatigue. The DTL will be replaced by a completely new section with almost same design parameters, i.e. pulsed current of up to 15 mA of $^{238}U^{28+}$ at 11.4 MeV/u. A dedicated source terminal & LEBT for operation with $^{238}U^{4+}$ is currently constructed. The uranium source needs to be upgraded in order to provide increased beam brilliances and for operation at 2.7 Hz.

INTRODUCTION

GSI is currently constructing the Facility for Ion and Antiproton Research (FAIR) [1]. It aims at provision of 3×10^{11}/s uranium ions at 1.5 GeV/u. Due to its high rigidity uranium imposes the highest challenges to the accelerator chain wrt fields and machine protection. Additionally, a total of 4×10^{12}/s cooled anti-protons are to be delivered. The complete accelerator chain is depicted in Fig. 1. The existing UNIversal Linear ACcelerator UNILAC will provide all primary ions but protons. A dedicated proton linac is currently under design and construction [2]. In order to deal with the FAIR requirements in the upcoming decades the UNILAC needs a considerable upgrade.

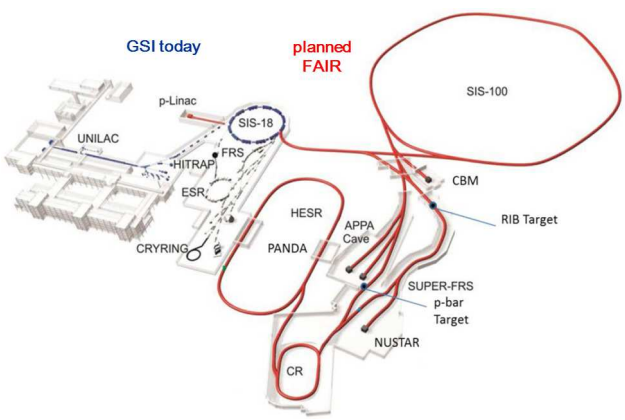

Figure 1: Facility for Anti proton and Ion Research (FAIR) under construction at GSI.

The existing UNILAC (Fig. 2) together with the subsequent synchrotron SIS18 serves as injector for FAIR. The

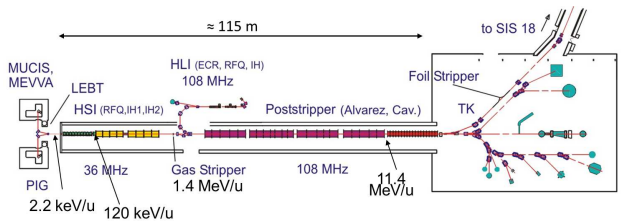

Figure 2: The UNIversal Linear ACcelerator (UNILAC) at GSI.

UNILAC has three ion source terminals that can be operated in pulse-to-pulse switching mode at 50 Hz. One terminal is equipped with an ECR source providing highly charged ions. Another terminal houses a Penning source providing low intensity beams at intermediate charge states. The third terminal is dedicated to provision of intense beams of low-charged ions. It can be equipped with various source types as MUCIS and CHORDIS for light to intermediate-mass ions for instance. Intense heavy ion beams are produced in a MEVVA or VARIS source at 2.2 keV/u. Beams are bunched and pre-accelerated to 120 keV/u along a 9 m long RFQ operated at 36 MHz. Afterwards two IH-cavities provide for acceleration to 1.4 MeV/u. For uranium the highest particle numbers are obtained by using the charge state $^{238}U^{4+}$. After the IH-DTL the acceleration efficiency is increased by passing the beam through a gaseous stripper which delivers a mean charge state of $^{238}U^{28+}$ at its exit. This increase of charge state is at the expense of intrinsic particle loss as prior to 2014 about 87% of the uranium ions are stripped to a charge state different from 28+. After dispersive selection of the desired charge state the beam is matched to the subsequent post stripper Alvarez DTL. The latter is operated at 108 MHz and comprises five tanks. Its exit beam energy is 11.4 MeV/u being the injection energy for the synchrotron SIS18. The UNILAC design parameters are listed in Table 1. The age of the UNILAC together with the requirement to provide reliable and intense beams for the upcoming FAIR era calls for a revision of the UNILAC. In the following the planned upgrade activities are described.

SOURCE, LEBT, MEBT, AND RFQ

In order to provide the mean uranium intensity required for FAIR the source has to be operated with a repetition rate of 2.7 Hz. Although this target has been reached for lead

ISBN 978-3-95450-131-1

Table 1: Beam Design Parameters for the Upgraded UNILAC

Ion A/q	≤ 8.5	
Beam Current	1.76·A/q	mA
Input Beam Energy	1.4	MeV/u
Beam Energy	11.4	MeV/u
Emit. (norm., tot.) hor/ver	0.8/2.5	µm
Beam Pulse Length	200	µs
Beam Repetition Rate	10	Hz
Rf Frequency	108.408	MHz

ions, reliable operation with uranium is currently limited to about 1.5 Hz. New uranium alloys shall be investigated as well as the reduction of the source beam pulse length in order to reduce the gas load in the plasma chamber. The latter mitigates the production of $^{238}U^{4+}$ ions by recombination. The existing LEBT includes two bends which impose dispersion and hexapolar fringe fields. Additionally, operation and handling of uranium comes along with restrictions from safety requirements. For these reasons a new and dedicated uranium branch is under design as shown in Fig. 3. It is a

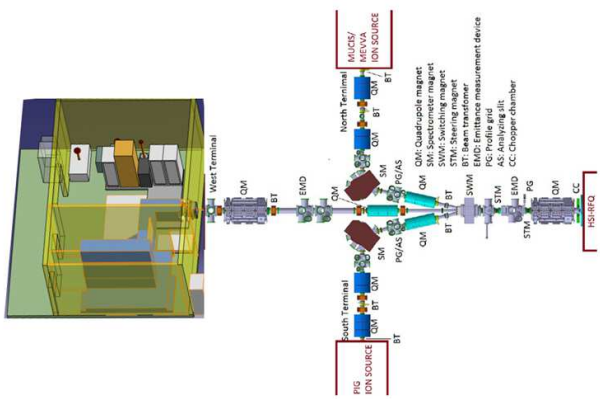

Figure 3: The existing north and south ion source terminals and LEBT branches together with the new uranium terminal (west).

straight LEBT comprising two quadruplets and one triplet. The source will deliver several charge states of uranium but only $^{238}U^{4+}$ is accepted by the RFQ. The fractions of other charge states (mainly 3+) are reduced by chromaticity together with an circular iris located at a beam waist of the charge state 4+. Reference [3] is on the detailed design of the new LEBT.

The RFQ suffered from sparking during operation with varying rf-duty cycles and rf-amplitudes. The attainable rf-voltages are about 10% below the required values for uranium. This leads to serious degradation of longitudinal beam quality from insufficient bunching. Additionally, the beam divergence at the RFQ exit is too large, triggering losses inside the subsequent super lens, which in consequence also has to be operated at lower voltages causing further degradation of beam quality. The design of the RFQ will be revised such that lower surface fields are applied at the expense of reduced acceptance.

The super lens is a non-accelerating RFQ, i.e. being used for focusing in all three planes. Accordingly, transverse and longitudinal focusing strengths are coupled. In total the present MEBT offers just four knobs to tune its matching performance to the IH-DTL: two quadrupole gradients, one rf-amplitude, and one rf-phase. This limitation together with too low rf-amplitudes (from sparking) causes poor longitudinal matching to the subsequent IH-DTL. A new MEBT design foresees two symmetric triplets and one buncher, i.e. four additional tuning knobs [4].

HIGH PRESSURE H_2-STRIPPER

For time being as stripping medium a continuous jet of nitrogen has been used at a back pressure of 4 bar. The achieved stripping efficiency from $^{238}U^{4+}$ to $^{238}U^{28+}$ was 13%. Last year a pulsed gas stripper cell has been tested. It injects short gas pulses (0.5 ms) at back-pressures of up to 120 bar into the stripping chamber. Measured charge state distributions behind the stripper for some stripper configurations are compared in Fig. 4. A relative increase of $^{238}U^{28+}$ intensity of 60% has been measured [5] using H_2. Future tests aim at increasing the back pressure to about 300 bar and at routine operation of this new stripping set-up. References [5–7] are on the successful campaign of increasing the stripping efficiency.

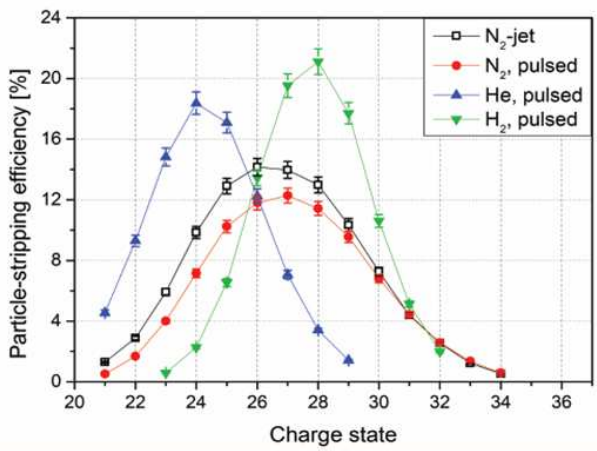

Figure 4: Uranium charge state distributions for an incoming beam of $^{238}U^{4+}$ at 1.4 MeV/u for different gas stripper configurations [7].

ROUND TO FLAT BEAM TRANSFORMATION

As seen from Table 1 the final transverse design emittances of the UNILAC differ by a factor of three. This requirement is imposed by the horizontal multi-turn injection (MTI) scheme to fill the synchrotron SIS18 [8]. Beams provided by linacs are generally round, i.e. the horizontal

ISBN 978-3-95450-131-1

and the vertical emittance are equal. Although the product of the two linac emittances is smaller than the product of the two corresponding effective synchrotron acceptances, the horizontal linac emittance exceeds the effective horizontal acceptance. Thus a scheme for convenient emittance re-partitioning has been proposed and experimentally demonstrated at GSI with a nitrogen beam [9–11]. The round-to-flat adopter is shown in Fig. 5 together with measured final phase space distributions at its exit. Charge state stripping inside a solenoid is required together with a skew triplet to arbitrarily partition the transverse emittances by varying the solenoid field strength only. A corresponding increase in MTI efficiency was measured [12].

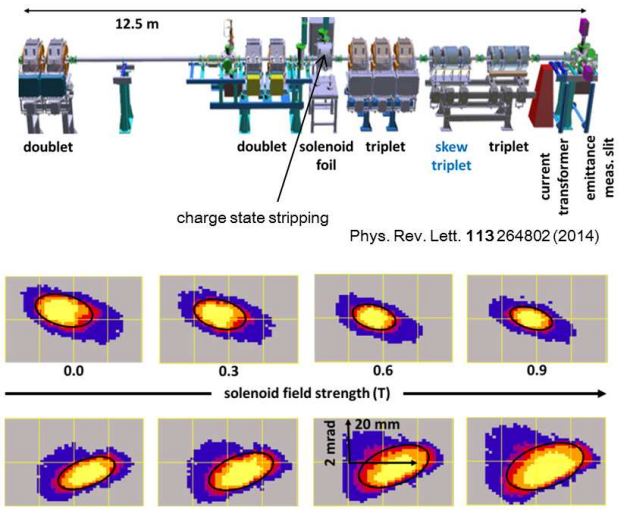

Figure 5: The EmTEx beam line providing round-to-flat transformation.

GSI currently designs a set-up to flatten beams of uranium along the gaseous stripper section. To this end 4d transverse beam diagnostics is required, i.e. the four 2nd order inter-plane correlations <xy>, <xy'>, <x'y>, and <x'y'>, must be measurable. To our knowledge such measurements never were conducted successfully before at ion energies beyond about 150 keV/u. Using the EmTEx set-up these correlations were measured for $^{238}U^{28+}$ ions at 11.4 MeV/u with a beam current of 1.7 mA. Regular slit/grid measurements were done in combination with skewed quadrupoles. Figure 6 compares horizontal and vertical emittance measurements behind the skew triplet together with calculations ignoring/including inter-plane correlations. As the measurements could be reproduced, the inter-plane correlations were determined to sufficient accuracy. A round-to-flat transformer will be installed along the gaseous stripper section if it is foreseeable that the other upgrade measures will not be sufficient to reach the UNILAC design beam parameters with uranium.

NEW POST STRIPPER ALVAREZ DTL

The existing post stripper DTL suffered considerably from material fatigue during that last four decades. Thus the amount of resources required for its maintenance increases

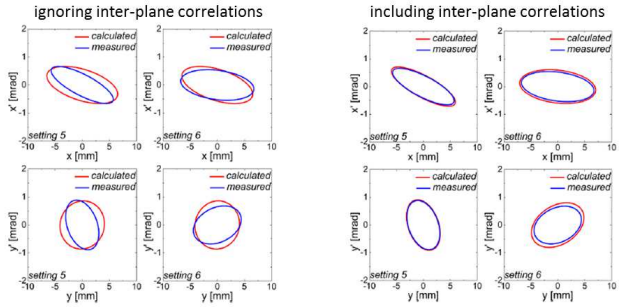

Figure 6: Projected rms ellipses from measurements (blue) and from calculations (red) ignoring inter-plane correlations (left) and including inter-plane correlations (right).

continuously. The section has to be replaced by a completely new DTL. The beam parameters of the new post stripper DTL are the same as for the existing one except the beam duty cycle. It will be limited to beam pulse lengths of 200 μs at a repetition rate of 10 Hz. The new UNILAC will serve just as an injector for the FAIR facility. Accordingly, the mixed operation between different rf-amplitudes and rf-pulse length, that caused damages at the cavity surface and limited the rf-amplitudes, will not be applied in the future. As beam quality is of utmost relevance for a low duty cycle injector, GSI aims at an Alvarez-type DTL. They proved to be reliable working horse accelerators. The related beam dynamics is fully understood even if considerable space charge is included. Periodic beam 3d-envelope solutions are properly defined as well as the procedure to match the incoming beam to these solutions. For IH-DTLs for time being we did not find a procedure to assure matched beam transport and acceleration that provides maximum mitigation of beam emittance growth from space charge [13].

Rf-Power Supply Chain

The existing rf-power systems are based on all-in-one technology of the 1970ies and are currently modernized to modular set-ups. Control and interlock units will be separated from the power units. A new 1.8 MW cavity amplifier prototype is under development. It is based on the widely-used THALES tetrode TH 558SC, thus promising availability for at least 25 years. The first new amplifier is tendered and will be installed and tested in the existing rf-gallery until 2017. New 150 kW solid state driver amplifiers will replace existing tube drivers. A digital LLRF system designed by industry was integrated into an existing amplifier driving a single gap resonator and was tested including ion beam tests. An overview of the RF system design and of the upgrades including results of digital LLRF tests is given in [14].

Drift Tube Geometry

The new DTL will comprise five tanks and the layout of the new cavities is progressing. It aims at optimization of the ratio of shunt-impedance to electric surface field [15]. The latter shall be limited to 1.0 Kilpatrick. For each tank a maximum rf-power of 1.8 MW is available of which about

ISBN 978-3-95450-131-1

0.25 MW is beam load. Currently the beta-profiles for acceleration to 5.39 MeV/u are available. A new shape of drift tube plates (Fig. 7) has been found that allows saving 17% of rf-power with an increase of surface field strength by 8% wrt the existing design. The shape of the tube plate does

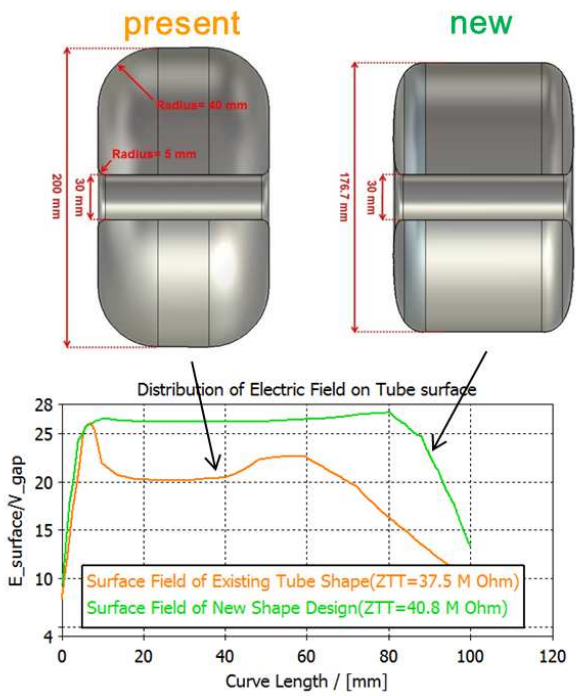

Figure 7: Comparison of the present and new drift tube design.

not include straight sections and is defined through about 200 fixed points. This approach provides a smooth surface field distribution and should lower the sparking rate. It does not cause significant additional cost for production nor it imposes restrictions wrt the achievable tolerances. Each drift tube along one tank will have the same end plate shape. The rf-frequency tuning of each cell is done through adoption of the drift tube length.

Stabilization of the accelerating field is done through well-considered orientations of the stems that keep the drift tubes [15]. As the drift tubes have to be provided with cooling water and electrical current for the quadrupoles, each tube is kept by two stems. It turned out that the orientation of the two stems plays a significant role in the suppression of parasitic modes as shown in Fig. 8. This innovative concept of field stabilization will be tested using a cold rf-model. Figure 9 illustrates how this model allows for variation of the stem orientation. Additionally, the end surfaces of each drift tube can be exchanged by simply unskrewing them from the main drift tube body.

Transverse Focusing

The transverse phase advance (zero current) has to be increased from 53° to 67° in order to avoid emittance growth

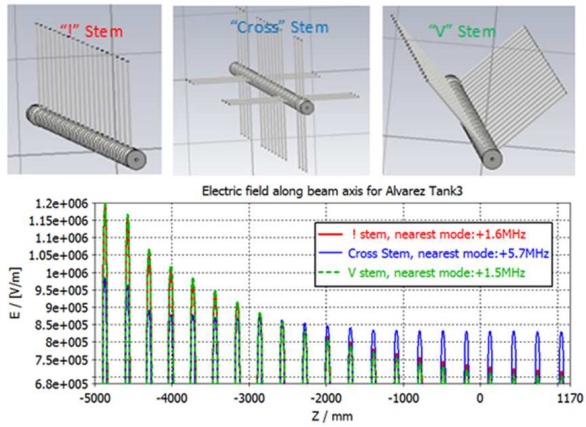

Figure 8: Several schemes of orientations of the DTL stems and their effect on the field stabilization.

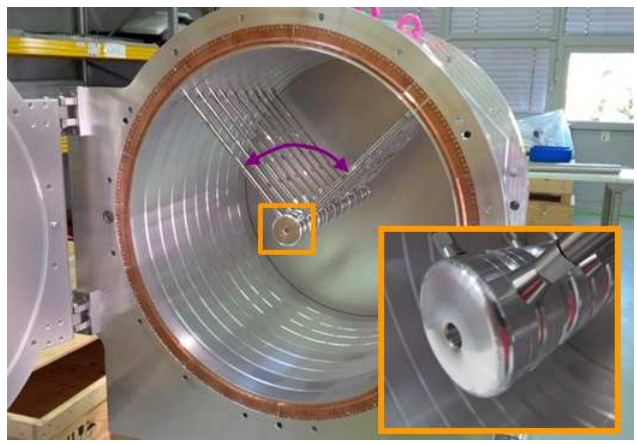

Figure 9: 1:3 scaled cold model of the first new Alvarez cavity.

from space charge driven resonances. Additionally, the emittance partition of flattened beams shall be preserved along the DTL by asymmetric focusing, i.e. the vertically focusing quadrupoles will be driven with stronger gradients wrt horizontally focusing quadrupoles [16]. Figure 10 shows how asymmetric transverse focusing avoids the corresponding transverse resonances driven by flat beams. Special care will be taken for proper beam envelope matching along inter-tank sections. These sections impose interruptions of the periodicity of the DTL lattice. If not being well-designed they will trigger emittance growth from mismatch in all three planes.

ALTERNATIVE DTL DESIGN BASED ON IH-CAVITIES

Compared to Alvarez cavities H-mode resonators feature much higher shunt impedances. Additionally, they require much less transverse focusing quadrupoles. They have the potential to impose an alternative to Alvarez-type DTLs at reduced cost and even allow for an eventual future energy upgrade to about 50 MeV/u using the existing linac tunnel. The Goethe University at Frankfurt designs a post-stripper

ISBN 978-3-95450-131-1

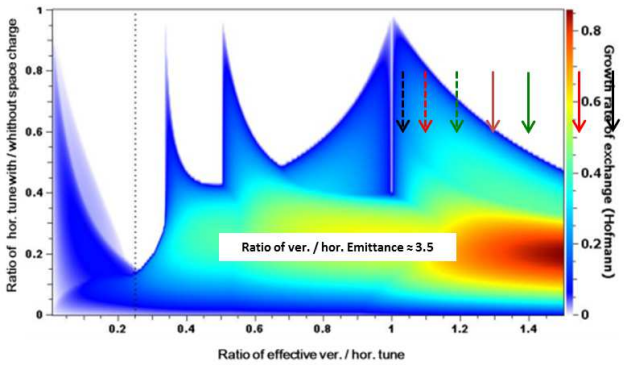

Figure 10: Stability chart and working points for the ver/hor emittance ratio of 3.5 at the entrance to the existing Alvarez type DTL of the GSI UNILAC assuming different focusing strengths in the transverse planes.

DTL for the UNILAC upgrade based on six IH-cavities as shown in Fig. 11. Currently extensive studies on the beam

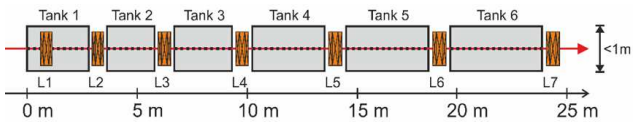

Figure 11: Conceptual layout of a DTL based on six IH cavities.

dynamics layout are performed. Figure 12 plots simulated emittance growth rates along the IH-DTL as functions of the depressed transverse phase advance. The study aims at providing straight forward procedures (comparable to Alvarez-DTLs) for setting phase advances, periodic envelopes, and properly matched settings.

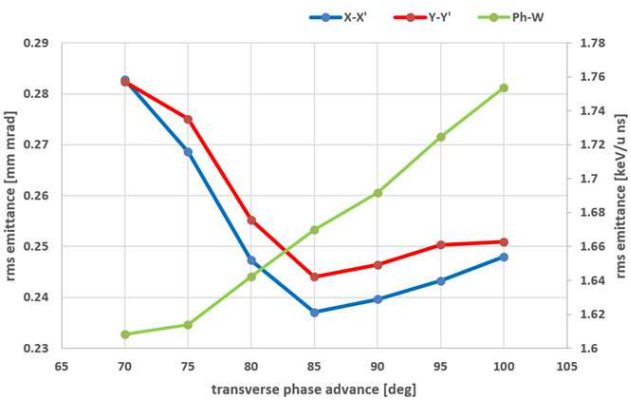

Figure 12: Simulated rms emittances at the exit of the IH-DTL as functions of the depressed transverse phase advance for a current of 17 mA of $^{238}U^{28+}$.

ESTIMATED PERFORMANCE AFTER UPGRADE

Table 2 summarizes the presented upgrade activities together with the corresponding estimated gains in beam current and emittance. The estimate assumes an Alvarez-type post-stripper DTL. Recent modifications of the source extraction system may indicate that currents in excess of 20 mA can be extracted under preservation of the emittances. But further investigations are required prior to commit to this value.

Table 2: Estimate of Expected $^{238}U^{28+}$ Performance After the Upgrade

section	I [mA]	ϵ_x [µm]	activity
	18.0	0.55	source development
LEBT + RFQ			new LEBT, RFQ upgrade
	16.2	0.63	
MEBT + IH-DTL			new MEBT
	14.6	1.1	
stripper			high press. H_2- jet
	18.4	1.2	
round-to-flat			installation
	16.5	0.49	
Alv. DTL			new DTL
	14.1	**0.73**	
target	*15.0*	*0.80*	

REFERENCES

[1] FAIR Baseline Technical Report, Vol. 2, GSI Darmstadt, Germany, 2006, p. 335.
[2] R. Brodhage et al., Proc. of IPAC2015 Conf. (2015).
[3] C. Xiao et al., NIM A 788 173 (2015).
[4] H. Hähnel et al., Proc. of LINAC2014 Conf. (2014).
[5] W. Barth et al., PRSTAB 18, 040101 (2015).
[6] P. Scharrer et al., J. Radioanal. Nucl. Chem. 305, 913 (2015).
[7] P. Scharrer et al., presented at HIAT'15, Yokohama, Japan, September 2015, paper TUA1C01, these proceedings.
[8] S. Appel et al., Proc. of IPAC2015 Conf (2015).
[9] L. Groening, PRSTAB 14, 064201 (2011).
[10] C. Xiao et al., PRSTAB 16, 044201 (2013).
[11] L. Groening et al., PRL 113 264802 (2014).
[12] L. Groening et al., Proc. of IPAC2015 Conf. (2015).
[13] A. Orzhekhovskaya et al., Proc. of IPAC2014 Conf. (2014).
[14] B. Schlitt et al., Proc. of LINAC2014 Conf. (2014).
[15] X. Du et al., Proc. of IPAC2015 Conf. (2015).
[16] L. Groening et al., Proc. of LINAC2014 Conf. (2014).

ISBN 978-3-95450-131-1

A PULSED GAS STRIPPER FOR STRIPPING OF HIGH-INTENSITY, HEAVY-ION BEAMS AT 1.4 MeV/u AT THE GSI UNILAC

P. Scharrer[1,2,3], W. Barth[1], M. Bevcic[2], Ch. E. Düllmann[1,2,3], L. Groening[2], K.P. Horn[2], E. Jäger[2], J. Khuyagbaatar[1], J. Krier[2], A. Yakushev[2]

[1]Helmholtz-Institut Mainz, 55099 Mainz, Germany
[2]GSI Helmholtzzentrum für Schwerionenforschung GmbH, 64291 Darmstadt, Germany
[3]Johannes Gutenberg-Universität Mainz, 55099 Mainz, Germany

Abstract

The GSI UNILAC in combination with SIS18 will serve as a high-current, heavy-ion injector for the future FAIR. It has to meet high demands in terms of beam brilliance at a low duty factor (100 µs beam pulse length, 2.7 Hz repetition rate). An advanced 1.4 MeV/u gas stripper setup has been developed, aiming at an enhanced yield into the required charge states. The setup delivers short, high-density gas pulses in synchronization with the beam pulse. This provides an increased gas density at a reduced gas load for the differential pumping system. In recent measurements, high-intensity, heavy-ion beams of U^{4+} were successfully stripped and separated for the desired charge state. The modified stripper setup, as well as major results, are presented, including a comparison to the present gas stripper based on a N_2 gas-jet. The stripping efficiency into the desired 28^+ charge state was significantly increased by up to 60 % using a hydrogen stripper target while the beam quality remained similar.

INTRODUCTION

The UNIversal Linear ACcelerator (UNILAC) will serve as part of an injector system for the Facility for Antiproton and Ion Research (FAIR), currently under construction at GSI in Darmstadt, Germany. A key projectile for FAIR is the heavy ion ^{238}U [1]. To meet the beam requirements for FAIR, an upgrade program of the UNILAC has started to increase the delivered uranium beam intensities. The aim is to deliver short-pulsed, high-current, high-intensity U^{28+} beams with a repetition rate of 2.7 Hz to the subsequent SIS18 accelerator.

In the UNILAC, a gas stripper is used to increase the charge state of the beam ions at an energy of 1.4 MeV/u. Currently, the gas stripper operates with a super-sonic N_2-jet as a target, created by a laval nozzle with a back-pressure of up to 0.45 MPa [2]. To be able to deliver the desired beam parameters for FAIR-injection, an upgrade program of the gas stripper is ongoing, aiming at increasing the stripping efficiency into the U^{28+} charge state. Improving the performance of the gas stripper for uranium operation has proved difficult in the past, predominantly because of the high gas load for the differential pumping system using the continuous gas-jet [3].

A new approach was tested by applying a pulsed gas injection to the existing stripper setup, using a newly developed setup replacing the laval nozzle. The aim is to temporally increase the gas density in the interaction zone of the gas stripper just when a beam pulse is passing. The reduction of the gas load allows increased gas densities, which enables the practical use of other promising gases as stripper targets by providing the conditions to reach equilibrated charge-state distributions.

In first measurements in February 2014, the functionality of the pulsed gas cell was tested. At the end of 2014, another measurement series was conducted using a wide range of different gases to test the stripping performance for uranium beams and to increase the stripping efficiency into U^{28+}.

HEAVY-ION STRIPPER OPERATION

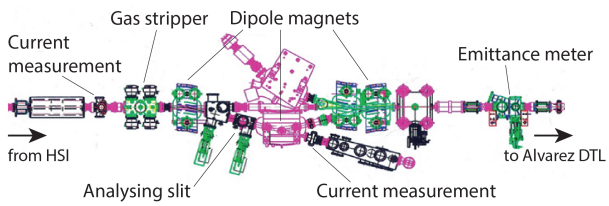

Figure 1: Layout of the UNILAC gas stripper section between the HSI and the Alvarez DTL.

In the UNILAC, the ion beams are delivered by three different ion sources in a time sharing mode. For the production of heavy ions like ^{238}U, a new Vacuum ARc Ion Source [4] is used. The prepared ion beams are delivered to the High Current Injector (HSI) [5]. The HSI comprises of a combination of a Radio Frequency Quadrupole structure (RFQ) and an interdigital H-structure drift tube linac (DTL), and accelerates the ion beams up to 1.4 MeV/u. Behind the HSI, the ion beams are focused onto a charge-analysing slit behind the gas stripper by two quadrupole doublets. The UNILAC stripper section is shown in Fig. 1. In the gas stripper, the charge state of the beam ions is increased by charge-changing processes occurring in the collisions between beam ions and neutral gas particles. Behind the stripper, the beam ions are separated by their charge state using a system of three dipole magnets. To select a charge state for further acceleration, an analysing slit is used behind the first dipole magnet at a deflection angle of 15°.

With the existing N_2-jet stripper, the stripping efficiency into the U^{28+} charge state at maximum back-pressure of

ISBN 978-3-95450-131-1

0.45 MPa is about 12.7 %. The average charge state of the corresponding charge-state distribution is about 26.8.

In the course of the ongoing upgrade program, several measurements were conducted with the aim to increasing the uranium stripping performance. In an attempt to use carbon foils instead of the N_2-jet, average charge states up to +39 were achieved at stripping efficiencies of about 20 % [6]. However, the lifetime of the foils was strongly limited to a few hours due to thermal and irradiation stress effects. At increased beam currents at FAIR, the use of stripper foils is not feasible for uranium beam operation and would set a limitation for the repetition rate. The practical use of other promising gas targets, like hydrogen, at sufficient densities was hindered by the limitation of the pumping system due to an increased gas load, using the continuous gas-jet stripper [3].

PULSED GAS CELL

To be able to increase the gas density, the continuous gas-jet is replaced with a pulsed gas injection. The short beam pulse width at a relatively low duty cycle is exploited to lower the total gas load for the pumping system, by only applying gas when a beam pulse passes the gas stripper. Due to this decrease of the gas-load, the back-pressure on the gas inlet can be increased significantly, enabling higher gas densities during the stripping process.

The short pulsed gas injection is realized by a pulsed gas valve, normally used in automotive applications. The valve is synchronized with a timing signal from the accelerator main control unit. When a beam pulse passes the gas stripper, the valve opens to increase the gas density during the stripping process and closes immediately afterwards.

The flange on top of the main stripper chamber was exchanged with a newly-developed flange featuring the pulsed gas valve. The pulsed gas valve is placed directly above the beam line in a specially designed build-up. To prevent the gas from instantaneous exhaustion, a T-fitting (44 mm length in beam direction) was added below the injection point matching the apperture of the beam line in the stripper (22 mm). The stripper-setup uses the same pumping system as the gas-jet stripper (see [7]). It consists of a roots vacuum pump (pumping performance: 8000 m^3/h) directly below the main stripper chamber and four turbo pumps (pumping performance: 1200 m^3/h each) in the adjacent differential pumping sections. Several additional vacuum pumps are installed along the adjacent beam line.

A first setup of the pulsed gas cell was tested in the beginning 2014 [8]. It was since adjusted to enable higher back-pressures as well as shorter opening times. This modified setup is described in [7, 9].

MEASUREMENTS AND RESULTS

During the second measurement series in November 2014, various different gases were applied covering a wide range for the back-pressure on the valve (2–12 MPa). The stripper gases H_2, He, Ne, N_2, O_2, Ar, and CO_2 were used. An U^{4+} beam with a beam pulse length of 0.1 ms at a repetition rate of 1 Hz was used as a reference beam for FAIR-injection. The opening time of the valve was set to 0.5 ms to achieve a maximum gas density during beam pulse transit for the applied back-pressure range.

To evaluate the quality as a stripper gas, the stripping efficiency into each populated charge state and the beam quality, namely the energy-loss and the horizontal and vertical beam emittance, were measured. The stripping efficiency into a specific charge state, q_i, is the ratio of the number of ions going into this charge state and the total number of ions in the incident charge state (+4 for uranium beam operation) in front of the stripper. To obtain the number of ions, the beam current is measured using beam transformers (see current measurements in Fig. 1) and then divided by the charge state of the ions. The energy of the beam ions is measured in time-of-flight measurements using phase probes along the beam line. To determine the energy-loss due to the collisions inside the stripper gas, the beam energy with and without applied gas is measured behind the stripper and subtracted from each other. The beam emittance was measured using a slit-grid measurement system behind the charge separation (see Fig. 1) [10]. At a certain target thickness, the cross-sections for the electron-capture and electron-loss processes reach an equilibrium. At this point, the charge-state distribution does not change anymore with increasing target-thickness. For all gases, except hydrogen, this equilibrium was reached within the measured pressure range of 2-12 MPa and the corresponding charge-state distributions are shown in Fig. 2. The charge-state distributions of uranium after passing different gas-targets is shown, plotting the stripping efficiency against the populated charge states. The heavier gases measured show broad charge-state distributions at average charge states between 25 and 27. For the light gases, H_2 and He, the charge-state distribution is more narrow, resulting in increased stripping efficiencies for the populated charge states. For H_2 compared to He, the average charge state of the distribution is increased. For H_2, the shown distribution was measured at 12 MPa. The charge-state distributions for uranium after passing through H_2 for an increasing target thickness are shown in Fig. 3. The target thickness is estimated from energy-loss measurements using SRIM2013 [11]. The solid lines are curves fitted to the data using a gaussian fit with a skewness correction. For increasing target thickness, the average charge state rises from about +23 to +28. The width of the distribution, as well as the maximum charge fraction, does not change within the error range for increasing target thickness.

By applying H_2 as a stripper gas, the stripping efficiency into U^{28+} could be increased from 12.7 % for the N_2-jet stripper to 20.4 %. Together with an optimization of the prestripper UNILAC for high-current uranium beam transport, an U^{28+}-intensity record was achieved behind the charge separation, using the new pulsed gas cell. An U^{28+}-beam current of 7.8 mA was measured behind the charge separation. The beam emittance as well as the energy-loss show a beam quality similar to the N_2-jet stripper. This achieve-

ISBN 978-3-95450-131-1

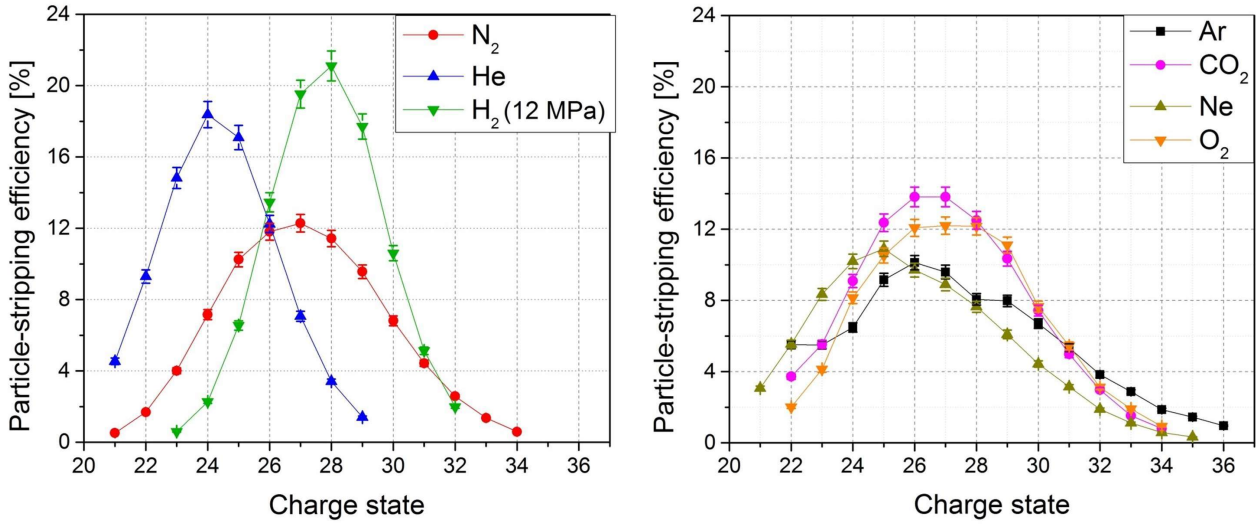

Figure 2: Equilibrated charge-state distributions showing the stripping efficiencies for U on He, Ne, N_2, O_2, Ar, and CO_2, measured with the pulsed gas cell at 1.4 MeV/u beam energy. For H_2, the shown charge-state distribution is still not equilibrated and obtained at 12 MPa.

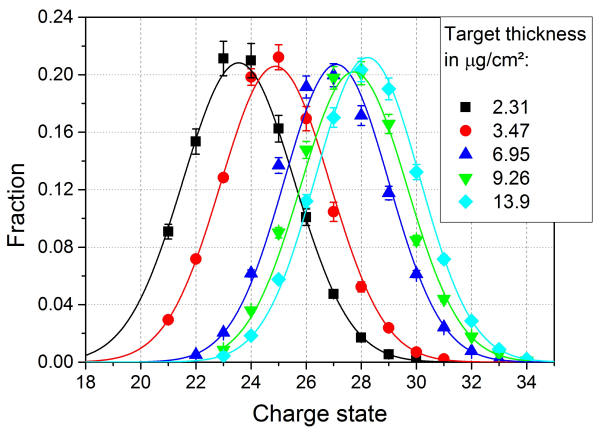

Figure 3: Charge-state distributions for U on H_2 at increasing target thickness, measured at 1.4 MeV/u beam energy. The solid curves are fitted to the data using a gaussian fit with a skewness correction.

ment is described in [9]. The beam quality, i.e. the measured beam emittance and energy-loss, compared to the preceding N_2-jet stripper is shown in Table 1.

Table 1: Comparison of U^{28+} Stripping Performance

Value	N_2-jet	pulsed H_2
Max. U^{28+} current	4.5 mA	7.8 mA
Stripping efficiency (U^{28+})	12.7 %	20.4 %
ϵ_x (90 %, total, norm.)	0.76 µm	0.7 µm
ϵ_y (90 %, total, norm.)	0.84 µm	0.93 µm
Energy-loss	20 keV/u	12 keV/u

CONCLUSION AND OUTLOOK

The modified setup of the pulsed gas cell was tested with an uranium beam applying various gases. The light gases hydrogen and helium show more narrow charge-state distributions then the heavier gases, resulting in increased stripping efficiencies into the populated charge states. Measurements with hydrogen at maximum back-pressure (12 MPa) show increased stripping efficiencies into the desired U^{28+}-charge state. This improvement resulted in higher beam currents behind the stripper, enabling a new U^{28+}-intensity record at the GSI UNILAC. However, an equilibrated charge-state distribution for uranium on hydrogen could not be observed in the applied back-pressure range.

To be able to measure equilibrated charge-state distributions using hydrogen, a new setup for the pulsed gas cell is currently being developed, featuring advanced pulsed gas valves. The new generation of valves enables increased back-pressures as well as an increased gas flow due to an enlarged opening. In addition to this, two valves are used to be able to increase the gas density inside the interaction zone even more. A new control unit for the valves enables a reduction of the opening time due to faster opening of the valve. In the course of a measurement series with this enhanced setup in July 2015, back-pressures up to 25 MPa were used at a reduced opening time of 0.4 ms. Increased gas densities for the stripping process are expected. With the new enhanced setup, additional measurements with uranium beams are envisaged.

ACKNOWLEDGEMENT

The authors are grateful for the support of the GSI ion-source and UNILAC staff. Stimulating discussions with V. P. Shevelko are gratefully acknowledged.

ISBN 978-3-95450-131-1

REFERENCES

[1] FAIR baseline technical report, Vol. 2 (2006) GSI Darmstadt, p. 335f.

[2] W. Barth, P. Forck, Proceedings of LINAC2000, 21–25th August, Monterey, USA, pp. 235–237.

[3] B. Schlitt et al., Proceedings of IPAC2013, 12–17th May, Shanghai, China, pp. 3779–3781.

[4] R. Hollinger et al., Nucl. Instr. Methods B 239 (2005) pp. 227–244.

[5] U. Ratzinger et al., Proceedings of LINAC1996, 26–30th August, Geneva, Switzerland, pp. 288–292.

[6] W. Barth et al., Proceedings of LINAC2010, 12–17th September, Tsukuba, Japan, pp. 154–156.

[7] P. Scharrer et al., Proceedings of IPAC2015, 3rd–8th May, Richmond VA, USA, pp. 3773–3775.

[8] P. Scharrer et al., J. Radioanal. Nucl. Chem., Vol. 305, Issue 3 (2015), pp. 837–842.

[9] W. Barth et al., Phys. Rev. ST AB 18 (2015) 040101.

[10] G. Riehl et al., Proceedings of EPAC1990, 12–16th June, Nice, France, pp. 756–758.

[11] J.F. Ziegler et al., The Stopping and Range of Ions in Solids, Vol. 1, Pergamon Press, New York, 1985.

ISBN 978-3-95450-131-1

ADVANCES OF THE SPIRAL 2 PROJECT

J-M. Lagniel, GANIL, Caen, France
for and with the SPIRAL 2 Team

Abstract

The first phase of the SPIRAL 2 project dealing with the high-power superconducting linac and the two experimental areas called Neutron for Science (NFS) and Super Separator Spectrometer (S3) is well advanced. The building and conventional facilities are now ready and the project has entered in a phase during which the linac components are successively installed and commissioned (the first beam was produced in December 2014). After having briefly recalled the project scope and parameters, the constraints linked to the safety rules and the way the installation and commissioning are done will be explained. The next steps which are the DESIR low-energy experimental area and the q/A = 1/7 heavy ion second injector will be also presented.

SPIRAL 2 STATUS

The agreement giving the start of the SPIRAL 2 project [1] [2] was signed in September 2006 by the French state, Basse-Normandy region, department of Calvados, town of Caen, urban community of Caen-la-Mer, CNRS and CEA. Fig. 1 gives a 3D view of the building; the construction of which started in December 2010. With more than 100 rooms the total surface is 7,200 m^2 consisting of 4 floors and 2 basement levels.

Most of the conventional facility equipment and some parts of the accelerator (parts of the ion sources, RFQ cavity, magnets and cryomodule supports…) were installed before the end of the construction of the building (September 2014). Ref. [3] describes the integration of the accelerator processes, construction of the building and process connections.

Fig. 2 gives an overview of the accelerator, beam lines and experimental halls at the -2 level (- 9.50 m underground). The large free space at the north of the two source rooms is reserved for the future installation of a new injector (source and RFQ) able to inject Q/A up to 1/7 heavy ions in the superconducting LINAC. One can also notice that the building has been built in such a way that a LINAC extension at higher energy and/or the installation of new experimental areas are possible.

Proton/Deuteron Source and LEBT

The SPIRAL 2 proton/deuteron source is a 2.45 GHz ECR source which uses permanent magnets, it is designed to produce 5 mA 20 keV proton and 40 keV deuteron beams in CW or pulsed modes.

This source and associated low energy beam transfer line have been constructed by the CEA/IRFU team and successfully tested at Saclay [4]. This work was completed in July 2012. Reliability and stability were improved; emittance was measured and optimized versus space-charge compensation measurements.

The source and beam line have then been dismantled and transported to the GANIL site.

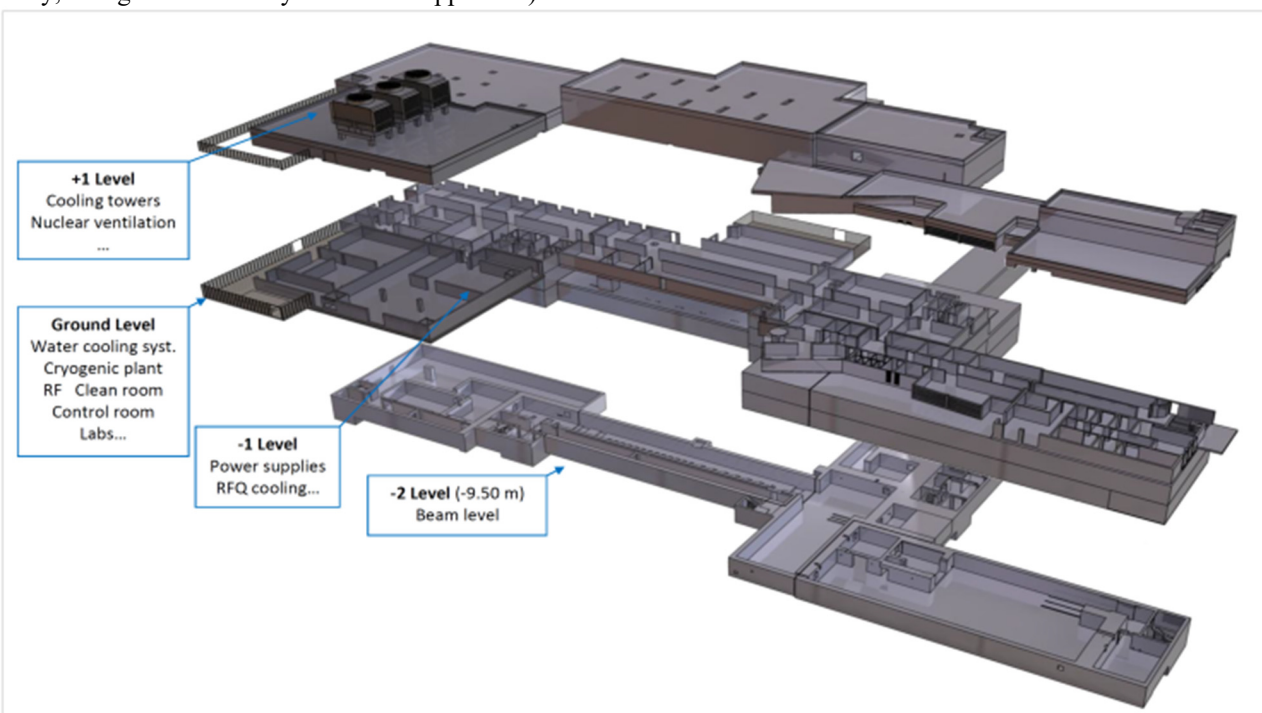

Figure 1: 3D view of the SPIRAL 2 building.

ISBN 978-3-95450-131-1

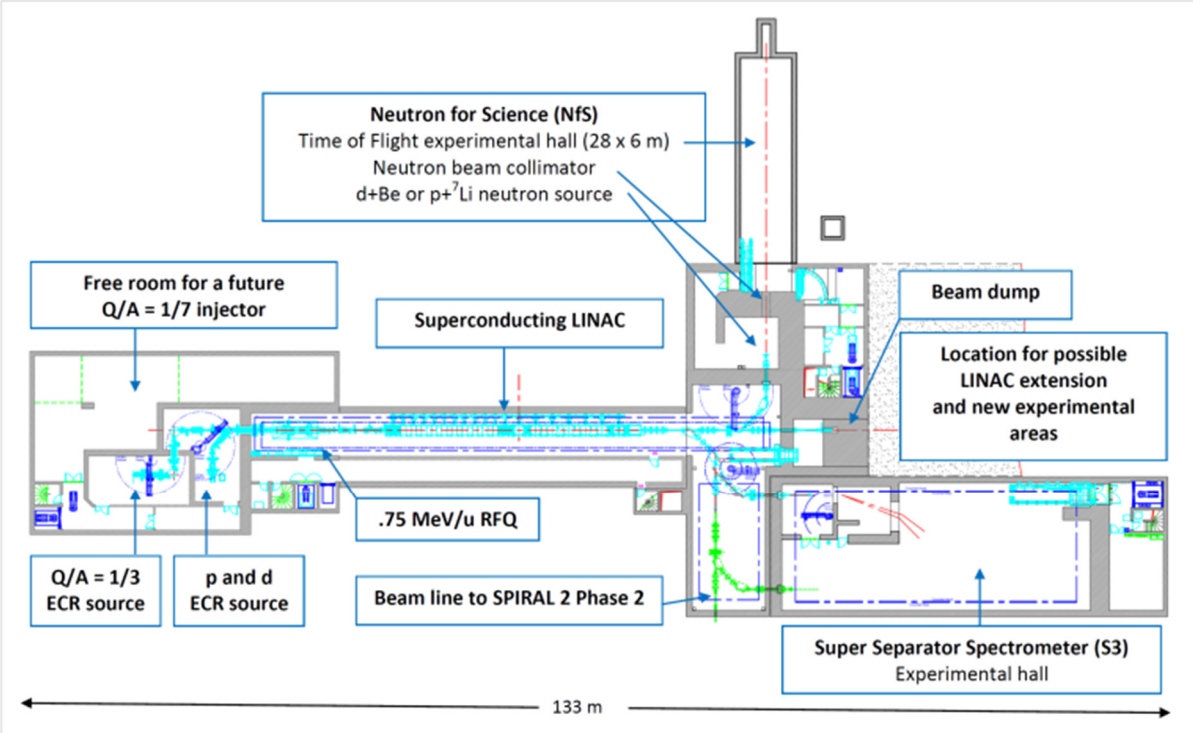

Figure 2: Overview of the accelerator, beam lines and experimental halls at the -2 level.

The first SPIRAL 2 beam at GANIL (protons) was produced by this proton/deuteron source on December 19, 2014. Since that time the periods of commissioning are scheduled taking into account the availability of the staff and the installation of the other equipment in the SPIRAL 2 building.

Up to now the goal has been to recover the excellent performances obtained at Saclay and to prepare the RFQ commissioning: proton proportion optimization, alignment and envelope tunings, intensity stability (including high-frequency noise), long run operation (6 mA CW during several nights (up to 14 h) without failure)... To obtain a 6 mA proton beam current at the LEBT end the extraction of 11 mA is required due to the low proton fraction.

The emittance measurement campaigns have been made to verify that H and V emittances of 0.2 π mm mrad rms norm. are still obtained with the 6 mA beam. Both beam intensity and emittance can be adjusted using the 6 H and 6 V pairs of slits installed along the LEBT.

Q/A = 1/3 Source and LEBT

The SPIRAL 2 heavy-ion source is the 18 GHz ECR source PHOENIX V2 which uses three normal conducting coils and a large permanent magnet hexapole. The magnetic field allows an operation at 18 GHz. This source and its LEBT are designed to produce heavy ions with Q/A up to 1/3 with a total extracted beam current up to 15 mA CW at 60 kV. The design allows the installation of a dedicated oven reaching 1,600°C for the production of metallic ion beams [5].

This equipment has been constructed by the CNRS/LPSC Grenoble team and successfully tested since 2010 at Grenoble before dismantling and transport to the GANIL site in June 2014.

In the SPIRAL 2 building (Fig. 3), a first Ar^{9+} beam has been successfully produced at 40 kV on July 2015. It has been analyzed using the first LEBT dipole.

PHOENIX V2 will be used for the SPIRAL 2 linac commissioning with heavy ions and also with $^4He^{2+}$ in order to mimic the deuteron beams before the safety authority authorization.

Figure 3: Q/A = 1/3 source and LEBT at GANIL.

RFQ and MEBT

The SPIRAL 2 RFQ cavity [6] has been designed by the CEA/IRFU Saclay team that also managed its realization and installation at GANIL (Fig. 4). The assembly of the five sections was done from September 2014 to November 2015), the vacuum tests done all along this operation have been successful.

ISBN 978-3-95450-131-1

Figure 4: SPIRAL 2 RFQ installed in the linac tunnel.

The low level RF tuning operations of the RFQ, including the voltage law bead-pull measurements and the 40 plunger adjustments ended in March 2015. The voltage errors are smaller than 2.3 % for the quadrupolar component, 0.9% for the dipolar longitudinal component and 1.4% for the dipolar transverse component. With such errors the expected transmission is 99.7 % (TOUTATIS code simulation). In air, at 38°C copper temperature, the resonance frequency is 88.0159 MHz, the quality factor is 13,526 and the total coupling coefficient is 1.021 (177 kW dissipated power expected at maximum voltage).

The first equipment of the Medium Energy Beam Transport line (MEBT, 0.75 MeV/u, between the RFQ and super-conducting linac) and the diagnostic plate are installed. They are ready and waiting for the first RFQ beam qualification. The fast chopper (bunch selector) development is being completed. The pulse generators and the vacuum chamber equipped with the electrodes are ready while the electronics to synchronize the two fast pulses to the 88 MHz beam is still under commissioning at INFN/LNS.

Superconducting LINAC

Table 1 gives the main linac parameters associated to the different ion species, including the ions produced by the future Q/A = 1/7 injector. This table shows the wide range of particles, intensities and energies which has to be managed in addition of the duty cycle range (from CW to single bunch using the fast chopper).

Table 1: SPIRAL 2 linac main beam parameters

Particle	I max (mA)	W (MeV/u)	Max beam power (kW)
Protons	5	2 – 33	165
Deuterons	5	2 – 20	**200**
Q/A = 1/3	1	2 – 14.5	45
Q/A = 1/7	1	2 – 8	48

The linac is composed of 19 cryomodules [7], 12 with one β = .07 cavity/cryomodule (CEA/IRFU Saclay) and 7 with two β = .12 cavities/cryomodule (CNRS/IPN Orsay). Both cavity types are equipped with RF couplers designed by CNRS/LPSC Grenoble.

Four low-beta and three high-beta are installed in the linac tunnel and connected to their valve box (Fig. 5). The first connections with the room temperature intermediate sections will be done mid September.

Figure 5: Low β (up) and high β (down) cryomodules installed in the linac tunnel (July 2015).

RF Systems

The RFQ cavity uses four 60 kW triode-based amplifiers and the superconducting cavities use individual solid state amplifiers (Fig. 6) able to deliver up to 20 kW. Amplifiers, distribution lines, circulators, LLRF and interlock PLC have been tested independently, installed in the building and interconnected. The commissioning has begun from the RFQ RF system, the RFQ cavity conditioning should begin by the end of October.

Cryogenic System

The cryogenic system (1,300 W equivalent 4.5 K) is installed and under validation. The first production of liquid helium has been done in July. The end of the liquefier tests and the receipt of the cryogenic installation are expected by the end of September.

ISBN 978-3-95450-131-1

Figure 6: Solid state 88.0525 MHz amplifiers.

HEBT and Beam Dump

The High Energy Beam Transfer lines drive the linac beam to the beam dump, to the NfS and S3 experimental halls and further on to the SPIRAL 2 Phase 2 production building (see Fig. 2). The HEBT magnet installation is in progress (Fig. 7) and the 200 kW beam dump designed by the CNRS-IPN Lyon team is already built.

Figure 7: HEBT installation in the SPIRAL 2 building.

Experimental Areas

NfS (Neutron for Science, Fig. 8) is the experimental area built to produce high power neutron beams from proton and deuteron beams ([1], see X. Ledoux, "NfS"). NfS plan to be ready for first SPIRAL 2 experiment from September 2016.

S3 (Super Separator Spectrometer), the experimental area built to produce very/super heavy elements ([1], see A. Drouart, "S3"), plan to be operational in 2017.

Both experimental halls are designed to have the possibility to use actinide targets.

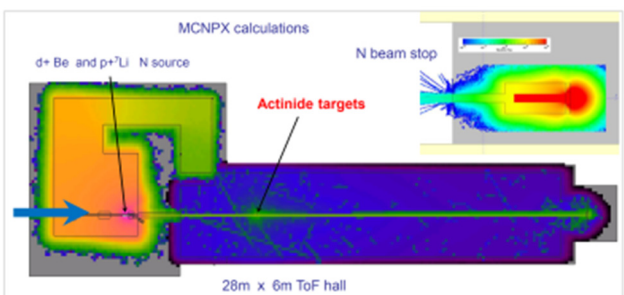

Figure 8: Neutron for Science (NfS) experimental area.

CHALLENGES

The issues arising when building and operating SPIRAL 2 type facilities are first of all the ones faced in any (accelerator based or not) project: construction of an efficient multi-competency project team, management of the collaborations, performance / cost / schedule / risk optimization... In addition, this new generation of RIB facilities induces at least two new important challenges.

Challenge Induced by the Safety Rules

SPIRAL 2 has been designed to produce high radioactive ion beam intensities and high neutron fluxes and, in addition, to allow the use of actinides targets. The challenges induced by the safety rules are then much more important than for the previous generations of RIB production facilities.

For SPIRAL 2, in addition to the classical "ALARA rule", the safety main objectives are to have an impact on the public lower than 10 μSv/y during normal operation and lower than 10 μSv/accident with a total release lower than 1 mSv/accident for accidental situations (electricity failure, fire, earthquake, plane crash...). These values have a severe impact on the schedule, cost, commissioning and operation of the facility ([1], see C. Brouillard and M. Wentzler, "Safety aspects").

A first example is the resistance requirements against earthquakes which forbid the use of light and cost saving industrial building structures. 15,000 m^3 of concrete and 2,200 T of iron (up to 400 kg/m^3) have been used for the SPIRAL 2 building (see Fig. 9). The equipment (magnets, cryomodules, helium tanks, cranes...) are also concerned since they must not damage the confinement barriers and shielding in case of earthquakes.

A second example is the obligation to build an expensive and constraining nuclear ventilation system to confine and monitor the activated gases and control their releases using very-high-efficiency filters. Three zones with a pressure gradient have been defined; all the cables and beam pipe wall traversals between two zones must be closed to minimize the air leaks.

The advances done with the French Nuclear Safety Authority are good but it must be pointed out that the safety constraints have been and still are a concern. The SPIRAL 2 experience could benefit to other projects.

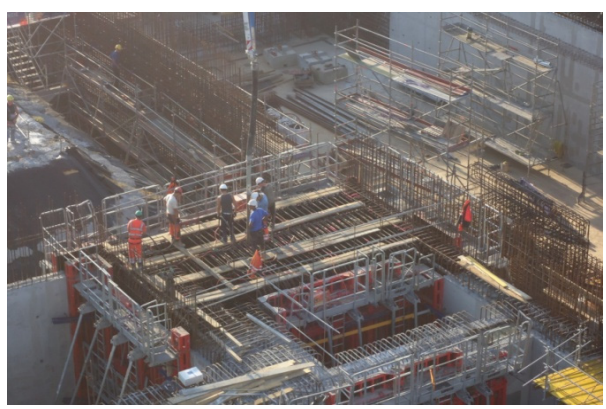

Figure 9: Iron mesh of the SPIRAL 2 building.

ISBN 978-3-95450-131-1

Commissioning and Tunings for Operation

For the commissioning and tunings for operation, SPIRAL 2 has issues shared with other high-power accelerators facilities (e.g. spallation neutron sources):

- The use of superconducting cavities forbids or strongly limits the use of interceptive diagnostics to minimize their pollution. Beam Position Monitors will be used for linac cavity tunings but they have a degraded accuracy below 150 µA and they work with bunched beams although the beam is bunched only when the cavities are tuned.
- Beam loss control is an issue to avoid damages (100 W enough to drill a vacuum chamber) and structure activation (the 1W/m limit).

In addition, the situation is complicated by the fact that:

- The tunings must be done for a large range of ions, energies, intensities and duty cycles (see Table 1).
- The beam loss monitors which are usually the key diagnostic to tune such machines have a weak efficiency at low energy.
- The long radial and longitudinal focusing periods imposed by the low frequency double gap cavities is such that the space charge effects (tune depression) are high at 5 mA.
- The limitation of the amount of activated material inventory imposed by the safety rules is such that the use of the beam dump is severely constrained: the authorized maximum beam power per day is 400 W, i.e. only 3 minutes per day to tune a 200 kW beam!

Advances on the SPIRAL 2 commissioning and tunings for operation strategy have been done in 2013 and 2014 by a working group gathering accelerator physicists, safety experts and the engineers in charge of the diagnostics and command/control. The NfS and S3 nuclear physicists in charge of the first experiments have been also consulted to make the choice of the ion species to be used during the commissioning phase ([1], see J-L. Biarrotte, "SPIRAL 2 linac diver commissioning").

Fig. 10 describes the phasing we plan to use to ramp up the beam power. During the two first phases both intensity and duty cycle must be low to be authorized to lose the whole beam. Diagnostics working well in these conditions are key for the commissioning success.

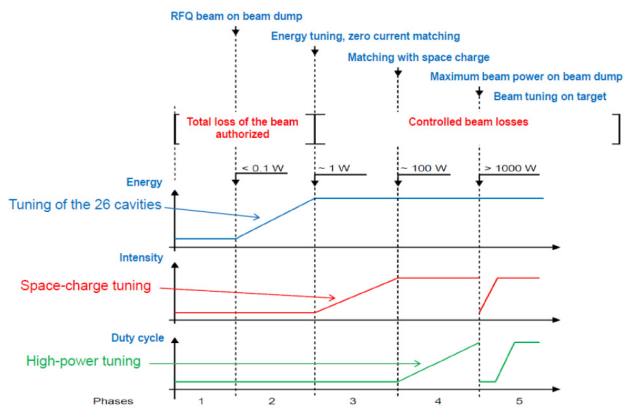

Figure 10: Commissioning / beam tuning strategy.

SPIRAL 2 1+ PHASE

The totality of the SPIRAL 2 1+ phase budget has been consolidated in June 2015. Fig. 11 gives a schematic view of this SPIRAL 2 extension ([1], see J-C Thomas, "DESIR"), its main components are:

- The DESIR experimental hall for low energy experiments (30 m x 50 m).
- Two beam lines from S3 and SPIRAL 1.
- The RFQ-cooler "SHIRaC" which has proven its ability to obtain 2 π mm mrd emittances with ΔE/E < 1 eV and 50 to 70% transmission for A = 40 to 130.
- A High Resolution Spectrometer (HRS) designed to obtain a M/ΔM > 20,000 resolution at 60 keV.

The detailed studies of the equipment and infrastructures are well advanced and some key pieces of equipment are already available (RFQ-cooler, HRS dipoles…). The first beam is expected in 2021, a date imposed by the safety procedures.

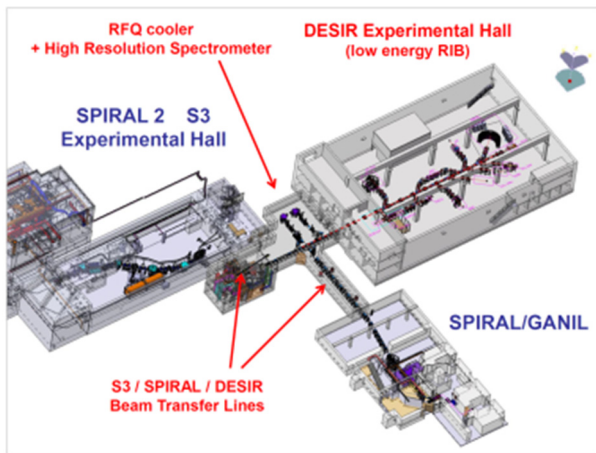

Figure 11: Schematic view of the SPIRAL 2 1+ phase.

ACKNOWLEDGMENTS

This paper has been prepared with more than a little help from my friends. Many thanks to them.

REFERENCES

[1] http://pro.ganil-spiral2.eu/events/weeks/ganil-spiral2-week-2014
[2] E. Petit, "Status of SPIRAL 2 project", HIAT'12, Chicago, USA, June 2012.
[3] P. Anger, "SPIRAL 2 integration of the accelerator processes, building construction and process connections", TUA2C01, these proceedings.
[4] D. Uriot et al., "Commissioning of SPIRAL 2 deuteron injector", IPAC'13, Shanghai, China.
[5] C. Barué et al., "Metallic beam developments for the SPIRAL 2 project", Rev. Sci. Instrum. 85, 02A946 (2014).
[6] R. Ferdinand, "SPIRAL 2 RFQ design", EPAC'04, Lucerne, Switzerland.
[7] P-E. Bernaudin et al., "SPIRAL2 cryomodule production result and analysis", LINAC'14, Geneva, Switzerland.

ISBN 978-3-95450-131-1

SPIRAL2 PROJECT: INTEGRATION OF THE ACCELERATOR PROCESSES, CONSTRUCTION OF THE BUILDINGS AND PROCESS CONNECTIONS

P. Anger, P. Bisson, O. Danna, X. Hulin, JM. Lagniel, F. Perocheau, E. Petit, L. Roupsard
GANIL Laboratory, Caen, France

Abstract

The GANIL SPIRAL 2 Project is based on the construction of a superconducting ion CW LINAC (up to 5 mA - 40 MeV deuteron and 33 MeV proton beams, up to 1 mA - 14.5 MeV/u heavy ion beams) with two experimental areas named S3 ("Super Separator Spectrometer" for very heavy and super heavy element production) and NFS ("Neutron For Science").

The building studies as well as the accelerator and experimental equipment integration started in 2009. The ground breaking started at the end of 2010. The integration task of the different equipments into the buildings is managed by a trade-oriented integration unit gathering the accelerator integration team, the building prime contractor and a dedicated contracting assistant. All work packages are synthesized at the same time using 3D models. 3D tools are used to carry out integration, synthesis, process connections and the preparation of the future assembly.

Since 2014, the buildings and process connections are received and the accelerator installation is well advanced.

This contribution will describe these 3D tools, the building construction, the process connection status and our experience feedback.

INTRODUCTION

Officially approved in May 2005, the GANIL SPIRAL2 radioactive ion beam facility (Figure 1) was launched in July 2005, with the participation of many French laboratories (CEA, CNRS) and international partners. In 2008, the decision was taken to build the SPIRAL2 complex in two phases: A first one including the accelerator, the Neutron-based research area (NFS) and the Super Separator Spectrometer (S3), and a second one including the RIB production process and building, and the low energy RIB experimental hall called DESIR [1][2][3].

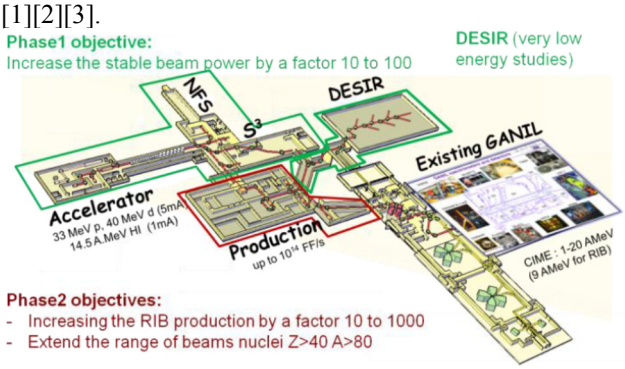

Figure 1: SPIRAL2 project layout, with experimental areas and connexion to the existing GANIL.

In October 2013, due to budget restrictions, the RIB production part was postponed, and DESIR was planned as a continuation of the first phase.

The first phase SPIRAL2 facility is now built, the installation and connecting tasks are in progress, with the aim of obtaining the first beam for physics (NFS) in 2016 [2][4].

DEFINITION OF THE NEEDS AND PRELIMINARY DESIGN

After the implementation of the Product Breakdown Structure (PBS), a global detailed specification was carried out to define the needs for each room of the building in terms of surface, mechanical stress for the floor, general servitudes to accommodate the accelerator and the experimental processes as well as for all the technical rooms receiving cryogenic, command control, RF power, vacuum systems.... The infrastructure needs (electricity, water cooling, nuclear ventilation, air conditioning, handling systems…) were also defined at that time.

These detailed specifications were used by the building prime contractor to make the building drafts and, in a second time, the preliminary design then the detailed design, with a cost estimate and control at each step.

The SPIRAL2 team took the decision to design the entire project with 3D tools due to the high degree of complexity of the processes and the very high level of the integration including connecting pipes and cables trays. We also wanted to be able to guarantee our ability to install, set up and maintain the equipments. For this 3D work the challenge comes from the fact that the same level of study is required for the building and conventional facilities, processes (ion sources, beam lines, RFQ, SC Linac and associated equipments) and for the process connections. A contracting assistant fully dedicated to these missions of 3D synthesis and 3D integration joined the SPIRAL 2 team in 2009.

The first difficulty was to define whole large reservations (floor or wall opening >1 m^2) for the infrastructure and process distributions in the concrete during the preliminary design phase. This request was due to obtain the authorization to build the facility taking into account the earthquake holding and the depth of the wall for the biological constraints.

The distribution principle was confirmed taking into account the position of electrical cabinets, the cable trays, fluid and RF distributions. The integration of all equipments (processes and infrastructure) was finally

ISBN 978-3-95450-131-1

validated. Figure 2 gives an example just limited of the process electrical cable tray integration.

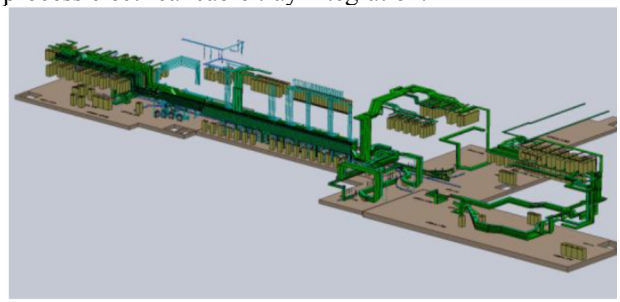

Figure 2: 3D view showing the electrical distributions for the process in the building.

After the synthesis and integration missions including the SPIRAL2 team with its assistant and the prime contractor, the integration references were defined for each work package (infrastructure and process equipments) so as to write the call for tender in April 2010.

IMPLEMENTATION STUDIES

The contracts for the different work packages of the building and process connections were signed in February 2011. Our major constraint was to be ready to define these "connection work packages" although the building and conventional facility implementation studies were progressing at the same time.

All the facility construction work packages must be synthesized at the same time using the same 3D tools!

The success of the implementation studies has been based on the synchronisation of the two synthesis cells (building and process) managed by the SPIRAL 2 system engineering group (see Figure 3).

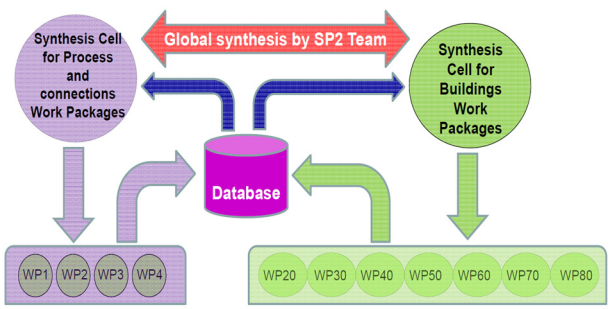

Figure 3: Organisation of the synthesis mission.

First, all companies had to work with the same 3D software (SolidWorks 2010) and use the same rules for each integration (3D absolute reference, graphics standards and arborescence).

Then the integration and synthesis process consisted in:

- Positioning equipments into the building via a modeling and providing these equipments with all services and connections necessary for their functioning.
- Ensuring the spatial coherence for all equipment in respect of the architectural constraints and technical capacities, for both exploitation and maintenance phases of the future facility and being translated into 2D or 3D synthesis drawings.

The SPIRAL 2 facility construction has been done managing 11 main contracts for the construction and then for the synthesis studies and implementation.

The synthesis process was carried out synchronizing nine companies, the building prime contractor, the assistant and the SPIRAL 2 project team, day after day over a twelve months period, to provide:

- A 3D high definition global integration without spatial interference (Figure 4).

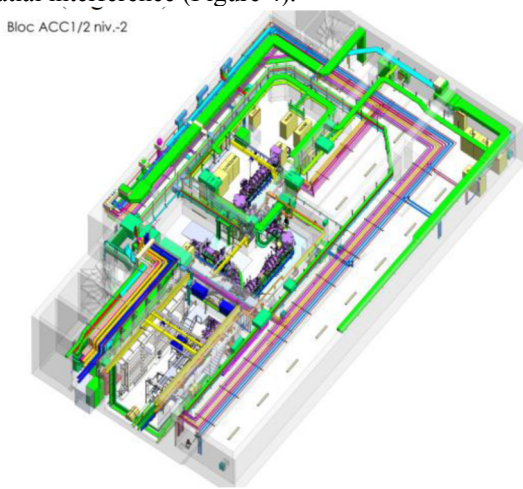

Figure 4: 3D views of processes + connections + buildings.

- The size and position of more than 1000 reservations in order to compute and draw the reinforcement needed to realize the concrete floors and walls.
- The size and position of the culverts in the floors for the servitude passages (cables...).
- The position of ground pin connections on the floors and walls to optimize the electromagnetic compatibility in order to achieve the requested high beam quality (Figure 5).

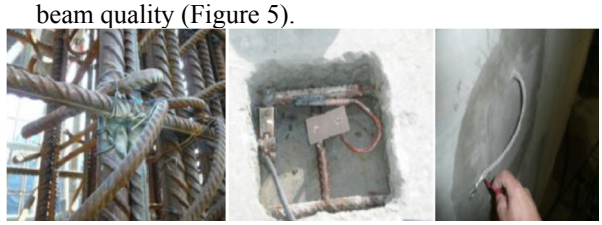

Figure 5: Welding of the iron frameworks and implementation of connection to link processes and cable trays to the global ground.

BUILDINGS CONSTRUCTION

The key dates of the building construction are:

- Construction permit: October 2010
- Excavation start: January 2011 (Figure 6)
- Pouring of first concrete: September 2011
- First process installation: November 2012
- Building handover: October 2014
- Process connection handover: April 2015

ISBN 978-3-95450-131-1

In October 2014, 14000 m^3 of concrete were poured, thanks to 450 000 work hours, and up to 120 workers on site. This can be seen in Figure 7.

Figure 6: Views of the construction site under way.

With a very high level of integration (number of element per unit volume) and an almost total absence of margins, 3D modelization has been the guide to build, to control the realizations and to study and adapt the integration for unavoidable modifications.

During the construction, several inspections were made by the French Safety Authorities, in order to check the conformity of the building with respect to the safety requirements (confinement barriers, earthquake resistance...).

Figure 7: Completion of the SPIRAL2 building (October 2014). The beam axis is 8 meters underground.

PROCESSES CONNECTION

Four work packages (Figure 8) directly managed by the SPIRAL 2 team have been contracted to realize this "connecting work":

- Two electrical work packages to install 10,000 m of cable trays, 400,000 m of cables, more than 20,000 connectors and the electrical distribution cabinets.
- One fluid work package for the water cooling connections with more than 700 valves.
- One RF power distribution work package to distribute the 600 kW 88 MHz radio frequency to the 33 accelerator cavities through 1,200 m of coaxial lines (broadcast).

The main difficulty has been to define in detail, during the execution, each one of the 20,000 connections (which wire colour corresponds to which pin number?) since a standardization is practically impossible to set up with the multitude of different technologies used to built an accelerator.

The second main difficulty has concerned the realization of specific connections (e.g. RF and small electronic connectors) by industrial companies not used to working on such specific connectors. After an initial period with permanent default on the braid shield for some connector families, we were forced to organized trainings and validated prototypes for landing to it. After that the default rate before correction became lower than 1%, a very good result.

Figure 8: Electrical, fluid and RF power distribution.

CONCLUSION

The buildings are now constructed, the main part of the cables and connections are installed, the injector is under tests and the superconducting LINAC is now being installed.

For the integration, synthesis, construction and set up of a complex facility such as SPIRAL 2 our main feedback concerns the followings:

- ✓ The contractors underestimated the complexity and the number of connections required by our processes.
- ✓ The data collection and synthesis is an enormous task which takes a lot of time and resources. The use of spreadsheet files for the synthesis is not the best tool. A database seems better adapted.
- ✓ A detailed numerical 3D modelization for a large facility with a high level of integration is required. It's the main way to minimize risks (spatial interference, difficulties of assembly and maintenance). It's a powerful tool to design and construct the building and infrastructures and then to control them.
- ✓ A 3D model generates enormous size files and global assemblies are often difficult to visualize. It requires a simpler model in particular for the processes.

The goal is reached: Such as designed = Such as built or 3D = Reality.

ACKNOWLEDGEMENT

The author addresses his thanks to the integration cell team and the whole SPIRAL2 project team.

REFERENCES

[1] SPIRAL2 project. http://pro.ganil-spiral2.eu/spiral2/what-is-spiral2/physics-case/at_download/file
[2] E. Petit, "progress of the SPIRAL2 project", IPAC 2011, San Sebastian, Spain, September 2011.
[3] P. Bertand, R. Ferdinand, "SPIRAL2 accelerator construction progress", Linac 2012, Tel Aviv, Israel.
[4] J-M. Lagniel, TUA2I01, HIAT2015, Yokohama, Japan.

ISBN 978-3-95450-131-1

THE PROJECT SPES AT LEGNARO NATIONAL LABORATORIES

M. Comunian, A. Pisent, A. Palmieri, L. Ferrari INFN-LNL, Legnaro, Italy
L. Bellan, INFN-LNL, Legnaro, Italy. Department of Physics and Astronomy, University of Padova, Padova, Italy.
A. D. Russo, INFN-LNS, Catania, Italy
B. Chalykh, ITEP, Moscow, Russia

Abstract

At LNL INFN is under construction a Rare Isotope Facility (SPES) based on a 35-70 MeV proton cyclotron, able to deliver two beams with a total current up to 0.5 mA, an ISOL fission target station and an existing ALPI superconducting accelerator as a post accelerator (up to 10 MeV/u for A/q=7). In this paper, some highlights are presented: the isotope separation part (low, medium and high-resolution classes), some highlights of the mechanical and RF aspects of the RFQ and the end to end simulation (from the charge breeder to the end of ALPI). High selectivity and high transmission for a beam of a very low intensity, plus the specific challenges related to the use of ALPI (with a reduced longitudinal acceptance) and related to the specific lay out led to specific and common problems which have been solved during the design stage.

INTRODUCTION

SPES, acronym of Selective Production of Exotic Species, is a CW radioactive ion beam facility under construction at LNL INFN in Italy. It will produce and accelerate neutron-rich radioactive ions, in order to perform nuclear physics experiments, which will require beams above Coulomb barrier.

The main functional steps of the facility are shown in Fig.1: the primary beam delivered by the cyclotron, the beam from the fission target (as an example, up to 10^{13} particle/s of ^{132}Sn), the beam cooler, the separators, the charge breeder and the accelerator (the existing ALPI with a new RFQ injector). The use of the continuous beam from the +1 source, which can use different configuration types LIS, PIS, SIS, maximizes the RNB efficiency but need a CW post accelerator (RFQ and ALPI). The beam is prepared for the post-accelerator stage with a charge breeder device (an ECR that woks in continuous). The energy on the transfer lines are determined by the chosen RFQ input energy (5.7 keV/u); for this reason, all the devices where the beam is approximately stopped (production target, charge breeder and RFQ cooler) lay at a voltage proportional to the ratio A/q. The charge state range (3.5<A/q<7) is bounded by the RFQ field level for the upper limit and by the minimum voltage on q=1 transport line.

METHOD FOR SIMULATIONS

The main software used for the simulations is TraceWin [1] a 3D multiparticle tracker, capable of field map usage. In such a way, the quarter-wave cavities of the linac ALPI were simulated via field-maps in order to take into account all nonlinear order effects. Due to that, the TraceWin code is capable to set all beam line for the runs of the LNL installed accelerators [2].

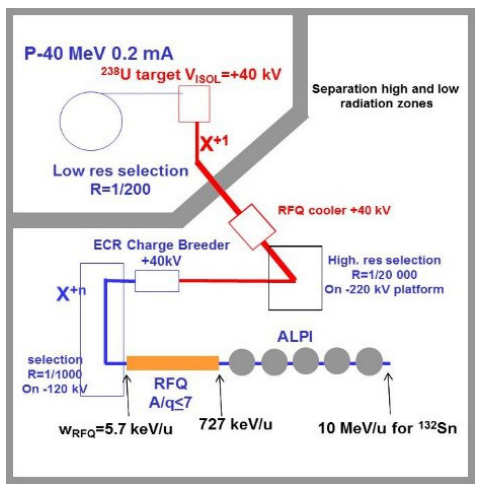

Figure 1: functional scheme of the SPES facility. There are two main areas: the 1+ line and the n+ line, where 1+ and n+ indicates the beam charge state.

THE SEPARATION STAGES

The general layout of the SPES facility is presented in Fig. 2.

The reference beam for the beam dynamics simulations is chosen to be the ^{132}Sn, extracted at 40 kV at the end of the target extraction system. It has been chosen a q=19 after the charge breeder i.e. A/q= 6.9, in such a way to test the maximum required electromagnetic fields of the line elements of the facility.

There are three normalized rms emittance regimes: after the target, it is chosen to be $\varepsilon_{n,rms}$=0.007 mm mrad, with an equivalent geometric emittance at 99% of $\varepsilon_{geo,99\%}$= 80.18 mm mrad. Then, the beam cooler prepares the beam to the HRMS stage, reducing the emittance down by a factor 5. After the CB, the emittance for the BD calculation is assumed to be $\varepsilon_{n,rms}$=0.1 mm mrad. As far as the longitudinal phase space is concerned, a uniform distribution between ±20 eV (reduced to ±1 eV

ISBN 978-3-95450-131-1

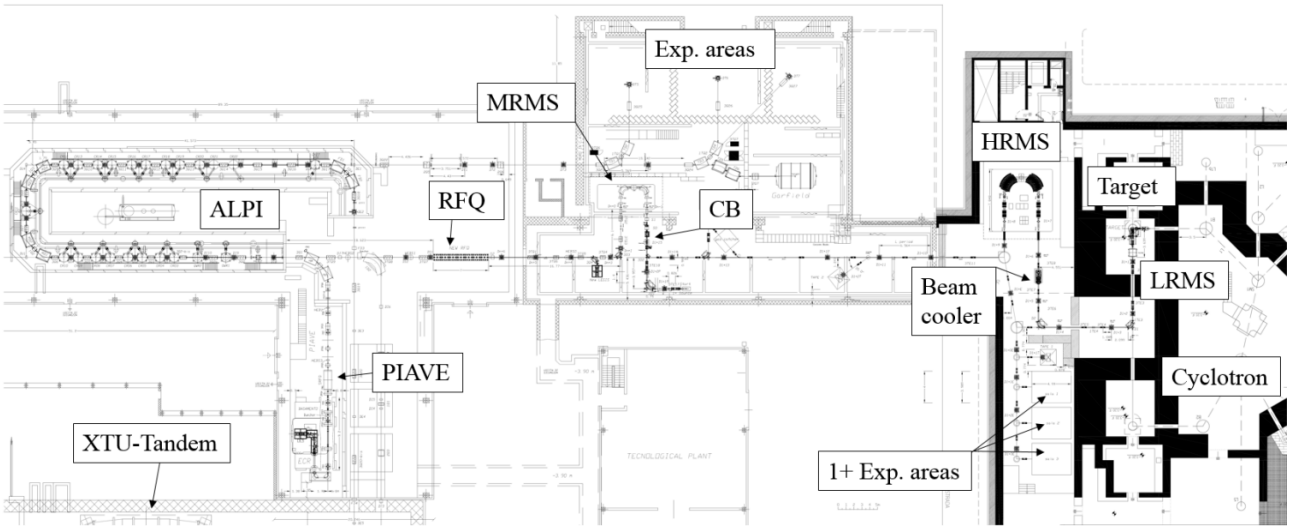

Figure 2: Full SPES layout with main areas.

after the beam cooler [3,4,5]) is considered. After the CB, the energy spread are set to ±15 eV. The low resolution section (LRMS) is the part of the line between the target and the beam cooler. Two mass spectrometers are placed between the target and the beam cooler: the Wien Filter and a 90° dipole. The overall resolution is of 1/200 in mass, sufficient to separate the isobars from the other isotopes.

Two similar type of spectrometers, the High Resolution Mass Spectrometer and the Medium Resolution Mass Spectrometer are provided for the SPES project. Both are composed by two 90° magnet with a multipole (up to 12° order pole) between them, placed onto platforms.

The HRMS is used to obtain the ions of interest, because it removes isobar ions coming from the source and the MRMS is used to clean the nominal beam from contaminants introduced by charge breeder.

After the 1/200 isotopes separator, the isobars separation is represented by HRMS placed on a 260 kV platform (the effect is a reduced divergence and energy spread). This separator is constituted by six quadrupole lens, two exapole lens, two dipoles and one multipole lens placed in the symmetry plane of the system to fix the curvature aberration. It is able to separate different isobar with $\Delta M / M$ =1/20000 and $\Delta W / W$ = ±1 eV (due to the beam cooler) like shown in Fig. 3 below. The optics improvement is still ongoing but it shows a fully resolving capability of isobars separated of 1/20000 in mass. It is important to take into account that its performance depend on the beam cooler efficiency. After the charge breeder, the next spectrometer is the MRMS, placed on a 120 kV platform (for the same reasons of the HRMS). The goal in resolving power of this spectrometer is 1000 with the interest beam fully separated. The Table 1 shows the overall capabilities of the two spectrometers.

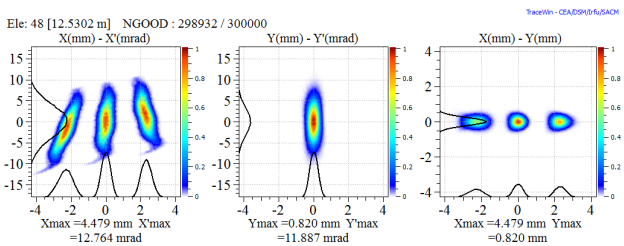

Figure 3: phase space at the HRMS image point. The three beam are separated of 1/20000 with ± 1eV energy spread.

Table 1: Medium and High Spectrometer Performances

Parameter	MRMS	*HRMS*
Input emit. n. rms mm mrad	0.1	0.0014
Emittance growth	10%	7%
Full res. ΔW = ±1 eV	1/1500	1/36000

After the selection, the beam is sent to the RFQ through a matching line.

THE SPES RFQ

The SPES RFQ is designed in order to accelerate beams with A/q ratios from 3 to 7 from the Charge Breeder through the MRMS and the selection and injection lines up to the MEBT. The main parameters of the RFQ are listed in Table 2. The RFQ is composed of 6 modules about 1.2 m long each. Each module is basically composed of a Stainless Steel Tank (AISI LN 304) and four OFE Copper Electrodes.

A copper layer will be electrodeposited on the tank inner surface and a spring joint between tank and electrode is used in order to seal the RF.

The voltage law is a linear function along z V(z)=V(0)+a·z with a=3.177 kV/m and V(0) depending on the A/q of the ion to be accelerated. Such law is

ISBN 978-3-95450-131-1

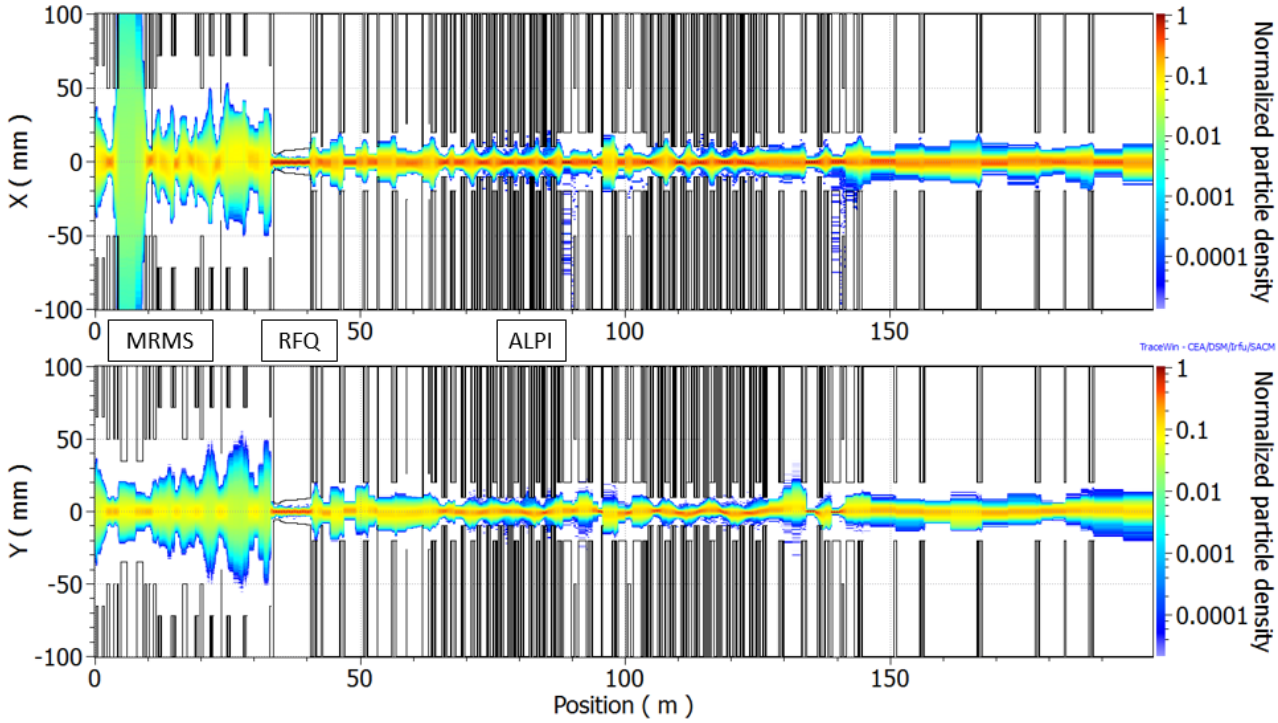

Figure 4: Multiparticle normalised-densities y and x of the whole line CB-RFQ-ALPI- Experimental hall.

Table 2: Main RFQ Parameters

Parameter [units]	Design value
Operational mode	CW
Frequency [MHz]	80
In/out. Energy [keV/u]	5.7-727 (β=0.0035-0.0359)
Vane length L [m]	6.95
RF Power [kW] (+30%)	98

implemented by designing the RFQ in order to obtain a constant TE_{21} cut-off frequency fc=79.5 MHz along the structure and by properly shaping the vane undercuts at the Low and High Energy Ends of the RFQ. In order to compensate the R0 variations, the capacitive region is varied along the RFQ. The electrode thickness is equal to 48 mm and the tank inner radius R is equal to 377 mm [6].

END TO END BEAM DYNAMICS SIMULATION

An end-to-end simulation from the CB to the end of ALPI was performed. The beam travels from the CB to the third hall, see fig. 4. The final kinetic energy is 1.2 GeV ($\Delta E / E < \pm 0.4\%$) with total losses of 14% in the nominal case. In Fig. 3 the multiparticle densities are shown for the x and y coordinates. An error study from the RFQ exit to the experimental hall was carried out.

The single preliminary errors study shows that the errors related to the QW cavities drive the losses through ALPI. The present precision of the cavity placement and on the synchronous phase setting is shown in Table 3. Therefore intrinsic losses of about 30% are foreseen unless new improvements.

Table 3: errors applied to the ALPI LINAC

Parameter	Value	Average losses
Cavity displacement	±1 mm	30%
Phase error	±1°	15%
Input beam phase error	±2°	10%

CONCLUSIONS

Several highlights of the SPES project were shown. The high-resolution mass separator is under refinement while the WF and the MRMS are under procurement. An end to end simulation of the line from the CB to the experimental hall was done, showing an overall transmission >85% in the nominal case. The full error study is under analysis.

REFERENCES

[1] D. Utriot and N. Pichoff, "TraceWin", CEA Saclay, June, 2014, website: http://irfu.cea.fr/Sacm/logiciels/index3.php

[2] M. Comunian et al., "Beam Dynamics Simulations of the Piave-Alpi Linac", WEPC014, IPAC'11, San Sebastian, SPAIN (2011).

[3] M. Maggiore et al., "Plasma-beam traps and radiofrequency quadrupole beam cooler", Review of

ISBN 978-3-95450-131-1

Scientific Instrument 85, AIP publishing, November 2013.
[4] A. Nieminen et al., "Beam Cooler for Low-Energy Radioactive Ions", Nuclear Instruments and Methods in Physics Research A 469, ELSEVIER, August 2001, p. 244-253; http://www.elsevier.org
[5] A. Pisent et al. "SPES Beam Dynamics", TUO4AB01, HB2014, East Lansing, USA(2014).
[6] L. Ferrari et al "Thermo-mechanical calculation of the SPES", HIAT2015, Yokohama, Japan, paper WEPB13, these proceedings.

ISBN 978-3-95450-131-1

THE SPES RIB PRODUCTION COMPLEX

A. Andrighetto, M. Ballan, E. Boratto, F. Borgna, S. Corradetti, M. Manzolaro, A. Monetti, A. Mozzi, D. Scarpa, R. Silingardi, M. Rossignoli, G. Vivian, G. Bisoffi and G. Prete, INFN, Laboratori di Legnaro, Italy
M. Guerzoni, A. Margotti, INFN Sezione di Bologna, Bologna, Italy
R. Oboe, Dipartimento di Tecnica e Gestione dei Sistemi Industriali dell'Università di Padova, Vicenza, Italy
G. Meneghetti, Dipartimento di Ingegneria Industriale dell'Università di Padova, Padova, Italy
M. Ferrari, A. Zenoni, Dipartimento di Ingegneria Meccanica e Industriale, Università degli Studi di Brescia, Italy

Abstract

SPES [1] is a second-generation ISOL RIB facility [2] of the National Institute of Nuclear Physics (INFN laboratory, Legnaro, Italy) actually in construction phase. The main goal is to provide intense neutron-rich Radioactive Ion Beams directly impinging a UC_x target with a proton beam of 40 MeV and current up to 0.2 mA. The production target follows an innovative approach which consists in a target configuration able to keep high the number of fissions, up to 10^{13} per second, low power deposition and fast release of the produced isotopes. The exotic isotopes generated in the target are then ionized, mass separated and re-accelerated by the ALPI [3] superconducting LINAC at energies of 10 AMeV and higher, for masses in the region of A=130 amu, with an expected rate on the secondary target up to 10^9 particles per second In this work, we will present the recent results on the R&D activities regarding the SPES RIB production complex (see Fig.1).

THE SPES FACILITY

The radioactive ions will be produced with the ISOL technique using the proton-induced fission of uranium contained in the UC_x [4] direct target and subsequently reaccelerated using the PIAVE-ALPI accelerator complex. The Best C70 cyclotron with a maximum current of 0.8 mA rows two exit ports those will be used as a primary proton beam driver, with variable energy (30-70 MeV). The cyclotron is able to accelerate H-beam, provided by an external multi-cusp ion source, up to the energy of 70 MeV. Since the stripping process does the proton extraction, the final energy varies within 35-70 MeV. Two independent extraction channels placed at 180° one with respect to the other, provide the simultaneous delivery of two beams. In order to reach an in-target uranium fission rate of 10^{13} fission/s, a proton beam current of 200 μA (40 MeV) is necessary; the second beam, up to 500 μA and 70 MeV, will be devoted both to neutron production for material research and to research on new isotopes for medical applications. The ISOL technique for radioactive beam production is based on a driver accelerator, which induces nuclear reactions inside a thick target. The reaction products are extracted from the target by thermal process (diffusion-effusion), ionized, mass separated and injected into a re-accelerator. The first mass selection is performed by a Wien Filter with 1/100 mass resolution, installed just after the first electrostatic quadrupole triplet inside the production bunker with the aim to confine the larger part of radioactivity inside the high shielded area. The transfer line toward ALPI is equipped with several beam handling systems to purify the beam. A Beam Cooler and a High Resolution Mass Separator (HRMS) with 1/20000 mass resolution will be installed inside the new building. Before the injection in the ALPI superconducting LINAC it is necessary an increase of the charge state from 1 + to n +. This is performed by means of a ECR Charge Breeder. The linear accelerator ALPI, with a range between about 0.04 and 0.2 and CW operation, represents an ideal re-accelerator for the radioactive beams.

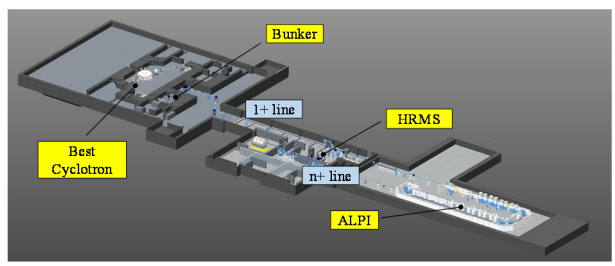

Figure 1: SPES facility. In the image, we can observe the location of cyclotron, production bunker, the path of 1+ line and n+ line toward ALPI, with the HRMS system in the middle.

THE TARGET SOURCE UNIT

In the ISOL facilities, the production target with the ion source constitutes the central component, which are capable to convert the primary beam into a radioactive ion beam. In particular, the reference version of the SPES production target is made of 7 UC_x [5] co-axial disks. These disks have diameter and thickness of 40 and 1 mm, respectively, and are impinged by a 40 MeV 0.2 mA proton beam, thus generating approximately 10^{13} fissions per second. In the SPES project, the primary proton beam is stopped in the target, dissipating its power and generating

ISBN 978-3-95450-131-1

by fission exotic nuclei in the intermediate mass range (80< A< 160). The desired exotic species must be extracted from the target, ionized and accelerated to make the RIB. This process is time demanding and usually unsuitable for atoms having half-lives lower than a few tens of ms.

The main elements produced in the fission process are represented in Figure 2, together with the optimum ionization mechanisms that will be adopted for the production of ion beams from isotopes of these elements.

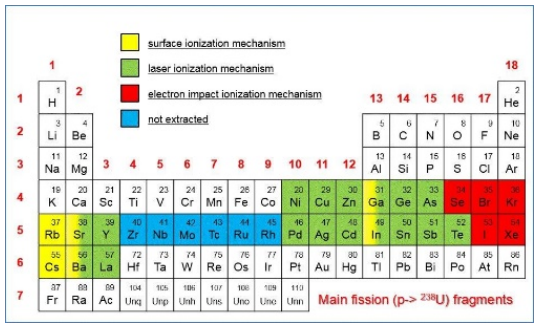

Figure 2: element table where are put in evidence the elements product with SPES beams.

In the context of the SPES project, two different ion source types will be adopted: the SPES surface ion source (SIS), and the SPES plasma ion source (PIS), shown in Figure 3. The former will be used to produce ions using both the surface and the laser ionization mechanisms, so it is named also as SPES laser ion source (LIS), whereas the latter will ionize the SPES fission fragments according to the electron impact ionization mechanism.

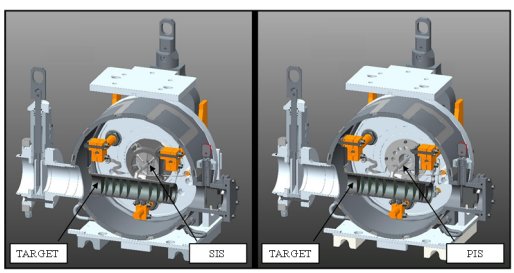

Figure 3: The two ion sources used in SPES project assembled with the target in the vacuum chamber:

- The SIS is the surface ion source;
- The PIS is the plasma ion source.

The target chamber unit, made in aluminium, has a water-cooled base plate and is covered by another water-cooled bell jar. The chamber unit, about 40 kg weight, is coupled to the proton and to the RIB beam lines, by means quick connectors. Two valves isolate the system respectively from the proton beam pipe and from the RIB pipeline. A drawing of the target-ion source chamber is shown in Figure 4.

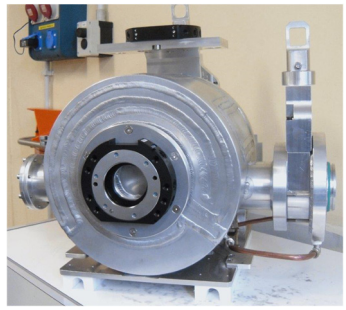

Figure 4: The SPES Target Unit.

THE TARGET MATERIAL

The properties required for the SPES target material, like in the case of other ISOL facilities, are directly related to the efficiency of the processes undergoing between the isotopes production and their release, which can be divided into two distinct phases [5]:

- The diffusion of the isotopes, generated inside the ceramic material grains, towards their surface. This mechanism is governed by Fick's laws.
- The effusion in high vacuum, either in the material pores or in the free spaces surrounding the target discs, towards the ion source.

The obtainment of a fast release of isotopes depends on a large number of parameters, both relative to the material properties and to the target operative conditions. The characteristics required for a material to work with a high efficiency as an ISOL target can be summarized as [5]:

- A sufficiently high cross section for the reaction between the target constituting atoms and the primary beam is required, in order to have a high probability of interaction.
- In order to speed up the aforementioned diffusion and effusion mechanisms, the target material must be able to work at high temperatures (more than 2000 °C) in high vacuum without degradation of its thermo-mechanical properties.
- The material should exhibit high thermal emissivity and conductivity in order to dissipate the power generated by its interaction with the primary beam without undergoing structural damage.
- The target should be highly permeable to exotic species during their path towards the ion source.

The research on materials for the SPES target, as in the case of other existing or future ISOL facilities, represents an important part of the entire facility development.

In recent years [4], the synthesis and characterization of uranium carbide thin discs (SPES target prototypes) have been successfully carried out, and the production methodology can be considered ready to be used to produce real UC_x targets when SPES will be operative.

The synthesis is based on the reaction between a proper uranium source, typically uranium dioxide, and graphite:

$$UO_2 + 6C \rightarrow UC_2 + 2C + 2CO$$

ISBN 978-3-95450-131-1

which is made to occur at high temperature (up to 1800 °C) in high vacuum (~10^{-6} mbar).

The production route of discs to be used as SPES targets consists of the following steps (the target during production phase is shown in Figure 5):

- Mixing of the precursors powders by means of an agate mortar or using a planetary ball mill. A small quantity of a phenolic resin binder, usually 2% wt., is used to provide a sufficient mechanical stability to be handled without damage and loss of powder.
- Uniaxial cold pressing of the mixed powders into pellets, making use of a hydraulic press and a specifically designed die. In the case of target prototypes, 13 mm diameter dies are commonly used.
- After extraction of the pressed pellet from the die, its thermal treatment is carried out in a high vacuum furnace specifically developed to reach very high temperatures (~ 2000 °C) as described in [5].

Figure 5: Making of the target unit.

THE TARGET REMOTE HANDLING

The target handling system consists of two independent apparatus, called vertical and horizontal devices that will move the target chamber to and from the bunker zone. The horizontal system will be the primary handling device while the vertical one is intended only as a backup solution.

The vertical handling device will access the bunker through a hole on the bunker roof. It will grab the target chamber using an interface tool placed on top of the chamber. On the other hand, the horizontal handling device will access the bunker using a door. In this case, the interface tool is located on the rear of the chamber. Both devices will place and grab the chamber on a coupling table where a series of electro-pneumatic actuators will couple and uncouple the target chamber to the beam lines and open and close the vacuum sectioning valves.

The horizontal system is made up of an Automatic Guide Vehicle (AGV) (see Fig. 6) that will move the target chamber to and from the bunker area and a Cartesian handling system, located on the top of the AGV, that will move the target chamber to and from the coupling table once the vehicle is in position. The AGV can travel following a impose path with reduced tolerances. One optical system will be the primary automatic guide system with a redundancy one to be defined (a possible solution will be chosen among magnetic line driving and laser distance driving). Moreover, manual operation of the AGV from an operator using a joystick and webcams installed onboard will be available.

The Cartesian system is implemented using screw type system and electrical motors.

A PLC on the AGV will control the operations and it will communicate with a user interface. The whole system will be operated on batteries and it works in a completely wireless way.

This kind of solution, even if more cost expensive rather than a fixed rail one, allows more flexibility and a complete isolation of the bunker when all the doors will be closed, due to the absence of holes for the rail.

Figure 6: horizontal handling device made up of the AGV, the Cartesian system and the PLC control.

CONCLUSION

The SPES facility is the main Nuclear Physics project in Italy for the next years. It is organized as a wide collaboration among the INFN Divisions, Italian Universities and international laboratories. SPES is an up to date project in the field of Nuclear Physics and in particular in the field of RIBs, with a very competitive know how, above all in the RIB production system. The SPES RIB complex will represent also an important step in the direction of the European project EURISOL.

ACKNOWLEDGMENT

The authors wish to thank Michele Lollo, Edoardo Visentin, Flavio Pasquato for their precious scientific and technological support.

REFERENCES

[1] G. Prete et al., Eur. Phys. J. Web Conf. 66 (2014) 11030.
[2] T. Stora, Nucl. Instrum. Meth. Phys. Res. B 317 (2013) 402.
[3] G. Bisoffi et al., Proceedings of HIAT 2012, Chicago, IL USA.
[4] S. Corradetti et al., Eur. Phys. J. Web Conf. 66 (2014) 11009.
[5] L. Biasetto et al., J. Nucl. Mater. 404 (2010) 68.

ISBN 978-3-95450-131-1

SUPERCONDUCTING CAVITY CRYOMODULES FOR HEAVY-ION ACCELERATORS AT ARGONNE*

Z.A. Conway, A. Barcikowski, G.L. Cherry, S.M. Gerbick, B.M. Guilfoyle, C.S. Hopper, M.J. Kedzie, M.P. Kelly, S.-h. Kim, S.W.T. MacDonald, B. Mustapha, P.N Ostroumov and T.C. Reid, ANL, Argonne, IL 60439, USA

Abstract

Over one year ago the ATLAS Efficiency and Intensity Upgrade (EIU) was finished. A major portion of this upgrade was the installation of a new superconducting cryomodule for the acceleration of β = 0.077 heavy-ion beams. The EIU cryomodule is capable of supplying a voltage gain greater than 17.5 MV with a total cryogenic load of 45 W to 4.5 K, 12 W static and 33 W dynamic. This unit is comprised of seven 72.75 MHz quarter-wave resonators and four 9 T solenoids. This presentation will review the technology advances that resulted in exceptional operational performance of the EIU cryomodule and the ongoing development work for a new eight-cavity beta = 0.11 half-wave cryomodule.

INTRODUCTION

Low-beta (β = v/c < 0.5) cryomodules occupy a significant portion of the length of proton/heavy ion accelerators. Two recent examples of this are: (1) The proposed 800 MeV booster linac for the Fermilab Proton Improvement Project-II (PIP-II) with low-beta cryomodules occupying 30% of its length which house 59 of the 116 SC cavities [1]. (2) The Michigan State University 200 MeV/u Facility for Rare Isotope Beams (FRIB) ~300 m driver linac where 100% of the cryomodules house low-beta co-axially loaded SC cavities [2]. The accelerator real-estate length occupied by the low-β cryomodules is a strong incentive to make them efficient and high performance.

At Argonne we installed a heavy-ion cryomodule capable of achieving high accelerating voltages with small cryogenic loads which has been in operation for over a year [3]. This cryomodule houses 7 72.75 MHz quarter-wave resonators (QWRs) optimized for the acceleration of beta = 0.077 ions and 4 9 T solenoids. In this paper we first discuss the measured thermal loads. This is followed by a comparison of the results to the previous split-ring cryomodule performance. Finally, a few concluding remarks are made.

The new QWR cryomodule was first cooled to 4.5 K in December 2013 and has been in full-time use supporting ATLAS operations since March 2014. This has given us ample time to characterize the cryomodule performance and the results presented here represent the highest measured thermal-load; e.g., with all cavities operating at 2.5 MV.

QWR CRYOMODULE

Cryomodule cold-mass hanging from the lid is shown in Figure 1. The EIU cryomodule is a modified version of our previous box-type cryomodule which has been in operation since 2009 [4]. Argonne box cryomodules implement current state-of-the-art techniques developed for electron accelerators such as separate cavity and insulating vacuum systems, surface processing and clean handling to achieve and preserve record single-cavity test performance [3, 5], and a design which enables the clean assembly to be complete and hermetically sealed prior to installing the "dirty" subsystems of the cryomodule. The cryomodule structure has been described in great detail in [6].

The cryomodule 4.5 K cryogenic system is gravity fed where each of the 7 QWR and 4 solenoids is attached to a common helium distribution manifold. All penetrations through the cryomodule 80 K thermal shield are baffled or covered such that the solid angle for room temperature surfaces viewing 4.5 K surfaces is minimal (a few square inches for the entire cryomodule) and much of the reflective path between room temperature and 4.5 K is coated with high-infrared-emissivity blackened surfaces [7]. Further reducing the 4.5 K heat load are the low-emissivity 80 K and 4.5 K surfaces which are either aluminized mylar or electropolished stainless steel. Finally, all of the connections to 4.5 K are very low-conductivity. This is accomplished by using very thin stainless steel walls (e.g., the beam-line gates valves and the helium manifold safety pressure relief) or by taking advantage of the acoustic impedance mis-match between titanium and stainless steel at low temperature to increase the contact impedance between these materials (e.g., the cold-mass hangers). The calculated 4.5 K static thermal load is 15 W where the major contributors are: 5 W from 80 K to 4.5 K radiation; 4 W from the helium manifold (with 1.5 W from the solenoid current lead feedthrough and 1 W from the safety pressure relief port); 3 W from the power couplers; and the remainder comes from several <1 W sources which are the beam-line gates valves, the cold-mass hangers, the cavity cool-down lines and the slow-tuner gas lines. We measured the 4.5 K static thermal load with two different methods: (1) The cryomodule helium system was sealed and the rate of

*This material is based upon work supported by the U.S. Department of Energy, Office of Science, Office of Nuclear Physics, under contract number DE-AC02-06CH11357, and the Office of High Energy Physics, under contract number DE-AC02-76CH03000. This research used resources of ANL's ATLAS facility, which is a DOE Office of Science User Facility.

#zconway@anl.gov

ISBN 978-3-95450-131-1

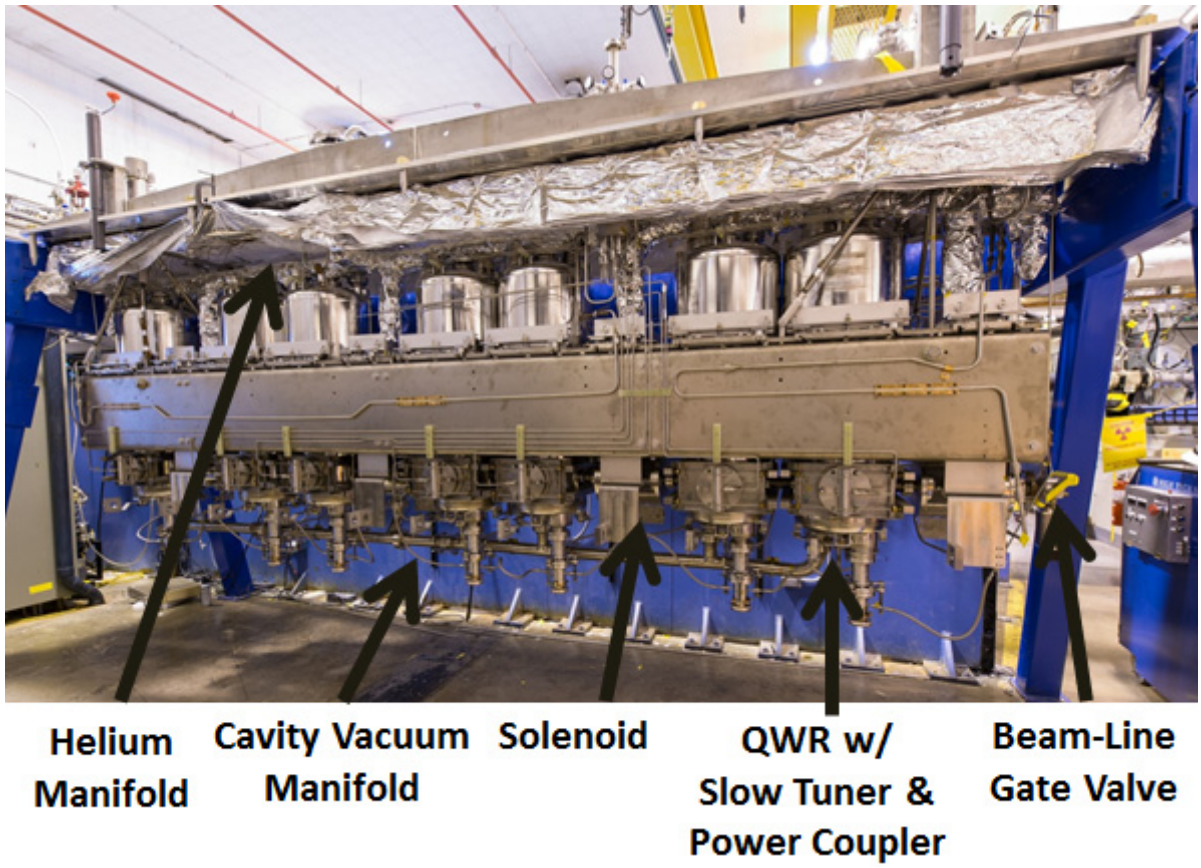

Figure 1: The cryomodule cold-mass hanging from the lid. Not shown are the solenoid gas purged lead feedthrough, the helium manifold relief port and the cold-mass hanger supports.

pressure rise was measured with two distinct heat loads. First, the pressure rise was observed with only the static thermal load warming the cryomodule. Next, the pressure rise was measured with several different known power levels applied to the helium bath through resistance heaters. For small ΔP, the rise in pressure observed for ~5 minutes was almost linear and the static heat load was extrapolated from comparing the pressure rise for heater powers of 5 W and 10 W to the no-heater case. (2) The cryomodule was vented to atmosphere and all of the venting boil-off gas was passed through a helium mass-flow meter. Figure 2 shows the reading from the mass-flow meter. The initial venting of the cryomodule was done through a different port and the initial mass-flow readings increase from 0 as this valve was closed. The maximum measured value was 12 W and this is used as the static heat load. It is not surprising that the measured value is less than the calculated value. The calculated values all assume shorter conduction paths and neglect thermal contact impedances.

The static 80 K load was measured by passing the nitrogen boil-off gas through a flow meter which was calibrated for room-temperature nitrogen gas flow. After the cryomodule came to thermal equilibrium the measured 80 K boil-off rate was measured to be 60 W. 5 days were required to reach thermal equilibrium. The 5 day cooldown is due to the poorly cooled titanium strong-back. The titanium strong-back is conductively cooled through the cavity and solenoid kinematic mounts which are very low-conductivity. We installed an active He cool-down circuit on the strong-back and will use it to pre-cool more in the future.

Dominating the total 4.5 K thermal load are the dynamic RF losses from the QWRs and couplers. Measuring the dynamic cryomodule losses was possible when the entire cryomodule was cooled with the upgraded ATLAS 4.5 K distribution system. First, the ATLAS 4.5 K refrigerator was operated at constant load. The load was kept constant through the operation of a load levelling resistive heater. The heater power was operated in a feedback loop to stabilize the entire system load such that it varied by 5 W peak-to-peak over the span of an hour prior to the measurements. The load levelling resistor was calibrated by energizing heaters internal to the QWR cryomodule. These heaters are rigidly attached to the helium manifold with hose clamps and there is indium wire between the heaters and the manifold to ensure good thermal contact. The cryomodule heaters were operated at 5 W, 10 W, 20 W 30 W and 40 W. Measureable changes in the 4.5 K helium system load levelling heater occurred for heater powers of 10 W and greater. Above 30 W the 4.5 K system pressure started to increase leading to a larger measurement error as reflected in the error bars. The day after the load levelling heater was calibrated the cryomodule QWRs were all energized to an average voltage gain of 2.5 MV per cavity. After the

ISBN 978-3-95450-131-1

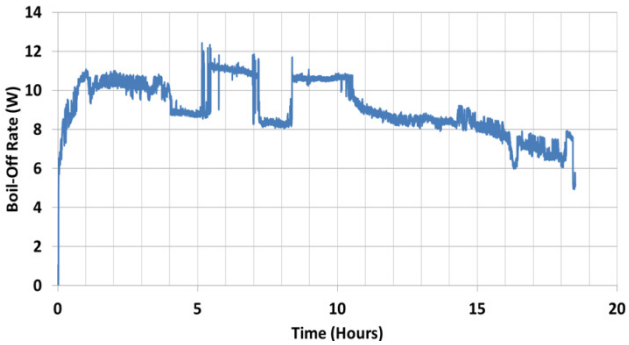

Figure 2: The helium mass-flow meter monitoring the helium boil-off after venting the cryomodule. The venting was done through a single port with all other ports sealed. The steps in the response correspond to the decreasing helium level dropping below the level of the helium manifold dam (a piece of metal welded into the pipe to regulate the maximum liquid level), the helium manifold, the top of the cavities, and the top of the solenoids. A 12 W load was largest reading observed.

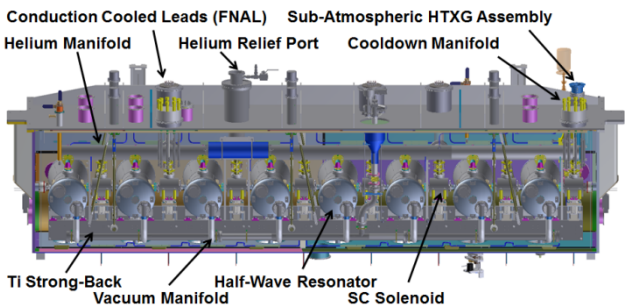

Figure 3: Cross section of the new HWR cryomodule.

last cavity was excited and the 4.5 K helium system came to equilibrium the load levelling resistor power was measured to be 33 +10/-5 W. The helium system pressure was constantly rising during this time indicating that the cryogenic load was somewhat higher giving the larger upper error bar.

PREVIOUS ATLAS PERFORMANCE

The 3 split-ring cryomodules which were removed consisted of a 4-cavity, an 8-cavity and a 6-cavity cryomodule. These cryomodules each had static 4.5 K thermal loads of 25 W static and the dynamic cavity loads were ~5 W per cavity. With the total 4.5 K load for all split-ring cryomodules being 165 W [8], 75 W static and 90 W dynamic. The new QWR cryomodule has a measured total 4.5 K load of 45 W, 12 W static and 33 W dynamic. This saves roughly 120 W of 4.5 K capacity relative to the older split-ring cryomodules. More importantly, this demonstrates the cryogenic savings gained by using fewer higher-performing superconducting cavities in a compact linear accelerator.

CONCLUDING REMARKS

The installation and commissioning of a new QWR cryomodule for ATLAS is complete. The new cryomodule has a measured 4.5 K thermal load of 45 W, 12 W static and 33 W dynamic. The 80 K load was observed to be 60 W. This has resulted in considerable saving for the ATLAS cryogenic system, equal to 120 W. Extra cryogenic capacity is now available for other liquid helium cooled devices and some of this is already being used. The reduced cryogenic loads clearly demonstrate the utility of using high-performance superconducting resonators to shrink the cryoplant size for new accelerators and the cost of future projects.

This work is now serving as the baseline for a new 2 Kelvin half-wave resonator (HWR) cryomodule being built as part of the FNAL PIP-II project. This cryomodule houses 8 HWRs and 8 superconducting solenoids, one in front of each cavity. Figure 3 shows a cross section view of the module. Two HWRs have been tested so far with exceptional results [9].

ACKNOWLEDGMENTS

We gratefully acknowledge the entire ATLAS operations staff for their help and support during the commissioning of this cryomodule.

REFERENCES

[1] *The PIP-II Reference Design Report*, Ed. V. Lebedev, Version 1.00, March 2015, http://pxie.fnal.gov/PIP-II_RDR/PIP-II_RDR.pdf.

[2] M. Leitner et al., "The FRIB project at MSU," SRF'13, Paris, France, September 2013, p. 1 (2013); www.jacow.org.

[3] P.N. Ostroumov, "Advances in CW Ion Linacs," IPAC'15, Richmond, Virginia, May 2015, p. 4085 (2015); www.jacow.org.

[4] J.D. Fuerst, "The ATLAS Energy Upgrade Cryomodule," SRF'09, Berlin, Germany, September 2009, p. 52 (2009); www.jacow.org.

[5] M.P. Kelly et al., "Commissioning of the 72 MHz Quarter-Wave Cavity Cryomodule at ATLAS," LINAC'14, Geneva, Switzerland, August 2014, p. 440 (2014); www.jacow.org.

[6] M. Kedzie et al., "Design and Development of a New SRF Cavity Cryomodule for the ATLAS Intensity Upgrade," in *Advances in Cryogenic Engineering* 57A, edited by J. G. Weisend II et al, American Institute of Physics, New York, 2012, Pg. 937.

[7] S.-h. Kim et al., "Emissivity Measurements of Coated Copper and Aluminium Samples at 80 K," in *Advances in Cryogenic Engineering* 59A, edited by J.G. Weisend II et al, American Institute of Physics, New York, 2014, Pg. 500.

[8] Private communication with S.W.T. MacDonald 2014.

[9] Z.A. Conway et al., "Achieving High Peak Fields and Low Residual Resistance in Half-Wave Cavities," SRF'15, Whistler, British Columbia, Canada, to be published.

ISBN 978-3-95450-131-1

STATUS AND OPERATION OF THE ATLAS SUPERCONDUCTING ACCELERATOR*

M. R. Hendricks, R.C. Pardo, A. Krupa, ANL, Argonne, IL 60439, USA

Abstract

ATLAS (the Argonne Tandem Linac Accelerator System) is a super conducting heavy ion accelerator which can accelerate nearly all stable, and some unstable, isotopes between protons and uranium with a charge to mass range of 1/1 to 1/7. The maximum energy ranges of these accelerated ions are 7-17 MeV per nucleon with intensities ranging from a few thousand ions/second to microampere currents. On average ATLAS delivers a different ion species and energy each week to one of six target areas. ATLAS currently operates 24 hours a day, 7 days per week, and at least 40 weeks per year. Topics discussed will be how we handle day to day operation of the facility including start up, reusing old accelerator configurations for new experiments (scaling), tuning for in-flight produced radioactive beams, troubleshooting problems, and maintenance.

THE ATLAS FACILITY

ATLAS is the worlds' first superconducting heavy ion accelerator [1]. From its origins in 1978 until now it has consistently pushed new boundaries for stable low energy ion beam production. Located at Argonne National Laboratory outside of Chicago, Illinois in the United States, ATLAS has been delivering beams consisting of stable isotopes between protons through uranium for 37 years. The facility (Fig. 1) has two ion sources, an ECR source for multipurpose use and a charge breeding source coupled to the CARIBU radioactive ion source [2]. Once ions are produced they are accelerated through a maximum of 50 superconducting RF resonators which can give beam energies of 10-20 MeV/A depending on the atomic mass of the ion. Typical beam currents of 5-500 electrical nanoamps to target are common. However, the facility has demonstrated 35 electrical micoamps through the first linear accelerating section. While the facility can accelerate ions in a mass range between protons and uranium, in 2014 the facility accelerated 29 unique ions species. Of those 29 species, 5 species delivered to target were radioactive ion beams (RIB). Two of the 5 species were from CARIBU, and 3 were produced in-flight from accelerated stable beam.

Staffing and Operations

The facility operates 24 hours a day, 7 days a week. Relying on a total staff of 21 full time employees, divided into the following specialities and full time employees: physicists (2), operations (8), ion source (2), control system (2), cryogenic (2), mechanical (2), and electronic (3).

New experiments are scheduled, on average, once a week and involve reconfiguring all elements of the accelerator. Two methods exist for this reconfiguration, either using an old saved configuration from a previous experiment, or by establishing a new configuration. The largest advantage to using an old saved configured is the amount of time saved versus establishing a new accelerator configuration. Even though a new configuration takes more time to create, it typically achieves the best beam quality. Depending on requirements for different experiments, it may take 8-24 hours to establish the accelerator and be delivering the requested ion species, energy, and intensity to target.

Accelerator configurations are saved via an offline computer. These saved configurations create a library of configurations which can be leveraged in future experiments. These configurations are scaled when applicable to future experiments. Resonators are scaled by the mass to charge ratio, but limited to approximately ±15% of the saved configuration's mass to charge ratio. This limit is driven by the lack of linearity when setting resonator phase and amplitude beyond this percentage. Magnetic devices are scaled based on the magnetic rigidity. The ability to scale accelerator configurations is critical for setup and delivering CARIBU beams, as well as for performing accelerator mass spectroscopy.

Facility Upgrades

The accelerator has undergone several improvements in the past 6 years, which have greatly benefited its operation and performance. In 2009 the last cryostat of the accelerator containing 1978 era RF resonators was replaced with a new cryostat containing, at that time, state of the art quarter wave resonators (QWR) [3]. These QWR had more than twice the voltage potential, a world record at the time, than the previous resonators. This cryostat had additional improvements as well, such as separating the cavity and cryostat vacuum spaces. Separating the vacuum spaces is motivated by the desire to keep the QWR RF surfaces as clean as possible. This cleanliness is import to maintaining cavity performance and is also a challenge to preserve. Since introduction there has been no degradation of quality or potential gradients for the QWR.

In 2011 a room temperature radio frequency quadrouple (RFQ) [4] was installed at the beginning of the accelerator. Since an RFQ maintains beam emittance, beam transmission through the first accelerating section, the PII Linac, improved to over 80%, instead of 60%, as was achievable under the previous configuration.

The most recent upgrade to the facility was a reconfiguration of the BOOSTER linac, including the

* This material is based upon work supported by the U.S. Department of Energy, Office of Science, Office of Nuclear Physics, under contract number DE-AC02-06CH11357

ISBN 978-3-95450-131-1

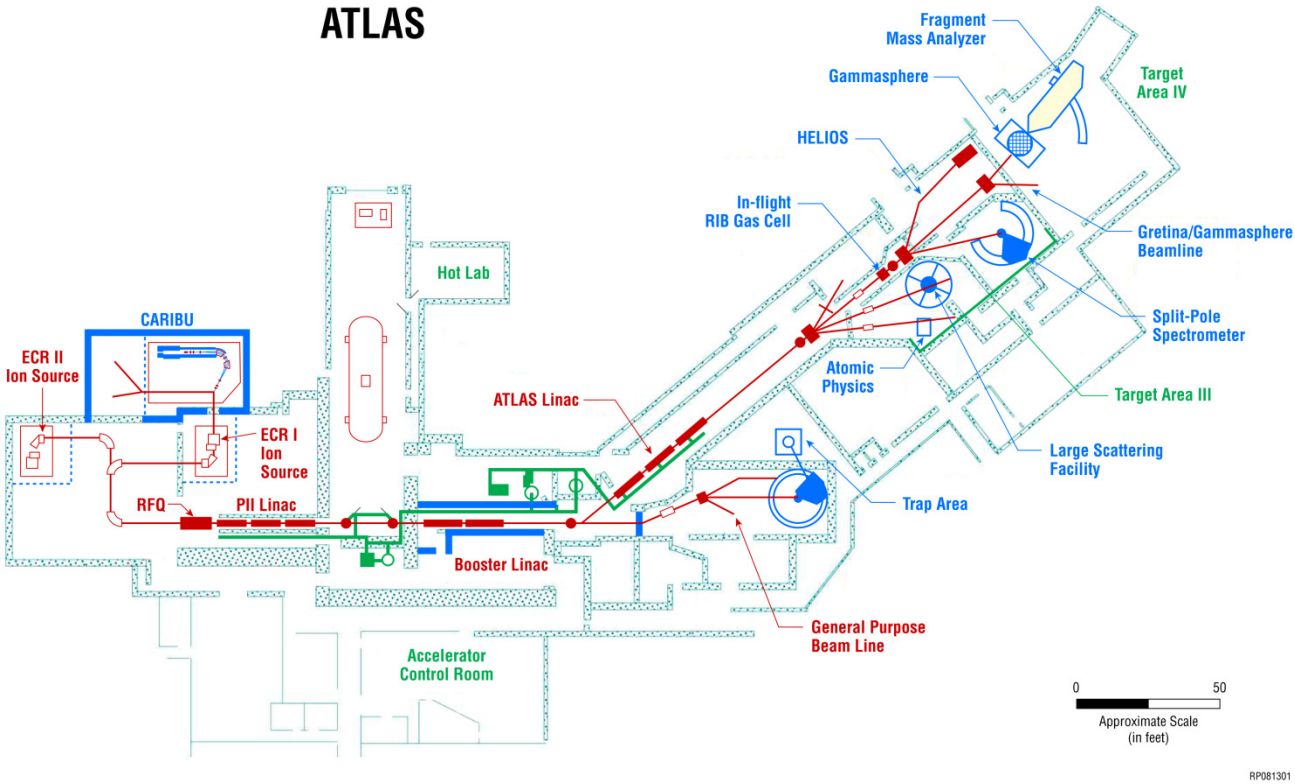

Figure 1: Overview of the ATLAS facility.

exchanging of three 1978 era cryostats, for a single new QWR cryostat [5]. Similar in implementation to the cryostat installed in 2009, it houses 7 QWR cavities, and achieves an average world record 2.5MV per resonator, while only contributing 45W of power into the 4.5K liquid helium system.

The existing ECR charge breeder ion source, currently coupled with CARIBU, will be replaced with an Electron Beam Ion Source (EBIS) early in 2016 [6]. This approximately doubles the charge breeding efficiency versus the ECR charge breeder. Additionally, EBIS will provide very clean background in the A/q range of CARIBU ion beams.

Before 2017 the facility plans to install the Argonne In-flight Radioactive Ion Separator (AIRIS). This new upgrade has many improvements versus the existing method of in-flight production. It will provide new regions of RIB, with a higher mass and further from stability, while improving the transmission. Its location will be moved upstream from the existing position which offers RIB to more target areas in the facility.

RIB Tuning

Tuning of radioactive ion beams is complicated versus stable ion beams. ATLAS as two different ways of producing radioactive beams, either from charge breeding the daughter products from a decaying ^{252}Cf source, or producing them in-flight from accelerated stable beam interacting with a gas cell or beryllium foil.

The process for delivering the in-flight produced RIBs, is as follows. First stable beam is delivered to the experimenter's detector area, where they may or may not use that beam for calibration of their detector. Next the gas target or beryllium foil is inserted into the beamline, and an energy degraded stable beam is then tuned to the detector area again. Finally to deliver RIB all beamline devices between the gas target or beryllium foil and the detector are scaled based on the expected rigidity of the RIB of interest. Additional tools are available to try and optimize the RIB, those include a superconducting solenoid after the gas cell or beryllium foil. Two different rebunching superconducting resonators, for time focusing both the stable and radioactive ion beams, are also configured. Finally, a RIB "sweeper" in some cases allows for the removal of undesired beam with similar rigidity but different timing.

RIB from CARIBU are tuned and delivered to target in a different way than in-flight beams. First a "guide beam" of similar A/q as the desired RIB is delivered to the detector area. The entire accelerator is then scaled by that A/q ratio difference between the "guide beam" and the desired RIB. Beams from CARIBU have an intensity of less than 10^5 particles/second, therefore special detectors are need throughout the accelerator are needed. These detectors rely on counting beta radiation emitted from the RIB once in implanted on an aluminium foil. Eight of these detectors are strategically placed in the accelerator and are used to optimize the CARIBU RIB transmission

ISBN 978-3-95450-131-1

after the scaling from the stable beam has been completed.

Maintenance and Troubleshooting

ATLAS has one planned maintenance period per year, which typically is 4 weeks long, and scheduled to occur in January. This period is used to address annual safety tests and inspections. Additional time is used to perform major repairs that are outstanding such as, cryostat repairs or cryogenic system repairs for example.

Aside from this planned maintenance period, the facility operates under the philosophy of run to failure. That means that ATLAS delivers beam to a target area unless there is a critical failure that requires maintenance. This attitude towards maintenance has given ATLAS an average reliability of nearly 92% over the past 6 years. The recent upgrades to the accelerator have improved reliability; however the upgrades and their operation require more diverse expertise to achieve.

Nearly all problems at ATLAS are first handled by the operators. The expectation is that the operator can troubleshoot and correct simple problems, and if they are not resolved by them, then the operator will contact the system expert for the affected subsystem experiencing difficulty. System experts are continually on call for troubleshooting problems.

SUMMARY

The ATLAS accelerator is versatile machine capable of delivering stable and radioactive beams to a wide variety of target areas. Recent upgrades have improved performance and reliability, while future upgrades will focus on improving the increasing the diversity of radioactive ion beams available to target. Tuning the accelerator for radioactive beams is well understood and becoming standardized.

ACKNOWLEDGMENT

The authors would like to thank the entire ATLAS staff for their continuous hard work and dedication to the facility.

REFERENCES

[1] L.M. Bollinger et al., “ATLAS: A Proposal for a Precision Heavy Ion Accelerator at Argonne National Laboratory”, Argonne National Laboratory, 1978, ANL-78-XX-68.

[2] R.C. Pardo et al., “Neutron-Rich Beams from 252Cf Fission at ATLAS – The CARIBU Project,” MO3GRI02, PAC proceedings, PAC’09, Vancouver, Canada (2009).

[3] M.P. Kelly et al., “Superconducting Quarter-Wave Resonators for the ATLAS Energy Upgrade,” THP025, LINAC proceedings, LINAC’08, Victoria, Canada (2008).

[4] P.N. Ostroumov et al., “Efficiency and Intensity Upgrade of the ATLAS Facility,” MOP045, LINAC proceedings, LINAC’10, Tsukuba, Japan (2010).

[5] P.N. Ostroumov et al., “Completion of Efficiency and Intensity Upgrade of the ATLAS Facility,” TUPP005, LINAC proceedings, LINAC’14, Geneva, Switzerland (2014).

[6] S. Kondrashev et al., “Commissioning of CARIBU EBIS Charge Breeder Sub-systems,” WEB02, HIAT proceedings, HIAT’12, Chicago, USA (2012).

ISBN 978-3-95450-131-1

INTEGRATING THE TRACK BEAM SIMULATION CODE TO IMPROVE ATLAS OPERATIONS*

C.A. Dickerson#, B. Mustapha, C.E. Peters, ANL, Argonne, IL 60439, USA

Abstract

At the Argonne Tandem Linear Accelerator System (ATLAS) we are integrating TRACK, three dimensional particle tracking software that numerically integrates the equations of motion, into the accelerator control system. ATLAS delivers a variety of ions (1 – 238 AMU) at various energies (1 – 15 MeV/u) to multiple targets. By comparing simulated and observed performance, model driven operations will improve the understanding of the facility, reduce tune times, and improve the beam quality for these diverse operating conditions. This paper will describe the work to interface TRACK with the real-time accelerator control system, and the results of simulations used to characterize and configure the accelerator.

INTRODUCTION

Accelerator operations at ATLAS need to be flexible and versatile to accommodate the variety of operating configurations. ATLAS operates two sources to six target lines, as shown in Fig. 1. Experiments are changed 1-2 times per week. Ion species range from protons to ^{238}U, and energies from 0.5 to >15 MeV/u. In addition to stable beam delivery, radioactive ion beams (RIB) can be produced via the in-flight method or by reaccelerating fission fragments from the CARIBU [1] source. RIB delivery poses a particularly difficult challenge since the RIB intensities are typically much too low <10^6 pps to monitor using conventional Faraday cups and wire scanners. For these cases the accelerator is first configured for a pilot beam of sufficient intensity then scaled to match the rigidity of RIB. While a compact particle detector is being developed to aid the tuning of low intensity beams at ATLAS [2], these situations could benefit particularly from component settings accurately predicted using simulation software.

To improve the efficiency and reliability of ATLAS operations, the beam tracking software TRACK [3] is being interfaced with the ATLAS control system. The goals of this effort are to identify regions of significant beam loss and areas of distortion which then lead to significant loss, and to reduce the setup time for accelerator configuration and optimization. Besides displaying beam characteristics for real time configurations, the simulations will be able to predict component fields for previously unencountered situations and configurations – when new equipment requires a reconfiguration, or during in-flight radioactive ion beam production when the 6D beam distribution changes dramatically at the production target. The graphics outputs of the simulations, which show the evolution of the beam through the accelerator (Fig. 2), will be a great training aid for operations staff and experimenters, and finally a more accurate understanding and model of the machine will evolve as the differences between the expected and observed accelerator performance are investigated.

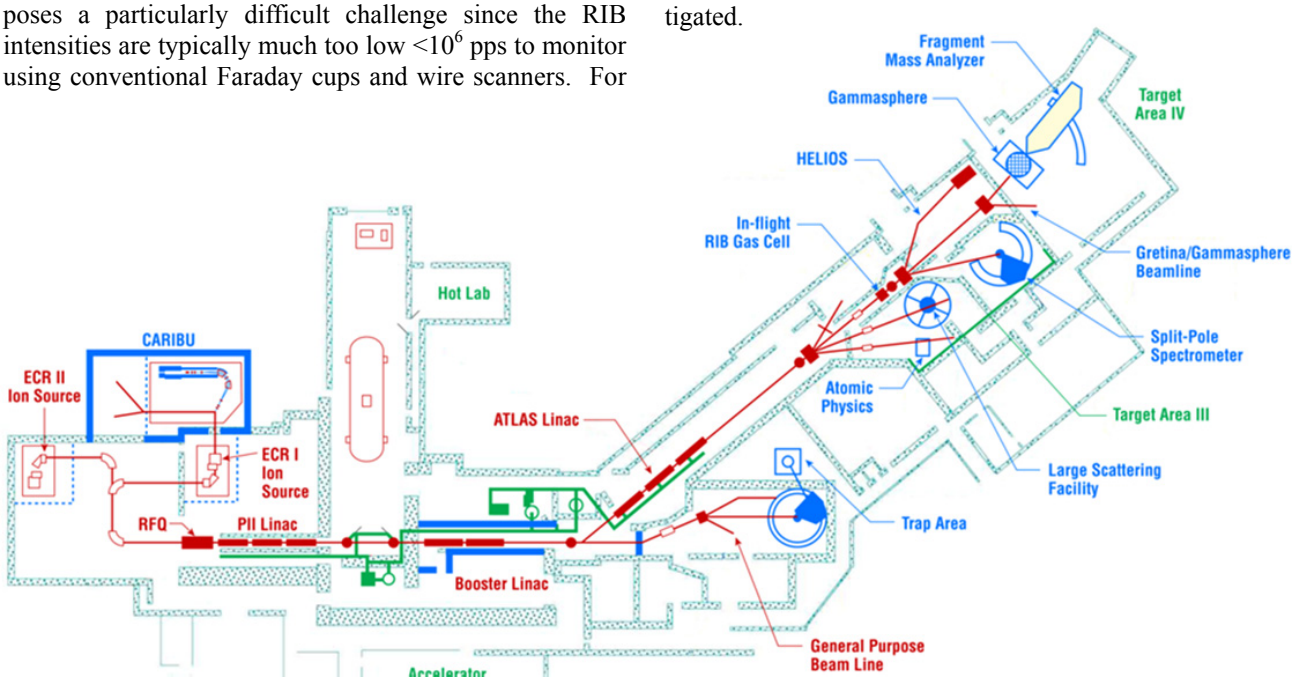

Figure 1: The ATLAS accelerator layout.

*Work supported by U.S. Department of Energy, Office of Nuclear Physics, under contract DE-AC02-06CH11357
#cdickerson@anl.gov

ISBN 978-3-95450-131-1

TRACK BACKGROUND

The TRACK simulation software was developed by the Argonne Physics Division to study beam evolution through superconducting linear accelerators, and is still maintained and upgraded regularly. TRACK numerically integrates the equations of motion for particles through 3D fields. Many basic component fields (dipole magnets, quadrupole magnets, acceleration tube, etc.) can be expressed analytically based on a few parameters, while more complicated geometries and more accurate fields can be mapped from third party software and imported into TRACK. TRACK also accounts for space charge forces using a Poisson solver, and includes matching and optimization routines.

Configured correctly, TRACK produces very accurate results by optimizing the number of integration steps independently for each component and by using realistic imported 3D fields. The accuracy of TRACK for predicting and characterizing both the transverse and longitudinal performance of complicated accelerating components was reported for the commissioning the ATLAS RFQ [4-5]. The measured time structure, transverse profile, and energy spread of the beams matched very well with the TRACK simulations.

BUILDING THE TRACK INPUT FILES

To interface TRACK with the real time accelerator configuration data for the component's set values, the component geometries and the beam characteristics are aggregated and parsed to create the two main TRACK input files: the accelerator configuration file and the beam configuration file. The accelerator configuration file includes the component sequence, the individual component geometries, and the associated electric and magnetic fields. The beam configuration file includes the beam species, the 6D distribution, and parameters for matching and optimization.

The sequence of accelerator components is dynamically created from the control system based on the beam source and the target listed for the experiment. An additional database was created to store all the relevant fixed information for each component such as length, aperture radius, etc. The component field levels are calculated using the control system set values and appropriate scaling. Scales from the RF control module output to a superconducting resonator field are based on energy gain measurements logged when configuring the resonator phasing. Based on the known input and output energies the effective voltage of the resonator can be calculated. It is then possible to determine the scale between the RF control module output and the effective resonator voltage by applying the normalization used to simulate the associated 3D resonator field. With years of logged resonator phase scans, statistically accurate resonator scale factors are possible. For magnetic components, dipoles and quadrupoles, power supply output current versus generated magnetic fields can be measured directly with a hall probe or the magnetic field can be continuously monitored using a hall probe.

The beam configuration file is generated from the species information, a beam distribution at a given plane, and energy information – from a Si detector, the ATLAS time of flight system, or the high resolution monitoring of the potential of the source high voltage platform. Before the beam is bunched a pepper pot emittance meter [6] can provide the necessary transverse 4D distribution information then TRACK can simulate the bunching process through the multi harmonic buncher before the RFQ. After the beam is bunched longitudinal information is available after each accelerating section from energy and timing signals generated with Si detectors.

TRACK RESULTS FOR ACCELERATOR OPERATIONS

The ATLAS control system runs on LINUX based computers, so the LINUX version of TRACK has been used for this application. Unfortunately there are no graphical outputs, so custom graphics were developed with the control system software libraries. Figure 2 shows the graphical display outputs. The top row from left to right shows the two transverse and the longitudinal phase space plots. The maximum and rms horizontal and vertical radii are plotted on the middle row, and the maximum and rms beam pulse length in degrees of the harmonic frequency are plotted on the bottom. The columns along the right show the component names in the control system listed by position. These labels will be incorporated into the envelope plots in the future.

TRACK has been used to provide nominal component settings for previously unencountered configurations, typically after significant upgrades like the recent efficiency and intensity upgrade [7]. With a pepper pot measured beam distribution upstream of the first buncher, TRACK simulations indicated quadrupole and superconducting solenoid settings to transport the beam through a completely new transport section, the new RFQ, and a reconfigured PII linac. Results were excellent as a significant portion of the beam was transported with these predicted settings and subsequent fine tuning was easily achievable. Recently a He leak in an old cryostat of split-ring resonators required the resonators and solenoids to be taken offline during the middle of beam delivery to an experiment. TRACK simulations successfully predicted the settings for the adjacent optical components to achieve 100% transmission.

ISBN 978-3-95450-131-1

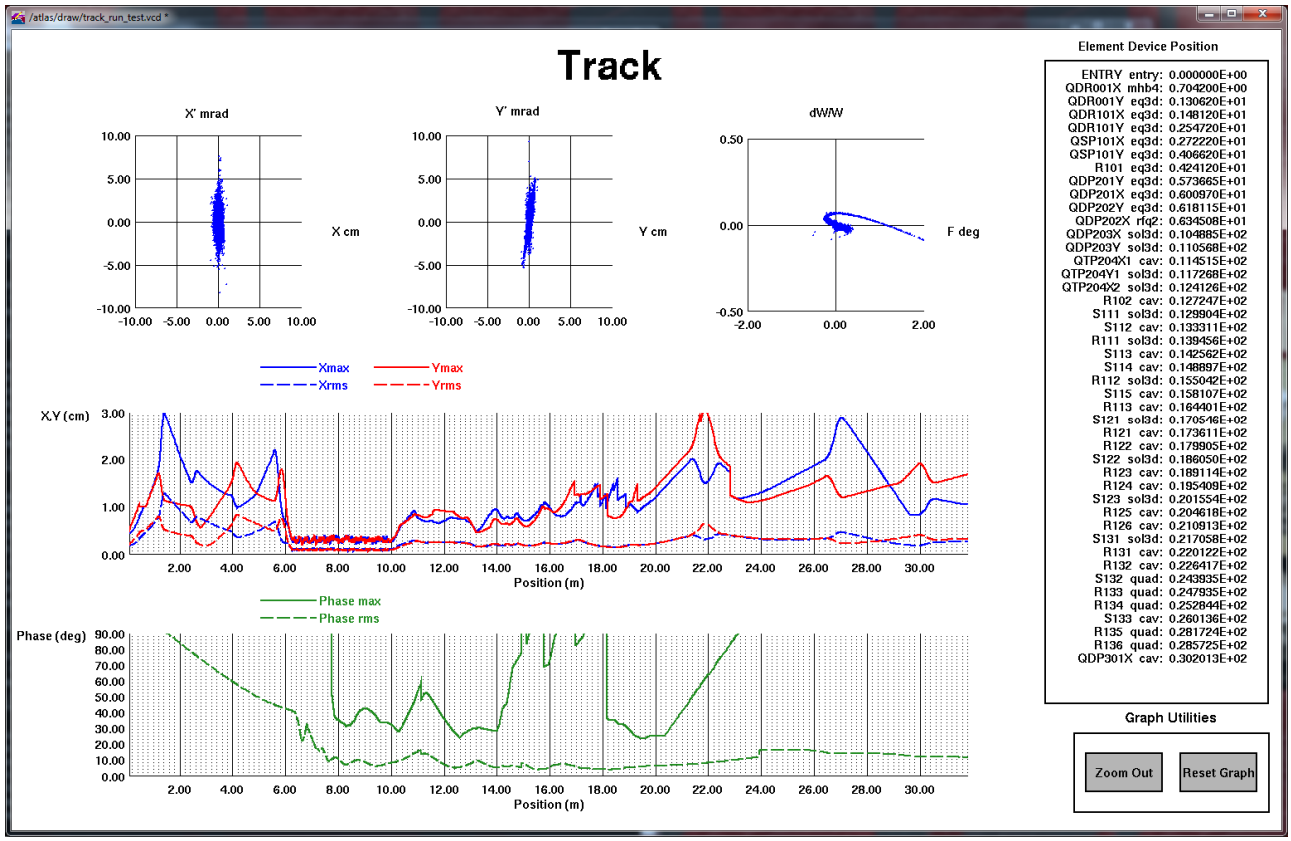

Figure 2: Graphics created for TRACK within the ATLAS control system: phase space distributions (top), maximum and rms envelope plots (middle), beam pulse width (bottom).

FUTURE WORK

As this effort continues the graphics output will be refined and functionality added to enable user interaction and rescaling of the plots. Custom scaling factors will be implemented for unmeasured components, and a special effort will be made to determine the field strength of the bunching cavities. Most importantly a user interface will be developed to allow simulation customization: user defined regions of the accelerator to simulate, and input of matching and optimization conditions.

SUMMARY

Operations at ATLAS need to be flexible and versatile; accelerator configurations are changed 1-2 times per week, and a wide range of masses and energies are delivered from a combination of sources and targets. We are integrating the TRACK beam simulation code into the ATLAS control system to improve operations, and increase the accelerator setup and optimization efficiency. TRACK is very accurate software, but this accuracy relies on realistic beam distributions and component definitions. Integrating TRACK into routine operations will refine the model and ultimately produce better results. TRACK simulations have already successfully predicted fields for previously unencountered accelerator configurations. The refinement of the accelerator model and development of a quality user interface will be a powerful tool for the ATLAS operations staff.

REFERENCES

[1] G. Savard et al., "Radioactive Beams from Gas Catchers: The CARIBU Facility", NIM B 266, 4086-4091 (2008).

[2] C.A. Dickerson et al., "A Fast, Compact Particle Detector for Tuning Radioactive Beams at ATLAS", MOPA29, these proceedings, HIAT15, Yokohama, Japan (2015).

[3] The beam dynamics code TRACK [http://www.phy.anl.gov/atlas/TRACK]

[4] P.N. Ostroumov et al., "Development and Beam Test of a Continuous Wave Radio Frequency Quadrupole Accelerator", PRST AB 15, 110101 (2012).

[5] A. Perry et al., "Beam Characterization of a New Continuous Wave Radio Frequency Quadrupole Accelerator", NIM A 735, 163-168 (2014).

[6] S. Kondrashev et al., "Emittance Measurements for Stable and Radioactive Ion Beams", LINAC10, Tsukuba, Sept. 2010, p. 208-210 (2010).

[7] P.N. Ostroumov et al., "Completion of the Efficiency and Intensity Upgrade of the ATLAS Facility," LINAC14, Geneva, Sept. 2014, p. 449-451 (2014); http://www.JACoW.org

ISBN 978-3-95450-131-1

THE ATLAS INTENSITY UPGRADE: PROJECT OVERVIEW AND ONLINE OPERATING EXPERIENCE*

R.C. Pardo, A. Barcikowski, Z. Conway, C. Dickerson, M. Hendricks, M. P. Kelly, S.H. Kim, Y. Luo, S. MacDonald, B. Mustapha, P. Ostroumov, C. Peters, M. Power, R. Scott, S. Sharamentov, R. Vondrasek, G. Zinkann
Physics Division, Argonne National Laboratory, IL 60439 USA

Abstract

ATLAS, the world's first accelerator to use RF superconductivity for ion acceleration, has undergone a major facility upgrade with the goals of significantly increased stable-beam current for experiments and improved transmission for all beams. The dominant components of the upgrade are a) new CW-RFQ to replace the first three low-β resonators, b) a new cryostat of seven β=0.077 quarter-wave resonators demonstrating world-record accelerating fields, c) an improved cryogenics system, and d) the retirement of the original tandem injector. This latest upgrade followed closely on the earlier development of a cryostat of β=0.14 quarter-wave resonators. The reconfigured ATLAS system has been in operation for over one year and its performance after the upgrade will be presented.

INTRODUCTION

ATLAS (the Argonne Tandem Linac Accelerator System) is the world's first superconducting accelerator for ions. ATLAS began as a proof-of-principle project in the early 1970s to demonstrate that a superconducting resonator's field amplitude and phase could be controlled with sufficient precision to enable the acceleration of ions [1]. In order to continue to meet current requirements of the experimental program, ATLAS has been continuously upgraded to provide the tools necessary to remain at the forefront of nuclear science.

A key component in ATLAS's continuing success has been the constant improvements to the facility including the evolution of best practices in constructing and operating superconducting resonators as well as new techniques for ECR ion source operation. Those developments are seen in the different classes of resonators that have been developed at Argonne and the new techniques in superconducting RF (SRF) technology that have been applied and the world best performance of the CARIBU ECR charge breeder ion source. From the split-ring resonator which was capable of approximately 3 MV/m accelerating field, to the quarter-wave resonators used in the Positive Ion Injector section of ATLAS installed in the early 1990s, and now to the fully helium immersed; pure niobium quarter-wave resonators used in an energy upgrade of the facility in 2009 as well as the most recent new upgrade to the center (Booster) section of ATLAS in 2014, one sees a continuing progression of state-of-the-art SRF technology now culminating in routine accelerating fields of up 8 MV/m.

This paper describes the overall facility operating performance and goals achieved in three major improvement projects going back to 2009. The goals of these projects are to improve the linac performance by increasing the maximum available beam current and improving the overall beam transmission and efficiency in order to increase beam currents for radioactive beams and high current stable beam operations.

PROJECTS OVERVIEW

In the last 6 years, the ATLAS accelerator has undergone a number of improvements that are aimed at addressing the current and future needs of the nuclear science community. These changes to the ATLAS accelerator have provided significant performance improvements in both accelerating fields and beam transmission. Thus four major accelerator improvement activities have been implemented at ATLAS in the past few years:

1. A new cryostat of seven quarter-wave (β=0.14) resonators has been installed as the last ATLAS cryostat restoring the maximum beam energy to approximately 21 MeV/u for the lightest ions and approximately 10 MeV/u for unstripped ^{238}U.

2. A new, room-temperature CW radio frequency quadrupole (RFQ) linac has been installed as the first accelerating resonator in the linac. It replaces three of the original, very low-velocity, superconducting resonators of the Positive Ion Injector (PII) Linac. This project has improved the overall bunching efficiency so that approximately 80% of the DC source current can be captured into a high-quality beam for acceleration through ATLAS.

3. A second new cryostat of seven quarter-wave (β=0.077) resonators has been constructed to replace three cryostats of split-ring resonators in the middle section (booster) of the ATLAS linac. These resonators are achieving world-record accelerating field performance for low-beta resonators, and reducing the total resonator count in the linac (from 64 to 51) while maintaining the total accelerating voltage. The center portion of the original ATLAS cryogenic system has been completely rebuilt, the beam optics in the center section of the ATLAS accelerator was redesigned and improved, and new shielding was installed to accommodate the higher intensity stable beams that are now available.

The ATLAS facility floor plan and identification of the location of these projects is shown in Figure 1.

* This work was supported by the U.S. Department of Energy, Office of Nuclear Physics, under Contract No. DE-AC02-06CH11357.

ISBN 978-3-95450-131-1

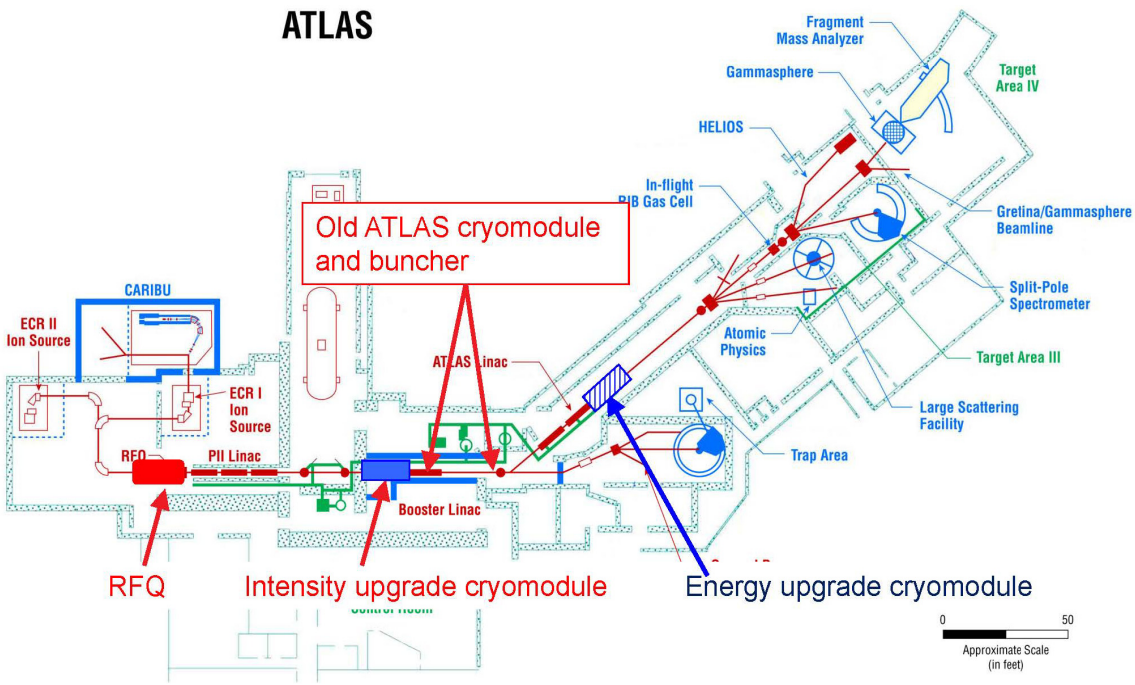

Figure 1: Floor plan of ATLAS showing the location of the major improvement projects discussed in this paper. The tandem injector, now retired, is shown but now disconnected from that ATLAS accelerator.

ENERGY UPGRADE CRYOSTAT

The energy upgrade cryostat with seven 'high' beta (β=0.14) cavities was completed and installed in 2009. The details of the resonator and cryostat design and commissioning performance can be found in reference [2]. Since then the resonators have provided over 2000 hours of accelerated beam for research.

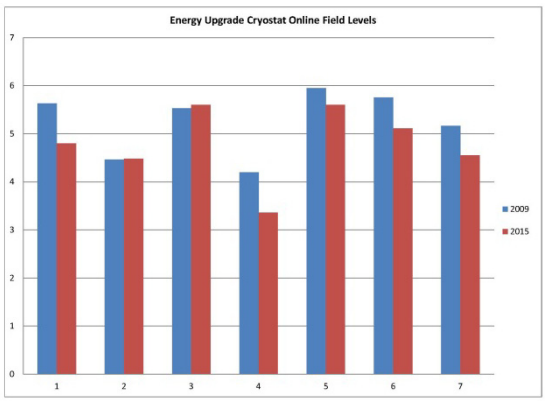

Figure 2: Comparison of on-line resonator field performance of the =0.14c QWR energy upgrade project resonators between 2009 and 2015. The average accelerating field performance in 2009 was 5.2 MV/m compared to 4.8MV/m in 2015.

The adoption of independent insulating vacuum and internal resonator/beamline vacuum space has greatly improved the long-term resonator online performance. After six years no clear degradation in field performance can be observed. The chart in Figure 2 compares the 2009 resonator commissioning performance and the present 'normal' operating performance for these resonators. One does notice that there is approximately a 10% decrease between the maximum commissioning fields achieved in 2009 and those routinely achieve today. But this decrease is due to desiring reliable operation and achieving a certain level of 'safety' with regard to the VCX PIN diode system. At this point, the field level in these resonators is limited by the power handling capability of the VCX system.

EFFICIENCY AND INTENSITY UPGRADE PROJECT

The Intensity and Efficiency Upgrade Project for ATLAS is designed to address the need for efficiently accelerating all beams (radioactive and stable) and to retire old split-ring resonators which have been in operation for over 35 years. Here 'efficient' means the highest possible transmission and bunching efficiency through the accelerator to target for all beams. The original PII linac design used quarter wave resonators that had a matched velocity as low as 0.009c. Only one resonator had such a low matched velocity but this resonator nearly doubled the beam energy from the ion source in a 10 cm total distance. The resonator was a 'split' drift tube design creating a 4-gap structure [3]. The beam optics of this one resonator created a small acceptance window and functioned in an alternating phase focusing mode. The result was significant emittance growth and loss of beam due to the mismatch condition in this early stage of acceleration. Therefore transmission through the PII linac was typically 60-65% and the transmission through the rest of the accelerator and beam transport was 80-85% at best.

ISBN 978-3-95450-131-1

Radio Frequency Quadrupole

The details of the design and commissioning performance of the RFQ linac can be found in reference [4]. The RFQ operates at 60.625 MHz, with a maximum vane voltage of 70 kW in CW mode. It is the first RFQ in the U.S. to operate on-line in CW mode and one of a very few in the world at this time. The RFQ is designed to accelerate ions with M/Q<7 from 30 to 295 keV/u.

The RFQ came into operation in January of 2013 and has now provided approximately 8000 hours of beam acceleration since then. Overall reliability has been over 92%. Up to the present, the highest M/Q beam delivered used an M/Q ~6.7.

The RFQ uses a novel high precision temperature control system to tune the RFQ eigenfrequency to the master oscillator. This system has worked extremely well but the original high resistivity water system caused electrolytic erosion in some parts. That system has recently been separated into two parts with only a small system that is required to cool the tetrode final stage tube of the RF transmitter requiring high resistance water.

The limitation on high field operation required for M/Q of 7 seems to partially be due to outgassing of the RFQ at high fields. Improved pumping is expected to be installed by the end of 2015 to improve reliability at the highest fields.

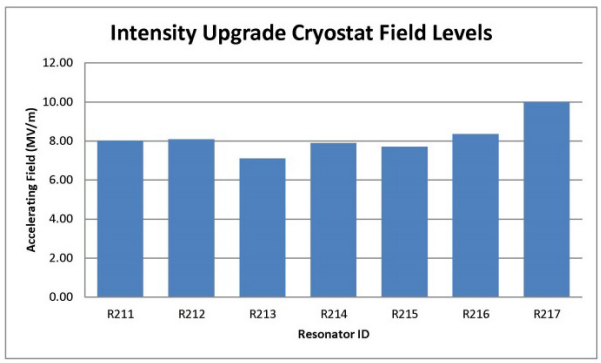

Figure 3: Performance of the ATLAS β=0.077 resonators during the first year of operation. The average field performance of these resonators has been 7.3 MV/m compared to the initial commissioning average of 8.2 MV/m.

Intensity Upgrade Cryostat

In February 2013 an additional new cryostat containing seven newly designed β=0.077 resonators was installed and commissioned. These resonators are described and their initial performance documented in [5]. The design choices made for these resonators and for the associated RF control system grew from the success achieved in the β=0.14 resonator developments of 2009. A major step was taken in this project by retiring the phase control system for all previous installations at ATLAS, the Voltage Controlled Reactance (VCX) PIN diode system and adopting a driven RF system for these resonators. They have now been operating for over one year and their online performance is shown in Figure 3.Compared to the field levels achieved in commissioning, the year over average is only reduce by 11%. This reduction is due to some difficulties with the new driven RF electronics and handling some vibrational situations with the cryogenics system. We see no degradation of resonator performance as seen by individual Q-curves for each resonator.

SUMMARY

The ATLAS upgrades implemented over the past 6 years have performed at or above the expected performance levels. We see no degradation in resonator field performance nor in the RFQ performance. The success of these projects has restored the original energy profile of the facility and sets the stage for the delivery of much higher beam currents than have been previously achieved.

REFERENCES

[1] P.K. Den Hartog, J.M. Bogaty, L.M. Bollinger, B.E. Clifft, S.L. Craig, R.E. Harden, P. Markovich, F.H. Munson, J.M. Nixon, R.C. Pardo, D.R. Phillips, K.W. Shepard, I.R. Tilbrook, and G.P. Zinkann, Proceedings of the 5th International Conference on Electrostatic Accelerators and Associated Boosters, Strasbourg, France and Heidelberg, West Germany, May 24-30, 1989; Nucl. Instrum. Methods A287, 235-239 (1990).

[2] P.N. Ostroumov, J.D. Fuerst, S. Gerbick, M. Kedzie, M.P. Kelly, S.W.T. MacDonald, R.C. Pardo, S. I. Sharamentov, K. Shepard, and G. Zinkann, Proceedings of the 23rd Particle Accelerator Conference (PAC09), Vancouver, BC, Canada, May 4-8, 2009, FR5REP045, pp. 4869-4871 (2010).

[3]] L. M. Bollinger, P. K. Den Hartog, R. C. Pardo, K.W. Shepard, R. Benaroya, P. J. Billquist, B.E. Clifft, P. Markovich, F. H. Munson, Jr., J.M. Nixon, and G. P. Zinkann, Proceedings of the 1989 IEEE Particle Accelerator Conference, Chicago, IL, March 20-23, 1989, eds. Floyd Bennett and Joyce Kopta (IEEE Publishing 1989) 2, 1120-1122

[4] P. N. Ostroumov, B. Mustapha, A. Barcikowski, C. Dickerson, A. A. Kolomiets, S. A. Kondrashev, Y. Luo, D. Paskvan, A. Perry, D. Schrage, S.I. Sharamentov, R. Sommer, W. Toter, and G. Zinkann, Phys. Rev. ST Accel. Beams **15**, 110101 14 November 2012

[5] M. P. Kelly, Z. A. Conway, S. M. Gerbick, M.R. Hendricks, M. Kedzie, S. H. Kim, S. MacDonald, R. C. Murphy, P. N. Ostroumov, T. Reid, S.I. Sharamentov, and G. Zinkann, 27th Linear Accelerator Conference (LINAC14), Geneva, Switzerland, August 31-September 5, 2014.

ISBN 978-3-95450-131-1

THE ISAC-II LINAC PERFORMANCE*

M. Marchetto, S. Kiy, R.E. Laxdal, Y. Ma, O. Shelbaya, Z. Yao, V. Zvyagintsev
TRIUMF, Vancouver, Canada

Abstract

The ISAC-II superconducting linac is operating for almost a decade. The linac first installation includes twenty cavities housed in five cryomodules. The Phase II linac upgrade consisted of the addition of twenty cavities housed in three cryomodules. The upgrade brings the linac to a nominal 40 MV of effective accelerating gradient according to the design specification. Moreover the upgrade was the first step to qualify a Canadian vendor (PAVAC) for the production of bulk niobium superconducting cavities. Each cryomodule includes bulk niobium quarter wave resonators and a 9 T superconducting solenoid for transverse focusing. The linac features a single vacuum space. Over the years the linac has experienced vacuum incidents and high power rf cable failures in vacuum that were addressed during maintenance. In a recent maintenance program cavities from a single cryomodule were removed and chemically etched to improve performance. Future cavity treatments are in the plan but they are restricted by the priority of the scientific program. The author will present the status of the linac performance and future development plans. Reliability and availability of the linac will be discussed, metrics that will be come even more important with the advent of ARIEL.

INTRODUCTION

The Isotope Separation and ACceleation (ISAC) facility at TRIUMF produces radioactive ion beams (RIB) (see Fig. 1).

The RIBs are produced using the isotope separation on line (ISOL) method [1] where an accelerator, the driver, produces light projectiles, the primary beam, that impinge on a thick target. The light projectiles, protons or light ions, break the target nuclei producing neutral radioactive isotopes. These neutral atoms diffuse into a source where they are ionized and extracted at source potential. The ISOL method produces high quality emittances but the complicated and relatively slow process reduces the possibility of extracting isotopes with few ms half-lives.

The produced radioactive ions are magnetically separated and sent to an experimental station. ISAC counts fifteen experimental stations distributed in three experimental areas characterized by different energy ranges: low, medium and high. In the high energy experimental area the beam is boosted by the ISAC-II superconducting linac.

Presently only a single RIB is available and can be sent to one of the fifteen stations at the time. The future ARIEL facility is going to increment the RIB availability to three ion beams that can be sent simultaneously to three different experimental stations.

* Funded under a contribution agreement with NRC (National Research Council Canada)

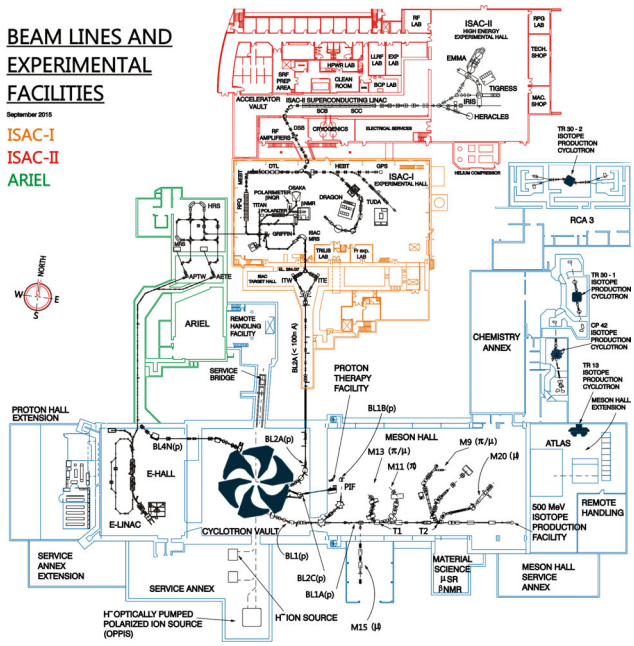

Figure 1: The TRIUMF site with the ISAC-I (red), ISAC-II (orange) and ARIEL (green) facilities.

ISAC OVERVIEW

ISAC uses the TRIUMF cyclotron as driver to accelerate protons at 500 MeV up to 100 μA of current. This is presently the highest power (up to 50 kW) driver beam for an ISOL facility. It allows to produce the most intense RIB of certain species like ^{11}Li for which yield of $2.2 \cdot 10^4$ s^{-1} has been achieved.

The overview of the ISAC facility is represented in Fig. 2 where the three experimental areas are highlighted.

Driver

The TRIUMF cyclotron accelerates H^- ions up to an intensity of 300 μA to a maximum energy of 500 MeV. The H^- are then stripped and protons are presently extracted in three different beam lines at different energies, one of which is dedicated for the ISAC radioactive beam production.

The simultaneous extraction of multiple beams with stable delivery is challenging. Nevertheless a 90% availability of the proton beam for the ISAC facility is regularly achieved.

The capability of multiple extractions can be expanded by refurbishing a fourth existing extraction beam line giving two simultaneous proton beams for RIB production [2] as represented in Fig. 3. This possibility together with an upgrade of the cyclotron [3] is key to the future ARIEL facility.

ISBN 978-3-95450-131-1

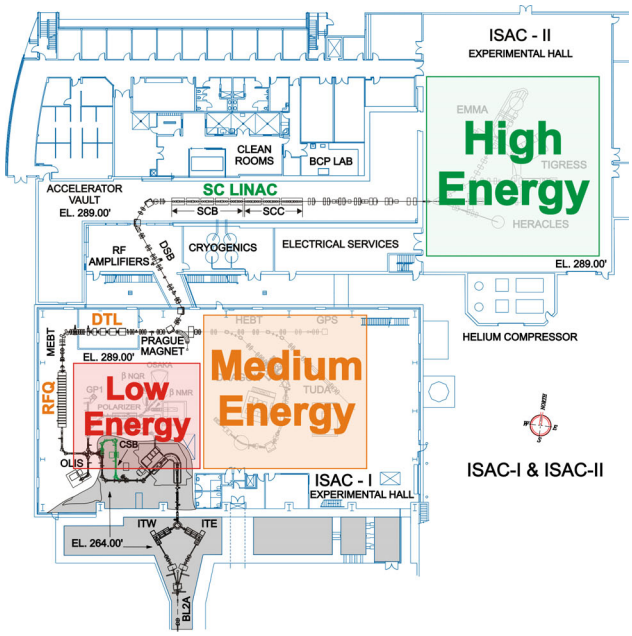

Figure 2: Overview of the ISAC facility at TRIUMF. The three experimental areas (low, medium and high) are highlighted. The grey shaded area is located two stories underground while the remaining is at ground level.

Target Station and Mass Separator

The ISAC facility has two independent target stations as represented in Fig. 4. The proton beam can be sent to one target station at a time.

Each target station is composed of five modules. The entrance module houses the diagnostic and protection monitors for the proton beam. The target module contains the target and the source; this module is routinely removed to change both target and source. The ionized species out of the source are singly charged. The beam dump module is located downstream of the target module. The last two are the extraction modules housing the optics elements. They are oriented perpendicular to the proton beam direction.

Target materials include silicon carbide, tantalum and uranium carbide. Two target configurations are available: low and high power respectively for proton beam powers up to 20 kW and 50 kW.

A common pre-separator magnet is located inside the target hall to contain most of the produced radioactivity inside the shielded target hall.

A finer selection is accomplished downstream by the mass separator, typically operating at a resolving power of few thousands. This device is installed on a biased platform to increase the resolution.

After selection it is possible to boost the single charge state of the radioactive ion by diverting them through an electron cyclotron resonance ion source (ECRIS). This charge breeder allows post acceleration of masses with $A > 30$.

The target stations and the separator area are located two stories underground. Once produced and selected the RIB is then transported to ground level where experimental stations are located.

ISAC-I Post Accelerators

The RIBs can be delivered to three experimental areas as represented in Fig. 2: a low energy area where the ions are accelerated at source potential (up to 60 kV), a medium energy area ($\beta = 1.8\% \rightarrow 6\%$) or a high energy area ($\beta = 6\% \rightarrow 18\%$) where the ions are post accelerated with linacs.

The first stage of acceleration uses a radio frequency quadrupole (RFQ) acting as an injector [4]. The RFQ boosts the energy from 2 keV/u to 150 keV/u. It can accelerate mass to charge ratio within $3 \leq A/q \leq 30$. The RFQ is a room

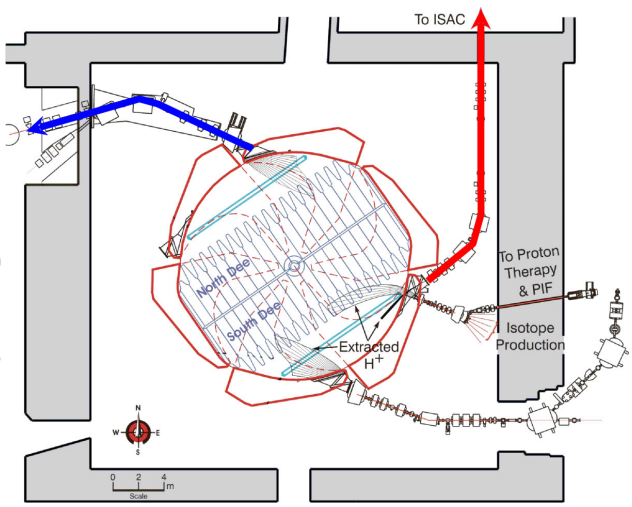

Figure 3: Schematic of the TRIUMF H^- cyclotron. Multiple beams can be extracted simultaneously at different energies. The proton beam is extracted at 500 MeV and up to 100 µA for RIB production in ISAC (red line) and in ARIEL (blue line - future).

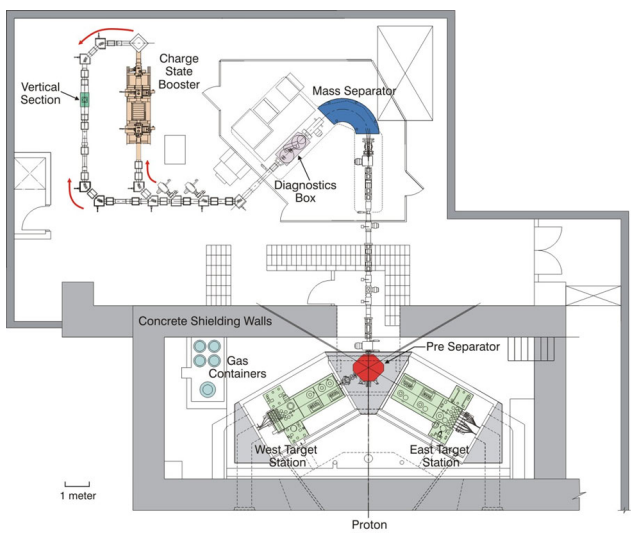

Figure 4: Representation of the two ISAC target stations and following separation stages.

ISBN 978-3-95450-131-1

temperature CW machine operating at 35.36ṀHz. The eight meter long resonant structure is composed of nineteen split rings supporting the electrodes. The RFQ doesn't have a bunching section; the beam is pre-bunched at the entrance with a three harmonics RF buncher, the fundamental being 11.78 MHz. This configuration produces a high quality longitudinal emittance after the RFQ (0.22 π keV/u·ns). Part of the beam transmitted but not accelerated is stopped into a fixed collimator downstream of the RFQ [5]. The beam inside the longitudinal emittance after the slit is around 80% of the injected.

After the RFQ the ion charge state is increased by means of stripping through a thin carbon foil (4 µg/cm^2). As a general rule the most populated charge state is selected using magnetic benders as long as the mass to charge ratio is within $2 \leq A/Q \leq 7$. These are the acceptance limits set by the following drift tube linac (DTL). The efficiency of the stripping foil depends on the mass of the stripped ions; in most of the cases it ranges between 30% to 50% for $A/q \leq 30$.

The DTL [6] is a variable energy machine covering the entire range of energies between 150 keV/u $\leq E \leq$ 1.8 MeV/u. The DTL is a separated function machine composed of five IH interdigital structure accelerating cavities and three split ring bunchers located between the first four cavities. This layout produces good beam quality at every energy. After the fourth cavity the time spread is sufficiently small that no buncher is required. The resonance frequency of the cavities and bunchers is 106.08 MHz; they operate at room temperature in CW mode. Transverse focus through the linac is provided by quadrupoles triplets between each cavity. The transmission through the linac is greater than 95%. The DTL is also used as injector for the ISAC II superconducting (SC) linac.

ISAC-II PROJECT

The ISAC-II project is an expansion of the ISAC capabilities in terms of final energies. The project specification is to accelerate heavy ions to and above the Coulomb barrier, specifically the goal is to reach an energy of $E \geq 6.5$ MeV/u for $A/q = 6$. This is equivalent to a minimum effective accelerating voltage of 30 MV. It was decided to develop a 40 MV superconducting linac. The linac installation was staged in two phases as represented in Fig. 5 . The total cost of the installed hardware is 15 M$ including cryogenics and power supplies.

Installation

The Phase-I installation (referred to as SCB section), completed in 2006 [7], is composed of five cryomodules.

The cryomodule design [8] consists of a top loading structure with a single vacuum as represented in Fig. 6. Each SCB cryomodule houses four superconducting cavities and one superconducting 9 T solenoid. All twenty cavities are fabricated in Italy by Zanon. The cavities and the solenoid hang from a strongback suspended by three posts. A helium reservoir keeps the the cavities and the solenoid in a helium

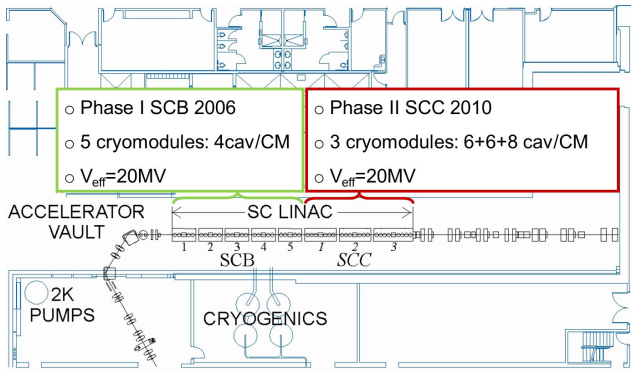

Figure 5: Final configuration of the ISAC-II superconducting linac. The first five cryomodules forms the SCB section, the last three forms the SCC section.

bath. The cryomodule has a heat shield cooled with liquid nitrogen to transition from 300 k to 4 k and a mu-metal shield to suppress external magnetic field.

Due to the single vacuum characteristic, each cryomodule is entirely assembled in a clean room.

The Phase-II installation (referred to as SCC section) is an upgrade consisting of twenty additional cavities to reach the total effective accelerating voltage of 40 MV. The twenty SCC cavities are housed in three cryomodules: six cavities in the first two cryomodules, eight in the third.

The cryomodule design is a duplicate of the phase-I module with some improvements based on the operational experience with the first installation. The strongback is suspended by four posts for added flexibility in the alignment stage. The

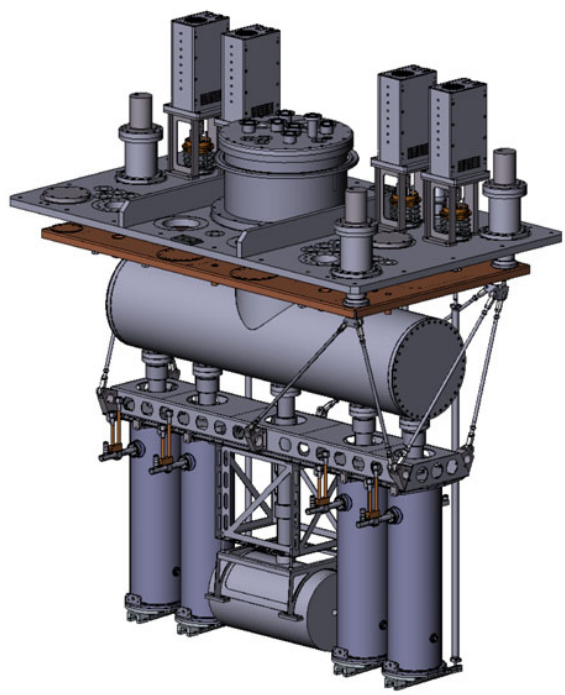

Figure 6: Superconducting linac cryomobule (SCB represented).

ISBN 978-3-95450-131-1

new module has a venting system through the RF pick-up ports of each cavity. The single vacuum inner space of the module is vented using dry filtered nitrogen from inside each cavity lowering the likelihood of contaminating the superconducting RF surface with impurities that may reduce the performance. The variable coupler is now guided by two linear bearings reducing the likelihood of a stuck coupler. The motor driving the mechanical tuner is changed in favour of a brushless servo and ball screw a cheaper unit that maintains the mechanical stability and rigidity required.

A key element of the upgrade is the development and fabrication of the cavities by PAVAC industries, a Canadian company located in the Vancouver area, in collaboration with TRIUMF. The cavity development started in 2007. The production cavities were ordered in March 2008. The phase-II installation was completed in March 2010 [9].

Rf Cavities

The basic accelerating cavity for both phases is a quarter wave bulk niobium resonator operating at 4 K.

Phase-I and Phase-II cavities resonate respectively at 106.08 MHz and 141.44 MHz. Two types of Phase-I cavities are installed with design β of 5.7% (cavity 1–8) and 7.1% (cavity 9-20). Phase-II cavities are of just one type with β = 11%. All types of cavities are represented in Fig. 7. The cavity specification requires an effective voltage of 1.1 MV at 7 W of helium power consumption.

Each cavity has an rf inductive coupler [10] and an electrical pickup. The rf coupler has liquid nitrogen cooling. A corrugated slotted niobium tuning plate provides compensation of frequency variation due to helium pressure fluctuations.

Each cavity is individually tested before being assembled in the cryomodule. All Phase-I meet or exceed the ISAC specification of 30 MV/m peak surface field at 7W of helium consumption when installed. The original average performance of the PAVAC cavities is 32 MV/m at 7 W; this significant result exceeds the ISAC specification.

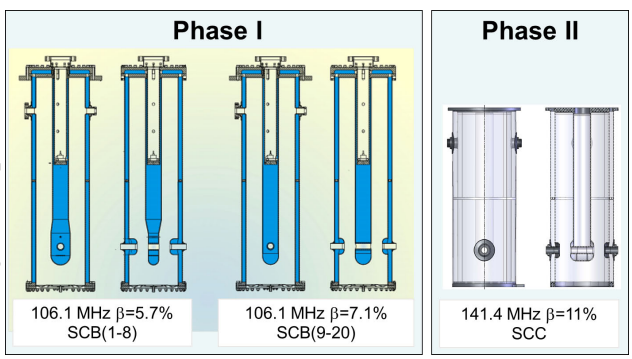

Figure 7: Superconducting linac cavities of the SCB (phase-I) and SCC (phase-II) section.

Cryogenic Distribution

The cryogenic plant [11] comprises two Linde TC50 (600 W at 4 K) refrigerator systems connected to a 10001 dewar. Each refrigerator is supplied with high pressure helium gas from a dedicated Keiser compressor.

The liquid helium at 4 K is transferred from the dewar to the cryomodules by differential pressure through the supply line. The helium gas can be sent back to the compressor via the cold return or the warm return line depending if the gas temperature is below or above 20 K.

When returned through the cold line the gas travels though the refrigerator before reaching the compressor. This return path increases the efficiency of the refrigerator itself.

An additional recovery compressor is installed to load the warm return gas into a buffer tank in case the main compressor is down.

The cryogenic system also supplies liquid nitrogen to the module for the heat shield and the rf coupling loops.

OPERATIONAL EXPERIENCE

In first decade of operation we experienced a few technical issues.

Some cavities require extensive multipacting conditioning that needs to be accounted for in the set-up time and in some cases causes down-time during operation. The choice of a variable coupler greatly reduces the amount of time required to recover from a cavity trip in the case where multipacting interferes with cavity turn-on.

In order to reduce the conditioning time, a technique is in place where all the twenty cavities in each phase are conditioned simultaneously using a single external signal generator to drive all the amplifiers of each cavity bypassing the low level rf system. The generator frequency is swept with a bandwidth that covers all the natural resonant frequencies of all the cavities. This technique reduces the conditioning time from days to hours.

The SCB section uses tube amplifiers while the SCC section uses solid state. The latter are proven to be more stable for operation. The tube amplifier needs to be phase tuned as the tube ages and their performance can degrade during the experimental run leading to downtime.

Some of the SCB cavities are affected by stuck variable couplers. This issue can result in the difficulty of conditioning the cavity or in achieving stable operation and therefore losing accelerating voltage. This issue is not present in the SCC section thanks to the improved design with linear bearings.

In 2009 the fourth cryomodule of the SCB section (SCB4) experienced a catastrophic failure of one of the turbo pumps. Debris from the exploded blades landed inside the cryomodule. An in situ cleaning and replacement of the pump occurred with no immediate degradation of the cryomodule performance.

Some rf cables developed in vacuum rf shorts rendering the relative cavity inoperable. This issue has been identified and corrected. The adopted solution consists in replacing the ANDREW 3/8″ FSJ2-50 cable with an ANDREW 1/2″ FSJ2-50 cable instead.

ISBN 978-3-95450-131-1

Linac Performance

The average effective gradients as measured after the initial installation is 6.98 MV/m and 5.02 MV/m respectively for the SCB and SCC section. After almost a decade of operation (as measured on August 2015) we experience a performance degradation of 19% and 14% respectively for SCB and SCC as shown in Fig. 8.

The SCB4 cryomodule shows more degradation in performance with respect to other cryomodules. This is attributed mainly to the vacuum accident and the single vacuum configuration. Since the SC linac is thermally cycled every year during the main shutdown, the fine particulate generated during the pump explosion eventually can migrate and contaminate the rf surface.

Two cavities, located in two different cryomodules (SCB1 and SCC2), still suffer from rf glow discharge in rf cables. These cables will be replaced in future shutdowns.

In general reduced maintenance activities due to other priority on site is one of the factor for the loss of performance. Nevertheless the linac is still capable of meeting the original ISAC-II specification of delivering effective accelerating voltage of 30 MV.

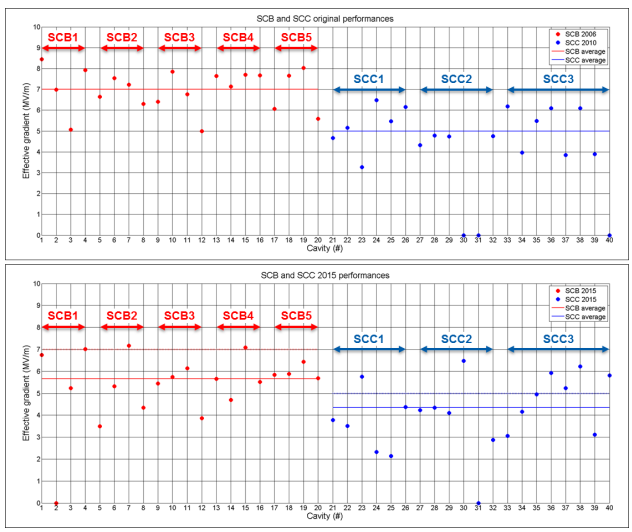

Figure 8: Linac performance in the original installation (top) and as of August 2015 (bottom). Two cavities (SCB1:CAV2 and SCC2:CAV5) are not operable due to damaged rf cables.

Future Plan

Presently the SC linac is capable of providing the effective accelerating voltage according to specifications, and hence accommodating energy requests from the user, as well it can maintained stable operation defined as > 90% of the scheduled beam time. In order to maintain this capability though it is necessary to invest in maintenance that requires long period of shutdown.

Treatment of the cavities such as degassing and additional buffer chemical polishing (BCP) followed by high pressure water rinsing (HPWR) can restore the rf surface and recover the original gradients.

Retrofitting of rf cables and couplers with linear bearings is also in the plan, as well as the upgrade to solid state amplifier for the SCB section.

All this planned maintenance aims at recovering effective accelerating voltage and stability during operation. This is critical in view of the ARIEL project [12] completion that is going to increase, an estimate four fold, the amount of RIB available for post-acceleration with the SC linac.

CONCLUSION

After a decade of operation the SC linac has experienced some degradation in performance. Nevertheless the accelerator is still capable of delivering the effective accelerating voltage of 30 MV as requested in the original specification of the ISAC-II project. A plan is conceived to restore the linac performance to the original installation and maintain stable operation. This is important for the future when the new ARIEL facility will increase the beam availability.

REFERENCES

[1] M. Marchetto, “ISAC-II operation and future plans”, LINAC08, Victoria, British Columbia, Canada, September 2008.

[2] G. Dutto et al., “Simultaneous Extraction of Two Stable Beams for ISAC”, EPAC08, Genova, Italy, June 2008 , p. 3505.

[3] I. Bylinskii et al., “TRIUMF 500 MeV Cyclotron Refurbishment”, Cyclotrons and Their Application, Giardini Naxos, Italy, September 2007 , p. 143.

[4] R.L. Poirier et al., “CW Performance of the TRIUMF 8 Meter Long RFQ for Exotic Ions”, LINAC2000, Monterey, California, USA, August 2000 , p. 1023.

[5] S. Koscielniak et al., “Beam Dynamics Studies on the ISAC RFQ at TRIUMF”, PAC’97, Vancouver, British Columbia, Canada, May 1997, p. 1102.

[6] R.E. Laxdal et al., “Beam Commissioning and First Operation of the ISAC DTL at TRIUMF”, PAC2001, Chicago, Illinoois, USA, June 2001, p. 3942.

[7] R.E. Laxdal, “Commissioning and Early Experiments with ISACII”, PAC07, Albuquerque, New Mexico, USA, June 2007, p. 2593.

[8] G. Stanford et al., “Engineering and Cryogenic Testing of the ISAC-II Medium Beta Cryomodule", THP16, LINAC 2004, Lübeck, Germany.

[9] M. Marchetto, “Commiss//ioning of the 20 MV Superconducting Linac Upgrade at TRIUMF ”, FROBN0, PAC 2011, New York, USA (2011).

[10] R. Poirier et al., “Rf Coupler Design for the TRIUMF ISACII Superconducting Quarter Wave Resonators”, LINAC2004, Lübeck, Germany (2004).

[11] I. Sekatchev et al., “ISAC SC Linac Phase-II Helium Refrigerator Commissioning and First Operational Experience at TRIUMF”, Advances in Cryogenics Engineering, AIP Conference Proceedings 1218, 823-830 (2010).

[12] L. Merminga et al., “ARIEL: TRIUMF’s RareIsotopE Laboratory”, WEOBA001, IPAC 2011, San Sebastian, Spain (2011).

ISBN 978-3-95450-131-1

PROGRESS ON SUPERCONDUCTING LINAC FOR THE RAON HEAVY ION ACCELERATOR

H. J. Kim* reprenting the RAON, IBS, Daejeon, Korea

Abstract

The RISP (Rare Isotope Science Project) has been proposed as a multi-purpose accelerator facility for providing beams of exotic rare isotopes of various energies. It can deliver ions from proton to uranium. Proton and uranium ions are accelerated upto 600 MeV and 200 MeV/u respectively. The facility consists of three superconducting linacs of which superconducting cavities are independently phased. Requirement of the linac design is especially high for acceleration of multiple charge beams. In this paper, we present the RISP linac design, the prototyping of superconducting cavity and cryomodule.

INTRODUCTION

The RISP accelerator has been planned to study heavy ions in nuclear, material and medical science at the Institute for Basic Science (IBS). It can deliver ions from protons to uranium atoms with a final beam energy, for example, 200 MeV/u for uranium and 600 MeV for protons, and with a beam current range from 8.3 pμA (uranium) to 660 pμA (protons) [1, 2]. The facility consists of three superconducting linacs of which superconducting cavities are independently phased and operating at three different frequencies, namely, 81.25, 162.5 and 325 MHz.

SUPERCONDUCTING LINAC

Lattice Design

The configuration of the accelerator facility within the RISP is shown in Fig. 1. An injector system accelerates a heavy ion beam to 500 keV/u and creates the desired bunch structure for injection into the superconducting linac. The injector system comprises an electron cyclotron resonance ion source, a low-energy beam transport, a radio-frequency quadrupole, and a medium-energy beam transport. The superconducting driver linac accelerates the beam to 200 MeV/u. The driver linac is divided into three different sections, as shown in Fig. 2: a low-energy superconducting linac (SCL1), a charge stripper section (CSS) and a high-energy superconducting linac (SCL2). The SCL1 accelerates the beam to 18.5 MeV/u. The SCL1 uses two different families of superconducting resonators, i.e., a quarter wave resonator (QWR) and a half wave resonator (HWR). The SCL11 consists of 22 QWRs whose geometrical β is 0.047 and 22 qudruopole doublets. The resonance frequency of the QWR is 81.25 MHz. The cryomodule of the SCL11 hosts one superconducting cavity. The SCL12 consists of 102 HWRs whose geometrical β is 0.12 and 62 quadrupole doublets. The resonance frequency of the HWR is 162.5 MHz. This

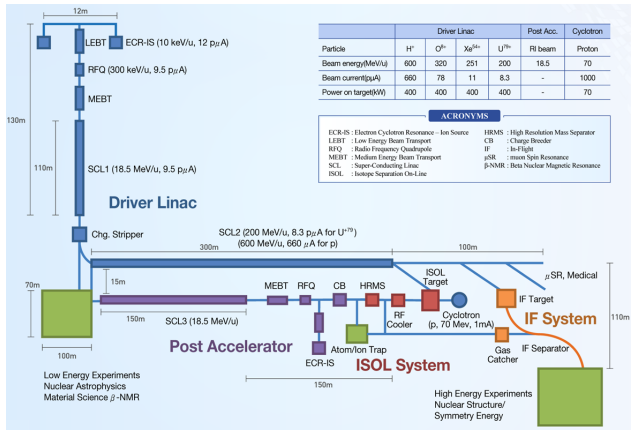

Figure 1: Layout of the RISP accelerator.

segment has two families of cryomodules: one type of cryomodule hosts two superconducting cavities, and the other hosts four superconducting cavities. The CSS accepts beams at 18.5 MeV/u. The charge stripper strips electrons from the heavy-ion beams to enhance the acceleration efficiency in the high-energy linac section. The charge stripping section consists of normal conducting quadrupoles and room-temperature 45-degree bending magnets. The quadrupole magnets provide adequate transverse focusing and beam matching to the SCL2, and the bending magnet provides momentum dispersion for charge selection. The SCL2 accepts a beam at 18.5 MeV/u and accelerates it to 200 MeV/u. The SCL2 uses two types of single spoke resonators, i.e., SSR1 and SSR2. The SCL2 consists of the SCL21 and the SCL22, each with geometric β 0.30, resonance-frequency 325-MHz SSR and a geometric β 0.51, resonance-frequency 325-MHz SSR. The single-spoke-resonator type is chosen mainly because it can have a larger bore radius compared with the half-wave-resonator type, which is very important for reducing the uncontrolled beam loss in the high-energy linac section. The numbers of cavities in the SCL21 and the SCL22 is 69 and 138 respectively. The cryomodules of the SCL21 and SCL22 host 3 and 6 cavities, respectively. The SCL2 provides a beam into the in-flight fragmentation (IF) system via a high-energy beam transport (HEBT).

The post accelerator (SCL3) is designed to accelerate the rare isotopes produced in the ISOL (Isotope Separation On-Line) system. The SCL3 is, in principle, a duplicate of the driver linac up to low energy linear accelerator. The accelerated rare isotope beams are reaccelerated in the SCL2. Hence, the RISP accelerator provides a large number of rare isotopes with high intensity and with various beam energies.

* hjkim@ibs.re.kr

ISBN 978-3-95450-131-1

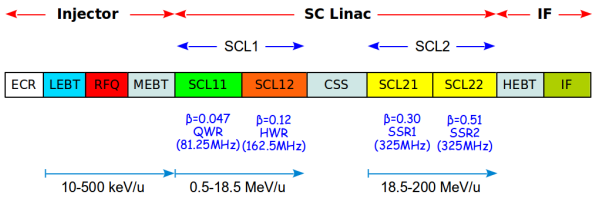

Figure 2: The RAON linear accelerator.

Table 1: Superconducting Cavity Parameters

Parameter	Unit	QWR	HWR	SSR1	SSR2
Frequency	MHz	81.25	162.5	325	325
β_g		0.047	0.12	0.30	0.51
$L_{eff} = \beta_g \lambda$	m	0.173	0.221	0.277	0.452
Q	10^9	2.1	4.1	9.2	10.5
QR_s	Ω	21	42	98	112
R/Q	Ω	470	310	246	296
E_{acc}	MV/m	6.6	6.4	6.9	8.6
E_{peak}/E_{acc}		5.3	5.5	6.3	7.2
B_{peak}/E_{acc}	mT/(MV/m)	9.5	8.1	6.63	7.2

Superconducting Cavity

In the optimization of the superconducting cavity, the resonant frequency, modes, and mechanical constraints in the cavity should be considered to design a high-efficient superconducting cavity. Figure of merits related with the cavity performance should be optimized. For particle beams passing through the cavity to get maximum energy gain, the acceleration gradient should be maximized while minimizing the peak electric and magnetic fields. Table 1 summarizes the parameters of four different superconducting cavities for the RISP superconducting linac. In order to achieve stable operation of the cavity, one of the critical issue is the multipacting effect inside of the cavity. It can cause damage to and external heating of the cavity. The multipactor effect is a phenomenon in which secondary electron emission occurs exponentially by electrons repeatedly hitting surface due to electron existing on the surface of the metal of the radio-frequency devices resonate with the RF electromagnetic field. Hence, the multipacting barriers of the QWR cavity are estimated with the secondary emission yield of 300°C-baked niobium. Several peaks are seen in the multipacting factors of four RF periods. The most serious multipactor occurs around the upper end of QWR at 1/8 the accelerating gradient. The detuning due to the tolerances of fabrication and the frequency sensitivities to mechanical deforming are estimated. The cavity is fabricated by using electron-beam welding of hydroformed 3-mm niobium sheets, drift tube and four additional ports. Two ports in the lower end are added for RF power and pickup coupling. The other two ports are installed for evacuation and high pressure rinsing. Figure 3 shows the prototype of quarter waver resonator. The detunings and the sensitivities of the bare cavity are shown in the Table 2. Figure 4 shows the result of measuring the Q-value versus acceleration electric field (E_{acc}) for

Figure 3: Quarter wave resonator after final electron beam welding.

Table 2: Frequency Shift Due to Various Sources

Frequency shift	Value (MHz)
Resonant frequency	81.25
External pressure (130 kPa)	81.27
Cool down (293 K → 4 K)	81.27
Vaccum	81.068
BCP (150 μm)	81.069
Welding shrikage (0.6 mm)	80.898
Clamp-up test	80.855

QWR cavity [3]. Normally, we cool down the cavity fast from room temperature to 4 K. The duration between 150 K and 4 K is around 25 minutes. In a measurement of 4K-1st and 4K-2nd, low-temperature (120°C) baking is not applied. After baking the cavity at 120°C, the Q-factor is improved twice at E_{acc}= 6.6 MV/m. In order to check the Q-disease effect, the cavity spends 7.5 hr in the Q-disease temperature window (50 K to 100 K). The 4K-QD in Fig. 4 shows the Q-disease performance and indicates some measure of hydrogen in the cavity. The performance reduction due to Q-disease is nearly recovered by a 250 K thermal cycle. The residual resistance is measured to be 2.5 nΩ. The maximum

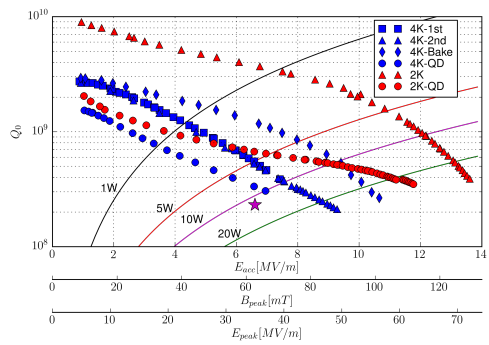

Figure 4: Measurement of Q-value of quarter wave resonator.

ISBN 978-3-95450-131-1

Table 3: Thermal Load (Watt at 4.5K) of Superconducting Linacs

	SCL11	SC12	SCL21	SCL22	SCL31	SCL33
Dynamic	532	2,016	1,014	5,009	532	2,016
Static	227	1,071	475	790	227	1,071
Sum	760	3,087	1,489	5,800	760	3,087

accelerating gradient achieved at 2 K is 13.6 MV/m without quench corresponding to an equivalent peak electric field of 72 MV/m and a peak magnetic field of 129 mT.

Cryomodule

The linac has five types of cryomodules for four different kinds of cavities [4]. The main roles of the cryomodules are maintaining the operating condition of the superconducting cavities and aligning the cavities along the beam line. A high level of vacuum and thermal insulation are required for the cryomodule to maintain the operating temperature of the superconducting cavities. The cryomodules hosting the QWR and the HWR cavities are box-type while those hosting the SSR1 and the SSR2 cavities are cylindrical. Both QWR and HWR cavities are vertically installed in the cryomodule. The main components of the cryomodule are dressed cavities, two-phase pipe, power couplers to supply RF power to the cavities, tuners to control the operation of the cavities, and support systems to fix the cavities along the beam line. Because the operating temperature of the superconducting cavities are 2 K, 40-K and 4.5-K thermal intercepts are installed to minimize the thermal load. The cold mass, including the cavity string, coupler and tuner, is installed on a strong back and is then inserted into a vacuum vessel with a thermal shield and a multi-layer insulator. The thermal loads of the superconducting linacs are summarized in Table 3. The dynamic and the static loads are 70% and 30% of the total thermal load, receptively. The designs of the cryomodule components have been conducted based on thermal and structural concerns. The thermal design starts by the estimating of the thermal loads that determine the required sizes of components such as the two phase pipes and the other cryogenic pipes. Three levels of cryogenic flow are necessary: 2 K, 4.5 K and 70K. Figure 5 shows the protype of quarter wave resonator cryomodule and P&ID diagram of cryogenic system. The static heat load is measured for QWR cryomodue. The helium flow rate and static thermal load versus time are shown in Fig. 6. The design and measured static loads are 4W and 3.9 W respectively.

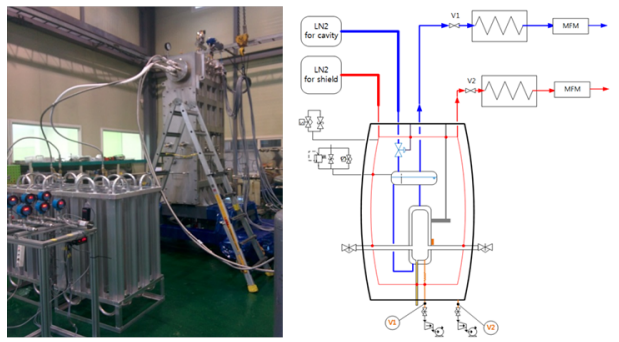

Figure 5: Prototype of quarter wave resonator cryomodule and P&ID.

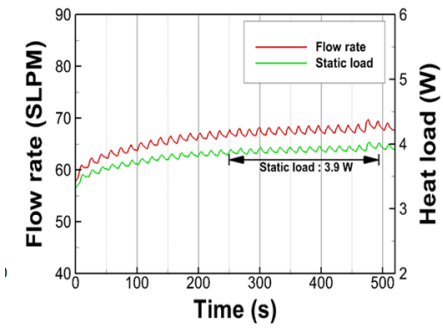

Figure 6: Measurement of static thermal load of quarter wave resonator cryomodule.

SUMMARY

The RISP linacs have been presented. In the design, four different cavities, QWR, HWR, SSR1 and SSR2, were used to accelerate the beam in the linac. The number of cavities per cryomodule at each section was optimized to minimize the total number of cavities required for efficient acceleration. We emphasized the stability of operation, the flexibility of maintenance, and the minimization of beam loss. The prototype of superconducting cavities have been fabricated and tested in the cryogenic temperature. The result shows that the target value of Q-factor is achieved with a magin. The box-shaped and cylindrical cryomodules are designed for hosting cavities. The testing of the cryomodules is under way.

ACKNOWLEDGMENTS

This work was supported by the Rare Isotope Science Project which is funded by the Ministry of Science, ICT and Future Planning (MSIP) and the National Research Foundation (NRF) of the Republic of Korea under Contract 2011-0032011.

REFERENCES

[1] S.K. Kim, Rare Isotope Science Project: Baseline Design Summary (2012).

[2] D. Jeon et al., in *Proceedings of LINAC2012*, TUPB030 (2012) p. 540.

[3] Z.Y. Yao et al., RISP QWR Initial Cold Test Report (2014).

[4] W.K. Kim et al., in *Proceedings of IPAC15*, WEPMN035 (2015).

ISBN 978-3-95450-131-1

STATUS AND PERSPECTIVES OF THE CW UPGRADE OF THE UNILAC HLI AT GSI

P. Gerhard*, L. Groening, W. Hartmann, S. Mickat, K. Tinschert, H. Vormann, K.-O. Voss
GSI, Darmstadt, Germany

Abstract

The High Charge State Injector (HochLadungsInjektor) HLI was commissioned in 1991 [1]. It was the first linac comprising of a Radio Frequency Quadrupole RFQ and an Interdigital H-Type cavity IH. For more than twenty years, it successfully provided essential heavy ion beams with high duty cycle for several lighthouse experiments and developments at GSI. Among them are the Super Heavy Element Research SHE, namely the experiments SHIP, TASCA, SHIPTRAP, and the heavy ion cancer therapy. Three out of the six transuranium elements found at GSI were discovered with ion beams from the HLI [2]. The ever increasing demand for beam intensity was met by the proposal of a SuperConducting Continuous Wave sc cw-Linac. As the HLI will serve as an injector for this new accelerator, a cw upgrade for the HLI was developed.

THE ORIGINAL HLI

The High Charge State Injector (see Fig. 1, and Table 1) is equipped with a Compacte A Plusieurs Résonances Ionisantes Cyclotron Electroniques (CAPRICE) ion source and a high resolution 135° spectrometer; the source was recently upgraded to slightly higher magnetic fields of 1.4 T.

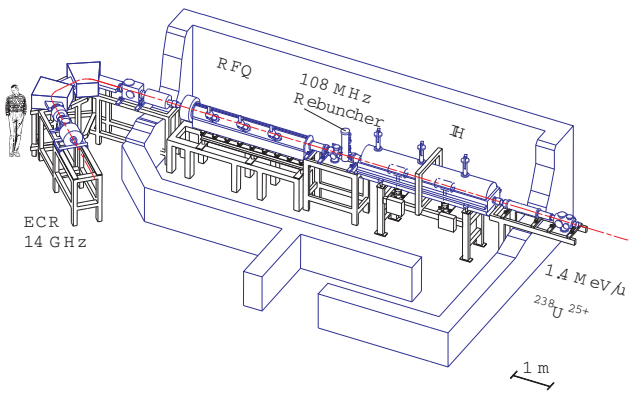

Figure 1: Overview of the HLI.

Behind the spectrometer the beam is matched to a 4-rod RFQ, which accelerates the ions from 2.5 to 300 keV/u. This is followed by a MEBT, which includes a magnetic quadrupole triplet and a doublet as well as a $\lambda/4$-buncher for transversal and longitudinal matching of the beam to the following IH cavity. The IH accelerates the beam to the final energy of 1.4 MeV/u. The beam is then transported to the UNIversal Linear ACcelerator UNILAC through a 180° bend (not shown in Fig. 1). A second $\lambda/4$-buncher provides for proper matching to the first Alvarez tank.

* p.gerhard@gsi.de

Table 1: Basic Parameters of the HLI

Property	Value
Mass resolution /(Δm/m)	$3 \cdot 10^{-3}$
Beam intensity /pnA	≤1
A/z 50% d.c. (cw)	≤8.5 (6.0)
Injection energy /(keV/u)	2.5
Extraction energy /(MeV/u)	1.4
RF Frequency /MHz	108.408
Design emittance /(π·mm·mrad)	1.5 (norm.)
Total length /m	10.8

The HLI was originally designed for a duty cycle (dc) of 50% and a pulse repetition rate of 50 Hz. Most of the magnets are operated at constant current, as it was not planned accelerating different ions in parallel. Thus, the HLI can be operated with cw beam as far as the magnets are concerned, but most other devices, like beam diagnostics, and the control system are designed for pulsed operation only.

The ECR ion source is ideal for stable, long lasting beams. Due to its low material consumption, rare isotope beams can be produced very efficiently. This has made the HLI the prominent injector for medium heavy ions requested by experiments at the Coulomb barrier up to now.

CURRENT STATUS AND CW UPGRADE

With no major changes, the HLI was in routine operation and successfully providing beams for coulomb barrier experiments and injection into the heavy ion synchrotron SIS for nearly 20 years. Nevertheless, the demand for higher (average) beam intensities grew with time, and two strategies were proposed to deal with this demand: An upgrade of the source to directly increase the beam current, and an upgrade of the whole accelerator to move from pulsed to cw operation, thereby raising the duty cycle and the average beam intensity by another factor of four.

MS-ECRIS

About ten years ago, an international project was started to develop a high performance ion source using the concept of electron cyclotron resonance. This source was called MS-ECRIS [3]. It was intended to install it as a second source in front of a new LEBT branch at the HLI. Key feature of the source was a strong confinement by higher magnetic fields, produced by sc magnet coils. The aim was to reach higher charge states and at the same time deliver more ions to the accelerator. In 2007, the magnet system was tested for the first time, and quenches occurred when both coils were

ISBN 978-3-95450-131-1

powered simultaneously to around 40% of the nominal value. Since then, several attempts and upgrades to the coil system have been made to increase this value, but no improvement could be achieved. Thus, the project recently had to be canceled, and the HLI operates with the existing CAPRICE until an alternative source will be evaluated and obtained.

First CW Upgrade: RFQ

In 2009 the HLI was equipped with a new 4-rod RFQ. This was intended as the first step of an upgrade of the whole linac [4] towards cw operation. It was initially designed to fit to the MS-ECRIS, but was redesigned as this project was delayed at that time, with an optional upgrade later. It turned out that the beam dynamics performed well, but the mechanical and thermal design of the structure was not able to meet the high requirements [5]. After an upgrade of the rf contacts of the tuning plates, operation up to 30 kW average power is now possible, while the design power for cw operation is 60 kW.

During commissioning, strong modulations of rf signals, like the reflected power, were observed (see Fig. 2). This

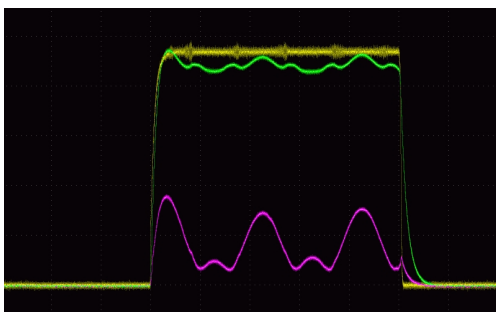

Figure 2: Modulation of the RFQ rf signals, caused by vibrations of the rods.

phenomenon was already known from the first HLI RFQ. It is attributed to mechanical vibrations of the structure. Later it was discovered, that operation at higher amplitudes is only possible for certain rf pulse lengths (at 50 Hz pulse repetition rate). Otherwise, the reflected power gets too high. It was verified by in situ investigations with a laser vibrometer [6], that mechanical vibrations of the rods are excited by the rf pulses. This leads to modulations of the rf field and deteriorates the beam quality substantially at high rf amplitudes. Operation is limited to moderate amplitudes with respect to the design values and requires a high degree of experience in operation. Due to fast and strong response of the structure to changes of the thermal load, cw operation is also not possible.

For the time being the HLI is still used as injector linac for medium heavy ions like ^{12}C, ^{40}Ar and ^{48}Ca with high duty cycles, and sometimes for rare heavy ions like ^{124}Xe.

Full CW Upgrade

The following describes the known measures necessary in order to turn the HLI into an injector linac capable of cw operation.

RF Cavities A thermally and mechanically improved RFQ will be build, but the other cavities have to be upgraded as well. Both bunchers are only capable of 50% dc due to their limited cooling. A new design for one of the bunchers is presently under development in the frame of the cw demonstrator project (see below).

The IH cavity in principle should be cw capable, but the plungers get too close to the drift tubes already at the present duty cycle due to the thermal load. This affects the field distribution and will not be tolerable at 100% dc. The proposed countermeasure is to build a new top shell.

Low Level RF and Power Amplifiers The existing low level rf is not suitable for cw operation. Since it was built on-site, a careful survey and consideration of possible alternatives has to be done.

All present rf transmitters are based on tubes. Their average power will not be sufficient for cw operation. The lower power systems for the bunchers may be replaced by solid state transmitters. The high power transmitters for the RFQ and the IH will again be tube based systems.

Beam Diagnostics and Control System The complete beam diagnostics, especially the electronics, are based on and designed for pulsed operation. Some parts, like beam current transformers, may be ordered from the shelf for cw operation, while for others this may not be the case and a considerable amount of development might be necessary. The same holds true for the control system.

CW LINAC

Nearly all beams from the HLI are accelerated to ion energies between 3.6 and 11.4 MeV/u by the UNILAC. On the other hand, the UNILAC is foreseen as the main injector linac for the FAIR project, which requires a short pulse, high brilliance beam. Therefore, an upgrade program for the UNILAC is running which, as a side effect, will reduce the dc of the UNILAC from 25 to 1%. With this, the cw upgrade of the HLI only makes sense if a new, cw capable linac is build, and this is what has already been proposed. The benefit is, that the two accelerators, the UNILAC and the cw linac, can independently be optimized for their specific tasks. Figure 3 shows the proposed integration of the cw linac into the existing facility at GSI.

The cw linac is based on a new type of rf accelerating cavities, namely superconducting crossbar H-Mode cavities [7]. Together with a new concept of the gap structure, in total nine sc CH-cavities will allow for flexible acceleration of the beam to energies between 3.5 and 7.3 MeV/u. This energy range is adapted to the requirements of most of the experiments that are now served by the UNILAC. The transverse focusing will be done by solenoids between the cavities.

Status of the CW Demonstrator

As the sc CH-cavities are a new technology, it was decided to build a demonstrator unit first. This project is called *sc*

ISBN 978-3-95450-131-1

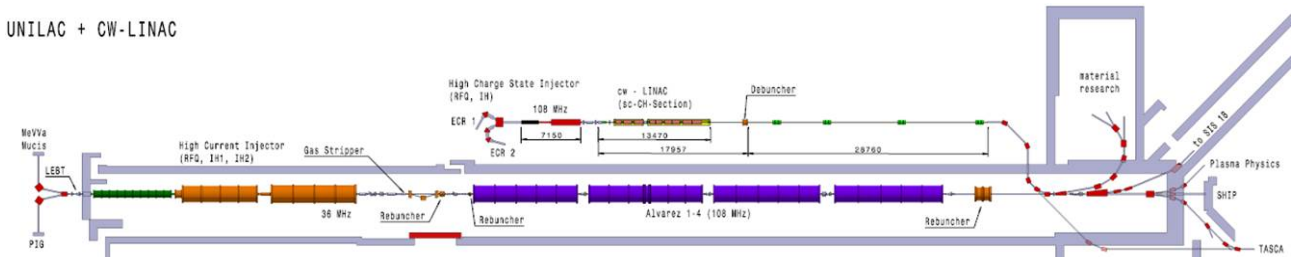

Figure 3: Present proposal for the integration of the cw linac at GSI.

cw-Linac Demonstrator. A test stand is being built behind the HLI. The concrete bunker is already set up (see Fig. 4), wherein a cryostat housing the cavity and a beam line will be placed.

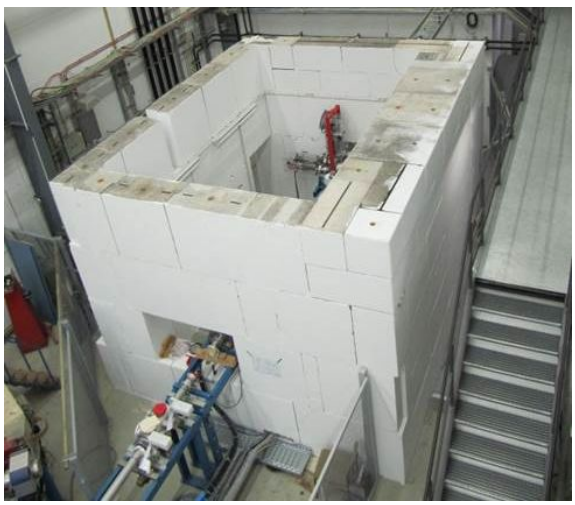

Figure 4: View on the sc CH-demonstrator test bunker and beamline.

Two sc solenoids and one sc CH-cavity (see Fig. 5) have been ordered, as well as the cryostat.

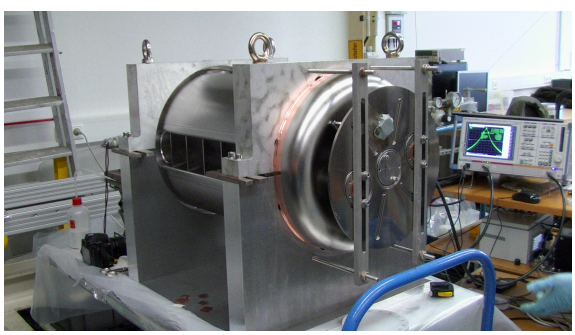

Figure 5: The first sc CH-cavity during manufacturing.

A detailed report on this project was given in this conference series [8]. The cryostat is expected to arrive at GSI in September, the first tests with beam are planned in 2016. Later, these devices will be used as the first section of the cw linac.

As the availability of this technology is essential for the cw linac project, all other upgrade activities are on hold until the first tests have been conducted successfully. The proposal for the next step, an advanced demonstrator consisting of five cavities, is already prepared [9].

SUMMARY & OUTLOOK

The high charge state injector is a very innovative and effective extension for the UNILAC. Today, it is an indispensable injector linac for many experiments at GSI, but the limitations become more perceptible. Increasing demands for higher beam intensities initiated upgrades for the source and for cw capability of the HLI. Both projects were not successful so far, while the road map to achieve these goals is clear. At the moment, all activities are concentrating on the performance demonstration of the sc CH-cavity which is planned for next year.

REFERENCES

[1] N. Angert et al., "Commissioning and First Operation Experience of the New Heavy Ion Injector of the UNILAC", EPAC'92, Berlin, Germany, March 1992, p. 167

[2] S. Hofmann and G. Münzenberg, The discovery of the heaviest elements, Rev. Mod. Phys. 72, 733 (2000)

[3] G. Ciavola et al., "A status report of the multipurpose superconducting electron cyclotron resonance ion source", Rev. Sci. Inst. 79, 02A326 (2008)

[4] P. Gerhard et al., "Commissioning of a new CW Radio Frequency Quadrupole at GSI", IPAC'10, Kyoto, Japan, May 2010, MOPD028, p. 741

[5] P. Gerhard et al., "Experience with a 4-rod CW Radio Frequency Quadrupole", LINAC'12, Tel Aviv, Israel, THPB035

[6] P. Gerhard et al., "In situ Measurement of Mechanical Vibrations of a 4-rod RFQ at GSI", LINAC'14, Geneva, Switzerland, THPB035

[7] F. Dziuba et al., "Superconducting CH Cavities for Heavy Ion Acceleration", IPAC'13, Shanghai, China, June 2013, THPWO016

[8] S. Mickat et al., "The SC CW Linac Demonstrator — 1st Test of an SC CH-Cavity with Heavy Ions", HIAT'12, Chicago, USA, June 2012, WEC03

[9] W. Barth et al., "Advanced superconducting cw Heavy Ion Linac R&D", IPAC'13, Shanghai, China, June 2013, THPWO007

ISBN 978-3-95450-131-1

CHARGE BREEDING EXPERIENCES WITH ECR AND EBIS FOR CARIBU

Richard Vondrasek#, A. Barcikowski, C.A. Dickerson, P.N. Ostroumov,
R. Pardo, A. Perry, G. Savard, R. Scott, S.I. Sharamentov
Physics Division, Argonne National Laboratory, Lemont, IL 60439, USA

Abstract

The efficient and rapid production of a high-quality, pure beam of highly charged ions is at the heart of any radioactive ion beam facility. An ECR charge breeder, as part of the Californium Rare Ion Breeder Upgrade (CARIBU) program at Argonne National Laboratory, was developed to fulfil this role. The charge breeding efficiency and high charge state production of the source are at the forefront of ECR charge breeders, but its overall performance as part of the accelerator system is limited by a pervasive stable ion background and relatively long breeding times. Steps have been taken to reduce the level of background contamination but have met with limited success. As such, an EBIS charge breeder has been developed and is now running in an off-line configuration. It has already demonstrated good breeding efficiencies, shorter residence times, and reduced background, and it is scheduled to replace the ECR charge breeder in late 2015. The resultant change in duty cycle and time structure necessitates changes to the overall facility operation. The experiences with these breeders – their strengths and their weaknesses - will be discussed.

CARIBU FACILITY

The CAlifornium Rare Isotope Breeder Upgrade (CARIBU)[1] provides radioactive beams to the Argonne Tandem Linac Accelerator System (ATLAS). The fission fragments are produced not by an ISOL facility but instead by a 1.3 Ci ^{252}Cf fission source. The Cf source is located inside a large-volume RF/DC helium gas catcher [2] which thermalizes the fission products and extracts them rapidly to form a low-energy beam of 1+ or 2+ ions from which the isotopes of interest are selected via a high-resolution magnetic separator. The beam is transported to either a low-energy area which includes a Penning trap and tape station or to an ECR source where the beam is charge bred for subsequent acceleration in the ATLAS linac.

The ECR breeder has been delivering charge bred radioactive species to the ATLAS experimental program for several years and in the last year has provided more than 81 days of beam. While its charge breeding efficiency and high charge state production have been at the forefront of ECR charge breeding, its overall performance as a part of the accelerator system has been hindered by the pervasive background present in ECR ion sources.

As such, an EBIS charge breeder is replacing the ECR in late 2015. The EBIS has a lower level of beam contamination than an ECR and exhibits improved charge breeding efficiency and faster breeding times [3, 4].

ECR CHARGE BREEDER

The ANL ECR breeder [5] is a room temperature source, and the plasma is excited with two RF frequencies – a 10.44 GHz klystron and an 11-13 GHz traveling wave tube amplifier (TWTA). It has an open hexapole structure providing good pumping to the plasma chamber region resulting in a base plasma chamber pressure of $2x10^{-8}$ mbar. The open structure also allows the RF and support gas to be introduced radially into the plasma chamber. This scheme eliminates the need for cut-outs in the field shaping iron to accept the RF waveguides and results in a highly symmetric axial magnetic field where the ions enter the plasma. This differs from other ECR breeders presently in existence which are closed hexapole devices with axial RF injection. The 1+ ions are introduced into the plasma through a grounded high-purity aluminum tube mounted on a linear motion stage. The stage has a 30 mm range of travel, and thus the deceleration point of the 1+ ions can be adjusted on-line without disturbing the source conditions. The source is designed to operate at a 50 kV potential although it typically operates at 36 kV. The source has produced beams primarily in the mid-mass regime but has also exhibited good performance for low mass beams such as sodium and potassium (see Table 1).

Table 1: Summary of Charge Breeding Performance for Both Stable Ions and CARIBU Provided Radioactive Ions

Ion	Half-life (s)	Efficiency (%)	A/Q
$^{23}Na^{7+}$		10.1	3.29
$^{39}K^{10+}$		17.9	3.90
$^{84}Kr^{17+}$		15.6	4.94
$^{85}Rb^{19+}$		13.7	4.47
$^{110}Ru^{22+}$	11.6	11.8	5.00
$^{135}Te^{26+}$	19.0	5.0	5.19
$^{129}Xe^{25+}$		13.4	5.16
$^{132}Xe^{27+}$		14.1	4.89
$^{133}Cs^{26+}$		14.7	5.11
$^{133}Cs^{27+}$		13.5	4.93
$^{141}Cs^{27+}$	24.8	12.3	5.22
$^{142}Cs^{27+}$	1.69	7.3	5.26
$^{143}Cs^{27+}$	1.79	11.7	5.30
$^{143}Ba^{27+}$	14.3	14.7	5.30
$^{144}Ba^{28+}$	11.5	14.3	5.14
$^{146}Ba^{28+}$	2.22	13.3	5.21

Charge Breeder Enhancements

The performance of the ANL ECR charge breeder can be attributed to several aspects: the open hexapole which

#vondrasek@anl.gov

ISBN 978-3-95450-131-1

allows better pumping to the plasma chamber region, the symmetric magnetic field at the point of 1+ ion injection, and multiple frequency heating.

The beneficial effect of a lower operating base pressure was first observed with rubidium through improved breeding efficiencies and peak charge state as a function of source pressure. Table 2 shows the breeding efficiencies for two periods – September 2008 when the operating pressure was 2.0×10^{-7} mbar and June 2009 when the pressure was 1.0×10^{-7} mbar. Source conditions, other than the pressure, were the same for both data sets.

In addition to better pumping, the open hexapole structure also allowed the RF waveguides to be inserted in between the hexapole bars. This resulted in a symmetrical iron plug on the injection side of the source which maintained the magnetic field symmetry where the 1+ ions enter the chamber.

Table 2: Summary of Charge Breeding Performance for Both Stable Ions and CARIBU Provided Radioactive Ions

Ion	Efficiency (2.0e-7 mbar)	Efficiency (1.0e-7 mbar)
$^{85}Rb^{11+}$	0.8	-
$^{85}Rb^{13+}$	1.8	-
$^{85}Rb^{15+}$	3.8	3.8
$^{85}Rb^{17+}$	0.8	5.2
$^{85}Rb^{19+}$	-	3.2
$^{85}Rb^{20+}$	-	2.9

1+ Ion Injection

Computer Simulation Technology Electromagnetic Studio was used to simulate 3D ion injection into the ECRCB using the source running conditions for the magnetic fields, electric potentials, and a ΔV potential of -10 V. The simulations did not take into account plasma collisional effects. Ions of Na^+, K^+, and Cs^+ were flown into the ECRCB plasma chamber and their depth of penetration was tracked. Cases were simulated for the symmetric iron configuration as well as a configuration in which the RF was launched on axis thus necessitating cut-outs in the injection iron and resulting in an asymmetric magnetic field. The simulation results are shown in Fig. 1. In the plot, the 0 cm position is defined as the end of the grounded tube where the 1+ ions enter the plasma chamber. The peak axial magnetic field on the injection side (B_{max}) is located at 8 cm. The chamber mid-point is at 23 cm (B_{min}), and the extractor is at 38 cm (B_{ext}). In all of the symmetrical iron cases, 100% of the injected 1+ ions penetrated past the B_{max} location, and 40-55% of the total injected ions penetrated as far as the extraction electrode. In the asymmetrical cases, 60-90% of the

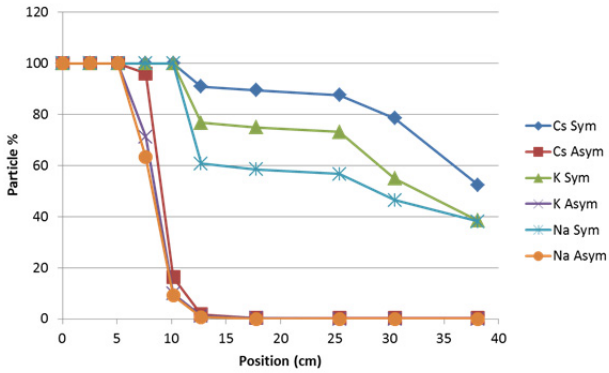

Figure 1: Simulated penetration of injected 1+ ions into ECR plasma chamber for symmetric (Sym) and asymmetric (Asym) iron cases.

injected 1+ ions penetrated past the B_{max} point, but only 1-2% passed the 13 cm mark and no ions reached the mid-point of the chamber. It is believed that this lack of penetration into the plasma region can hinder the capture of the 1+ ions and thus reduce the breeding efficiency. Recent modifications to the SPIRAL Phoenix charge breeder appear to support this conclusion [6]. The injection iron configuration was modified to eliminate field asymmetries where the 1+ ions enter the plasma chamber. In off-line testing, the source has demonstrated high breeding efficiencies including for the low mass species.

Multiple Frequency Heating

The first test of multiple frequency heating's effect on breeding efficiency was with ^{129}Xe. Three RF schemes were investigated: 1) klystron only, 2) TWTA only, 3) klystron+TWTA. To serve as a direct comparison of the various RF injection schemes, the total RF power launched into the source was kept constant at 245 W, only the power distribution between the klystron and TWTA was varied. With the source running an oxygen plasma and an extraction voltage of 20 kV, a 65 nA beam of $^{129}Xe^+$ was injected into the ECRCB and the breeding efficiency measured as a function of RF power distribution with the results shown in Fig. 2. When going from single to two-frequency heating, the peak of the

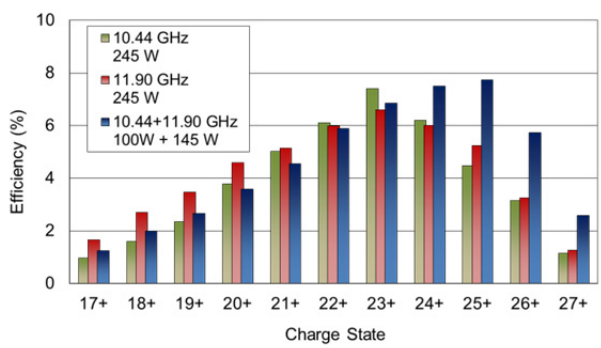

Figure 2: Simulated penetration of injected 1+ ions into ECR plasma chamber for symmetric (Sym) and asymmetric (Asym) iron cases.

ISBN 978-3-95450-131-1

charge state distribution shifted from 23+ to 25+ accompanied by a doubling of the breeding efficiency for 26+ and 27+.

Charge Breeding Time

It was observed that changes in the charge breeding efficiency due to RF power levels and operating frequency could be accompanied by dramatic changes in the charge breeding time. Fig 3 shows the observed efficiencies and rise times for ^{132}Xe as a function of the TWTA operating frequency. The $^{132}Xe^{+}$ was provided by an RF discharge source with an intensity of 17 enA. The ECRCB was run with an oxygen plasma and single frequency heating employing only the TWTA. When the frequency of the TWTA was shifted from 11.762 GHz to 11.765 GHz (300 W) several effects were observed: 1) the charge state distribution shifted to higher charge states, 2) the breeding efficiencies for the high charge state ions increased, 3) the charge breeding times increased. No other source parameters were changed between these two data sets implying that the frequency shift was the sole cause of the change in the plasma properties, possibly due to a change in the plasma potential as observed in Ref. [7]. Clearly the choice of operating frequency is just as critical with charge breeding as has been demonstrated in normal ECR operation [8]. While the exact mechanism of the operating frequency effect is still being investigated, it does give the source operator another convenient knob with which to optimize the ion source performance.

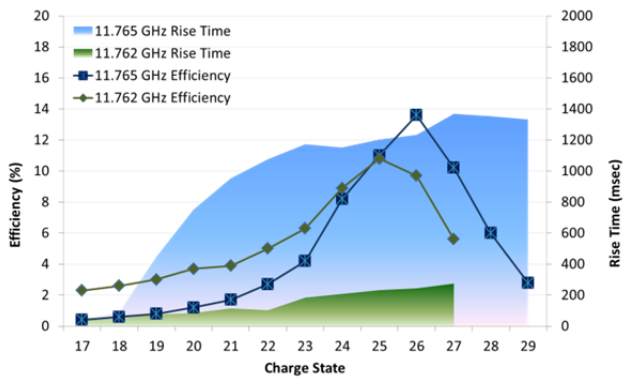

Figure 3: Xe-132 breeding efficiencies and rise times for TWTA operating frequencies of 11.762 GHz (in green) and 11.765 GHz (in blue).

Charge Breeder Background

The ubiquitous background contamination of ECR ion sources is well known [9,10]. Examples of this background are shown in Figs. 4 and 5, silicon barrier detector spectrums of a $^{144}Ba^{28+}$ and a $^{146}Ba^{28+}$ beam after acceleration in the ATLAS linac. The ^{144}Ba shows several contaminants ($^{36}Ar^{7+}$, $^{72}Ge^{14+}$, $^{108}Cd^{21+}$, $^{180}Hf^{35+}$) with the dominant contaminant being ^{36}Ar. In [11], the source of the ^{36}Ar was attributed solely to surface desorption and not o-ring permeation. In that analysis, however, the fact that the permeation rate of Viton increases with temperature was not taken into account and this could also explain the increase in ^{36}Ar rates observed in that

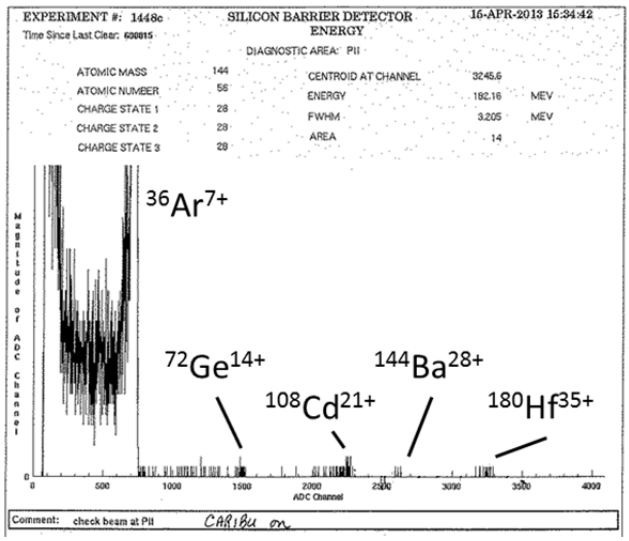

Figure 4: Beam of accelerated Ba-144 and its contaminants observed with a silicon barrier detector.

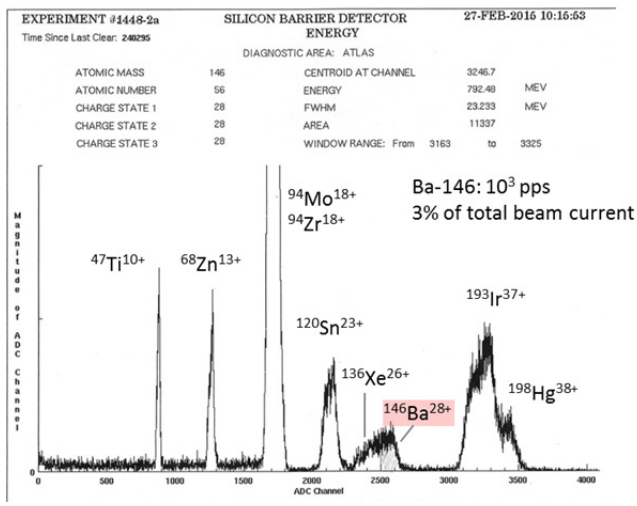

Figure 5: Beam of accelerated Ba-146 and its contaminants observed with a silicon barrier detector.

work. Calculations show that the 17 Viton o-rings on the source produce at room temperature an equivalent leak rate of 10^{-5} torr-l/s limiting the ultimate base pressure of the ion source to $2x10^{-8}$ mbar. The other species in the spectrum are due to either contamination of the plasma chamber surfaces or the bulk aluminum. The ^{144}Ba peak, while still visible at channel 2600 in the spectrum, represents <0.5% of the overall detector rate.

The impact of surface and bulk material contamination is more clearly seen in the ^{146}Ba spectrum where the stable beam components account for 97% of the total rate into the detector. Titanium and zinc are components of 6061 aluminum, the material used for the plasma chamber body. The source of the molybdenum, tin, iridium, and mercury is less understood. Only 7 contaminants out of a possible 47 [(m/q)/(Δm/q)>300)] are observed, and due to there being no strong contaminant near mass 146, the $^{146}Ba^{28+}$ radioactive beam component is still easily identified.

ISBN 978-3-95450-131-1

Charge Breeder Cleaning

Cleaning of the chamber surfaces with sand blasting and high pressure rinsing has been successfully demonstrated to reduce the background contamination [9]. However, these procedures would necessitate disassembling the ECR ion source and constructing a clean room to ensure a clean environment for source reassembly, and this was not compatible with the accelerator run schedule. It was decided to utilize CO_2 snow cleaning of the plasma chamber surfaces as well as the injection and extraction hardware. It is a non-destructive, non-abrasive, and residue-free method based upon the expansion of either liquid or gaseous carbon dioxide through an orifice leading to the nucleation of small dry ice particles in a high velocity gas carrier stream. The CO_2 pellets remove micron and submicron particulates by momentum transfer and hydrocarbons via a freeze-fracture mechanism. The high-velocity carrier gas propels the contaminants out of the system thus eliminating the need for high pressure rinsing and allowing the entire process to be done in situ.

In order to shield the 6061 aluminum wall from direct exposure to the plasma and thus address the bulk contaminant issue, the chamber was coated with ultra-high purity aluminum (99.9995%). A tungsten coil which had been saturated with the aluminum was suspended in the middle of the plasma chamber. The source was evacuated to 10^{-7} mbar and the coil heated resulting in an average surface deposition of 1 micron. Although not all surfaces were adequately coated, namely an injection side disk and mating piece both of which are constructed of 6061 aluminum, the majority of the plasma chamber was coated.

Before the CO_2 cleaning, a detailed mass scan of the entire source output was performed with analyzing slits set at +/-0.1 mm recording all peaks with an intensity >1 epA. After the CO_2 cleaning, the scan was repeated with the exact same source conditions. We observed reductions in three major observed contaminants – a factor of 20 reduction for fluorine, a factor of 4 for chlorine, and a factor of 50 for iron.

After the aluminum coating, the mass scan was repeated with the same source settings. The three contaminants were further reduced – a factor of 160 reduction for fluorine, a factor of 17 reduction for chlorine, and iron was no longer detectable.

Figure 6 shows silicon barrier spectra taken before and after the aluminum coating. As a result of the coating, several of the stable contaminants observed in the silicon barrier spectrum have either been eliminated (iron, cadmium, cerium) or have come down significantly (titanium). A significant ^{98}Mo peak remains and two new contaminants have been introduced – ^{181}Ta and ^{186}W – presumably due to the tungsten heating coil used for the evaporation which had a 20 ppm component of tantalum and a 10 ppm component of molybdenum. On the experimenter's detector, the ^{98}Mo was reduced by a factor of 5, the ^{142}Ce was eliminated (the Fe and Cd were not observed), but the Ta and W now dominated the spectrum.

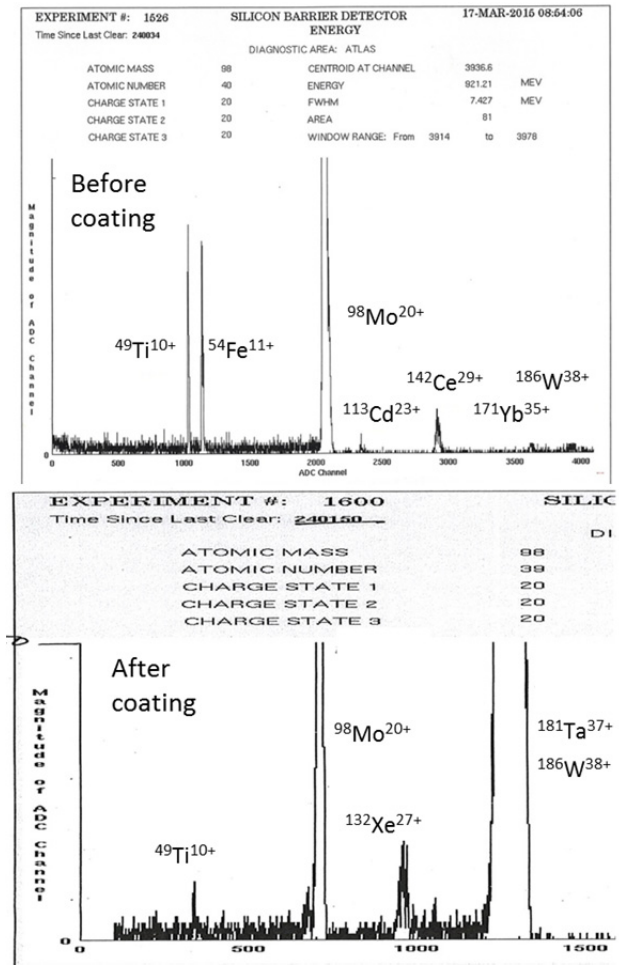

Figure 6: Silicon barrier detector spectra for before and after aluminum coating. The Mo-98 has been reduced by a factor of 5, and the Fe-54, Cd-113, Ce-142 have been eliminated. New contaminants of Ta and W are now present.

While the above techniques have demonstrated significant reductions in the level of background, especially that due to surface contamination, there are several refinements which can be made. The o-rings need to be eliminated from the source design to establish a truly UHV system. This advancement has been incorporated into the construction of the SPIRAL PHOENIX ECR charge breeder. A new technique to evaporate the aluminum needs to be developed. It is possible that a greater reduction in the ^{98}Mo component could have been realized if not for the 10 ppm molybdenum content of the heating coil, as inferred by the significant increase in Ta and W. Several off-line tests with various carbon-based heating elements have been performed with limited success.

EBIS PERFORMANCE

The demonstrated higher efficiencies, shorter breeding times, and greater purity of charge-bred radioactive ion beams achievable with an EBIS have led ANL to develop an EBIS in collaboration with the Brookhaven group [12]. However, the parameters of the electron gun, potential

ISBN 978-3-95450-131-1

distribution in the ion trap region, electron collector and injection/extraction beam lines are substantially modified from the Brookhaven design in order to obtain the highest acceptance and breeding efficiency of low intensity rare isotope beams. Special attention was paid to the design of the vacuum system to maintain high purity of the charge-bred radioactive ion beams. Parameters and some design details of the CARIBU EBIS CB are described elsewhere [13].

The first off-line charge breeding results were obtained in May 2014 [14]. With the injection of a Cs^{+} beam, a charge breeding efficiency of 10% into 14+ was realized with a modest solenoid field (4 T) and electron beam density (170 A/cm^2). There was still a high level of residual background due to several small vacuum leaks which were eventually identified and fixed.

After performing a multi-day bake-out and utilizing a higher magnetic field (5 T) and electron beam density (385 A/cm^2), the background was substantially lower and we achieved a 20% breeding efficiency into 28+ for 28 ms breeding time, 10^7 ions/pulse without preparation in a cooler/buncher, and a repetition rate of 10 Hz [15] (Fig. 7). For comparison, the best the ECR breeder has achieved is 13% into 27+ with a breeding time on the order of 300 ms.

The EBIS will replace the ECR charge breeder in late 2015. In addition, the beamline on the CARIBU deck will be reconfigured to incorporate an MR-TOF providing greater mass resolution in the 1:40000 range with >50% transmission and a capacity of 10^4 ions/bunch. The system will work at repetition rates between 1-30 Hz. Other than the dipole magnets and a few steerers, all transport elements in the low energy line will be electrostatic. The system is scheduled to be operational in early 2016.

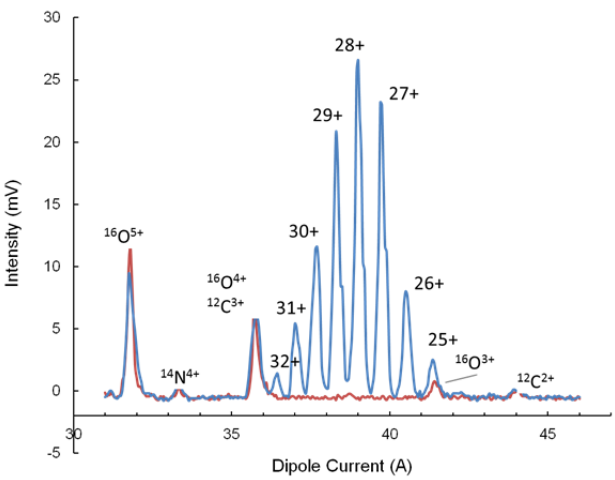

Figure 7: Spectrum of charge bred cesium from the EBIS.

ACKNOWLEDGEMENTS

This work was supported by the U.S. Department of Energy, Office of Nuclear Physics, under Contract No. DE-AC02-06CH11357 and used resources of ANL's ATLAS facility, an Office of Science User Facility.

REFERENCES

[1] R. Pardo, G. Savard, S. Baker, C. Davids, E.F. Moore, R. Vondrasek, G. Zinkann, NIM-B 261, Issues 1-2 (2007) 965.

[2] G. Savard, Journal of Physics: Conference Series, 312 (2011), p. 052004.

[3] F. Wenander, Nucl. Instrum. Meth. B266 (2008) p.4346-4353.

[4] P. Delahaye, NIM-B, Volume 317, Part B, 15 December 2013, Pages 389-394.

[5] R.C. Vondrasek, R. Scott, J. Carr and R.C. Pardo, Rev. Sci. Instrum. 79, 02A901 (2008).

[6] L. Maunoury, "Charge breeder for the SPIRAL1 upgrade: preliminary results", ICIS2015, New York, NY, August 23-28, 2015.

[7] O. Tarvainen, P. Suominen, T. Ropponen, and H. Koivisto, Rev. Sci. Instrum. 77, 03A309 (2006).

[8] L. Celona, G. Ciavola, F. Consoli, S. Gammino, F. Maimone, D. Mascali, P. Spädtke, K. Tinschert, R. Lang, J. Mäder, J. Roßbach, S. Barbarin, R.S. Catalano, Rev. Sci. Instrum. 79, 023305 (2008).

[9] N. Imai, S. C. Jeong, M. Oyaizu, S. Arai, Y. Fuchi, Y Hirayama, H. Ishiyama, H. Miyatake, M.H. Tanaka, M. Okada, and Y. X. Watanabe, Rev. Sci. Instrum. 79, 02A906 (2008).

[10] F. Ames, R. Baartman, P. Bricault, K. Jayamanna, T. Lamy, M. McDonald, Rev. Sci. Instrum. 81, 02A903 (2010).

[11] R. Vondrasek, J. Clark, A. Levand, T. Palchan, R. Pardo, G. Savard, R. Scott, Rev. Sci. Instrum.85, 02B903 (2014).

[12] S. Kondrashev, C. Dickerson, A. Levand, P. N. Ostroumov, R. C. Pardo, G. Savard, R. Vondrasek, J. Alessi, E. Beebe, A. Pikin, G. I. Kuznetsov and M. A. Batazova, Rev. Sci. Instrum. 83, 02A902 (2012) .

[13] S. Kondrashev, A. Barcikowski, C. Dickerson, R. Fischer, P. N. Ostroumov, R. Vondrasek and A. Pikin, Rev. Sci. Instrum. 85, 02B901 (2014).

[14] S. Kondrashev, A. Barcikowski, C. Dickerson, P.N. Ostroumov, S. Sharamentov, R. Vondrasek and A. Pikin, AIP Conf. Proc. 1640, 54 (2015).

[15] P. Ostroumov, A. Barcikowski , C. Dickerson , A. Perry , A. Pikin , S. I. Sharamentov , R. Vondrasek , G. Zinkann, Rev. Sci. Instrum., Accepted for publication.

ISBN 978-3-95450-131-1

STATUS REPORT ON THE OPERATION OF THE RIBF RING CYCLOTRONS

K. Ozeki#, T. Dantsuka, M. Fujimaki, T. Fujinawa, N. Fukunishi, H. Hasebe, Y. Higurashi, E. Ikezawa, H. Imao, T. Kageyama, O. Kamigaito, M. Kase, M. Kidera, M. Komiyama, K. Kumagai, T. Maie, M. Nagase, T. Nagatomo, T. Nakagawa, M. Nakamura, J. Ohnishi, H. Okuno, N. Sakamoto, K. Suda, A. Uchiyama, S. Watanabe, T. Watanabe, Y. Watanabe, K. Yamada, H. Yamasawa, RIKEN Nishina Center, Wako, Japan
S. Fukuzawa, M. Hamanaka, S. Ishikawa, K. Kobayashi, R. Koyama, T. Nakamura, M. Nishida, M. Nishimura, J. Shibata, N. Tsukiori, K. Yadomi, SHI Accelerator Service Ltd., Tokyo, Japan
Y. Kotaka, CNS, University of Tokyo, Saitama, Japan

Abstract

Operating status of four ring cyclotrons (RRC, fRC, IRC, SRC) from August 2014 to July 2015 is reported. We are engaging in the improvements and adjustments for increasing beam intensities year after year, and maintenances for the stabilization of beam supply. In these contributions, we will report the past performances of accelerated beams, statistics of operational and tuning time on corresponding period, as well as failures and copings with them.

INTRODUCTION

At RIKEN Nishina Center, the Radioactive Isotope Beam Factory (RIBF) [1] consists of four ring cyclotrons and three injectors. The four ring cyclotrons are: the RIKEN ring cyclotron (RRC) [2], which was commissioned in 1986; fixed-frequency ring cyclotron (fRC) [3], which was commissioned in 2006; intermediate stage ring cyclotron (IRC) [4]; and superconducting ring cyclotron (SRC) [5]. The three injectors are: the RIKEN heavy ion linear accelerator (RILAC) [6], RILAC2 [7], and AVF cyclotron (hereafter, AVF) [8,9]. The list of nuclei accelerated in the RIBF so far is shown in Fig. 1. Several acceleration modes are available through selection of a combination of accelerators. All ions from hydrogen to uranium can be accelerated up to 345 MeV/u (400 MeV/u for A/Z~2). There are three types of acceleration modes corresponding to each injector, which use the SRC. The beam extracted from the RRC can also be used at the experimental laboratories in the old facility. In addition, high-energy light ions recently became available at the biological irradiation laboratory in the old facility (E5B), which were accelerated using AVF, RRC, and IRC and then transported back to the old facility. Figure 2 shows the examples of energy attained at each stage in multiple-stage acceleration for each acceleration mode using SRC and IRC. The solid line shows the fixed-frequency mode, in which RILAC2 is used as the injector and all the ring cyclotrons are connected in series. The dashed line represents the variable-frequency mode, in which RILAC is used as the injector. The dotted line denotes the light-ion mode, in which AVF is used as the injector [10]. The dashed-dotted line shows a mode, which utilizes the newly installed IRC-E5 beam line. In this contribution, the status of the ring cyclotron system in the RIBF from August 2014 to July 2015 is reported.

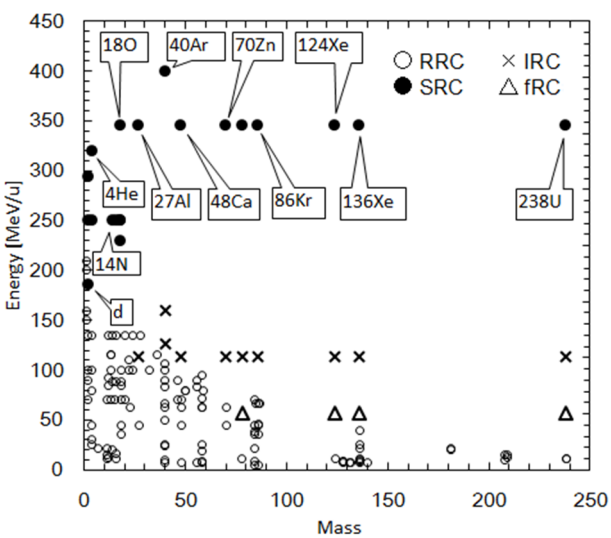

Figure 1: List of nuclei accelerated in the RIBF so far.

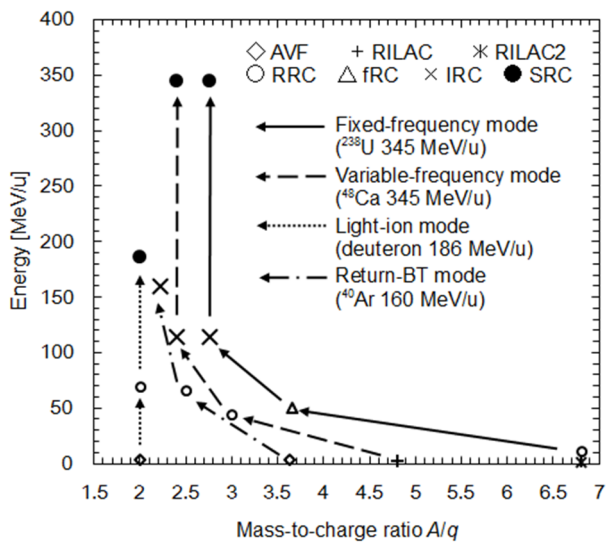

Figure 2: Transitions of energy and mass-to-charge ratio of accelerated nuclei in each acceleration mode in the RIBF.

#k_ozeki@riken.jp

ISBN 978-3-95450-131-1

OPERATING STATUS

The operating statistics of the RIBF are summarized in Table 1. Availability is defined as the ratio of the actual beam supply time to scheduled beam supply time. If the availability is greater than 100%, it denotes that actual time exceeds the scheduled time for various reasons such as shortening of beam tuning time. For the experiments in which the beam was not constantly used, such as material irradiation experiments, the availability was considered as 100% if the irradiation of the predetermined samples was completed without any delay. Multiple experiments using a similar beam are put together except for the long-term experiments using SRC; they are described separately.

The accelerations of ^{238}U using SRC were carried out three times. The total beam supply time and availability were 1,233 h and 94%, respectively. The intensity of the ^{238}U beam increased gradually, as shown in Fig. 3. In the operation on May 2015, the maximum beam intensity was 39.5 particle nA because of several factors, such as the enhancement of beam intensity supplied from the ion source, conversion of the injection buncher from the mesh type to cavity type, implementation of a new carbon material for the rotating charge stripper [11], and improvement of transit efficiency in the cyclotrons by the proficient beam tuning. On the other hand, the degradation of transit efficiency in the RRC caused by the loss of vacuum has become obvious [12].

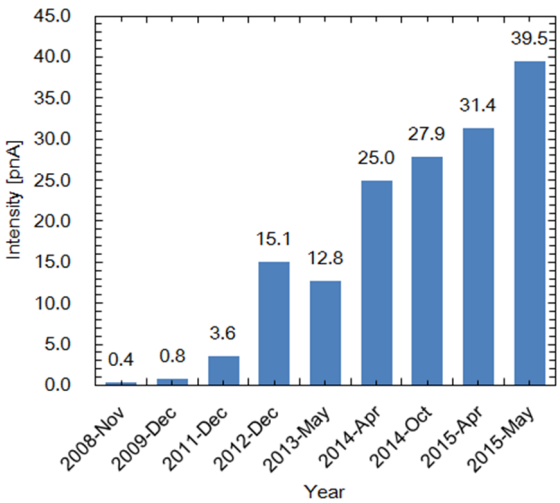

Figure 3: Beam intensity record of obtained in each ^{238}U beam service.

In the acceleration of ^{48}Ca, the beams were supplied to four experiment groups. The electrostatic deflection channel in the SRC was operated at 128 kV, the voltage of which was close to the upper limit of specification. The beam with a beam power of more than 8 kW was stably supplied.

The acceleration of polarized deuterons with the energy of 190 MeV/u was lower than the lower limit of the energy certified by the design of SRC (250 MeV/u). The acceleration test showed that a single-turn extraction was possible at this energy. In order to maintain the ratio of the half bunch to the main bunch in the beam extracted from the SRC below 1%, which was an index of the mixture of turns, beam tunings were performed frequently. Nevertheless, the availability exceeded 100% because the beam supply was started ahead of schedule because of the shortening of accelerator tunings.

Although the medium-heavy nuclei were typically accelerated using the variable-frequency mode in the RIBF, the fixed-frequency mode was adopted for the acceleration of ^{78}Kr. Adoption of this mode has several advantages: a high intensity 28-GHz superconducting ECR ion source can be used, as well as only one charge stripping is needed. However, a thick charge stripper foil must be used because of the difference between the extraction energy from the fRC and injection energy into the IRC. This mode was not adopted so far because degradation in beam quality was expected. As a result of the acceleration test, it was found that the high-intensity operation was possible in spite of the degraded beam quality. The beam with the maximum intensity of 310 particle nA was supplied to six experiments. In addition, the high-intensity beam production test was conducted using a beam dump in a projectile-fragment separator (BigRIPS), which was installed downstream of the SRC, to record a beam power of 13.1 kW (486 particle nA), which is the highest value recorded in the RIBF.

Table 1: Operation Statistics of RIBF

Beam particle	Energy (MeV/u)	Acceleration mode	Beam course	Beam current(particle nA) Requested	Beam current(particle nA) Actual	Beam time(h) Scheduled	Beam time(h) Actual	Down time (h)	Availability (%)
12C	70	AVF-RRC	E6(RIPS)	10.0	350.0	36.0	36.0	0.0	100.0
12C	135		E5B(Biology)	1.0	393.2	47.0	47.0	0.0	100.0
40Ar	95		E5B(Biology)	1.0	76.5	32.0	32.0	0.0	100.0
56Fe	90		E5B(Biology)	1.0	6.3	21.0	21.0	0.0	100.0
84Kr	70		E5A(Industry)	0.1	5.6	121.0	121.0	0.0	100.0
86Kr	36	RILAC-RRC	E3A(JAXA)	1.0	8.8	12.0	12.0	0.0	100.0
48Ca	63		E6(RIPS)	200.0	235.3	108.0	104.3	1.2	95.4
136Xe	10.75	RILAC2-RRC	E2B(KEK/KISS)	50.0	405.0	96.0	106.0	0.9	109.4
238U	10.75		A01(MS)/E5A(Material)	2.0	2500.0	48.0	48.0	0.0	100.0
40Ar	160	AVF-RRC-IRC	E5B(MS)	—	1.6	48.0	48.0	0.0	100.0
pol.d	190	AVF-RRC-SRC	BigD-pol	10.0	290.0	96.0	123.9	22.5	105.6
48Ca	345	RILAC-RRC-IRC-SRC	BigRIPS/SAMURAI	500.0	530.0	492.2	492.2	18.1	96.3
78Kr	345	RILAC2-RRC-fRC-IRC-SRC	BigRIPS/ZDS/EURICA/Rare-RI Ring	300.0	486.1	732.0	732.0	72.2	90.1
238U(1st)	345		BigRIPS/ZDS	15.0	27.9	532.1	532.1	31.1	94.2
238U(2nd)	345		BigRIPS/ZDS	15.0	31.4	552.0	553.0	47.9	91.5
238U(3rd)	345		BigRIPS/ZDS	20.0	39.5	228.0	252.0	25.3	99.5

ISBN 978-3-95450-131-1

In the old facility, biological experiments were conducted at the E5B, the industrial uses were conducted at the E5A, and nuclear experiments were conducted at the E6 (RIPS) and E2 (KISS). Stable beams were supplied as usual.

IRC-E5 BEAM LINE

In order to increase the beam energy used for biological experiments, a new beam line, which connects the IRC and an old experimental laboratory E5, was installed.

The newly installed beam line diverges from the SRC injection line at the deflection electromagnet DAKR, passes through a part of the bypass line, which connects the RRC and SRC bypassing the IRC, and joins the existing beam line at the deflection electromagnet DMA1 (See Fig. 4). The installation of each component was completed on January 2015, and a two-day commissioning was conducted. In order to obtain a high-energy beam from the IRC, a new acceleration mode that uses AVF, RRC, and IRC in series was tested. The ^{40}Ar beam was successfully accelerated up to 160 MeV/u, and transported to the old facility. In addition, a test to supply the beam to the biological irradiation device in E5B was conducted.

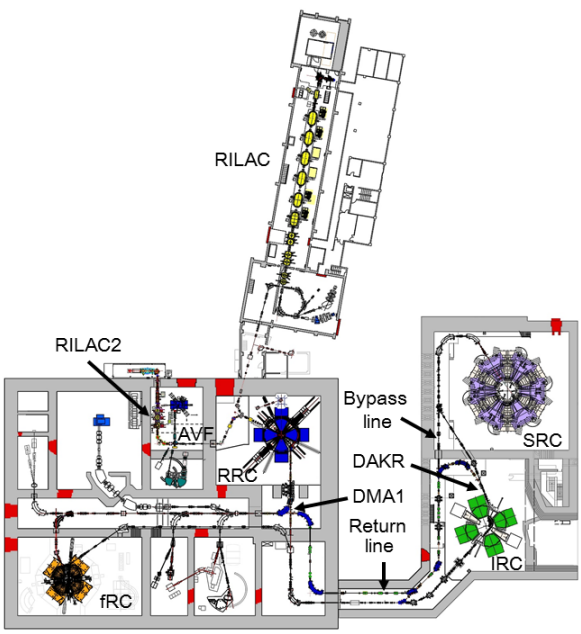

Figure 4: The layout of the accelerator facility in RIBF at RIKEN.

SUMMARY

For the duration from August 2014 to July 2015, the total beam supply time was 3,041 h. The ratio of experiments in which users use the beams directly extracted from RRC to all experiments was 19%. The total availability was 95%. The supplied beam intensities increased annually. A practical operation of the ^{48}Ca beam with the beam power of 13 kW is scheduled this autumn. Attempts for further enhancement of beam intensities and improvement of availability are made continuously.

REFERENCES

[1] Y. Yano, The RIKEN RI beam factory project: A status report, Nucl. Instrum. Methods B261 (2007) 1009-1013.

[2] H. Kamitsubo, Progress in RIKEN Ring Cyclotron Project, Cyclotrons'86, Tokyo, Oct. 1986, pp. 17-23.

[3] N. Inabe et al., Fixed-frequency ring cyclotron (fRC) in RIBF, Cyclotrons'04, Tokyo, Oct. 2004, 18P15, pp. 200-202;
T. Mitsumoto et al., Construction of the fRC sector magnet for RIKEN RI Beam Factory, ibid, 20P12, pp. 384-386.

[4] J. Ohnishi et al., Construction status of the RIKEN inter-mediate-stage ring cyclotron (IRC), Cyclotrons'04, Tokyo, Oct. 2004, 18P14, pp. 197-199.

[5] H. Okuno et al., The Superconducting Ring Cyclotron in RIKEN, IEEE Trans. Appl. Supercond. 17 (2007) 1063-1068.

[6] M. Odera et al., Variable frequency heavy-ion linac, RILAC: I. Design, construction and operation of its accelerating structure, Nucl. Instrum. & Methods 227 (1984) 187-195.

[7] K. Yamada et al., Beam commissioning and operation of new linac injector for RIKEN RI beam factory, IPAC12, New Orleans, May 2012, TUOBA02, pp. 1071-1073.

[8] A. Goto et al., Injector AVF cyclotron at RIKEN, Cyclotrons'89, Berlin, Germany, 1989, pp. 51-54.

[9] K. Suda et al., Status report of the operation of the RIKEN AVF cyclotron, in these proceedings, MOPA12.

[10] N. Sakamoto et al., High intensity heavy-ion-beam operation of RIKEN RIBF, Proceedings of PASJ9, WEPL02 (2012) 7-11.

[11] H. Hasebe, History of solid disk improvement for rotating charge stripper, in these proceedings, MOA1C01.

[12] Y. Watanabe et al., RIKEN Ring Cyclotron (RRC), in these proceedings, MOPA09.

ISBN 978-3-95450-131-1

ELECTRON-BEAM-DRIVEN RI SEPARATOR FOR SCRIT AT RIKEN RI BEAM FACTORY

T. Ohnishi*, S. Ichikawa, and M. Wakasugi
RIKEN Nishina Center for Accelerator-Based Science, Wako, Saitama, Japan

Abstract

Electron-beam-driven RI separator for SCRIT (ERIS) was constructed for the SCRIT (Self-Confinement RI Target) electron scattering facility at RIKEN RI Beam Factory. It is employed to produce low-energy, high-quality, and high-intensity RI beams used for the electron scattering of unstable nuclei. For RI production, ERIS uses the photofission of uranium driven by an electron beam, and the estimated production rate of fission products is 2.2×10^{11} fissions/s with 30-g uranium and a 1-kW electron beam. The RI production in ERIS was started at 2013. After several improvements of production target and ion source, the rate of ^{132}Sn was achieved to 2.6×10^{5} atoms/s with 15-g uranium and a 10-W electron beam. Further studies in ERIS are in progress to supply intense RI beams stably for the electron scattering with RI.

INTRODUCTION

Electron scattering is an unambiguous probing method to study the nuclear structure because of the well-known interaction and no internal structure of electron [1]. Thus, electron scattering has been applied to the study of stable nuclei for many years. As for short-lived unstable nuclei, it has not been applied due to the difficulty of preparing unstable nuclei target. To overcome this problem and realize electron scattering of short-lived nuclei, a novel target forming technique, named as SCRIT(Self-Confinement RI Target) [2], was proposed. SCRIT harnesses the ion trapping phenomenon in an electron storage ring. The validity and performance of SCRIT was already demonstrated [3,4]. Based on this successful achievement, the SCRIT electron scattering facility [5] was constructed at RIKEN RI Beam factory, and it has been operated from 2009.

Electron-beam-driven RI separator for SCRIT (ERIS) [6] is constructed as an online isotope separator (ISOL) system which is dedicated to produce a radioactive isotope (RI) beam for the SCRIT facility. In ERIS, the photofission of uranium driven by the electron beam is used for the RI production, because this reaction is effective for producing more neutron-rich isotopes around the tin region compared with other fission reactions [7]. This region is the first target of our project, and ^{132}Sn, especially, is an important nucleus in the study of unstable nuclei owing to its double magic number structure. After the commissioning of the beam line of ERIS, the RI production was started from 2013, and ^{132}Sn was clearly observed in the first attempt [6].

* oonishi@ribf.riken.jp

In this paper, we introduce ERIS briefly, and report the recent progress of the production target and the RI production.

EXPERIMENTAL SETUP OF ERIS

Figure 1 shows the schematic layout of ERIS. ERIS consists of a production target, a forced electron beam induced arc discharge (FEBIAD) type ion source, and a beam analyzing transport line. Produced RIs are transported to the SCRIT device installed inside the electron storage ring. Details of the components of ERIS and the result of the commissioning are described in Ref. [6].

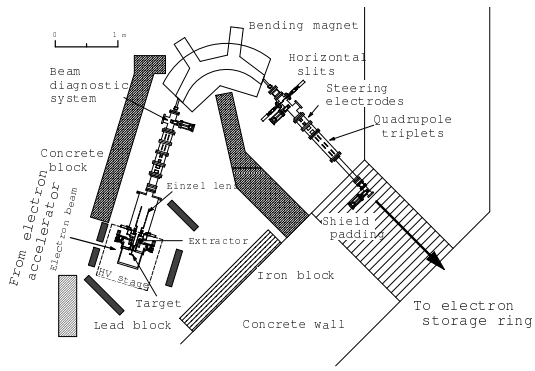

Figure 1: Schematic layout of ERIS. ERIS is surrounded with a concrete wall 2 m in thickness and local shields in the form of concrete, iron, and lead blocks are also installed.

The production target is installed inside a graphite container, which is 21 mm in inner diameter and 60 mm in inner length. This container is surrounded with a tantalum heater, and it is connected to the ion source by the transfer tube. For fast effusion and diffusion, all components are heated up to around 2000 °C. Figure 2 shows a tantalum heater and its setting.

In ERIS, the FEBIAD type ion source is used, because of its applicability to a wide range of elements and its stable operability with high ionization efficiency. The basic design of the ion source is based on CERN ISOLDE [8] and HRIBF [9] at Oak Ridge National Laboratory. Details of the ion source including the electrical connections is described in Ref [6]. This ion source is placed on a high-voltage stage (<50kV) for acceleration.

The beam transport line consists of an einzel lens, a doublet and a triplet electrostatic quadrupoles, four steering electrodes, and a 120° bending magnet with radius of 0.8 m. The diameters of the apertures of the einzel lens and the quadrupole electrodes are 120 and 40 mm, respectively. The maximum magnetic rigidity of the bending magnet is

ISBN 978-3-95450-131-1

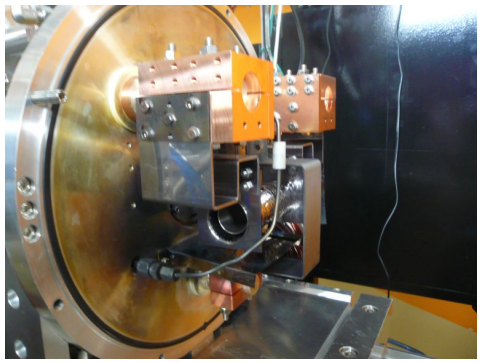

Figure 2: Photograph of tantalum heater and its setting. Cu blocks are heater electrodes connected with tantalum heaters. A thin tube which is connected to transfer tube is a gas inlet.

0.96 Tm. As a result of the commissioning, the mass resolution (M/ΔM) was obtained as about 1600 in σ.

The particle identification system consists of a rotating disk and a Ge detector, and it is installed at the exit of ERIS. The RI beam is stopped inside the rotating disk, and it is moved to the front of the Ge detector. The identification of the stopped RI is performed if specific γ rays corresponding to the decay of the stopped RIs are detected.

The total rate of fission products is estimated from the γ-ray production rate obtained from a Monte Carlo simulation and the measured cross section of the photofission of uranium [10]. In the calculation, a UC_2 target is used, and its density is set to 4.8 g/cm^3. With 60-mm thick target and 1-kW electron beam, the total fission products is estimated to be 2×10^{11} fissions/s. The production rate of ^{132}Sn is estimated be 2×10^9 particles/s from the independent chain yield (1%) [11].

PREPARATION OF PRODUCTION TARGET

As a production target, we prepared thin uranium-carbide disks for several merits.: 1) Using a thin target disk, such as 1-mm disk, the efficiency of release from the target is expected to be improved, because the total surface area of target disks becomes large. 2) Uranium carbide is more suitable for production target than uranium oxide, because its vapor pressure and density are lower and higher than those of uranium oxide, respectively. 3) With small amount of oxygen, damages to the material of ion source can be reduced.

Uranium carbide is obtained by the carbothermal reduction of uranium oxide in presence of carbon around 1100–1600°C [12]. First, uranyl nitrate solution was mixed with 20μm graphite grains. After the oxidization under air flow at 500°C, uranium-oxide-coated graphite powders were obtained. Next, these powders were manually ground, and formed into a disk without a binder at 180-MPa compression. The formed disk was 20 mm in a diameter and around 1 mm in a thickness, shown in Fig. 3. Finally, uranium-oxide-coated graphite disk was converted into uranium carbide disk at around 1100–1600°C. The obtained disk was 18 mm in a diameter and 0.8 mm in a thickness. In total, 23 disks were prepared. Total amount of uranium was about 15 g, and the average mass concentration of uranium in the disk was estimated as 3.4 g/cm^3.

Figure 3: Photograph of 1-mm uranium-oxide-coated target disks. These disks are 20 mm in a diameter and 1 mm in a thickness.

RI PRODUCTION AT ERIS

The prepared uranium-carbide disks were irradiated with an electron beam accelerated to 150 MeV. The maximum electron beam power was nearly 10 W. During the measurement, the electron beam power was adjusted to keep the acceptable counting rate of the detector. Total amount of uranium was about 15 g using 23 prepared thin uranium carbide disks. Tantalum disks with a thickness of 5 mm and a diameter of 20 mm were inserted in front of the production target to increase the production of γ rays. The temperature of the target and the transfer tube was approximately 2000°C. Produced RIs were accelerated to 20 kV and mass-separated by the beam transport line of ERIS. They were identified by the particle identification system.

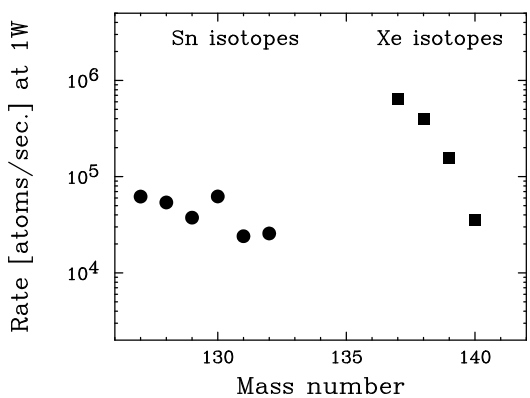

Figure 4: Rate of Sn and Xe isotopes at the particle identification detector at ERIS. Total amount of uranium is 15 g. The electron beam power is normalized to 1 W.

Figure 4 shows the rate of tin and xenon isotopes at the Ge detector. These rates are estimated from the observed γ-ray yield using the efficiency of the Ge detector and the

ISBN 978-3-95450-131-1

half-life of each isotope. These rates are normalized using the measured electron beam power. The overall efficiency is the ratio of the observed rate to the expected production rate inside the target. This efficiency includes the efficiency of release from the target, ionization in the ion source, and efficiency of transport from the ion source to the detector. The overall efficiency of stable xenon with a calibrated gas flow was also measured during the experiment. Since stable xenon was introduced into the ionization chamber through a gas inlet, the measured overall efficiency of stable xenon includes only ionization and transport efficiencies. In the case of tin isotopes, the same ionization and transport efficiency as those of xenon can be used, which is supported by the results at ALTO [13]. As a result, the release efficiency of xenon and tin isotopes can be estimated. Table 1 shows the summary of rate and efficiency in the case of ^{137}Xe and ^{132}Sn. The expected rate is calculated with the measured target density.

Table 1: Summary of Rate and Efficiency with 1-W Beam

	^{137}Xe	^{132}Sn
Observed rate (atoms/sec)	6.4×10^5	2.6×10^4
Expected rate (atoms/sec)	7.5×10^6	1.3×10^6
Overall efficiency	8.4%	2.1%
Overall efficiency of stable xenon	14%	15%
Release efficiency	61%	14%

The release efficiency includes the decay inside the target during the release process and the absorption in the target and the transport line. For ^{132}Sn, the reason of the low release efficiency is considered as the long time for effusion and diffusion due to its chemical property. In order to improve the release efficiency, it is needed to develop the poromeric structure target and achieve the better thermal uniformity in the transport line.

The stability of the production target at high temperature was also examined measuring the time dependence of the release efficiency. During the measurement period, the temperature of the production target was kept over 2000°C and the irradiation of the electron beam was only performed during the measurement of the efficiency. After 120 hours from the first measurement, the power of the target heater was increased from 4.4 kW to 5 kW. This was corresponding to almost 50 degree temperature rise around 2000°C.

Figure 5 shows the time dependence of the release efficiency of ^{130}Sn and ^{132}Sn. After about 4 days, the release efficiency becomes half of the values at the first measurement. Furthermore, the release efficiency was not fully recovered in spite of the temperature rise. From these results, the sintering of the target proceeded and the target crystal structure was expected to became more dense. Therefore, the effusion time from the target became much longer. To improve this situation, the thermal stability of the crystal structure is required. For example, a carbon nanotube is one of a candidate material. More study of the target crystal structure is needed.

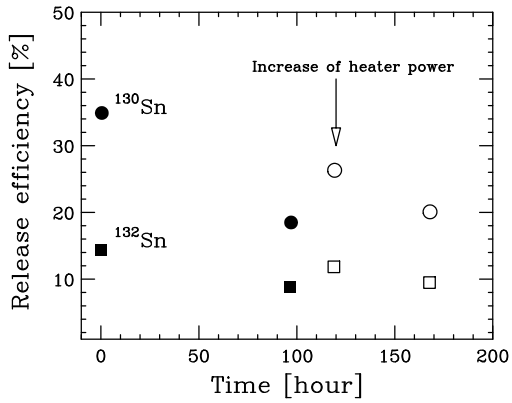

Figure 5: Time dependence of the release efficiency of ^{130}Sn and ^{132}Sn. Circles and squares show the result of ^{130}Sn and ^{132}Sn, respectively. Black and white show the target heater power 4.4 and 5 kW, respectively.

CONCLUSIONS

ERIS was constructed for the production of the RI beams at the SCRIT electron scattering facility. The RI prodcution at ERIS has been successfully performed and the development of increasing the rate of RI has been proceeded. To improve the efficiency of relase from the target, the stable supply of a 1-mm uranium-carbide disk was established, and the stability of the target was examined. Further studies in ERIS are in progress to supply the stable and intense RI beam, and realize the electron scattering with short lived nuclei.

REFERENCES

[1] T. Suda el al., Prog. Theor. Exp. Phys. 2012, 03C008 (2012), and references there in.

[2] M. Wakasugi et al., Nucl. Instrum. Methods A 532, 216 (2004).

[3] M. Wakasugi et al., Phys Rev. Lett. 100, 164801 (2008).

[4] T. Suda et al., Phys Rev. Lett. 102, 102501 (2009).

[5] M. Wakasugi et al., Nucl. Instrum. Methods B 317, 668 (2013).

[6] T. Ohnishi et al., Nucl. Instrum. Methods B 317, 357 (2013).

[7] Yu. Ts. Organessian et al., Nucl. Phys. A 701, 87c (2002).

[8] S. Sundell et al., Nucl. Instrum. Methods B 70, 160 (1992), and references there in.

[9] G. D. Alton, Nucl. Instrum. Methods A 382, 207 (1996), and references there in.

[10] M. Giaeri, ENDF/BB MT-18, NNDC and H. Reis et al., Phys. Rev. C 29, 2346 (1984).

[11] D. De Frenne et al., Phys. Rev. C 29, 1908 (1984).

[12] Gmelin handbook of inorganic chemistry, Supplememnt Volume C12.

[13] M. Cheikh Mhamed et. al., Nucl. Instr. Meth. B 266, 4092 (2008).

ISBN 978-3-95450-131-1

ACCELERATION SCHEME OF RADIOACTIVE ION BEAM WITH HIMAC AND ITS INJECTOR LINAC

Akira Noda#, Satoru Hojo, Ken Katagiri, Masao Nakao, Etsuo Noda, Koji Noda, Akinori Sugiura, Kazutoshi Suzuki, Takashi Wakui , NIRS, Inage, Chiba, 263-8555, Japan
Manfred Grieser, MPI-K, 69117, Heidelberg, Germany

Abstract

At the National Institute of Sciences (NIRS), cancer therapy with the use of a carbon beam has been successfully applied since 1994 by using 'HIMAC' (Heavy Ion Medical Accelerator in Chiba). Recently the number of treated patients has been increased to nearly 1000 per year. For the purpose of real-time verification of the irradiation distribution in the patient's body during a heavy ion cancer treatment, the capability of the so-called "Open PET" with a radioactive $^{11}C^{6+}$ ion beam has been proposed[1] and projectile fragment ^{11}C ion beams, already has been tried to be applied[2], but the beam intensity was rather poor, about 10^5 pps, and a good S/N ratio had not been attained[1]. Therefore to remedy this situation, the acceleration of radioactive ions created by the "Target Fragment" scheme, where beams from the cyclotron irradiate a target, has been proposed[3]. In the present paper, in connection with recent developments[4], an acceleration scheme of secondary produced radioactive ^{11}C ion beams with HIMAC and its injector is investigated.

INTRODUCTION

Radiation cancer therapy utilizing heavy ions has increased its importance by a steady increase of the treatment numbers in addition to the fact that it is improving the "Quality of Life" of the patients. Up to now the irradiated region by heavy ion beams has been estimated with a preparatory irradiation into a water phantom and by using computer simulation. However, recent innovations of imaging technology might enable a direct detection of the irradiation area during the real therapy treatment with the use of an "OPEN PET"[1]. For such purpose, it is inevitable to provide enough ions (>10^7 pps) to the irradiation port of HIMAC for attaining a good S/N ratio.

Up to now, radioactive ion beams of ^{11}C, produced by projectile fragmentation of stable ^{12}C ion beams have been created[2] and transferred to the secondary beam port of HIMAC for the purpose of visualization of the beam stopping point. Its intensity, however, was rather limitted (less than 10^5 pps) and it is not strong enough for real clinical usage.

In order to attain enough intensity of a radioactive ^{11}C ion beam, a scheme utilizing target fragments, produced by high intensity proton beam irradiation with the use of the cyclotron; NIRS HM18, has been considered[3], which is a similar scheme used at ISOLDE of CERN[5] , although the energy region of the primary proton beam is much lower. Originally a N_2 gas target has been proposed using a $^{14}N(p, \alpha)^{11}C$ reaction[6]. The collection efficiency of molecules containing radioactive ^{11}C ions, however, is rather limited with the use of a N_2 gas target, because separation of the huge amount of the impurity N_2 gas is a serious problem to provide the ^{11}C molecules to the 1+ ion source under vacuum condition, which is different from radioactive drug generation case. Therefore a new scheme using a solid $NaBH_4$ target for $^{11}B(p,n)$ ^{11}C reaction is utilized where the ^{11}C gas can be ionized and efficiently collected[4].

RADIOACTIVE ISOTOPE PRODUCTION

Radionuclide Production with Cyclotrons at NIRS

At NIRS since its establishment, various knowledge and experiences have been accumulated concerning treatment and imaging with the use of radioactivity. Recently more than 200 radiopharmaceuticals have been developed and been globally utilized for diagnostic imaging. Reflecting the rapid progress of imaging and medical treatment utilizing radio-pharmaceuticals, Targeted Radionuclide Therapy (TRT) has been also investigated and basic experiments with animals have been applied using α-particle with high LET (Linear Energy Transfer) or radioisotopes with Auger electron emission. In table 1 and table 2, lists of radionuclides produced by

Table 1: Ion Beams from the NIRS930 Cyclotron and their Created Radionuclides

Beam Particle	Radionuclide
Proton	^{89}Zr
	^{11}C
	$^{62}Zn/^{62}Cu$
	^{68}Ge
	^{67}Cu
H_2^+	^{64}Cu
	^{124}I
Deuteron	^{177}Lu
Helium	^{67}Cu
	^{43}Sc
	^{47}Sc
	^{74}As
	^{155}Tb
	^{186}Re
	^{211}At
	^{28}Mg

Table 2: Ion Beams from HM-18 Cyclotron and their Created Radionuclides

Beam Particle	Radionuclide
Proton	^{11}C
	^{13}N
	^{18}F
Deuteron	^{15}O

#a_noda@nirs.go.jo

ISBN 978-3-95450-131-1

the irradiation with a beam from cyclotron, NIRS-930 and a small HM-18 cyclotron, respectively, are shown. Based on such an activity, a new project to extend the TRT has been proposed.

Radioactive ^{11}C Ion Production at NIRS930 Beam Line

At the beam line of NIRS930 used for neutron therapy just after construction about 40 years ago, a modification utilizing wobblers to enlarge the beam size for various radiopharmaceuticals production is being applied[7]. With this beam line, the scheme above mentioned to create $^{11}C^{+}$ beams will also be tested experimentally using proton beams from NIRS-930 as a preparatory study before the beams are further accelerated.

At NIRS, on the basis of such an activity as described before, ^{11}C of the amount of about 10^{13} are produced in 20 minutes with the $^{11}B(p, n)^{11}C$ reaction by irradiation with 18 MeV proton beams onto a solid $NaBH_4$ target. A ^{11}C beam with an intensity of 10^8 pps can be provided in each 20 minute cycle. Recent scheme utilizes irradiation onto a solid target under the vacuum condition[8].

ACCELRERATION SCHEME OF ^{11}C BEAMS WITH HIMAC

Injector Linac System of HIMAC

The beams from the ion source are accelerated by the RFQ and the drift tube linac of Alvarez type, both with the operation RF frequency of 100 MHz, before the beam is injected into the HIMAC synchrotron. In table 3, the main acceleration performance parameters of the injector linac are listed up[9]. Ions with charge to mass ratio (q/M) larger than 1/7 times e/m_0 (e and m_0 are unit charge and atomic mass unit, respectively) can be accelerated. The normalized emittance (90 %) of the injector linac is 0.7 πmm・mrad and the momentum spread is ±0.1%.

Acceleration of Radioactive ^{11}C Ion with HIMAC and its Injector

For the purpose of acceleration of a radioactive ^{11}C ion with a life time of about 20min by the injector linac of HIMAC as shown in Fig. 1, the CMPS (^{11}C molecule production and separation system) has to be followed with a singly charged ion source and a charge breeder (shown in Fig. 2). The ISOL system for ^{11}C ion production has to be close to the linac, for example at the position A or B shown in Fig. 1. We are now considering the construction of a small cyclotron, HM-20[10] with an irradiation room for the unsealed radiation. The final decision of the position of HM-20 and CMPS depends on the usage of the area next to the RFQ.

Table 3: Main Parameters of the Injector Linacs (Borrowed from Ref.[9])

Injection Energy	8 keV/u
Output Energy	800 keV/u(RFQ), 6 MeV/u (DTL)
Input Current	140eμA(C^{4+}), 300eμA(C^{2+})
Transport Efficiency LEBT RFQ Alvarez	 93%(C^{4+}), 80%(C^{2+}) 92%(C^{4+}), 92%(C^{2+}) 96%(C^{4+}), 86%(C^{2+})
Stripping Efficiency	93%
MEBT Transmission	95%(C^{4+}),84%(C^{4+})
Normalized emittance (90%)	0.7 πmm・mrad
Momentum Spread	±0.1%

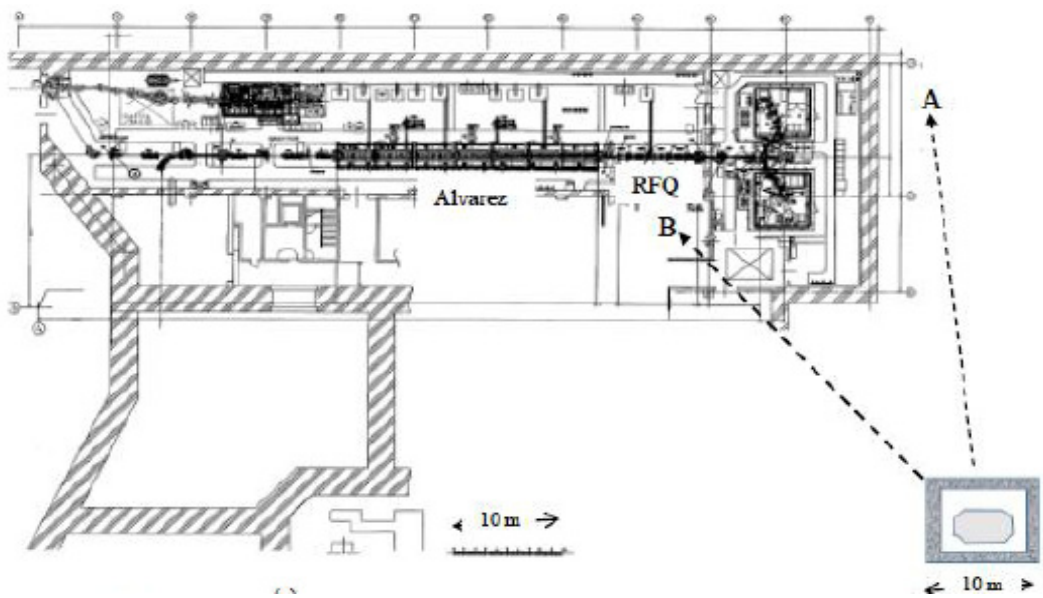

(a) (b)

Figure 1: (a) Layout of the injector linac system of HIMAC, (b) Rough scale of HM20 (with shielding).

ISBN 978-3-95450-131-1

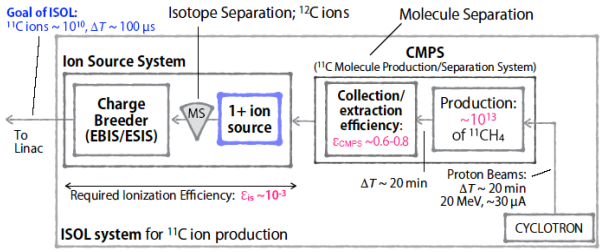

Figure 2: A scheme to provide ^{11}C ion beam (borrowed from Ref. [8]).

The performance of the above scheme composed of CMPS and 1+ ion source followed by a charge breeder has to be experimentally investigated. The studies will start early next year. The beam emittance and momentum spread of the ^{11}C ion beam will be measured as soon as the irradiation system becomes available.

Beam Dynamics Evaluation

Because the initial parameters of the radioative ^{11}C ion beam from the ISOL system for ^{11}C ion production shown in Fig.2, are not yet known so far, beam dynamics simulations of the ^{11}C ion beam has to be carried out with a computer simulation code such as PARMTEQ[11], assuming similar beam parameters (emittance and momentum spread) of a usual ^{12}C ion source. It is expected that by modification of the intervene voltage according to the difference of the charge to mass ratio, similar beam behaviour as shown in Fig.3 can be obtained.

CONCLUSION

Using the above scheme, we expect to be able to provide totally about 10^9 ^{11}C ions every 20 minutes. If the beam extraction from HIMAC and the beam supply to the treatment room is performed during 10 seconds, beam rates of about 10^8 pps will be realized for a limited part (10 sec.) of the 20 minutes period, which is around 10^3 times larger compared with the already applied scheme utilizing the

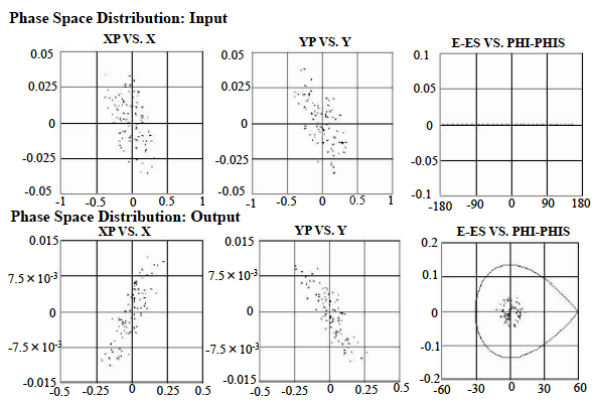

Figure 3: Example of beam distribution at the input and output of the RFQ calculated by PARMTEQ.

"Projectile Fragment" scheme and the S/N ratio for online PET imaging is expected to be well enhanced.

Possibility of Acceleration of Other Ions

As shown in table 2, the small cyclotron can produce other ions like ^{13}N, ^{18}F and ^{15}O. ^{15}O ions with a rather short life time (2 minutes) needs a deuteron beam for the production and is not usable for further acceleration. The available accelerated radioactive ion beams are rather limited due to the required charge to mass ratio larger than 1/7 (e/m_0) by the injector linac. However the combination with HIMAC might give us a possibility of unique higher energy radioactive ion beams and seems to require further deep discussions for the future.

ACKNOWLEDGEMENT

One of the author (A. N) would like to present his sincere thanks to Dr. Y. Iwata at NIRS and Dr. V. Kapin at Fermi Nat. Lab. for their kind advice to utilize computer calculation CODEs PARMTEQ and PARMILA for linac beam dynamics calculation.

REFERENCES

[1] T. Yamaya, et al., "A proposal of an open PET geometry", Phys. Med. Biol., 53, (2008), pp757-773.
[2] E. Urakabe et al., "Spot scanning using radioactive 11C beams for heavy-ion radiotherapy", Jap. J Appl. Phys., 40, AIP Accel.(2001), pp2540-2548.
[3] S. Hojo et al., "Production of 11C-beam for particle therapy", Nucl. Instr. Meth. B240,(2005), pp75-78.
[4] K. Katagiri et al., "11CH4 molecule production using a NaBH4 target for 11C ion acceleration", Rev. Sci. Instrum. 85, 02C305 (2014).
[5] http://isolde.web.cern.ch/
[6] K. Suzuki et al., "Specific activity of [11C]CO2 generated in a N2 gas target: effect of irradiation dose, irradiation history, oxygen content and beam energy", Radiochem. Acta 88, pp211-215 (2000).
[7] K. Katagiri et al., "Design of Beam Transport Lines For Radioisotope Production Systems in NIRS Cyclotron Facility", Proc. of IPAC14, Dresden, Germany, pp2162-2164.
[8] K. Katagiri et al., "A singly charged ion source for radioactive 11C ion acceleration", Proc. of the International Conference of Ion Sources 2015 (ICIS2015), New York City, USA.
[9] S. Yamada et al., "Present status of the HIMAC injector", Proc. of 1994 International Linac Conference, Tsukuba, Japan, pp. 768-770, (1994).
[10] http://www.shi.co.jp/quantum/jp/product/pet/hm20.html
[11] K.R. Crandall and T.P Wangler, "PARMTEQ---A beam dynamics code to the RFQ linear accelerator", AIP Conference Proc. Vol. 177 (1988), pp22-28.

ISBN 978-3-95450-131-1

PUSHING THE INTENSITY ENVELOPE AT THE ATLAS LINAC*

B. Mustapha#, C. Dickerson, P. Ostroumov, R. Pardo, M. Hendricks, R. Scott and G. Zinkann
ANL, Argonne, IL 60439, USA

Abstract

The ATLAS linac at Argonne National Laboratory has recently been upgraded for higher beam intensity and transport efficiency. A new 60 MHz RFQ replacing the first few cavities of the Positive Ion Injector (PII) section and a new superconducting module replaced three old cryomodules of split-ring resonators in the Booster section of the linac. Following the installation of the new RFQ, we performed a high-intensity run using a $^{40}Ar^{8+}$ beam. A beam current of 7 pμA was successfully injected and accelerated in the RFQ and PII section of the linac to an energy of 1.5 MeV/u. The results of this run are presented and the limitations to reach higher currents are discussed. A second run is planned to try to push the beam current higher and farther into the Booster and ATLAS sections of the linac. Finally, a future intensity upgrade plan, motivated by the inflight production of radioactive beams using the AIRIS separator and the proposed multi-user upgrade with potential stable beam applications is presented and discussed. The ultimate goal of this upgrade plan is to reach 10 pμA or higher for most beams at the full ATLAS energy.

THE RECENT ATLAS UPGRADE AND IMPROUVEMENT IN BEAM CHARACTERISTICS

The Argonne Tandem Linear Accelerator System (ATLAS) was the first superconducting linac for ion beams in the world [1]. It has been operating and delivering ion beams for over thirty years at different capacities. Over the same period, ATLAS has undergone several upgrades [2]. The most recent is the Efficiency and Intensity upgrade [3].

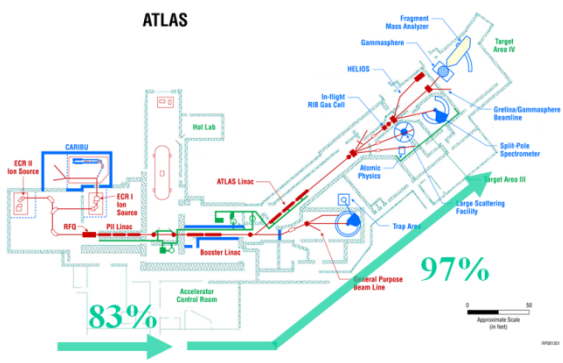

Figure 1: ATLAS layout after the recent Intensity and Efficiency Upgrade showing typical beam transmission through the different linac sections.

The Efficiency and Intensity upgrade consisted of a new RFQ [4] and a new superconducting module [5]. The RFQ replaced the first three superconducting cavities of the Positive Ion Injector (PII) to avoid deterioration of the beam quality due to fast acceleration of low energy beams. The RFQ uses the existing multi-harmonic buncher (MHB) as a pre-buncher. Two notable features of the ATLAS RFQ are trapezoidal modulations in the accelerating section and a compact output matcher to produce an axially-symmetric beam for direct beam injection into the PII which uses solenoidal focusing [6]. The new cryomodule replaced three old modules with split-ring resonators [7]. The split-ring cavities steer the beam resulting in beam loss and the subsequent quench of solenoids. The new cryomodule is made of 7 quarter-wave resonators (QWR) and 4 superconducting solenoids. The QWRs were designed and built with steering correction [8]. The new module should be able to accelerate 10 to 100 times higher intensity stable beams without significant beam loss.

Both the new RFQ and cryomodule have been successfully commissioned and are now being used for routine ATLAS operations. The improved beam quality from the RFQ, both transverse and longitudinal, has increased the transmission by 50 to 100% for all beams accelerated in ATLAS [9]. The overall transmission is now routinely over 80%, which is dictated by the MHB used to produce a small longitudinal emittance for more efficient beam transport and acceleration in ATLAS [10]. Figure 1 shows the current layout of ATLAS after the recent intensity and efficiency upgrade.

HIGH INTENSITY RUN AT ATLAS

A high-intensity run was performed at ATLAS in February 2014, just before the installation of the new cryomodule. The goal of this run was to inject and accelerate 10 pμA of a heavy-ion beam through the RFQ+PII section of ATLAS.

An ~ 120 eμA $^{40}Ar^{8+}$ beam was produced at the ECR-2 ion source. The LEBT, RFQ and PII were first tuned with low current beam using attenuators to control the beam intensity and collimating slits to control the beam emittance. A transmission of 80% or more through the RFQ+PII is essential. A lower transmission would mean a substantial beam loss that will prevent ramping up the beam current. The beam intensity was increased by gradually removing beam attenuators, opening slits and adjusting the gas in the ECR. The final results were: 72 eμA injected into the RFQ+PII section with 58 eμA transmitted and accelerated (consistent with the simulated MHB-RFQ transmission) to the full 1.5 MeV/u energy. That is a 7.2 pμA $^{40}Ar^{8+}$ beam, which is a significant

* This material is based upon work supported by the U.S. Department of Energy, Office of Science, Office of Nuclear Physics, under Contract number DE-AC02-06CH11357. This research used resources of ANL's ATLAS facility, which is a DOE Office of Science User Facility.
#brahim@anl.gov

ISBN 978-3-95450-131-1

improvement over the previous maximum of 2 pμA for this beam.

Among the limitations preventing us from reaching higher currents are: (i) The current ECR source produces enough beam current but with such a large emittance that it requires significant collimation to be effectively transported through the LEBT and injected into the RFQ, (ii) beam loss in PII due to the large emittance and not enough steering correction to control the beam center, as well as (iii) the loss of the RFQ satellite bunches in PII due to the frequency change. Both of these effects lead to solenoid quenching and resonator heating in PII, which are the main limiting factors. A second run is planned in the near future to try to push the beam current higher and farther into the Booster and ATLAS sections of the linac.

OPPORTUNITY FOR A FUTURE INTESNITY UPGRADE AT ATLAS

The Argonne In-flight Radioactive Isotope Separator (AIRIS) [11] project has recently been approved, by the US Department of Energy's (DOE) Office of Nuclear Physics, to be built and installed at the ATLAS facility. AIRIS, shown in Figure 2, will use stable beams from ATLAS to produce secondary radioactive beams (RIBs) using transfer reactions. Secondary beams with masses up to 50 with energies variable over the full ATLAS energy range will be available to the same experimental areas served by ATLAS stable beams. The existing radioactive beam facility [12] has been limited to primary beam intensities of about 100 pnA by both the gas cell target used to produce the secondary beams and the insufficient 20 year old radiation shielding in the production area. AIRIS is a dedicated device, where a liquid film target will be used along with the appropriate radiation shielding. The starting primary beam intensity for AIRIS is 1 pμA, that is ten times the current limit. However, the production of radioactive beams at AIRIS could benefit significantly from an intensity upgrade of ATLAS. A 10 pμA primary beam current will shorten the run time for typical RIBs and allow the production of more rare isotope beams at rates useful for experiments.

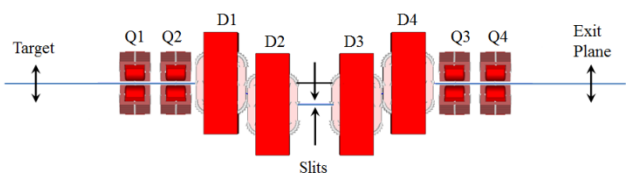

Figure 2: Layout of AIRIS, recently approved for construction and installation at ATLAS.

On the other hand, with the upcoming installation of the recently commissioned CARIBU-EBIS charge breeder [13], it will be possible to simultaneously accelerate one radioactive and one stable beam in ATLAS. The EBIS produces a 10 μs to 1 ms beam pulse with a repetition rate of up to 30 Hz, or 3% of the duty cycle. ATLAS, being a CW machine, enables the possibility of injecting stable beams during the remaining 97% of the duty cycle. Considering the fact that a stable beam with a charge-to-mass ratio close to that of the CARIBU beam is usually used as a guide beam to tune the linac, it would be straightforward to inject any stable beam with a charge-to-mass ratio within 3% without retuning the machine. Such a multi-user capability could also benefit from an intensity upgrade at ATLAS where we can envision splitting an intense stable beam to serve different experimental areas simultaneously, including possible applications. In particular, this could be done right after the PII section of the linac for high-intensity beam irradiation experiments, or at the end of the linac for isotope production, which requires high intensity beams at the full ATLAS energy. Figure 3 shows the proposed layout for the ATLAS multi-user upgrade with beam splitting to the different experimental areas.

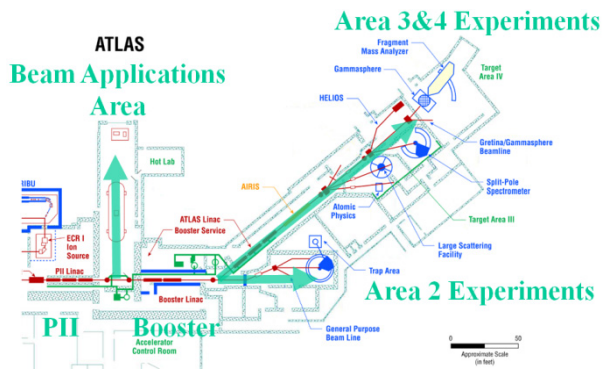

Figure 3: Layout of the proposed ATLAS multi-user upgrade with possible beam splitting after PII for beam applications and after Booster for the different experimental areas.

THE PATH TO HIGHER BEAM INTENSITY AT ATLAS

The ultimate goal of a future intensity upgrade is to deliver 10 pμA or more for most beams at the full ATLAS energy. The proposed approach to reach this goal is:

1) Install a new VENUS-type [14] superconducting ECR ion source to provide the required input current for all beams within acceptable emittances.
2) Adopt achromatic beam transport to limit emittance growth in the LEBT, using more compact electrostatic focusing. This will be implemented with the upcoming CARIBU-EBIS installation and integration into ATLAS [15].
3) Locate where the RFQ satellite bunches are lost and, if needed, install beam collimators inside or between cryomodules to intercept them and avoid quenching of solenoids and cavities.
4) Add beam steering elements in PII to better control beam center. Few existing solenoids could be replaced by solenoids with steering correctors.
5) Install a second re-buncher after PII. Using a single re-buncher is enough for low current operations,

ISBN 978-3-95450-131-1

but the second re-buncher will be needed for high intensity runs.

6) Replace the remaining three split-ring cryomodules with at least one new QWR cryomodule, similar to the recent 72 MHz module. The split-rings are limiting the beam current in ATLAS to 2-3 pμA due to their intrinsic beam steering.
7) A second high-beta QWR cryomodule, similar to the existing 109 MHz module [16], may be needed to achieve the energy goal for heavy ions..
8) Install high-power diagnostics throughout the linac.

With such a plan, we believe we could achieve the desired goal of higher beam intensity at ATLAS.

SUMMARY

Following the recent ATLAS Intensity and Efficiency Upgrade [3], we have performed a high-intensity run in the RFQ+PII section. A 7.2 pμA $^{40}Ar^{8+}$ beam was successfully transported and accelerated to 1.5 MeV/u. This is a significant improvement over the previous limit of 2 pμA for this particular beam. Work is ongoing to increase the available beam current, and we have identified several limitations and presented possible solutions. This first run was performed prior to the installation of the new intensity upgrade QWR cryomodule. We are planning a second high-intensity run in the near future to attempt to push the beam current higher and farther into the Booster and ATLAS sections of the linac.

With the upcoming AIRIS project and the proposed ATLAS multi-user upgrade, we see an opportunity for a future intensity upgrade of ATLAS. The goal of such an upgrade is to be able to deliver 10 pμA or higher for most beams at the full ATLAS energy. This would allow higher intensity radioactive beams from AIRIS. It would also allow potential high-intensity stable beam applications that could run simultaneously with the experimental nuclear physics program following the ATLAS multi-user upgrade.

REFERENCES

[1] L.M. Bollinger et al., "The Argonne Superconducting heavy-ion linac", Proceedings of the Conference on Proton Linear Accelerators, Chalk River, Ontario, 14-17 September 1976, AECL-5677, p95 (1976).
[2] K.W. Shepard et al., "Superconducting Low-Velocity Linac For The Argonne Positive-Ion Injector", Proceedings of the 1989 IEEE Particle Accelerator Conference, Chicago, Illinois, March 20-23, 1989, IEEE Publishing Vol. 2, p974 (1989).
[3] P.N. Ostroumov et al., "Completion of Efficiency and Intensity Upgrade of the ATLAS Facility", Proceedings of the 2014 Linear Accelerator Conference (LINAC-14), Geneva, Switzerland, August 31 - September 5, 2014.
[4] P.N. Ostroumov et al., "Development and beam test of a continuous wave radio-frequency quadrupole accelerator", Phys. Rev. ST–AB 15 (2012) 110101.
[5] M.P. Kelly et al., "Commissioning of the 72 MHz Quarter-Wave Cavity Cryomodule at ATLAS", Proceedings of the 2014 Linear Accelerator Conference (LINAC-14), Geneva, Switzerland, August 31 - September 5, 2014.
[6] B. Mustapha et al., "A full three-dimensional approach to the design and simulation of a radio-frequency quadrupole", Phys. Rev. ST–AB 16 (2013) 120101.
[7] K.W. Shepard et al., "Split-ring Resonator for the Argonne Superconducting Heavy-ion Booster", IEEE Trans. Nucl. Sci. NS-24, p1147 (1977).
[8] B. Mustapha and P.N. Ostroumov, "Electro-Magnetic Optimization of a Quarter-Wave Resonator", Proceedings of the XXV Linear Accelerator Conference (LINAC-10), Tsukuba, Japan, September 12-17, 2010.
[9] C. Dickerson et al., "Improved beam characteristics from the ATLAS upgrade", HB-2014, East Lansing, MI, November 10-14, 2014.
[10] B. Mustapha P. N. Ostroumov and J. A. Nolen, "A Driver Linac for the Advanced Exotic Beam Laboratory: Physics Design and Beam Dynamics Simulations", Proceedings of PAC-07 Conference, Albuquerque, New Mexico, June 25-29, 2007, p1601.
[11] S. Manikonda et al., "Argonne In-flight Radioactive Ion Separator", Proceedings of HIAT-2012, Chicago, IL, USA.
[12] B.B. Back et al., "Astrophysics experiments with radioactive beams at ATLAS", AIP Advances 4, 041005 (2014).
[13] P. Ostroumov et al., "Fast and efficient charge breeding of the Californium rare isotope breeder upgrade electron beam ion source", Rev. of Sci. Instr. 86, 083311 (2015)
[14] The VENUS ECR ion source, @ http://cyclotron.lbl.gov/ionsources/venus
[15] P. Ostroumov et al., "Off-line Commissioning of EBIS and Plans for Its Integration into ATLAS and CARIBUEBIS", Proceedings of the ICIS-2015 Conference, New York, NY, August 23-28, 2015.
[16] J.D. Fuerst, "The ATLAS Energy Upgrade Cryomodule", Proceedings of SRF 2009, Berlin, Germany.

ISBN 978-3-95450-131-1

OPTIMIZATION DESIGN OF THE RFQ TRAPEZOIDAL ELECTRODE

Li Chenxing#, He Yuan, Wang Zhijun, Institute of Modern Physics, CAS, Lanzhou, China

Abstract

In order to reduce the length of a deuteron beam RFQ, trapezoidal modulation is used in the last 3-meter-long section. Because there is no existing tested design procedure fitting for designing this type of unconventional structure, a VBA code used for designing trapezoidal modulation RFQ electrode was developed. VBA is an effective and efficient tool for completing repetitive work. So it can be used to design repetitive analogous cells of electrode of RFQ or DTL or other periodic acceleration structures. By using this VBA code, cell length and the exit energy can be obtained accurately. The feasibility and accuracy of this method have been validated by beam dynamics simulation.

INTRODUCTION

The conventional method to design RF cavities such as RFQ or DTL can be divided into three steps [1]. First, generate the basic parameters of acceleration cells. Second, model and optimize the cavity structure. Third, evaluate the beam performance by beam dynamics simulation using the RF field generated from the RF simulation done in the second step. To achieve a reasonable solution, iterations of these three steps will be necessary. It is predictable that the repetitive work will occupy the most time of the design. The electric field in the RF cavities such as RFQ or DTL is concentrated mainly in small regions near the electrode gaps. This makes it feasible to design the local regions where the electric field concentrated independently by using 3D electrostatic codes such as CST EM Studio [2].

The secondary development based on VBA (Visual Basic for Applications) has been extensively utilized in mechanical design. The design efficiency can be improved and the design period can be shortened due to the repetitive work in the design procedure can be completed by computer code. By means of the VBA in CST, the automated design and optimization of RFQ electrode or DTL tubes using CST EM Studio can be achieved. Based on CST EM Studio, a VBA code that aims to optimization of longitudinal structure of RFQ electrodes and DTL tubes has been developed. By utilizing this code, the design of the trapezoidal modulation electrode of the last 3-m-long section of a deuteron beam RFQ has been done.

DEUTERON BEAM RFQ DESIGN

The main design parameters for the deuteron beam RFQ are listed in table 1. The RFQ will consist of five identical ~ 105 cm long segments. Figure 1 shows the full five-segment engineering model.

#lichenxing@impcas.ac.cn

Table 1: The Main Parameters for the Deuteron Beam RFQ

Parameter/Feature	Value
Input Energy	20 keV/u
Output Energy	1.7 MeV/u
Frequency	162.5 MHz
Vane Voltage	65 kV
Average Aperture Radius	4.8 mm
Length	5.25 m
Bunching	Internal

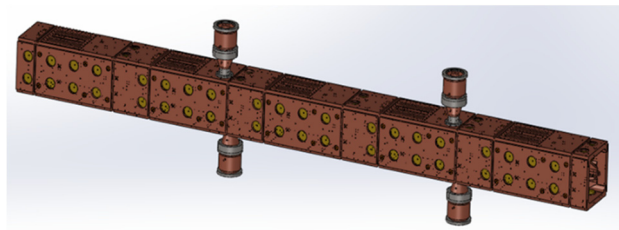

Figure 1: 3D model of the deuteron beam RFQ.

In order to increase the acceleration efficiency of the RFQ, the trapezoidal modulation electrode is introduced in this RFQ. The first 2 m section of the electrode is sinusoidal and the last 3.25 m section of the electrode is trapezoidal. As the design result, the energy at the exit is nearly 1.7 MeV/u. The first 2 m section is designed by the code DESRFQ [3]. Because there's no ready-made code to design the unconventional structure of the trapezoidal modulation electrode, a VBA code based on CST EM Studio has been developed for the design of the trapezoidal modulation electrode.

THE DESIGN OF ELECTRODE WITH TRAPEZOIDAL MODULATION

The idea utilizing trapezoidal modulation electrode to increase the acceleration efficiency was initially actualized by the IHEP-Protvino group [4] and also has been implemented in ATLAS RFQ [5]. Figure 2 shows the longitudinal section of one cell trapezoidal modulation RFQ electrode and the 3D model. It can be seen that each cell of the trapezoidal modulation RFQ electrode is comprised of two flat parts and one sinusoidal transition part between them. The proportion of the flat parts in the cell length is represented by k. The electrostatic simulation can be done when the 3D model is generated. Figure 3 shows the axial component of the electrostatic field for different proportions of the flat parts. As expected, the maximum of the axial component of the electrostatic field increase as the proportion enlarges

ISBN 978-3-95450-131-1

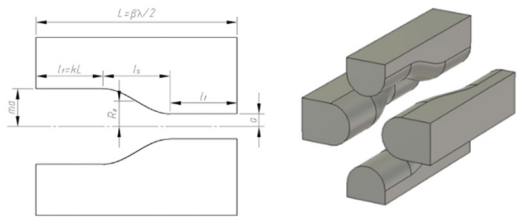

Figure 2: The longitudinal section of one cell trapezoidal modulation RFQ electrode and the 3D model.

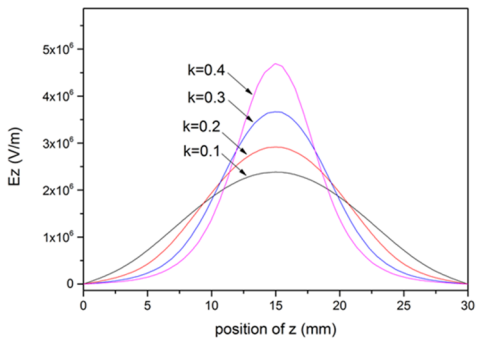

Figure 3: The axial component of the electrostatic field for different proportion of the flat part.

The input parameters are the ion energy at the entrance of the trapezoidal section of the RFQ, the RF frequency, synchronous phase, transit time factor. In order to setting the transit time factor and the proportion of the flat part in the cell length reasonably, parameter sweeps of the proportion k have been done at several certain cell length (L=30 mm, 40 mm, 50 mm, 60 mm). Figure 4 shows the results obtained when L=30 mm. As illustrated in Figure 4, the acceleration efficiency increases when the proportion enlarges. But the proportion is limited by the maximum surface electric field on the electrode in case electric break down. Through the parameter sweeps, the ranges of the trapezoidal proportions and the transit time factors are determined.

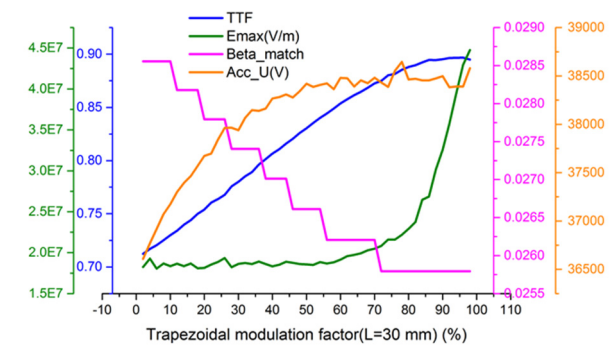

Figure 4: Parameter sweep of trapezoidal modulation factor (L=30 mm).

In the design of multi cell trapezoidal modulation RFQ electrode, the VBA code based on CST EM Studio was utilized to perform the repetitive calculation and adjustment. The algorithm of this code is elaborated in the flow chart in Figure 5. In the flow chart, the phase of a synchronous particle at the entrance of one cell is calculated by finding the zeropoint of the following function [6] using the bisection method.

$$\mathrm{F}(\varphi_{in}) = \tan^{-1}\left[\frac{\int_0^L qE_z(s)\cdot\sin\left[\varphi_{in}+\frac{\omega_{rf}}{c}\int_0^s\frac{ds'}{\beta_z(s')}\right]\cdot ds}{\int_0^L qE_z(s)\cdot\cos\left[\varphi_{in}+\frac{\omega_{rf}}{c}\int_0^s\frac{ds'}{\beta_z(s')}\right]\cdot ds}\right]-\varphi_s$$

And the exit phase of the synchronous particle can be calculated by an integral method. Then the adjusted quantity of the cell length can be calculated. After several iterations, the difference between the phase at the exit of the cell under adjustment and the phase at the entrance of the next cell will be small enough. And the longitudinal structure of the trapezoidal modulation RFQ electrode will be ultimately determined.

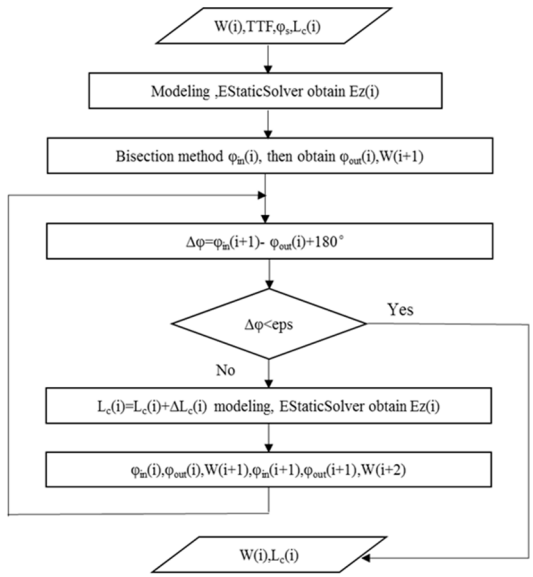

Figure 5: The flow chart of the code to design the longitudinal structure of RFQ electrode.

After running the VBA macro code, multi cell 3D model will be modelled and several results will be generated: particle energy at the exit of each cell, the length of each cell, phase differences between cells. These results are shown in Figure 6. Figure 6 (a) and (b) indicate that after adjustment the phase differences between cells can be greatly reduced and controlled into a small level below 0.015 degrees.

The code can also generate the 3D multi cell model directly and do electrostatic simulation. And then the 3D electrostatic field can be exported and utilized in beam dynamics simulation based on TraceWin [7] or CST Particle Studio [2]. Figure 7 shows the 3D model and the beam dynamics simulation using CST Particle Studio.

ISBN 978-3-95450-131-1

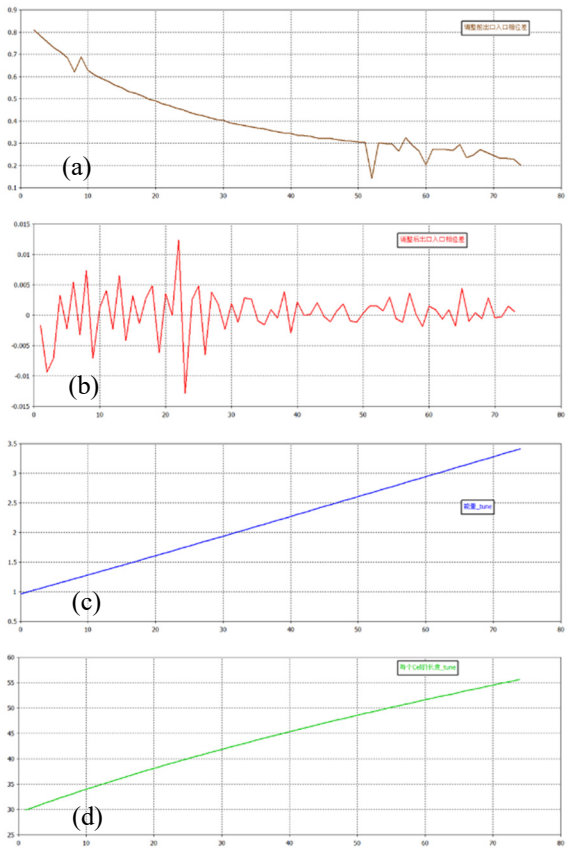

Figure 6: (a) phase differences between cells before adjustment (b) phase differences between cells after adjustment (c) energy at the exit of each cell (d) ultimate cell length of each cell.

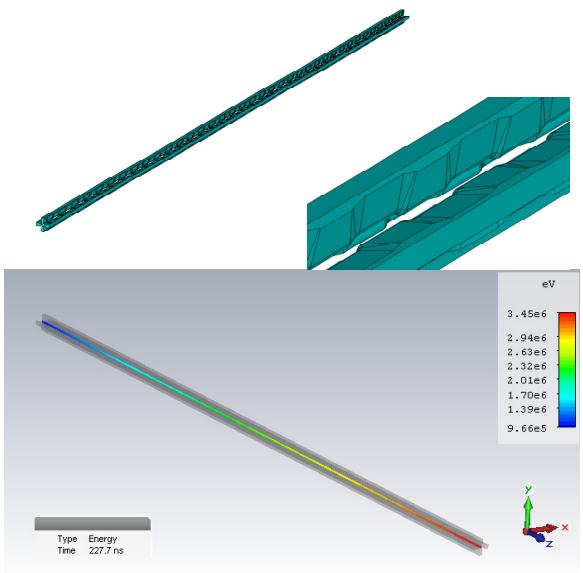

Figure 7: 3D model of trapezoidal modulation RFQ electrode and the result of beam dynamics simulation.

FABRICATION TEST

A fabrication test also was performed to validate the feasibility of fabricating the trapezoidal modulation electrode using ready-made flying cutter. In order to generate the trajectory of cutter center be suitable for fabrication, the sinusoidal transition part is substituted by two arcs and their internal common tangent (Figure 8). The trajectory of the cutter center can be generated by a simple code. After fabrication is completed, the measurement is also performed. As measured by a coordinate measuring machine (CMM), the error of fabrication is lower than 0.0309(31) mm (Figure 9).

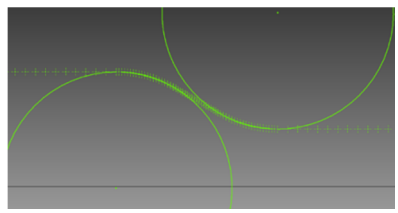

Figure 8: Substitute the sinusoidal transition part by two arcs and their internal common tangent.

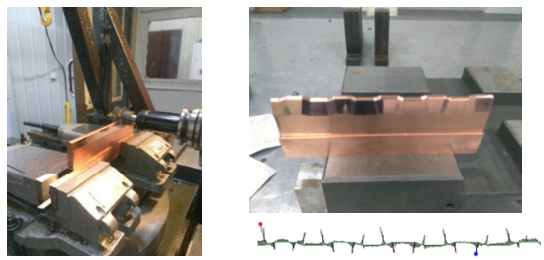

Figure 9: Fabrication and measurement of the trapezoidal modulation RFQ electrode.

CONCLUSION

A code aimed to the design of longitudinal structure of RFQ electrode has been developed based on the VBA of CST. Using this code, the trapezoidal modulation RFQ electrode of a deuteron beam RFQ was designed. The results have been validated by beam dynamics simulation using CST Particle Studio. A fabrication test was performed to validate the feasibility of fabricating the designed trapezoidal modulated RFQ electrode.

REFERENCES

[1] A. Bandyopadhyay, O. Kamigaito, S.K. Nayak, H.K. Pandey, M. Mondal, Alok Chakrabarti, Nucl. Instrum. Method A, 560 (2006), p. 182.
[2] CST EM-Studio, CST Particle Studio, CST, GmbH, Darmstadt, Germany: http://www.cst.de
[3] A.A. Kolomiets, The code DESRFQ, ITEP/ANL, Technical note, 2005.
[4] O. K. Belyaev et al, Proceedings of the 20th Linac Conference, Monterey, California, page 259.
[5] P. N. Ostroumov et al., Phys. Rev. ST Accel. Beams 15, 110101 (2012).
[6] D. Uriot, TraceWin documentation, CEA/SACLAY-DSM/Irfu/SACM.
[7] Trace Win CEA, http://irfu.cea.fr/Sacm/logiciels/index.php

ISBN 978-3-95450-131-1

THE QUALITY ASSURANCE AND ACCEPTANCE SYSTEM OF NIOBIUM MATERIAL FOR RAON CAVITIES

Mijoung Joung#, Yoochul Jung, Hyungjin Kim, IBS, Deajeon, Korea

Abstract

The QAAS (Quality Assurance and Acceptance System) of superconducting material for RAON's cavities has been set up. The subject was selected by how the part is affected by RF (Radio Frequency) in the cavity operation at cryo-temperature. The QAAS consist of property analysis and checking the surface condition. Each step has criteria its own to pass the assurance and acceptance system. The method to analyze the properties and to inspect the niobium surface was described. The certificates were classified by RRR values of Nb pieces due to distribution of RRR value. The Nb properties slightly different by RRR values, so we will set a bunch of niobium pieces for one specific cavity with Nb pieces having similar RRR value.

INTRODUCTION

The high quality material is needed to make a high performance resonator. The niobium is widely used as superconducting material for SRF (Superconducting Radio Frequency) cavity and the niobium surface condition is one of the important factors to determine the cavity performance because the surface resistance is related to the energy of the cavity and the surface resistance depending on material quality and surface condition. There are two aspects about quality control of material. One is to control the material's chemical, mechanical, electrical and optical properties. The other is that to control the niobium surface. Many other institutes carry out the checking the properties and surface inspection using various methods before doing machining [1-5]. The material properties are determined at the production stage by project demands, so it is necessary to verify the properties by sampling. In case of surface checking, it is necessary step for mass production. However, it is practically impossible to inspect all of the niobium because of the time limitation and man power. For this reason, the subject for inspection was selected by considering RF (Radio Frequency) effect. The parts where the highest electric and magnetic field is exerted was selected and it is called as RDP (Radio frequency Dominant Part). It will be explained about the kind of inspection, inspection process, subject selection, the criteria of acceptance and the inspection and measurement method. Also the certificates of Nb provided by the ATI metallurgy were classified.

QAAS OF NIOBIUM FOR RAON

QAAS (Quality Assurance and Acceptance System) will be introduced in this section.

The Type of Niobium and the Subject Selection

There are three types of niobium for RAON's cavity.

- Big sheet (635*1200 mm, 3t)
  (600*800 mm, 3t)
  (450*600 mm, 5t)
- Cut set (specific size corresponding to the part, 3t)
- Rod or Tube (Φ 60, 3t)

Big sheet is used for cavity prototype and extra sheet. Cut set is a bunch of Nb pieces which were cut by a required size of each cavity part with extra margin. The rod or tube of Nb is for beam port. And big sheet has two types of grade, which are RRR (Residual Resistivity Ratio) 300 and RRR 50 (Reactor grade). And it has different thickness which are 3mm and 5mm. The RRR 50 grade sheet is only used for supporting structure such as ribs for upper part or doubler of beam port cup. All of Nb cut set and Nb rod have 3mm thickness.

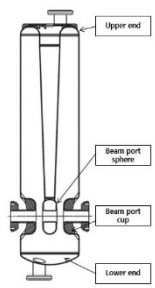

Figure 1: QWR cross section.

Figure 1 shows the RDPs (Radio frequency Dominant Part) which are strongly affected by RF field in the cross section of QWR (Quarter Wave Resonator). In case of QWR, upper, lower and beam tube parts are RF dominant part. The RISP (Rare Isotope Science Project) will make four kinds of the cavities which are QWR, HWR (Half Wave Resonator and two kinds of SSRs (Single Spoke Resonators).

Whole Process

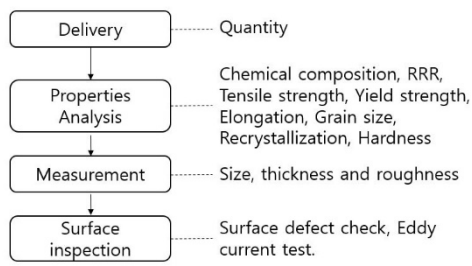

Figure 2: Whole process of QAAS.

#mijoung@ibs.re.kr

ISBN 978-3-95450-131-1

Figure 2 shows the whole process of QAAS. First of all, quantity checking is needed when Nb is delivered to IBS from the vendor. Secondly, the analysis of Nb property is carried out in various aspects to verify the certificates of the niobium. Thirdly, only RDPs undergo size, thickness and surface roughness measurements. Fourthly, only RDPs are inspected the surface to detect the defects, such as pit, scratch, dent and so on. Lastly, only RDPs are tested with the ECT (Eddy current test) to find the defect under the surface which is effected by RF in cavity operation at 2K.

Criteria of Acceptance

Table 1: Criteria of each steps

	Criteria	Unit	Chemical composition	Max. Weight (ppm)
Tensile strength	> 100	Mpa	C	20
Yield strength	50<Rp<80	Mpa	N	20
Elongation	> 40 (Longitudinal)	%	O	40
	> 35 (Transverse)	%	H	5
Hardness	< 50	HV10	Ta	1000
Grain size	64	μm	Fe	50
Recrystallization	> 95	%	Si	50
RRR	> 300		W	70
Size	± 3.175	mm	Mo	50
Thickness	± 0.254	mm	Ti	40
Surface defect	< depth 25	μm	ECT : No defect under the surface	

Table 1 shows the criteria of all steps. The criteria of chemical, mechanical, electrical and optical properties were determined from the specification of niobium for RAON's cavities. Each property is widely used in linear accelerator field [6-8]. The defect on the niobium surface is allowed only when the size is less than 25μm in depth. According to the inspection result, the defects which exist on the niobium surface have the size of around 10μm in depth. And other defects are not allowed under the surface of niobium.

Inspection & Measurement Method

Figure 3 shows the samples for property analysis and the chemical, mechanical, electrical and optical properties were analysed by table 2.

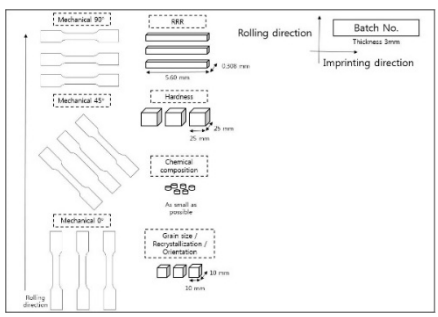

Figure 3: The samples for properties analysis.

The property analysis was carried out with niobium pieces which have 3 different types of RRR values, which are RRR 363, RRR 434 and RRR 500. Each analysis is carried out 3 times to verify the results. Different RRR values of niobium will be discussed in the section of certificates analysis. All of the niobium pieces have the identification number. This number is imprinted in a vertical direction to the rolling direction of sheet. We call this identification number as batch number.

The measurements of size, thickness and surface roughness were carried out with a special ruler, thickness measurement and surface finish measurement. The size checking is not tested fastidiously because pieces have extra margin. When Nb pieces fit in or is bigger than the special ruler corresponding to specific size, that piece is passed. In case of thickness measurement, 5 positions on the surface were measured, four corners and a center of each Nb piece. The surface roughness is tested with same position regardless of the piece size because this result will be used to compare with the surface roughness result after doing machining.

Table 2: The method of each analysis

Properties		Standard	Method	Spec.Min	Spec.Max	
Longitudinal	Tensile Strength	ASTM E8	Tensile test	100 Mpa		
	Yield Strength	ASTM E8		50 Mpa	100 Mpa	Offset 0.2%
	Elongation	ASTM E8		40 %		Gage 1"
Transverse	Tensile Strength	ASTM E8		100 Mpa		
	Yield Strength	ASTM E8		50 Mpa	100 Mpa	Offset 0.2%
	Elongation	ASTM E8		35 %		Gage 1"
RRR			PPMS	300	-	
Chemical composition			ICP(metal impurities) / EA(C,H,O,N)	-	Ta <1000ppm	
Hardness		ASTM E-384	Vicker's hardness	-	60 HV10	Long./ Trans.
Recrystallization			EBSD	95%	-	
Grain size		ASTM E112	EBSD	-	< 64μm	Long./ Trans.
Orientation			EBSD	-		

ICP : Inductively Coupled Plasma
EA : Elemental analyzer
EBSD : Electron Back Scatter Diffraction

The surface defect checking is carried out by visual inspection. If there is suspicious part on the niobium surface, the size of depth will be measured with surface finish measurement and the size of depth is represented by Rz (Average maximum height of the profile) and Ry (Maximum height of the profile). The ECT (Eddy Current Test) is tested with optimal frequency of niobium. The optimal frequency depends on the material, probe design and the target depth. The optimal frequency of niobium for RAON's cavity has been submitted to the journal name of Nondestructive Testing and Evaluation.

CERTIFICATES ANALYSIS

The certificates of niobium were provided by the vender of niobium, ATI, USA and the data on the certificates were obtained at a stage of resource batch. We ordered the niobium which can meet the requirement of specification for RAON's cavities, but it dose not mean all of the niobium pieces have same properties. Because of this reason, the certificates were classified according to different RRR value. There is the distribution of RRR value and figure 4 shows the result.

Figure 4 shows the number of RRR value type in the niobium sets for RAON's QWR, HWR cavities. There are 11 types of RRR values which are between minimum 338 and maximum 500. According to figure 4, we observed two results. One is all of the Nb products satisfied RAON's RRR requirement : average RRR should be large than 300.

ISBN 978-3-95450-131-1

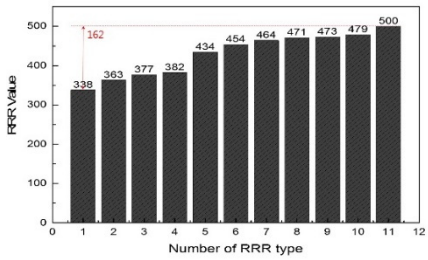

Figure 4: The number of RRR value type.

The other is that RRR distribution is substantial, which means the maximum difference in RRR is about 162. Each piece for one cavity wasn't from the same resource because the pieces were cut in the way that they can make pieces as many as possible in the one big sheet. So we are planning to set the bunch of pieces having similar RRR values. Because the Nb pieces with similar RRR values can give a similar environment to the interface between Nb pieces. And this interface which is called as welding zone usually causes the problem in the cavity operation at cryo-temperature.

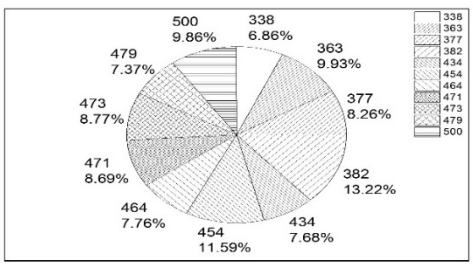

Figure 5: Distribution of RRR value.

Figure 5 and 6 show the distribution of RRR in QWR, HWR niobium cut set. According to figure 5 and 6, the distribution of RRR values over the whole pieces in relatively uniform than RDPs.

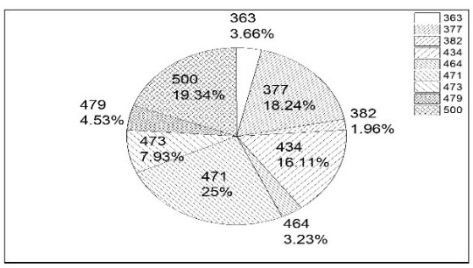

Figure 6: Distribution of RRR value in RDPs.

The RRR values of over 470 account for 56.8% of all of RDPs. We have to focus on the RDPs more than whole pieces because the RDRs will affect to the cavity performance than the rest parts. The RRR value degradation occur by e-beam welding in the range of between 8% and 22% depending on welding condition Especially, this degradation occur around welding zone which is called as HAZ (Heat affected zone) because of the impurity incorporation into the HAZ, such as H_2, N_2 and O_2. RISP set the minimum RRR value as 275, so only less than 8% of degradation is allowable in RISP [9].

CONCLUSION

The QAAS (Quality Assurance and Acceptance System) of superconducting material has been set up for RAON's cavities. The system cover the niobium properties and surface condition. The properties of Nb are analyzed by typical methods, according to ASTM (American Society for Testing and Materials) standard. The niobium surface condition was inspected in the way of visual inspection and eddy current test. The Nb certificates proved by the vendor was classified by RRR values and it will be used to make a bunch of Nb pieces for one cavity. We performed QAAS to guarantee the superconducting material properties and we categorized Nb pieces having similar properties with the certificate.

ACKNOWLEDGMENT

This work was supported by the Rare Isotope Science Project of Institute for Basic Science funded by the Ministry of Science, ICT and Future Planning (MSIP) and the National Research Foundation (NRF) of the Republic of Korea under Contract 2013M7A1A1075764.

REFERENCES

[1] C. Compton et al., "Quality Assurance and Acceptance Testing of Niobium Material for use in the Construction of the Facility for Rare Isotope Beam (FRIB) at Michigan State University (MSU)", MOP033, SRF2013, Paris, France (2013).

[2] A.Brinkmann et al., "Statistic to Eddy-Current Scanning of Niobium Sheets for the European XFEL" MOP032, SRF2013, Paris, France (2013).

[3] Q.-S. Shu et al., "Squid Based Non-destructive Testing Instrument of Dished Nb Sheets for SRF Cavities", WEPMS055, PAC07, Albuquerque, USA (2007).

[4] Cristian Boffo et al., "Eddy Current Scanning of Niobium for SRF Cavities at Fermialb", IEEE Transactions on Applied Superconductivity, VOL. 17, NO. 2, 1326-1329 (2007).

[5] Y. Iwashita et al., "Updates on R&D of Nondestructive Inspection Systems for SRF Cavities", TUPO032, SRF2011, Chicago, USA (2011).

[6] XFEL/007,"Technical Specifications, Niobium Material", 2010.

[7] Fermilab, "Technical Specification for High RRR grade Niobium Sheet for Use in Superconducting Radio Frequency Cavities", 5500.000-EC-371037 Rev B.

[8] R.M. Silzer et al., "CLS Superconducting Cavity Niobium Specification", CLS2.40.32.001 Rev.1, 2000.

[9] [RRR] Y.C. Jung et al., "RRR Characteristics for SRF Cavities", ICABU, Deajeon, Korea, 2014.

ISBN 978-3-95450-131-1

STUDY OF ELECTRODE CONFIGURATION OF THE FOUR BEAM IH-RFQ LINAC

Shota Ikeda, Tatsunori Shibuya,
Graduate School of Science and Engineering, Tokyo Institute of Technology, Tokyo, Japan
Noriyosu Hayashizaki,
Research Laboratory for Nuclear Reactors, Tokyo Institute of Technology, Tokyo, Japan

Abstract

The multi-beam acceleration method, which is technique for accelerating low energy, high intensity, heavy ion beams by accelerating multiple beams to decreasing the space charge effect, and integrating these beams by a beam funneling system [1]. Working towards the commercialization of this method, at the Tokyo Institute of Technology we have been developing a 4 beam IH-RFQ linac. As part of the design work for the 4 beam IH-RFQ linac, we evaluated the cell parameters of the RFQ electrodes using a RFQ design code and a beam dynamics simulation code. Also, we evaluated the RF properties of several electrode layouts using a three dimensional electromagnetic simulation code. This paper reports on the results.

INTRODUCTION

The multi-beam acceleration method utilizes multiple beams to decreasing the space charge effect, then integrates these beams by a beam funneling system. The space charge effect has a property that is inversely proportional to the square of beam velocity and proportional to the beam current. Therefore, low-energy (from keV/u to several MeV/u) high-intensity (over 10 mA) heavy ion beam acceleration is the most severe condition.

We have been developing a 4 beam IH-RFQ linac shown in Figure 1, which consists of sixteen RFQ electrodes (4x4 set) and the stem electrodes installed alternately on upper and lower ridge electrodes. The RF electromagnetic field is stimulated by the TE111 mode. The electric field and magnetic flux distribution in a 4 beam IH-RFQ linac is shown in Figure 2. The RFQ electric field is generated by induced current through the ridge electrodes and the stem electrodes.

The electrical capacitance of the 4 beam IH-RFQ linac is large compared with that of a single beam type, because there of the large volume of the stem electrodes and the 4 set RFQ electrodes in the cavity. Therefore the resonance frequency of the 4 beam IH-RFQ linac is lower than that of a single beam type.

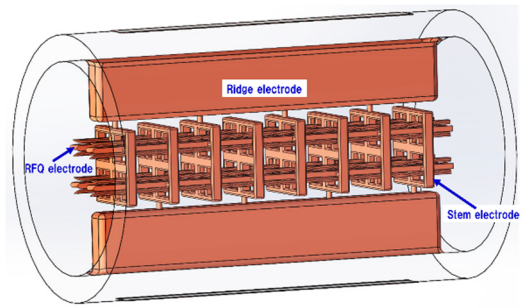

Figure 1: Configuration of the 4 beam IH-RFQ linac.

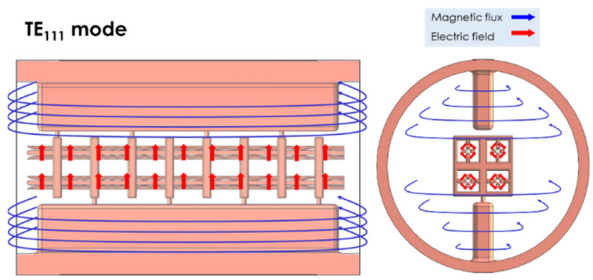

Figure 2: Electric field and magnetic flux distribution.

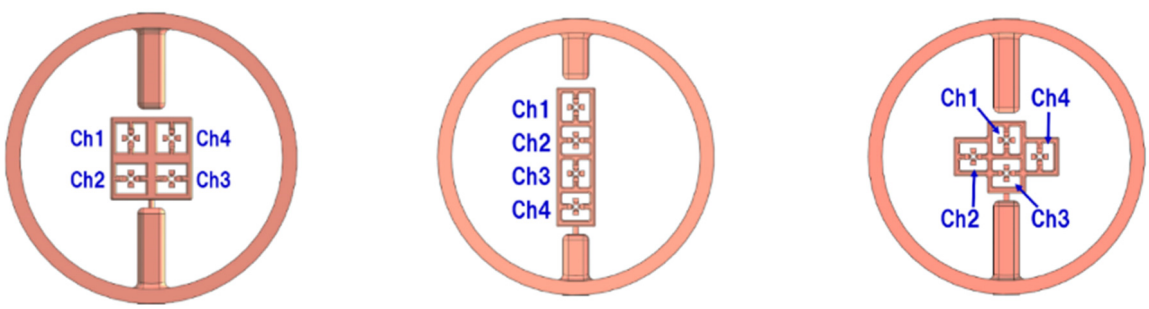

Layout 1 Layout 2 Layout 3

Figure 3: Electrode layouts of the 4 beam IH-RFQ linac.

ISBN 978-3-95450-131-1

RF SIMULATION

We simulated the RF properties of the 4 beam IH-RFQ linac using the eigenmode solver of the three dimensional electromagnetic simulation software CST MICROWAVE STUDIO [2]. The simulated electrode layouts are shown in Figure 3. In addition, the cavity parameters of the 4 beam IH-RFQ linac are shown in Table 1. The result of the simulation is shown in Figure 4.

The resonance frequency and the unloaded quality factor (Q_0) calculated in each electrode layout are shown in Table 2. The resonance frequencies of layout 1 and 3 are approximated and are around 2 MHz higher than that of layout 2.

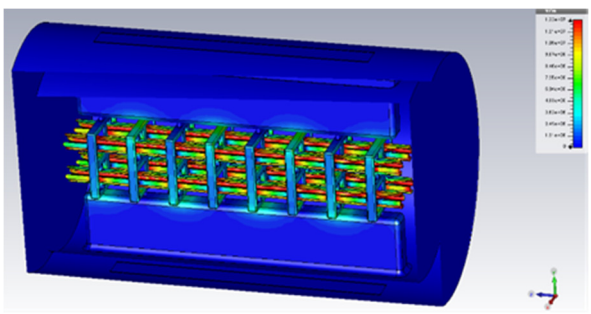

Figure 4: The state of the electric field simulation.

Table 1: Cavity Parameters of the 4 Beam IH-RFQ Linac

Cavity diameter [mm]	410
Cavity length [mm]	800
Ridge electrode width [mm]	47
Stem electrode number	8
Stem-ridge electrodes distance [mm]	15
RFQ electrodes length [mm]	770

BEAM DYNAMICS SIMULATION

The cell parameters of the RFQ electrodes have been evaluated using the RFQ design code RFQUICK [3]. Currently, we confirmed the cell parameters which can accelerate C^{2+} ion up to 39.6 mA in a length of 770 mm. The cell parameters are shown in Figure 5 and Figure 6. The results simulated using the RFQ beam dynamics code PARMTEQM [4] are shown Figure 7 and Table 3.

Table 2: The Simulated Resonance Frequency and Q_0

Layout	Resonance frequency [MHz]	Q_0
1	47.7	4549
2	45.6	4430
3	48.1	4439

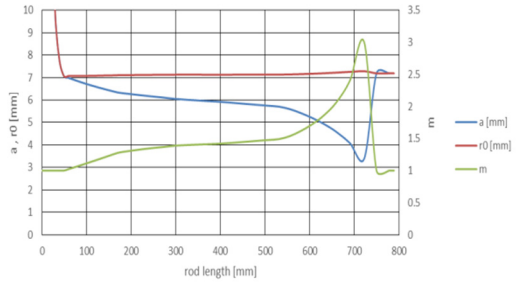

Figure 5: Cell parameters (1).

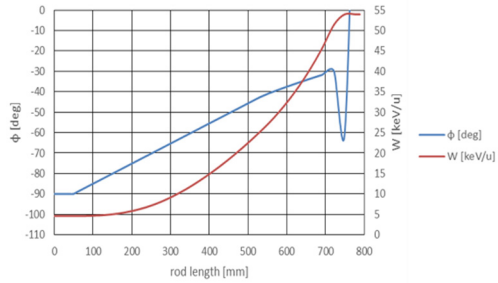

Figure 6: Cell parameters (2).

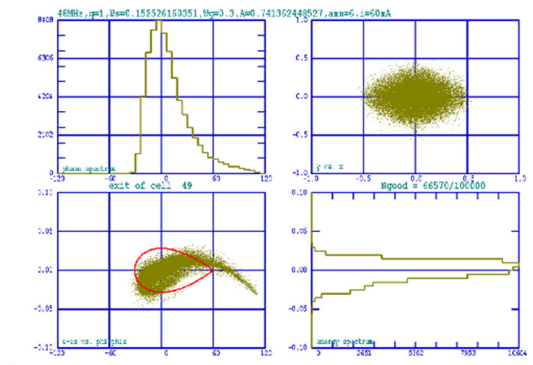

Figure 7: Beam simulation results.

Table 3: Designed Beam Parameters

Operation frequency [MHz]	48
Charge to mass ratio (q/a)	1/6
Input beam current [mA]	60
Output beam current [mA]	39.6
Transmission [%]	66.4
Input beam energy [keV/u]	4.58
Output beam energy [keV/u]	53.9
Input beam emittance [π mm mrad RMS]	0.1
Output beam emittance ε_x [π mm mrad RMS]	0.31
Output beam emittance ε_y [π mm mrad RMS]	0.37
Max. field at inter-electrode gap [Kilpatrick]	1.8

ISBN 978-3-95450-131-1

SUMMARY

As part of a feasibility study of a 4 beam IH-RFQ linac, the resonance frequency and the unloaded quality factor of the acceleration cavity were simulated for three electrode layouts. The RFQ cell parameters were evaluated using RFQUICK and PARMTEQM. In the near future, we will complete the prototype design for the 4 beam RFQ linac with a 4 beam laser ion source using a direct plasma injection scheme.

REFERENCES

[1] Ratzinger, U., et al., "The GSI 36MHz high-current IH-type RFQ and HIIF–relevant extensions." Nuclear Instruments and Methods in Physics Research Section A: Accelerators, Spectrometers, Detectors and Associated Equipment 415.1 (1998): 281-286.
[2] http://www.cst.com/
[3] K. R. Crandall RFQ Design Codes, LA-UR-96-1836(2005).
[4] K. R. Crandall and T.P Wangler, Workshop on Linear Accelerator and Beam Optics Codes, La Jolla, CA, USA, 1988, AIP Conference Proceedings No177 (1988).

ISBN 978-3-95450-131-1

LINAC OPTIONS FOR THE ION INJECTOR OF MEIC*

J. Guo#, Y. Zhang
Thomas Jefferson national Accelerator Facility, Newport News, VA 23606 USA

Abstract

In the current baseline design of the Medium-energy Electron-Ion Collider (MEIC) proposed by Jefferson Lab, a green field ion injector complex is composed of several ion sources, one linac with charge stripper, and one booster ring. The original linac design contains a short warm front end and a long SRF section with QWR/HWR cavities, capable of accelerating H^- to 285 MeV or Pb^{67+} to 100 MeV/u. Such a linac is a major cost driver of the project, despite that the required duty factor of this linac is very low. In this paper, we will compare alternative options for this ion linac, including the possibilities to lower the linac energy and choose a warm linac.

ION BEAM FORMATION AND THE CHOICE OF LINAC ENERGY

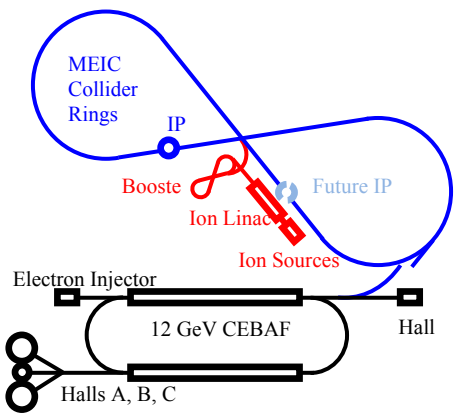

Figure 1: Layout of MEIC.

The MEIC proposed by JLab is a high luminosity electron-ion collider with 3-10 GeV electrons and 20-100 GeV protons (or ions with the same range of magnetic rigidity, i.e. lead ion with 12-40 GeV per nucleon) [1, 2]. The ion collider ring's beam current design goal is 0.5A, with the possibility for further upgrade. Figure 1 shows the layout of the collider with electron and ion injectors. The baseline ion injector complex contains the following components: 1) ion sources providing polarized H^- and other light ions, as well as un-polarized heavy ions up to lead; 2) a pulsed SRF linac; 3) a booster ring with 1/9 of the circumference of the collider ring (239.4m), kinetic energy E_k up to 7.9 GeV for proton (momentum 8.79 GeV/c/q for different ions) with DC cooling. The process to accumulate and accelerate ion beam toward collision is illustrated in Fig. 2 and outlined below [3]:

1. Eject the used beam from the collider ring, cycle the magnets
2. Accumulate strip-injected beam from the linac into the booster, perform DC electron cooling if needed
3. Capture the beam into a bucket of 0.7 circumference
4. (proton only) Ramp the booster to 2 GeV and perform DC electron cooling
5. Ramp to 7.9 GeV for proton, or to the same momentum per elementary charge for the other ion species
6. Compress the bunch length to 0.7/N of the booster circumference (N determined by booster charge)
7. Transfer the beam into the collider ring bucket to bucket, cycle the booster magnets
8. Repeat steps 2-7 by 9×N times, perform bunched beam (BB) electron cooling while stacking
9. Ramp the collider ring to the collision energy 12-100 GeV; perform bunch splitting; ready for collision.

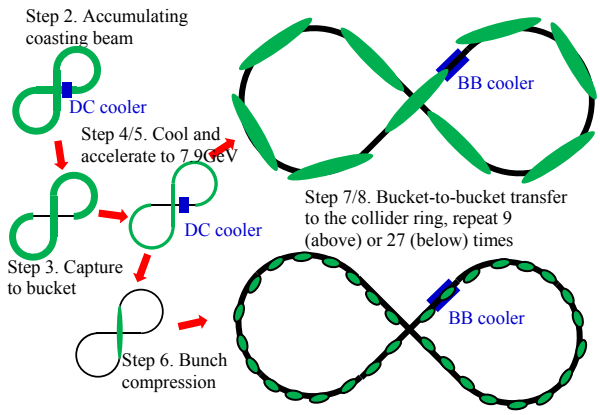

Figure 2: Illustration of the ion beam formation process, step 2-8 as listed above.

The major bottleneck for the ion injection is the space charge (SC) tune shift in the booster ring and the collider ring, especially during step 3 and 8. With given aperture (or emittance) and space charge tune shift in the collider ring at step 8, the booster's extracted beam energy determines the maximum beam current of the collider ring; the linac's extracted beam energy determines how much charge the booster ring can accumulate in each booster cycle.

Table 1 lists the space charge tune shift and the beam aperture for different linac and booster extraction energies and beam charges, with the maximum tune shift set at 0.15. With the original 285 MeV proton linac energy, it takes 9 booster cycles to form 0.5 A proton beam current in the collider ring; for 100 MeV/u lead ions from the linac, 9 booster cycles are not enough for 0.5 A colliding beam current, we need to double the number of booster cycles to 18. If we drop the linac energy to 120 MeV for proton and 40 MeV for lead, we need to increase the

* Authored by Jefferson Science Associates, LLC under U.S. DOE Contract No. DE-AC05-06OR23177
#jguo@jlab.org

ISBN 978-3-95450-131-1

number of booster cycles to 27 (proton) and 36 (lead). Currently we assume that each booster cycle takes 1 minute, dominated by magnet ramping and electron cooling. With the low energy linac option, the estimated time for the full beam formation cycle is acceptable.

We also considered lowering the booster ring extraction energy to 6.5 GeV to distribute the magnet ramping range in the collider ring and booster ring more evenly. The SC tune shift in the collider ring at the end of stacking (step 8) is acceptable. However, this leaves little room for future beam current upgrade, so we should keep the 7.9 GeV booster energy as long as the ramping range is reasonably achievable. The magnet rigidity ratio between 120 MeV and 7.9GeV proton is 18.

Table 1: Selected Parameters of Ion Beam Formation in the MEIC Ion Injector

Particle	**Proton**			**Pb**		
Collider ring current (A)	0.5	0.5	0.5	0.5	0.5	0.5
Linac extraction energy (MeV/u)	285	120	95	100	40	53
Booster cycles	1×9	3×9	4×9	2×9	4×9	3×9
Booster charge (μC)	0.4	0.13	0.1	0.2	0.1	0.13
Normalized emittance, step 3 (μm)	2.66	1.64	1.43	1.49	0.93	1.06
SC tune shift, step 3	0.150	0.150	0.150	0.110	0.150	0.150
6σ aperture, step 3 (mm)	40.0	39.8	39.5	39.7	39.8	39.8
Booster extraction energy (GeV/u)	7.90	6.50	6.50	2.65	2.12	2.12
Booster extraction momentum (GeV/c/q)	8.79	7.38	7.38	8.79	7.38	7.38
Normalized emittance, step 8 (μm)	0.5	0.5	0.5	1.0	1.0	1.0
SC tune shift, step 8	0.089	0.125	0.125	0.109	0.153	0.153
6σ aperture, step 8 (mm)	5.2	5.7	5.7	11.7	12.8	12.8

SRF LINAC DESIGN

The original pulsed SRF linac was designed by our collaborators at Argonne National Lab [1]. The linac starts with a warm front end including ion sources, an RFQ and an IH DTL up to 4.8 MeV/u, then an SRF section with 42 QWR cavities and 80 HWR cavities, as shown in Fig. 3. The ion source will generate Pb^{30+} beam, and a charge stripper is put in the middle of the SRF section to reduce the accelerating voltage. For 100MeV/u lead, the stripping energy is chosen at 13.2 MeV/u to minimize the total effective linac voltage to ~385 MV. The extracted Pb beam will have a charge state of 67+. The proton energy is only 285 Me V/u because the RFQ and DTL need to operate at lower voltage to keep the same velocity profile, and the SRF cavities have lower transit time factor for proton. The linac will provide 2 mA 0.5 ms pulsed light ion beams, or 0.5 mA 0.25 ms pulsed heavy ion beams. The pulse repetition rate is up to 10 Hz. The beam current is mainly limited by the ion sources and the loss during charge stripping.

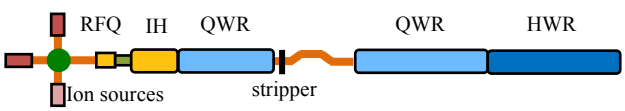

Figure 3: Layout of the SRF linac.

Recently, our Argonne collaborators updated the design to a short linac [4], capable to deliver 130 MeV proton and 42 MeV Pb^{61+} beam with only 45 cavities and enhanced accelerating gradient. The energies are slightly higher than the energies listed in table 1, providing a little more margin. The Pb charge stripping energy is 8.2 MeV/u, with ~175 MV total effective linac voltage.

WARM LINAC CONCEPTUAL DESIGN

The duty factor required for the MEIC linac is extremely low. For each booster cycle shown in table 1, the injected charge is less than 1 μC. With the significant beam loss during strip-injection, the booster accumulation can be done in one or several linac pulses for light ions and 10s of pulses for heavy ions, taking just a few seconds. For each full ion beam formation cycle (which occur once in several hours), the beam in the linac will be turned on for only 10s or 100s of milliseconds. Even during the several seconds of booster accumulation, the duty factor is only up to 0.5%. Considering that the static heat load in the cryomodules will consume cryogenic power 24 by 7 even when the SRF linac is idling, it's natural to consider warm linac as an alternative. Adding to the warm linac's advantage is the lower particle energy and velocity required. When β<=0.3, warm DTL structures, especially the IH (Interdigital H-mode) and CH (Cross-bar H-mode) types [5], have very high R/Q for low beta ions and can generate competitive shunt impedance per unit structure length. The SRF linac design also includes a warm IH DTL up to 4.8 MeV/u.

Multi-gap structures like DTL have very narrow velocity range for peak transit time factor (TTF), due to the invariable phase between gaps. So DTL must operate at fixed β profile. The structure will be optimized for the heaviest ions (lowest q/a), and need to lower the

ISBN 978-3-95450-131-1

accelerating voltage for lighter ions, so that all the particles will have the same exit E_k/u. Single/double gap structures in the SRF linac can operate at close to full voltage for different ion species and give about the same E_k/q.

We conceptually designed a DTL linac with 95 MeV proton (increases the booster cycles to 36) and 53 MeV/u Pb^{61+} (decreases the booster cycles to 27), as shown in Fig. 4. The choice of energy makes the performance comparable to the SRF linac with 120 MeV proton and 40 MeV/u Pb.

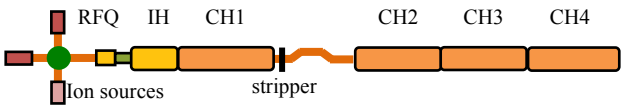

Figure 4: Layout of the DTL linac.

Table 2: CH DTL Conceptual Design Parameters

DTL Section	CH1	CH2	CH3	CH4
Lowest q/a particle	Pb^{32+}	Pb^{61+}	D^-	H^-
Exit energy (MeV/u)	8.1	53.0	67.7	95.2
Exit β	0.130	0.322	0.361	0.417
Number of structures	1	9	2	2
Average V_{eff} per structure (MV)	21.3	17.0	14.7	13.2
Average Z_{eff}/L (MΩ/m)	91	58	43	38

The warm linac has an identical warm front end up to the IH as in the SRF linac. The rest are 4 sections of totally 14 CH DTLs. Every two CH structures share the split power from a 325 MHz (or 352 MHz) 2.5 MW (or 2.8 MW) pulsed klystrons, which are the most cost effective commercially available pulsed RF sources in this frequency range. Each structure is ~5m long and takes ~1MW cavity power when accelerating the lowest q/a particles. The pulsed beam power in each structure ranges from several to 30 kW, depending on the structure and ion species. The power from each klystron will be split into two structures. CH1 is one structure optimized for Pb^{32+}, delivering 8.1 MeV/u for charge stripping. This is slightly closer to the optimal stripping energy than putting two structures in CH1 before the stripper. CH2 has nine structures optimized for Pb^{61+}, with exit energy at 53 MeV/u. CH3 has two structures optimized for D^- and will be turned off during Pb operation, with exit energy 68 MeV/u. CH4 has the last two structures that accelerate H^- to 95 MeV. The effective voltage of each CH structure is estimated from the effective shunt impedance per unit length parameter of the FAIR proton linac structures (up to 70 MeV) with the closest β [6]. The total effective linac voltage is 261 MV. Table 2 lists some parameters of the CH DTL linac. The total length of the CH structures is about 70 m, which is longer than the SRF linac.

Given the extremely low duty factor, the RF power consumption in the structures can be negligible in both cases of the warm and SRF linac. The SRF linac's power consumption is dominated by the static cryogenic heat load. With 5 cryomodule and 45 cavities operating at 4K, the wall plug power in the cryo-plant would be close to 30 kW, which might be higher than the equipment idle power for the warm linac, but still insignificant.

The cost comparison between the SRF and warm DTL options is very primitive at this stage. So far the difference between the two options is smaller than the error bar of our estimation; the SRF option may cost less with some cost savings achieved in the updated design, such as higher gradient in the cavities. The main reason for higher cost in the warm linac is the extra accelerating voltage needed in CH3/4, as CH1/2 have to lower the voltage when accelerating light ions. If an upgrade to higher linac energy is needed in the future, the SRF advantage will be more obvious, as the DTL efficiency deteriorates at higher β.

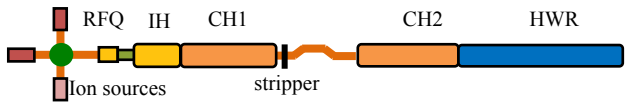

Figure 5: Alternative SRF linac design with extended warm section.

Another option is to extend the warm DTL section of the SRF linac to a higher energy of ~25 MeV/u with four CH structures and two 2.5 MW klystrons, and then use 3 SRF HWR cryomodules (7-9 cavities each) to accelerate Pb^{61+} to 55 MeV and H^- to 130 MeV, as shown in Fig. 5. This design will fully utilize the high efficiency of pulsed CH structures at low β, but avoid building sections of warm structures that can only accelerate light ions, so the total linac voltage is about 205 MV. The QWRs in the SRF design replaced by the CH structures also have degraded TTF in part of the β range for the light ions. For this option, the extraction energy for most ion species will meet the requirement of 27 booster cycles injection into the MEIC collider ring, and the cost-effectiveness might be improved further.

SUMMARY

We updated the MEIC ion formation scheme with the low energy linac option. With 40 MeV/u Pb and 120 MeV proton, the ion injection of 0.5 A beam current can be done within 27-36 booster cycles. We compared the SRF and DTL options for such a linac. With the beam current and duty factor required for MEIC, the two options are close in operation and construction cost, as well as the performance. However, SRF will have obvious advantage if we plan to increase the energy or find a side program in the future. A third option is to extend the warm section in the SRF linac to 25 MeV/u, which may optimize the design further.

REFERENCES

[1] S. Abeyratne et al., Science Requirements and Conceptual Design for a Polarized Medium Energy

ISBN 978-3-95450-131-1

Electron-Ion Collider at Jefferson Lab, edited by Y. Zhang and J. Bisognano, (2012).
[2] S. Abeyratne et al., MEIC Design Summary for NSAC EIC Cost Estimate Sub-Committee, edited by G. A. Krafft, (2015).
[3] Y. Zhang, "MEIC Proton Beam Formation with a Low Energy Linac", TUPWI035, Proc. of IPAC'2015.
[4] P. N. Ostroumov et al., "Pulsed SC Ion Linac as an Injector to Booster of Electron Ion Collider", MOPB068, Proc. of SRF'2015.
[5] U. Ratzinger, "H-type Linac Structures," CERN-2005-003, p351.
[6] W. Barth et al., Technical Design Report, FAIR Proton Linac, 2008.

ISBN 978-3-95450-131-1

CHARGE STATE SELECTIVE ION BEAM ACCELERATION WITH RFQ LINAC

J. Tamura*, Japan Atomic Energy Agency, Ibaraki, Japan
Y. Fuwa, Kyoto University, Kyoto, Japan
T. Kanesue and M. Okamura, Brookhaven National Laboratory, New York, USA

Abstract

DPIS (Direct Plasma Injection Scheme) is one of the effective methods for high-intensity heavy ion beam acceleration. In the DPIS, multiple charge state ions are simultaneously injected into an RFQ. And then, ions whose charge states are comparable with that of ions desired for an RFQ acceleration are captured by the RF bucket. To prevent the unneeded ions from being accelerated, we investigated the motion of multiple charge state ions in an RFQ. We found that the discontinuous transition of a synchronous phase inhibits the unneeded ion's acceleration without a significant loss of desired ions. The particle tracking simulation for C^{5+} acceleration shows that 89% of C^{5+} and 9% of C^{6+} are accelerated with the discontinuous transition of the synchronous phase, whereas 96% of C^{5+} and 73% of C^{6+} are accelerated with the smooth transition. To validate the designed cell parameters, we manufactured new 4-rod RFQ electrodes and planed to perform beam acceleration test using the new RFQ electrodes.

BACKGROUND

We have been investigating high-intensity carbon beam acceleration using DPIS (Direct Plasma Injection Scheme). In this scheme, high-intensity carbon plasma generated by irradiating a graphite target with a pulsed laser is directly injected into an RFQ [1, 2]. And then, ions are extracted at the entrance of the RFQ. Because the DPIS doesn't have an LEBT (Low Energy Beam Transport), multiple charge state ions are simultaneously injected into the RFQ. The simultaneous injection of multiple charge state ions is unavoidable. And also, the beam is not matched for the RFQ injection [3].

Ions whose charge states are comparable with that of ions desired for the RFQ acceleration are captured by RF bucket and accelerated with the desired ions [4]. Therefore, we have investigated an RFQ which doesn't accelerate unneeded ions (different charge state ions) [5]. And then, we manufactured new RFQ electrodes based on the result of particle tracking simulation. In this paper, the designed RFQ cell parameters and the tracking simulation result are shown.

MANUFACTURED RFQ ELECTRODES

The new RFQ was designed to accelerate C^{5+} and not to accelerate different charge state carbon ions such as C^{6+} and C^{4+}. The differences of A/Q gives the smallest value for carbon ion under this condition. Ions which charge state is higher than that of ions desired for an RFQ acceleration are captured by the longitudinal RF bucket more than lower charge state ions. Therefore, the requirement for the new RFQ is to prevent C^{6+} from being accelerated and not to decrease the rate of the accelerated C^{5+}.

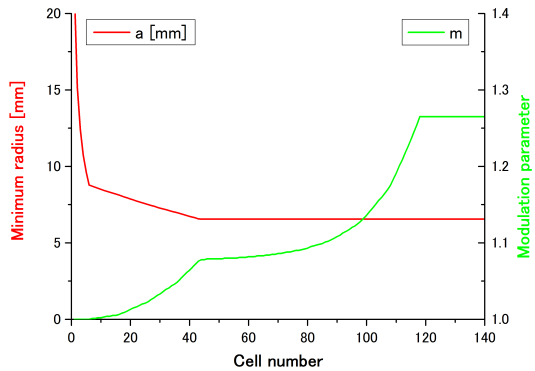

Figure 1: The minimum aperture and modulation factor.

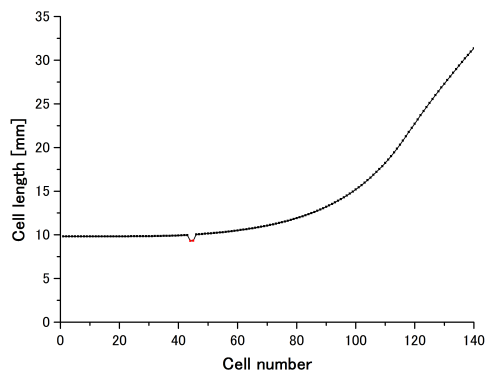

Figure 2: The cell length.

The designed RFQ have a discontinuous transition of the synchronous phase in the bunching section. The cell parameters for the RFQ are shown in Fig. 1 and Fig. 2. The cell length is shorten at the 43th and 44th cell as shown in Fig. 2, whereas the cell length is smoothly increased in an usual RFQ acceleration. This shortening of the cell length shifts the synchronous phase smaller (to negative direction) and leads to the discontinuous transition of the synchronous phase. In the smooth transition of the synchronous phase, the synchronous phase is gradually increased from -90 degree to positive direction.

The new 4-rod RFQ electrodes were manufactured in Hiroshima and delivered to J-PARC in Tokai site of Japan

* jtamura@post.j-parc.jp

ISBN 978-3-95450-131-1

Figure 3: The manufactured RFQ electrodes.

Atomic Energy Agency. Parts of the manufactured electrodes are shown in Fig. 3. We are planning to ship these electrodes to Brookhaven National Laboratory and perform beam acceleration test by applying these electrodes to the DPIS.

LONGITUDINAL MOTION

Using the cell parameters shown in Fig. 1 and Fig. 2, particle tracking simulation was conducted. In this simulation, motions of C^{4+}, C^{5+}, C^{6+} were tracked without a space charge effect. The resonant frequency of the RFQ is 100 MHz and the inter-vane voltage was set to 96 kV for C^{5+} acceleration. This RFQ accelerates ions from 20 keV/u to 200 keV/u with 2 m long of electrodes. The injection energy of each charge state is shown in Table. 1. These values were derived from 48 kV of extraction voltage for C^{5+} acceleration. The initial longitudinal distribution is shown in Fig. 4. C^{4+}, C^{5+} and C^{6+} are shown by green, red and blue dots, respectively. ΔW in each charge state was set to zero because the energy spread of the laser-produced plasma is incomparably small compared with the extraction voltage. The transverse emittance was set to 1 π mm-mrad of normalized emittance for both horizontal and vertical direction. And also, the ellipse parameters (shown in Fig. 5) were set to match the RFQ injection to eliminate the transverse loss. In this simulation, we focused only on longitudinal motion to discuss how the acceleration of the unneeded ion is avoided.

The result of the particle tracking simulation shows that 89% of C^{5+} and 9% of C^{6+} are accelerated with the discontinuous transition of a synchronous phase, whereas 96% of

Table 1: Injection Energy of Each Charge State

Ion	Energy [keV]	Energy [keV/u]
C^{4+}	192	16
C^{5+}	240	20
C^{6+}	288	24

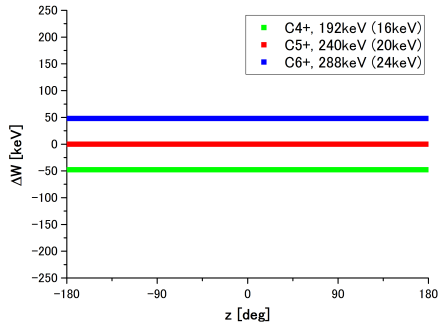

Figure 4: Initial distribution for z-z' plane.

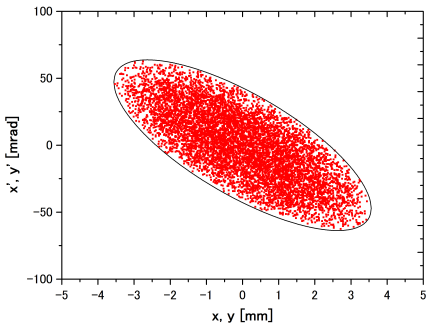

Figure 5: Initial distribution for x-x' and y-y' plane.

C^{5+} and 73% of C^{6+} are accelerated with the smooth transition. Figure. 6 shows the rates of unaccelerated ions in each charge state. Particles that have more than 250 keV of ΔW are identified as longitudinally lost particles. C^{4+} cannot be accelerated due to the lack of injection energy with both smooth and discontinuous transition of a synchronous phase. No particles are lost in the transverse direction (All the particles goes through the RFQ even under unaccelerated condition).

The deceleration induced by the shortened cell at 43th and 44th cell contributes to the feature of non-accelerating

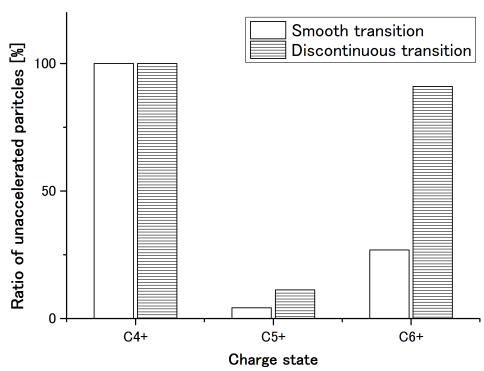

Figure 6: Rates of unaccelerated ions in each charge state.

ISBN 978-3-95450-131-1

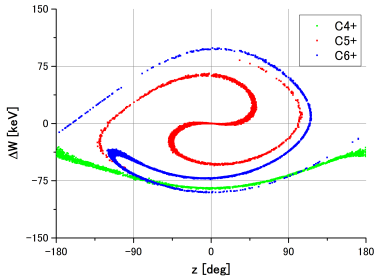

Figure 7: 50th cell (smooth).

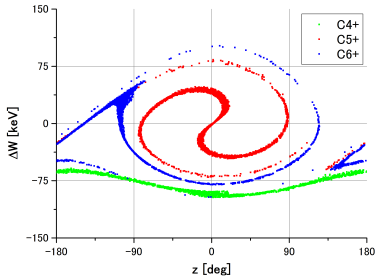

Figure 8: 58th cell (smooth).

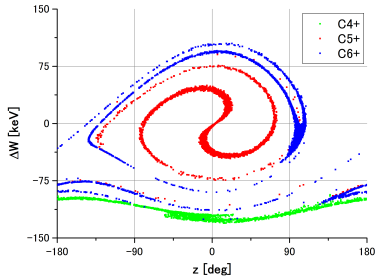

Figure 9: 70th cell (smooth).

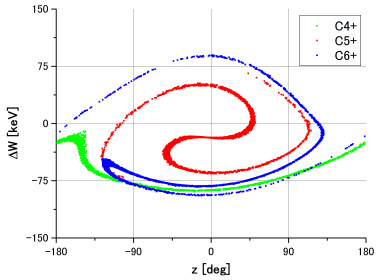

Figure 10: 50th cell (discontinuous).

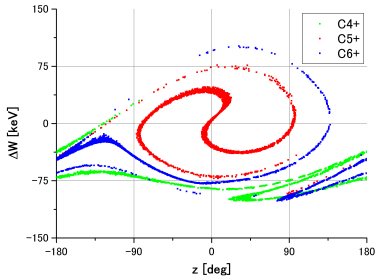

Figure 11: 58th cell (discontinuous).

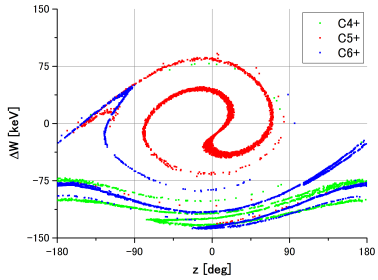

Figure 12: 70th cell (discontinuous).

C^{6+}. The longitudinal motion with smooth transition of the synchronous phase are shown in Fig. 7, Fig. 8 and Fig. 9. In case of the discontinuous transition, ions move as in Fig. 10, Fig. 11 and Fig. 12. In the 43th and 44th cell, most of the C^{6+} ions are located in the bottom part of the separatrix (longitudinal acceptance for successive acceleration). By choosing the synchronous phase lower than -90 degree, most of the ions are decelerated and shifted further to bottom side in the longitudinal phase space. When the synchronous phase returns to the original value, most of the shifted C^{6+} are located outside of (below) the separatrix.

SUMMARY

To prevent unneeded ions from being accelerated, we performed particle tracking simulation for multiple charge state ions in the RFQ. According to the simulation result, the discontinuous transition of a synchronous phase inhibits the acceleration of the unneeded ions without significant loss of the desired ions. To validate the designed modulation parameters, we manufactured new RFQ electrodes based on the simulation result. We are planning to perform a beam acceleration test by applying the new electrodes to the DPIS.

ACKNOWLEDGMENT

We would like to thank the staff of TIME.,Ltd for manufacturing the RFQ electrodes.

REFERENCES

[1] M. Okamura, H. Kashiwagi, K. Sakakibara, J. Takano, T. Hattori, N. Hayashizaki, R. A. Jameson and K. Yamamoto, Rev. Sci. Instrum. 77, 03B303 (2006).

[2] M. Okamura, T. Takeushi, R. A. Jameson, S. Kondrashev, H. Kashiwagi, K. Sakakibara, T. Kanesue, J. Tamura and T. Hattori, Rev. Sci. Instrum. 79, 02B314 (2008).

[3] J. Tamura, T. Hattori, N. Hayashizaki, T. Ishibashi, T. Kanesue, H. Kashiwagi, K. Kondo and M. Okamura, Rev. Sci. Instrum. 81, 02B726 (2010).

[4] J. Tamura, T. Hattori, N. Hayashizaki, T. Ishibashi, T. Ito, T. Kanesue, H. Kashiwagi and M. Okamura, Proceedings of HIAT09, Venice, Italy, TH-08, 179.

[5] Y. Fuwa, S. Ikeda, M. Kumaki, T. Kanesue, M. Okamura and Y. Iwashita, Proceedings of LINAC2014, Geneva, Switzerland, MOPP112, 317.

ISBN 978-3-95450-131-1

THERMO-MECHANICAL CALCULATIONS FOR THE SPES RFQ

L. Ferrari, A. Palmieri, A. Pisent, INFN-LNL, Legnaro (PD), Italy

Abstract

Within the SPES project at INFN-LNL[1] a new injection line will be built at INFN LNL [2]in order to transport and match the RIBs to the existing ALPI superconducting linac. This line includes a new RFQ that will operate in a CW mode (100% duty factor) at the operating frequency of 80 MHz. The RFQ is composed of 6 modules about 1.2 m long each. Each module is basically composed of a Stainless Steel Tank (AISI LN 304) and four OFE Copper Electrodes. A copper layer will be electrodeposited on the tank inner surface and a spring joint between tank and electrode is used in order to seal the RF. Moreover, the electrodes are equipped with two brazed SS inserts in order to allow coupling with the tank. In order to remove the RF power (about 100 kW) as well as to allow frequency control during high power operation for a given cooling channel layout, a set of thermo-structural simulations was performed, whose input data were the RF Power densities calculated with 2D and 3D codes. In this paper the analytical and numerical methods used, as well as the main outcomes of these studies are presented.

THE SPES RFQ

The SPES RFQ is designed in order to accelerate beams in CW with A/q ratios from 3 to 7 from the Charge Breeder through the MRMS and the selection and injection lines up to the MEBT. The main parameters of the RFQ are listed in Table 1:

Table 1: Main RFQ Parameters

Paramater [units]	Design value
Frequency [MHz]	80
In/out. Energy [keV/u]	5.7-727 (β=0.0035-0.0359)
Accelerated beam current [μA]	100
Inter-vane voltage V [kV, A/q=7]	63.8 – 85.84
Vane length L [m]	6.95
Average radius R_0 [mm]	5.27÷ 7.89
Synchronous phase (deg.)	-90 ÷ -20
Focusing Strength B	4.7 ÷ 4
Pole tip radius ρ	4.01÷5.97 (0.76 R_0)
Stored Energy [J]	2.87
RF Power [kW] (30% margin)	98
Q value (30% margin)	14000
Max power density [W/cm^2]	0.31 (2D), 11 (3D)

The voltage law is a linear function along z V(z)=V(0)+a·z with a=3.177 kV/m and V(0) depending on the A/q of the ion to be accelerated. Such law is implemented by designing the RFQ in order to obtain a constant TE_{21} cut-off frequency fc=79.5 MHz along the structure and by properly shaping the vane undercuts at the Low and High Energy Ends of the RFQ. This choice sets the tuner tuning range of the RFQ in the interval [79.5 MHz, 80.5 MHz]. In order to compensate the R_0 variations, the capacitive region is varied along the RFQ (Fig.1). Therefore the electrode thickness is constant and equal to 48 mm and the tank inner radius R is equal to 377 mm.

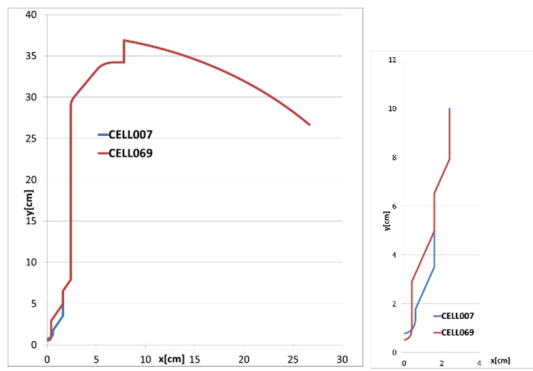

Figure 1: Capacitive tuning of the RFQ sections corresponding to the highest (Cell007) and lowest (Cell069) R_0 values.

The RFQ Cooling system is designed to remove power and to finely tune the cavity resonant frequency during operation by temperature regulation. For such a purpose, it is necessary to have two independent water loops with two temperature set points: a “cold” circuit for the tank, and a “warm” one for the vanes. By mixing with a 3-way valve the cold inlet water with part of the warm water coming from the cavity, it is possible to vary the resonant frequency of the RFQ and to tune the cavity accordingly. Therefore a thorough thermo-structural analysis of the RFQ is needed in order to determine, for s given cooling channel layout and inlet temperature, the associated temperature and displacement fields in the RFQ as well as the mechanical stresses. The outcomes of this analysis are the frequency sensitivities vs water temperatures and/or RF input powers in order to determine the actual tuning range with water temperature during RFQ operation. This analysis was carried out both in 2D (SUPERFISH) for the input parameters (power densities) and in 3D (ANSYS Electromagnetic Suite and ANSYS 16).

Preliminary simulations permitted to determine the position of the cooling channel and the cooling water path arrangements (Figs. 2 and 3) and the water input temperatures for vane and tank. It is important to notice

ISBN 978-3-95450-131-1

two main aspects of this RFQ: first, the vane and the tank are thermally insulated and second the RF power balance is approximately 60% on the vanes (Cu) and 40% on the tank (SS). The channel radii are Rc_2= 6 mm on the vane and Rc_1=4 mm on the tank, the inlet water velocity is 3 m/s and consequently the heat convection coefficient h_c was chosen to be equal to 10000 W/m^2·K. For the reference case study the inlet vane temperature (T_2) is 20°C and the inlet tank temperature (T_1) is 15°C. The channel heights on the vane are 125 mm (90 mm for the 1st and 6th module) and 305 mm, while the channel angles on the tank with respect to the electrode symmetry plane are 15° and 33° respectively (Fig.2).

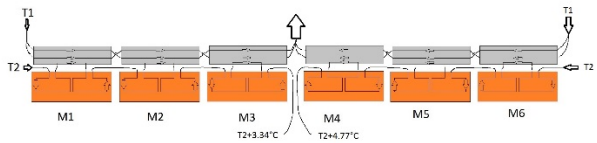

Figure 2: Cooling channel connections.

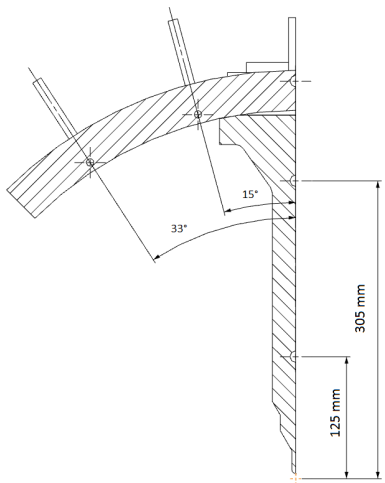

Figure 3: Transverse cooling channel layout.

From the above figures, it is possible to notice that

- The vane and tank channels are connected in series from modules 1 to 3 and then from modules 6 to 4.
- In order to reduce the thermal stress on the adaptation piece between tank and electrode, an additional cooling channel on the tank is foreseen with same radius inlet temperature of the vane ones.

As for the water temperature calculations to be used as input data for thermo-structural calculations, they were derived from the knowledge of the power per unit length $p_{d2}(z)$ [p_{d1} (z)] on the vane [tank] [W/m] via the relationship

$$T_{out\,1[2]} = T_{in[2]} + (1/\dot{m}c_p)\int_{z_{in}}^{z_{out}} p_{d\,1[2]}(z)dz \quad (1)$$

T_{in} [T_{out}] being the inlet [outlet] water temperatures, $\dot{m}$ the mass flow rate and c_p the water specific heat.

2D CALCULATIONS

2D calculations were performed in order to determine, via the SUPERFISH code, the input power densities to be inserted in the thermo-structural 3D simulations. For such a purpose 21 significant RFQ section (1/4 of RFQ) were taken into account and the related power densities were calculated. Moreover, from the same simulations, the frequency sensitivities vs. R_0 and R variations were determined. In particular, the dissipated power per unit length profile p_{dSF} [W/m] is calculated as.

$$p_{dSF}(z) = \oint_{\gamma} p_{densSF}(z,s)ds \quad (2)$$

$p_{densSF}(s,z)$ being the surface power density [W/m^2] given by the code and γ is the RFQ profile.

In the following figure 4 such profile is shown and it is compared with the scaling law $p_d(z)=p_d(0)(V(z)/V(0))^2$.

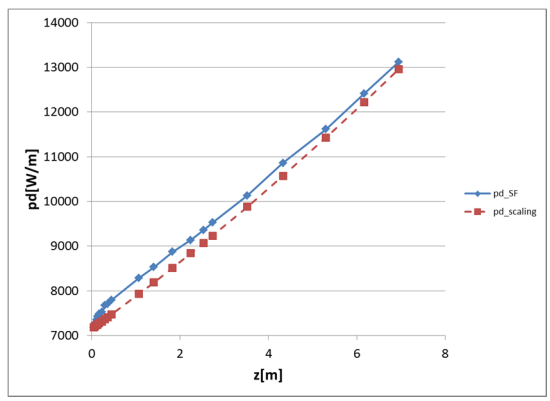

Figure 4: Comparison between the pd(z) functions given by SUPERFISH (solid curve) and the scaling law (dotted curve).

Now, since the differences between the two calculations are below 5%, this scaling law will be used for the input surface power densities for thermal calculations.

As for frequency sensitivities is concerned, it results that $\chi_{R0}=\partial f/\partial R_0$ varies from 2.5 MHz/mm to 3.7 MHz/mm (average value 3.3 MHz/mm) and $\chi_R=\partial f/\partial R$=-0.2 MHz/mm. The frequency shift can be calculated as $\Delta f=\chi_{R0}\Delta R_0 + +\chi_R\Delta R \approx =\chi_{R0}\Delta R_0$ (in most cases the second term can be neglected).

3D CALCULATIONS

The 3D simulations were performed with the ANSYS Workbench v.15 software on 1/8 of the overall RFQ, including, brazed inserts and vane undercuts. Such simulations consisted in stationary thermal and structural calculations. The Power densities from the electromagnetic solver were used as an input for the thermal calculation. Finally, from the knowledge of the deformation profile, it was possible to determine the frequency shift. In these simulations the simplified assumption that each channel of the vanes and of the tank absorbs the same amount of

ISBN 978-3-95450-131-1

power respectively was made. In particular, input data power densities p_{dens} [W/cm^2] were given by SUPERFISH at each RFQ section according to the scaling law introduced in the preceding paragraph. Indeed, on the vane undercuts the power densities were calculated with ANSYS Electromagnetic Suite v 16.1. The average and outlet temperatures for each channel were determined according to (1). Then, from temperature distribution on the RFQ bulk, the corresponding deformation and stress fields were calculated. In this simulation 1'800'000 nodes, 1'100'000 and Tethraedral elements were set, for the Thermal steady state and static Structural.
In Fig.5 the temperature distribution on the RFQ is shown.

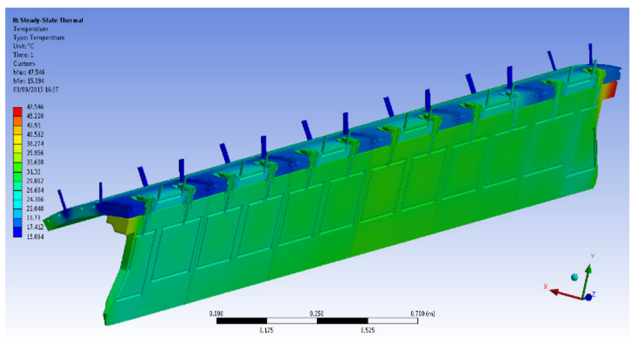

Figure 5: Temperature distribution on the 1/8 of the RFQ. The maximum value of 48°C occurs on the tank in the plane between electrodes at the High Energy side.

As for the deformation pattern is concerned, in the following figure the ΔR_0 (z) deformation is shown for the case T_1=15°C, T_2=20°C.

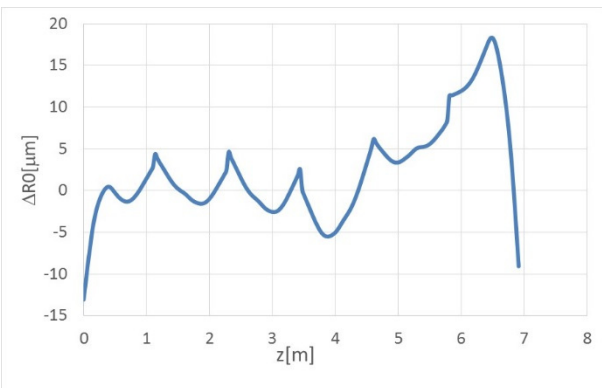

Figure 6: Average aperture perturbation for the case study (vane undercuts included).

This perturbation provokes a frequency shift of 7 kHz and a voltage perturbation $|\Delta V(z)/V(z)|<0.005$, to be compared with the maximum admittable value of 0.03, as for beam dynamics specifications. The frequency temperature sensitivity in this case was investigated as well. The vane temperature coefficient $\partial f/\partial T_2$ is equal to about -17 kHz/°C. Moreover the frequency shift $\Delta f_{on\text{-}off}$ from maximum input power to zero input power is +85 kHz, and the vane+tank temperature coefficient $\partial f/\partial T_{1,2}$ (that is the frequency shift due to both T_1 and T_2 increase is -2kHz/°C. Therefore a temperature tuning range of about ±85 kHz can be established for a T_2 variation in the range [15°C, 25°C]. Moreover, as power increases frequency increases, as well as water temperature. Nevertheless, since $\partial f/\partial T_{1,2}<0$, then a stabilizing mechanism is established and a thermal runaway is avoided. This phenomenon is similar to the one encountered both for TRASCO [3] and IFMIF [4] RFQs. Finally, the behaviour of the Von Mises Stress σ_{eqVM} was studied, with particular reference to the effect of the additional cooling channel on the vane. In particular, the $\sigma_{eqVM}(z)$ function was evaluated on a path between two consecutive adaptation piece between tank and electrode on Module #4, considering different values of the product $\Pi_c=A_C \cdot h_c$, $Ac=2\pi l_c R_{C1}$ being the channel surface (l_c = =channel length). The results are shown in Fig. 7 in the case T_1=15°C, T_2=25°C

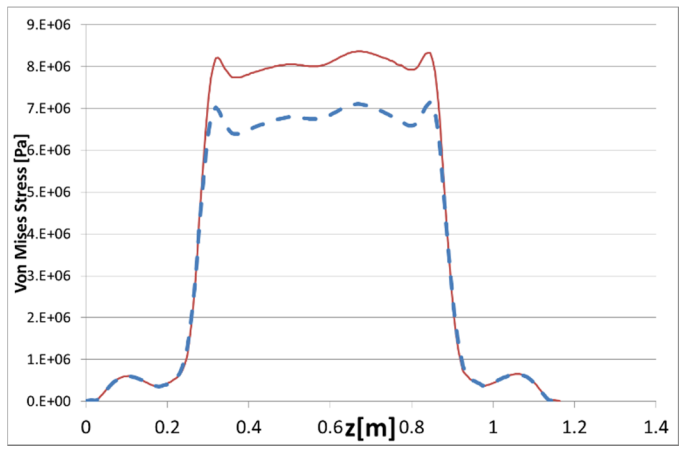

Figure 7: The von Mises stress for hc=0 (solid line) and hc=10000 W/m^2·K (dotted line).

From this figure it is possible to notice that actually the σ_{eqVM} decreases with Π_c, moreover the maximum value is kept below the safe limit of 20 MPa in any RFQ point.

CONCLUSIONS

The outcomes of the combined Electromagnetic and thermo-structural studies validate the current channel layout. Further refinement in this study include the precise pointwise determination of the water temperatures via the usage of the 1D Fluid thermal elements [5].

REFERENCES

[1] A. Pisent, HB 2014 East Lansing (USA) p.220.
[2] M. Comunian et. al, these proceedings.
[3] E. Fagotti et al LINAC 2012 Tel Aviv (Israel) p. 945.
[4] F. Scantamburlo et al LINAC 2010 p.539.
[5] Raatikainen et. al CERN CLIC Note 881.

ISBN 978-3-95450-131-1

HEAVY-ION BEAM ACCELERATION AT RIKEN FOR SUPER-HEAVY ELEMENT SEARCH

E. Ikezawa, M. Fujimaki, Y. Higurashi, O. Kamigaito, M. Kase, M. Komiyama,
T. Nakagawa, K. Ozeki, N. Sakamoto, K. Suda, A. Uchiyama, K. Yamada
RIKEN Nishina Center, Wako, Saitama, Japan
K. Kaneko, T. Ohki, K. Oyamada, M. Tamura, H. Yamauchi, A. Yusa
SHI Accelerator Service Ltd., Tokyo, Japan

Abstract

The RIKEN heavy-ion linear accelerator (RILAC) comprises a variable-frequency Wideröe linac as the main linac, an 18 GHz electron cyclotron resonance ion source, a variable-frequency folded-coaxial radiofrequency quadrupole linac as a pre-injector, and a charge-state multiplier system as a booster. An experiment to search for a super-heavy element (Z=113) was carried out using the RILAC at the RIKEN Nishina Center for Accelerator-Based Science, from September 2003 to August 2012. As a result, three events for Z=113 were successfully observed. This paper presents heavy-ion beam acceleration at RIKEN for the super-heavy element search.

INTRODUCTION

The project to construct a heavy-ion accelerator complex (linac-cyclotron) at RIKEN was initiated in 1974. The construction of six RIKEN heavy-ion linear accelerator (RILAC) resonators (RILAC No.1 - No.6) was completed in 1980 [1]. These are variable-frequency Wideröe linac-type resonators. The frequency tunable range of the resonators is from 17 to 45 MHz. The stand-alone mode operation of the RILAC to supply ion beams for experiments was started in 1981. The injection-mode operation of the RILAC to inject ion beams into the K540MeV RIKEN Ring Cyclotron (RRC) [2] was initiated in 1986.

In 1996, the pre-injector of the RILAC, a direct-current (DC) high-voltage terminal, was converted into a combination of a powerful 18 GHz electron cyclotron resonance ion source (18GHz-ECRIS) [3] and a very efficient low-β accelerator, which is a variable-frequency folded-coaxial radiofrequency quadrupole linac (FC-RFQ) [4]. The frequency tunable range of the FC-RFQ is from 17.7 to 39.2 MHz.

A new project for the RIKEN Radioactive Isotope Beam Factory (RIBF) [5] was proposed to extend radioactive isotope beams to heavy mass range. Since the project aimed principally at producing an intense heaviest-ion (uranium) beam, a charge-state multiplier system (CSM) [6] was proposed to minimize the inevitable beam-loss during the charge stripping process after the RILAC. In 2000, as an energy upgrade program of the RILAC in collaboration with the Center for Nuclear Study, University of Tokyo, six CSM resonators (CSM A1-A6) were installed after the existing accelerator of the RILAC. CSM A1 and CSM A2 are variable-frequency type resonators that have a frequency tunable range from 36.0 to 76.4 MHz. The other four resonators (CSM A3-A6) are

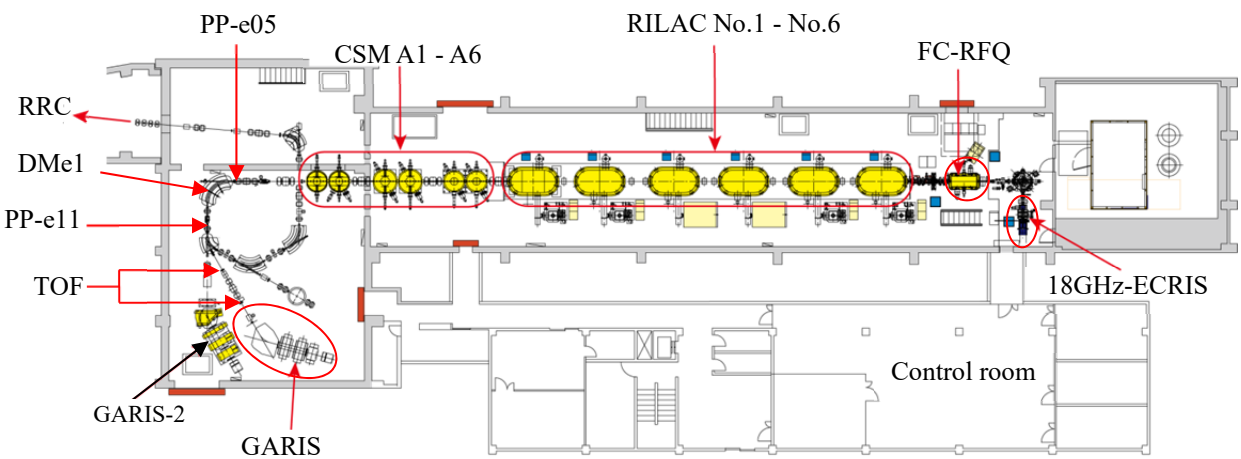

Figure 1: Layout of RILAC and GARIS.

ikezawa@riken.jp

ISBN 978-3-95450-131-1

fixed-frequency type set at 75.5 MHz. Therefore, the RILAC operation with these accelerators improved the maximum beam energy to 6 MeV/nucleon [7], meeting the requirement of the gas-filled recoil ion separator (GARIS) [8]. The GARIS was moved from the E1 experiment room of the RRC to the experiment room of the RILAC in 2000. The layout of the RILAC and the GARIS is shown in Fig. 1.

RILAC OPERATION

Ion Source

The photograph of the 18GHz-ECRIS is shown in Fig. 2. The micro wave frequency is 18 GHz. The maximum magnetic field on-axis of the normal-conducting mirror coils is 1.4 T. The field strength on the surface of the permanent hexapole magnet is 1.4 T. ^{70}Zn (enrichment of 80-95%) vapor was generated from a ceramic rod (4×4×40 mm^3), which was inserted into the ECR plasma. By adjusting the relative position of the rod to the plasma, ^{70}Zn was charged into the plasma by heating. At the beginning, $^{70}Zn^{16+}$ was used, which subsequently changed to $^{70}Zn^{15+}$ to produce higher intensity beam without minding $^{14}N^{3+}$ being mixed in the projectiles. The beam current at the ion source was maintained above 19 eμA (1.2 pμA), and a periodic decrease of approximately 10% was always observed; the current loss was usually recovered by adjusting the rod position. The ion source could function very well, at least, for more than one month without the need to clean or exchange the ceramic rod. The consumption rate of ^{70}Zn was usually approximately 0.4 mg/h.

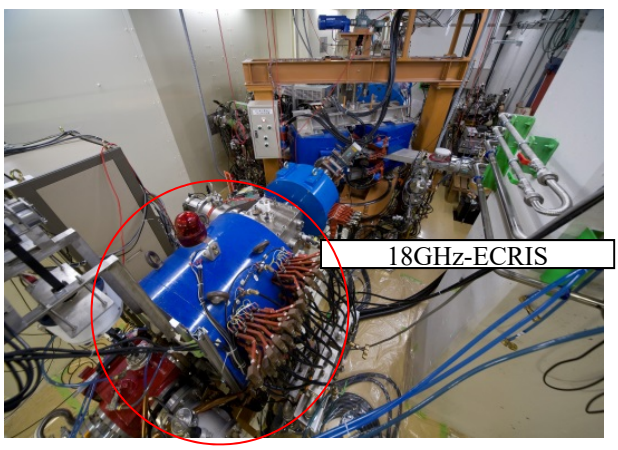

Figure 2: Photograph of 18GHz-ECRIS.

Accelerator

The photograph of the FC-RFQ resonator, the RILAC resonators, and the CSM resonators is shown in Fig. 3. The FC-RFQ resonator and the six RILAC resonators were operated at a frequency of 37.75 MHz. The six CSM resonators were operated at 75.5 MHz. The final energy of the ion beam could be varied continuously by tuning radiofrequency voltages and/or radiofrequency phases in the last two CSM resonators (CSM A5 and CSM A6). The RILAC had been providing the around 5 MeV/nucleon beam with an intensity of 0.4-0.7 pμA.

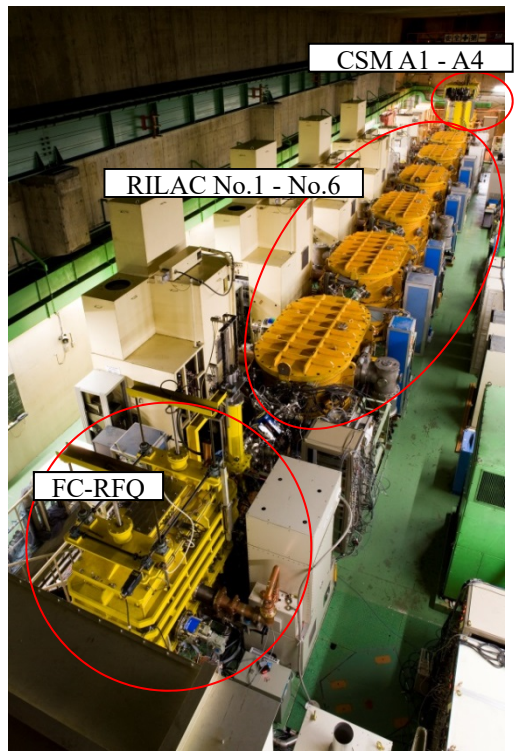

Figure 3: Photograph of FC-RFQ, RILAC, and CSM.

Beam Monitor

The ion beam energy was checked with a 90° analyzing magnet (DMe1) placed after CSM A6. Moreover, the time of flight (TOF) measurements were performed using two sets of beam phase picked-up that were installed along the straight beam line right in front of the GARIS target, as shown in Fig. 1. During the GARIS experiment, the signals from two sets of phase probes, denoted as PP-e05 and PP-e11 in Fig. 1, were analyzed, and the amplitude and phase of the third harmonic signal were always displayed. Therefore, the $^{70}Zn^{+15}$ beam intensity could be maintained at more than 0.5 pμA.

GARIS EXPERIMENT

Target

A plan view of the GARIS is shown in Fig. 4. The target was located right in front of the dipole magnet. The ^{209}Bi target [9], a metallic bismuth layer, which is such as a 450 μg/cm^2 thick, was attached to such as a 60 μg/cm^2 thick backing carbon foil. Several targets were mounted on the rotating wheel. The wheel was rotated during irra-

ISBN 978-3-95450-131-1

diation at around 3000 rpm. To prevent the beam from hitting the frame, it was chopped with a duty cycle of 80% by a parallel-plate deflector placed after the 18GHz-ECRIS. A set of targets were replaced with new targets every week. After the experiment was started, the elastic scattering of the projectile on the target was observed continuously using a solid-state detector. The spectrum of them showed how the target was damaged and indicated when it should be changed.

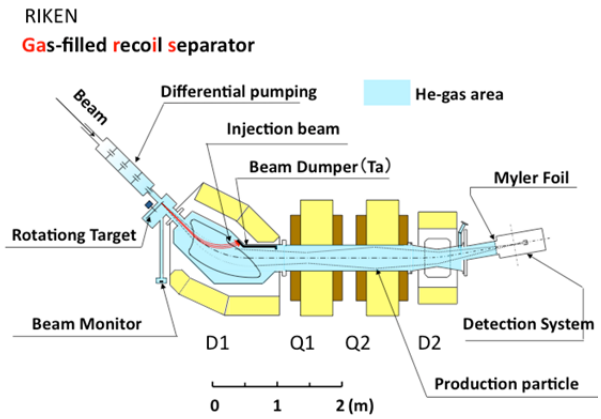

Figure 4: A plan view of GARIS.

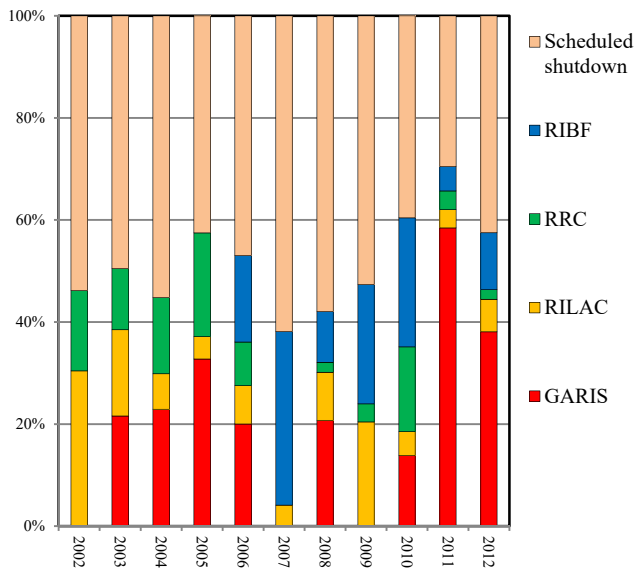

Figure 5: The operation statistics of RILAC from 2002 to 2012. In each year, 8760hr corresponds to 100%.

Experiment

The operation statistics of the RILAC from 2002 to 2012 are shown in Fig. 5. After the preliminary experiments for identification of the super-heavy element, the GARIS experiment, a search for the super-heavy element (Z=113), was carried out from September 2003 to August 2012, as shown by the red bars in Fig. 5. In 2007 and 2009, the GARIS experiment was not conducted because the RILAC was engaged in the commissioning of the RIBF, as shown by the blue bars in Fig. 5. In 2011, after the completion of construction of a new linac injector (RILAC2) for the RIBF [10], the GARIS experiment was conducted exclusively. The beam availability for this experiment was about 90%.

CONCLUSION

The GARIS experiment, a challenging search for the super-heavy element (Z=113), was conducted at the RIKEN Nishina Center for Accelerator-Based Science in the period from September 5, 2003 to August 18, 2012. The RILAC provided an around 5 MeV/nucleon ^{70}Zn beam with an intensity of around 0.6 pμA [11,12]. The net irradiation time was 553 days with a total beam dose of 1.351×10^{20}. As a result, three convincing candidate events for the isotope of the 113th element were successfully observed for the first time on July 23, 2004 [13], followed by the observations on April 2, 2005 [14] and finally August 12, 2012 [15].

REFERENCES

[1] M. Odera et al., Nucl. Instrum. Methods 227, 187 (1984).
[2] Y. Yano, Proc. 13th Int. Cyclo. Conf., 102 (1992).
[3] T. Nakagawa et al., Nucl. Instrum. Methods B226, 392 (2004).
[4] O. Kamigaito et al., Rev. Sci. Instrum. 70, 4523 (1999).
[5] Y. Yano, Nucl. Instrum. Methods B261, 1009 (2007).
[6] Y. Yano et al., Proc. PAC97, TRIUMF (1997).
[7] O. Kamigaito et al., Rev. Sci. Instrum. 76, 013306 (2005) .
[8] K. Morita et al.; Eur. Phys. J. A21, 257 (2004).
[9] D. Kaji et al., Nucl. Instrum. Methods A590, 198 (2007).
[10] K. Yamada, et al., IPAC2012, TUOBA02, 1071 (2012).
[11] E. Ikezawa, et al., PASJ3-LAM31, WP02, 272 (2006).
[12] M. Kase, et al., IPAC2012, THPPP040, 3823 (2012).
[13] K. Morita et al., J. Phys. Soc. Jpn. 73, 2593 (2004).
[14] K. Morita et al., J. Phys. Soc. Jpn. 76, 045001 (2007).
[15] K. Morita et al., J. Phys. Soc. Jpn. 81, 103201 (2012).

ISBN 978-3-95450-131-1

THE COST OPTIMIZATION STUDIES OF THE SUPERCONDUCTING LINAC*

Y. Tao[a,b], Z.J. Wang[a], Y. He[a,*], S.H. Liu[a], W.S. Wang[a], C. Feng[a], P.Y. Jiang[a], H. Jia[a], W.L. Chen[a,b]
[a]Institute of Modern Physics, the Chinese Academy of Sciences, Lanzhou 73000, China
[b]University of the Chinese Academy of Sciences, Beijing 100049, China

Abstract

The research superconducting linac is growing in energy and power which induces an increase of the project cost. The RF cavities and RF power supplies mainly contributes the cost of the superconducting linac, which is a competitive technology for high power machine. A code internally with optimization algorithm is developed to optimize the geometric beta value of superconducting cavity family and transition energy to increase the acceleration efficiency of the whole linac. In this paper, the CADS Linac is taken as example to demonstrate the design procedure and the preliminary results of the CADS linac is also presented. The new method can be also used in other high power superconducting facilities.

INTRODUCTION

The applications of the research accelerator are becoming more and more diverse, from the very low power medical accelerators to the high power driven sub-critical accelerators. One of the main advantages of the linear accelerator is its capability for producing high-energy and high-intensity charged-particle beams with high beam quality, where high beam quality can be related to a capacity for producing a small beam diameter and small energy spread, which make it widely used sufficient to resolve problems. With the development of superconducting RF technology, the high energy high intensity superconducting linac is becoming more and more popular. The main superconducting linac projects all over the world are shown in the Fig.1. From the Fig.1, the beam power of the existed projects is round 1 MW, while for the further planned projects, the beam power will be ten times higher. The huge cost of the superconducting linac has been a factor, which is limit to the development of the linac. However, for the time being the accelerator optimization is concentrated on optimizing the lattice; the linac is merely matching the beam to transport line. It is necessary to find a new method to optimize the cost of superconducting linac.

The China Accelerator Driven Sub-critical System (CADS) [1] which aim to solve the nuclear waste problem is a 1.5 GeV and 10 mA continue wave superconducting linac project consists of two injectors and a main superconducting linac. The CADS roadmap is shown in the Fig. 2. The beam power will reach 10-15 MW. There will be more than two hundred of superconducting cavities and 20-25 MW RF power need for the whole project. Increasing the acceleration efficiency and utility of RF power is necessary and essential for the project cost optimization.

In this paper, the optimization concept as well as optimization procedures are presented in detail.

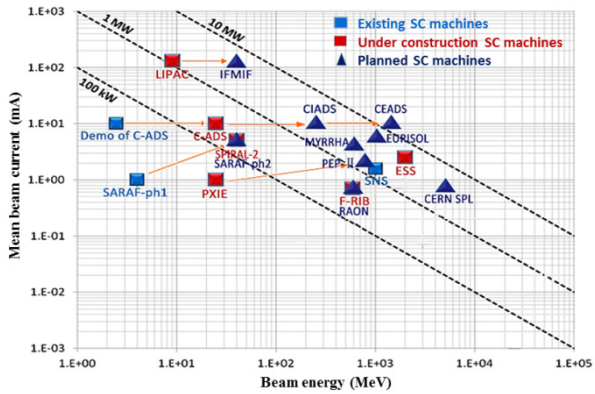

Figure 1: The superconducting linac in the world.

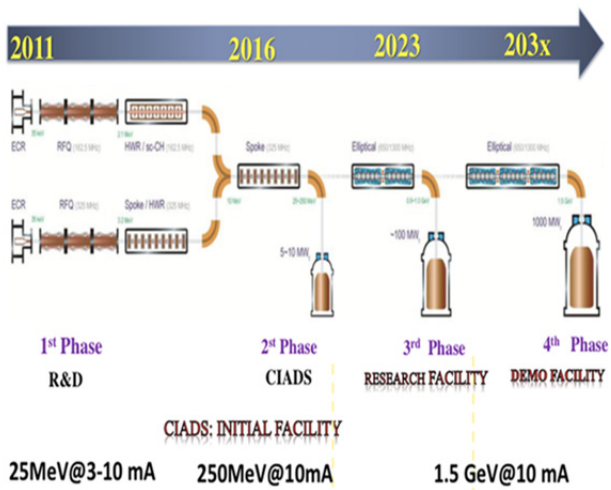

Figure 2: The roadmap of CADS project.

THE FOUNDATION OF PHYSICS

To select a reasonable geometric beta and transition energy is of great importance for the superconducting linac since an over specified value which will not be reached will result to a linac reduce the cost. How to choose the geometric beta and transition energy is an optimized problem, and the optimization result cannot be easily found by using the traditional method. As few papers studying the cost optimization of the superconducting linac [2], the new method which using a

*Work supported by IMP
*hey@impcas.ac.cn

ISBN 978-3-95450-131-1

code and choosing normalized transit time factor (TTF) and cavity number as objectives is presented.

All of these parameters dependents on each other, the optimization has to be performed in the 2 dimensional space. The energy gain of each cavity is defined as:

$$\Delta W_i = qV_0 \cos(\phi_i), \quad (1)$$

where q is charge of the particles respectively, ϕ_i is the synchronous phase, and V_0 the efficient voltage that could be written down as :

$$V_0 = \frac{E_{acc} L_i}{T_i}, \quad (2)$$

where E_{acc} is the max accelerating gradient, L_i is the cavity length and T_i is the TTF. Some of these parameters are functions of other parameters. The length of the cavity is a function of the gap number of the cavity N_{cell}, geometric beta of the cavity βg and wavelength of high frequency electric field λ_i. The cell length measured from the centre of one drift tube to the centre of the next. The equation for the length for this case becomes:

$$L_i = N_{cell} \frac{\beta_{gi} \lambda_i}{2}, \quad (3)$$

The TTF of cavities operating on π-mode of electromagnetic oscillations which is the case for practically all known types of superconducting cavities [3]:

$$T_c(N,\beta,\beta_g) = \begin{cases} (\frac{\beta}{\beta_g})^2 \cos(\frac{\pi N}{2\beta/\beta_g}) \frac{(-1)^{(N-1)/2}}{N((\beta/\beta_g)^2 - 1)} \\ \frac{\pi}{4} \end{cases}, \quad (4)$$

$$T_s(N,\beta,\beta_g) = \begin{cases} (\frac{\beta}{\beta_g})^2 \sin(\frac{\pi N}{2\beta/\beta_g}) \frac{(-1)^{(N+1)/2}}{N((\beta/\beta_g)^2 - 1)} \\ \frac{\pi}{4} \end{cases}, \quad (5)$$

where T_c is for the odd number of cells N in the cavity and T_s is for the even.

For the superconducting cavity, there is a relationship between the peak electric surface field E_{peak} and acceleration field E_{acc} [4]. Consulted a number of papers, the date which consists of lots of E_{peak}/E_{acc} value is from research accelerator project all over the world, such as CADS, ESS, and SPIRAL-2 and so on. The red line in Fig. 3 is plotted using [5]:

$$E_{acc} = \frac{E_{peak}}{k_1 * \exp(-\beta_g / k_2) + k_3}, \quad (6)$$

By fitting, values of k_1, k_2 and k_3 constants will be found. For the optimistic case, k_1=14.45, k_2=3.68, k_3=-9.13.

The cavity number and TTF which are not good consistency for each other are factors that used to weigh the cost of the superconducting linac against the power it will bring. The totals of cavity number N_c which depends on the output energy 1.5 GeV are shown in Eq. (7). As synchronous phase ϕ_s is a constant, there is an only one affecting factor V_0 which shows radio of the applied power to the maximum power means TTF influence the cost. In order to choose the right geometric beta and right transition energy, the study of the factors is necessary.

$$N_c = \frac{1.5GeV}{V_0 \cos(\phi_s)} \quad (7)$$

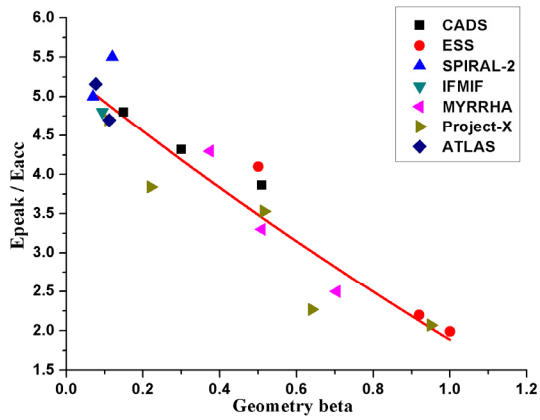

Figure 3: Ratio of the peak electric surface field to accelerating field vs geometric beta.

OPTIZATION OF CADS LINAC

Particle Swarm Optimization (PSO) [6] is relatively new swarm intelligence based heuristic global optimization technique. It seems with the other technique, also based on the concept of population and evolution, through cooperation and competition with other particle to find the global optimal solution.

The accelerating efficiency of the cavity, TTF, is a parameter that shows the ratio of the max accelerating. The accelerated particles are formed in stable bunches. When the particle inject speed is matching with the cavity speed, the max accelerating wave will be created. To come true these ideas, the optimization is provided by an appropriate choice of the objective normalized TTF and cavity number to optimize the geometric beta and transition energy to reduce the cost. The normalized TTF means the TTF of the cavities closely to the max TTF, defined as:

$$F = \sum_{j=1}^{S} \sum_{i=1}^{N} (T_i - T_{\max})^2 / S, \quad (8)$$

where S is cavity section, N is each cavity number, T_i is cavity TTF and T_{max} is max TTF of each cavity type.

THE PRELIMINARY STUDIES

As the optimization has long time to go, in order to verify the method combining design with optimize, using the method to design the CADS demo facility from 2.1 MeV to 250 MeV. The Fig. 4 shows the results of the optimization of cavity number. There are no good results, because cavity number and TTF are not accord with the

ISBN 978-3-95450-131-1

physics. The cavity number, which measured for the efficiency of the cavity, is least when the TTF is very high. But in fact, from the results, it is on the contrary.

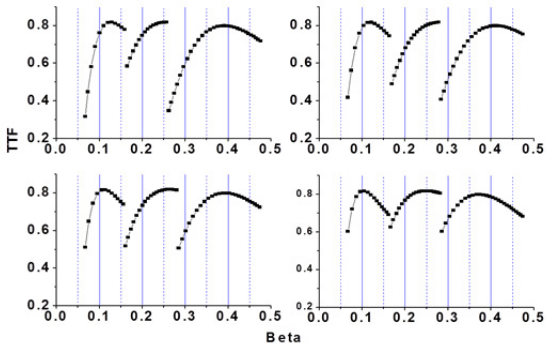

Figure 4: The cavity number optimization results.

The other result which choice of the normalized TTF as objective is to choosing the right geometric beta and the right transition energy in main linac of CADS to improves the average transit time factor, and therefore the acceleration efficiency of the linac. Figure 5 shows the results of the geometric beta and transition energy choose.

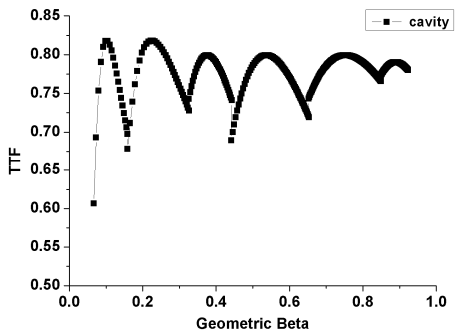

Figure 5: The geometric beta and transition energy results.

To gain the maximum acceleration efficiency this transition should happen when the accelerating efficiency of the normal conducting linac reaches that of the following superconducting linac. But the third and fourth transition energy is disconnected. Two objectives cavity number and normalized TTF cannot separate.

CONCLUSION

The objectives are essential for optimization problem. The preliminary results have been obtained from the previous work. The objectives are modified for time to get more and more reasonable. The multi-optimization objections included normalized TTF and cavity number has been figured out and the optimization process is ongoing.

ACKNOWLEDGMENT

The authors want to special thanks to W. Li, Z. H. Li and China ADS Linac centre collaboration.

REFERENCES

[1] Z.H. Li, P. Cheng, H.P. Geng, et al., Physics design of an accelerator for an accelerator-driven subcritical system, Phys. Rev. ST Accel. Beams, 16, 080101 (2013).

[2] M. Eshraqi, cost optimized design of high power linac, in proc. LINAC 2014.

[3] P N Ostroumov, Physics design of the 8 GeV H-minus linac, New Journal of Physics 8 (2006) 281.

[4] P. Pierini, Analysis of gradients for proton linac, Gradients and Betas for ESS LINAC, Lund, September 2010, Sweden.

[5] M. Eshraqi, The Optimization of ESS Superconducting LINAC, ESS AD Technical Note/AD/0010, 21 March, 2011.

[6] Carlos A. Coello Coello, Member, Handling Multiple Objectives With Particle Swarm Optimization, IEEE, VOL. 8, NO. 3, JUNE 2004.

ISBN 978-3-95450-131-1

CONCEPTUAL DESIGN OF LEBT FOR C-ADS LINAC ACCELERATOR*

W.L.Chen, Z.J.Wang, Y. He, H.Jia, Q.Wu, Y.Tao, IMPCAS, Lanzhou, China.

Abstract

In order to avoid the hybrid ions like H_2^+, H_3^+ injecting into the RFQ and the residual gas H_2 tracing through the RFQ which may lead the RFQ cavity performance degradation, we present the conceptual design of the Low Energy Beam Transport (LEBT) for the China Accelerator Driven Sub-Critical reactor system (C-ADS) accelerator. The LEBT, consisting of one bending magnet and three solenoids and four short-drift sections, match the CW proton beam with 35KeV and 10mA to the entrance of a radio frequency quadrupole (RFQ). This bending LEBT can easily separate the unwanted ions. With the edge angles and one quadrupole to correct the beam asymmetry causing by the bending magnet, the simulation results meet the RFQ entrance requirements.

INTRODUCTION

A project named China Initiative Accelerator Driven Sub-Critical System (C-IADS) has been proposed to treat the spent nuclear fuel and began construction since 2011[1]. Under three years commissioning, the demo facility had accelerated 10mA CW proton beam to 2.56MeV, and recently 2.7mA CW proton beam had accelerated up to 5.17MeV. The layout of the demo facility is shown in the Fig 1.Some beam experiments in the CW mode had taken on the LEBT recently, and find that the component of H_2^+ and H_3^+ is about 32% and 5% at 1.6E-3Pa vacuum degree. And in our accelerator we find the transmission efficient from the LEBT to the RFQ is almost 62.5% (FC1=16mA, ACCT1=10mA). Another question is the H_2 removal from the ion source to the RFQ and even to the downstream superconducting cavity. Long-time operation with residual gas RFQ performance may decline has reported in paper, and residual gas removal to the SC may lead the cavity quench. This paper presents the detailed description about a new LEBT for C-ADS accelerator.

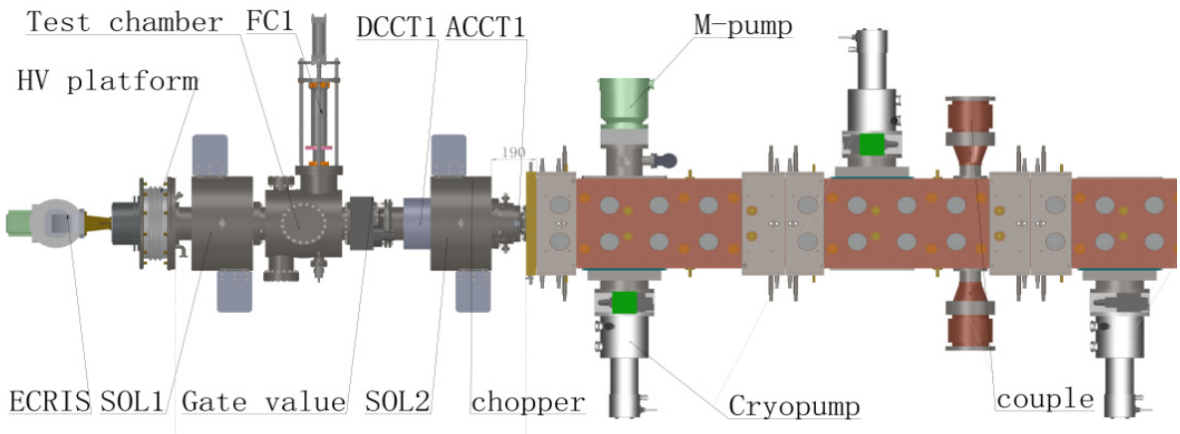

Figure 1: The layout of the ADS LEBT and parts of RFQ.

LEBT SYSTEM

The 10mA proton DC beam with the energy of 35KeV is extracted from a 2.45 GHz ECR ion source, after the LEBT transmission, focusing to the RFQ accelerator with the normalized RMS emittance at the entrance of RFQ less than 0.2 π.mm.mrad. The LEBT is used to transport and match the proton beam to the RFQ. Table 1 shows the key parameters of the front end to the RFQ which had met well with the downstream in the demo facility commissioning.

To meet the proton fraction requirement, a bending magnet and collimator have been considered to substantially reduce the contaminants, such as H2+ and H_3^+[3]. In order to decrease the beam divergence, we shorten the distance from the ion source to the first solenoid. And in order to reduce the space charge effect, the bending magnet is installed as close as possible to the first solenoid. Bending magnet will contribute the asymmetric ingredient to transverse axis, so we chose a little rotation angle into the magnet. After the separator, another two solenoids is used to match the Twiss parameters to the requirements. The next section will show the simulation results by TraceWin [2].

Table 1: required parameters before the RFQ

Parameters	Numbers	Units
Energy	35	KeV
Current	20	mA
Repetition frequency	50	Hz
Pulse width	CW	-
Twiss parameter α	1.21	-
Twiss parameter β	0.0479	mm/π.mrad

*Work supported by IMPCAS

ISBN 978-3-95450-131-1

$\epsilon(nRMS)$	<0.2	π.mm.mrad
Proton fraction	>95	%

To meet the proton fraction requirement, a bending magnet and collimator have been considered to substantially reduce the contaminants, such as H_2^+ and H_3^+. In order to decrease the beam divergence, we shorten the distance from the ion source to the first solenoid. And in order to reduce the space charge effect, the bending magnet is installed as close as possible to the first solenoid. Bending magnet will contribute the asymmetric ingredient to transverse axis, so we chose a little rotation angle into the magnet. After the separator, another two solenoids is used to match the Twiss parameters to the requirements. The next section will show the simulation results by TraceWin.

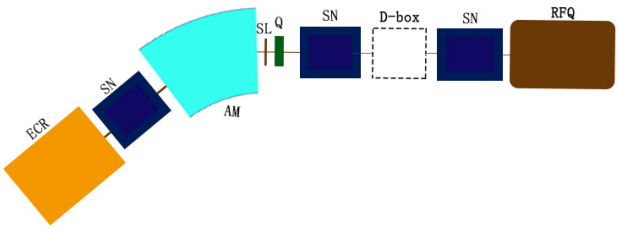

Figure 2: The layout of the LEBT.

SIMULATION RESULTS

Figure 2 shows the layout of the new conceptual designed LEBT. In this construction, the whole length of the LEBT is 2.714m from the source to RFQ entrance. The beam coming from the ion source dose not just consist of proton ion only. In the simulation, 10mA (62.5%) H^+, 5.2mA (32.5%) H_2^+ and 0.8mA (5%) H_3^+ was used to simulate the hybrid beam respectively of the total beam. Typical values of the initial parameters from the ion source are listed in Table 2. In order to prevent the unwanted species from transporting to downstream, the bending magnet will work as the separator. Figure 3 shows the simulation results with analysis magnet or not when the beam passes through three solenoids.

Table 2: required parameters before the RFQ

Twiss Parameters	Numbers	Units
$\alpha x = \alpha y$	-1.865	-
$\beta x = \beta y$	0.1835	mm/π.mrad
$\epsilon(nRMS)$	0.1885	π.mm.mrad

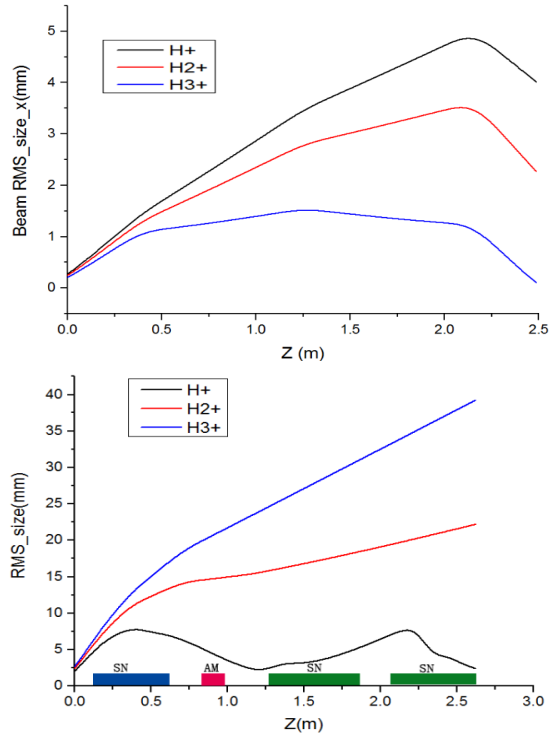

Figure 3: Comparison of the evolution of the beam profile along the LEBT with analysis magnet (the upper one without analysis magnet, the below one one with it).

As to the aperture studies, it can be seen from the Figure 3 that an aperture of radius 8mm slit is sufficient for full transmission of the H^+ beam. Hybrid ions can be eliminated in horizontal axis. In the figure 4 shows the simulation results about the beam scrapped in the LEBT. The unwanted ions about H_2^+ and H_3^+ all lost in the LEBT. Drifts have been chosen to be able to accommodate beam diagnostics, steers, gate valves, vacuum pumps.

The transfer matrix of the charged particle between the beginning of the bending magnet and the export are defined by the following linear model:

$$M_{sector} = \begin{pmatrix} \mathrm{Cos}[K_x\Delta s] & \frac{\mathrm{Sin}[K_x\Delta s]}{K_x} & 0 & 0 \\ -K_x\mathrm{Sin}[K_x\Delta s] & \mathrm{Cos}[K_x\Delta s] & 0 & 0 \\ 0 & 0 & \mathrm{Cos}[K_y\Delta s] & \frac{\mathrm{Sin}[K_y\Delta s]}{K_y} \\ 0 & 0 & -K_y\mathrm{Sin}[K_y\Delta s] & \mathrm{Cos}[K_y\Delta s] \end{pmatrix};$$

Where: $h = \frac{1}{\rho}\frac{\Delta\alpha}{\Delta\alpha}$, $K_x = \sqrt{(1-n)h^2}$, $K_y = \sqrt{nh^2}$, $\Delta s = \rho\Delta\alpha$. this are the bending magnet parameters.

The edge angle matrix is defined by the following linear model:

$$R_{edge} = \begin{pmatrix} 1 & 0 & 0 & 0 \\ \frac{\mathrm{Tan}[\beta]}{|\rho|} & 1 & 0 & 0 \\ 0 & 0 & 1 & 0 \\ 0 & 0 & \frac{-\mathrm{Tan}[\beta-\psi]}{|\rho|} & 1 \end{pmatrix};$$

ISBN 978-3-95450-131-1

$$\psi = K_1 \frac{g}{|\rho|}\left(\frac{1+\mathrm{Sin}^2[\beta]}{\mathrm{Cos}[\beta]}\right).\left(1 - K_1 K_2 \frac{g}{|\rho|}\mathrm{Tan}[\beta]\right);$$

The upper formula is the fringe-field correction.

In order to achieve the beam symmetry both in X and Y axis, the bending magnet is designed with a little angle about 20° and a 6°rotation angles at the bending magnet edge. A quadrupole installed behind the bending magnet is used to match the asymmetry action in Y direction.

The combinatorial matrix consisting of the edge angle, rotation angle, drift matrix and quadruple matrix are the following results:

$$R_{comb} = \begin{pmatrix} 0.89749 & 0.62389 & 0 & 0 \\ -0.27677 & 0.92181 & 0 & 0 \\ 0 & 0 & 0.91240 & 0.63096 \\ 0 & 0 & -0.24082 & 0.92946 \end{pmatrix};$$

This combinatorial matrix meets enough accuracy for the symmetry requirement. This configuration of the LEBT was used in the simulations.

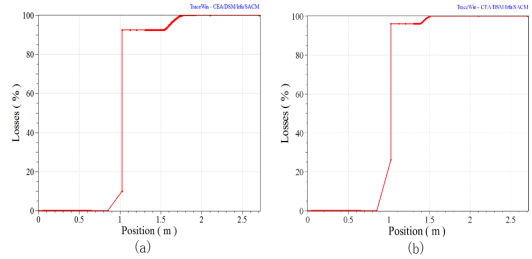

Figure 4: Comparison of the evolution of the beam profile along the LEBT with the slit, (a) shows the H_2^+ ion losses and (b) shows the H_3^+ ion losses.

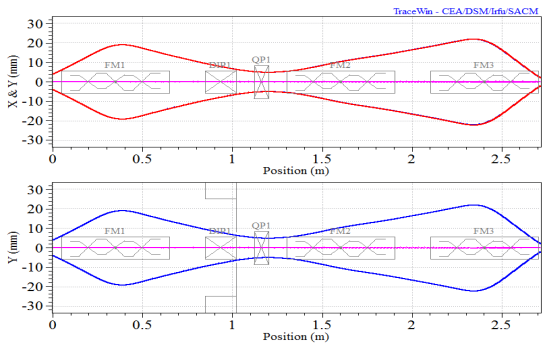

Figure 5: Beam trajectory in LEBT as calculated from partarn envelope calculation in TraceWin.

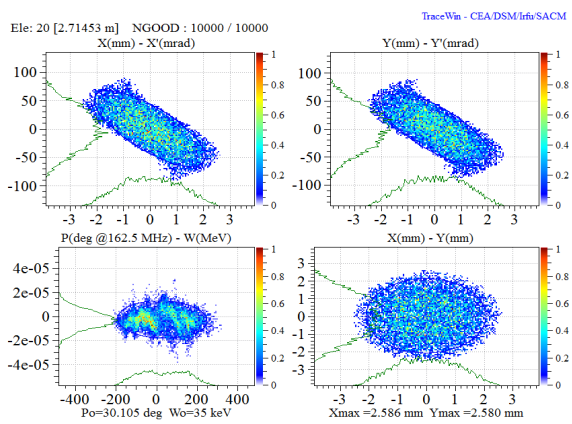

Figure 6: Beam phase spaces in LEBT at the end of the LEBT with 4D ellipse input distribution type.

Table 3: Twiss parameters out of LEBT

Twiss Parameters	Numbers	Units
αx	1.1425	-
αy	1.1408	-
βx	0.0474	mm/π.mrad
βy	0.0476	mm/π.mrad
$\epsilon(nRMS)$xx	0.1968	π.mm.mrad
$\epsilon(nRMS)$yy	0.1992	π.mm.mrad

In the figure 5, it can see that with the 6° rotation angle and quadrupole modulation, the beam trajectory both in X and Y axis is symmetry. Figure 6 shows the beam phase spaces distribution at the end of the LEBT, and the Twiss parameters shows in the table 3. It was found that the simulation results meet the requirements.

SUMMARY AND CONCLUSIONS

A bending-magnet based with three-solenoids LEBT has been designed for C-ADS accelerator at IMPCAS. The main design criterion is to match the beam from ECR ion source to the RFQ without hybrid ions and less H_2 tracing through the RFQ to the downstream. The detailed hybrid ions scrapped and beam dynamic simulation shows in the section 3. The 2.714m LEBT designed with bending magnet will also do well in machine protection system. Faraday cup and Chopper will be considered to be installed behind the first solenoid. With the bending magnet the beam can be cut freely and safely. Furthermore, the H_2 migration will be simulated with VSim code later to observe the residual gas trace into the RFQ and interaction with the beam for space charge compensation.

REFERENCES

[1] Y.Yang. et al, “A low energy beam transport system for proton beam”, ‘Review of Science Instruments’84, p.033306 (2013).

[2] D. Uriot, TraceWin documentation, CEA/SACLAY-DSM/Irfu/SACM.

[3] P.Pande. et al, “Optimization of solenoid based low energy beam transport line for high current H+ beam”, ‘IOP Science’, P02001(2015).

ISBN 978-3-95450-131-1

STATUS OF SUPERCONDUCTING QUARTER WAVE RESONATOR DEVELOPMENT AT MHI

T. Yanagisawa #, K. Sennyu, H. Hara, A. Miyamoto, R. Matsuda, Mitsubishi Heavy Industries, Ltd (MHI), Tokyo, Japan
O. Kamigaito, H. Okuno,N. Sakamoto, K. Yamada, K. Suda
K. Ozeki, Y. Watanabe, RIKEN Nishina Center, Wako, Saitama, Japan
E. Kako, H. Nakai, K. Umemori, KEK, Tsukuba, Ibaraki, Japan

Abstract

MHI's activities for development of Superconducting Quarter Wave Resonator (QWR) are reported. MHI has experiences of developments and fabrications of several superconducting ellipse cavities. And now MHI is developing the superconducting QWR for heavy ion accelerators.

INTRODUCTION

Mitsubishi Heavy Industries (MHI) has supplied the superconducting RF cavities and the cryomodules for various electron accelerator projects, such as a STF and c-ERL project at KEK [1][2]. Moreover, MHI is developing the superconducting low beta cavities for proton or heavy ion accelerator using cultivated technique by electron accelerator development. Now MHI develops the superconducting Quarter Wave resonator and cryomodule for RIKEN RI beam Factory(RIBF) upgrade project[3][4] in collaboration with RIKEN and High Energy Accelerator Research Organization (KEK).

This report describes Frequency analysis of QWR cavity, forming test for cavity parts and status of preparation of manufacturing equipment for QWR cavity.

QWR CAVITY AND CRYO MODULE

In collaboration with RIKEN and KEK, MHI designs the prototyping of the superconducting QWR cavity and cryomodule. The cross section and the structure of QWR cavity are shown in Figure 1. The superconducting QWR cavity is made by pure niobium, and the formed or machined parts of QWR cavity are assembled by electron beam welding (EBW). The resonance frequency of the prototype superconducting QWR cavity for RIKEN RIBF upgrade is 75.5MHz, Height is 1055mm and inner diameter is 300mm.In order to correct a machining error and a welding error in process of manufacture, after the subassembly of cavity, it is necessary to perform adjustment processing.

Scheme drawing of the prototype cryostat for QWR cavity is shown in Figure 2. It is the design which can store two superconducting QWR cavities. An operating temperature is 4.2K and 40K Thermal shield cooled by a small refrigerator is installed. [5]

#takeshi_yanagisawa@mhi.co.jp

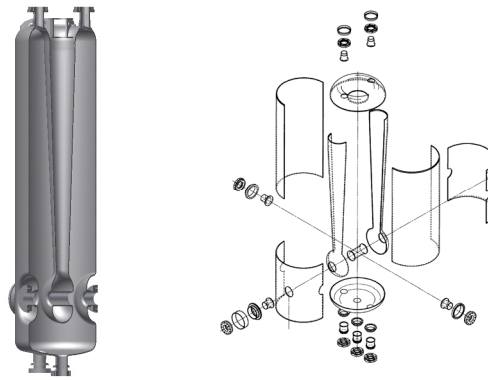

Figure 1: QWR cavity.

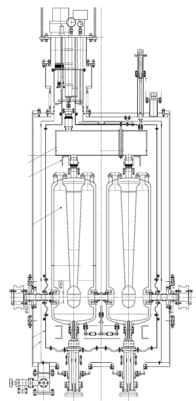

Figure 2: Cryomodule for QWR cavities.

FREQUENCY ANALYSIS OF QWR CAVITY

In order to determine the manufacturing procedure and the adjustment value of parts for frequency tuning, MHI did the frequency analysis using electromagnetic field analysis software MWS in collaboration with KEK. The model of analysis is shown in Figure 3. The following cases were assumed as a dimensional change in a process of manufacture.

A: The length change of the body lower part
B: The length change of the body upper part (A stem is also included)
C: A gap of a drift tube and the body

ISBN 978-3-95450-131-1

Case A is most important. The body lower part would be the last point of welding. If the length change of the body lower part shows the sufficient frequency sensitivity, the frequency adjustment procedure would become simple and easy.

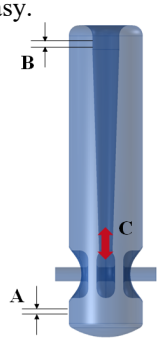

Figure 3: Calculation model of QWR.

Analysis results are shown in Figure 4. The frequency sensitivity of case A is 1.2 kHz/mm, and is about 1/60 of the sensitivity of case B and case C. For example, when a 0.3-mm error occurs into the portions of B or C in welding etc., if it adjusts only in the portion of A, about 18-mm adjustment length is needed, and it is not realistic. These results show that the case A is not enough and the frequency adjustment of QWR cavity needs the combined methods including case A.

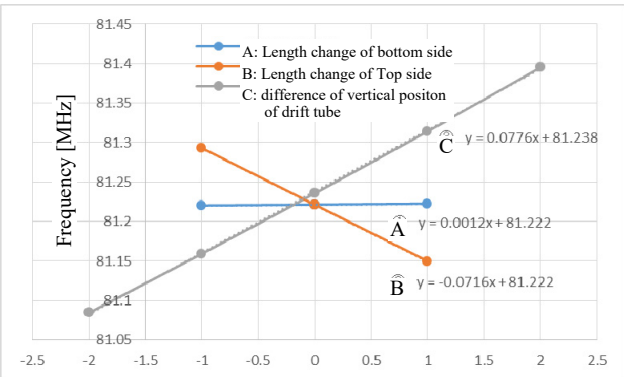

Figure 4: Results of calculation.

STEM PART FORMING TEST

The drift tube part and stem part of the center of a QWR cavity can be manufactured separately, but in order to reduce the number of welding point, we have tested to press drift tube and stem in one piece.

When MHI develops the forming method for niobium part of superconducting cavity, following procedure is generally adopted.

1) The check of the fabricability and the design of forming tools by forming analysis.
2) The forming test using test material
3) Modification of forming tools and condition
4) The forming test using niobium material.

Elastic-plastic analysis was carried out using analysis software LS-DYNA. We checked the existence of generating of a crack and wrinkles, board thickness distribution, required pressing load, forming die shape, etc (see Figure. 5). Then the forming tools ware designed.

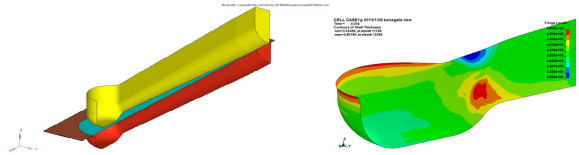

a) Model b) Contour plot of thickness

Figure 5: Forming analysis model and result.

The forming test was done using test material (aluminum), and we checked that it could fabricate without a crack and wrinkles. The drift tube part was 0.5 mm or less in accuracy, and change of thickness was ±10% or less. Although the influence of spring back was seen in the stem part, it was considered that this influence can be repaired by the correction press using a partial forming tool.

Finally, the forming test using a niobium material was carried out. This test region was around the drift tube part which was the most transformation area. We checked that it was being able to fabricate also with a niobium material without a crack and wrinkles. The accuracy of form was of 0.5 mm or less and thickness was ±15% or less (see Figure. 6).

a) Aluminum b) Niobium

Figure 6: Forming test.

QWR CAVITY PRODUCTION EQUIPMENT

MHI is planning to install equipment for surface preparation in order to integrate total process of production of superconducting RF cavity.

MHI already had the electron beam welding equipment, a vacuum heat treatment furnace, and Class10000 (ISO-7) clean room.

In addition to this equipment, the following equipment is due to be installed.

These specifications which are based on the specifications of KEK's equipment were decided after consultation with KEK.

Moreover, MHI and KEK will carry out together the verifications of equipment after introduction.

BCP Equipment

MHI will install the Buffered Chemical Polishing (BCP) equipment for the inner surface polish of QWR cavity. The acid is injected from lower port of QWR cavity, and circulated (see Figure 7).

ISBN 978-3-95450-131-1

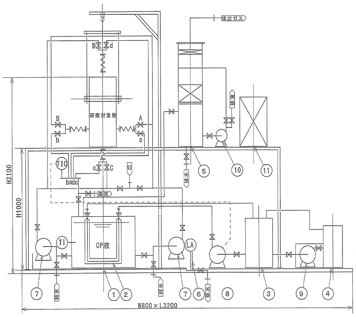

Bath:
$HF+HNO_3+H_3PO_4$
Capacity:
100 L
Temperature control:
14~20 degree C

Figure 7: BCP facility.

Ultrasonic Cleansing Apparatus

The ultrasonic cleansing apparatus for washing the cavity after BCP will be installed. The cleaning position of cavity is vertical. The rinsing liquid is pure water (see Figure 8).

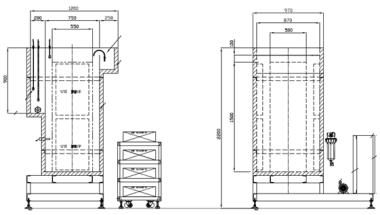

Size:
L500mm x W550mm
x H1500mm
Vibrator:
40kHz, 2000W x 4
Rinsing liquid:
Pure water

Figure 8: Ultrasonic rinsing equipment.

HPR Equipment

The High Pressure Rinse (HPR) equipment and the ultrapure water system for injecting and washing high-pressure ultrapure water on the surface in a cavity will be installed. This equipment is installed in Class10000 clean room in our factory, and the cavity after washing is taken out in the clean area as described in Figure 9.

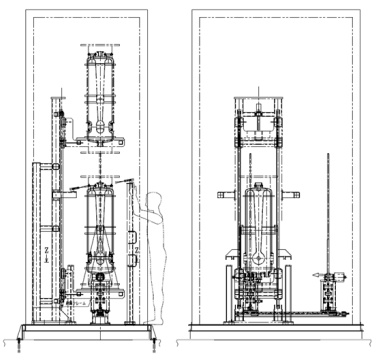

Water pressure:
10MPa (Max)
Flow rate:
10 L/min
Rinsing liquid:
Ultra-pure water

Figure 9: HPR Equipment.

Clean Area

Class100 (ISO-4) clean area is newly established in the existing Class10000 (ISO-7) clean room. Clean area passes a coherent air current from a side wall, and generates clean room (See Figure 10).

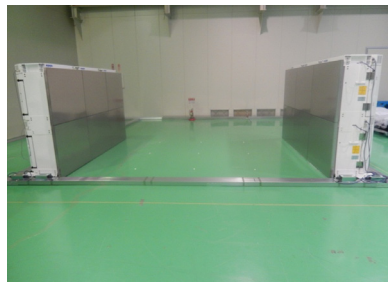

Cleanliness:
Class 100 (ISO-4)
Type:
Horizontal coherent flow from side wall
Location:
Inside of class 10000 clean room

Figure 10: Clean area.

FUTURE SCHEDULE

MHI will finish the detail design of superconducting QWR cavity and cryostat in collaboration with RIKEN and KEK and a prototype QWR cavity is manufactured. Moreover, the Introduction of new production equipment will be completed by October, 2015, and a verification examination will be carried out in collaboration with KEK after that. The inner surface-preparation work of the prototype superconducting QWR cavity is due to be done from February, 2016 after the completion of verification test.

REFERENCES

[1] T.Tsuiki, et al., " Development of superconducting RF cryomodule for STF2", 11th conference of particle accelerator society of Japan, SUP040
[2] T.Yanagisawa, et al., "Status of superconducting cavity and cryomodule development at MHI", IPAC15, THPP099
[3] K.Yamada, et al., "Conceptual design of SC Linac for RIBF-upgrade plan", SRF2013, MOP021
[4] K.Yamada, et al., "Design of a new superconducting Linac for the RIBF upgrade", Linac2014, THPP118
[5] K.Ozeki, et al., " Heat flow estimation of the cryomodule for superconducting quarter-wavelength resonator", 12th conference of particle accelerator society of Japan, THP059

ISBN 978-3-95450-131-1

LASER ABLATION ION SOURCE FOR HIGHLY CHARGE-STATE ION BEAMS

Naoya Munemoto[#, A ,B], Naoto Takakura[C], Susumu Takano[B], Isao Yamane[B], Ken Takayama[A,B,D,E]
[A)] Tokyo institute of Technology, Nagatsuta, Kanagawa, Japan
[B)] High Energy Accelerator Research Organization, Tsukuba, Ibaraki, Japan
[C)] Nagaoka University of Technology, Nagaoka, Niigata, Japan
[D)]The Graduate University for Advanced Studies, Hayama, Kanagawa, Japan
[E)] Tokyo City University, Tamadsutsumi, Tokyo, Japan

Abstract

KEK Laser ablation ion source (KEK-LAIS) has been developed to generate highly ionized metal ions and fully ionized carbon ions since 2012. Laser ablation experiment has been carried out by using Nd-YAG laser (838 mJ/pulse, 20 ns) at the KEK test bench. Basic parameters such as momentum spectrum and plasma current have been obtained. Experimental results are compared with the existing results, which had been obtained by Munemoto at BNL. In addition, the newly designed electrostatic analyzer and a plan of the future experiment are discussed.

INTRODUCTION

The High Energy Accelerator Research Organization Digital Accelerator (KEK-DA) is a 10 Hz fast-cycling induction synchrotron without a large-scale injector [1] The KEK-DA is capable of accelerating any species of ion, regardless of its possible charge state. At this moment, low-charge-state gaseous ions are provided from the X-band ECRIS [2], which is installed in the high-voltage platform.

Induction synchrotron was proposed as an alternative to a RF synchrotron. Recently an ideal induction synchrotron has been designed as a hadron driver for cancer therapies [3]. It does not use a conventional injector system consisting of RFQ, DTL, and carbon stripper foil. It is indispensable to produce full-stripped carbon ions in the ion source. Demonstration of such an ion source is strongly demanded.

The laser abrasion ion source (LAIS) has been developed at KEK since 2012, as a method to easily produce highly charged ions at low cost. R&D works on the LAIS to produce high intensity ion beam is going on based on preceding studies [4]. Plasma in the LAIS is produced as a result of interaction between the laser and a target substance, and drifts downstream to the extraction region, where an ion beam is extracted from the plasma by applying a few tens kV across the acceleration gap.

Laser irradiation on the graphite target was tried at BNL by using two laser systems of Quantel Brilliant b (1064 nm, τ=6 ns, E=750 mJ) and Ekspla (1064 nm, τ=150 ~ 550 ps, E=500 mJ) in 2013. Then a similar ion source test bench employing the Spectron SL800 was constructed at KEK in 2014 and the laser irradiation experiment has been conducted. Its first priority is to reproduce the experiment results obtained at BNL and to acquire further information.

Comparison between the existing experimental results and recent results newly obtained at the test bench of the KEK-LAIS is discussed here.

EXPERIMENTAL SETUP

Layout of the KEK-DA LAIS Chamber is depicted in Fig. 1. The chamber consists of the optical components and target unit. Graphite (IG-110) is used as a target material, which has the density of 1.77 g/cm^3, the homogeneous fine grain structure, and 5 mm in thickness. The maximum laser irradiation area on the target is 169 cm^2. All of optical components are located inside the chamber. The laser beam is guided into the chamber through the anti-reflection coated BK7 window (ϕ40 mm), reflected by the coated mirror (ϕ30 mm), and delivered to the focusing lens (ϕ25 mm, f=200 mm). Spot size on the target is controlled by adjusting the focusing lens position so as to minimize the TOF of plasma from the target to the Faraday cup (FC) (see Fig. 1). In the other ward, the laser focusing parameter is determined so that the observed velocities of particle become maximum. The laser has an incident angle of 30° against the target surface. These optical components are securely protected from vapor contamination from the target by the thin aluminum shielding. Schematic of the KEK-LAIS test bench is depicted in Fig. 2, where LAIS chamber, solenoid guide system, FC measuring system, and static electric analyzer are shown.

Vacuum of plasma chamber and FC chamber are 2×10^{-4} Pa and 2.5×10^{-5} Pa, respectively. Spectron Laser system SL800 Nd-YAG laser (λ=1064 nm, τ=20 ns, E=838 mJ) is used. If its laser profile is assumed to be Gaussian, the spot size and energy density can be calculated using following formula [5]:

#munemoto.n.ad@m.titech.ac.jp

ISBN 978-3-95450-131-1

$$d_0 \approx M^2 \frac{2f\lambda}{D} \quad (1)$$

$$I_0 = \frac{2P}{\pi d_0^2} \quad (2)$$

d_0 : spot diameter, f: focus distance, λ: wavelength,
D:incident beam diameter
I_0 : Laser power density, P : Laser power, M^2 : Gussian beam=1

The focused laser power density is about 1.42×10^{13} W/cm^2 in an ideal condition. To obtain reproducible carbon ion beams, the irradiated surface is refreshed by moving the X-Y stage by 1mm per shot. The time constant of the FC is τ=0.1 μs. The aperture of the FC is 1 cm in diameter, and the bias voltage applied to the FC is -50 V. The distance from the target to the FC is 2.6 m. As the trigger signal to measure a FC current, an output signal from the PIN photo diode (Cutoff frequency = 200-300 MHz) observing scattered laser light is used.

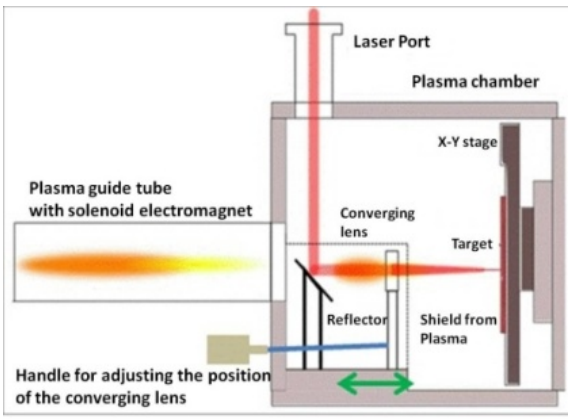

Figure 1: KEK LAIS plasma chamber layout.

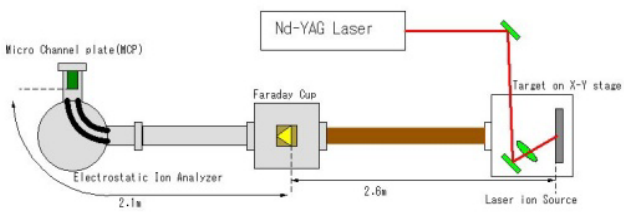

Figure 2: Set-up of the KEK LAIS experiment.

EXPERIMENTAL RESULTS

Analytical Method

Obtained data are scaled to a value at the distance of 1m from the target using following relation,

$$T \sim L \quad (3)$$
$$N \sim 1/L^2 \quad (4)$$
$$I \sim 1/L^3 \quad (5)$$

T is time of flight from the target to the FC, N is number of particle, I is beam current, L is distance between the target to the FC.

Results and Discussion

Table 1 is summarized in the obtained laser plasma parameter. Figure 3 shows the current density as a function of the drift energy, which is measured by the FC. Here, the drift energy is expressed by the following equation.

$$E_{Drift} = \frac{A}{2}mc^2 \frac{1}{c^2}\left(\frac{L}{T}\right)^2 = \frac{A}{2}mc^2\beta^2 \quad (6)$$

A : Mass number, mc^2 : 939[MeV], c : Light speed,
L : Distance from the target to the Faraday cup,
T : Time of flight, β : Relaticistic beta

$$T_e[eV] = 100\left(\frac{\bar{Z}P[GW]}{d[mm]}\right)^{\frac{7}{2}} \quad (7)$$

$$E_{kin}^{\max} \approx \frac{15}{2}(Z+1)T_e[eV] \quad (8)$$

T_e : Electron temperture, Z: Charge state, $\bar{Z}$: Averaged charge state,
d : spot size, P : Laser power

Substituting the experimentally obtained largest drift energy into Eq. (8), we have the plasma temperature T_i. Substitution of this T_i into Eq. (7) gives the spot size of 223 μm [6]. Meanwhile, the spot size derived from Eq. (1) is 19.4 [μm]. We find a fact that the factor M^2 is around 11 and the laser is not focused at its focal point as expected.

The experimental results obtained at KEK and BNL are summarized together in Figs. 4 and 5, where the maximum drift energy and the current density are given as functions of the laser power, respectively. From Fig. 4 we know that the larger the laser power, the higher plasma energy is obtained. However, the plasma energy decreases beyond 1 TW. This region of the laser power density is outside the region where classical absorption is dominant and close to the region where non-linear forces appear [7, 8]. It is found in Fig.5 that the current density decreases below 100 GW in contract to our expectation. This may be attributed to the fact that the laser of 850[mJ] 20[ns] employed at KEK is not well focused and the produced plasma is not sufficiently ionized.

Table 1: The Obtained Laser Plasma Parameter

Max plasma current densty	18.8 [mA/cm^2]
Fastest arriving time	3.28 [μs]
Fastest drift energy	5.72[keV]
Pulse width(half width)	0.85 [μs]
Drift energy of centre	3.57 [keV]
Half width of drift energy	+1.05~-0.56 [keV]

ISBN 978-3-95450-131-1

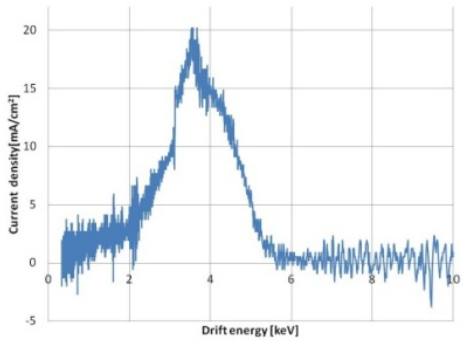

Figure 3: Current density vs. Drift energy (KEK LAIS).

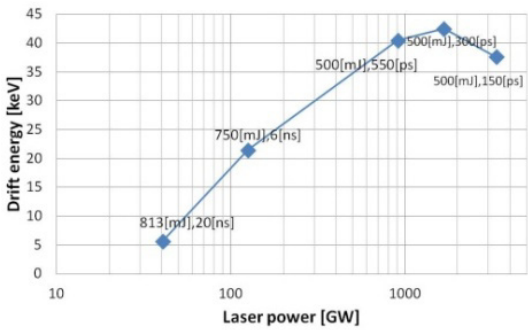

Figure: 4 Drift energy vs. Laser power.

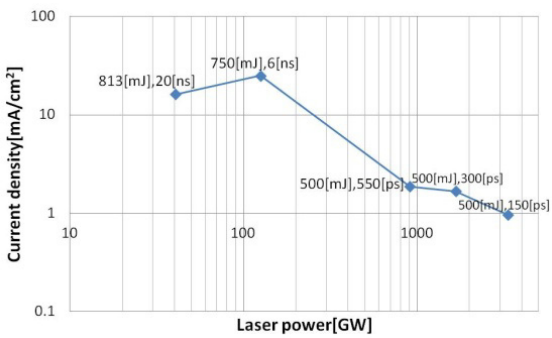

Figure 5: Current density vs. Laser power.

DEVELOPMENT OF ELECTROSTATIC ANALYZER

Figure 6 shows the newly designed electrostatic analyzer, which is used to obtain the charge-state spectrum with a good accuracy. Two 90 degree electrode plates with the radius of 15.3 cm and 15.8 cm are placed in parallel. Slit plates are placed at the entrance and exit of the parallel plate region (at 5 mm upstream and 5 mm downstream). Their aperture is 0.5 mm in the transverse direction and 5 mm in the vertical direction. The simulation software CST has been used for analysing the performance of the electrostatic analyzer system. Orbits of Carbon 6+ macro particles 10,000, which have a energy spread of 10 % and a tilt in the moving direction of 20 degrees, were tracked under the 3D entire field distribution.

The centre energy of a fraction of macro particles that can propagate through the downstream slit is determined by the following equation,

$$V_2 - V_1 = 2\left(\ln\frac{R_2}{R_1}\right)\frac{T}{Z} \quad (9)$$

V_i : Voltage applied to the electrode plate

R_i: The radius of the electrode

T: Drift energy of plasma, Z:Charge state

It is found in Fig. 7 that the simulation result with respect to the analyzed average energy agrees with the analytical solution well. The energy resolution was within 2 % (see Fig. 8).

FUTURE PLAN

- Analysis of the charge state distribution using the electrostatic analyser discussed here.
- Emittance measurement.
- Optimization of the solenoid magnetic field applied to the laser plasma.
- Pre-acceleration with 20 kV, post-acceleration with 180 kV, beam transport thorough the LEBT, and injection into the KEK-DA.

CONCLUSION

The Laser ablation experiment using the laser SL-800 has been carried out and their results have been compared with the existing results. It turns out that the obtained plasma is not sufficiently heated, because the laser pulse is too long. Numerical simulations to confirm the operational performance of the assembled electrostatic analyzer has been done. They suggest that our electrostatic analyzer will work as expected.

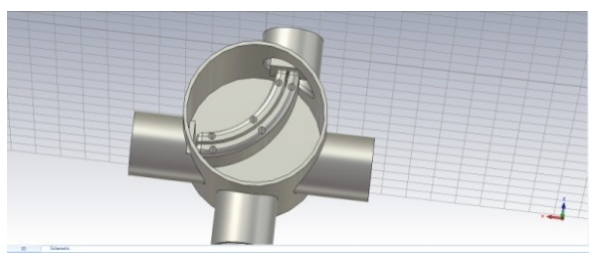

Figure 6: Simulation model of the electrostatic analyzer.

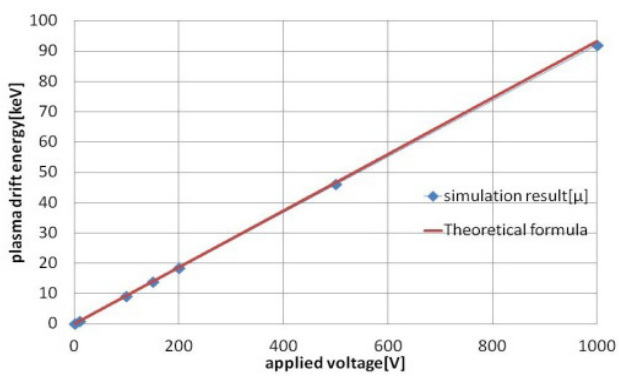

Figure 7: Averaged drift energy vs. Applied voltage.

ISBN 978-3-95450-131-1

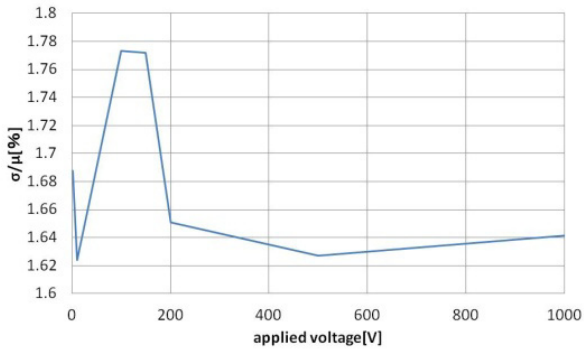

Figure 8: Beam resolution vs. Applied voltage.

REFERENCES

[1] K.Takayama *et al., Phys. Rev. ST-AB* **17,** 010101 (2014).
[2] Leo Kwee Wah et al., in *Proceedings of ECRIS2010*, August 23-26, 2010 Grenoble, France, TUPOT15.
[3] Leo Kwee Wah et al. submitted to Phys. Rev. ST-AB (2015).
[4] N.Munemoto et al., *Rev. Sci. Inst.* **85**, 02B922 (2014)
[5] A. E, Siegman LASERS Sec17.2 .
[6] I. V. Roudskoy Laser and Particle Beams **14**, 369 (1996).
[7] P.Mora *Phys.Fluids,* **25**,1051(1982).
[8] L. Láska et al., *Appl. Phys. Lett.* **86**, 081502 (2005).

ISBN 978-3-95450-131-1

DEVELOPMENT OF THE NEW DECRIS-PM ION SOURCE.

V. Bekhterev, S. Bogomolov, A. Efremov,FLNR, JINR, Dubna, Moscow Reg., Russia
N. Konev, ITT-Group, Moscow, Russia

Abstract

Super-heavy-element factory is under development at the Flerov Laboratory for Nuclear Reactions, JINR, Dubna. The factory will include DC-280 cyclotron, which will be equipped with two 100 kV high voltage platforms. All-permanent magnet ECRIS will be installed on one of the platforms. The request for the source is a production of medium mass ions with A/q=4÷7.5 such as $^{48}Ca^{8+}$. Results of the detailed design of the DECRIS-PM ion source will be presented.

INTRODUCTION

One of the basic scientific programs which are carried out at the FLNR is a synthesis of new elements requiring intensive beams of heavy ions. To enhance the efficiency of experiments for next few years it is necessary to obtain accelerated ion beams with the following parameters:

Ion energy	4÷8 MeV/n
Ion masses	10÷238
Beam intensity (up to A=50)	10 pμA
Beam emittance	≤ 30 π mm×mrad
Efficiency of beam transfer	> 50%

These parameters have formed the base for the new cyclotron DC-280 [1]. Some expected beam intensities are collected in Table 1.

Table 1: DC-280 Cyclotron - Basic Technical Parameters

Ion	Intensity from ion source μA	Intensity on physical target pps
$^{20}Ne^{3+}$	150	1×10^{14}
$^{40}Ar^{7+}$	300	1×10^{14}
$^{48}Ca^{8+}$	150	5×10^{13}
$^{58}Fe^{10+}$	125	4×10^{13}
$^{136}Xe^{23+}$	150	2×10^{13}
$^{238}U^{40+}$	1	1×10^{11}

The axial injection system of the DC-280 cyclotron will include two high voltage platforms which will allow for efficient injection of ions from helium to uranium with an atomic mass to charge ratio in the range of 4÷7. Each HV-platform will be equipped with the low power consuming ECR ion source. For production of ions with the medium masses (from He to Kr) the all permanent magnet (PM) ECR ion source will be used. In this paper we report the design of the magnetic system of the new DECRIS-PM ion source.

SOURCE DESIGN

Many good performance all-permanent magnet ECRISs have been built around the world: NANOGAN series [2], BIE series [3], LAPECR2 [4] and others. The main advantages of all permanent magnet ECRISs are low power consumption, low pressure in the cooling water system, simplified operation, etc. However there are few significant drawbacks of all permanent magnet ECRISs. First of them is the fixed distribution of the magnetic field and comparatively low field strength. Thus, the designed magnetic configuration should be optimized for the desired operation mode from the very beginning. Another drawback is strong mechanical force acting on the individual parts of the system. As a result the correction of the magnetic field after the assembly of the magnetic system is practically impossible without the degaussing of it.

Some deviations from the required field distribution can occur for many reasons. The magnetic material itself has scatter in parameters of up to 5%. Furthermore, the magnetic rings that form the axial magnetic field consist of several blocks. In calculations of the magnetic field it is almost impossible to take into account the influence of gaps between individual blocks. Figure 1 illustrates this problem. The figure shows the distribution of the magnetic field in front of one of the hexapole poles which is made of five blocks of identical magnetic material. With the gaps of about 0.1 mm the oscillations in the magnetic field measured at a distance of 3 mm from the pole are around 10%.

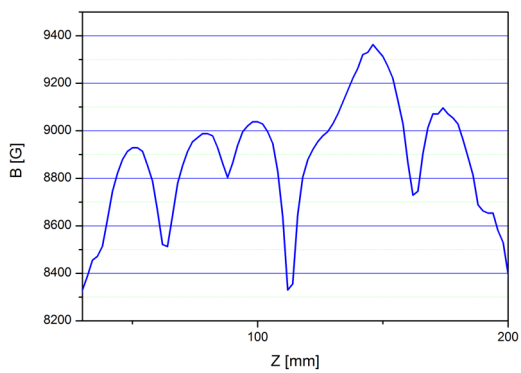

Figure 1: Measured magnetic field distribution along the hexapole pole.

For this reason it is desirable to provide a possibility for correction of the field distribution in the case of finding an

ISBN 978-3-95450-131-1

inconsistency between the measured and desired magnetic fields.

The operating frequency selected to be 14 GHz for the source. The corresponding values of B_{inj}, B_{min} and B_r were chosen according to scaling laws for the axial magnetic field configuration [5]. The injection magnetic field maximum was chosen to be around 1.3 T to have a reasonable weight of the system and basing on the earlier experience of conventional ion sources. The desired parameters of the magnetic system of DECRIS-PM are listed in Table 2.

Table 2: Design Parameters of DECRIS-PM

Frequency	**14 GHz**
B_{inj}	≥ 1.3 T
B_{min}	0.4 T
B_{extr}	1.0 ÷1.1 T
B_r	1.05÷1.15 T
Plasma chamber internal diameter	70 mm

By further consideration of the different magnetic structures we came to the version which fully satisfies the stated objectives. The structure is shown in Fig. 2. The magnetic structure consists of five large 36-segmented axial magnetic rings with corresponding axial or radial magnetization.

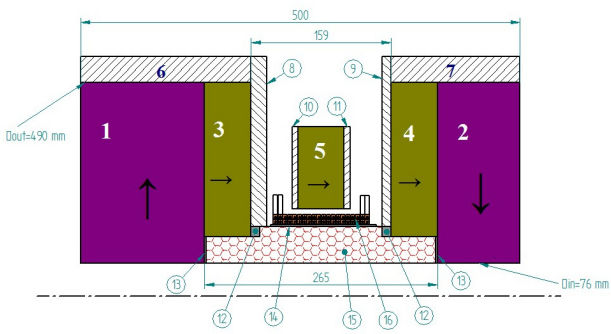

Figure 2: Magnetic structure of DERIS-PM. 1÷5 – PM rings; 6, 7 – soft iron rings; 8÷11 – soft iron plates, 12÷14, 16 - auxiliary elements, 15 – hexapole.

Permanent magnet (PM) rings at the extraction and at the injection sides are inserted into the soft iron rings which slightly increase the magnetic field peaks and strongly suppress the stray field around the source. The soft iron plates around the PM rings with the axial magnetization play an important role in the final magnetic field distribution. The effect of thickness of one of the plate on the B_{min} is shown on Fig. 3. By changing the thickness, it is possible to tune the minimum field when necessary.

Figure 4 shows the axial magnetic field distribution of DECRIS-PM. A distance between the injection and

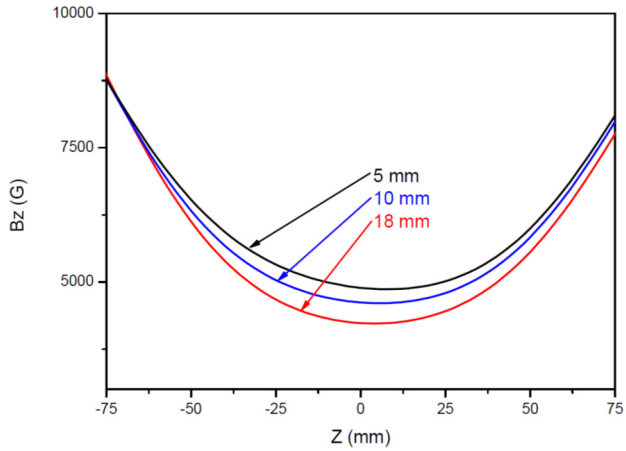

Figure 3: The effect of the soft iron plate thickness.

extraction maxima is 24.5 cm. The field is changing its sign and reaching 0.8 T at extraction gap, which influences the ion beam extraction and transport.

The magnetic field of DECRIS-PM is the superposition of axial and hexapole fields similar to conventional ECRIS. The hexapole is a 24-segmented Halbach structure magnet which provides a radial field of 1.05 T at the inner wall of the Ø70 mm ID plasma chamber. The result of 3D magnetic field calculation is shown in Fig. 6. The ECR zone length is around 7 cm, the $2B_{res}$ zone is closed according to the commonly accepted requirements.

The total weight of the permanent magnets is around 525 kg and total weight of the system is about 1000 kg.

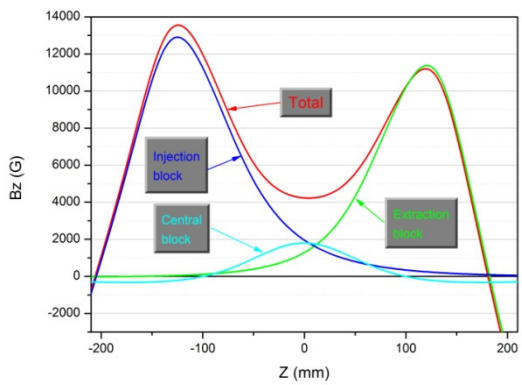

Figure 4: Axial magnetic field distribution of DECRIS-PM.

Other specific feature of the source is an additional coil placed at the centre of the structure between the hexapole and central PM ring. The coil will be used to tune the Bmin value during the source operation. According to [6], the optimal value of Bmin depends on the level of the injected microwave power and it should be changed on- line. Use of such the tuning can assist in improving the source performance.

The coil consumes less than 1.5 kW of electric power and shares the cooling system with the plasma chamber. The influence of the coil on the Bmin value is shown in

ISBN 978-3-95450-131-1

Fig.5. When the coil is excited to maximum current, the Bmin value is shifted by ±0.05 T depending on the current polarity.

The assembling procedure is planned to be the following: first, the extraction and injection groups of magnets (see Fig. 4) are assembled, and then the axial magnetic field in each group is measured separately. The total magnetic field is calculated basing on the real magnet properties. When necessary, dimensions of soft iron component are defined as the final step.

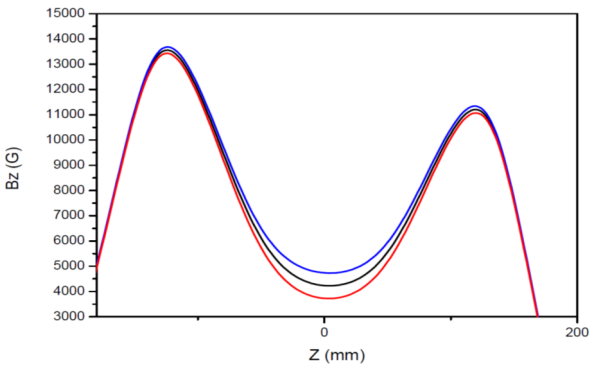

Figure 5: Coil effect.

PRELIMINARY MAGNETIC FIELD MEASUREMENT

We started the preliminary magnetic field measurements in the beginning of September 2015. The

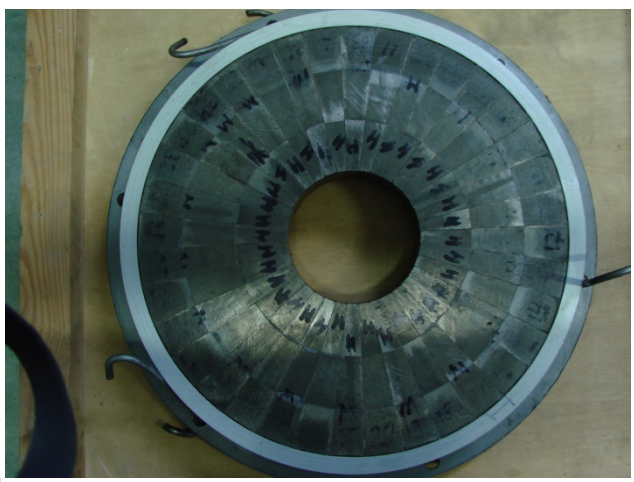

Figure 6: Axially magnetized ring.

axial magnetic field distribution of the axially magnetized ring (see Fig. 6) is presented on Fig. 7. The results of measurement and calculations are in good agreement: calculated field in maximum is 0.290 T and the same measured is 0.298 T. Manufacturing of the magnetic system is planned to be finished in the beginning of October 2015.

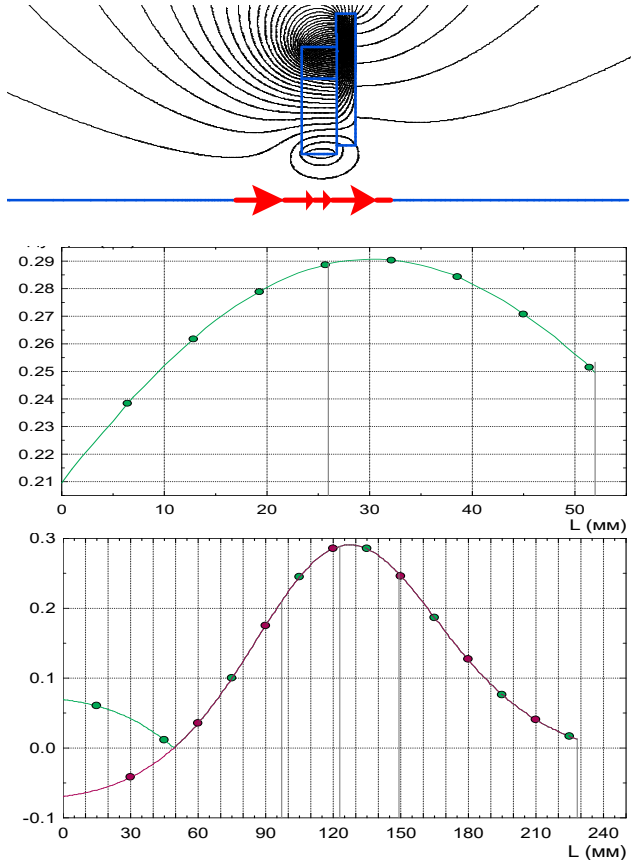

Figure 7: Calculated (top) and measured (bottom) magnetic field distribution.

REFERENCES

[1] G. Gulbekyan et. al., Development of FLNR JINR heavy ion accelerator complex in the next 7 years. New DC-280 cyclotron project, Proceedings of IPAC 2011, San Sebastián, Spain, 2011, WEPS082, p. 2700.

[2] C. Bieth, J.L. Bouly, J.C. Curdy, S. Kantas, P.S Sole, and J.L. Vieux-Rochaz, Rev. Sci. Instrum. 71, 899 (2000).

[3] Dan. Z. Xie, Rev. Sci. Instrum. 73, 531 (2002).

[4] L.T. Sun et. al., Nucl. Instr. Meth., B 263 (2007) 503–512.

[5] 2. S. Gammino, G. Ciavola, L. Celona, D. Hitz, A. Girard, and G. Melin. Rev. Sci. Instrum. 72, 4090 (2001).

[6] T. Nakagawa, M. Kidera, Y. Higurasi, J. Ohnishi, T. Kageyama, T. Aihara, A. Goto, Y. Yano, Magnetic field configuration effect and new ECRISs for RIKEN RIBF project, Proceedings of the 17th International Workshop on ECR ion sources and Their Applications, IMP-Lanzhou, China, September 17 – 21, 2006, p. 23

ISBN 978-3-95450-131-1

NEW DUAL-TYPE ELECTRON CYCLOTRON RESONANCE ION SOURCE FOR A UNIVERSAL SOURCE OF SYNTHESIZED ION BEAMS*

Y. Kato,# F. Sato and T. Iida, Osaka Univ., 2-1, Yamada-oka, Suita-shi, Osaka, Japan

Abstract

A new dual-type source has been constructing on the basis of electron cyclotron resonance (ECR) plasma for producing synthesized ion beams in Osaka Univ. Magnetic field in the 1st stage consists of all permanent magnets, *i.e.*, cylindrically comb shaped one, and that of the 2nd stage consists of a pair of mirror coil, a supplemental coil and the octupole magnets. Both stage plasmas can be individually operated, and produced ions which energy controlled by large bore extractor also can be transported from the 1st to the 2nd stage. Fundamental operations and effects of this source, and analysis of ion beams and investigation of plasma parameters are conducted on produced plasmas in dual plasmas operation as well as each single operation.

INTRODUCTION

A new concept on magnetic field of plasma production and confinement has been proposed to enhance efficiency of an electron cyclotron resonance (ECR) plasma for broad and dense ion beam source under the low pressure [1]. We make this source a part of new dual-type ion source for the 1st stage. We are also constructing the large bore 2nd stage for synthesizing ions, extraction and beam analysis [2]. We investigate feasibility and hope to realize the device which has wide range operation window in a single device to produce many kinds of ion beams, *e.g.*, from multiply charged, to molecular, cluster ions, nanotube, fullerenes, including impurities trapped as iron-endohedral fullerene, *etc.*, as like to universal source based on ECR ion source (ECRIS). We consider to being necessary to device that is available to individual operations with different plasma parameters, and then obtain concept of dual ECRIS from relevant previous works.

EXPERIMENTAL APPARATUS

The top view of the dual-type ECRIS and the beam line for the ion extraction and the analysis are shown in Fig.1. The 1st stage of the device is large-bore one using cylindrically comb-shaped permanent magnets, *i.e.* octupole magnets with a pair of ring magnets whose polarity is opposite each other [3-5]. Two frequencies microwaves are supplied to the plasma chamber (200mm in diameter and 320mm in length) [6]. Incident and reflected microwaves are tuned by the stainless steel/aluminum plate tuner. We are investigating positional dependence of this tuner to ion beam currents and plasma parameters in detail [7].

Ion produced in the 1st stage is extracted and transferred to the 2nd stage by the large bore extractor consisted of three electrode plates CE1-3 ($V_{CE1\text{-}3}$) with multi-holes (200 holes of 8mm in diameter) and the effective diameter 154mm, and the ion beam current $I_{FCx,y}$ is measured by two faraday cups. The typical extraction voltages range within about 1.0kV.

The magnetic configuration of the 2nd stage is mirror field formed by the coil A, B, and C, and superimposed the octupole magnetic field by permanent magnets [8]. The ECRIS performance is very sensitive to shape, intensity, and gradient nearby the ECR zone around bottom of mirror field, and we are available to control them precisely by the coil C [8]. The plasma chamber of the 2nd stage is about 160mm in diameter and 1000mm in length. 2.45 GHz microwaves are launched by the Ti rod antenna from the side wall. The single aperture extractor assembly is set at the mirror end plate with the aluminium plate for the microwave mode. The extractor consists of three electrodes, *i.e.*, the plasma electrode PE, the mid-electrode E1, and the extractor electrode E2. The typical extraction voltage (V_{PE}) and the extractor voltage (V_{E2}) are usually 10kV and the ground, respectively. The mid-electrode voltage (V_{E1}) is used on optimizing extraction of each ion species. We also install the ion-beam irradiation system (IBIS) in the downstream beam line for beam profiles, emittance measurements, and various beam-material applications.

In the both stages, plasma parameters and pressures are measured by Langmuir probe and Bayard-Alpert (B-A) gauges. The electron density n_e and the temperature T_e are measured from the probe current I_p and voltage V_p characteristics. We have also estimated electron energy distribution function (EEDF) from these probe data [9].

We confirmed that the ion beam is flowed from the 1st to the 2nd stage. From the result, we can become possible to conduct experiment at least on the dual-type ECRIS.

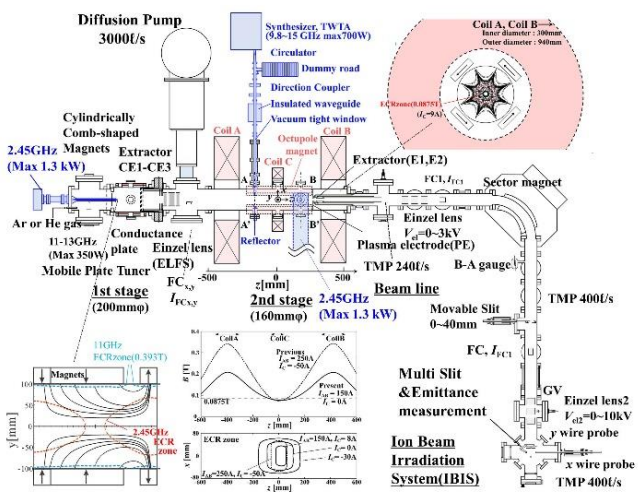

Figure 1: Schematic drawing of the top view of the new dual-type ECRIS (Osaka Univ.).

*Work supported by Operating Grants of Osaka Univ. as National University Corporation in Japan.

#kato@eei.eng.osaka-u.ac.jp

ISBN 978-3-95450-131-1

EXPERIMENTAL RESULTS AND DISCUSSIONS

Typical Experimental Results on the 1st Stage

Beam current profile control by multi-frequency microwaves We have investigated the effect of launching multi-frequencies microwaves to ECRIS plasma on constructing ion beams. In the 1st stage, 2.45 GHz and 11–13 GHz microwaves can be supplied to plasma chamber individually and simultaneously. The resonance zones of 2.45 GHz and 11–13 GHz microwaves are located at the center and the peripheral regions of the chamber, respectively. It has been found that controlling beam profiles is available by feeding multi-frequencies microwaves and adjusting their powers to the ECRIS [6].

Beam current optimization with mobile plate tuner position The $I_{FCx,y}$ from the 1st stage and ion saturation current I_{is} in the 1st stage plasma oscillate with respect to the position of the mobile plate tuner. It is clear that the $I_{FCx,y}$ coincides reproducibly with the I_{is} in both cases of multi-frequency and each single frequency. The variation level and the number of peaks in 11 GHz are larger than those of 2.45 GHz [7].

Selective microwave modes excitation for efficient ECR It is known the beam current is affected by the position of the mobile plate tuner in the vacuum chamber as like a circular cavity resonator. The $I_{FCx,y}$ and the I_{is} change periodically in moving the position of the mobile plate tuner. For each microwave mode TE_{nm}, we analyse the electric field distribution and the microwave power absorbed by electrons per unit area S_{nm}. We obtain that a new guiding principle for the number of efficient microwave mode is selected to fit to that of the multipole number of the comb-shaped magnet for 11 and 2.45 GHz We made a new mobile plate tuner from the theoretical analysis. We measured the $I_{FCx,y}$ and the I_{is} in using it, and we obtained excitation of selective microwave modes to enhance ECR efficiency [10].

Typical CSDs of beams from the 1st stage We investigate the CSDs of the 1st stage plasma on the dual-type ECRIS for first time. We conduct measurement of them by extracting ion beam from the 2nd stage where there is no plasma but exits magnetic mirror fields. We can observe the Ar charge state up to q=4, despite all magnets and large bore source. The values of the beam currents increase significantly by $V_{EC1,2}$. In addition to increase of the ion beam current, sifts of the CSD spectrum by extracting from the 1st to the 2nd stage (<1kV) are observed on the basis of the V_{PE}, usually about 10kV. Ion beam currents is loosely proportional to the $V_{EC1,2}$, but each fraction is almost constant at their various values [11].

Typical plasma parameters in the 1st stage We measure the profiles of the n_e and the T_e in the 1st stage plasma corresponding to mobile plate positions. The n_e at the peak position is much larger than one at the minimum positions, while the T_e is almost same value. It is considered enhancement of the ion beam currents $I_{FCx,y}$ by excitation of selective microwave mode is caused by increase of the n_e, not rather one of the T_e as similar results in the cases of 11-GHz frequency microwaves [7]. On basis of plasma theory, I_{is} is proportional to n_e and $T_e^{1/2}$. Therefore increments of the $I_{FCx,y}$ are strongly due to the n_e inside the ECRIS plasma, and selective mode excitation of microwaves is useful to enhance n_e values and the $I_{FCx,y}$.

Typical Experimental Results on the 2nd Stage

Beam currents affected by shape of ECR zones The total ion beam currents I_{FC1} extracted from the 2nd stage are measured at just downstream of extractor assembly and einzel lens against various Coil C currents I_c, *i.e.* various shapes of ECR zone. According to the typical dependence, the maximum current is usually obtained around I_c = 10A, where the minimum ECR zone is constructed around the mirror bottom with the mirror coil A, B currents $I_{A,B}$=150A. The I_{FC1} decreases, as the I_c decreases. But the 2nd peak is recognized again around I_c~-30A. Now we are paying attention to this phenomenon as a new heating mechanism as we will discuss later.

Typical CSDs of beams from the 2nd stage We investigated the CSD of the extracted ion beams I_{FC} from the 2nd stage and their dependence on the intensity of the I_C corresponding to the above mentioned results. The $Ar^{3+\sim8+}$ beam currents attain their peak values at the minimum ECR zone constructing around the mirror bottom at I_C~5A in the case of I_{AB}=150A and I_c~0A in that of I_{AB}=170A, respectively. In the case of I_{AB}=150A, the 2nd peak of the I_{FC1} around I_C~-30A is found to be corresponding to the 2nd peak of Ar^+ and Ar^{2+}. These experimental results will be recalled in the consideration of the accessibility condition.

ECR efficiency by microwave mode analysis We have already proposed a concept for enhanced efficiency of the ECR plasma for production of multicharged ions by constructing a microwave cavity, and then making the maximum electric field correspond to the ECR zone [12]. We investigate available microwave modes in circular cavity resonator. Microwave modes existing are mainly several transvers electric modes, *i.e.* TE_{01}, TE_{11}, and TE_{21}. It is found that the 1st peak of the I_{FC1} against the I_C coincides to the each peak position of the S_{nm} for each TE_{nm} mode, except for the decreasing behaviours. But the 2nd peak cannot be explained by discussion of microwave modes including the 2nd harmonics ECR.

Typical plasma parameters in the 2nd stage After preparation of the electricity and cooling system for mirror coils to some extent 60% for the maximum in the 2nd stage, we are available to sustain discharge in low pressures ($10^{-4\sim-5}$Pa). First beam have been successfully extracted at November 2013. We can measure and observe the ECR plasma continuously on various intensities of the magnetic field. The n_e is over the cut-off density ($7.4x10^{16}m^{-3}$) for 2.45GHz microwave, and then it suggests propagation of whistler modes. Because the measured n_e is no longer over cut-off density of launched microwave frequency, we must consider dispersion relations and propagation of waves in the magnetized plasma, *i.e.* accessibility condition of electromagnetic and electrostatic waves in the ECR plasma.

ISBN 978-3-95450-131-1

We use these data for estimating accessibility condition of wave propagation in the ECR plasma in changing various magnetic fields.

Accessibility condition of microwaves in ECR plasma and additional heating possibility We investigate the accessibility condition of waves in the ECR plasma by using profiles of the magnetic field and the n_e in the 2nd stage of the dual-type ECRIS at various I_C values. We estimate ray traces of propagating microwaves launched from the antenna with various direction in real spaces in the 2nd stage chamber and in the space of Clemmow-Mullaly-Allis (CMA) diagram corresponding to the former trace [13]. There exists four principle modes, *i.e.*, the ordinary (O-made), the extraordinary (X-mode), the right hand polarization (R-mode), and the left hand polarization (L-mode) waves, of waves propagations in the magnetized plasma [13]. It is found that the 2nd peak of the I_{FC1} and their behaviour coincides the appearance of the upper hybrid resonance (UHR) and their development and decrease of the ECR efficiency. The UHR may be strong candidate for explanation of the experimental results. It is suggested that there are some room for additional enhancing efficiency of the electron heating on ECR, and then moreover enhance production of multicharged ions.

Preliminary Experimental Results on Effects of Dual Operation and Each Single Operation

We investigated the CSD in the case of both stages and each single plasma operations. We have been conducting preliminary experiments on investigating effects of dual operation and each single operation. Produced ions in the 1st stage can be transported to the 2nd stage with imparted energy (<1kV) by the large bore extractor. It is found that drastic changes in the CSD's of the 2nd stage plasma with or without the flow from the 1st stage plasma at the extreme low microwave power in the 2nd stage. As the extraction energies from the 1st stage increase gradually, the I_{FC} increase, and we use to observe the splitting spectrum for each Ar^{q+} beams as already mentioned [11].

New Applications on the Dual-Type ECRIS, Future Planning, and Perspective

We will investigate both stage plasmas' characteristics and the effects of the dual-type ECRIS. We will also investigate new wave heating/cooling methods in the device as also a universal theme in ECRIS in near future.

It is also found that the more pressure difference between the 1st and the 2nd stage are needed for applications.

We have been developing the pure vapour sources for fullerene and iron. We have succeeded in producing iron ion beam from the 1st stage and multi-charged fullerene beams from the 2nd stage. We will try to synthesize iron-endohedral fullerene by using this dual-type ECRIS in near future. Furthermore we are planning to implant many kind ion beams to materials having potential and new functionality, *e.g.*, visible reaction of photocatalytic titanium dioxide and strontium titanate, *etc.*, in future material beam-processing.

ACKNOWLEDGMENT

The authors would like to wish to thank Dr. A. Kitagawa and Dr. M. Muramatsu, Professor. A. G. Drentje, KVI, Professor Y. Yoshida and Dr. T. Uchida, Toyo Univ., and Dr. S. Biri and R. Rácz, ATOMKI for continuous encouragements and helpful discussions. The authors also would like to wish to thank gratefully all of graduates, past member of their group staff for preparation and dedicated assistance.

REFERENCES

[1] Y. Kato *et al*, in Proc. HIAT09, Venice, Italy, 2009, p326, http://accelconf.web.cern.ch/AccelConf/HIAT2009/papers/e-03.pdf

[2] Y. Kato, Y. Kurisu, D. Nozaki, K. Yano, D. Kimura, S. Kumakura, Y. Imai, T. Nishiokada, F. Sato, and T. Iida, Rev. Sci. Instrum., 85, 02A950-1-3(2014).

[3] T. Asaji, Y. Kato, F. Sato, T. Iida, and J. Saito, Rev. Sci. Instrum., 77, 113503-1-6(2006).

[4] Y. Kato, T. Satani, T. Asaji, F. Sato, and T. Iida, Rev. Sci. Instrum., 79, 02A323-1-3(2008).

[5] Y.Kato, H. Sasaki, T. Asaji, T. Kubo, Fuminobu Sato, T. Iida, AIP Conference Proceeding 866, 373-376(2006); Y. Kato, T. Satani, Y. Matsui, T. Watanbe, M. Muramatsu, K. Tanaka, T. Asaji, A. Kitagawa, F. Sato, and T. Iida, AIP Conference Proceeding 1066, 348-351(2008).

[6] Y.Kato, T. Watanabe, Y. Matsui, Y. Hirai, O. Kutsumi, N. Sakamoto, F. Sato, T. Iida, Rev. Sci. Instrum., 81, 02A313-1-3(2010).

[7] Y. Kurisu, R. Kiriyama, T. Takenaka, D. Nozaki, F. Sato, Y. Kato, T. Iida, Rev. Sci. Instrum., 83. 02A310-1-3(2012).

[8] K. Yano, Y. Kurisu, D. Nozaki, D. Kimura, Y. Imai, S. Kumakura, F. Sato, Y. Kato, and Toshiyuki Iida, Rev. Sci. Instrum., 85, 02A937-1-3(2014).

[9] S. Kumakura, Y. Kurisu, D. Kimura, K. Yano, Y. Imai, F. Sato, Y. Kato, and T. Iida, Rev. Sci. Instrum., 85, 02A925-1-3(2014,).

[10] D. Kimura, Y. Kurisu, D. Nozaki, K. Yano, Y. Imai, S. Kumakura, F. Sato, Y. Kato, and T. Iida, 85, 02A938-1-3(2014).

[11] Y. Kato, D. Kimura, K. Yano, S. Kumakura, Y. Imai, T. Nishiokada, F. Sato, and T. Iida, AIP Conference Proceeding 1109, 6940031-1-4(2014).

[12] Y.Kato, H. Furuki, T. Asaji, F. Sato, and T. Iida, Rev. Sci. Instrum., 77, pp.03A336-1-4(2006).

[13] T. H. Stix, "*Waves in plasmas*", AIP, 1992, Chap. 2.; R. Geller, "*Electron Cyclotron Resonance Ion Sources and ECR plasma*", Institute of Physics Publishing, 1996, Chap. 2.; M. A. Lieberman and J. Lichtenberg, "*Principles of Plasma Discharges and Material Processing*", 2nd Ed., Wiley-Interscience, 2005, Chap. 4 and 13.

ISBN 978-3-95450-131-1

SUPPLY OF METALLIC BEAMS FROM RIKEN 18-GHz ECRIS USING LOW-TEMPERATURE OVEN

K. Ozeki#, M. Kidera, Y. Higurashi, T. Nakagawa, RIKEN Nishina Center, Saitama, Japan

Abstract

At the RIKEN 18-GHz ECR ion source, in order to enhance the intensity and stability of medium-heavy metallic beams, a low-temperature oven has been put into practical use. The supply methods, operational test results, and operational statuses for several metallic beams are reported herein.

INTRODUCTION

At the RIKEN Radioactive Isotope Beam Factory (RIBF) [1], beams of medium-heavy metals, such as ^{23}Na, ^{24}Mg, ^{27}Al, ^{48}Ca, ^{58}Ni, and ^{70}Zn, are supplied from the RIKEN 18-GHz electron cyclotron resonance ion source (ECRIS) [2]. Until recently, these metallic beams were produced using the rod-insertion method (except for Ni beams, which were produced using the Metal Ions from VOlatile Compounds (MIVOC) method [3]). In this method, a sintered rod of metallic oxide (fluoride for a Na beam) is inserted directly into the plasma generated in the ECRIS. The rod is heated by the plasma, and the metallic atoms are evaporated and fed into the plasma. The typical intensities of the $^{48}Ca^{10+}$ and $^{70}Zn^{15+}$ beams produced using this method were slightly below 20 eμA. However, the ECRIS required frequent tuning to maintain constant beam intensity. Therefore, we had tried to produce beams of medium-heavy metals using a low-temperature oven, which was already in use at several facilities [4-7], with the goal of enhancing the beam intensity and stability.

In this contribution, the supply methods and conditions, operational test results, and operational statuses of beam supplies to the experiments for ^{48}Ca, ^{70}Zn, and ^{27}Al beams are reported. The temperature dependences of the vapor pressures of Ca, CaO, Zn, ZnO, and Al, which are obtained obtained from Ref. [8], are shown in Fig. 1.

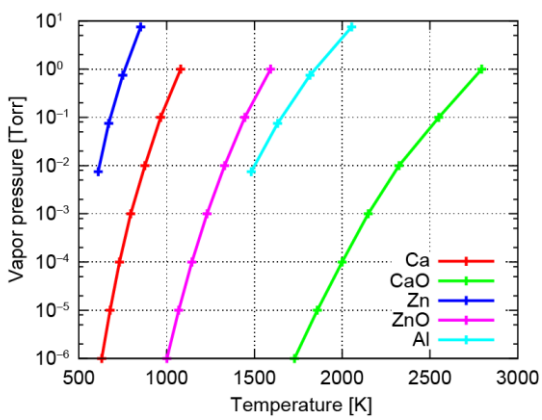

Figure 1: Temperature dependences of vapor pressures of Ca, CaO, Zn, ZnO, and Al (obtained from Ref. [8]).

#k_ozeki@riken.jp

STRUCTURE OF LOW-TEMPERATURE OVEN

The details of the structure of the low-temperature oven is described in Ref. [9]. It has been found that the oven temperature can be increased up to about 1000°C without damaging the oven. The crucible and Pt wire are replaced after each operation.

CALCIUM BEAM

For the supply of a ^{48}Ca beam, $CaCO_3$ which is highly enriched with ^{48}Ca (from a natural abundance of 0.2% to 70%-80%) is prepared. $CaCO_3$ is reduced to CaO by heating $CaCO_3$ to above 900°C. A mixture of CaO and Al powders is placed in the crucible. Then, the low-temperature oven is installed in the ECRIS. By heating the material to about 850°C, metallic Ca is produced through the following reductive reaction:

$$3CaO + 2Al \rightarrow 3Ca + Al_2O_3.$$

Ionized helium gas is used to generate the plasma.

Because the material is so expensive, it is quite important to reduce its consumption rate. Therefore, we adopted the so-called “hot liner” method [5,10,11]. In this technique, the inner surface of the plasma chamber in the ECRIS is thermally decoupled from the cooling water jacket to be kept at a high temperature heated by the plasma. Using this method causes the metallic atoms attached to the inner surface to re-evaporate. The details of operational tests that confirm the effectivity of using a hot liner, as well as the effectivity of applying a negative bias to the low-temperature oven itself, are reported in Refs. [9, 12].

The $^{48}Ca^{11+}$ beams produced using a low-temperature oven were first supplied twice to the experiments in the old RIBF facility [12]. After that, the $^{48}Ca^{10+}$ beams produced using a low-temperature oven were supplied to the new RIBF accelerator complex, from November 2014 until December 2014. Figure 3 shows the obtained charge distribution of ^{48}Ca ions. The RF power fed to the ECRIS was 370 W. The beam intensity at the exit of the ECRIS and the oven current are shown in Fig. 4. The beam intensity was adjusted to meet the experimental requirements by changing the slit aperture at the exit of the ECRIS. A beam intensity of about 35 eμA with the maximum slit aperture was maintained throughout the experiments. The status of beam supply is summarized in Table 1.

We succeeded in supplying ^{48}Ca beams twice as intense as those using the rod-insertion method, with nearly one-tenth of the material consumption rate.

ISBN 978-3-95450-131-1

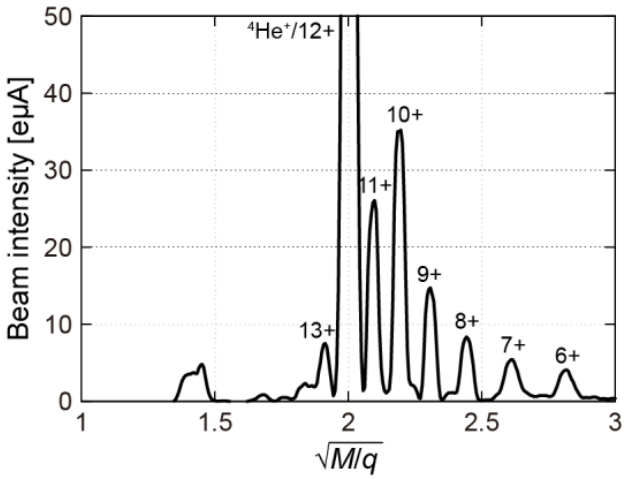

Figure 3: Charge distribution of ^{48}Ca ions.

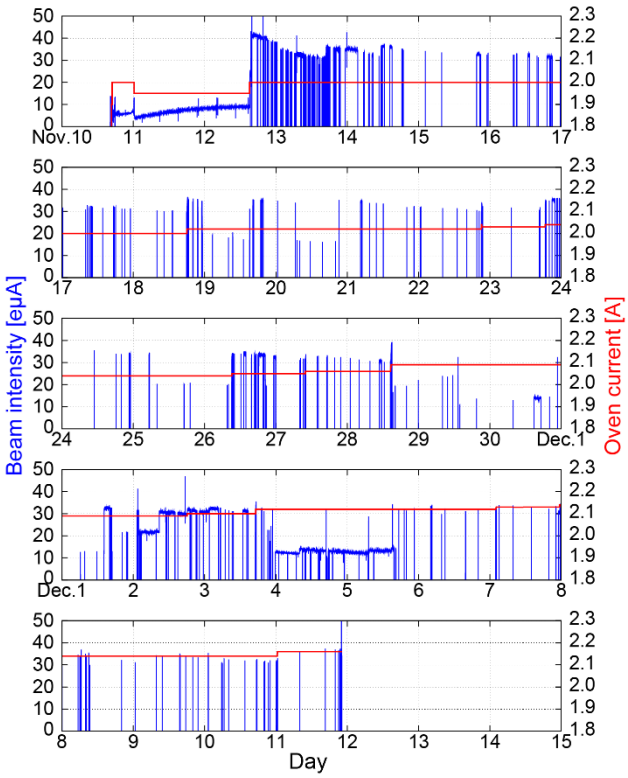

Figure 4: Long-term supply of $^{48}Ca^{10+}$ beam for experiments in new RIBF facility. Intensity of $^{48}Ca^{10+}$ beam (blue) and oven current (red) are shown.

Table 1: Status of $^{48}Ca^{10+}$ Beam Supply

Averaged beam intensity [eμA]	35
Amount of material prepared [mg]	299
Amount of material consumed [mg]	98
Consumption rate of material [mg/h]	0.13

ZINC BEAM

For the supply of a ^{70}Zn beam, ZnO which is highly enriched with ^{70}Zn (from a natural abundance of 0.6% to more than 80%) is prepared. In contrast to the procedure for the Ca beam, only the powder of ZnO is placed in the crucible because of the sufficiently high ZnO vapor pressure. Ionized helium gas is used to generate the plasma. The hot liner is not used because a high RF power of 550 W is required to produce an adequate intensity of highly charged Zn^{15+} ions. In an operational test in which the hot liner was installed in the ECRIS and the RF power fed to the ECRIS was limited to 400 W, the beam intensity hit a peak at an inadequate level even if the oven current was increased.

When the oven current is gradually increased, following the evaporation of the water, Zn beam production is observed at an oven current lower than that at which the Ca beam is produced. The production of the Zn beam at a lower oven current is likely due to the evaporation of the traces of metallic Zn which exist in ZnO. The Zn beam production at this oven current rapidly ceases. By further increasing the oven current, Zn beam production is observed again at an oven current higher than that at which the Ca beam is produced.

A $^{70}Zn^{15+}$ beam produced using the low-temperature oven was first supplied to the experiment in the RIBF from May 2014 until June 2014. Figure 5 shows the obtained charge distribution of ^{70}Zn ions. The RF power fed to the ECRIS was 550 W. The beam intensity at the exit of the ECRIS and the oven current are shown in Fig. 6. In order to reduce material consumption, the oven current was decreased when the beam was not in use. Because there was a break period (from May 27th until May 29th in Fig. 6), the material was replaced as a precaution. The statuses of beam supplies before and after the break are summarized in Table 2. The consumption rate throughout the experiment was 0.14 mg/h.

Table 2: Status of $^{70}Zn^{15+}$ Beam Supply

	Before	After
Averaged beam intensity [eμA]	30	33
Amount of material prepared [mg]	1007	835
Amount of material consumed [mg]	59	22
Consumption rate of material [mg/h]	0.16	0.10

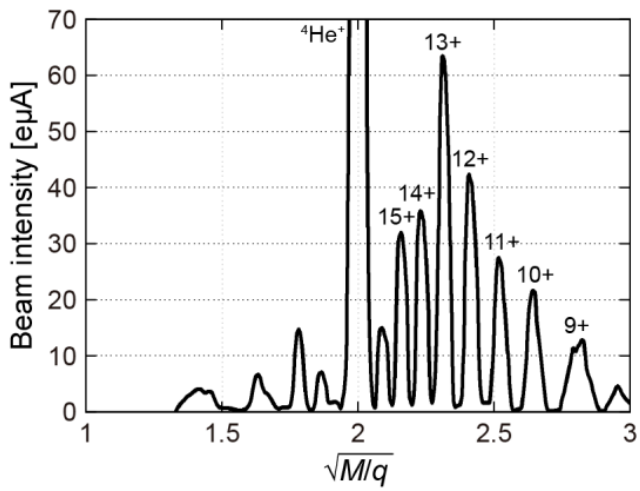

Figure 5: Charge distribution of ^{70}Zn ions.

ISBN 978-3-95450-131-1

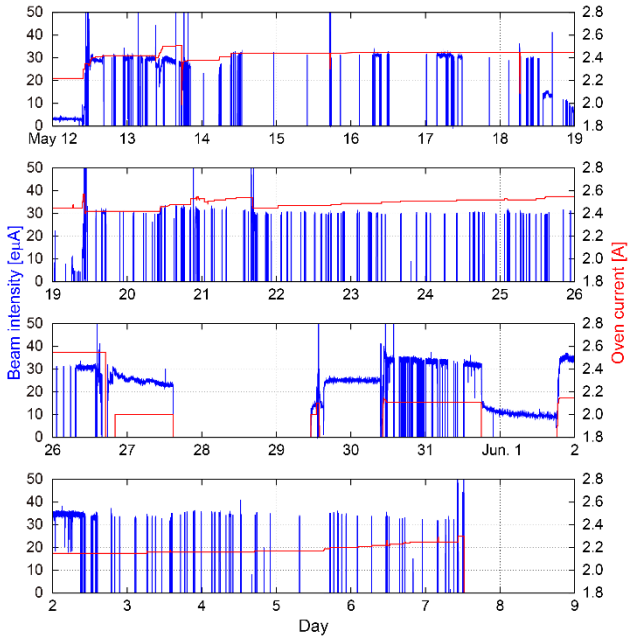

Figure 6: Long-term supply of $^{70}Zn^{15+}$ beam for experiment in RIBF. Intensity of $^{70}Zn^{15+}$ beam (blue) and oven current (red) are shown.

As shown in Fig. 1, since the vapor pressure of ZnO is lower than that of Ca, ZnO requires an oven temperature higher than that required by Ca. However, after ZnO is decomposed into Zn and O by the plasma, the vapor pressure of Zn is higher than that of Ca, enabling the beam to be supplied with a sufficiently low consumption rate, even if a hot liner is not used.

ALUMINIUM BEAM

As Fig. 1 shows, the vapor pressure of Al is slightly lower than that of ZnO. Thus, Al atoms should be evaporated at a slightly higher oven temperature. In the Al beam production test conducted using the low-temperature oven, metallic Al was placed in the crucible, and the hot liner was not used. The maximum RF power fed to the ECRIS was 500 W. Ionized helium and oxygen gases were tested to generate the plasma. Unfortunately, the obtained $^{27}Al^{8+}$ beam had an intensity of no more than a few eμA, even when the oven current was increased to a level at which previous empirical evidence had indicated that Pt wire should burn out within one week.

At the RIKEN 28-GHz superconducting ECRIS [13,14], a high-temperature oven for the production of a highly intense ^{238}U beam is currently under development [15]. The temperature of this oven can be increased to above 2000°C. Therefore, it is expected that an Al beam can be produced using this high-temperature oven without any difficulty.

SUMMARY

At the RIKEN 18-GHz ECRIS, a low-temperature oven has been put into practical use to supply highly intense and stable beams of medium-heavy metals. Ca and Zn beams have been successfully produced, and supplied to the long-term experiments in the RIBF. The upper temperature limit of the low-temperature oven seems to be slightly lower than the temperature at which an Al beam can be produced with an adequate intensity.

REFERENCES

[1] Y. Yano, Nucl. Instrum. Methods Phys. Res. B **261**, 1009 (2007).
[2] T. Nakagawa et al., Nucl. Instrum. Methods Phys. Res. B **226**, 392 (2004).
[3] H. Koivisto et al., Nucl. Instrum. Methods Phys. Res. B **94**, 291 (1994).
[4] R. Harkewicz, Rev. Sci. Instrum. **67**,2176 (1996).
[5] V. B. Kutner et al., Rev. Sci. Instrum. **71**, 860 (2000).
[6] D. Wutte et al., Rev. Sci. Instrum. 73, 521 (2002).
[7] R. Lang et al., Proc. of ECRIS'02, p. 180.
[8] Edited by JSPS, *Hakumaku handbook*, (Tokyo: Ohmsha, 2008).
[9] K. Ozeki et al., Rev. Sci. Instrum. **85**, 02A924 (2014).
[10] A. Efremov et al., Rev. Sci. Instrum. **69**, 662 (1998).
[11] P. Lehérissier et al., Rev. Sci. Instrum. **73**, 558 (2002).
[12] K. Ozeki et al., Rev. Sci. Instrum. **86**, 016114 (2015).
[13] T. Nakagawa et al., Rev. Sci. Instrum. **81**, 02A320 (2010).
[14] Y. Higurashi et al., Rev. Sci. Instrum. **83**, 02A308 (2012).
[15] J. Ohnishi et al., Rev. Sci. Instrum. **85**, 02A941 (2014).

ISBN 978-3-95450-131-1

DEVELOPMENT OF ELECTRON CYCLOTRON RESONANCE ION SOURCES FOR CARBON-ION RADIOTHERAPY

M. Muramatsu, A. G. Drentje, and A. Kitagawa,
National Institute of Radiological Sciences, Chiba, Japan

Abstract

Compact Electron Cyclotron Resonance (ECR) ion sources have been developed for high energy carbon-ion radiotherapy (C-ion RT). Three compact ECR ion sources have been developed as the prototype at National Institute of Radiological Sciences (NIRS). The first ion source was used the microwave of 2.45 GHz to reduce the construction cost of the source as much as possible. It was required to produce 150 μA for C^{2+}. This ion source could not obtain enough intensity of C^{2+} because there were problems in microwave injection and beam extraction system. The second and third ion sources, named Kei and Kei2, solved these problems and set a target of 200 μA for C^{4+}. The structure of Kei and Kei2 were similar, however Kei2 improved on the magnetic field configuration and the beam extraction system. The beam intensity of 260 μA and 780 μA for C^{4+} were obtained by Kei and by Kei2, respectively. Kei2 was modified to connect with an injector linac for C-ion RT facility.

All of later C-ion RT facilities in Japan, the Gunma University Heavy Ion Medical Center, the Saga Heavy Ion Medical Accelerator in Tosu, and the Ion-beam Radiation Oncology Center in Kanagawa, installed copies of Kei2 and named them KeiGM, KeiSA, and KeiGM3. On the other hand, the original Kei2 have been installed in the Heavy Ion Medical Accelerator in Chiba (HIMAC) at NIRS and produces carbon beams for experimental use. Kei2 is still improving and is utilized for the development of ion sources at present.

KEI SERIES

The NIRS-ECR ion source [1] with normal conducting coil has been supplied the carbon ion for medical use with good stability. However, NIRS-ECR has large electric power supply (maximum current and voltage are 600 A and 60 V) for mirror magnet in same high voltage platform. Therefore, the size of high voltage platform include ion source, electric power supplies, vacuum system and controllers is large with 5.3 m length and 6.9 m width. Case of the NIRS-ECR, there is a fault that the running cost increases by occasion of three of the following. 1) A large amount of water is needed to cooling the electromagnet and power supply. 2) From the operating experience with about ten years, the klystron power amplifier (KPA) for microwave source had many troubles. 3) The breakdowns in the control system for power supply etc. by the aged deterioration has increased from there are a lot of numbers of parts that compose the ion source, too.

In order to solve these problems, a compact ECR ion source for the carbon ion production with all permanent magnet has been developed. The electric power and cooling water can be decreased by using a permanent magnet. Therefore, size of ion source with utility such as water cooling can be reduced. Moreover, a permanent magnet is given maintain easy because the number of parts is less than that of the electromagnet. However, it is difficult to obtain an optimal magnetic field for production of target ion under the uncontrollable magnet.

Three compact ECR ion sources have been developed as the prototype. The first prototype ion source is used the microwave frequency of 2.45 GHz aiming to reduce the cost of the source as much as possible. It was required to produce the C^{2+} by 150 μA in this ion source [2]. Figure 1 shows schematic view and magnetic field of the first prototype ion source. An enough performance was not obtained in this ion source because there were problems in microwave injection and beam extraction system [3]. In the microwave injection, the introduced microwave reflected almost from the plasma chamber, and was not absorbed to plasma. The production of the highly charged ion was difficult as the result. In the beam extraction, the puller was made by iron because increasing the mirror field at extraction side. However, distance between puller and plasma electrode could not be optimize for beam extraction. From this problem, the beam defocuses immediately extraction, and was not able to transport the beam to the downstream side. And the cost and size of the accelerator is increased because target ion was C^{2+}.

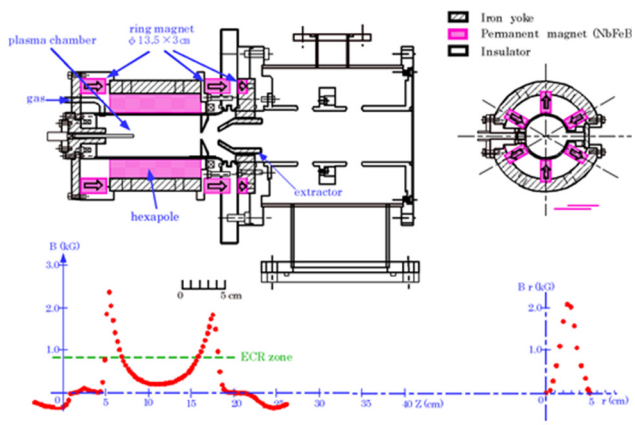

Figure 1: Schematic drawing of 2.45 GHz compact ECR ion source.

The second and third prototype ECR sources (Kei and Kei2), these were developed for solution of problem of the 2.45 GHz compact ECR ion source. The target is change to 200 μA for C^{4+}. Figure 2 shows schematic drawing of Kei source. The fixed magnetic field of the Kei and the Kei2 are copied from that of the 10 GHz NIRS-ECR source at HIMAC, which has already been proven to be reliable

ISBN 978-3-95450-131-1

and stable for the production of C^{4+}. This particular field profile seems to be suitable for the production of C^{4+}, but not for C^{5+} or C^{6+}.

The upstream-chamber is placed upstream from ion source for installation of waveguide, gas pipe and biased disk. A Traveling-Wave-Tube (TWT) amplifier is used in the Kei and Kei2, in order to find the optimum frequency under a fixed and uncontrollable magnetic field. The TWT amplifier operated at a frequency of 8-10 GHz, and can be driven both in cw and pulse modes with a maximum output power of 300 W. Microwave power is fed into the plasma chamber through a rectangular wave guide from the axial direction. An rf window is used for vacuum. The diameter of the biased disk is 8 mm, and is made of molybdenum. The disk position is movable between 7 mm upstream and 25 mm downstream in the direction from the peak of the mirror field (gas injection side). From our experience, this method seems to be suitable for such a compact ECRIS, since the disk does not need a large space for installation. Extraction electrode is installing in down stream from ion source. Einzel lens is set up on the downstream side of the extraction electrode. The Turbo Molecular Pump (TMP) (150 l/sec and 500 l/sec) are installed respectively with the upstream vacuum chamber and under the einzel lens The beam intensity of 260 μA at C^{4+} was obtained in the Kei source [4-6].

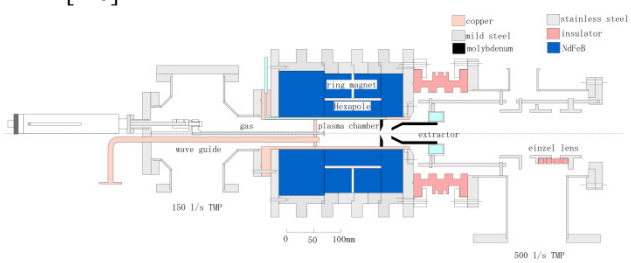

Figure 2: Schematic drawing of Kei source.

The structure of Kei and Kei2 were similar, however Kei2 improved on the magnetic field configuration and the beam extraction system. Figure 3 shows schematic drawing of Kei2 source. Mirror field of Kei2 was increased from Kei source about 13.8% and 13.6% at injection side and extraction side, respectively [7,8]. The extraction electrode is cooled directly by water. This is very effective to reduce any outgassing from the electrode and to keep a good vacuum at the extraction region. The disk was installed in the extraction electrode so that the carbon ion is not adhering to the insulator.

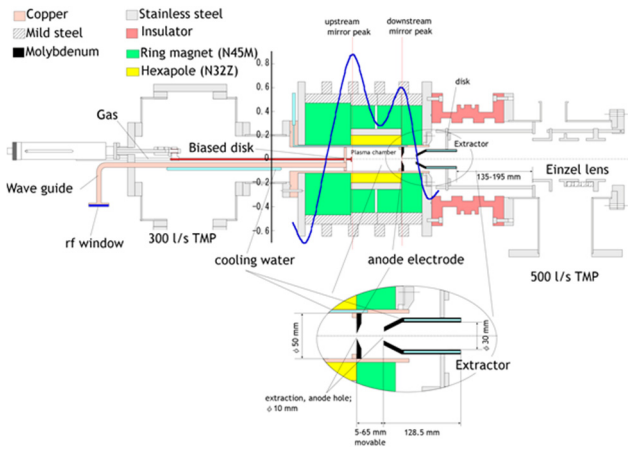

Figure 3: Schematic drawing of Kei2 source.

In order to increase the intensity of C^{4+}, we test gas mixing technique. Gas mixing technique is suitable for all-permanent-magnet ion source Kei2, because, this technique don't need big modification and complicated structure parts. Figure 4 shows charge distribution of carbon with CH_4, C_4H_{10} and C_2H_2. Beam intensity of C^{4+} was reached to 600 μA using C_2H_2 gas.

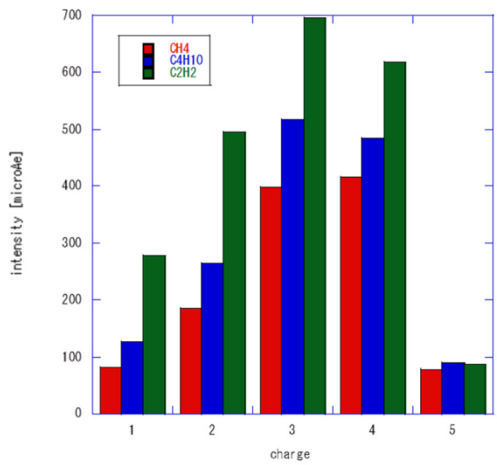

Figure 4: Charge state distribution of carbon.

Moreover, the TWTA with high output power is used for production of highly charged carbon. We change the TWT amplifier. Microwave frequency and output power are 9.75-10.25 GHz and 750 W, respectively. The maximum beam intensity of C^{4+} under the extraction voltage of 30 kV and 40 kV were 760 and 1017 μA, respectively. Figure 5 shows dependence of extraction voltage.

ISBN 978-3-95450-131-1

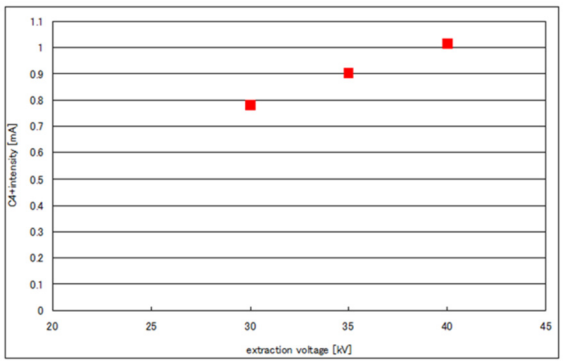

Figure 5: Dependence of extraction voltage.

All of later C-ion RT facilities in Japan, the Gunma University Heavy Ion Medical Center, the Saga Heavy Ion Medical Accelerator in Tosu, and the Ion-beam Radiation Oncology Center in Kanagawa, installed copies of Kei2 and named them KeiGM, KeiSA, and KeiGM3. These ion sources have been manufactured by Sumitomo Heavy Industries. The general structure including the magnetic field was copied from Kei2. A microwave source with the TWT was adopted, with a frequency range and maximum output power of 9.75 - 10.25 GHz and 750 W, respectively. Microwave power is fed into the plasma chamber through a rectangular wave guide from the axial direction. A biased disk is also used for optimizing. The plasma chamber is made of copper for a good cooling efficiency, in order to avoid a decrease in the magnetic field due to high temperature. The plasma chamber has an inner diameter of 50 mm. Extraction voltage is 30 kV. The CH_4 gas was chosen for production of carbon ions. There are two reason for choose the CH_4 gas, (1) enough beam intensity of C^{4+} is obtained for medical use under the CH_4 operation. (2) There is experience of long operation of the source used the CH_4 gas at HIMAC.

REFERENCES

[1] A. Kitagawa et al., Review of Scientific Instruments, Vol. 65, 1087 (1994).
[2] S. Shibuya et al., Proc. Int. Workshop on ECR Ion Sources, 1995, Wako, ISN-j-182(Univ. Tokyo, 1995), 264 (1995).
[3] M. Muramatsu et al., Rev. Sci. Instrum. 69(2), 1076 (1998).
[4] M. Muramatsu et al., Rev. Sci. Instrum. 71(2), 984 (2000).
[5] M. Muramatsu et al., Rev. Sci. Instrum. 73(2), 573 (2002).
[6] M. Muramatsu et al., Proceedings of the 15th International Workshop on ECRIS, 59 (2002).
[7] M. Muramatsu et al., Rev. Sci. Instrum. 75(5), 1925 (2004).
[8] M. Muramatsu et al., Rev. Sci. Instrum. 76, 113304 (2005).

ISBN 978-3-95450-131-1

DEVELOPMENT OF AN ONLINE EMITTANCE MONITOR FOR LOW ENERGY HEAVY ION BEAMS*

V. Tzoganis#, RIKEN, Saitama, Japan , Liverpool University, Liverpool, UK, The Cockcroft Institute, Warrington, UK
T. Nagatomo, M. Kase, O. Kamigaito, T. Nakagawa, RIKEN, Saitama, Japan
C.P. Welsch, Liverpool University, Liverpool, UK, The Cockcroft Institute, Warrington, UK

Abstract

RIKEN's 18 GHz ECR [1] (electron cyclotron resonance) ion source supplies the AVF cyclotron with beams ranging from protons to heavy ions as xenon. From comparison with the use of the RILAC (RIKEN Linear Accelerator) and beam transport simulations it was found that the transport efficiency is much lower. To this extend and with the aim to understand the ECR beam production, beam dynamics and optimize the beam transfer we have developed an emittance monitor based on the pepperpot method. The device is composed of a perforated copper plate, transparent scintillator and a CMOS camera for image capturing. Parameters of interest for scintillator's performance are the light yield and radiation hardness. Quartz was found to be resilient to damage and having linear light emission. A real time algorithm written in LabVIEW manages the data acquisition and the 4D phase space distribution calculation. Provided this information, we can investigate parameters such as inter-plane correlation and emittance dependence on extraction specifications, beam current and the magnetic field in the ion source. In this contribution we are presenting the emittance meter design, algorithm description and a set of typical measurements.

INTRODUCTION

For efficient beam transport in LEBT (low energy beam transfer) lines, the understanding of the beam production and beam dynamics is of very high importance. Beam transverse emittances are key parameters to quantify the beam quality and for an improved beam transfer, emittance matching between the ion source and the LEBT's acceptance is required.

For the case of RIKEN's 18 GHz superconducting ECR ion source, user experience has shown that the transport efficiency is much lower compared to the use of RIKEN's linear accelerator as injector. It has been confirmed experimentally with use of a scintillating screen at the entrance of the LEBT, that the beam size is larger than the LEBT aperture while the beam diameter at the extraction is around 1 cm. Moreover, preliminary beam dynamics studies suggested that the transport efficiency is about 16% and the beam emittance blows up in the area between the ion source and LEBT (~ 1m).

Studies by L. Groening et al and C. Xiao et al [2–4] on the concept of emittance reduction and emittance exchange have shown that it is possible to improve ion beam quality transport efficiency by exchange between the 2 transverse emittances.

With those considerations in mind and the goal to better understand beam transfer and improve beam quality we have developed an emittance monitor that allows for real time beam emittance measurements. The device is based on the pepperpot method which has been well studied and applied in multiple beam sources of electrons and ions..

EMITTANCE MONITOR

ECR Ion Source

The 18 GHz ECR ion source is used to provide various ion beams to the RIKEN AVF cyclotron. From there they are either further accelerated for RIBF or used for RI production and nuclear physics experiments. The ion source design is based on 4 superconducting solenoid magnets and a permanent hexapole magnet that generate a mirror magnetic field for plasma confinement. Different gases depending on the desired ions are injected in the ion source and heated up by microwaves produced by an 18 GHz reference source and amplified by a TWTA (traveling wave tube amplifier).

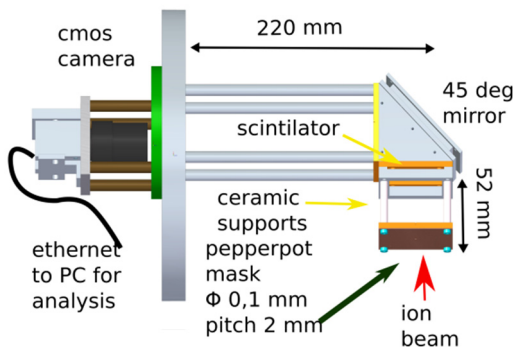

Figure 1: Emittance monitor schematic.

Pepperpot Device

The pepperpot device used here, Figure 1, is mounted on an ICF203 flange about 3m from the beginning of the LEBT. A 70x70 mm perforated copper plate with hole diameter of 0,1mm and pitch 2 mm intercepts the ion beam and splits it in small beamlets. The plate is electrically isolated so it can be used for direct beam current measurements for a measure of beam stability. Absolute current measurements are not possible as there is no secondary electrons suppression. The ion beamlets

*Work supported by STFC, Cockcroft Institute grant and Liverpool - Riken collaboration.
#Vasileios.tzoganis@riken.jp

ISBN 978-3-95450-131-1

imping on a transparent scintillator 52mm downstream that produces visible light. Scintillators tested include CaF2 (Eu), CsI (Th), KBr and SiO2 (quartz) with quartz being the most suitable. Light produced by the ion-scintillator interaction is then recorded from the back side of the scintillator after being reflected by a 45^0 tilted mirror. The image captured device used here is a CMOS based (BFLY-PGE-13E4M-CS) Ethernet camera sitting behind a transparent glass viewport. The camera is water cooled for improved performance in high gain and high exposure time operation mode. A windows 7 operated PC running Labview is used for data acquisition and camera control.

Algorithm Description

A labview custom written algorithm acquires the images and calculates the 4D phase space distribution. It starts with an offline calibration for a fixed pepperpot position and size. This input provides the pixel to mm ratio and compensates for any rotation due to alignment tolerances of the device.

In the real time operation the software acquires images and isolates the beamlets while removing noise based on intensity and size thresholds. Every beamlet location corresponds to a pepperpot hole location with a known X and Y coordinate. From the difference between the hole's location and the actual beamlet location the beam divergence X′ and Y′are calculated and later used for the transverse rms emittances calculation E_x and E_y as given in literature [5]. Furthermore and to investigate interplane correlation the E_{4D} is calculated as described by Groeningen [2–4] that results in the coupling parameter t as:

$$t = \frac{E_x E_y}{E_{4D}}. \quad (1)$$

If this parameter is larger than 1 it indicates emittance interplane coupling that can be used to reduce the one of the 2 transverse emittances by emittance exchange.

The algorithm also plots the 6 combinations among X,Y, X′ and Y′ of the 4D phase space projections (Figure 2 top left) and the same plots after applying a different colour in groups or particle every 10 mm (Figure 2 top right). These plots provide a better visualization of any interplane correlations. Other parameters visualized depend on the performed measurements and they can be beam current, extraction voltage, etc.

It has to be stated that the user can highlight an area of the beam (Figure 2 bottom left) and plot the phase space distribution of it. This selection takes place on a binary image for better performance in real time. The usual operation speed of the algorithm is a few fps (1-5).

EXPERIMENTAL

For the current contribution, experimental results obtained by a 6.5 keV proton beam will be discussed. The beam current varied from a few euA to around 800 as measured from the pepperpot plate and not the absolute value. For the different beam currents, transverse emittances and the coupling factors were calculated (Figure *3*).

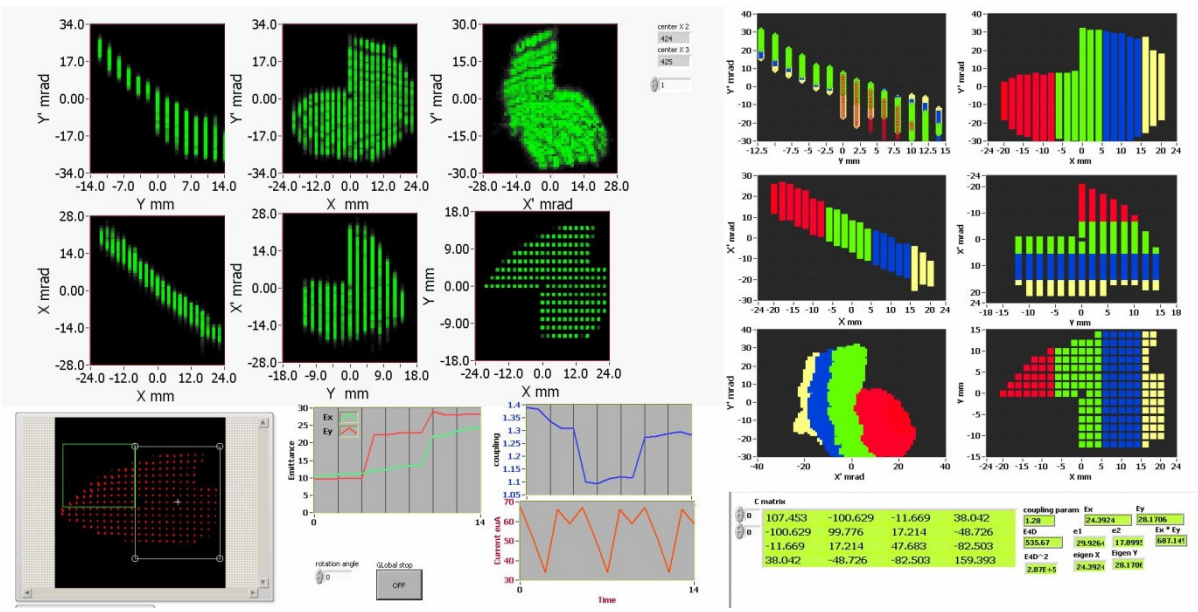

Figure 2: Sample image of the emittance meter algorithm. Various visualizations of phase space projections are shown as well as a binary beam image for selection of only a subset to plot.

ISBN 978-3-95450-131-1

Secondly we measured the emittance while varying the position of the extraction electrode from 25 mm to 55 mm from the end of the ion source chamber, Figure 4. Final measurement is the emittance as a function of the mirror magnetic field by adjusting the solenoid current, Figure 5. For the last case the current values were such that the magnetic fields changed only locally around the 3rd solenoid downstream in the ion source. This only affects the beam near the extraction point as the fringe field decays past the ion source chamber.

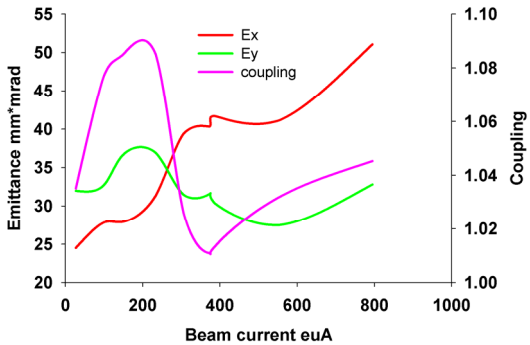

Figure 3: Emittance and coupling factor against beam current.

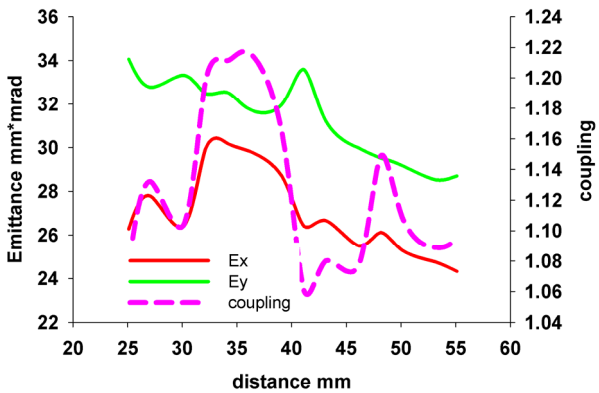

Figure 4: Emittances versus extraction electrode location.

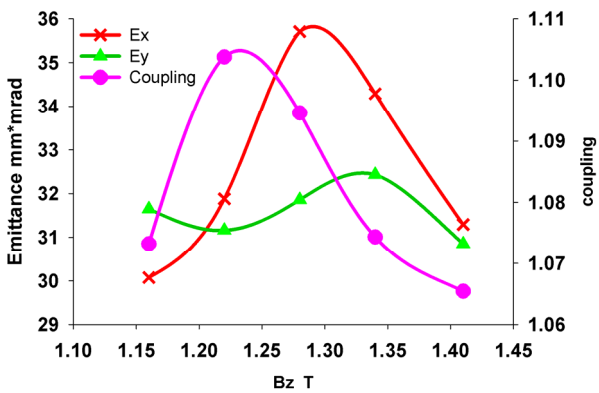

Figure 5: Emittances versus solenoid magnetic field.

RESULTS

As it can be seen here, variation in operating parameters of the ion source affects the beam emittance. The aim of this study is to investigate the operation of the ion source and find optimized value of the all the parameters for more efficient beam transport. The interplane coupling is small in all the measurements and reduces the possibility of emittance reduction by exchange between the 2 planes.

The beam emittance changes by up to 50% with beam current variations as *seen in Figure 3*. For the specific case the beam current was increased by increasing the microwave power that heats up the plasma. Nevertheless the beam current can be increased by other factors too such as the injected gas flow-rate. The very high values of current do not represent reality because of the lack of secondary electron suppression by the pepperpot plate.

The position of the extraction electrode affects the emittance too but it has a much smaller contribution. Variation of the solenoid magnetic field seems to have a greater effect and on the E_x than the E_y component.

SUMMARY

A real time emittance monitor is valuable tool for beam transport optimization and tuning. It will assist to the more efficient operation of the ion source when it will be completed. In the current state is can provide emittance measurements and plot in real time all the phase space components as shown here.

Further developments include better noise immunity, automatic parameters scans and. A new prototype is being prepared that includes retractable emittance monitor and a movable pepperpot plate to better fit the very tight space constrains.

REFERENCES

[1] T. Nakagawa, AIP Conf. Proc. **600**, 232 (2001).
[2] L. Groening et al., *Emittance Transfer in Linacs, oral presentation*, HB2014 (2014) http://epaper.kek.jp/HB2014/talks/weo3lr04_talk.pdf.
[3] L. Groening, Phys. Rev. Spec. Top. - Accel. Beams **14**, 1 (2011).
[4] C. Xiao et al., Phys. Rev. Spec. Top. - Accel. Beams **16**, 1 (2013).
[5] M. Zhang, Emittance *Formula for Slits and Pepper-Pot Measurement* (1988).

ISBN 978-3-95450-131-1

DEVELOPMENT OF A BUFFER GAS-FREE BUNCHER FOR LOW ENERGY RI ION BEAM

M. Togasaki, K. Kurita, K. Yamada, Rikkyo University, Tokyo, Japan
R. Toba, Nagaoka University of Technology, Nagaoka, Niigata, Japan
M. Hara, T. Ohnishi, and M. Wakasugi, RIKEN Nishina Center, Wako, Japan

Abstract

A new-type buncher which is buffer gas-free and workable under the ultra-high vacuum for low energy RI ion beams based on a linear RFQ ion trap was developed. Our idea is to make active use of the fringing fields in a region close to the entrance or the exit of the RFQ to decelerate and stack ions continuously injected into the buncher. As a result of performance experiments, ion beams extracted from the buncher with pulse width of about 500 µs and a stacking efficiency of $^{133}Cs^{+}$ of 10 % were obtained for the operating frequency of 10Hz. It is usable for bunching ion beams provided from the ERIS (Electron-beam-driven RI separator for SCRIT) in the SCRIT (Self-Confining RI Ion Target) electron scattering facility at RIKEN RI Beam Factory.

INTRODUCTION

The SCRIT (Self-Confining RI Ion Target) is an internal target formation technique for electron scattering off short lived unstable nuclei [1–3]. In the SCRIT electron scattering facility at RIKEN RI Beam Factory [4], we constructed an ISOL-type RI beam generator named ERIS (Electron-beam-driven RI separator for SCRIT) [5]. the ERIS supplys continuous RI ion beam with the energy of 50 keV at maximum. In order to efficiently inject the RI beam from the ERIS into the SCRIT device equipped in an electron storage ring and to produce a sufficiently high luminosity for SCRIT experiment, it is absolutely necessary to bunch the beam with a pulse width of about 500 µs without deteriorating of a vacuum level of less than 10^{-7} Pa.

Therefore, we developed a new-type buncher system for the RI ion beam based on a technique of a linear radiofrequency quadrupole (RFQ) ion trap such as in reference [6] but without using buffer gas and working under the ultra-high vacuum. Our idea is to make active use of the fringing fields in a region close to the entrance or the exit of the RFQ. In this paper, we report results of a verification of the new technique using numerical simulations, and of performance experiments of the buncher system.

PRINCIPLE OF THE BUFFER GAS-FREE BUNCHER

Fringing fields of a linear RFQ

an ideal electrostatic potential generated by rods of a linear RFQ [7] lying along the z-axis with a bore radius r_0, $\phi(x,y,t)$, is given by

$$\phi(x,y,t) = V_{\mathrm{DC}} + \frac{x^2 - y^2}{r_0^2} V_{\mathrm{RF}} \cos \omega t \qquad (1)$$

where V_{RF} and ω are amplitude and angular frequency of an RF voltage respectively, and V_{DC} is an adittional DC voltage applied to the rods. In a region close to end-cap electrodes (hereafter called "barrier" electrodes), however, fringing fields [8–10] are not negligible. The potential $F(x,y,z,t)$ in this region is expressed approximately by

$$F(x,y,z,t) = f(z)\phi(x,y,t) \qquad (2)$$

$$f(z) = 1 - \exp[-az - bz^2] \qquad (3)$$

where a and b are coefficients dependent on the ratio of a distance from the rods to the barrier electrode to r_0, and $z = 0$ corresponds to the position of the barrier electrode [9, 10].

According to the above equations, ions in this region are longitudinally accelerated or decelerated by the RF fringing fields. If energys of the decelerated ions come to be lower than the DC voltage applied to the barrier electrode, the ions should be stacked in the longitudinal barrier-potential well and a bunch beam can be produced by extracting the stacked ions within a short time.

Ion stacking by the fringing fields

We verified the ion stacking phenomenon by the fringing fields using Monte Carlo particle simulations. Numerical solutions of the three-dimensional Laplace equation were employed as models of the fringing fields. Where DC voltage applied to the barrier electrodes is $V_{\mathrm{Barr}} = V_{\mathrm{Acc}} - 0.70$ V, as an example, Figure 1 shows the time evolution of averaged survival rate $\langle S \rangle_{\mathrm{RF}}(t)$ of $^{133}Cs^{+}$ ions injected into the RFQ within one RF cycle T_{RF} from $t = 0$ for some different values of V_{DC}. $V_{\mathrm{Acc}} = 6.0$ kV is accelerating voltage of ions, and amplitude and frequency of the RF voltage are $V_{\mathrm{RF}} = 300$ V and $\omega/2\pi = 1.6$ MHz respectively.

Total number of stacked ions $N(t)$ in RFQ with continuous beam-injection time t is expressed by

$$N(t) = \frac{I_{\mathrm{inj}} T_{\mathrm{RF}}}{e} \sum_{i=0}^{n} \langle S \rangle_{\mathrm{RF}}(t - iT_{\mathrm{RF}}) \qquad (4)$$

where I_{inj} is the injected beam current, time t is multiple of the RF cycle T_{RF} and

$$n = \frac{t}{T_{\mathrm{RF}}} \qquad (5)$$

Therefore, ion stacking efficiency $\epsilon(t)$ defined as the ratio of the $N(t)$ and total number of injected ions $I_{\mathrm{inj}} t/e$ can be written as

$$\epsilon(t) = \frac{T_{\mathrm{RF}}}{t} \sum_{i=0}^{n} \langle S \rangle_{\mathrm{RF}}(t - iT_{\mathrm{RF}}) \qquad (6)$$

ISBN 978-3-95450-131-1

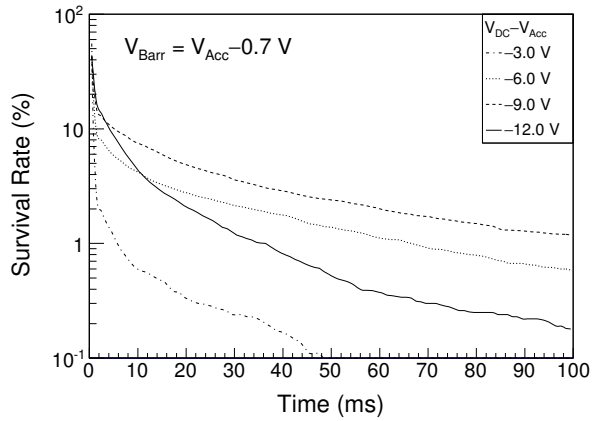

Figure 1: Averaged survival rate $\langle S \rangle_{\mathrm{RF}}(t)$ of $^{133}Cs^{+}$. Accelerating voltage of the ions is $V_{\mathrm{Acc}} = 6.0\,\mathrm{kV}$, DC voltage applied to the barrier electrodes is $V_{\mathrm{Barr}} = V_{\mathrm{Acc}} - 0.70\,\mathrm{V}$, and amplitude and frequency of the RF voltage are $V_{\mathrm{RF}} = 300\,\mathrm{V}$ and $\omega/2\pi = 1.6\,\mathrm{MHz}$ respectively.

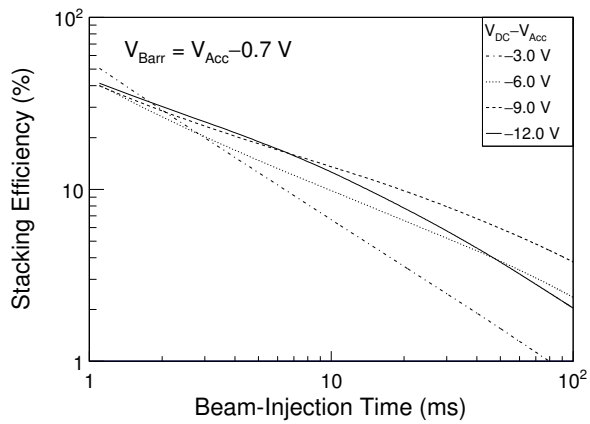

Figure 2: Ion stacking efficiency $\epsilon(t)$ of $^{133}Cs^{+}$ where t is the beam injection time. V_{Acc}, V_{Barr}, V_{RF}, ω and V_{DC} have same values as in Figure 1.

The $\epsilon(t)$ numerically-calculated from the $\langle S \rangle_{\mathrm{RF}}(t)$ in Figure 1 are shown in Figure 2. Moreover, Figure 3 shows the $\epsilon(t)$ of $^{133}Cs^{+}$ plotted versus $V_{\mathrm{DC}} - V_{\mathrm{Acc}}$ for $t = 100\,\mathrm{ms}$, and for some different values of V_{Barr}.

EXPERIMENTAL SETUP

Figure 4 shows the experimental setup of our buncher system together with the longitudinal potential diagram. The RFQ has a total length of 914 mm along the beam axis and a bore radius of $r_0 = 8.0\,\mathrm{mm}$. A resonant circuit technique is employed for the RF system. RF voltage of up to 500-V amplitude can be supplied with frequency range from 0.3 MHz to 3 MHz by tuning the resonant condition of the circuit. The ion source is surface ionization type and provides continuous alkali metal ion ($^{133}Cs^{+}$, $^{39}K^{+}$ or $^{23}Na^{+}$) beam with accelerating voltage $V_{\mathrm{Acc}} = 6.0\,\mathrm{kV}$ constantly. The voltage V_{Barr} applied to the barrier electrode 1 and 2 is a few volts lower than V_{Acc} and higher than the DC voltage V_{DC} applied

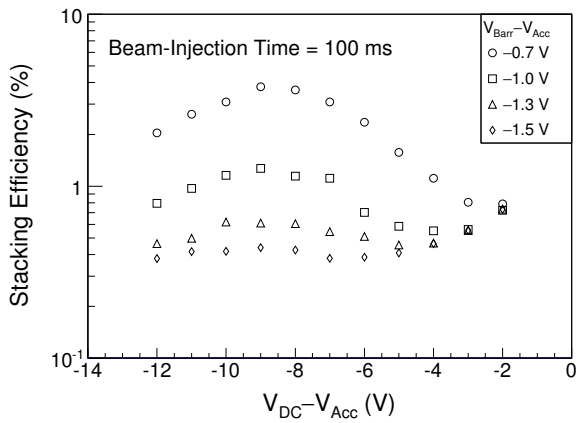

Figure 3: Ion stacking efficiency $\epsilon(t)$ of $^{133}Cs^{+}$ plotted versus $V_{\mathrm{DC}} - V_{\mathrm{Acc}}$ for the beam injection time of $t = 100\,\mathrm{ms}$. V_{Acc}, V_{RF} and ω have same values as in Figure 1.

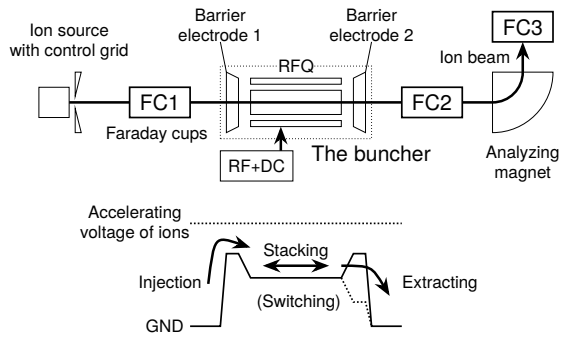

Figure 4: Experimental setup of the buncher system together with the longitudinal potential diagram.

to the RFQ rods for the injection of the ions into and stacking in the buncher. For the extraction of the stacked ions from the buncher the potential of the barrier electrode 2 is switched from V_{Barr} to $\approx V_{\mathrm{Acc}} - 100\,\mathrm{V}$ within less than ten microseconds by a fast transistor switch. The injected beam current I_{inj} and the total number of stacked ions (number of ions contained in the beam extracted from the buncher) $N(t)$ is measured by the Faraday cups named FC1-3.

MEASUREMENT OF THE ION STACKING EFFICIENCY

Figure 5 shows typical waveforms of the $^{23}Na^{+}$ beam extracted from the buncher observed by FC2 for the beam-injection time of $t = 100\,\mathrm{ms}$, 500 ms and 900 ms. The ion beams extracted from the buncher with pulse width of about 500 µs which naturally depends on V_{DC} was obtained. In the case of $t = 100\,\mathrm{ms}$, as an example, the number of ions contained in the waveform is $N(t) \approx 1.0 \times 10^{8}$ and the injected beam current observed by FC1 is $I_{\mathrm{inj}} \approx 4.3\,\mathrm{nA}$. Therefore, the ion stacking efficiency including an injection and an extraction efficiency is

$$\epsilon(t) = N(t)\frac{e}{I_{\mathrm{inj}}t} = 3.8\,\% \qquad (7)$$

ISBN 978-3-95450-131-1

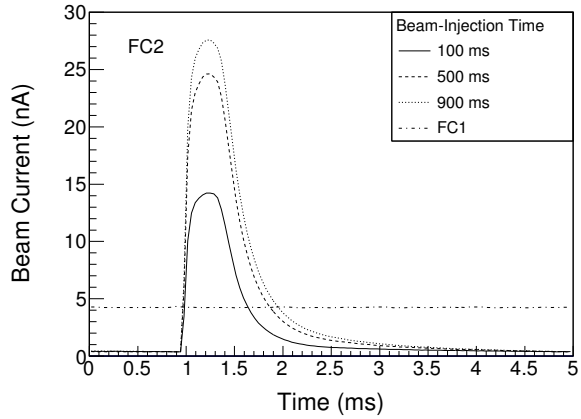

Figure 5: Typical waveforms of the $^{23}Na^{+}$ beam extracted from the buncher observed by FC2 for the beam-injection time of 100 ms, 500 ms and 900 ms where $V_{\mathrm{Barr}} = V_{\mathrm{acc}} - 1.3\,\mathrm{V}$, $V_{\mathrm{DC}} = V_{\mathrm{acc}} - 6.7\,\mathrm{V}$, $V_{\mathrm{RF}} = 150\,\mathrm{V}$ and $\omega/2\pi = 1.9\,\mathrm{MHz}$. The dot-and-dash line shows the waveform of the injected beam observed by FC1.

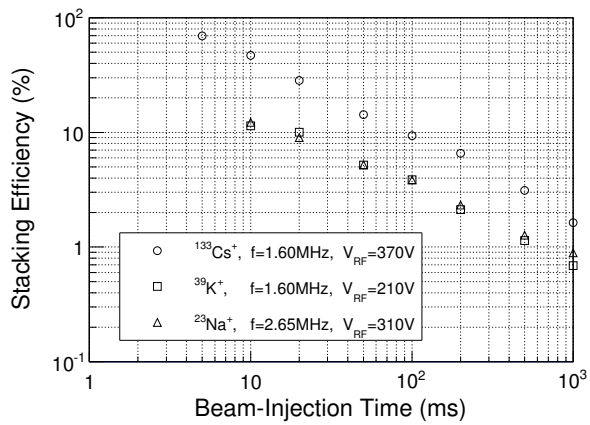

Figure 6: Experimental ion stacking efficiencys $\epsilon(t)$ of the $^{133}Cs^{+}$, $^{39}K^{+}$ and $^{23}Na^{+}$ beams. Values of V_{Barr}, V_{DC}, V_{RF} and ω have been optimized for each beam.

Such the experimental ion stacking efficiencys $\epsilon(t)$ of the $^{133}Cs^{+}$, $^{39}K^{+}$ and $^{23}Na^{+}$ beams are shown in Figure 6. Here, values of V_{Barr}, V_{DC}, V_{RF} and ω have been optimized for each beam, and it is known that ω have no effect on $\epsilon(t)$ essentially. Although the experimental result for the heavy $^{133}Cs^{+}$ beam reasonably reproduced the computational one shown in Figure 2, higher stacking efficiency of nearly 10 % was obtained for $t = 100\,\mathrm{ms}$ or an operating frequency of the buncher of 10 Hz. Figure 7 shows dependency of the experimental $\epsilon(t)$ of $^{23}Na^{+}$ on V_{Barr} and V_{DC} for $t = 100\,\mathrm{ms}$ where $V_{\mathrm{RF}} = 210\,\mathrm{V}$, and $\omega/2\pi = 1.9\,\mathrm{MHz}$. The computational result shown in Figure 3 was reproduced well. It is show that the ion stacking efficiency $\epsilon(t)$ heavily depend on V_{Barr} and V_{DC}.

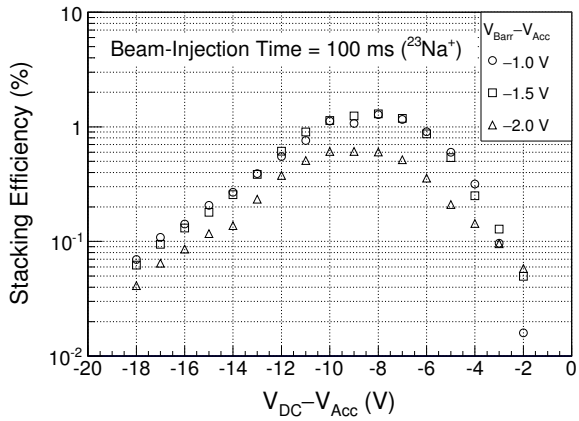

Figure 7: Dependency of the experimental ion stacking efficiencys $\epsilon(t)$ of $^{23}Na^{+}$ on V_{Barr} and V_{DC} for $t = 100\,\mathrm{ms}$ where $V_{\mathrm{RF}} = 210\,\mathrm{V}$, and $\omega/2\pi = 1.9\,\mathrm{MHz}$.

CONCLUSIONS

The new-type buncher which is buffer gas-free and workable under the ultra-high vacuum for low energy RI ion beams was developed. Ion beams extracted from the buncher with pulse width of about 500 µs and the stacking efficiency of heavy ions such as $^{133}Cs^{+}$ of 10 % was obtained for the operating frequency of 10Hz. it has already been observed taht the efficiency is further enhanced by providing cooling force on the ions or by combination with pre-bunching at the ion source. The buncher system can be expected to be applied to various applications.

REFERENCES

[1] M. Wakasugi et al., Nucl. Instrum. Methods A 532, 216 (2004).

[2] M. Wakasugi et al., Phys. Rev. Lett. 100, 164801 (2008).

[3] T. Suda et al., Phys. Rev. Lett. 102, 102501 (2009).

[4] M. Wakasugi et al., Nucl. Instrum. Methods B 317, 668 (2013).

[5] T. Ohnishi et al., Nucl. Instrum. Methods B 317, 357 (2013).

[6] F. Herfurth et al., Nucl. Instrum. Methods A 469, 254 (2001).

[7] R. E. March and J. F. Todd, *Quadrupole Ion Trap Mass Spectrometry, 2nd Edition*, Wiley, Hoboken (2005).

[8] P. H. Dawson (Ed.), *Quadrupole Mass Spectrometry And Its Applications*, Elsevier, Amsterdam (1976).

[9] K. L. Hunter and B. J. McIntosh, Int. J. Mass Spectrom. Ion Processes, 87, 157 (1989).

[10] B. J. McIntosh and K. L. Hunter, Int. J. Mass Spectrom. Ion Processes, 87, 165 (1989).

ISBN 978-3-95450-131-1

DEVELOPMENTS OF LEBT AND INJECTION SYSTEMS FOR CYCLOTRONS AT RCNP

T. Yorita#, K. Hatanaka, M. Fukuda, H. Ueda, K. Shimada,
Y. Yasuda, T. Saito, H. Tamura, S. Morinobu, K. Kamakura
RCNP, Osaka University, Osaka, Japan

Abstract

Developments of injection systems for cyclotrons at Research Center for Nuclear Physics (RCNP) Osaka University have been carried recently in order to improve the highly intense heavy ions in MeV region for the secondary RI beam, et al. The cyclotron cascade consists with injector AVF cyclotron of K=140 and Ring cyclotron of K=400. The additional glazer lens on axial injection of AVF cyclotron is one of those and it has been installed for the purpose of increasing beam transmission to the inflector in center region of cyclotron. Another development is additional buncher for the heavy ion injection like Xe which requires high voltage in comparison with proton case. Extension of baffle slits on injection line of Ring Cyclotron also has been done to extend the flexibility of injection orbit. Modification of low energy beam transport (LEBT) from 18 GHz Superconducting (SC)-ECR ion source [1] to AVF injection axis also has been carried.

LEBT FOR 18 GHz SC-ECR

Modification of LEBT from 18GHz SC-ECR to injection of AVF cyclotron has been done. Schematic views of previous LEBT and modified LEBT are shown in Fig 1. Previous LEBT has 110 degree bending magnet and 20 degree electrostatic deflector. With this geometry, beam transmission from FC1 to FC3 shown in Fig. 1 was reaching an upper limit of 80 %. According to the calculation of beam envelope using MadX code [2], it is proved that the beam with emittance of more than 200 pi*mm*mrad is limited by baffle of 80 mm in diameter [3]. (See upper figure in Fig. 2.) In the case that these bending magnet and electrostatic deflector are changed by simple 90 degree bending magnet, it is expected that beam transmission would be improve due to the looser limitation as shown in lower figure in Fig. 2. After this modification of LEBT, beam transmission more than 90 % has been achieved except the case that large magnetic field leakage from AVF cyclotron which median plane locates 6m below the LEBT, even additional steering magnets shown in Figure 1 have been used to cancel the leakage field. It is also confirmed that beam with more than 200*pi*mm*mrad emittance measured by emittance monitor shown as EM in Fig. 1 has been transported.

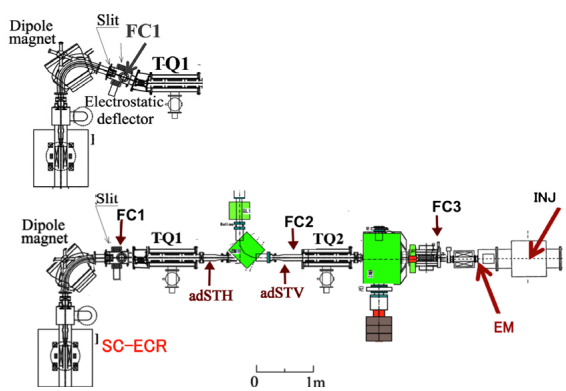

Figure 1: Schematic views of 18 GHz SC-ECR and LEBT components: upper figure shows previous LEBT and lower shows new LEBT. adSTH and adSTV are steering magnets, TQ1 and TQ2 are electrostatic Triplet Q lenses and FC1~3 are Faraday cup.

#yorita@rcnp.osaka-u.ac.jp

INJECTION AXIS OF AVF CYCLOTRON

To improve the beam current accelerated by AVF cyclotron, some components have been added to injection axis. Those are additional buncher and glaser lens.

Buncher

To improve the beam current of heavy ion, especially of Xe, additional buncher has been installed on injection axis. In Fig. 3, existing buncher is shown by “b” and located 2550mm above median plane (MP) of AVF. This existing one makes saw wave by RF combining with 1x, 2x and 3x harmonics and maximum saw voltage is

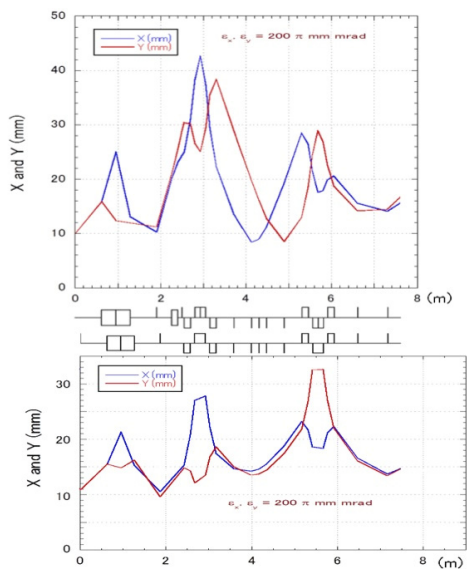

Figure 2: The beam envelopes for previous LEBT and new LEBT calculated by MadX[1]. Both envelopes are assumed the beam emittance of 200 pi*mm*mrad.

ISBN 978-3-95450-131-1

±600 V. This buncher can bunch lighter ion which has small m/q and is accelerated with higher frequency, but the voltage is not enough for heavy ion like Xe. So additional new buncher is expected to help to improve beam current in combination with existing one. New buncher also makes saw wave by charge-discharge circuit with maximum voltage of 0-1200 V at 2 MHz, 0-600 V at 6 MHz and 0-200 V at 20 MHz. The installation position is 4600 mm above the median plane as shown in Figure 3 by "a". The beam test has been done by $^{22}Ne^{8+}$ with acceleration frequency 9.32 MHz. First optimized beam current at extraction of AVF cyclotron is 2.5 μA with existing buncher only, and is 0.4 μA without any buncher. With this condition and no further optimization for magnets on injection axis, the beam current with only new buncher is 1.7 μA and it is confirmed that the new buncher works well. For the next step, beam test to improve beam current by the combination of these two bunchers would be done.

Glaser Lens

To improve the efficiency of AVF injection, additional glaser lens has also been installed. In previous situation of injection axis with only 3 glasers shown as d, e and f in Fig. 1, it was hard to deliver the beam through the region of 0~2000 mm above the median plane where the beam pipe size is narrow of 57 mm in diameter and only the beam with the size up to 5 mm at the iris slit shown by "g" in Fig. 3 can be delivered. So new additional glaser is installed at the position of "c" shown in Fig. 3. With new additional glaser, now the beam with the size of 10 mm at the iris slit can be delivered.

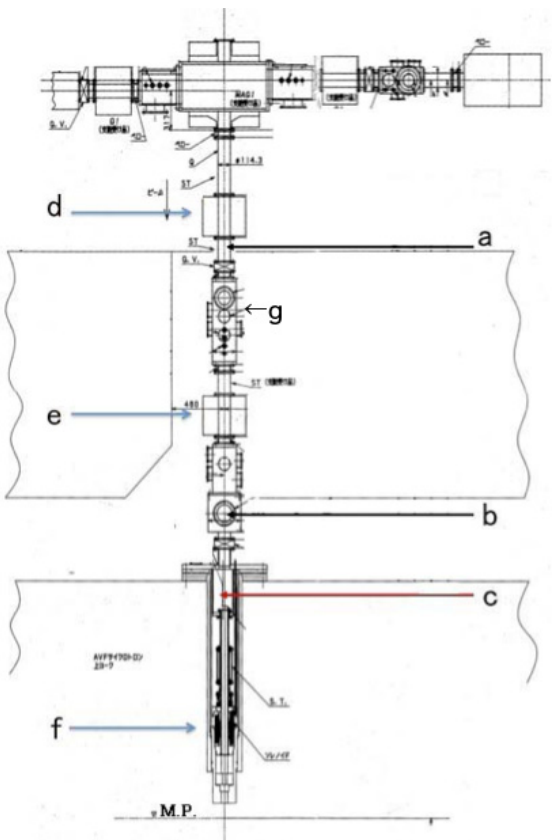

Figure 3: Schematic view of injection axis of AVF Cyclotron. a: new buncher, b: existing buncher, c: new glaser, d~f: existing glaser, g: iris slit.

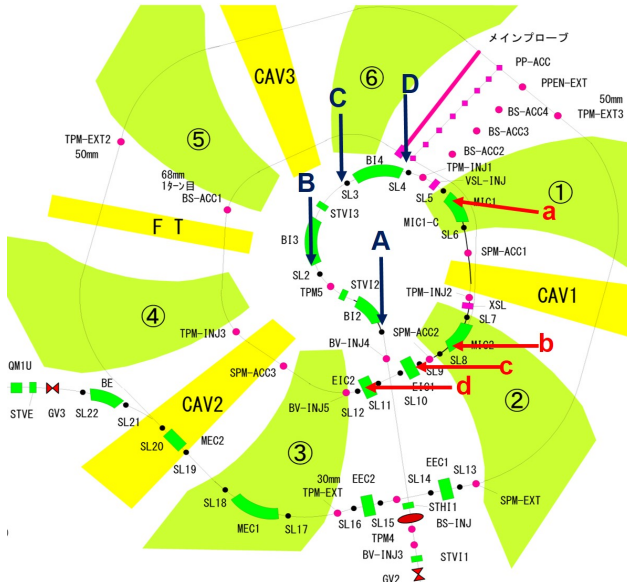

Figure 4: Schematic view of Ring cyclotron: A~D are baffle slits on injection line, a and b are slits of magnetic channel and c and d are electrostatic channel.

INJECTION TO RING CYCLOTRON

To improve the injection efficiency of Ring cyclotron, extentions of baffle slits on beam injection line have been done to expand the flexibility of beam injection orbit. In Fig. 4, A~D show the baffle slits of injection line, a and b are the slit of magnetic channel, and c and d are electrostatic channel. These slits have been extended as far as protection of components works. Figure 5 shows the examples of the extension. After these slit extension, optimum current of MIC2 shown in Fig. 4 has drastically decreased, the current ratio of this MIC2 and analyzing magnet downstream of AVF extraction takes smaller

Figure 5: Examples of baffle slit extension: left figure shows magnetic channel slit extended from 15 mm×15 mm to 33mm×30mm and right figure shows slit of B in Fig. 4 which extended from 30mm×24mm to 36mm×30mm.

ISBN 978-3-95450-131-1

value of 1.3~1.9 than the previous of 2.0~2.5. This means that the optimum trajectory has been changed due to slit extensions. The injection efficiency represented by the ratio of beam current at BS_ACC1 and BS_INJ shown in figure 4 also seems to be improved from 25~65% to 67~97%. To clarify that this efficiency improvement is due to slit extension and to improve the efficiency more, further study should to be done for transport line between AVF cyclotron and Ring cyclotron.

CONCLUSION

Several developments have been done for the purpose of improve the current of the beam accelerated by cyclotrons: LEBT of ion sources has been modified, additional buncher and glaser have been install on injection axis of AVF cyclotron and baffle slits on injection of Ring cyclotron have been extended. Those components work well. For further improvement of beam current, more detail development with those components and existing components combination would be done.

REFERENCES

[1] T. Yorita, et al., Rev. Sci. Instrum. 81, 02A332 (2010), T. Yorita, et al., Rev. Sci. Instrum. 79, 02A311 (2008).
[2] CERN MAD-X Page: http://frs.home.cern.ch/frs/Xdoc/, MAD-X Primer CERN-AB-2004-027-ABP
[3] T. Yorita, et. al, Rev. Sci. Instrum. 85 , 02A741 (2014).

ISBN 978-3-95450-131-1

CONTROL OF LASER ABLATION PLASMA BY PULSED MAGNETIC FIELD FOR HEAVY ION BEAM PRODUCTION*

S. Ikeda#, Tokyo Institute of Technology, Yokohama, Kanagawa 226-8502, Japan, and
RIKEN, Wako, Saitama 351-0198, Japan
M. Costanzo, T. Kaneuse, R. Lambiase, C-J. Liaw, and M. Okamura
BNL, Upton, NY 11973, USA

Abstract

To improve the total charge and quality of a beam pulse from the laser ion source (LIS) operated at Brookhaven National Laboratory (BNL), we attempt to modify the beam current profile to be flatter by applying a pulsed magnetic field to the plasma. For this purpose, we investigated the suitable magnetic field experimentally with a quasi-steady field. We found that a magnetic field decreasing from 90 G to 60 G within 10 μs is expected to create a flat current profile. To drive such a current, we designed a coil and a modified LC discharge circuit. The coil will be installed into LIS at BNL and the effect will be tested.

INTRODUCTION

In the laser ion source (LIS), a pulsed ion beam is extracted from plasma generated by laser irradiation on a solid. The source provides many ion species such as Li, C, Al, Si, Fe, and Au ions to the Relativistic Heavy Ion Collider and the NASA Space Radiation Laboratory (NSRL) at Brookhaven National Laboratory (BNL) [1]. Typically, the plasma drifts and spreads three-dimensionally with a constant velocity distribution in the absence of an external force [2]. The current of the ion beam extracted from the freely spreading plasma varies drastically in time within a single beam pulse. The shape of the current waveform is determined by the velocity distribution and cannot be controlled without applying an external force. In this case, the total charge in a pulse is maximized when the peak current is equal to the space charge limit current while current in most part of beam pulse is less than the limit current by several tens of percent. This means that we can increase the total charge if we can control the current waveform. In addition, the extraction from the varying plasma flux causes larger emittance than estimated by the thermal energy spread. Therefore, as an upgrade of LIS for NSRL operation, we attempt to generate a flat-topped, long beam pulse by controlling the plasma plume with a pulsed magnetic field. A magnetic field can modify the plasma shape. Therefore, we expect to generate a flat-topped beam current by changing the magnetic field in accordance with the plasma density distribution.

To predict a suitable pulsed magnetic field, we investigated the dependence of the plasma flux waveform on the strength of a quasi-steady magnetic field. We designed a coil and a pulse circuit for Fe plasma on the basis of the experimental results.

EXPERIMENTAL SETUP

The experimental setup is shown in Fig. 1. The laser target was a Fe plate. Laser energy, spot size, and power density on the target were 380 mJ, 0.1 cm^2, and $6x10^8$ W/cm^2, respectively. The power density was almost the same as that of LIS at BNL and mainly produces singly charged ions. A six-turn coil with a 50 mm diameter and 5 mm length was placed at a distance of 260 mm from the target. The distance was determined with the configuration of the present LIS at BNL. The coil current was generated by a pulse circuit composed of 50 μF storage capacitor. The time scale of the current change was much larger than the duration of plasma passing through the coil. The decrease in magnetic field during the plasma traversal was 10%, small enough to consider the field generated by the coil as steady. A negatively biased ion probe with a 2 mm diameter aperture was used to measure the plasma flux as an ion-saturated current density. The bias voltage was -180 V. The probe was placed at a distance of 690 mm from the target.

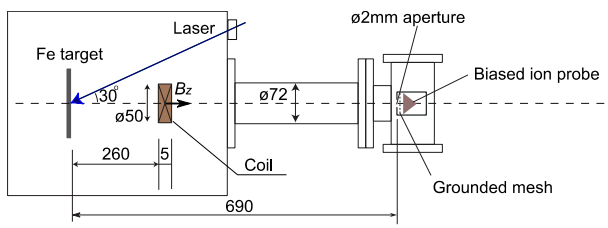

Figure 1: Experimental setup.

RESULTS AND DISCUSSIONS

Figure 2 is the graph of the measured plasma flux. The horizontal axis is time from laser shot. The red curve is the flux without the magnetic field and the other curves are with the field. As shown in the figure, the fast and slow parts of the plasma were enhanced by several tens of gauss magnetic field. In addition, as the field increased, the peaks of both parts increased more while the peak times of the fast part were almost constant and those of the slow part shifted forward.

Based on these results, we can design a suitable pulsed magnetic field. Because the two parts of the plasma were

*Work supported by RIKEN, DoE and NASA
#ikeda.s.ae@m.titech.ac.jp

ISBN 978-3-95450-131-1

affected, the time profile of magnetic field would be complicated if we control both parts. Therefore, to avoid this complication, we do not control the fast part and do not apply the magnetic field to it. This can be achieved by raising the field rapidly after the fast part of plasma passes through the coil. After that, we control the slow part to increase the plasma flux to make the magnitude equal the original peak around 20 μs. As experimental results showed, the peak of slow part was slower as the magnetic field was weaker. Therefore, if we apply 90 G on the region of the plasma around 25 μs, 70 G on the region around 40 μs, and 60 G on the region around 60 μs, the plasma flux of each region is expected to be almost matched to that of the original peak. To apply each magnetic field strength on each region of the plasma, we need to generate the appropriate magnetic field at the time when each region arrives at the coil. The arrival time at the coil for each region can be calculated from the arrival time at the ion probe. Because each region moves with constant velocity, each arrival time is proportional to the flight distance. So, if we fix the position of the coil, the arrival times are determined and then, the fall time of the magnetic field is determined accordingly.

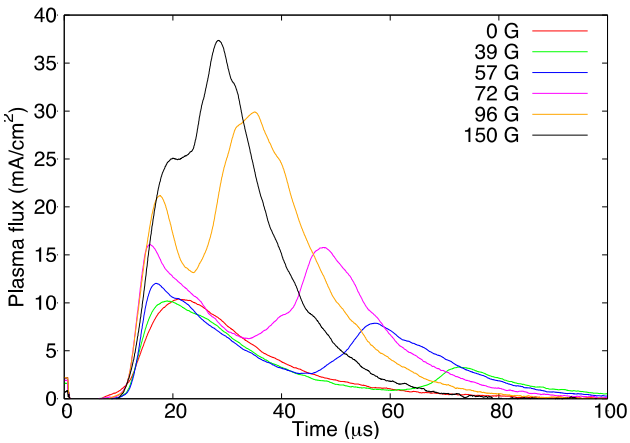

Figure 2: Plasma flux measured at a distance of 690 mm from the laser target with and without magnetic field.

DESIGN OF COIL AND PULSED CIRCUIT

Mechanical Design

To avoid obstructing the plasma, the diameter of coil is 75 mm, matching the vacuum pipe in the LIS at BNL. The length of the coil is 75 mm; that is larger than what is used in the present experiment to decrease the current in the coil and obtain a more uniform magnetic field profile. The coil center is at a distance of 220 mm from the target, this is determined by the configuration of the present LIS. A wire is wound 100 times and there are two layers of coil. The winding number determines the inductance of the coil and the field strength generated by a given current. Therefore, the number was determined by the design of the pulsed circuit driving the coil. When the coil current rises rapidly, the coil is charged up and the electric field can affect the plasma if it is not shielded. To shield the coil, we insert a thin aluminium tube into the coil. The tube has a longitudinal slit to prevent the rising magnetic field from inducing an azimuthal eddy current.

Design of Pulsed Circuit

Because the velocity distribution was constant [2], plasma flux waveform at a distance from the target is similar. Namely, if the normalized waveform at a distance z from the target is described as $i(t)/i_{peak}(z)$, the normalized waveform at the other distance z' is described as $i(tz/z')/i_{peak}(z')$. Therefore, we can calculate the plasma flux waveform at the coil center at a distance of 220 mm from the taret with the waveform at 690 mm. The red curve in Fig. 3 is the calculated waveform without a magnetic field. We can find that the arrival time of original peak at the coil center is around 8 μs and the time of the part reaching the ion probe at 60 μs is around 19 μs. Therefore, the required time profile for the magnetic field rapidly rises to 90 G around 8 μs and then decreases to 60 G around 19 μs.

To drive such a current, we designed an LC circuit modified to set rise and fall time independently as shown in Fig.4. Capacitor C1 is a discharge capacitor that determines the rise time. The discharge starts when switch S1 is turned on. Capacitors C3 and C4 determine the fall time. If switch S2 is on, C4 is connected to C3 in parallel and the fall time becomes longer. After the plasma passes through the coil, S1 is turned off and the circuit begins recovering. During recovery, C1 is recharged by V1 through R1 and C3 and C4 are discharged through resistors R3 and R4. Because the LIS at BNL produces beam to NSRL around once per four seconds, R1, R3, and R4 are determined to complete recovery within four seconds. The calculated coil current is shown by the green curve in Fig.3. The peak current can be adjusted by varying the charging voltage. The pulsed coil will be installed into the present LIS and the performance will be tested.

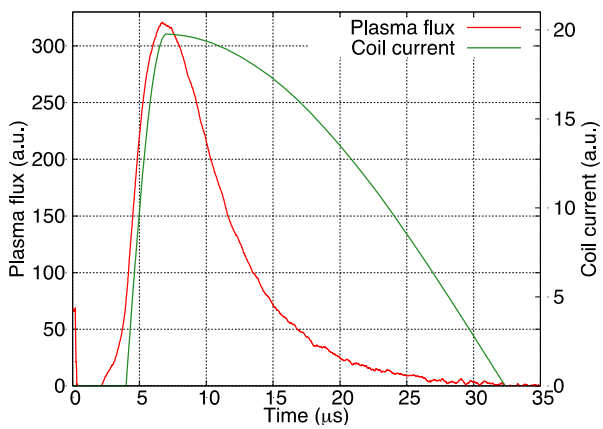

Figure 3: Plasma flux at center of coil and coil current.

ISBN 978-3-95450-131-1

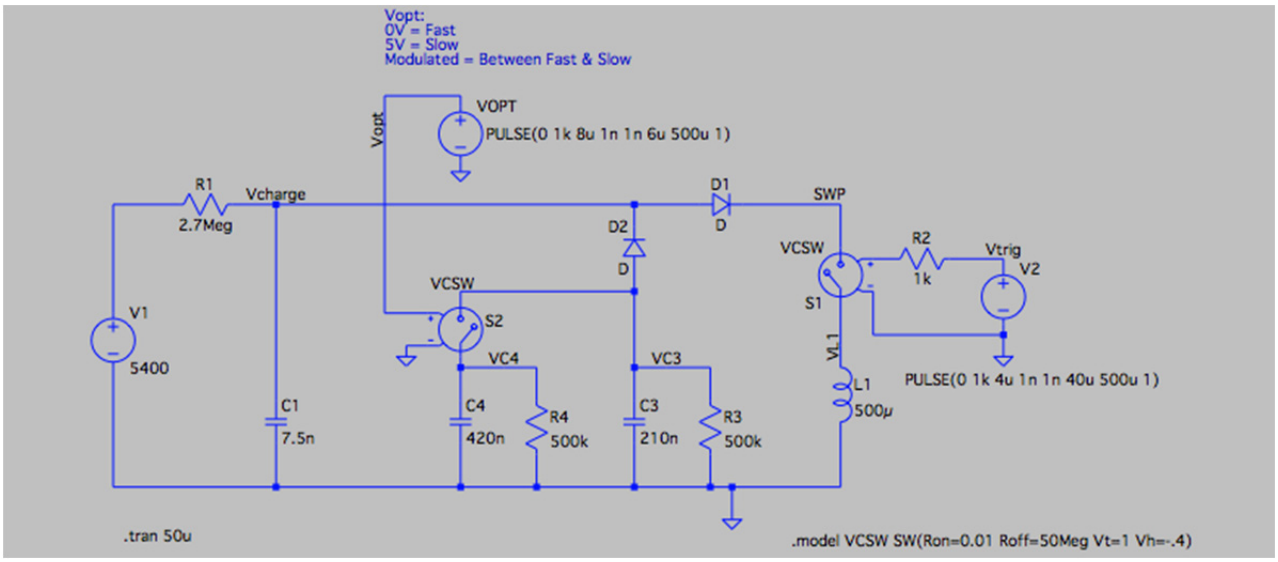

Figure 4: Pulse circuit diagram.

SUMMARY

We are studying the effect of a pulsed solenoid field on laser ablation plasma to improve quality and total charge within a signle pulse of an ion beam. We collected the basic data on a test bench and then found that the magnetic field decreasing from 90 G to 60 G within 10 µs is expected to produce a flat current profile. To prove the advantage of the pulsed solenoid, we will install a specially designed pulsed solenoid in the Laser Ion Source for the RHIC-EBIS (LION) at BNL. The electrical and mechanical design was finished and we started fabrication.

ACKNOWLEDGMENT

We would like to thank Dr. H. En'yo of Radiation Laboratory, RIKEN for supporting this study. This work was performed under the supports of the DoE and National Aeronautics and Space Administration, and supported by RIKEN Junior Research Associate Program.

REFERENCES

[1] T. Kanesue *et al.*, Proc. IPAC'14. Dresden, Germany, (2014)
[2] R. Kelly, and R. W. Dreyfus, Surf. Sci., vol. 198, nos. 1-2, pp. 263-276 (1988)

ISBN 978-3-95450-131-1

OBSERVATION OF SUBLIMATION EFFECT OF MG AND TI IONS AT THE HYPER-ELECTRON CYCLOTRON RESONANCE ION SOURCE

H. Muto#, Center of General Education, Tokyo University of Science, Suwa, 5000-1, Toyohira, Chino Nagano 391-0292, Japan
Y. Ohshiro, Y. Kotaka, S. Yamaka, S. Watanabe, H. Yamaguchi, S. Shimoura, Center for Nuclear Study, University of Tokyo, 2-1 Hirosawa, Wako Saitama 351-0198, Japan
M. Kase, S. Kubono, K. Kobayashi, M. Nishimura, Nishina Center for Accelerator-Based Science, RIKEN, 2-1 Hirosawa, Wako Saitama 351-0198, Japan
M.Oyaizu, Institute of Particle and Nuclear Studies, High Energy Accelerator Research Organization, 1-1 Oho, Tsukuba Ibaraki 305-0801, Japan
T. Hattori, Heavy Ion Cancer Therapy Center, National Institute of Radiological Sciences, 49-1 Anagawa, Inage Chiba 263-8555, Japan

Abstract

Light intensities of a grating monochromator during plasma chamber baking, $^{24}Mg^{8+}$ and $^{48}Ti^{13+}$ beam operation were observed at the Hyper -Electron Cyclotron Resonance (ECR) ion source. During chamber baking almost all light intensities were Fe I and Fe II. However, when MgO or TiO_2 rod was inserted into the plasma, and the beam operation was started, the light intensity spectrum significantly changed. In particular, most of the Fe I and Fe II lights disappeared, and Mg or Ti light intensities appeared. In this paper we describe the sublimation pump effect of Mg and Ti ions of ECR ion source during chamber baking and beam tuning.

INTRODUCTION

A grating monochromator with a photomultiplier has been used for beam tuning at the Center for Nuclear Study Hyper-ECR ion source [1,2]. Hyper-ECR ion source has been successfully used as an injector of the multi-charged ion beams of high intensity for RIKEN Azimuthal Varying Field (AVF) cyclotron [3]. Light intensity observation is an especially useful technique for an identification of the ions of the same charge to mass ratio in the plasma [4]. These ions are difficult to separate by an analyzer magnet. Before the operation of multi-charged metal ion beams chamber baking (degassing from the plasma wall) must be done to obtain a required vacuum condition. At the beginning low RF power (~100W) is fed to the residual gas in the plasma chamber, and a degassing process is conducted with increasing RF power gradually until the vacuum gauge reading is settled (1~5 x 10^{-5} Pa order) to start a metal rod insertion into the plasma chamber. In this paper we describe the light intensities during baking, $^{24}Mg^{8+}$ and $^{48}Ti^{13+}$ beam operation.

EXPERIMENTAL

$^{24}Mg^{8+}$ and $^{48}Ti^{13+}$ ions have been produced in the 14.2 GHz Hyper-ECR ion source. The structure and present operation condition of the ion source are described in Ref. 3. At the beginning of the chamber baking RF power of ~100 W was fed to the residual gas of the plasma chamber. Extraction voltage was set to 10 kV. Then a vacuum gauge reading rapidly dropped down to less than 10^{-4} Pa from 10-5 Pa order, and a brake-down of the high voltage power supply happened because of a huge extraction current. Several hours later the extraction voltage was recovered, and vacuum gauge reading also reached 10-5 Pa order. RF power gradually increased to ~ 600 W until obtaining a required vacuum condition (1~5 x 10^{-5} Pa), and a row extraction current of less than 2 mA. After baking of the plasma chamber, a pure metal or an oxidized metal rod was gradually inserted into the chamber without an excessive heat. An excessive heat causes a brake-down of the power supply because of a huge extraction current. The RF power was ranging between 500 and 600W for a highly multi-charged ion production. Argon, Neon, Oxygen and Helium gases were used as supporting gases to keep the plasma condition stable. A grating monochromator (JASCO CT-25C) and a photomultiplier (Photosensor module H11462-031, Hamamatsu Photonics) were used for a light intensity observation during chamber baking and beam operation. Beam resolution of the grating is 0.1 nm (FWHM). L-37 and R-64 filters are used for preventing both second and third order light signals. Wavelengths of the observed lines were determined in accordance with the NIST Atomic Spectra Database [5].

RESULTS AND DISCUSSIONS

Figure 1 shows the optical line spectrum of the Hyper-ECR ion source under plasma chamber baking after three hours from the start. A vacuum gauge reading was 5.7 x 10^{-5} Pa. A drain current (an extraction current) was 12 mA. RF power was 100 W. In this figure most of all peaks were Fe I and Fe II. There were some C, N and O optical lines in the spectrum. However, those lines were all disturbed by Fe I and Fe II strong lights, and therefore it was difficult to separate those. Relative intensities of those Fe I and Fe II are quite strong. Figure 2 shows the optical line spectrum of the ECR plasma during $^{24}Mg^{8+}$ ion beam tuning. A vacuum gauge reading was 1.7 x 10^{-5} Pa. A drain current was 1. 8 mA. RF power was 611 W.

#guatemalacocoa@gmail.com

ISBN 978-3-95450-131-1

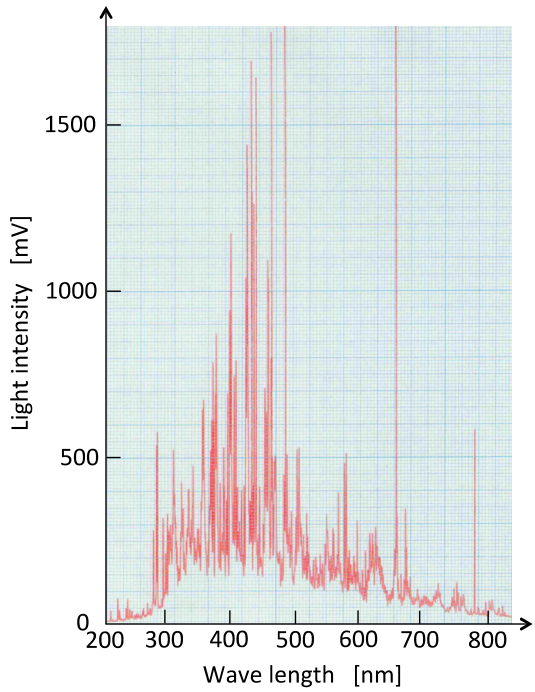

Figure 1: Light intensity spectrum of the residual gas ions after baking for three hours. The peaks of the spectrum are mostly Fe I and Fe II. The pressure and microwave power were 5.7 x 10^{-5} Pa and 100 W, respectively.

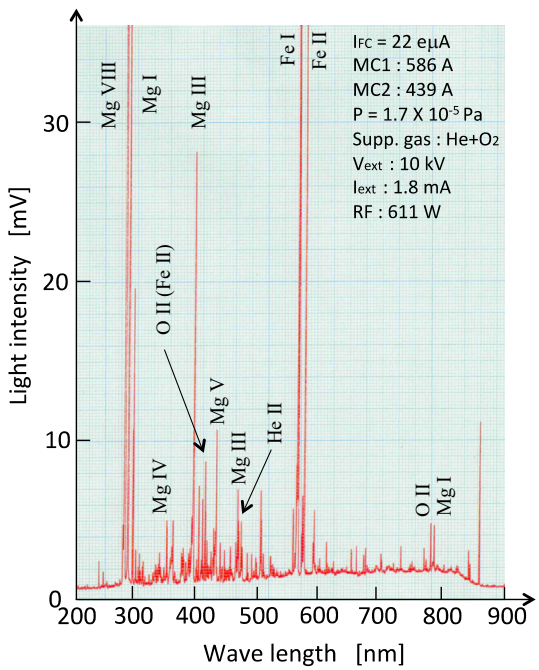

Figure 2: Optical line spectrum during $^{24}Mg^{8+}$ ion beam tuning. The shape of the spectrum drastically changed from that of residual gas plasmas. Fe light intensities of residual gas disappeared, and Mg I, III, IV and VIII lines were clearly observed.

Line intensities of Fe I and Fe II almost disappeared, and Mg light intensities appeared. Especially, Mg VIII line spectrum (λ=279.64 nm) was clearly obtained to identify the existence of $^{24}Mg^{8+}$ ions in the ECR plasma. In this figure new Fe I (λ=559.2 nm) and Fe II (λ=570.3 nm) light intensities were observed. A non-magnetic stainless steel cover was used for a smooth heat transfer to the tip of the MgO rod from the plasma. The edge of the cover was melted by plasma as shown in fig.3. Therefore, these two strong Fe lines are thought to be present because of the melted stainless cover.

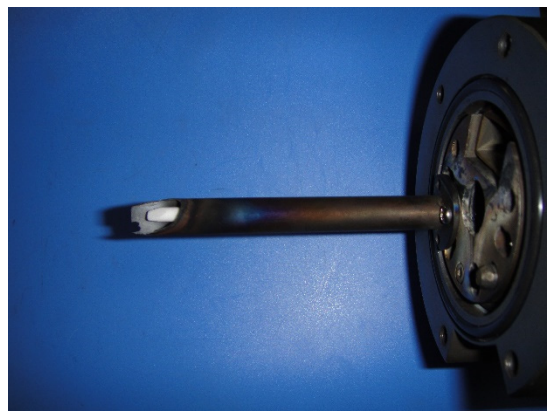

Figure 3: MgO rod with a stainless steel cover.

Oxygen and Helium lines also appeared in the spectrum because Helium and Oxygen gases were fed during the beam tuning as supporting gases to keep a required plasma condition. The ion source was tuned for the production of the $^{24}Mg8^{+}$ ions. Beam intensity of the $^{24}Mg^{8+}$ ions was set at 22 eμA. Figure 4 shows light intensity spectrum of residual gas plasma just after inserting TiO2 rod. Vacuum condition became stable after insertion of TiO2 rod. However, a sublimation effect is too strong, and a production of highly multi-charged Ti ions was complex. Then, a pure Ti rod instead of TiO2 rod was used to make $^{48}Ti^{13+}$ beam. Figure 5 shows the optical line spectrum during $^{48}Ti^{13+}$ beam tuning with Ne supporting gas. Natural Neon gas has ~ 9.22 % of ^{22}Ne and $^{22}Ne^{6+}$ is the same charge to mass ratio of $^{48}Ti^{13+}$ (q/m=0.27). Beam intensity of these beams was 3.0 eμA. Ti XIII light intensity was observed clearly. However, it was difficult to separate these ions by a magnetic analyser.

Then, Ar was selected as a supporting gas instead of Ne to separate $^{48}Ti^{13+}$ ions. However, the plasma condition became unstable, and the desired $^{48}Ti^{13+}$ ions were not obtained. As a result, He gas was selected as a supporting gas in order to produce $^{48}Ti^{13+}$ ion beam. Figure 6 shows light intensity spectrum during $^{48}Ti^{13+}$ ion beam tuning with He supporting gas. Ti XIII line was clearly observed and $^{48}Ti^{13+}$ beam intensity was 1.0 eμA. Beam intensity of $^{48}Ti^{11+}$ was also set at 9.6 eμA.

From these results sublimation pump effect of Magnesium and Titanium ions were visually demonstrated by the grating monochromator with photomultiplier.

ISBN 978-3-95450-131-1

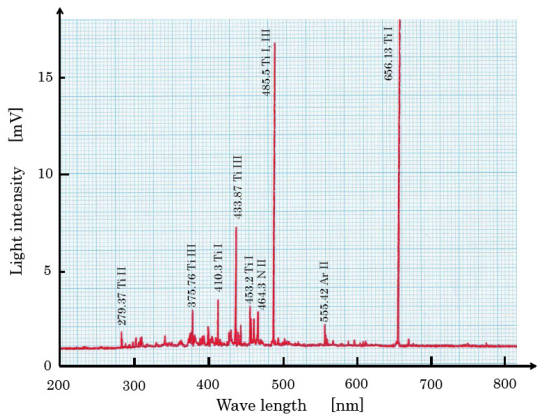

Figure 4: Optical line spectrum of residual gas plasma just after inserting TiO2 rod. Vacuum gauge reading was 1.9 x 10^{-5} Pa and RF power was 100 W.

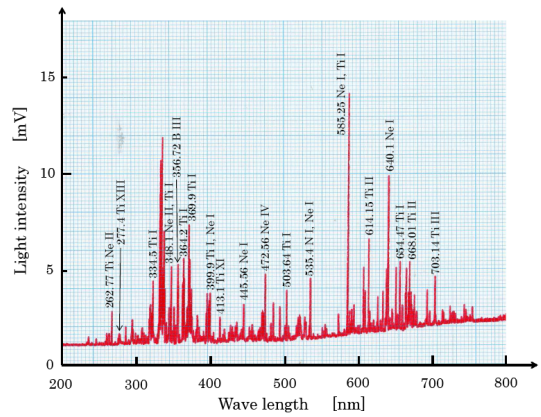

Figure 5: Optical line spectrum during $^{48}Ti1^{3+}$ ion beam tuning with Ne supporting gas. Ti XIII line was clearly observed. However, Ne lines also were present.

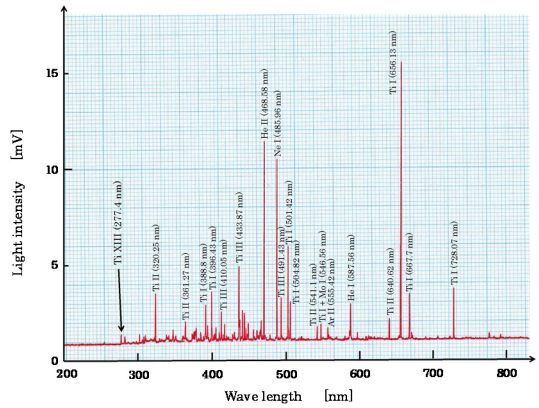

Figure 6: Optical line spectrum during $^{48}Ti^{13+}$ ion beam tuning with He supporting gas. Ti XIII line was clearly observed and 1.0 eμA of $^{48}Ti^{13+}$ ion beam was obtained.

CONCLUSIONS

During plasma chamber baking observed light intensities were mostly Fe I and Fe II. Fe ions were relatively heavy and not easy to extract from the plasma chamber. Those atoms were present for a long time in the vacuum chamber. Therefore, stainless steel is thought to be an unsuitable material for a plasma chamber to extract multi-charged ions. Aluminium or Magnesium based light alloy is better for plasma chamber materials for degassing and extraction.

REFERENCES

[1] H. Muto et al., Rev. Sci. Instrum. 84, 073304 (2013).
[2] H. Muto et al. , Rev. Sci. Instrum. 85, 02A905 (2014).
[3] Y. Ohshiro et al., Rev. Sci. Instrum. 85, 02A912 (2014).
[4] H. Muto et al., Rev. Sci. Instrum. 84, 073304 (2013).
[5] www.nist.gov/pml/data/asd.cfm for NIST Atomic Spectra Data base.

ISBN 978-3-95450-131-1

OPTICAL DESIGN OF THE EBIS CHARGE BREEDER SYSTEM FOR RAON IN KOREA

Hyock-Jun Son, Handong Global University, Pohang 791-708, Rep. of Korea
Jongwon Kim ,RISP, Institute for Basic Science, Daejeon 305-811, Rep. of Korea
Young-Ho Park RISP, Institute for Basic Science, Daejeon 305-811, Rep. of Korea
Moses Chung ,Ulsan National Institute of Science and Technology, Ulsan 689-798, Rep. of Korea

Abstract

Electron beam ion source (EBIS) will be used for charge breeding of rare isotope beams in Rare Isotope Science Project (RISP) the ISOL system. Simulations of EBIS charge breeder system are reported here. The electron beam simulation has been performed by using TRAK code. The electron beam collector deign was optimized based on these electron beam simulation. Ion beam simulation, including acceptance calculation, has also been performed by using TRAK and SIMION codes. In this work, we will also report simulation results on the charge breeding processes in addition to the electron and ion beam dynamics.

INTRODUCTION

In Korea, a heavy ion accelerator facility called RAON is being designed to produce various rare isotopes under the Rare Isotope Science Project (RISP). The RAON has a unique feature of having both Isotope Separation On-Line (ISOL) and In-Flight fragmentation (IF) systems for the various rare isotope productions. Electron beam ion source (EBIS) will be used for main charge breeder in the ISOL system. The EBIS charge breeder has significant advantages over the ECR option for high ion beam intensities, providing higher efficiency, shorter breeding times and significantly better purity of highly charged radioactive ion beams for further acceleration [1]. To reduce emittance of a beam injected into the EBIS, an RFQ cooler is planned to be used as in other facilities. Beam emittance is expected to be reduced by an order of magnitude to around 3 π mm·mrad at 50 keV [2]. The main design and simulation parameters were chosen based on those of the EBIS for the CARIBU project at Argonne National Laboratory [1].

SIMULATION AND OPTICAL DESIGN

The simulation of EBIS system is mainly classified into three parts such as the electron beam dynamics, the ion beam dynamics and electron-ion beam interaction. The TRAK, SIMION and CBSIM codes have been used to design the EBIS charge breeder system for the RISP.

Electron Beam Simulation

The electron gun with IrCe cathode is designed by BINP. The electron beam current is set to be 3 A at the beam energy of 20 keV. The electron beam simulation has been performed from an E-gun cathode to a collector by using TRAK code [3]. The electron beam trajectories are shown in Figure 1. The electron beam current density can reach up to 500 A/cm^2 by maximum magnetic field of about 6 T. This region, which has a maximum electron beam current density, is called ion trap region. The electron beam radius is around 0.45 mm in this region. The radial ion trapping is achieved through the space charge of the electron beam in the ion trap region. The axial trapping is achieved by biasing drift tubes.

The electron beam trajectories in the collector are shown in Figure 2. The electron beam is rapidly spread out from the entrance of the collector because magnetic fields are decreased by a magnetic shield. Furthermore, the electron beam trajecories depend on the potential applied to the repeller and collector body electrode. For the case of Figure 2, the applied voltages of the collector body and the repeller are 1 kV and -10 kV, respectively. The trajectories of electron beam are directly related to the corresponding power density distributions along the inner cylindrical collector surface. Figure 3 presents the corresponding power density distributions under different electrode voltage conditions.

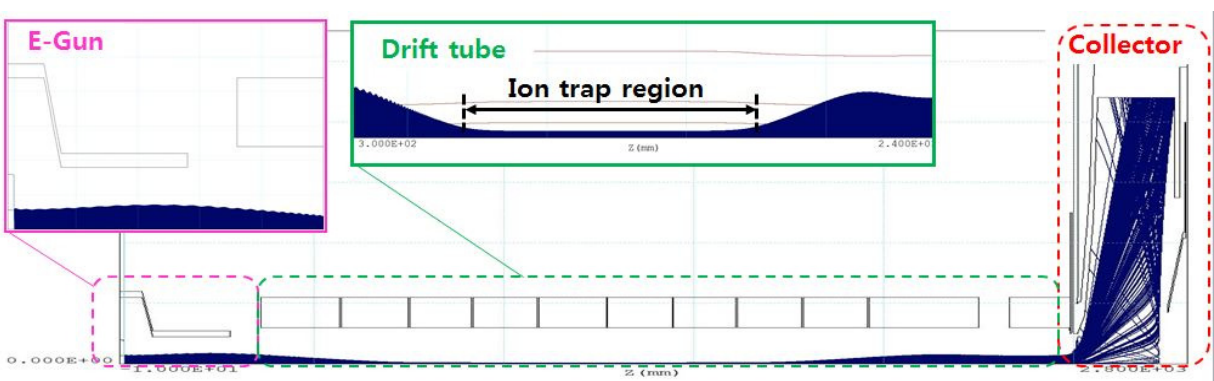

Figure 1: The electron beam trajectories from an E-gun cathode to a collector.

ISBN 978-3-95450-131-1

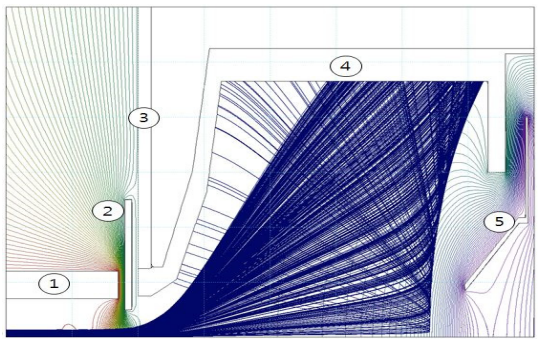

Figure 2: Electron beam trajectories in the collector (①drift tube, ② suppressor, ③ magnetic shield, ④ collector body, ⑤ repeller).

If the absolute repeller voltage increases, the end position of the electron beam dump will be placed further inside of the collector. Whereas the lower collector body voltage, the lower peak power density and the broader power density distribution. For each case of dashed line and straight lines in Figure 3, total power consumptions are 12kW and 15kW, respectively.

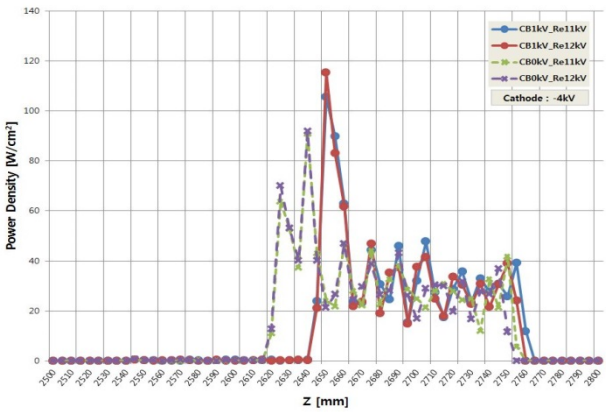

Figure 3: Power density distributions along the collector body for several different voltage settings.

Charge Breeding Progress

The charge breeding was simulated using CBSIM codes [4]. The breeding time of $^{132}Sn^{33+}$ is calculated to be 61 ms under the electron beam conditions of 3A and 20keV. In case of $^{133}Cs^{33+}$, the breeding time is about 67 ms. The estimated charge breeding results of Sn ions are shown in Figure 4.

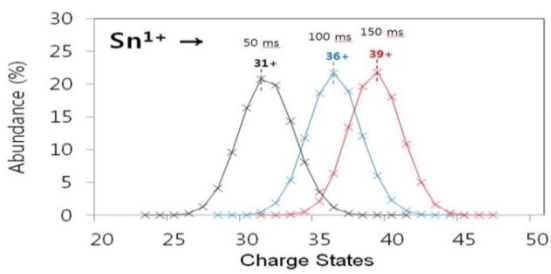

Figure 4: Charge state distribution of Sn ions after breeding times of 50ms, 100ms and 150ms.

Acceptance

An RMS acceptance of the EBIS system is estimated to be 52π mm·mrad assuming partial overlap between ion and electron beams. If 100% of ion-electron overlap is assumed, the acceptance is 14π mm·mrad (Fig. 5).

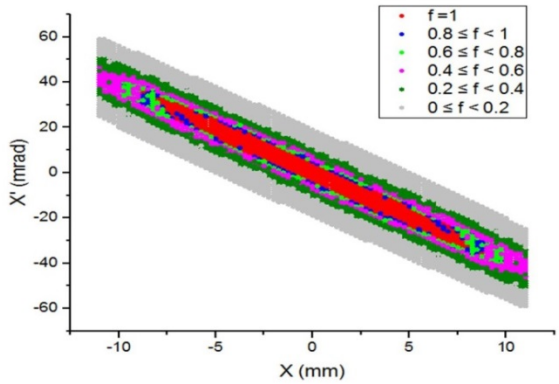

Figure 5: Phase-space of accepted ions.

Ion Beam Extraction Simulation

Figure 6 shows the ion beam trajectories in the presence of the electron beam in the extraction mode.

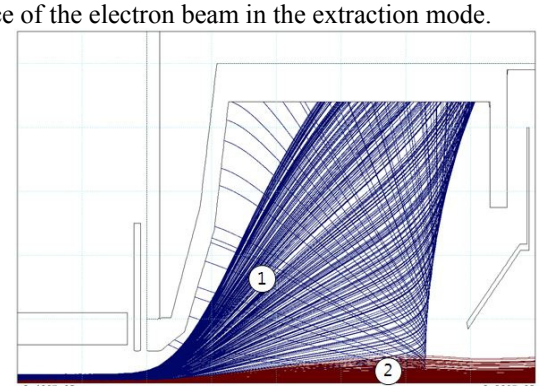

Figure 6: The trajectories of beam in the extraction mode (① electron beam trajectories, ② The $^{132}Sn^{32+}$ ion beam trajectories).

The ion transport simulation has been performed by using SIMION code [5]. The transport optics basically consists of two Einzel lenses. In particular, the repeller is shared for one component of the Einzel lens. Figure 7 shows the structure of the ion transport optics and ion beam distributions at each monitoring plane. The RMS emittance in the X-X' phase space is 44.4π mm·mrad at the starting plane. However, the emittance is increased to 60.6π mm·mrad at the plane #2, and the phase space is also distorted. For this type of ion transport structure with simple Einzel lenses, the potential distribution is asymmetric, and the acceleration section exists inside of the collector. Consequently, we expect that the emittance growth and phase space distortion occur in this case.

In case of CARIBU EBIS charge breeder, a steerer type Einzel lens is adopted to reduce the emittance growth rate [6]. Hence, in this study, we also have performed the ion transport simulations for case of an ion transport structure with the steerer type Einzel lens.

ISBN 978-3-95450-131-1

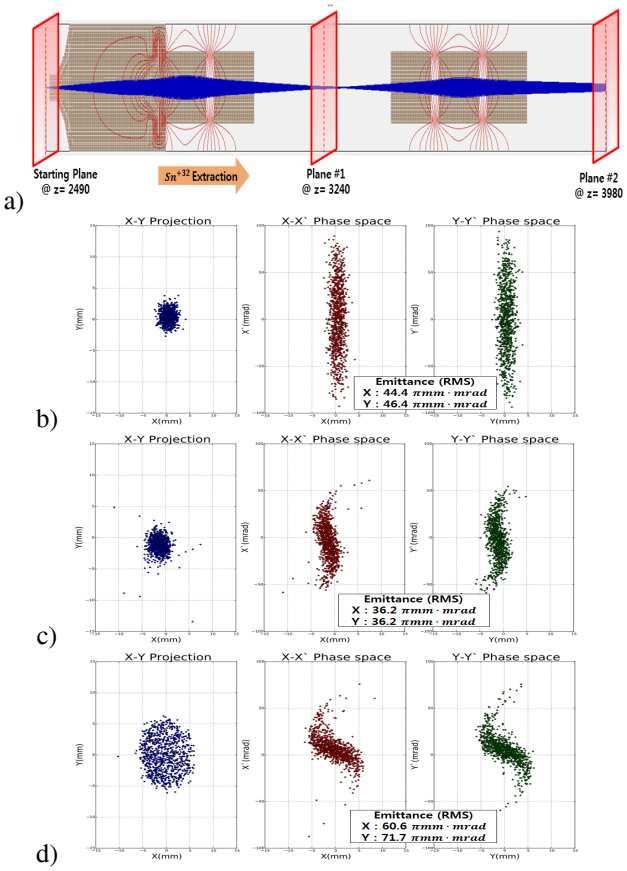

Figure 7: (a) Schematic of the ion transort optics and ion trajectories. Ion beam distributions at starting plane (b), plane #1 (c), and plane #2 (d).

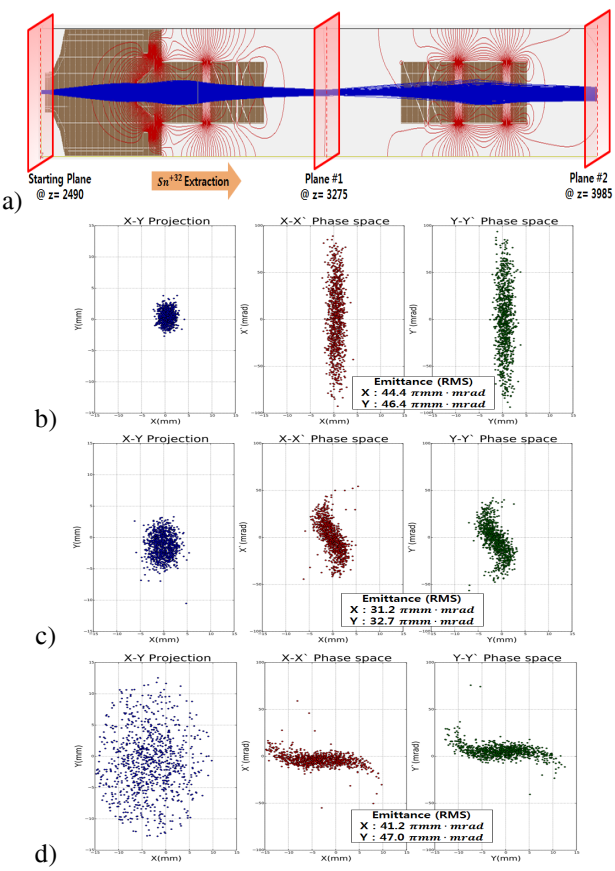

Figure 8: (a) Schematic of the ion transort optics and ion trajectories. Ion beam distributions at starting plane (b), plane #1 (c), and plane #2 (d).

Figure 8 shows the structure of the steerer type Einzel lens ion transport optics and ion beam distributions. The emittance growth is suppressed under this structure. The RMS emittances in the X-X' phase space are 44.4π mm·mrad and 41.2π mm·mrad, respectively at starting plane and plane #2.

However, a shift in beam position and a broadening of beam distribution in the X-Y projection are resulted at the plane #2. We need to further optimize the simulation and to perform careful design studies of the ion transport optics.

CONCLUSION

Based on the numerous simulations presented in this paper, design of the electron gun test stand is finished for the RISP EBIS system. For the ion transport part, we plan to perform more detailed simulations and careful design studies for future work.

ACKNOWLEDGMENT

This work is supported by the Ministry of Science, ICT and Future Planning (MSIP) and Technology and the National Research Foundation (NRF) of the Republic of Korea under Contract No. 2011-0032011.

REFERENCES

[1] S. Kondrashev, C. Dickerson, A. Levand, P. Ostroumov, R. Vondrashek, A. Pikin, G. Kuznestov, M. Batazova, "Commissioning of CARIBU EBIS charge breeder sub-systems," in Proceedings of 12th Heavy Ion Accelerator Technology Conference (JACoW, 2012), pp. 165-169.

[2] Jongwon Kim, Jae-Eun Han, Hyock-Jun Son, Kun-Hui Yi, Liangji Zhao, Jin-Soo Kim, "An EBIS System for Rare Isotope Science Project in Korea", AIP Conference Proceedings;2015, Vol. 1640 Issue 1, p38.

[3] TRAK8.0, Field Precision LLC, New Mexico, U.S.A.

[4] R. Becker, O. Kester, Th. Stoehlker, "Simulation of charge breeding for trapped ions," in Journal of Physics: Conference Series 58 (IOP Publishing, 2007), pp. 443-446.

[5] SIMION8, Scientific Instrument Services, NJ, U.S.A

[6] C. Dickerson, B. Mustapha, A. Pikin, S. Kondrashev, P. Ostroumov, A. Levand, and R. Fischer, "Simulation and design of an electron beam ion source charge breeder for the californium rare isotope breeder upgrade", Physical Review Special Topics – Accelerators and Beams 16, 024201 (2013).

ISBN 978-3-95450-131-1

CHALLENGES FOR THE NEXT GENERATION ECRIS

L. Sun#, H. W. Zhao, J. W. Guo, Y. Yang, W. Lu, W. Wu, L. Z. Ma
Institute of Modern Physics, CAS, 509 Nanchang Rd., Lanzhou 730000, China

Abstract

As an indispensible device to produce intense highly charged ion beams, ECR ion source has evolved into the 4th generation or the next generation. Knowledge from the development of the 3rd generation ECR ion sources could provide valuable reference for the next generation machine design and fabrication, however there are still many challenges with regards to several key technical issues and physics approaches. This paper will review what we have learned from the state of the art ECR ion sources, and then critical aspects concerning the higher performance next generation ECR ion sources development will be discussed.

INTRODUCTION

For existing facilities, or projects to be done, such as FRIB project, SPIRAL2 project, HIRFL facility, RIBF project, RHIC, LHC, FAIR and etc., the preinjectors are essentially important. Higher Q/M or charge state Q from an ion source makes the downstream accelerators more compact and less costly. High Charge state Ion (or HCI) beam at the preinjector is delivered from a HCI source. But because of the capacity and characteristics of an ion source is inherent, the choice of ion beam charge state is a tradeoff between ion beam intensity and charge state. Therefore, the choice of the ion source is also strongly depending on the accelerator needs, for instance, EBIS is the ion source solution to RHIC preinjector [1], and ECRIS is the must-have choice for FRIB project [2]. For high charge state intense CW or long pulse (~ms) ion beams solution, ECR in source is still the dispensable one. HIAF or High Intensity heavy ion Accelerator Facility project to be launched in China, 50 pμA of U^{34+} beam production performance should be demonstrated by the injector ion source so as to ensure the possibility to operate the ion source routinely with an intensity of 40 pμA. The state of the art high performance ECR ion source such as VENUS can produce a beam intensity of ~11.7 pμA U^{34+} [3]which is barely 1/4 of the desired beam intensity. Thanks to the recent intense development with SECRAL, 22 pμA Bi^{31+} has been obtained, which is an indication that with a proper oven that gives sufficient uranium vapour, ECR ion source of 3rd G. can also produce an equivalent beam intensity of U^{34+}. However, this value still needs to be multiplied by a factor of 2.3 to get the HIAF goal.

ECRIS development stepped into the era of the 3rd G. when the LBNL colleagues got the 1st beam with VENUS at 18 GHz in 2002[4]. Together with the following-up development of superconducting ECR ion sources in IMP, MSU and RIKEN, it have been evidenced that the 3rd G. ECR ion source is virtually a very powerful machine in terms of intense highly charged ion beam production. The empirical frequency scaling laws still works well with a 3rd G. ECRIS. According to the scaling laws, one must build a min-B device with high enough magnetic field to confine the much denser plasma that are induced by higher frequency microwave heating, so as to produce intense HCI beams since $\Sigma n_q = n_e$ and $n_e \propto \omega^2$, where n_q is the ion density of charge state q and ω is the microwave frequency. Therefore, to produce highly charged ion beam intensities beyond the 3rd G. ECRIS capacity, a 4th G. ECRIS is very likely the only economical solution. Learned from experience during the development of a 3rd G. ECRIS, there are many technical and physics challenges that need long-term R&D and probably some big break-through. In this paper, we will review and discuss the challenges and difficulties that we could envision during the development of a 4th G. ECRIS.

DEVELOPMENT OF 3RD G. ECRIS

3rd G. ECRISs have shown obvious performance enhancement over the 2nd G. ones, however there are many technical and physics challenges during the ion source development that makes the device more complicated and expensive. In this section, a general review of the typical issues that the ECRIS community have learned during a high performance superconducting ECR ion source development. Figure 1 gives the layout of a typical ECR ion source and the analysing beam line system which.

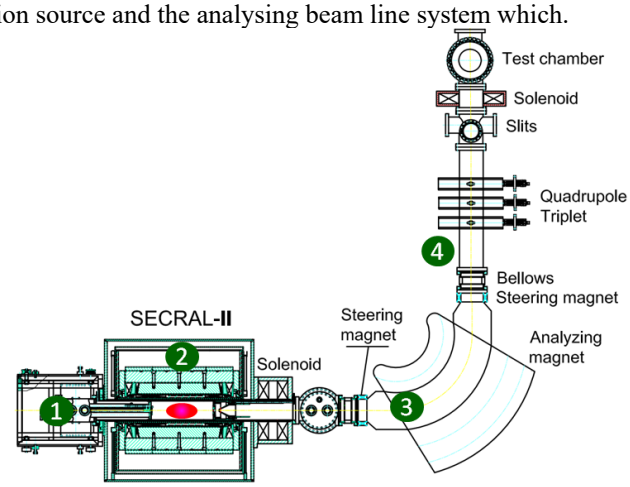

Figure 1: Layout of a typical ECRIS test bench, 1-Ion source injection part; 2-Ion source magnet; 3-ECR beam line; 4-Ananlysing beam line and beam diagnostics.

Superconducting Magnet

One typical feature of the 3rd G. ECRIS is that they are all incorporated with NbTi superconducting magnet technique so as to provide sufficient magnetic field confinement for the optimum operation at 24~28 GHz. Superconducting magnet design and construction is of the

#sunlt@impcas.ac.cn

ISBN 978-3-95450-131-1

highest challenge in a 3rd G. ECRIS development. ECR ion source magnet has a sophisticated structure which has a superimposed configuration of axial solenoids and radial sextupole magnet. For superconducting ECRIS magnet, because of the very high field produced and the high currents in the coils, strong Lorentz forces are induced in the coils. Therefore, it is essential to do sufficient clamping to all of the superconducting coils to prevent any slight movement during the magnet coil ramping and operation. Insufficient coil clamping will most likely cause quenches and probably magnet failure. The most critical forces in a superconducting ECRIS magnet are the EM forces at the sextupole coils ends, where the sextupole coil currents in the return ends see the magnetic field components from the axial solenoids, and consequently strong Lorentz forces created at the sextupole coil ends. To reduce the strong forces, design with conventional structure has to extend the ends to a certain distance from the axial solenoids so as to lower the forces to safe values for operation, which makes the conventional structure magnet more bulky and engineering complicated. An alternative and also very effective solution to this issue is to place the sextupole coils external to the solenoids. With this design, the sextupole coils see much lower axial fields and therefore, the sextupole magnet could be designed with a short length that makes the whole magnet very compact. The schematic structure of the conventional one (adopted by VENUS, SuSI and Riken SCECRIS, an etc.) and the alternative one (SECRAL) are shown in Fig.2. Nevertheless, with either design configuration, magnet clamping and coil pre-stress is very critical. VENUS source magnet incorporated a very innovative pre-stress technique by using liquid metal bladder [5]. The similar technical approach was also employed during the fabrication of SuSI ion source [6]. For SECRAL magnet, massive cold iron had been used in the design so as to boost the radial field and also to shield the stray field. The cold iron sections together with the coils are efficiently clamped by big aluminium rings installed through hot jacket fit. Besides proper pre-stress or clamping, precise calculation and mechanical design taking into account of the thermal contraction from room temperature to 4.2 K are required essentially.

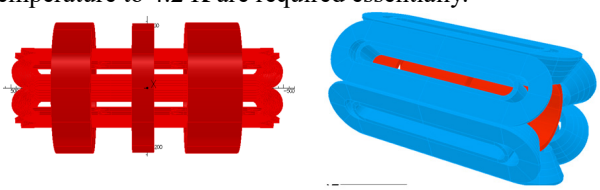

Figure 2: Conventional superconducting ECRIS magnet structure (left) vs. SECRAL type magnet structure (right).

Cryogenic System

For most of the superconducting ECR ion sources in operation now, the cold mass is immersed in 4.2 K LHe atmosphere, therefore sufficient LHe level must be kept to guarantee their continuous operation. Two feasible approaches have been adopted in different labs, i.e. the LHe supply tube is connected to the cryogenic circulation loop of a cryo-plant, such as SuSI in NSCL, or by using cryo-coolers to recirculate the evaporated He from the LHe reservoir, such as VENUS in LBNL. Since the second option is more flexible and convenient for operation, it is the most recommendable and widely adopted one. However, unlike the other cryogenic system, ECRIS cryogenic system has strong subsequent influence of the plasma condition. When ECR plasma is heated with high microwave power, strong bremsstrahlung radiation is created which induces dynamics radiation heat load to the 4.2 K region. This plasma radiation dynamic heat load dominates the heat load to the 4.2 K when the ion source is working at higher frequency. For instance, the static heat load at 4.2 K of SECRAL magnet is about 1.0 W, but when operated at 24 GHz, typically 1.0W/kW dynamics heat load has been observed. When higher B_{min} is tuned for the highly charged ion production, this rate becomes much higher. More cryo-coolers or high cooling capacity coolers on the service turret could be a straight-forward solution. For example, SCECRIS in Riken has utilized 2 GM-JT coolers and 1 GM cooler to solve the problem, and have enough redundancy for high power operation at 28 GHz (Fig. 3) [7]. However, for the successful operation of the ion source at 10 kW/28 GHz, a $\geqslant$10 W dynamics heat load could be induced, which is still a big challenge for all the 3rd G. ECRISs.

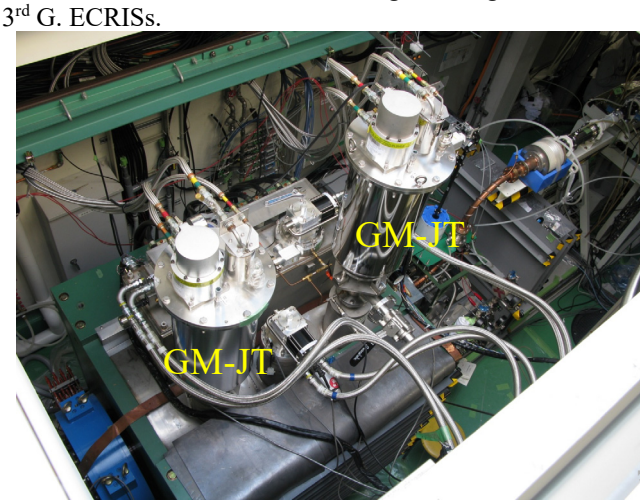

Figure 3: Service turret of Riken SCECRIS ion source.

Conventional Parts

A high performance 3rd G. ECRIS will deal with maximum 10 kW microwave power heating inside the plasma chamber. This is a challenge for the conventional parts' cooling design, especially those sections facing the plasma directly, i.e. biased disk, plasma chamber, and plasma electrode. Different labs have alternative approaches to a successful design. But long-term reliable operation at high power is still a big issue. Additionally, strong bremsstrahlung radiation will cause insulation performance degradation of the high voltage insulator housing the plasma chamber, and ultimately result in high voltage insulation failure. Presently, insertion of a 1.5~2 mm tantalum sheet between the plasma chamber and HV

ISBN 978-3-95450-131-1

insulator column seems to be an applicable solution (Fig.4), but after certain long operation period at high microwave power, degradation is still witnessed inside the insulator.

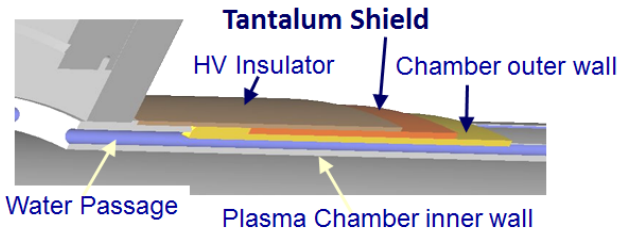

Figure 4: Ta shielding design for a 3rd G. ECR ion source.

Intense Beam Transmission

When operated for intense highly charged ion beam production, a 3rd G. ECRIS typically extracts 10~15 emA total current from the plasma with a maximum energy of 25~30 keV/q. Space charge is very server during such an intense beam transmission with low energy. Thanks to the space charge compensation in the ECR beam line, typically ~70% space charge has been compensated [8]. However, severe beam divergence is still obvious at the entrance of the analyser magnet. The ECR beam line is intentionally designed very short for high transmission efficiency, therefore, no extra space is left for additional beam focusing elements. When large envelope beam passing through the dipole, it might be exposed to the high order component therein, which causes high order aberration to the analysed beams. Larger gap magnet with proper pole surface trimming will be very helpful to improve the beam quality (Fig. 5) [9]. An alternative solution might be a sextupole magnet corrector installed either upstream or downstream of the dipole magnet. However, it is not easy to make a high quality beam for the downstream accelerators. The ion beam condition at the ECR beam line is far from been better understood, as a cause of insufficient diagnostic, which makes the downstream beam matching challengeable. Besides, the ion beam extracted from an ECR ion source is inhomogeneous and highly coupled in transverse space [10].

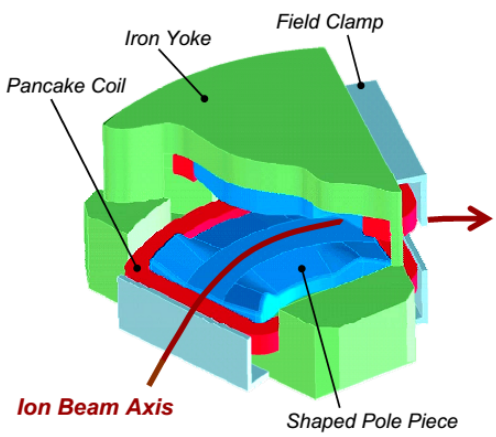

Figure 5: *Batman* analyser dipole magnet design for VENUS ion source beam line.

TOWARDS A 4TH G. ECRIS

A 4th G. ECRIS is expected to be operated at the frequency of 40 GHz or higher. Compared to a 3rd G. ECRIS, the challenges to build a 4th G. ECRIS will be more or less similar. But since the next generation ion source will be operated at higher frequency, higher microwave power under the condition of higher magnetic field confinement to the plasma, the challenges existing with a 3rd G. ECRIS will become more severe that makes the development of a 4th G. ECRIS more difficult.

Nb_3Sn Superconducting Magnet

As discussed in the former section, to meet the highly charged ion beam intensity needs of a next generation heavy ion accelerator, such as HIAF, an intensity gain by a factor of ~2.3 should be made. According to ω_{ecr}^2 scaling, the next generation ECRIS is desired to be operated at ω_{ecr}= $(2.3)^{0.5}$ * 28~43 GHz. At IMP, a 45 GHz ECRIS is under construction with this guiding rule.

To make an ECRIS optimum for operation at the frequency of 45 GHz, magnetic fields of two mirror maxima 6.5 T and 3.5 T at source injection and extraction sides respectively, 3.4 T at the ion source plasma chamber wall are desired. For this purpose, approximately 1400 A/mm^2@12 T will be seen inside the superconductor. Obviously, this parameter is far beyond the NbTi superconducting technology. The state of the art Nb_3Sn technology is therefore the feasible solution to the 4th G. ECRIS magnet. Unlike NbTi, which is ductile and can withstand high compressive force, Nb_3Sn is brittle and strain sensitive. As a result, the current carrying capability of Nb_3Sn coils is affected by mechanical stresses in the windings. The actual behaviour depends on several factors, such as the wire design and the fabrication process. However, reversible degradation is generally observed above 150 MPa with severe and permanent degradation occurring above 200 MPa [11].

When designing a 4th G. ECRIS magnet, there several choices must be made first with series of comparison of pros and cons. As shown in Fig. 6, Nb_3Sn wire with Bronze method can barely meet the requirement of a 45 GHz ECRIS magnet, therefore it is better to go with the selection of Internal Tin method, typically the rod-restack processed or RRP Nb_3Sn. To have a 15~20% operation safety margin, it is better to go with M-grade RRP wire as shown in the picture. However, as mentioned in the former paragraph, Nb_3Sn is brittle and non-ductile, winding of the coils with one single strand will have high risk of magnet break-down if one of the strand could be broken for any reasons. The scheme with Nb_3Sn cable winding will be a more robust one, but it also has many subsequent issues. Cable solution means that the magnet coils will be excited with currents up to 10 kA for our application. More expensive power supplies and current leads will be used. Since for >1000 A excitation currents, HTS leads are no longer applicable, heat load to the 4.2 K region will be high, therefore traditional solution with cryocoolers will not be applicable. Two technical approaches are recommended, i.e.

ISBN 978-3-95450-131-1

connection the LHe feeding port to the main cryogenic system of the accelerator, or place a dedicated LHe liquefier system (such as Linde L70 liquefier) adjacent to the ion source magnet. But most of the high performance ECR ion source as an injector ion source will be placed on a high voltage platform, for instance ECRIS for HIAF is going to be floated to 100 kV or higher. The solution of LHe lines connected to the main cryogenic pipes at ground potential will be very technically challengeable in terms of the HV insulation. The solution with a LHe liquefier placed on the high voltage platform will increase enormously the footprint and electricity capacity needs of the high voltage platform, and of course a much higher budget tolerance must be made as well.

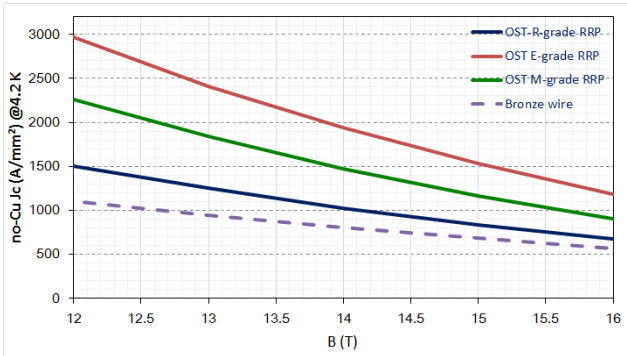

Figure 6: Typical performances of Internal tin Nb_3Sn wires vs. Bronze Nb_3Sn wire.

Economical Nb_3Sn strand is commercially available within the length of 1 km for the diameter control of Ø0.8 mm to Ø1.8 mm. For the 4th G. ECRIS magnet coils, if wound with single strand, maximum wire length of 4.0 km might be necessary, which means superconducting wire joints must be made for the incident coils. This is very a challengeable technique, especially when many joints should be made inside such a high field magnet. Winding with Nb_3Sn cable can avoid such a trouble, but with the other problems as discussed above.

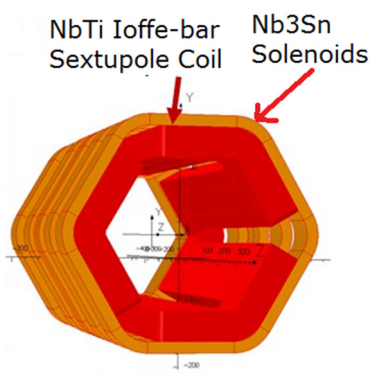

Figure 7: Ioffe-bar sketch for a 45 GHz ECRIS.

Besides the superconductor issue, the choice of the magnet configuration is another very critical aspect in the 4th G. ECRIS development. As for the moment, three magnetic configurations are available for choice, i.e. the conventional type, SECRAL type, and the latest proposed Ioffe-bar type (Fig. 7). Each of these configurations has its specific features and advantages. Both SECRAL and conventional configuration ECRIS magnets have been practically tested with the 3rd G. ECRISs. Ioffe-bar configuration has the biggest advantage by using NbTi wire to get the radial fields for the optimum operation of an ECRIS at 45 GHz, which can avoid the risk of complicated Nb_3Sn sextupole coil fabrication and also make the magnet more cost efficient [12]. However, this innovative idea needs further proof of principle test to demonstrate the feasibility.

Cryogenic System

Several issues concerning the cryogenic system have already been discussed in the former section. In the Nb_3Sn cable scheme, either support with the cryogenic plant or a dedicated LHe liquefier could be the solution with sufficient 4.2 K heat load tolerance. While winding with a single Nb_3Sn strand, it is more preferable to utilize GM-JT coolers. Two GM-JT coolers could provide maximum 9.0 W (50 Hz) cooling capacity at 4.2 K, which might not be enough for a 45 GHz microwave power heating ECR plasma operation at $\geqslant$10 kW. A dynamic heat load of >1.5 W/kW is predicated according to the operation experience with a 3rd G. ECRIS. How to get sufficient 4.2 K cooling capacity is one challengeable issue for the development of a next generation ECRIS. Alternative approach other than providing higher 4.2 K cooling capacity, effective X-ray shielding in the warmbore or 70 K shield might help to lower the 4.2 K dynamic heat load.

Quench protection is another critical issue needs to be considered. As a 4th G. ECRIS operated at 45 GHz has a stored energy up to 1.8 MJ, to dump such a high energy in a short time without any potential damage to the superconductor when magnet quenches needs a robust quench protection scheme. The winding scheme with Nb_3Sn cable allows high operation currents and much less coil turns that indicates much lower inductance and mutual inductance in the coils. Provided with a limit on the maximum voltage inside the quench protection loop (typically 1000 V), the maximum temperature rise will be much lower and within the safe operation margin which does not need a specific design on the quench protection loop. While for the single strand winding scheme, higher inductance and mutual inductance will be created, which could be problematic for the quench protection system design. Sectional protection loop for each coil could be a feasible approach.

Microwave Coupling and Heating

Gyrotron frequency microwave was incorporated into ECR ion source firstly in INFN/Catania during the commissioning of SERSE source [13]. And it becomes a standard ancillary hardware when ECRIS evolves into 3rd G. machines. As a conventional technique, the existing 3rd G. ECRISs are all using TE_{01} mode as the gyrotron microwave power coupling scheme, which is actually a directly borrowed technique from fusion community. Ion

ISBN 978-3-95450-131-1

sources working at gyrotron frequency have been tested and verified having the capacity to produce more intense highly charged ion beams with sufficient magnetic confinement, which has been predicted by the frequency scaling laws. However, at the same microwave power level or same power density level, gyrotron frequency heating is not doing well as predicted. In most occasions, compared to 18 GHz, it is behaving just like a linear extrapolation of power effect to get more intense highly charged ion beams. Figure 8 gives the recent Xe^{27+} beam results with SECRAL. At 24 GHz, SECRAL can produce the beam intensity of the ω^2 scaling, but at much higher microwave power level compared to that at 18 GHz. Similar results have also been observed with SuSI [14]. This raised the question about the coupling efficiency of gyrotron microwave power into ECR ion source plasma. This question remains a very puzzling one for the ECRIS community in the 3rd G. ECRIS development. Without any progress, this would become a severe problem for a 4th G. ECRIS development, i.e. one can't achieve the desired performance with a 4th G. ECRIS. Technically and physically understanding and improving the microwave coupling and heating efficiency of a gyrotron frequency microwave is one of the critical topics in ECRIS source development and very essential for the 4th G. ECRIS development.

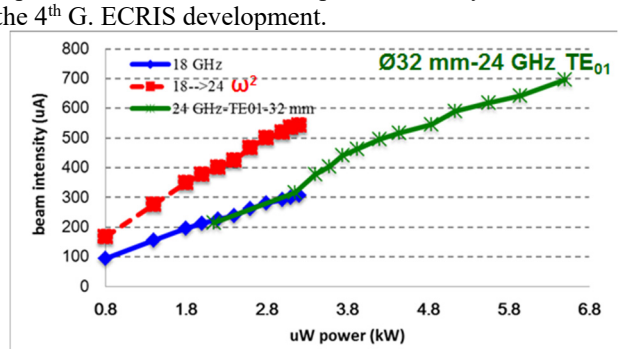

Figure 8: Recent Xe^{27+} results with SECRAL ion source at 24 GHz in comparison with the results at 18 GHz and the extrapolated results from 18 GHz to 24 GHz.

Since the wavelength of 45 GHz microwave is ~6.67 mm, quasi-optical transmission scheme is routinely utilized for high power transmission. This scheme has already been widely utilized in the fusion machines, but to accommodate with an ECRIS, the outcome is not evidenced yet. Many technical details and modifications will be made accordingly.

Intense Beam Extraction and Transmission

While the typical highest extracted beam currents from a 3rd G. ECRIS for the production of intense highly charged ion beams are of 10~15 emA, the extractable beam intensity from a 4th G. ECRIS might exceed 20 emA. How to realize the efficient extraction of very intense ion beam from the much denser ECR plasma needs further investigation. Higher extraction HV might be helpful, for instance 35~40 kV, but the operation stability at strong stray magnetic field needs to be investigated.

Transmission of intense ion beam in the ECR beam line remains a problem for the 4th G. ECRIS. As the intensity gets higher, much stronger space charge will be observed in the beam line. For the analysing beam line (or ECR beam line), stronger space charge will weaken the focusing force of the Glaser lens at source extraction and deteriorate the mass separation resolution at the image point of the analyser magnet, and under the worst case, it is impossible to separate two adjacent heavy ion charge states at the faraday cup, such as U^{33+} and U^{34+}. It is mandatory to take into account of the worst case of very intense beam extraction and transmission in the beam dynamics simulation. A 110° large gap analyser magnet is an applicable solution [15].

Miscellaneous Aspects

Strong bremsstrahlung radiation remains a very severe problem for a 4th G. ECRIS development. Besides the cryogenic issues discussed above, the potential damage to the magnet coil impregnation epoxy is still not very clear. Strong X-ray radiation will also induce photoelectric effect in metals, which might cause malfunction of electronic units. Sufficient lead shielding is desired, but the utility will be very bulky and costly. One ultimate goal of the 4th G. ECRIS is to produce very intense highly charged uranium ion beams. The obvious barrier so far the ECRIS community can foresee is the capacity of the high temperature oven. To produce 50 pμA U^{34+} beam, the oven must be very reliable at high temperature up to 2100 ℃ and have a large loading capacity. Uranium beam is just one example. How to produce enough metal vapour to the ECR plasma is one of the biggest challenges to the next generation ion source development. Last but not least, the routine operation of an ECRIS with ~1 emA highly charged ion beam has never been evidenced. The long-term stability and reliability really concerns the operation of next generation heavy ion accelerators.

CONCLUSION

By reviewing the problems and challenges existing with the development of a 3rd G. ECRIS operated at 24 or 28 GHz, we could envision the possible challenges we might have for the next generation ECR ion source development, which is most likely to be operated at 45 GHz. Even after more than 10 years after the first plasma at 28 GHz with a 3rd G. ECRIS, promising improvement has been made annually among the ECR community, which also gives strong support to the successful development of a 4th G. ECRIS which is under design at IMP. And also with the rapid improvement of accelerator technologies, many challenges to the 4th G. ECRIS development will be properly handled.

ACKNOWLEDGEMENT

This work is supported by the 100 Talents Program of the CAS (No. Y214160BR0), NSF (contract No. 11375244) and MOST (contract No. 2014CB845500). The fruitful discussion with OST scientists from New Jersey, USA and

ISBN 978-3-95450-131-1

C. M. Lyneis, D. Z. Xie, S. Prestemon from LBNL is warmly acknowledged.

REFERENCES

[1] E. N. Beebe, et al., Rev. Sci. Instr. 73 (2002) 699.
[2] R. C. York, "JACoW, FRIB: A NEW ACCELERATOR FACILITY FOR THE PRODUCTION OF AND EXPERIMENTS WITH RARE ISOTOPE BEAMS", PAC'09, Vancouver, May 2009, MO3GRI03, p. 70 (2009); http://www.JACoW.org
[3] J. Benitez, K. Y. Franzen, C. Lyneis, L. Phair, M. Strohmeier, G. Machicoane, L. T. Sun, "JACoW, Current Development of the VENUS Ion Source in Research and Operations", ECRIS'12, Sydney, Australia, Sept. 2012,THO02, p.153; http://www.JACoW.org
[4] C. M. Lyneis, D. Leitner, S. R. Abbott, R. D. Dwinell, M. Leitner, C. S. Silver and C. Taylor, Rev. Sci. Instr. 75, (2004) 1389.
[5] M.A. Leitner, S. A. Lundgren, C.M. Lyneis, C.E. Taylor, D.C. Wutte, "Progress Report of the 3rd Generation ECR Ion Source Fabrication", ECRIS'99, CERN, Geneva, Switzerland, May 1999, p.66; http://www.osti.gov/scitech/biblio/751770
[6] J. C. DeKamp, P. A. Zavodszky, B. Arend, S. Hitchcock, J. Moskalik, J. Ottarson, and A. F. Zeller, IEEE TRANSACTIONS ON APPLIED SUPERCONDUCTIVITY, 17(2007)1217.
[7] T. Nakagawa, et al., Rev. Sci. Instr. 81 (2010) 02A320.
[8] Daniel Winklehner, Daniela Leitner, Guillaume Machicoane, Dallas Cole, Larry Tobos, "JACoW, Space Charge Compensation Measurements in The Injector Beam Lines of The NSCL Coupled Cyclotron Facility", Cyclotrons'13, Vancouver, Canada, Sept. 2013, WE3PB03, p.417; http://www.JACoW.org
[9] M. Leitner, S.R. Abbott, D. Leitner, C. Lyneis, "A High Transmission Analyzing Magnet for Intense High Charge State Beams", ECRIS'02, Jyväskylä, Finland, June, 2002, p.32 (2002).
[10] L. Sun, et al., "JACoW, ECRIS Development Towards Intense High Brightness Highly-Charged Ion Beams", HB2014, East Lasning, USA, Nov. 2014, TH02AB01, p.363; http://www.JACoW.org
[11] P. Ferracin, S. Caspi, H. Felice, D. Leitner, C. M. Lyneis, S. Prestemon, G. L. Sabbi, and D. S. Todd, Rev. Sci. Instr. 81 (2010) 02A309.
[12] D. Z. Xie, et al., "Development Status of a Next Generation ECRIS: MARS-D at LBNL", to be published at Rev. Sci. Instr., proceedings of 16th International Conference on Ion Source, New York, USA, Aug. 2015.
[13] S. Gammino, G. Ciavola, L. Celona, D. Hitz, A. Girard, G. Melin, Rev. Sci. Instr. 72 (2002) 4090.
[14] G. Machicoane, D. Cole, K. Holland, D. Leitner, D. Morris, D. Neben and L. Tobos, "JACoW, First Results at 24 GHz with the Superconducting Source for Ions (SuSI)", ECRIS'14, NN, Russia, Aug. 2014, MOOMMH03, p.1 (2014); http://www.jacow.org
[15] Y. Yang, L. T. Sun, X. Z. Zhang, H. W. Zhao, Y. He, "JACoW, Preliminary Design of a LEBT for HIAF Linac at IMP", IPAC2014, Dresden, Germany, June 2014, TUPRO054, p.1153; http://www.jacow.org

ISBN 978-3-95450-131-1

PERFORMANCE OF THE LOW CHARGE STATE LASER ION SOURCE IN BNL*

M. Okamura#, J. Alessi, E. Beebe, M. Costanzo, L. DeSanto, J. Jamilkowski, T. Kanesue, R. Lambiase, D. Lehn, CJ. Liaw. D. McCafferty, J. Morris, R. Olsen. A. Pikin, D. Raparia, A. Steszyn
BNL, Upton, NY 11973, USA
S. Ikeda, TITech, Yokohama, Japan/RIKEN, Saitama, Japan

Abstract

On March 2014, a Laser Ion Source (LIS) was commissioned which delivers high brightness low charge state heavy ions for the hadron accelerator complex in Brookhaven National Laboratory (BNL). Since then, the LIS has provided many heavy ion species successfully. The low charge state (mostly singly charged) beams are injected to the Electron Beam Ion Source (EBIS) where ions are then highly ionized to fit to the following accelerator's Q/M acceptance, like Au^{32+}. Recently we upgraded the LIS to be able to provide two different beams into EBIS on a pulse-to-pulse basis. Now the LIS is simultaneously providing beams for both the Relativistic Heavy Ion Collider (RHIC) and NASA Space Radiation Laboratory (NSRL).

INTRODUCTION

In 2007, we started to study low charge state heavy ion beam creation using a laser ion has been originally studied for high current highly charged beam production. It was confirmed that by adjusting the laser power density between a few 10^8 W/cm^2 and about 10^9 W/cm^2, the induced ablation plasma contains mostly singly charged ions from various materials [1]. Although highly charged beam has high intensity with short pulse length, the observed low charge state beams had a much longer pulse of more than a few tens μs at a position of 1 m away from the laser target, with moderate beam currents. Also it was found that the damage of the target surface was quite small since the low charge state production mode needs gently focused spot on the target. This enabled us to apply multiple shots on the same target spot. In 2010, the low charge state laser ion source project was funded by NASA. The project was to enhance the versatility of the EBIS pre-injector [2], which provides various heavy ions to NSRL, by establishing fast species switching in a few second. Unlike other ion sources, the plasma created in a LIS is formed independently from surrounding environments including vacuum chamber wall, residual gases, magnetic confinement field or resonant modes of microwave. Thus, in a LIS, by only mechanically changing target material, we can change the ion species provided without any hysteresis effects.

*This work has been supported by Brookhaven Science Associates, LLC under Contract No. DE-AC02-98CH10886 with the U.S. Department of Energy, and by the National Aeronautics and Space Administration.
okamura@bnl.gov

In March 2014, the first beam was delivered to the EBIS and then ten days later, the beam was supplied to NSRL. Since then most of the solid based ions used in NSRL have been supplied by the LIS [3].

UPGRADE FOR RUN15

Upon the successful beam commissioning of the LIS, we decided to install another laser and target in the system to provide beams to the Relativistic Heavy Ion Collider (RHIC) without any interferences in providing beams to NSRL. The over view of the LIS is shown in the Fig.1.

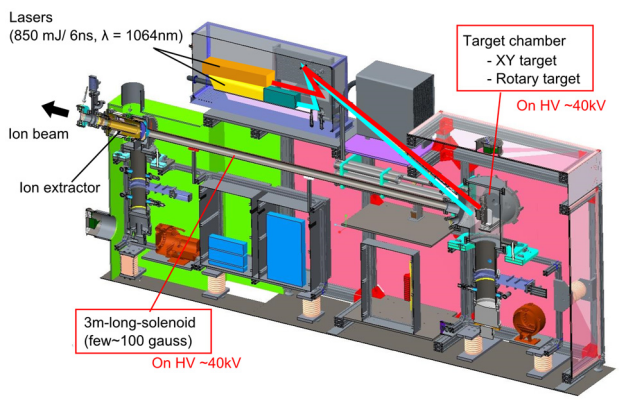

Figure 1: Cut view of the LIS.

In the enclosure made of aluminium on the top of the frame, we have a Quantel Brilliant B Twin laser (6 ns, 1064 nm) which has two independent oscillators [4]. One of the oscillators is used as a backup in case of a failure. In the same enclosure, we added another Quantel Brilliant B laser (single oscillator model). The beam paths of lasers in the enclosure are shown in Fig. 2.

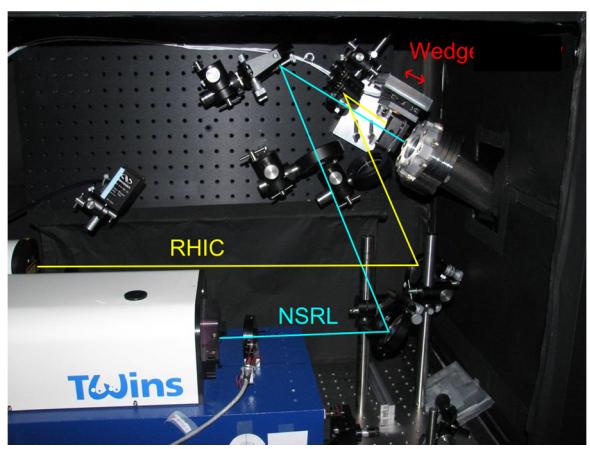

Figure 2: Laser paths in enclosure.

ISBN 978-3-95450-131-1

In RHIC RUN15, aluminium beam was requested in addition to gold beam. To irradiate the both materials, we installed a retractable AR coated wedge in the laser path for the RHIC. By inserting the wedge, the beam direction is deflected by 0.3 degree aiming to an aluminium target which is next to the gold target.

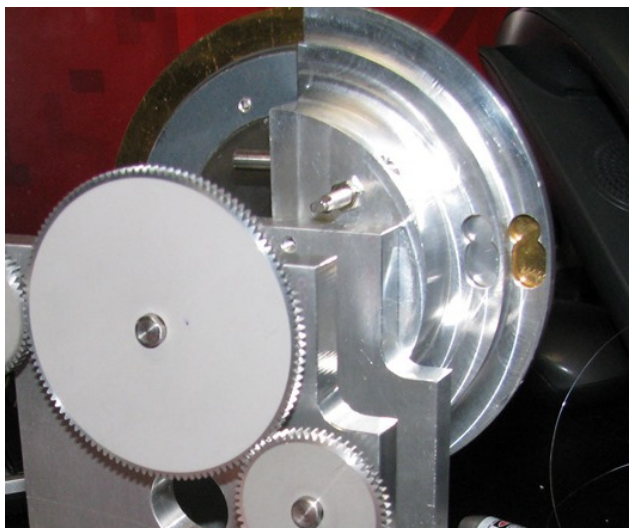

Figure 3: Rotating target for RUN15.

Figure 3 shows a photo of the installed target moving structure. The drive motor was mounted outside of the vacuum and the motor axis is connected to a reduction gear, a magnetic coupling mechanical feedthrough and another gear to drive the gold and aluminium rings. The ring's O.Ds are 120 mm and 100 mm. The laser irradiation surfaces are seen through holes in the aluminium shroud in the photo. The target rotated at least at 5 rpm to avoid consecutive exposures on the same position on the ring surface, when running at 5 Hz.

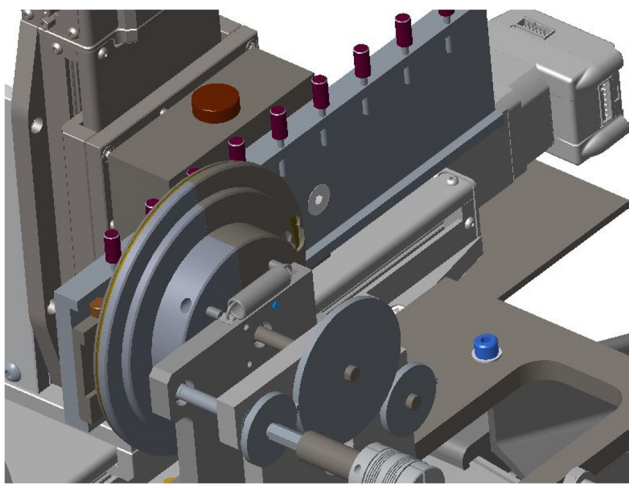

Figure 4: Rotating target and XY target mounted in the vacuum chamber.

Behind the rotating target, as shown in the Fig. 4, we have a XY motorized stage which has 250 mm and 50 mm of movable range in horizontal and vertical directions respectively. The laser irradiation spot on the XY stage was aligned to the common axis of the solenoid and extraction electrode. The laser spots on the gold and aluminium rotating targets were offset 15 mm and 25 mm from the axis. This is because the NSRL beams are mainly lighter ions and require more effective solenoid enhancement, which was explained at [5, 6]. The gold beam for RHIC doesn't need a strong enhancement by the solenoid and can be set at the off-centre position. In the Fig 5 from left to right, aluminium, gold, aluminium, lithium(top), calcium(bottom), silicon, titanium, iron and graphite mounted on the tungsten target holder are shown as used in RUN2015.

Figure 5: Various materials mounted on the target holder for the NSRL.

OPERATION

The entire hadron accelerator complex is triggered every ~5 seconds and the interval of the triggers is called the supercycle. In a supercycle, the LIS delivers beams to the NSRL only once. This means that the repetition rate for the NSRL beam is ~0.2 Hz and the exposed spot on the target has enough time to be cooled down before having the next laser irradiation. On the other hand, RHIC needs 8 pulses at 5 Hz within a super cycle. The continuously rotating target reduces the degradation of the beam current due to the excessive exposure on the same spot.

Operation for NSRL

Typically beam time for NSRL is 8 hours a day 5 days a week. To optimize other devices, the LIS was operated longer than the beam time. In the RUN, the LIS has provided, Li, C, Ca, Si, Ti, Fe, Ta and Au. Due to strong demands, Si and Fe targets were heavily used.

Operation for RHIC

During a RUN period, RHIC runs 24 hours a day. Once beams are injected and accelerated up to desired energy, the RHIC tunes into storage mode and continues for several hours. This means the LIS needs to provide 8 pulses in every super cycle for around 5 minutes to fill RHIC and then wait for another injection request. However, to keep other devices in a standby state, the LIS provides at least one pulse in a super cycle continuously. Also, tuning optimization of AGS and booster need the beams. In the most of daytime, the LIS was occupied to deliver the beams with 8 pulse mode operation.

ISBN 978-3-95450-131-1

Hours of operation

The total days when the beams were provided by LIS to the users are summarized in Table 1.

Table 1: Species and Number of Days

		Li	C	Al	Ca	Si	Ti	Fe	Ta	Au
Run14	NSRL(days)		2			11	1	18	1	3
	RHIC(days)									33
Run15	NSRL(days)	1	3		1	19	4	30		6
	RHIC(days)			14						42

The days listed in the table show the beam time for NSRL and RHIC. Commissioning or tuning days are excluded. For example, the total days of the LIS operation for multiple species, aluminium for RHIC, and gold for RHIC reached 99, 24, and 96 days respectively.

Failures of the system

Just after the commissioning in 2014, we experienced a failure at one of the stepping motors which is used in the XY stage for the target manipulation. To achieve even target consumption and to stabilize beam condition for a long time operation, the target needs to be scanned with very low speed. Initially we drove the motor continuously and this incessant electric current in the motor induced excessive heat. This was clearly seen in the vacuum monitor and damaged the motor. Then we changed the operation mode of the motor to step motion, like 0.1 mm every several minutes. In the RUN 2015, we had a problem with the moving mechanism in the rotating target system. A ceramic bearing was used to hold the axes of the gears and target. Those bearings were exposed to laser plasmas and evaporated gas from the target. Also the torque control of the drive motor was not optimized. This caused a halt in the target rotation. For the next run, we are developing a new robust mechanism for the gold rotating target.

Deposition in the system

After the RUN15 was finished, we disassembled the extraction chamber, 3 m solenoid pipe and target chamber. The inner surface of the target chamber was coated by target materials as expected. However, we did not find obvious deposition at the extraction electrodes. The beam extraction system seems likely to last for several years without maintenance work.

CONCLUSION

We have developed a laser ion source to provide low charge state heavy ions to the EBIS. In the RUN15, most of the solid based ions provided to the NSRL and RHIC originated in the LIS. The overall performance including beam stability and the fast species switching capability was satisfactory.

ACKNOWLEDGMENT

In the R&D phase, many students from U.S. and Japan have contributed for the project, and equipment brought from RIKEN was used. We also thank D. Lowenstein for promoting the project.

REFERENCES

[1] T. Kanesue et al., “Measurement of Ion Beam from Laser Ion Source for RHIC EBIS”, MOPC147, EPAC’08, Genoa, Italy (2008).
[2] J. Alessi et al., “Performance of the New EBIS Preinjector”, WEP261, PAC’11, New York, USA (2011).
[3] T. Kanesue et al., “The Commissioning of the Laser Ion Source for RHIC EBIS”, WEOAB01, IPAC’14, Dresden, Germany (2011).
[4] Quantel laser, website: http://www.quantel-laser.com
[5] K. Kondo et al., “Laser Ion Source with Solenoid for Brookhaven National Laboratory-Electron Beam Ion Source”, Rev. Sci. Instrum. **83**, 02B319 (2012).
[6] K. Kondo et al., “Laser Ion Source with Long Pulse Width for RHIC-EBIS”, WEP264, PAC’11, New York, USA (2011).

ISBN 978-3-95450-131-1

60 GHz ECR ION SOURCES*

T. Lamy, J. Jacob, J. Angot, P. Sole, T. Thuillier
LPSC, Université Grenoble - Alpes, CNRS/IN2P3, Grenoble, France
M. Bakulin, GYCOM Ltd, Nizhny Novgorod, Russia
A.G. Eremeev, I. Izotov, B. Movshevich, V. Skalyga, IAP/RAS, Nizhny Novgorod, Russia
F. Debray, J. Dumas, C. Grandclement, P. Sala, C. Trophime, LNCMI, Grenoble, France

Abstract

Electron Cyclotron Resonance Ion Sources (ECRIS) deliver high intensities of multicharged heavy ions to accelerators; nowadays the evolution of science requires extremely intense ion beams. Since 1987, semi empirical scaling laws state that the ECR plasma density, in a minimum-B magnetic field configuration, varies like the square of the electromagnetic waves (EM) frequency or of the resonant magnetic induction. The present most performing ECRIS are operated at 28 GHz. In order to significantly increase the ion beam intensities, the use of EM with frequencies of the order of 60 GHz is evaluated worldwide. Conceptual studies based on superconductors are performed and different magnetic configurations accepting such a high ECR frequency are proposed by several groups. Since 2009, LPSC collaborates with IAP-RAS (Russia) and LNCMI (CNRS) and has built the first ECRIS with a topologically closed 60 GHz ECR resonance zone, using radially cooled polyhelices. Unique ion beam intensities have been extracted from this prototype, like 1.1 mA of O^{3+} through a 1mm hole representing a current density of 140 mA/cm^2. The worldwide high frequency ECRIS research status is presented along with a focus on the present LPSC-IAP-LNCMI strategy.

ECRIS STATE OF THE ART

The production of intense multi charged heavy ion beams is performed worldwide with Electron Cyclotron Resonance Ion Sources (ECRIS) using a minimum-B magnetic field to confine the ECR plasma. It is generated by the superimposition of an axial field, produced by at least two solenoids, with a hexapolar radial field produced by permanent magnets or superconducting coils. Until now, the ECRIS development and optimization has been driven by scaling laws [1] specifying semi-empirical values for the optimal magnetic induction on the peak fields of the axial mirror and the radial field at wall. This magnetic field insuring the plasma confinement has to be much higher than the ECR magnetic field value B_{ECR}:

$$B_{ECR} = \frac{\omega_{\mu w} \times m_e}{e}, \quad (1)$$

where $\omega_{\mu w}$ is the frequency of the microwaves (μw), m_e and e, the mass and the charge of the electron. Following the scaling laws, the axial magnetic induction on the axis of an ECRIS, at the injection side, has to be of the order of three to four times B_{ECR}, and the radial magnetic field has to be at least twice this value inside the plasma chamber. Presently, the highest μW frequency injected into a minimum-B ECRIS is 28 GHz [2–6] ($B_{ECR} = 1$ T), that means 3 to 4T for the axial field on the axis and more than 2T for the hexapolar radial field. In such an ECRIS, it is considered that the plasma density is close to the critical one, this assumption allows to say that the plasma density varies like the square of $\omega_{\mu w}$ or B_{ECR}.

These ECRIS, using NbTi superconductors to provide the appropriate magnetic induction, are called 3rd generation ones. Their performances are excellent and more or less in the same range, they produce about 800 to 1400 μA of Ar^{12+} (see previous references for various ion beam data). However their cost is high (a few M€), the development time is long (~5 years) and their construction process presents non negligible risks of failure. The new generation accelerator facilities requiring higher intensities of highly charged heavy ions, a strong research and development activity is necessary to define the so-called 4th generation ECRIS (higher ECR frequencies in the range 40-60 GHz). Such ECRIS are expected to operate with a plasma density up to four times higher than the present 3rd generation. However it necessitates the doubling of the magnetic field induction. A 60 GHz ECRIS magnet, featuring a 3 to 4 T hexapole with a 7T injection peak field requires the use of Nb3Sn superconductor technology [7]. The construction of Nb3Sn magnet is very difficult and risky, because once reacted, the Nb3Sn cable is very brittle. So far, no one has built such a prototype. Experimental research and development activities on ECRIS have reached a bottle neck. We will describe in the next paragraphs the different options evaluated worldwide for ~ 60 GHz ECRIS.

MAGNETIC FIELD CONFIGURATIONS FOR ~60 GHz ECRIS

A few groups in the world began to evaluate and design the next generation ECRIS. The Lawrence Berkeley National Laboratory in USA and Institute of Modern Physics at Lanzhou in China worked on the optimization of the present magnetic structures associating superconducting solenoids and hexapole using either NbTi or Nb_3Sn or both material [7, 8], and they show the difficulty to build such systems. Some other original minimum-B magnetic structures issued from fusion devices are proposed too, like the ARC-ECRIS source [9, 10], consisting in a 'yin-yang' coil creating magnetic field inductions and mirror

*We acknowledge the support of LNCMI-CNRS, member of the European Magnetic Field Laboratory (EMFL), and the support of the International Science and Technology Center (project#3965).

ISBN 978-3-95450-131-1

ratio very close to classical ECRIS ones. It is interesting to note that the use of NbTi for such a coil may allow the injection of 60 GHz microwaves in a minimum-B structure. A more recent publication [11] proposes to make a rather sophisticated toroidal ECRIS (56 GHz) with a twisted hexapolar field along the torus and a radial extraction. The configuration studied is based on the use of high currents flowing through solid material and coils (3.5 MA and 300 kA for the generation of toroidal and poloidal fields respectively). A lot of modelling work needs to be performed to evaluate the potential of such a device and the realization could be a technical challenge.

In the frame of the European Isotope Separation On-Line project, and later in EUROnu (Beta Beams) [12], P. Sortais, proposed the concept of a "60 GHz ECR – duoplasmatron" [13], to ionize and bunch, with high efficiency, a continuous flux of radioactive atoms and provide an intense pulsed ion beam with the time structure suitable for the CERN accelerator facility. In the frame of a collaboration between LPSC and the high magnetic laboratory in Grenoble (LNCMI), we designed and built a cheap prototype (~150 k€) [14]. It uses high field magnets techniques (radially cooled copper polyhelices), to establish a magnetic field for a 60 GHz ECRIS. This first configuration is a spindle cusp with a closed resonance zone at 2.14 T (Fig. 1). It is a minimum-B structure; iso-B surfaces are slightly deformed ellipsoids centered on the null value.

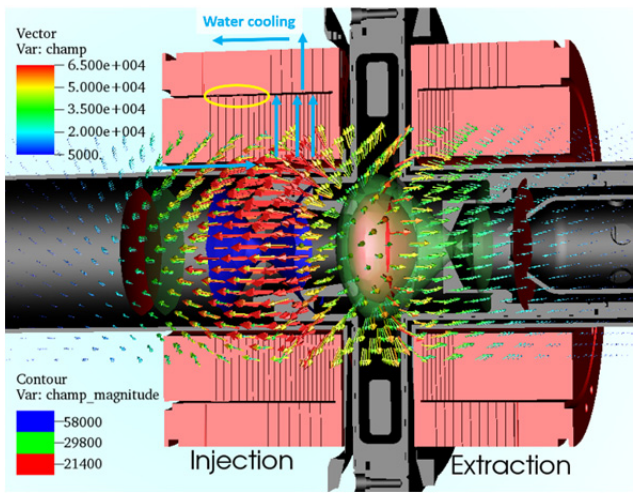

Figure 1: Simulated magnetic field with a 2.14 T quasi ellipsoidal surface at the center, 6T at the injection, 3T at the extraction, and 4T at the radial cusp.

MAGNETIC FIELD MEASUREMENTS

LNCMI High Magnetic Field Facility

The high magnetic field laboratory LNCMI in Grenoble, is equipped with 4 AC/DC convertors delivering 16 kA each, and a maximum voltage of 400 V (maximum available power is 24 MW). It provides high magnetic fields up to 36 T for fundamental physics and applications. A group of the laboratory performs research and development for the generation of high magnetic fields with resistive and superconducting magnets [15]. Our prototype has been designed to deliver its maximum magnetic field (7T at the injection) for an intensity of 30 kA. It is thus possible to use only two of the LNCMI convertors connected in parallel which allows more flexibility for the experiments planning. However, in such a situation, the extraction magnet is connected in series with the injection one, depriving us of an independent tuning of the magnetic field on each coil.

Magnetic Field Measurements at 26 kA

The magnetic field of the prototype was previously measured for an intensity of 15 kA allowing an operation at 18 GHz [16]. For an operation at 60 GHz it has been decided to operate the magnets up to 26 kA.

To validate the operation at such intensity, the prototype was connected to four 7.5 kA water cooled cables.

The intensity was ramped in successive cycles from zero to a maximum value increased at each ramp. During a ramp, the voltage was monitored and fitted. At the next ramp, the experimental voltage was compared to the fit of the previous one. In case of a significant voltage deviation, the procedure was stopped, due to a possible problem with the magnet. During the procedure, at 21 kA, the monitoring system measured an irreversible drop of about 8% of the resistance of the helices at the injection side. As a reminder, the width of the slits between each winding and the electric insulation are held by numerous small insulator strips glued in an oven with a special epoxy resin. The prototype disassembly showed short circuits between a few windings of the internal helix 'compensated' by the ungluing of the insulators at the basis of the helix (Fig. 2).

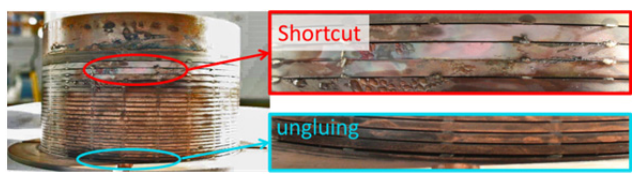

Figure 2: Internal injection helix defaults observed at 21 kA during the first test to reach 26 kA.

The analysis of the problem has shown that the water cooling channel design was at stake. In the magnet tank, cold water is introduced in the inner coils diameter. It then flows radially through the thin slits between the coil turns. On the top left of Fig. 1, the water path is shown in cyan, the position of the short circuit in yellow. The number of slits is much higher in the inner helix than in the outer one, creating a water speed decrease on the inner helix rear part and a subsequent overheating. The problem was solved by machining supplementary axial slits in the inactive part of the outer coil, taking care to minimize the effect on the electrical current path (Fig. 3).

ISBN 978-3-95450-131-1

Figure 3: Perpendicular slits machined in the internal injection helix.

After this modification, the source was successfully operated up to the full current (26 kA) for hours. Let us remark that this result is important for the high field magnets technology, some windings having the highest ever reached current density in a radially cooled helix (600 A/mm^2). This validation allowed us to measure the magnetic field of the source. We can see on Fig. 4 the plot of the axial magnetic field on the axis, for three different intensities (10, 20, and 26 kA). These results are in full agreement with the simulations performed and allow a satisfying operation of the source at 60 GHz.

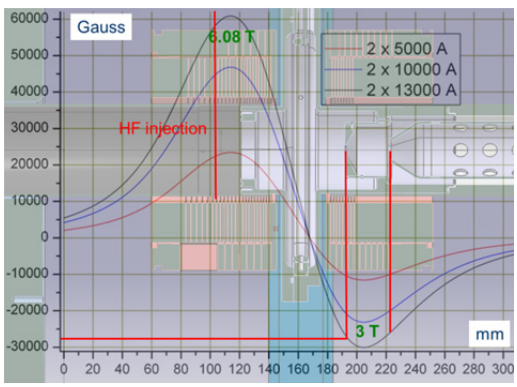

Figure 4: Magnetic field measurements at 10, 20 and 26 kA, superimposed on a cut view of the source.

60 GHz GYROTRON AND BEAM LINE

Gyrotron Setup

A pulsed 60 GHz - 300 kW gyrotron has been designed, constructed, and tested, by the GYCOM Company and the IAP-RAS in Nizhny Novgorod (Russia) in the frame of an International Science and Technology Center contract, funded by LPSC-CNRS and the European Community. Presently the μw pulse width can be varied from 50μs to 1 ms and the repetition rate can reach 2Hz at full power, 5Hz at 100 kW. Let us note that by means of some modifications and by the change of high voltage power supplies, this gyrotron could be operated in CW up to a power of 15 kW.

The gyrotron was setup at LNCMI at the end of 2012, its main components can be seen Fig. 5, more details can be found in [17]. The electromagnetic waves are launched as a quasi-Gaussian beam, vertically polarized. A dedicated microwave launching system has been designed by I. Isotov (IAP-RAS) to optimize the power density on the resonance surface. It has been realized at LPSC.

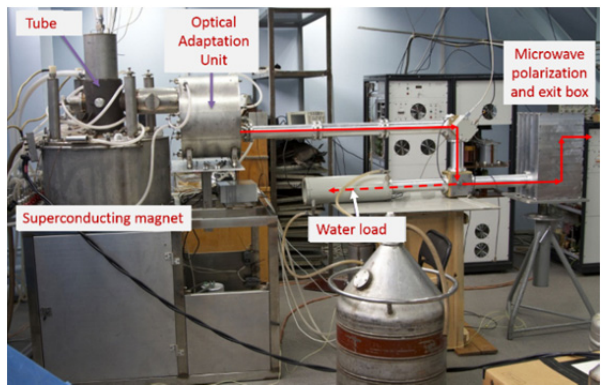

Figure 5: 60 GHz, 300 kW pulsed gyrotron.

Beam Line Setup

The experiment is located in a dedicated room at LNCMI, with a floor having a limited weight resistance, preventing us from setting up a high acceptance magnetic spectrometer. Due to our present budget constraints, we have not yet implemented a beam line and diagnostics suitable to the full characterization of intense ion beams. The beam line is equipped with two faraday cups, the first on the axis of the extraction, the other after a 60 mm gap magnetic spectrometer. A general view of the experiment is shown Fig. 6. The gyrotron system is easily tuned from a user-friendly interface; the operation of the helices is controlled from a dedicated rack and supervised by an adapted LNCMI automated system.

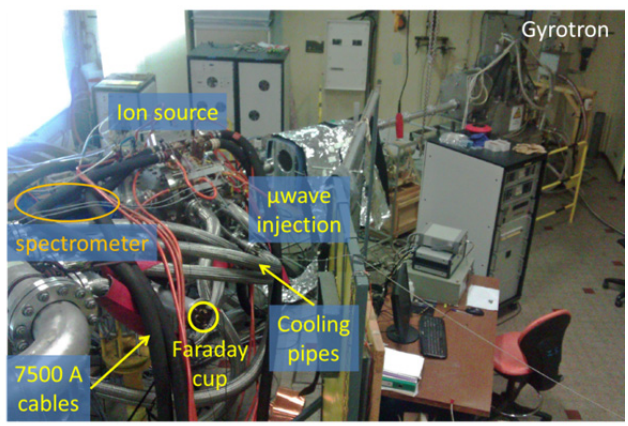

Figure 6: Overview of the beam line setup at LNCMI.

FIRST 60 GHz ECR PLASMA AND ION BEAMS

The plasma chamber and the microwave injection system are at high voltage with a Peek insulation allowing operation up to 30 kV. The microwaves are optically injected through a quartz window into the microwave adaptation system under vacuum. The source was operat-

ISBN 978-3-95450-131-1

ed with oxygen in order to analyse all the charge states extracted at 20 kV with the available dipole. In order to limit the space charge effect, ions were extracted through a 1mm diameter hole in the plasma electrode. Oblique holes were present on the plasma electrode to enhance source pumping. The first experiments consisted in measuring the total current extracted from the ion source.

High Voltage Dependence of the Total Current Extracted

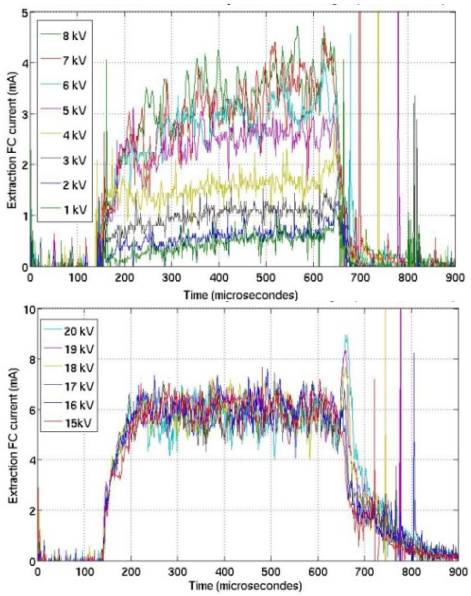

Figure 7: Total ion current intensity extracted on the axis of the source for extraction voltages from 1 to 8 kV (top) and 15 to 20 kV (bottom).

The initial pressure in the beam line is 2.3×10^{-06} mbar, oxygen gas is injected to reach 1.1 E-05 mbar. The current in the helices is set to 22 kA (~5T at the injection), the gyrotron power is adjusted to 80 kW to limit X-ray emission from the plasma, and the pulse duration is set to 500 µs. The ignition of the plasma is immediate, and this remark can be generalized for any tuning parameters. The total current is measured in the faraday cup on the axis of the extraction. Two sets of measurements are shown in Fig. 7: in the ranges from 1 to 8 kV, and from 15 to 20 kV. One can see the intensity gain during the µw pulse when increasing the extraction high voltage (~270 µA/kV) in the lower range. In the upper range there is no more gain for extraction voltages higher than 15 kV during the µw pulse, giving indication that the beam was fully transported up to the first faraday cup. However, an afterglow signal appears and its intensity increases with the high voltage, higher voltage will be required to transport the full afterglow intensity. The plateau signals are relatively stable and reach about 6 mA which means an ion beam current density of 760 mA/cm^2 (for other tunings, 900 mA/cm^2 was observed). During the afterglow this value increases up to 1.1 A/cm^2. The peaks appearing after the classical afterglow are much shorter in duration, seem to be reproducible, and represent an ion beam current density of 1.8 A/cm^2.

MULTICHARGED ION BEAMS EXTRACTED FROM THE 60 GHz ION SOURCE

3D Spectra

Afterglows being seen in the total ion beam intensity extracted, it is interesting to analyse the different Q/A intensities as a function of time. Fig. 8 shows such measurements, the colour is the intensity, the X-axis is the magnetic field of the spectrometer, and the Y-axis is the time. In order to maximize the afterglows, the extraction high voltage was set to 22 kV. The charge states from 2+ to 5+ are clearly observed. The black and white spectra on the right of the Fig. 8 are a cut view, at a specific time (horizontal yellow line), during the pulse. It is striking to see that during the plateau, the 2 to 4+ beams have about the same intensity. We can see too that the afterglows appear at different times, the 5+ being measured about 15 µs before the 1+ (not seen on the figure). If we only take into account the extraction voltage, the 5+ should appear about 90 ns before the 1+. This time difference appears to be physical and a plasma phenomenon is possibly the cause. Further analysis is required.

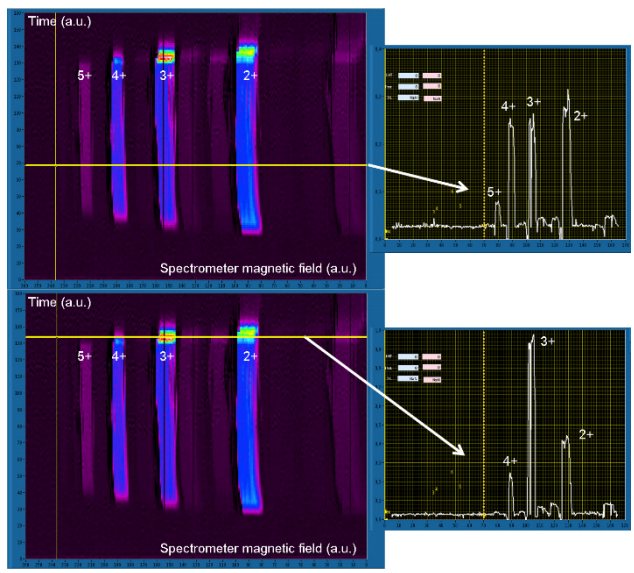

Figure 8: Multicharged oxygen ions spectrum, time evolution of the charge state distribution.

Oxygen 3+ Afterglow Intensity

The analysis of O^{3+} pulses at different extraction voltages show a remarkable stability of the signals (Fig. 9). At 25 kV, through the 1mm hole we have an afterglow of 1.1 mA (the maximum among the different charge states), reaching about 4 times the plateau intensity, so

ISBN 978-3-95450-131-1

140 mA/cm^2. Further afterglow current increase is expected at higher voltage.

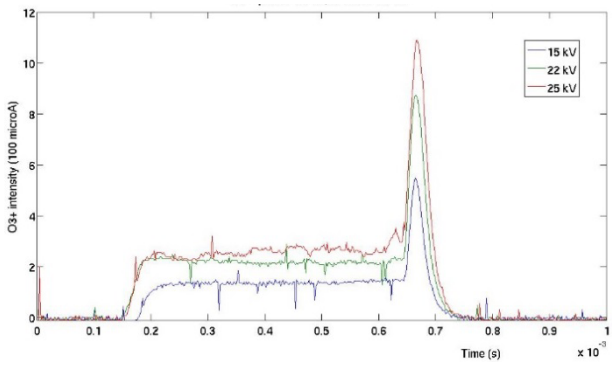

Figure 9: O^{3+} afterglows extracted at 15, 22, and 25 kV

CONCLUSION

The first results obtained during a one week experiment with our 60 GHz ion source showed unique features: extremely high intensities are extracted, presence of afterglows peaks proving electron confinement as predicted in [18]. The next steps will be to vary the length of the magnetic trap, then to test its properties as a magnetic bottle. In the future, we plan to improve the beam line transport, study plasma characteristics obtained with different magnetic structures in a European context. A dedicated experiment to study the transition between gasdynamic and Pastukov confinement is also planned by enhancing the control of the ion source pressure. This research may help to the definition of the 4th generation ECRIS.

REFERENCES

[1] R. Geller et al., "The Grenoble ECRIS Status 1987 and Proposals for ECRIS Scaling," Proceedings of the International Conference on ECR Ion Sources and Their Applications, NSCL Report Nb. MSUCP-47, Michigan State University, East Lansing, USA (1987).

[2] J. Y. Benitez et al., "Current developments of the VENUS ion source in research and operations", proceedings of the 20th International Workshop on Electron Cyclotron Resonance Ion Sources ECRIS2012, Sydney, Australia, pp. 153–158, www.JACoW.org

[3] L. Sun et al., "Progress of superconducting electron cyclotron resonance ion sources at Institute of Modern Physics (IMP)", Rev. Sci. Instrum. 85, 02A942 (2014).

[4] Y. Higurashi et al., "Recent development of RIKEN 28 GHz superconducting electron cyclotron resonance ion source", Rev. Sci. Instrum. 85, 02A953 (2014).

[5] G. Machicoane et al., "First results at 24 GHz with the superconducting source for ions (SUSI), proceedings of the 21th International Workshop on Electron Cyclotron Resonance Ion Sources ECRIS2014, Nizhny Novgorod, Russia, pp. 1-4, www.JACoW.org

[6] Jin Yong Park et al., "The installation of the 28 GHz superconducting ECR ion source at KBSI", proceedings of the International Workshop on Electron Cyclotron Resonance Ion Sources ECRIS2014, Nizhny Novgorod, Russia, pp. 104–106, www.JACoW.org

[7] C. Lyneis et al., "Concept for a fourth generation electron cyclotron resonance ion source", Rev. Sci. Instrum. 83, 02A301 (2012).

[8] D.Z. Xie et al., "Development Status of a Next Generation ECRIS: MARS-D at LBNL", to be published in proceedings of the 16th International Conference on ion sources, August 23-28, New York City, USA (2015).

[9] P. Suominen et al., "First results with the yin-yang type electron cyclotron resonance ion source", Nucl. Instrum. Methods Phys. Res., Sect. A 578, 370–378 (2007).

[10] P. Suominen and F. Wenander, "Electron cyclotron resonance ion sources with arc-shaped coils", Rev. Sci. Instrum. 79, 02A305 (2008).

[11] C. Caliri et al., "Modeling of ion extraction from a toroidal Electron Cyclotron Resonance Ion Source", Nucl. Instrum. Methods Phys. Res., Sect. A 790, 57–63 (2015).

[12] E. Wildner et al., "Design of a neutrino source based on beta beams", Phys. Rev. ST Accel. Beams 17, 071002 (2014).

[13] P. Sortais, "ECR technique for RIB production", Radioactive beams for nuclear physics and neutrino physics, Rencontres de Moriond, Les Arcs, France (March 2003), http://moriond.in2p3.fr/mor_fr.html

[14] T. Thuillier et al., "High frequency ECR ion source (60 GHz) in pre-glow mode for bunching of beta-beam isotopes", Proceedings of the 10th International Workshop on Neutrino Factories, Super Beams and Beta Beams, Jul 2008, Valencia, Spain. Proceedings of Science, Nufact08, pp.089 (2008).

[15] F. Debray et al., "State of the art and developments of high field magnets at the Laboratoire National des Champs Magnétiques Intenses", Comptes Rendus Physique 14, 2–14 (2013).

[16] M. Marie-Jeanne et al., "Status of the SEISM experiment", proceedings of the 20th International Workshop on Electron Cyclotron Resonance Ion Sources ECRIS2012, Sydney, Australia, pp. 111–113, http://www.JACoW.org

[17] M.I. Bakulin et al., "The 60 GHz 300 kW Gyrotron System for ECR Ion Source of New Generation" presentation at the International Workshop on Electron Cyclotron Resonance Ion Sources ECRIS2014, Nizhny Novgorod, Russia, TUOBMH01.pdf, http://www.JACoW.org

[18] M.H. Rashid et al., "New spindle cusp zero-b field for ecr ion and plasma sources", proceedings of the 18th International Workshop on Electron Cyclotron Resonance Ion Sources ECRIS08, Chicago, pp. 123–125, http://www.JACoW.org

ISBN 978-3-95450-131-1

ULTRA HIGH IMPEDANCE DIAGNOSTICS OF ELECTROSTATIC ACCELERATORS WITH IMPROVED RESOLUTION

N.R. Lobanov#, P. Linardakis, D. Tsifakis and T. Tunningley
The Department of Nuclear Physics, Research School of Physics and Engineering,
The Australian National University, Canberra, Australia

Abstract

This contribution describes a new technique to diagnose faults with high-voltage components in electrostatic accelerators. The main applications of this technique are non-invasive testing of high-voltage grading systems; measuring insulation resistance or determining the volume and surface resistivity of insulation materials used in column posts and acceleration tubes. A simple and practical fault finding data interpretation procedure has been established based on simple concepts. As a result of efficient in-situ troubleshooting and fault elimination techniques, the relative resistance deviation ΔR/R is kept below ±2.5% at the conclusion of maintenance procedures. In 2015 the technique was enhanced by increasing the test voltage from 40 V to 100 V. Experimental verification of the improved resolution was conducted during recent scheduled accelerator maintenance in May-June 2015.

INTRODUCTION

In electrostatic accelerators, a voltage gradient between electrodes in acceleration tubes is established by resistors conducting current from the high voltage terminal to ground at the entry (low energy) and exit (high energy) of the insulating gas containment tank. The configuration of the 14UD accelerator produced by National Electrostatic Corporation is described in [1]. Typical resistors and ceramic failure modes have been classified by severity in [1–3].

A novel technique to diagnose issues with high-voltage components of electrostatic accelerators is described in [1, 4]. Recently, the resolution of the technique was improved by increasing the test voltage from 40 V to 100 V. The verification of the resolution improvement at higher test voltage is the main purpose of the investigation of this paper. The first section outlines the general concept of high impedance measurement and describes the experimental design, together with the protocols for collecting data and the data analysis procedures. The second section presents key experimental results collected from maintenance performed on the 14UD in May-June 2015 during tank opening (TO) #124. The third section presents the interpretation of the main test results.

METHODS

A good voltage measuring technique for electrostatic accelerators can be accomplished in the most efficient way by using an electrometer [5]. The basic configuration of the method is shown in Fig. 1.

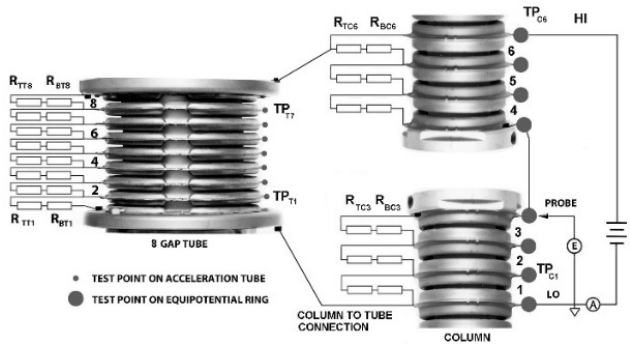

Figure 1: The constant voltage method for diagnostics of the high voltage grading system. The eight gap acceleration tube and the three gaps of the bottom and top section of the column posts are shown. There is a pair of resistors for each column post gap, R_{TCi} and R_{BCi}, and a pair for each acceleration tube gap, R_{TTi} and R_{BTi} where i is the gap number. E and A are the electrometers.

The measured voltage distribution across an eight gap acceleration tube and the corresponding six column post gaps is recorded and shown in Table 1. The measurement set up shown in Fig. 1 illustrates the configuration for an eight gap acceleration tube. A voltage of 100 V is applied to six gaps on the column post by connecting cable leads to equipotential rings marked as LO and HI. Through the column to tube connection, this same voltage is consequently applied to the top and bottom gaps of the eight gap tube. The voltages U_{meas} at each test point is recorded. The voltage drop per tube or column gap U_{gap} is then calculated leading to a mean value of voltage drop per gap $<U_{gap}>$. The error value is calculated by $\Delta[\%]=100(U_{gap}/<U_{gap}>-1)$.

For a chain of N identical resistors of value R in series with applied voltage U_{meas}, if the value of single resistor is changed by ΔR, the relative resistance change is $\Delta R/R = \Delta U \times N/(U_{meas} - \Delta U)$. The resolution of this method is limited by the electrometer accuracy of the voltage measurement, $\Delta U/U = 0.1\%$. For an eight and eleven gap tube structure and U_{meas}= 100 V, the $\Delta R/R_{8GT} = 0.8\%$ and $\Delta R/R_{11GT} = 1.1\%$ correspondingly. For six and five gap post structure and the same test voltage, the calculated $\Delta R/R_{6GP} = 0.6\%$ and $\Delta R/R_{5GP} = 0.5\%$. Evaluation of the data presented in a table provides a feel of what is going on in the high impedance circuit under examination. Components with a measured error above ± 2.5% are considered faulty. In the example results presented in Table 1, two faults are highlighted. It suggests that there

*Work supported by Heavy Ion Accelerators Education Investment Fund
#Nikolai.Lobanov@anu.edu.au

ISBN 978-3-95450-131-1

is a lower than expected resistivity in the second tube gap and higher resistance across the second column gap. The comprehensive analysis of a particular pattern collected during the primary non-invasive test is presented in the form of a troubleshooting chart in [1].

Table 1: Voltage Distribution across an Eight Gap Acceleration Tube and the Corresponding Six Gaps on the Column Post with Suspected Faults Highlighted

TP_T	U_{meas}, V	U_{gap}, V	Δ_T, %	TP_C	U_{meas}, V	U_{gap}, V	Δ_C, %
8	100.0	12.6	0.80	6	100.00	16.50	-1.02
7	87.4	12.6	0.80	5	83.50	16.40	-1.62
6	74.8	12.5	0.00	4	67.10	16.30	-2.22
5	62.3	12.5	0.00	3	50.80	16.40	-1.62
4	49.8	12.7	1.60	2	34.40	17.60	5.58
3	37.1	12.5	0.00	1	16.80	16.80	0.78
2	24.6	12.0	-4.00	LO	0.00	<U_{gap}>	
1	12.6	12.5	0.00			16.67	
LO	0.1	<U_{gap}>					
		12.5					

TP_T - test point on tube
TP_C - test point on column

The adaptors shown in Fig. 2 have been developed to position the sensor on the equipotential rings. The adaptor device shown in Fig. 2 (b) features a shorter slot geometry and more open space between the insulator and the probe tip electrode. This modification substantially reduces electrostatic interference.

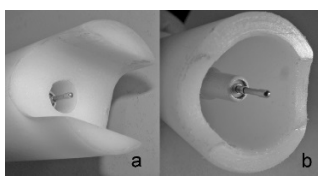

Figure 2: Adaptor devices developed for reproducible positioning of the sensor on equipotential rings.

RESULTS

The experimental results described in this paper were collected from the 14UD during recent scheduled accelerator maintenance in May-June 2015 (TO#124). The associated Tank Opening Report #124 can be downloaded from http://physics.anu.edu.au/nuclear/tor.php.

Figure 3 and Fig. 4 illustrate the electrometer results of service entry and exit tests of the accelerator resistive grading systems associated with acceleration tubes and column posts. Note that gap voltage distributions do not reflect the actual voltage distribution during accelerator operation, as all distributions are measured at the same test voltage of 100 V, even though there are a different number of gaps. The aim of the exit test is to confirm that the resistive grading system is well balanced within the acceptance margin of ±2.5% after appropriate maintenance has been performed. The chart in Fig. 3 displays the entry and exit distributions of gap voltage in the accelerating tubes. This is also a graphic display of the current configuration of tube resistive dividers taking into account shorted gaps. The entry distribution is shown in red and the exit data presented in green. The horizontal axis is the number of the accelerating tube from low-to high-energy end. Dashed lines display the ±2.5% acceptance margin at different tube gap voltages U_{gapT}, corresponding to the following measurement conditions: 9.1±0.23 V for tubes with eleven gaps; 10.0±0.25 V for eleven gap tubes with one shorted gap; 11.1±0.28 V for eleven gap tubes with two shorted gaps and; 12.5±0.3 V for eight gap tubes.

The chart in Fig. 4 shows the service entry and exit test distributions of gap voltages in the column post structure linked to the acceleration tube by means of column-to-tube connection wires. The horizontal axis is the number of the post gap from the low- to high-energy end of the machine. Dashed lines display ±2.5% acceptance margin at different column gap voltages U_{gapP} corresponding to the following measurement conditions: 16.7±0.4 V for six gaps on posts linked to eight gap tubes; 20.0±0.5 V for five gaps on the posts linked to eleven gap tubes; 22.2±0.56 V for column sections where the voltage distribution is set with nine active resistors and remaining resistors are shorted. In case of sections with five gaps, only one resistor is shorted.

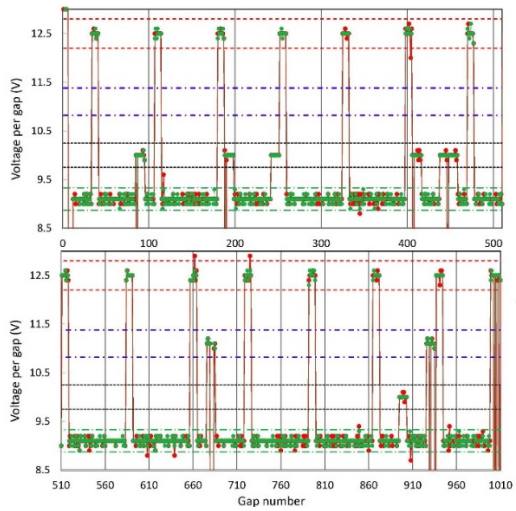

Figure 3: The distribution of gap voltage in the acceleration tubes. The horizontal axis is the gap number in the acceleration tubes starting from low energy to high energy. The red series is the compilation of entry test distribution. The green series is the exit distribution. Dashed lines display the ±2.5% acceptance margin at different gap voltages: dashed/dotted green line is the per gap voltage range 9.1±0.23 V for eleven gap tube; dashed black line is 10.0±0.25 V for eleven gap tube with one shorted gap; dashed/dotted blue line is 11.1±0.28 V for eleven gap tube with two shorted gaps and dashed red line is 12.5±0.3 V for eight gap tube.

A test voltage of 100 V is applied to an assembly incorporating an eleven gap acceleration tube in parallel with five column post gaps or an eight gap acceleration tube in parallel with six gaps on the column post. Each end of an acceleration tube is connected to the column section. In the case of ceramic gap failure in an acceleration tube, a quick fix solution is to short out the gap. Since the number of the gaps on the column post is nearly half of the corresponding number of gaps on the accelera-

ISBN 978-3-95450-131-1

tion tube, only one of two resistors bridging across the column post gap is shorted in order to maintain a uniform voltage distribution. The calculated voltage distributions across an arbitrary number of column post gaps is shown in Table 2.

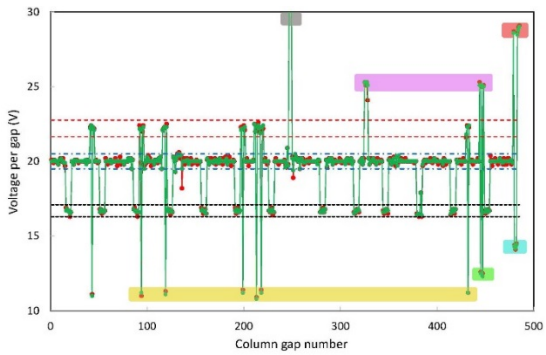

Figure 4: The distribution of gap voltage in the column posts obtained during tests with the electrometer. The horizontal axis is the gap in the column posts numbered from the low-to high-energy end. The red series is the compilation of the entry test distribution accrued during TO#124. The green series is the exit distribution collected in the end of TO#124. Dashed lines display the ±2.5% acceptance margin at different gap voltages: the dashed black line is the per gap voltage margin 16.7±0.4 V for six gaps on the posts linked to eight gap tubes; dashed blue line is 20.0±0.5 V for five gaps on the posts linked to eleven gap tubes; dashed red line is 22.2±0.56 V for five gap posts with one resistor shorted.

Table 2: Calculated Voltage Distribution across an Arbitrary Number of Column Gaps at a Test Voltage of 100 V

Number of resistors per section	6	7	8	9	10	11	12
U_{meas} per gap with two resistors	33.3	28.6	25.0	22.2	20.0	18.2	16.7
U_{meas} per gap with one resistor	16.7	14.3	12.5	11.1	10.0	9.1	8.3

Table 2 represents the current configuration of the resistive divider of the 14UD accelerator. The Data highlighted in Table 2 corresponds to boxes of the same colour shown in Fig. 4. For instance, the column post gaps from the section in which the voltage distribution is set with nine active resistors and remaining resistors shorted can be seen highlighted in yellow in Fig. 4 and Table 2. For this, the voltage per gap containing one resistor is 11.1 V and 22.2 V across gaps with two resistors.

The classification of faults observed during TO#124 is shown in the Pareto chart in Fig. 5.

DISCUSSION

According to the Pareto chart shown in Fig. 5, the most common failure mode is lack of continuity or poor electrical connection between the column to tube connection at approximately 30%. Of these, failures of the rivet style mountings are the most common.

The next most common fault is an open circuit or poor continuity between pairs of resistors with a fault proportion of 20% for tube resistors and 8% for column post resistors. Pairs of resistors are connected together with a wire inserted into a machined nut at the end of each resistor. The design has proved to be very successful based on operational performance over last two decades. Spark damaged wire leads are still found but are easily replaced.

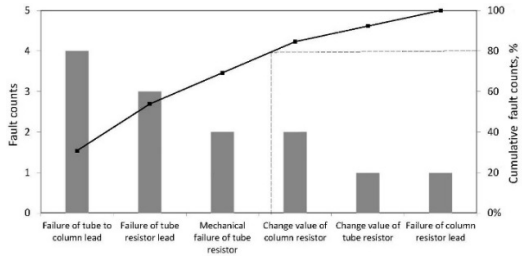

Figure 5: Pareto chart showing the number of 14UD electrostatic structure faults. The dashed line starting at 80% of the right y-axis highlights 80-20 rule.

The next most commonly observed fault category, at 15%, is mechanical failure of the acceleration tube resistor. An example is when the resistor or its spark gap electrode becomes loose in its shield.

The next important fault is a variation of the column post resistor value at 15% or tube resistor value at 8%. The erosion of the resistor conductive layer can occur due to exposure to corona discharge.

The total proportion of faults is 46% for tube components and 23% for column posts. This higher proportion of faults on acceleration tubes is consistent with results reported in [1]. Despite acceleration tubes usually being better protected when compared to column posts, the posts and their resistors are more accessible and historically have been replaced more often as a part of a post refurbishing program.

Finally, the green series in Fig. 3 and Fig. 4 denotes the exit test distribution of gap voltage U_{gap}. Overall, it can be seen that as a result of in-situ diagnostics and fault elimination, the maximum deviation of ΔU_{gap} is kept well within the acceptable level ±2.5%.

REFERENCES

[1] N.R. Lobanov, P. Linardakis, and D. Tsifakis, Ultrahigh impedance method to assess electrostatic accelerator performance, Phys. Rev. ST Accel. Beams **18**, 060101 (2015).

[2] J. Noe, Proc. Symposium of North Eastern Accelerator Personnel, Notre Dame, France, 1986, pp.168–185.

[3] D.C. Weisser, Nuclear Instruments and Methods in Physics Research Section A, vol. 328, pp. 138–145 (1993).

[4] N.R. Lobanov, P. Linardakis, D. Tsifakis, Nuclear Instruments and Methods in Physics Research Section A, vol. 767, pp. 433–438 (2014).

[5] M.A. Noras, Industry Applications Conference, Industry Applications Conference, 2005. 40th IAS Annual Meeting. Conference Record of the 2005 IEEE, Volume 3, 2–6 Oct., 2005, Hong Kong, pp. 2194–2197.

ISBN 978-3-95450-131-1

CONSTRUCTION OF THE 6 MV TANDEM ACCELERATOR SYSTEM FOR VARIOUS ION BEAM APPLICATIONS AT THE UNIVERSITY OF TSUKUBA*

K. Sasa#, S. Ishii, H. Oshima, Y. Tajima, T. Takahashi, Y. Yamato, D. Sekiba, T. Moriguchi, E.Kita
UTTAC, University of Tsukuba, Tsukuba, Ibaraki, Japan

Abstract

The 12UD Pelletron tandem accelerator at the University of Tsukuba was completely destroyed by the Great East Japan Earthquake on 11 March 2011. A replacement has been designed and constructed at the university as part of the post-quake reconstruction project. We planned to install a new horizontal-type 6 MV tandem accelerator. A three-year plan for the new accelerator's construction was started in 2012. The new accelerator system consists of the 6 MV tandem accelerator, four new ion sources, the Lamb-shift polarized ion source, and twelve beam courses. The 6 MV tandem accelerator will be used for various ion beam applications. Routine beam delivery and experiments will start in 2015.

INTRODUCTION

The University of Tsukuba's Tandem Accelerator Complex (UTTAC) is a major center of ion beam research in Japan. We had the 12UD Pelletron tandem accelerator, a 1 MV Tandetron accelerator, a 1 MV high-resolution Rutherford back scattering (RBS) system, and a positron annihilation spectrometry system. The 12UD Pelletron accelerator was a vertical-type large tandem accelerator made by National Electrostatic Corp. (NEC), USA; and was installed at UTTAC as a first Pelletron tandem accelerator in Asia in 1975 [1]. Its main accelerator tank was 17.9 m long and 4.8 m in diameter; its total weight was 120 metric tons. The maximum terminal voltage of 12 MV was available for various ion beam applications.

The Great East Japan Earthquake (9.0 magnitude) of 11 March 2011 severely damaged the 12UD Pelletron tandem accelerator [2]. A seismograph at the University of Tsukuba (part of the National Research Institute for Earth Science and Disaster Prevention, Kyoshin-Net infrastructure [3]) measured the earthquake's maximum acceleration as 371.7 cm/s^2 (gal) and its duration as about 300 s. The vertical-type tandem accelerator was damaged by the sustained shock of the earthquake, and all the high-voltage accelerating columns collapsed in the accelerator tank. Repairing the 12UD Pelletron tandem accelerator was not feasible, and it was shut down in 2011.

We planned to install a new horizontal-type 6 MV tandem accelerator in the experimental room on the first floor to replace the damaged accelerator. The 6 MV tandem accelerator will be used for various ion-beam research projects, such as accelerator mass spectrometry (AMS), microbeam applications, particle-induced X-ray emission (PIXE) analysis for geoscience and materials research, heavy ion RBS and elastic recoil detection analysis, nuclear reaction analysis for hydrogen in materials, and high-energy ion irradiation for semiconductor and nuclear physics.

In this paper, we report the construction status of the 6 MV tandem accelerator and the research programs at the University of Tsukuba.

DESIGN OF THE 6 MV TANDEM ACCELERATOR FACILITY

All experimental equipment is installed on the first floor at UTTAC. Figure 1 gives an overview of the equipment on the first floor. The new accelerator system consists of a horizontal-type 6 MV tandem accelerator, four new ion sources, the Lamb-shift polarized ion source (S1 in Figure 1), and five new beam courses. After the 105° analyzer magnet, the beam line is separated in two directions by the 40° switching magnet in the accelerator room. A high-energy beam transport line equipped with a vertical ion-irradiation system is connected from the accelerator room to the existing experimental room, which houses seven beam courses. A total of 12 beam courses will be available for nuclear physics, ion beam applications, and AMS.

The Lamb-shift polarized ion source was used as the injector of polarized proton and deuteron beams to the old tandem accelerator on the 9th floor at UTTAC [4]. After the earthquake, this ion source was moved to a new experimental building outside the accelerator building. In the accelerator room, there are four negative-ion sources. In Figure 1, S2 is a high-current Cs-sputtering negative-ion source (SNICS II), and S3 is a radio frequency charge exchange ion source (Alphatross) to produce He^- beams for injection into the 6 MV Pelletron tandem accelerator. S4 and S5 are the multi-cathode Cs-sputtering negative-ion sources (MC-SNICSs) for AMS.

In the accelerator room, the ion beam analysis (IBA) system equipped with a high-precision four-axis goniometer is located on the L1 beam course. The L2 beam course has a large environmental testing chamber (1 m diameter) that will be mainly used for the radiation-resistant testing of semiconductor devices for space satellites. The L3 beam course is constructed as the microbeam system for high-sensitivity PIXE analysis of structural materials. The L4 beam course is the rare-particle detection system for AMS. The L5 beam course is a general-purpose line for ion beam applications. Figure 2 shows a photograph of the accelerator room.

* Work supported by the Ministry of Education, Culture, Sports, Science and Technology
# ksasa@tac.tsukuba.ac.jp

ISBN 978-3-95450-131-1

In the experimental room, there are two large magnetic spectrographs (A6 and A7 beam courses) for nuclear physics. Other beam lines are used for ion beam channeling (A2 beam course), 3D fabrications with swift heavy ions (A3 beam course), and hydrogen analysis (A4 beam course). There is also a large general-purpose chamber (A5 beam course).

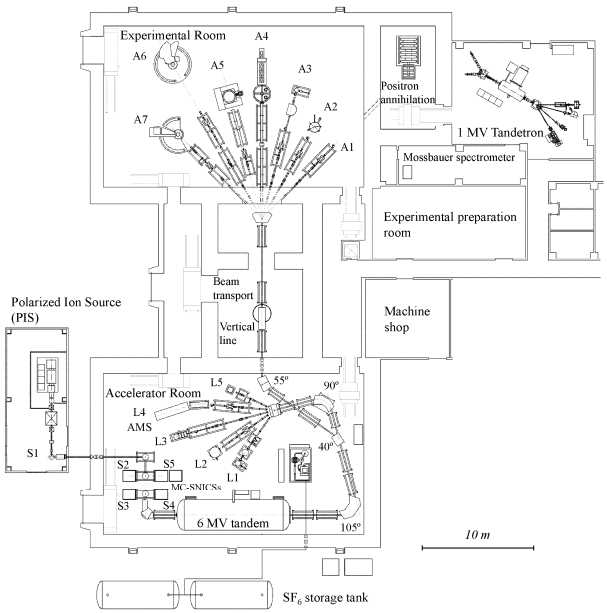

Figure 1: Overall view of the first floor at UTTAC.

Figure 2: Full view of the accelerator room.

DETAILED DESCRIPTION OF THE 6 MV TANDEM ACCELERATOR

Injector (Ion Sources)

At the low-energy side, the injection energy from the ion sources is 65 keV. There are three 90° retractable electrostatic spherical analyzers (ESAs) with a 200 mm radius and 35 mm plate separation to provide for each of the five ion sources. The 90° high-mass-resolution double-focusing magnetic analyzer with a 457 mm radius has a mass energy product of ME/Z^2 = 15 amu MeV with a mass resolution of up to 200. A 15 kV pulsed power supply is provided to bias the 90° magnetic analyzer chamber for the sequential injection of up to four different beams. Downstream of the 90° magnetic analyzer, two movable offset Faraday cups are located to measure particle transmission through the accelerator and the beam intensities of lower-mass beams during higher-mass beam injection. In front of the accelerator tank, there is a beam attenuator to adjust the transport for high-beam current by decreasing one-tenth of the beam current. Figure 3 details the injection system of the 6 MV tandem accelerator.

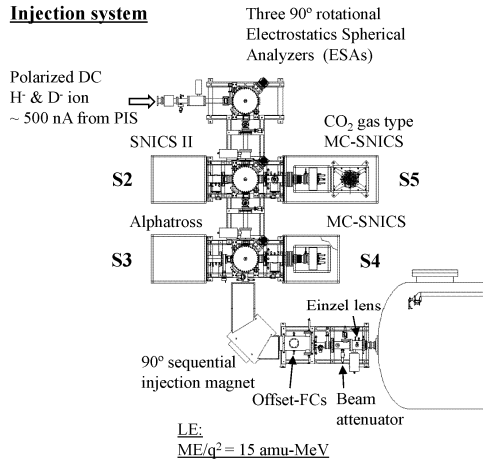

Figure 3: Injection system of the 6 MV tandem accelerator.

Accelerator

The main accelerator (model 18SDH-2 Pelletron accelerator developed by NEC, USA) is a dual acceleration electrostatic accelerator. The accelerator tank is about 2.74 m in diameter and 10.5 m long. Figure 4 shows a cross-section drawing of the accelerator tank. It was delivered to Tsukuba in March 2014.

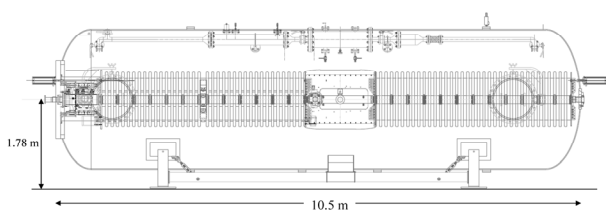

Figure 4: Cross-section drawing of the accelerator tank.

The high-voltage terminal has a long gas stripper tube assembly and a foil changer with 80 foil holders for equilibrium stripping ions. Carbon stripper foils will be mainly used for heavy ions to obtain a high charge state. The stripper gas canal is about 10 mm in diameter and 95 cm long. The generator operates reliably to terminal voltages as high as 6.3 MV. Stability is estimated to be better than

ISBN 978-3-95450-131-1

1 kV at a 6.0 MV terminal voltage. Maximum beam currents are predicted to be up to 50 μA for heavy ions. Specifications for the 6 MV tandem accelerator are shown in Table 1. It will be capable of accelerating various ions with a wide range of energy. Figure 5 shows an estimation of ion beam energy range.

Table 1: Specifications of the 6 MV Tandem Accelerator

・Model: 6 MV Pelletron Tandem (18SDH−2, National Electrostaics Corp., USA)		
・Accelerator Tank Size:	Length:	10.5 m
	Diameter:	2.74 m
	Line Height:	1.78 m
	Weight :	17,420 kg
・Terminal Voltage:	0.5 − 6.0 MV	
・Voltage Ripple:	≤ 750 V p−p at 6.0 MV	
・Voltage control: GVM & Slit Current Feedback System		
・Maximum Beam Current:	H :	3 μA
	Heavy ions:	~50 μA
・Terminal Stripper:	Gas (Ar or N_2)	
	Foil Unit (80 Foil Holders)	
・Insulation Gas:	SF_6 (0.6 MPa)	
・Beam Courses : 12 Lines and Vertical Transport Line		
・Ion Sources:		
Cs Sputtering Negative Ion Sources		
NEC SNICS II		
NEC MC-SNICS		
NEC CO_2 Gas Type MC-SNICS		
RF Ion Source (NEC Alphatross)		
Lamb-shift Polarized Negative Ion Source		
・Mass Energy Product (ME/Z^2): 15 amu MeV (LEBT)		
176 amu MeV (HEBT)		

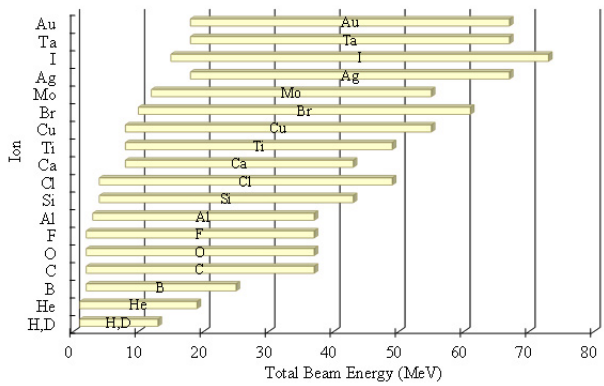

Figure 5: Ion beam energy range for the 6 MV tandem accelerator.

High-energy Beam Transport Line

A high-energy beam transport line after the accelerator has a mass energy product of ME/Z^2 = 176 amu MeV. The 105° analyzer double-focusing magnet (1.27 m radius) has a resolution of $M/\Delta M$ = 725. After the 105° analyzer magnet, three movable Faraday cups are set to intercept precisely the various beams of interest. A 90° deflection double focusing magnet (1.27 m radius) is provided along the beam line. Two magnetic quadrupole triplet lenses are arranged to control divergence and focus ion beams between the 105° analyzer magnet and the switching magnet. The switching magnet is installed at the end of the beam line in the accelerator room, and has five beam ports.

Rare-particle Detection System for AMS

One of the important researches in ion beam application is AMS for the 6 MV tandem accelerator. The rare-particle detection system (Tsukuba 6 MV AMS system) is set on the −20° port on the switching magnet (L4 beam course). A 22.5° ESA (3.81 m radius) is provided to filter out unwanted ions whose mass energy product (ME/Z^2) is the same as the rare isotope of interest. The 22.5° ESA has a resolution of $E/\Delta E$ = 200. A five-electrode gas ionization detector is installed on the end station of the rare-particle detection system. The Tsukuba 6 MV AMS system is expected to measure all standard AMS species routinely (e.g., ^{10}Be, ^{14}C, ^{26}Al, ^{36}Cl, ^{41}Ca, and ^{129}I) [5].

CONCLUSION

The 12UD Pelletron tandem accelerator that was over 35 years old at the University of Tsukuba was destroyed by the Great East Japan Earthquake in 2011. It was replaced by the new 6 MV tandem accelerator that was installed at UTTAC in 2014, and then used to regulate beam transport. This new multi-purpose tandem accelerator will see various uses, including, AMS, IBA, ion irradiation, and nuclear physics. The new system will start routine experiments on ion beam applications in 2015.

ACKNOWLEDGMENT

We would like to acknowledge Hakuto Co., Ltd. Japan and National Electrostatics Corp., USA for installation support for the 6 MV tandem accelerator.

REFERENCES

[1] S. Seki et al., “The 12 UD pelletron accelerator at the University of Tsukuba”, Nucl. Instrum. Methods 184, p. 113 (1981).

[2] K. Sasa, “Damage Situation of the 12UD Pelletron Tandem Accelerator at the University of Tsukuba by the Great East Japan Earthquake”, June 2012, p. 80 (2012); http://www.JACoW.org

[3] K-NET, the National Research Institute for Earth Science and Disaster Prevention (NIED), Japan. http://www.kyoshin.bosai.go.jp/

[4] Y. Tagishi et al., “A Lamb-shift polarized ion source for the Tandem Accelerator Center, The University of Tsukuba”, Nucl. Instrum. Methods 164, p. 411 (1979).

[5] K. Sasa et al., “The new 6 MV multi-nuclide AMS facility at the University of Tsukuba”, Nucl. Instrum. Methods B, in press (2015).

ISBN 978-3-95450-131-1

PRESENT STATUS OF A SUPERCONDUCTING ROTATING-GANTRY FOR CARBON THERAPY

Y. Iwata#, K. Noda, T. Shirai, T. Fujita, T. Furukawa, K. Mizushima, Y. Hara, Y. Saraya,
R. Tansho, S. Matsuba, S. Mori, S. Sato, K. Shoda, NIRS, Chiba 263-8555, Japan
T. Fujimoto, H. Arai, AEC, Chiba 263-0043, Japan
T. Ogitsu, KEK, Ibaraki 305-0801, Japan
N. Amemiya, Kyoto University, Kyoto 615-8530, Japan
Y. Nagamoto, T. Orikasa, S. Takayama, Toshiba, Tokyo 105-8001, Japan

Abstract

A superconducting rotating-gantry for carbon therapy is being developed. This isocentric rotating gantry can transport carbon ions with the maximum energy of 430 MeV/u to an isocenter with irradiation angles of over ±180 degrees, and is further capable of performing three-dimensional raster-scanning irradiation. The combined-function superconducting magnets were employed for the rotating gantry. The superconducting magnets with optimized beam optics allowed a compact gantry design with a large scan size at the isocenter; the length and the radius of the gantry are approximately 13 and 5.5 m, respectively, which are comparable to those for the existing proton gantries. A construction and installation of the superconducting gantry is in progress, and beam commissioning will begin from this autumn. We will report an overview as well as a present status of the superconducting rotating-gantry.

INTRODUCTION

In recent years, an application of high-energy particle accelerators to cancer therapy has attracted many attentions, and a number of medical particle accelerators were constructed around the world. In the ion radiotherapy, the rotating gantry is a very attractive tool, because a treatment beam can be directed to a target from any of medically desirable directions, while a patient is kept in the best position. This flexibility of the beam delivery for this type of the gantry, *isocentric rotating gantry*, is advantageous to treat tumors having wide range of tumor sites and sizes.

For proton cancer therapy, rotating gantries were commonly constructed around the world. However, it would be very difficult to construct a rotating gantry for carbon therapy, because the required magnetic rigidity for carbon beams having energy of 430 MeV/u is roughly three times higher than that for proton beams having energy of 250 MeV/u, and hence the size and weight for the gantry structure, including magnets and its counterweight, would become considerably larger. To overcome this problem, a superconducting rotating gantry for carbon therapy is being developed [1]. The construction as well as installation of the superconducting gantry is in progress, and beam commissioning will begin from this autumn. In this paper, an overview as well as a present status of the gantry is presented.

#y_iwata@nirs.go.jp

OVERVIEW OF THE GANTRY

Figure 1 shows a three-dimensional image of the superconducting rotating gantry. This rotating gantry has a cylindrical structure with two large rings at both ends. The end rings support the total weight of the entire structure, and are placed on turning rollers so as to rotate the beam line on the rotating gantry along the central axis over ±180 degrees. Carbon beams, provided by the HIMAC, are transported with ten sector-bending superconducting magnets, mounted on the gantry structure through each of their supporting structures; they are directed on a target located at the isocenter

Figure 2 shows a schematic drawing of the beam line, installed in the rotating part of the gantry. The beam line consists of ten sector-bending superconducting magnets (BM01-10), a pair of scanning magnets (SCM-X and SCM-Y), and three pairs of steering magnets as well as a beam profile monitor (STR01-03 and PRN01-03). To design the compact gantry, combined-function superconducting magnets are employed except for BM07 and BM08. These superconducting magnets have a surface-winding coil structure, and can provide both dipole and quadrupole fields.

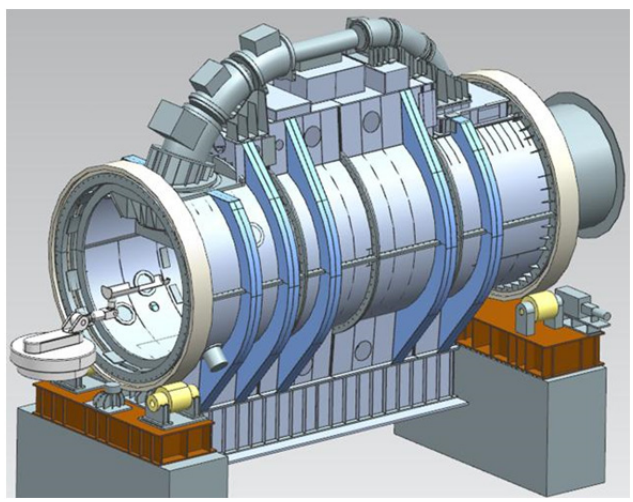

Figure 1: Schematic drawing of the superconducting rotating gantry.

ISBN 978-3-95450-131-1

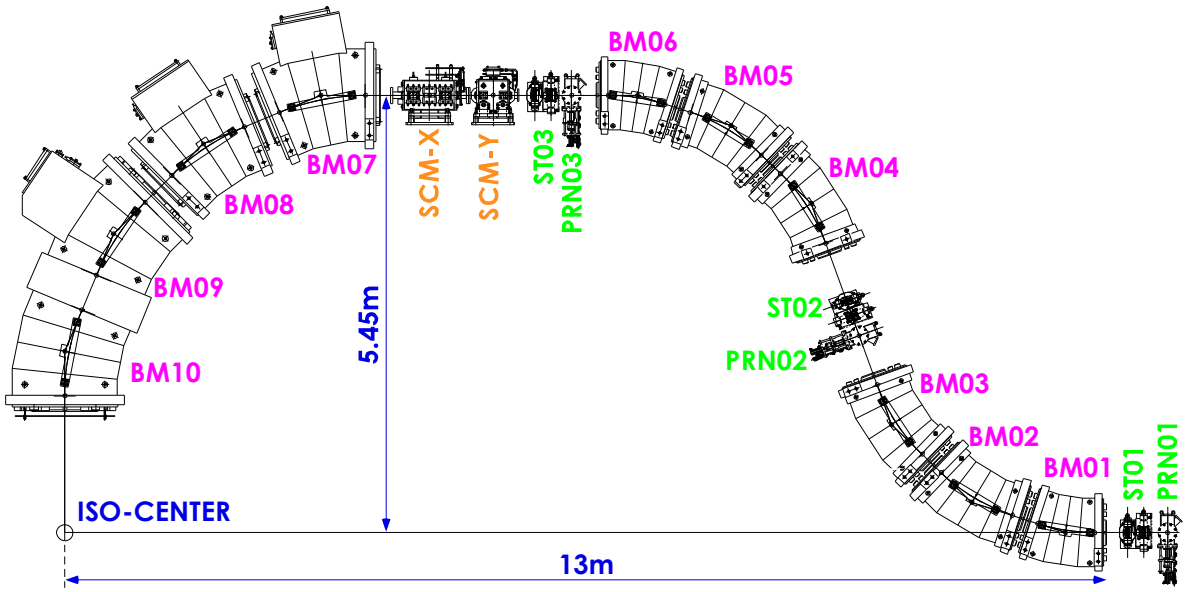

Figure 2: Layout of the superconducting rotating gantry. The gantry consists of ten superconducting magnets (BM01-10), a pair of the scanning magnets (SCM-X and SCM-Y), and three pairs of beam profile-monitor and steering magnets (ST01-03 and PRN01-03).

Figure 3 shows the beta and dispersion functions along the beam line of the rotating gantry. The blue and red curves in Fig. 3 represent those for the horizontal and vertical coordinates, respectively. The twiss parameters at the entrance of the gantry is $\beta_x=\beta_y=30$ m, $\alpha_x=\alpha_y=0$, $D_x=D_y=0$ m, $D'_x=D'_y=0$, while the twiss parameters for the isocenter is designed to be $\beta_x=\beta_y=1$ m, $\alpha_x=\alpha_y=0$, $D_x=D_y=0$ m, $D'_x=D'_y=0$. Since a typical 2σ beam emittance for energy of 430 MeV/u is $\varepsilon\sim1$ πmm·mrad, the beam size at the isocenter is $\sqrt{\beta\varepsilon}$ ~1 mm.

All of the superconducting magnets were designed using the "Opera-3d" code [2]. A result of the calculation for BM02-05 is presented in Fig. 4. The positions of the superconducting wires were optimized so as to provide uniform magnetic field over the effective aperture of ϕ40 mm for BM02-05. With the calculated magnetic fields for all the superconducting magnets, beam-tracking simulations were made. The simulation results agreed well with those of the linear beam-optics calculation, proving validity of the final design for the superconducting magnets [3].

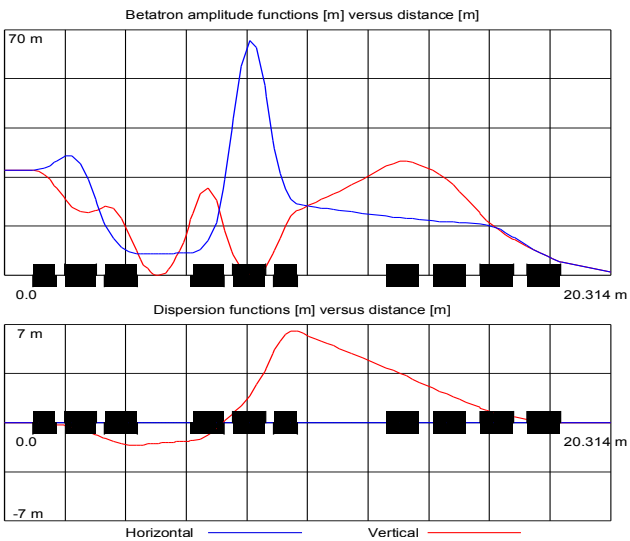

Figure 3: Beta and dispersion functions along the gantry beam line.

CONSTRUCTION AND INSTALLATION

Having completed the design, all the superconducting magnets were constructed, and field measurements using Hall probes as well as NMR probes were performed. The measured field map over the magnet aperture agreed with that, calculated by the "Opera-3d" code, although we observed quadrupole field, originated from the dipole coil [4]. However, since the magnets have the dipole and quadrupole coils, this quadrupole field from the dipole coil can be corrected by adding or reducing coil current from the designed quadrupole coil current.

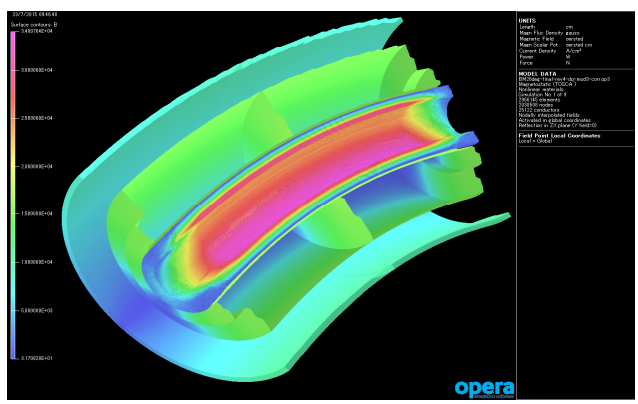

Figure 4: Result of three-dimensional field calculations for BM02-05 using the "Opera-3d" code.

ISBN 978-3-95450-131-1

Figure 5: Rotation tests of the gantry structure at the Toshiba Keihin Product Operations.

The gantry structure was designed to have a cylindrical shape with the two large rings at both ends as shown in Fig. 1. The length between the two end rings is approximately 14 m, and the outer diameter of the end rings is 6.5 m. In the design, the detailed FEM calculations were performed, and the gantry structure was optimized so as to minimize deformation of the structure, as caused by rotating the entire structure of the gantry. Finally, the maximum displacement of the each superconducting magnet was estimated by the calculations to be less than 1 mm.

Because of the construction and transportation issues, the cylindrical structure of the rotating gantry was divided into eight large parts. The eight parts as well as the two end rigs were made at the Toshiba Keihin Product Operations. At Toshiba, the gantry structure was assembled with dummy weights, instead of the magnets, and rotation tests were performed as shown in Fig. 5. The deformation was precisely measured by a laser tracker, and we found that measured deformations roughly agreed with those predicted by the FEM calculations.

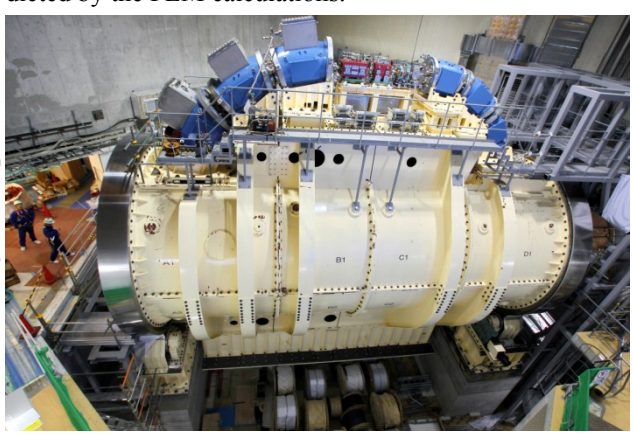

Figure 6: Picture of the superconducting rotating-gantry, as installed in NIRS. All the magnets as well as the profile monitors were mounted on the gantry structure.

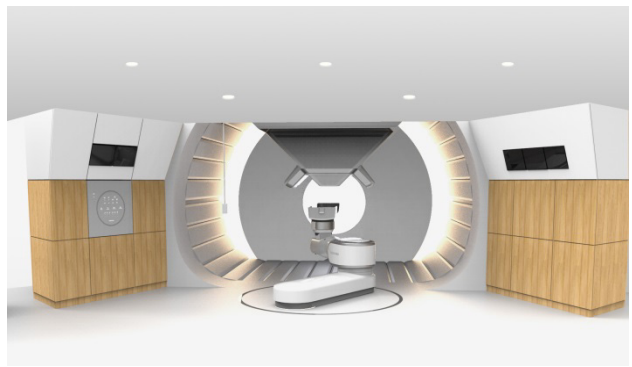

Figure 7: Image of the treatment room for the rotating gantry.

Having made a series of the tests at Toshiba, the rotating gantry was disassembled into the parts, and they were transported to the gantry room in NIRS. Then, the parts were installed and reassembled in the gantry room, and further the superconducting magnets as well as all the other beam transport devices were mounted on the gantry structure as presented in Fig. 6. Having activated cryocoolers, all the superconducting magnets were now cooled down below 4 K.

A design image of the treatment room is given in Fig. 7, and its construction is in progress. All the construction is planned to be completed by the end of September.

SUMMARY

A superconducting rotating-gantry for carbon therapy is being developed. By using the combined function superconducting magnets, the size and weight of the gantry structure is considerably reduced. After finalizing the construction of the treatment room, we will begin beam commissioning from this autumn.

ACKNOWLEDGEMENTS

We thank the other members of Toshiba Corporation for their help in the design and construction. This work is supported by Ministry of Education, Culture, Sports, Science and Technology (MEXT), Japan.†

REFERENCES

[1] Y. Iwata et al., “Design of a superconducting rotating gantry for heavy-ion therapy”, Phys. Rev. ST Accel. Beams. 15, 044701 (2012).
[2] “Opera-3d” software, http://www.cobham.com/.
[3] Y. Iwata et al., “Development of a superconducting rotating-gantry for heavy-ion therapy”, Nucl. Instrum. and Meth. in Phys. Res. B 317, 793 (2013).
[4] Y. Iwata et al., “Development of curved combined-function superconducting-magnets for a heavy-ion rotating-gantry”, IEEE Trans. on Appl. Supercon-ductivity, Vol. 27, Issue3, 4400505 (2014).

†Product names mentioned herein may be trademarks of their respective companies.

ISBN 978-3-95450-131-1

A COMPACT HADRON DRIVER FOR CANCER THERAPIES WITH CONTINUOS ENERGY SWEEP SCANNING

Leo Kwee Wah[1], Toshikazu Adachi[2,3], Tadamichi Kawakubo[2], Takumi Monma[2,4], Tanuja Dixit[5], and Ken Takayama[2,3,4,6]
[1]Malaysian Nuclear Agency, Bangi, Kajang, Malaysia
[2]High Energy Accelerator Research Organization (KEK), Tsukuba, Ibaraki, Japan
[3]The Graduate University for Advanced Studies (SOKENDAI), Hayama, Kanagawa, Japan
[4]Tokyo Institute of Technology, Nagatsuda, Kanagawa, Japan
[5]Society for Applied Microwave Electronics Engineering & Research (SAMEER), Mumbai, India
[6]Tokyo City University, Setagaya, Tokyo, Japan

Abstract

The compact hadron driver for future cancer therapies based on the induction synchrotron concept, which has been proposed recently, is discussed. This is a fast cycling synchrotron that allows the energy sweep beam scanning. Assuming a 1.5 T bending magnet, the ring can deliver heavy ions of 200 MeV/au at 10 Hz. A beam fraction is dropped from the barrier bucket at the desired timing and the increasing negative momentum deviation of this beam fraction becomes enough large for the fraction to fall in the electrostatic septum extraction gap, which is placed at the large *D(s)* region. The programmed energy sweeping extraction makes spot scanning beam irradiation on a cancer area in depth possible.

INTRODUCTION

3D spot scanning of hadron beams to cancer tissues of human organs is of most concern in this society [1]. We will focus on spot scanning by the energy sweeping extraction from a fast cycling induction synchrotron [2]. A hadron bunch captured in the barrier bucket is continuously accelerated by the induction flat voltage and a fraction of the beam bunch is spilled out from the stable barrier bucket by non-adiabatically changing timing of the acceleration voltage controlling trigger signal in the desired time period. Equilibrium orbits of spilled out particles move inward depending on the dispersion function *D(s)* and those particles enter into the electrostatic septum gap region to be further deflected inward, and then propagate through the extraction region downstream consisting of extraction device such as a Lamberson magnet to put on the extraction beam line. Start of the extraction and a number of spilled out particles are simply determined by controlling of the gate signal. Thus, we can obtain a driver beam for the cancer therapy with the function of 3D spot scanning, the energy of which changes continuously in the same acceleration cycle as shown in Fig. 1 by integrated with the ramping pattern of guiding magnet. Details of this scheme have been proposed in Reference [3]. Its essence will be described here.

Details of this scheme has been proposed in Reference [3]. Its essence will be described here.

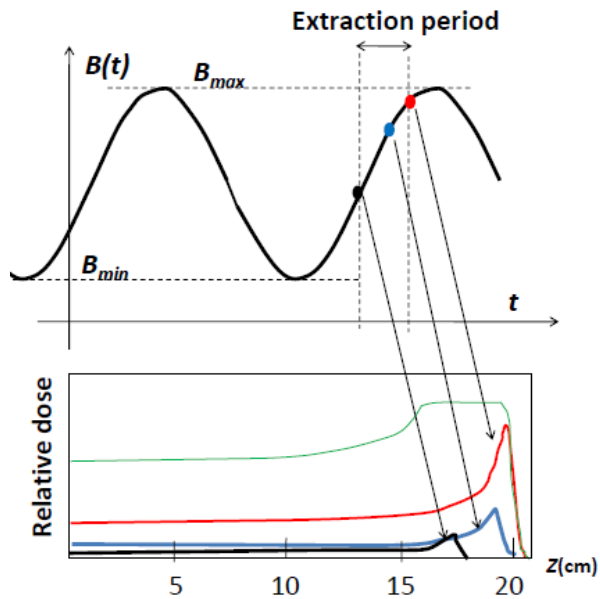

Figure 1: Energy sweep extraction in the same acceleration cycle and integrated dose along the path, where *B(t)* is the magnetic flux density of the guiding magnet.

In this paper, a practical method to realize the energy sweeping extraction from a fast cycling synchrotron is proposed.

Ring Lattice

Properties of the lattice design and machine parameters [3] as shown in Fig. 2 and Table 1must comprise of:

i) Dispersion-free region for induction acceleration devices and injection device.
ii) Localized large flat dispersion region for the extraction device with the length of 3 m.
iii) Local betatron phase advance of π/2 for the fast extraction.

leo@nuclearmalaysia.gov.my

ISBN 978-3-95450-131-1

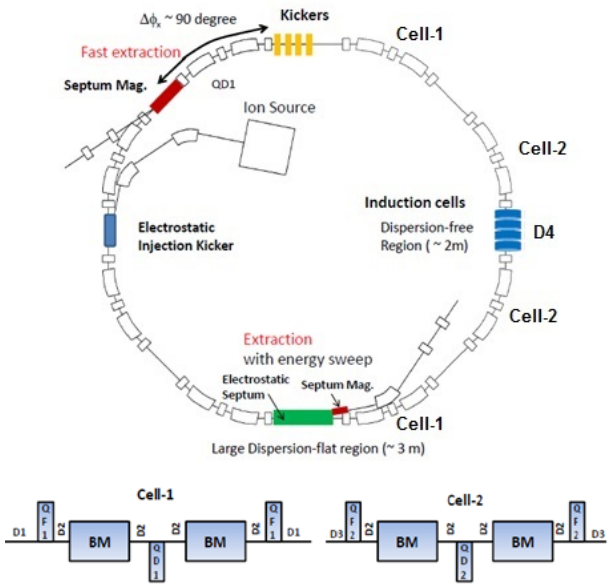

Figure 2: Outline of the driver ring and cell structure.

Table 1: Machine and Beam Parameters

Energy	656 MeV for proton 200 MeV/nucleon for $A/Q = 2$ ion
C_0	52.8 m
Ion species	Gaseous/Metal ions
Ion source	Laser ablation IS, ECRIS
Injector	200 kV (electrostatic)
Ring	fast cycling (10 Hz)
	B_{max} = 1.5 Tesla
	ρ = 2.8662 m
	FODOF cell with edge focus of B
	Mirror symmetry
	ν_x / ν_y = 1.3143/1.4635
	2m long dispersion-free region 3m long flat large dispersion region
	α_p=0.273088 γ_T=1.92, E_T=864.7 MeV
Acceleration	Induction cells driven by SPS employing SiC-MOSFET $V_{acc} = \rho C_0 dB/dt$ (max 7 kV)
Vacuum	10^{-8} Pascal

SIMULATION FOR EXTRACTION

Energy Sweeping Extraction

In this driver ring, a hadron bunch is trapped in the barrier bucket and accelerated with the induction voltage pulse as shown in Fig. 3. Particles in a normal acceleration, where an entire bunch is accelerated to the end of acceleration cycle, behave as shown in Fig. 4. In the energy sweep extraction mode, the flat edge of V_{acc} pulse is moved to the rising edge of positive V_{bb} pulse just in 1 turn at the extraction timing. Insufficient magnitude of the acceleration voltage allows an artificial and continuous leak of a fraction of macro-particles beyond the assumed extraction timing.

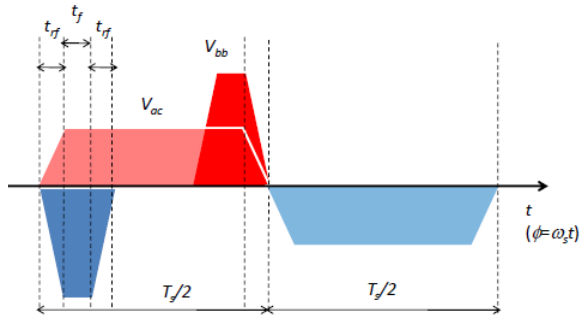

Figure 3: V_{ac} and V_{bb} profile in time before extraction, where T_s and ω_s are the revolution time period and angular revolution frequency of the synchronous particle t_{rf} is the rising and falling time period of both voltage.

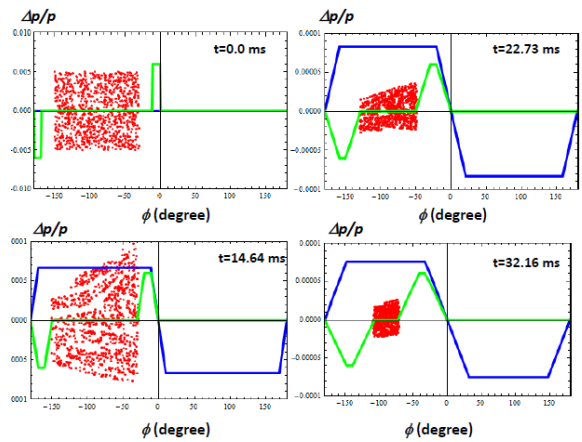

Figure 4: Phase plots of tracked macro-particles in the phase space with V_{ac} *(Blue)* and V_{bb} *(Green)*, where the voltage heights are shown in a relative unit.

Spill Drop from the Barrier Bucket

For this simulation, the gate signals for the V_{ac} voltage pulses are changed beyond the starting time of extraction so that the flat edge of V_{ac} becomes to be equal to the rising bottom of positive V_{bb}. Particles entering into the positive barrier region, where the V_{ac} voltage profile has a negative slope are affected by an insufficient acceleration voltage. As the result, a lager negative momentum deviation is generated. These particles leave the barrier bucket region or trapped region to move downward further. Eventually, they arrive the boundary region of $\Delta p/p = -10^{-2}$, beyond which a particle entering into the electrostatic septum region is kicked inward in the horizontal direction by the electrostatic fields. Typical examples of the phase plot with the spill drop from the barrier bucket are shown in Fig. 5. One finds that the small fraction of macro-particles continuously drifts down in the momentum space. At this stage, the spill is not controlled because any parameters are not optimized.

ISBN 978-3-95450-131-1

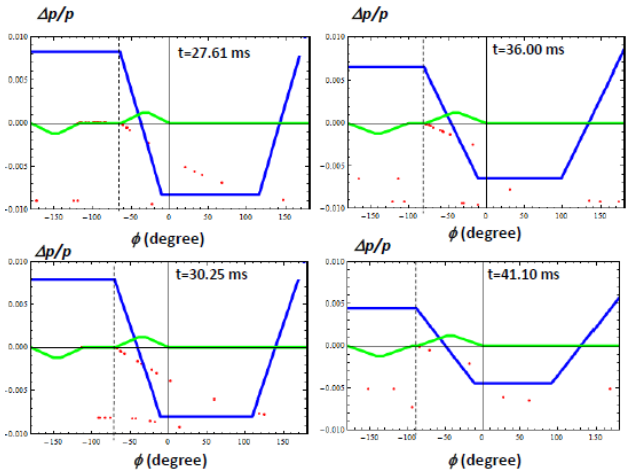

Figure 5: Phase plots of macro-particles leaving the barrier bucket region, where the bunch core is invisible, because its momentum spread is quite small. The position of broken lines, from which particles leak, must be noted.

SPILL CONTROL

The spill size can be controlled, where the turning-off time of V_{ac} is changed in a programmed manner. If some of particles being trapped in the barrier bucket are not given a required energy matching to the guiding magnet pattern, they will leave the trapping region or the barrier bucket and drifting downward in the longitudinal phase space. This is a key feature of spill control. Acceleration is uniquely determined by V_{ac}. Its downhill profile in time is steep and its starting phase of falling-down in V_{ac}, which is indicated by ϕ_{ext} in Fig. 6, is maneuvered by gate-control for the switching power supply. This timing is always adjusted in the programmed manner or by means of feed-back from the spill monitoring system. The procedure for spill control is shown below.

(1) ϕ_{ext} is instantaneously moved to near the left edge of the right barrier voltage pulse (ϕ_{bb}) at the starting time of spill extraction.
(2) Then, ϕ_{ext} is changed so as to satisfy the expected spill profile in the programmed manner or watching an actually extracted spill profile.

As shown in Fig. 7, The integrated spill profile as a function of time for three extraction cases with different timing of V_{ac} but constant ϕ_{ext} and 1,000 macro particles. It is clear that the spill profile depends on the extraction parameter δ. This parameter can be controlled so as to meet a requirement on the spill profile. Such a typical example is given in Reference 3, where the constant spill is maintained up to the end of acceleration. Actually the programmed spill profile is realized by a program loaded on the field programmed gate array (FPGA). Real time feedback control may be also possible by watching an actual spill in the acceleration cycle.

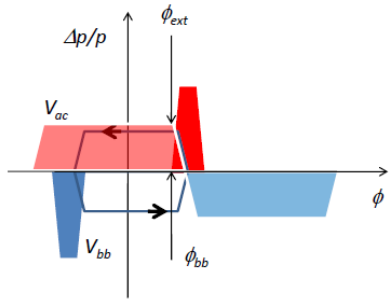

Figure 6: Phase space with the Vac profile adjusted for extraction.

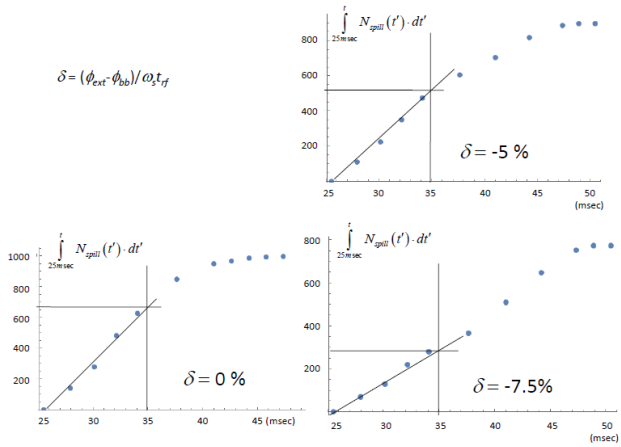

Figure 7: Integrated spill for different δ.

SUMMARY

The hadron machine with continuous energy scanning for cancer therapies has been designed and its performance has been confirmed by macro-particle simulations. There is no space to discuss a key device for energy sweep extraction, that is, electrostatic septum. We believe that this is realized utilizing the modern technology of variable voltage power supply employing a solid-state switch [3]. However, there are still several issues related with beam transverse emittance that must be studied hereafter.

REFERENCES

[1] K. Hiramato, talk at *Workshop on Hadron Beam Therapy of Cancer*, 27th April, 2009, Erice, Italy.
[2] K. Takayama, T. Yoshimoto M. Barata, Leo Kwee Wah, Liu Xingguang, T. Iwashita, S. Harada, T. Adachi, T. Arai, D. Arakawa, H. Asao, E. KAdokura, T. Kawakubo, H. Nakanishi, Y. Okada, K. Okamura, K. Okazaki, A, Takagi, S. Takano and M. Wake, *Phys. Rev. ST-AB* **17**, 010101 1(2014).
[3] Leo Kwee Wah, T. Adachi, T. Kwakubo, T. Monma, T. Dixit, and K. Takayama, "A Compact Energy Hadron Driver for Cancer Therapies with Continuous Energy Sweep Scanning" submitted to *Phys. Rev. ST-AB(2015)*.

ISBN 978-3-95450-131-1

DESIGN, FABRICATION AND TESTING OF COMPACT DIAGNOSTIC SYSTEM AT IUAC

R.V.Hariwal, [1, 2, #] H.K.Malik, [2] R. Mehta, [1] S.Kedia, [1] and V. Verzilov [3]
[1]Inter-University Accelerator Centre, Aruna Asaf Ali Marg, New Delhi 110067, INDIA
[2]Plasma Waves and Particle Acceleration Lab, Department of Physics, I.I.T Delhi 110016, INDIA
[3]Accelerator Division, TRIUMF, 4004 Wesbrook Mall, Vancouver, B.C. V6T2A3, CANADA

Abstract

High Current Injector (HCI) [1] is an upcoming accelerator facility at Inter-University Accelerator Centre, New Delhi, India. This comprises of high temperature superconducting Electron Cyclotron Resonance (HTS-ECR) ion source [2], normal temperature Radio Frequency Quadrupole (RFQ), IH-type Drift Tube Linear (DTL) resonators [3] and low beta superconducting Quarter Wave Resonator (QWR) cavities to accelerate heavy ions having A/q ≤ 6. The compact diagnostic system consists of Faraday cup, slit scanner and capacitive pick up to measure the current, profile, position and bunch length of incident ion beam respectively. It is especially designed and fabricated to measure the beam parameters at the entrance of each of six IH-DTL resonators. The compactness is preferred to minimize the transverse and longitudinal emittance growth at the entrance of DTL resonators. The beam current and profile measurements of various heavy ion beams at different energy have been carried out to validate the design and fabrication of the diagnostic system. Here we are presenting the detailed information about its design, fabrication and various test results.

DEVELOPMENT OF COMPACT DIAGNOSTIC SYSTEM

Compact Diagnostic Box (CDB)

A compact diagnostic chamber (Fig.1) is made of 12 mm thick stainless steel (SS-304) material. As the drift space between two DTL cavities is crucial, to accommodate the diagnostic chamber and quadrupole triplet, we need to minimize the drift. A highly compact diagnostic chamber has been designed and fabricated indigenously. The diagnostic chamber is of 70 mm longitudinal length. The radial dimension of the box is approximately 160 mm and the beam aperture is 20 mm. It has eight faces, in which two of them are orthogonal to each other and they have been designed specifically to mount the Faraday cup and slit scanner. The chamber was leak tested at the leak rate of $1x10^{-11}$ mbar.l/s. Without any separate pumping station, the vacuum of $1x10^{-7}$ mbar was achieved, but this can be further improved by adding a separate pumping station.

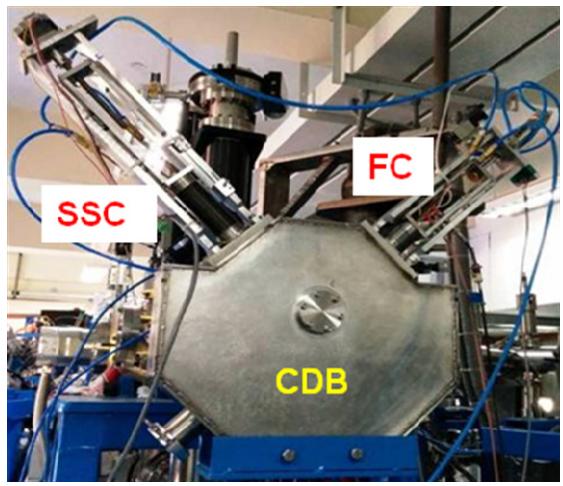

Figure 1: Compact Diagnostic Box.

Faraday Cup (FC)

A water cooled Faraday cup (FC) has been fabricated to measure the current. The cup has a beam aperture of 25 mm and its length is 20 mm along the beam direction (Fig. 2). It is made of Oxygen Free High Conductivity (OFHC) copper material. Based on the expected beam power from HCI the FC is designed for few hundred watts of beam power. The suppressor ring, which retains the secondary electrons on the cup, is made of SS 304 material. The FC is completely shielded by the 3 mm thick tantalum sheet. The linear movement of FC is controlled by a pneumatic cylinder, which provides the 60 mm strokes in the diagnostic box.

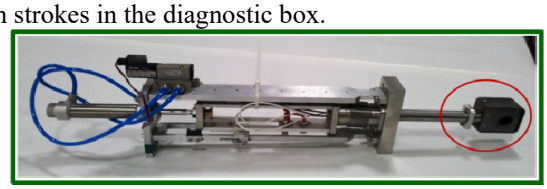

Figure 2: Faraday Cup.

It is a very compact design and can be used to measure the current of the order of few nanoamperes to hundreds of microampere current.

Slit Scanner (SSC)

The slit scanner (Fig. 3) is fabricated indigenously for the measurements of beam positions and beam profiles in HCI beam line. It scans the beam in both transverse directions with the help of two 500 micron slits. The slits are made orthogonal to each other and moves linearly in such a way that they cut the ion beam in x and y directions.

#hariwal@gmail.com

ISBN 978-3-95450-131-1

The linear motion of the slit scanner is done by a computer controlled stepper motor. The microcontroller programming and data processing have been done with the help of LabVIEW programs.

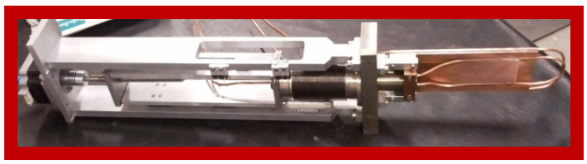

Figure 3: Slit Scanner.

It is possible to see the online beam profiles on the two dimensional graphs of the beam intensity versus the beam positions. The linear movement and position can also be controlled with two limit switches.

EXPERIMENTAL SET-UP FOR ONLINE BEAM TEST

Diagnostic Box Installation in LEIBF

HCI development is underway so the compact diagnostic box, along with the Faraday cup and slit scanner, was installed in the Low Energy Ion Beam Facility (LEIBF) at IUAC (Fig.4) to perform the online ion beam test.

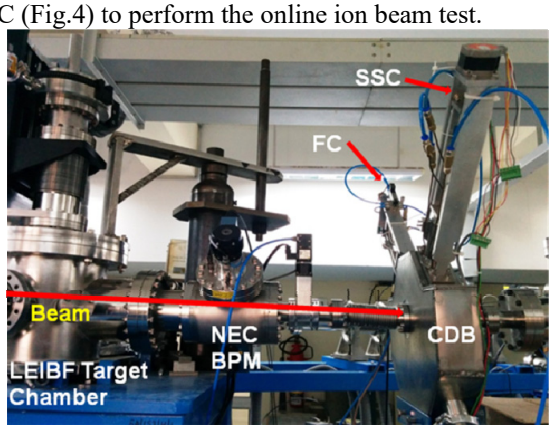

Figure 4: Diagnostic installed at IUAC beam line.

The beam profile and current measured by the diagnostic system matched very closely to the one measured by the National Electrostatics Corporation (USA) made FC and BPM devices. The diagnostic system was further verified by the measurements of currents and beam profiles of the various ion beams such as N and O ion beams with different energy and currents. All the results demonstrated good agreement with those measured by standard devices confirming the operational aspect of the system.

Online Beam Test Set-up

A Keithely 6517 B electrometer is used to measure the ion beam current directly from the Faraday Cup. The current signal from the Faraday cup can also be displayed on the control panel by using log amplifier. The linear motion of the slit scanner has been controlled by the stepper motor controller unit which is connected to a computer running the LabVIEW program (Fig 5).

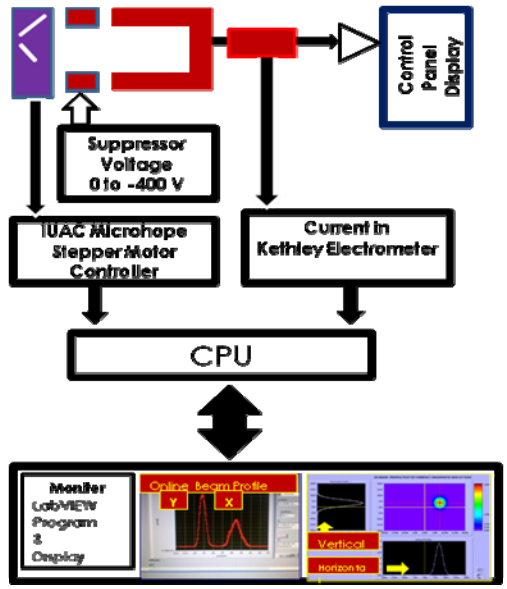

Figure 5: Electronic set up.

When the scanner moves, FC collects the charged particles passed through the slits. It provides current signal and thus measures the ion beam current intensity vs the beam position.

RESULTS AND DISCUSSION

The beam current and profile measurements of various heavy ion beams at different energy have been carried out to validate the design and fabrication of the Faraday cup and slit scanner. We have tested the Faraday cup and slit scanner by measuring the current and profiles of various ion beam viz. Nitrogen and Oxygen at different energy and current. The experimental details and its results are given below.

Beam Profile and Beam Position Measurements

The Faraday cup and beam profile monitor have been tested and verified with the following ion beams. (Table 1).

Table1: Current Measurement by Faraday Cup

Ion Beam	Energy (keV)	Current(FC) (μA)	Current(NEC) (μA)
N^{1+}	250	72.5	74
N^{5+}	1250	1.3	1.3
O^{1+}	250	2.77	2.77
O^{5+}	1250	0.421	0.421

Nitrogen and Oxygen Ion Beam Test

The determinations of beam profiles through the slit scanner have been carried out for N and O ion beam in the material science beam line. The measurements of various types of the beams at various energies and current are really useful for the evaluation of the performance of

ISBN 978-3-95450-131-1

the various optical devices installed into the beam line [4-8]. The results are shown in the following figure (Fig.6).

The lower as well as higher currents were measured by the Faraday cup very accurately from tens of picoamperes to few hundreds of microamperes. Various ion beam profiles, obtained with the LabVIEW program, provide the digital signature of the charged particles distribution, i.e. the current intensity along the ion beam positions.

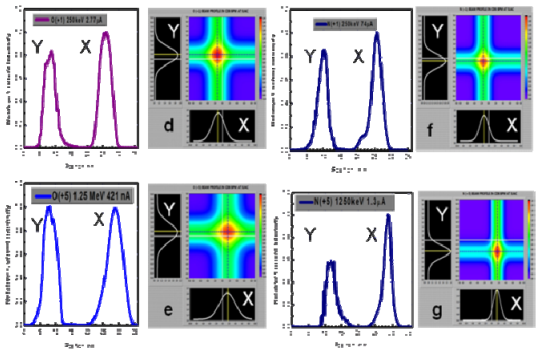

Figure 6: Beam Profiles.

The experimental results provide the information not only on the beam profile and spot size but the beam positions also. The Oxygen and Nitrogen ion beam profiles along with their positions from the centre point of the beam line are shown above.

CONCLUSIONS

We have developed indigenously a very compact diagnostic system, which can replace any conventional beam diagnostic components in the beam line. The motivation behind the development of such devices came to investigate and avoid the beam losses in the low energy ion beam line section of an accelerating system. The low cost, high accuracy, high reliability and simplicity are the figures of merit of this system. This system plays a significant role in the current measurements and beam tuning to enhance the performance of accelerators by providing the good quality beam, especially at the entrance of each DTL cavities in the HCI accelerator system.

ACKNOWLEDGEMENTS

The author would like to acknowledge the IUAC workshop to provide the machining and welding facilities during the fabrication of complete diagnostic system. The author is also thankful to the Director, IUAC New Delhi for giving the permission for installation of diagnostic system and online testing with the various ion beams in LEIBF. Lia Merminga, R. Laxdal and Josef Holek from TRIUMF Canada are specially acknowledged for their support and fruitful technical suggestions.

REFERENCES

[1] A. Roy, Curr. Sci.**76**, 149(1999).
[2] G.Rodrigues,P.S.Lakshmy, Sarvesh Kumar, A.Mandal and D.Kanjilal, Rev. Sci. Instrum. **81**, 02B713 (2010).
[3] R. Mehta, J. Sacharias, R.V. Hariwal et .al, Design Validation of IH Type Drift Tube Resonator at IUAC in ADS conference 2011, BARC, Mumbai, India.
[4] Valery Dolgashev et al, Appl. Phy. Lett. **97**,171501 (2010).
[5] O.Kamigaito, M.Kase, N.Sakamoto, Y.Miyazawa, Eikezawa et al., Rev. Sci. Instrum.**76**, 013306 (2005).
[6] R.B. Fair, J. Phys. E: Sci. Instrum. **4,** 35 (1971).
[7] Probyn B. A., J. Appl. Phys.D:Appl.Phys. 1, **457-65** (1968)
[8] Jacob L Phil, Mag**. 28,** 81-85 (1939) [1]Peter Fork, Lecture Notes on Beam instrumentation And Diagnostics, Joint University Accelerator School, 2008

ISBN 978-3-95450-131-1

HEAVY ION LABORATORY, UNIVERSITY OF WARSAW – A UNIQUE RESEARCH CENTER IN POLAND

J. Choinski, P. Gmaj, Heavy Ion Laboratory University of Warsaw, Warsaw, Poland

Abstract

On behalf of the staff of the Heavy Ion Laboratory of the University of Warsaw (HIL) we present the current state of development of the laboratory. HIL is a user facility operating a K_{max}=160 isochronous heavy ion cyclotron, unique in central Europe. Two ECR ion sources, a homemade 10 GHz and a commercial (Supernanogan Pantechnik) 14.5 GHz, supply ions to the machine. In the center of the machine a "spiral" type inflector bends the ion beams into the median plane. The current system allows ions from He up to Xe to be accelerated with energies up to 10 A MeV. The research program of HIL includes nuclear physics, solid state physics, medical radioisotope production, biology and detector testing. In 2012 HIL launched a new facility - the Radiopharmaceuticals Production and Research Center (RPRC). This is a fully GMP compliant production facility of radiopharmaceuticals for PET. It operates a General Electric PETtrace 840 cyclotron and a complete production line of FDG. An external beam line with target station, designed and constructed by the Laboratory, allows metallic and powdered samples to be irradiated, extending medical isotope research by using proton and deuteron beams.

THE HEAVY ION LABORATORY OF THE UNIVERSITY OF WARSAW

The Heavy Ion Laboratory [1] is situated in the centre of the University of Warsaw and the Polish Academy of Sciences Scientific Campus Ochota, 500 m from the Public Central Teaching Hospital affiliated to the Medical University of Warsaw (MUW) - see Figure 1.

Figure 1: Scientific Campus Ochota.

HIL was founded in 1979 by an agreement between three state institutions: the Ministry of Science and Higher Education, the Polish Academy of Sciences and the National Atomic Energy Agency. The Laboratory plays the role of a user facility and is an inter–faculty unit of the University of Warsaw. Currently, HIL operates two cyclotrons: a U-200P heavy ion cyclotron and a compact cyclotron accelerating protons and deuterons. In order to host both accelerators the HIL building was divided into two parts. The main part is assigned to the heavy ion cyclotron with its research infrastructure. The second part is dedicated to the compact cyclotron and is located in the underground part of the HIL building, see Figure 2.

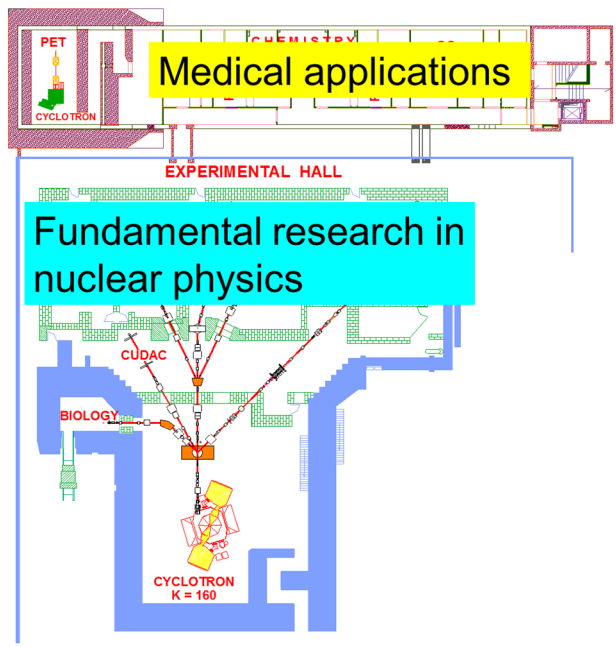

Figure 2: A scheme of the building.

With two cyclotrons HIL is the perfect place to carry out fundamental research in nuclear physics, solid state physics, medical radioisotope production, biology and detector testing. All the above mentioned activities are based on the heavy ion cyclotron with a K value varying from 120 to 160. This is an isochronous cyclotron with four straight sectors. The stripper foil system allows ions with energies from 2 to 10 MeV/A to be extracted.

Two ECR ion sources supply ions to the machine. The older ECRIS, homemade, operates at 10 GHz and delivers beams of light elements from He to Ar. The second ion source, a commercial Supernanogan from Pantechnik, bought a few years ago, operates at 14.5 GHz and delivers beams up to Xe. It is equipped with a high temperature oven and a “Sputtering” system. With this source not only gaseous but also metallic ions are available for acceleration. The sources are mounted in the basement of the cyclotron cave and connected to the machine via an

ISBN 978-3-95450-131-1

injection line. The beams from the ion sources and injection line are transferred to the first cyclotron orbit through a spiral inflector. As a result of recent crucial improvements, i.e. adding the commercial ECRIS and implementation of the spiral inflector, the accelerator has been able to deliver an average of 3300 h/y of beam time for almost 100 users/y during recent years. The new inflector was developed in collaboration with the cyclotron team from Dubna (Russia).

Currently two new R.F. generators are under construction. Their commissioning is expected at the beginning of 2016.

The ECR ion source team is also involved in work associated with the international project 'EMILIE' [2]. As can be seen in Figure 2, beams from the U-200P are transferred to an experimental hall equipped with a number of stationary experimental set-ups.

THE RESEARCH PROGRAM OF HIL

The research program is defined by each experimental set-up. Short description is provided below.

EAGLE (Figure 3)

The acronym EAGLE denotes the central European Array for Gamma Levels Evaluation. This is our newest multi-detector gamma ray spectrometer [3]. It started operation in 2009. Its frame is able to host up to 30 HPGe detectors with Anti-Compton Shielding. This measuring system can be modified by adding existing auxiliary detectors such as a 4π Si-ball, an electron spectrometer (ULESE) [4], the so-called 'Munich chamber' equipped with 48 PiN diodes (max. 110) or the 'Bucharest' plunger [5]. The latter device is available within the framework of our collaboration with IFIN-HH, Romania.

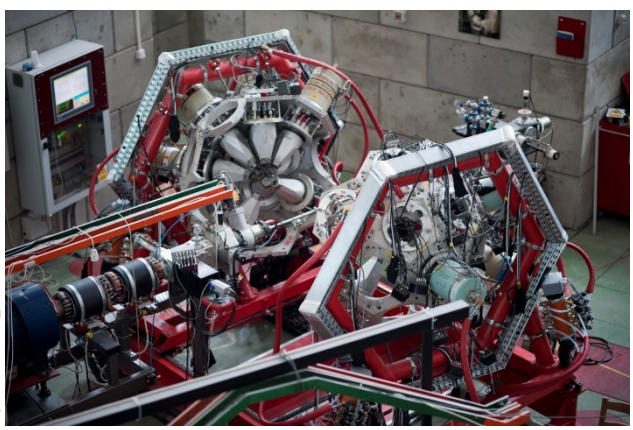

Figure 3: EAGLE set-up.

This modern experimental set-up allows us to conduct research on nuclear structure by γ-spectroscopy techniques such as: γ-γ angular correlations with the EAGLE HPGe array, e-γ spectroscopy with the ULESE spectrometer, lifetime measurements using tools such as the Doppler Shift Attenuation Method [6] and the Recoil Distance Doppler Shift technique, and complex Coulomb excitation experiments relevant for nuclear structure physics [7] but also complementary to RIB experiments by providing additional experimental data derived from independent experiments, crucial when going towards more exotic nuclei. During the last few months the effort of the research groups was focused on the search for chiral symmetry breaking in atomic nuclei by Doppler-shift measurements of picosecond lifetimes, a study of the violation of K-selection rules by measurements of internal conversion coefficients for transitions deexciting K isomers, studies of non-spherical and non-axial shapes of nuclei by direct measurements of electromagnetic matrix elements using the Coulomb excitation method (GOSIA code) and a study of the reaction mechanism for complete and incomplete fusion by measurements of gamma radiation in coincidence with emitted charged particles (protons, alphas).

CUDAC

This experimental set-up is a small scattering chamber, equipped with an array of backward hemisphere semiconductor detectors (PiN diode type) and forward hemisphere monitoring Si counters. It is mostly used for Coulomb excitation studies and measurements of fusion barrier level distributions. A new version of the scattering chamber is currently under construction.

ICARE (Figure 4)

The acronym ICARE denotes 'Identificateur de Charges A Rendement Eleve'. ICARE is a particle spectroscopy chamber from IReS Strasburg (France), present at HIL since 2007. Its huge size (Φ1.0m x 0.7m) allows the use of up to 48 telescopes for charged particle detection, identification and energy measurements.

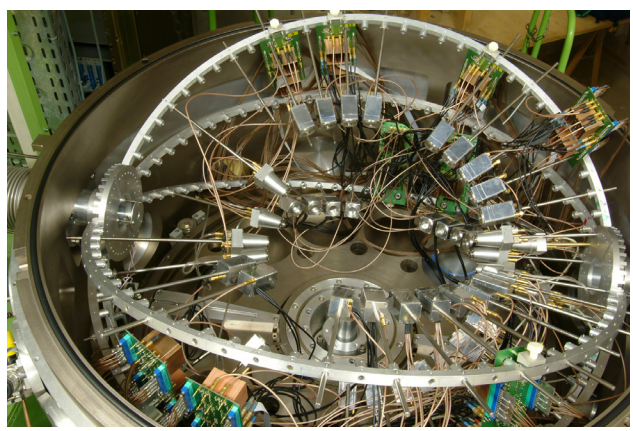

Figure 4: ICARE set-up.

The scientific program assigned to this set-up includes barrier distribution measurements, reaction mechanism studies and novel detector tests [8,9]. Recent experiments were devoted to:

- barrier level distribution studies – *CUDAC & ICARE;*
- a series of experiments using ^{11,10}B, ^{18}O, ^{14,15} N beams on light targets: ^{6,7}Li, ^{9}Be, ^{12,13}C – energies 4-6 MeV/c;
- backward angle structure in the ^{20}Ne+^{28}Si quasi-elastic scattering at near-barrier energies – a study of the reactions of α-clustering nuclei;

ISBN 978-3-95450-131-1

- measurements of elastic scattering cross sections for ^{16}O and ^{13}C on light nuclei (^{12}C, ^{9}Be) at energies of 2–3 MeV/n – optical model parameters of the nucleus-nucleus interaction and cluster transfer studies;
- an indirect study of the astrophysical ^{16}O+^{16}O fusion reaction by the Trojan Horse Method;
- a search for heavy ion molecular resonances with an Ar beam using the Thick Target Inverse Kinematics method.

Applications of Heavy Ions

In recent years one of the research groups from HIL has been actively engaged in an investigation of the production capabilities of ^{211}At, ^{43}Sc, ^{44}Sc, ^{72}Se/^{72}As radioisotopes and their potential medical applications. For this purpose a consortium of HIL, the Inst. of Nucl. Chemistry and Technology and Polatom – National Centre for Nuclear Research was established. The radioisotopes are produced by alpha beam reactions using the internal target station of the heavy ion cyclotron [10].

Supplementary Services

In addition to the research infrastructure described above HIL also has an on-line mass separator IGISOL, a detector laboratory, a target laboratory, a set-up for biological sample irradiation experiments [11] and a laboratory for medical imaging equipped with a DST-XL Gamma camera. The latter laboratory is mainly dedicated for use by students specializing in 'Medical Physics'.

THE RADIOPHARMACEUTICALS PRODUCTION AND RESEARCH CENTER

RPRC (Figure 5) was constructed for radiopharmaceuticals production for PET [12–14]. This is a fully GMP compliant production centre certified by the Polish authorities which has been operating since May, 2012.

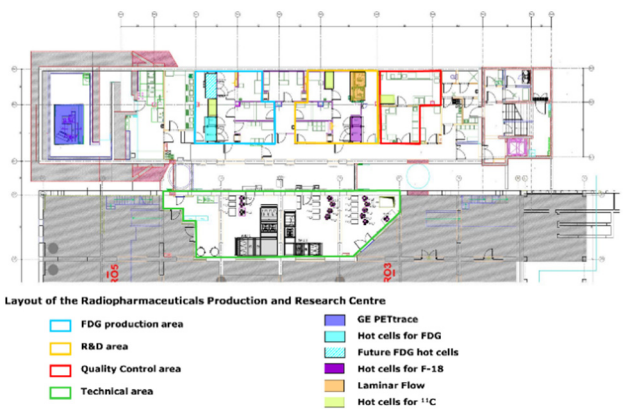

Figure 5: The layout of RPRC.

The facility consists of the cyclotron vault, two "hot chemistry" production laboratories, a quality control department, administration rooms, technical rooms and different kinds of store rooms including the archives. RPRC operates a GE PETtrace 840 cyclotron and a complete production line of 18F-fluorodeoxyglucose. The second production lab is dedicated to R&D and is equipped with several synthesizers and dispenser units. The apparatus collected in this lab allows the production of radiopharmaceuticals containing ^{18}F, ^{15}O and ^{11}C radioisotopes. Besides ^{18}F, ^{15}O and ^{11}C targets the cyclo-tron is additionally equipped with an external short beam line with a target station. This latter is the outcome of the ALTECH project. The station allows the irradiation of metallic and powdered samples. Currently the ^{99m}Tc isotope is produced from a ^{100}Mo target. After a small modification the device will also be used to carry out the PET-SKAND project, focused on the production and utilization of Sc isotopes.

CONCLUSION

HIL is a one-of-its-kind Polish nuclear physics center, a place for research, education and medical applications studies. It is also a member of the European Transnational Access Facility. This national nuclear physics laboratory is open for external researchers and it also serves as an educational center for local and foreign students [15].

ACKNOWLEDGMENT

The authors would like to acknowledge the financial support of the ERA-NET NuPNET. The Polish team's activities within the international 'EMILIE' project are supported by the Polish National Centre for Research and Development (PNCRD), Project No. ERA-NET-NUPNET/02/12. The production of Sc radioisotopes, project 'PET-SKAND' has financial support from the PNCRD, Project No. PBS3/A9/28/2015. The project 'ALTECH' is financially supported by PNCRD, Project No. PBS1/A9/2/2012.

REFERENCES

[1] J. Choinski at al., Nukleonika 48 (2003)109.
[2] O. Tarvainen et al., Plasma Sources Sci. Technol. 24 (2015) 035014.
[3] J. Mierzejewski et al., NIM A659 (2011)84.
[4] J. Perkowski at al., RSI v.85, 043303 (2014).
[5] F. Bello et al., Phys. Rev. C 92, 024317 (2015).
[6] E. Grodner et al., Physics Letters B 703 (2011).
[7] K. Wrzosek-Lipska et al., PRC 86 064305 (2012).
[8] E. Piasecki et al., Phys. Rev. C 85, 054604 (2012).
[9] A. Trzcińska et al., Acta Phys. Pol. 45, 383 (2014).
[10] K. Szkliniarz at al., Acta Phys. Pol. A, 127 (2015).
[11] U. Kazmierczak et al., Acta Phys. Pol. B 45, 553 (2014).
[12] J. Choiński et al., EPJ Web of Conferences 66, 10003 (2014).
[13] J. Jastrzębski, Acta Phys. Pol. 43, 193 (2012).
[14] J. Choiński and J. Jastrzębski, Nucl. Med. Rev. 15, 85 (2012).
[15] www.slcj.uw.edu.pl

ISBN 978-3-95450-131-1

RADIOACTIVE ION BEAMS PROGRAMME AT VECC-KOLKATA, INDIAN EFFORTS

Alok Chakrabarti#, VECC, Kolkata, India

Abstract

An ISOL type Radioactive Ion Beam (RIB) facility has been built at VECC with *K*130 cyclotron that delivers proton and alpha particle beams as the driver accelerator. So far ion beams of $A/q \leq 14$ have been accelerated up to 414 keV/u using a Radio Frequency Quadrupole (RFQ) linac and three IH-Linacs. Two more IH Linac modules are being added to increase the energy to 1.0 MeV/u. A few RIBs have been accelerated with typical intensities of 10^3 to 10^4 pps at the separator focal plane.

In the next phase, the plan is to construct a new facility called ANURIB (Advanced National facility for Unstable and Rare Isotope Beams) at the upcoming new campus of VECC at New Town in Kolkata. ANURIB aims to attract a wider user community in nuclear physics, nuclear-astrophysics, and materials science and is being built as a national facility. There will be two primary accelerators in ANURIB aimed at producing both neutron-rich and proton-rich beams. One is a 50 MeV 100 kW superconducting electron linac photo-fission driver that is being developed in collaboration with TRIUMF Canada and the other a 50 MeV proton injector to be developed indigenously. To be built in phases starting from low energy of few keV/u in Phase-I to a final energy of 100 MeV/u in Phase-II, ANURIB will be a combined ISOL and PFS type facility.

INTRODUCTION

It was in the mid-nineties that the idea of developing a Radioactive Ion Beam facility took shape at VECC, prompted by exciting physics opportunities in study of exotic nuclei that led to activities world-wide for construction of RIB facilities. It was realized that this would need design and development of advanced accelerators, ion-sources and detector systems. It was decided: a) to proceed in small R&D steps to acquire the capability, and b) to collaborate with an international laboratory that has already started working in this field and has the experience of designing and building advanced accelerators.

To meet these objectives and to keep the budget small, it was decided to use the existing *K*130 room temperature cyclotron as the driver or the primary accelerator and construct an ISOL type RIB facility around the same [1-3]. A collaboration agreement with RIKEN, where RI Beam Factory project was just about to start, was signed in 1996. The VECC RIB project received some seed money in 1998 for design of the facility. Funding for construction of accelerators was made available in 2003 and again in 2007. These have led to development of a number of linear accelerators [4-10], the physics designs of which were mostly done in collaboration with RIKEN. Also, facilities for material science and laser spectroscopy of exotic nuclei have been built. Proton and alpha particle beams from the cyclotron have been used to produce rare isotopes using suitable targets. Using a gas-jet recoil transport coupled ECR technique [11, 12] radioactive atoms, ion beams of ^{14}O ($t_{1/2}$=71 sec), ^{42}K ($t_{1/2}$=12.4 hrs), ^{43}K ($t_{1/2}$=22.2 hrs), ^{41}Ar ($t_{1/2}$=109 min) have been produced at the facility. RIB of ^{111}In ($t_{1/2}$= 2.8 d) has been developed in the off-line mode.

ACCELERATOR DEVELOPMENT

A layout of the facility is shown in Fig. 1. The scheme is to produce rare isotopes using a suitable target in alpha/proton induced nuclear reactions, ionize the reaction products in two ion-sources in tandem [2, 6], mass separate the reaction products to choose the rare isotope of interest and finally accelerate the beam in a series of linear accelerators. The charge breeder is an ECR ion-source operating at 6.4 GHz. The post- accelerators are – a Radio Frequency Quadrupole (RFQ) linac that accelerates heavy-ions of $A/q \leq 14$ to 100 keV/u, followed by five IH linac tanks for further acceleration to 1 MeV/u. Two superconducting QWR modules to boost the energy to 2 MeV/u are also planned.

First, a 1.7 metre long RFQ [4, 5, 8] was constructed with the aim to study machining and fabrication aspects and conduct comprehensive beam tests. Commissioned in September 2005 this was the first RFQ to be built in India and was a major milestone in the RIB project. Operating in CW mode at 33.7 MHz, this RFQ accelerates ion beams from energy 1.38 to 29 keV/u. Typical measured beam transmission is 85%. This RFQ is now a part of the material science beam-line (Figure 1). A second RFQ (Fig. 2), operating at 37.8 MHz and 3.4 m long has been commissioned in year 2008 [9]. The high power RF sources for RFQ and linacs have been developed indigenously in collaboration with SAMEER, Mumbai. The critical components of the RFQ viz. the copper electrodes and supporting posts have been machined at Central Mechanical Engineering Research Institute, a CSIR laboratory at Durgapur, 200 km from Kolkata. Other components have been made in Indian industry.

#alok@vecc.gov.in

ISBN 978-3-95450-131-1

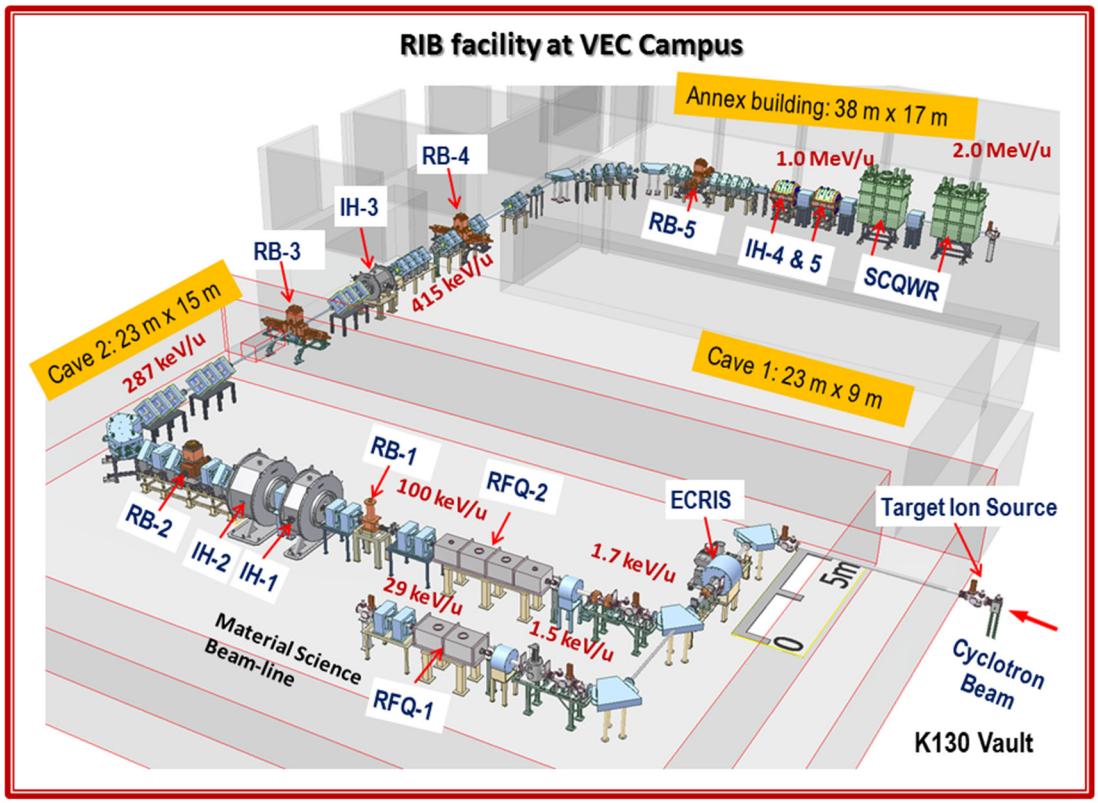

Figure 1: Layout of the RIB facility at VECC Kolkata.

The first three Linac modules have also been designed and built indigenously. Facility up to third linac (Linac-3) has been successfully commissioned by accelerating $^{14}N^{4+}$ beam to 414 keV/u (5.8 MeV) in year 2010 [7].The first two Linacs operate at 37.8 MHz and the subsequent ones, third to fifth, operate at 75.6 MHz. After the third Linac (Fig. 3) a charge stripper would be used for obtaining *A/q* of 7 needed for Linac 4& 5.

Linacs 4 & 5 have already been fabricated and are awaiting installation in a 20 m long beam line [10] that additionally has several quadrupoles, di-poles and bunchers. These are to be housed in a new annex building which is almost complete. The 1.0 MeV/u beam after Linac-5 will be accelerated further to about 2 MeV/u in two super-conducting heavy-ion QWR modules. The design and development of the Superconducting QWR linacs is now in progress in collaboration with TRIUMF.

A good deal of R&D effort has gone into designing targets for RIB production, ion sources, and for trying out various techniques for RIB production. Apart from these studies, the stable ion beams from the facility have been regularly used for material science research especially for ion beam induced nano-structure formation and studies on room temperature ferro-magnetism in ZnO and other oxides. Also a laser spectroscopy hut has been set up for pursuing quantum optics studies relevant to photo-ionization and for measurements of atomic hyperfine splitting and isotopic shift of exotic nuclei using collinear laser spectroscopy.

Experiments to study decay spectroscopy of short-lived nuclei are being planned / carried out using the low energy RI Beams. These efforts together with accelerator design and development have so far led to about 60 publications in Journals and 7 *PhD* theses.

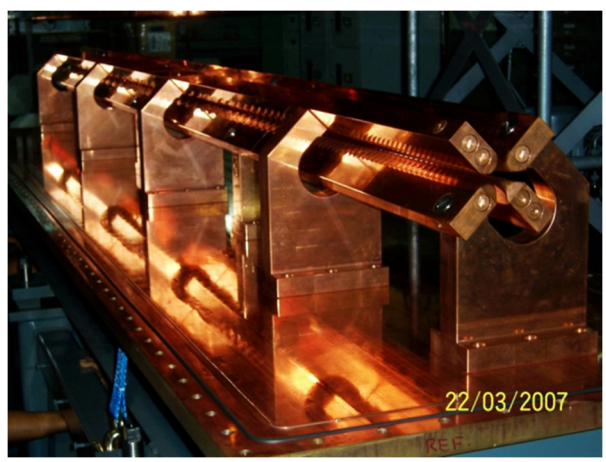

Figure 2: Photograph of the internal post-vane structure of 3.4 m long RFQ linac taken during installation at VECC.

ISBN 978-3-95450-131-1

ANURIB – VECC'S UPCOMING FLAGSHIP PROJECT

The next step for us is to take up the development of an internationally competitive RIB facility, named ANURIB (**A**dvanced **N**ational facility for **U**nstable and **R**are **I**sotope **B**eams), as the flagship project of the centre [13, 14]. The ANURIB will be a green-field project and will be built at VECC's new 25 acre campus in New Town, Kolkata. An International Advisory Committee has been constituted by Department of Atomic Energy to review the ANURIB project proposal. The committee gave a favourable recommendation, accepted the entire proposal, and suggested several measures for speedy and successful implementation of ANURIB.

The RIB production and acceleration scheme in ANURIB is shown in figure 4. A 50 MeV, 100 kW cw electron linac and a high current proton accelerator would be the driver accelerators for production of neutron-rich & proton-rich isotopes. The facility has been planned such that experiments can be done at each stage of development. The physics opportunities that will open up at various stages are indicated in figure 4. After initial acceleration in RFQ and room temperature linacs, Superconducting Linac Boosters (SLBs) will increase the beam energy to around 7 MeV/u opening up the regime of coulomb barrier physics and production of Super Heavy Nuclei (SHE) using RIBs as well as Stable Ion Beams. For ANURIB a novel acceleration scheme using Asymmetric Alternate Phase Focussing will be employed in the SLBs that would allow simultaneous acceleration of multiple charge states of heavy-ions [15, 16].

Figure 3: Photograph showing third heavy-ion Linac module with the front cover open. Designed at VECC this linac was fabricated in an industry at Bangalore.

A separated sector cyclotron will be used to accelerate 7 MeV/u beams after the SLB to about 100 MeV/u. The fragmentation of these RIBs in a secondary target is expected to produce highly exotic rare isotopes, which cannot be sufficiently produced through fragmentation of stable ion beams [17]. Also 5 to 7 MeV/u beams of p-rich nuclei are very effective in producing very exotic p-rich species using compound nuclear evaporation reactions.

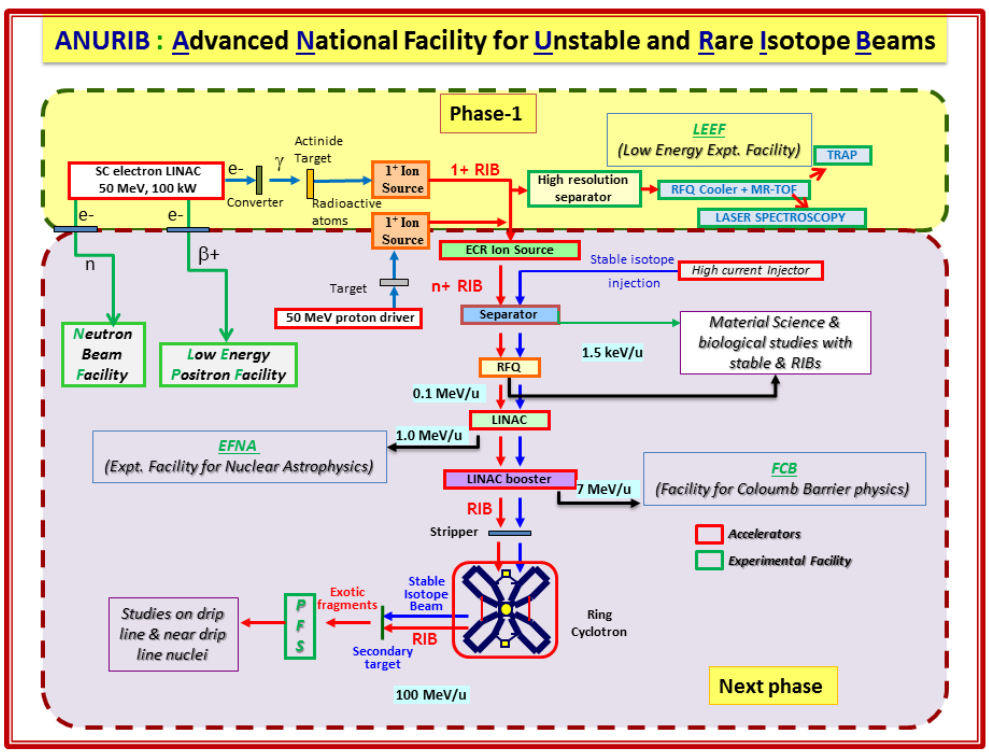

Figure 4: Schematic layout of ANURIB facility.

ISBN 978-3-95450-131-1

ANURIB will be built in two phases with an estimated budget of Rs. 1200 crores and will need 12 years for completion. In 2013, the project has received funding for phase-1. In this phase (2013-2020) the electron driver accelerator, electron target module and low energy experimental facility (LEEF) will be built along with the phase-1 building. Facilities such as RFQ cooler and buncher, Multiple Reflection Time of Flight spectrometer, Penning traps, and Laser spectroscopy set up, are being planned for LEEF along with Neutron and the Positron beam lines for multidisciplinary research.

The superconducting electron accelerator (e-Linac) [18], presently under development jointly with TRIUMF, will be the main driver accelerators for ANURIB. An identical machine is being built at TRIUMF for the ARIEL-Advanced Rare Isotope Laboratory project. In the e-Linac, electron beam from a 300 kV thermionic gun will be accelerated first to 10 MeV in an Injector Cryo-Module (ICM) housing one 1.3 GHz, 2K 9-cell cavity. The 10 MeV electron beam would be then accelerated to 50 MeV in two Accelerator Cryo-Modules (ACM) each housing two 9-cell cavities. Last year in a test run at TRIUMF, electron beam has been accelerated to 23 MeV using the ICM and one nine cell cavity inside the ACM1. A second ICM meant for VECC is presently under construction at TRIUMF (figure 5.) and is scheduled to be tested in early 2016.

Figure 5: Injector Cryo Module for the VECC superconducting Electron Linac (e-Linac) at TRIUMF.

The electron accelerator will produce neutron-rich rare isotopes through gamma induced fission of actinides. The design and development of actinide target capable of handling high beam power is a challenging task, and is also being pursued jointly with TRIUMF.

The use of electron driver for production of *n*-rich RI Beams, combination of both ISOL and PFS methods, fragmentation and fusion reactions with RI Beams, and availability of intense stable heavy-ion beams together would make ANURIB an internationally competitive facility.

REFERENCES

[1] Alok Chakrabarti, J. Phys. G: Nucl. Part. Phys. **24** (1998) 1361.
[2] Vaishali Banerjee, et. al., Nucl. Instrum. & Meth. **A447** (2000)345.
[3] Alok Chakrabarti, Pramana **59** (2002) 923
[4] Vaishali Banerjee,et. al., Pramana **59** (2002) 957.
[5] Alok Chakrabarti, et. al.,Nucl. Instrum. & Meth. **A535** (2004) 599.
[6] D. Naik, et.al., Nucl. Instrum. & Meth. **A547** (2005) 270.
[7] Arup Bandyopadhyay, et. al., Nucl. Instrum. & Method **A560** (2006) 182.
[8] Alok Chakrabarti, et. al., Rev. Sci. Instrum. **78** (2007) 043303.
[9] S. Dechoudhury, et. al., Rev. Sci. Instrum. **81** 023301 (2010).
[10] Md. Sabir Ali, et. al., Nucl. Instrum. & Method **A636** (2011)1.
[11] Vaishali Naik, et. al., Rev. of Sci. Instrum. **84** (2013) 033301.
[12] Vaishali Naik, et. al., Nucl. Instrum. & Method B **317** (2013) 227.
[13] Alok Chakrabarti, Nucl. Instru. & Meth. **B261** (2007) 1018.
[14] Alok Chakrabarti, et. al., Nucl. Instrum. & Meth. **B317** (2013) 253.
[15] S. Dechoudhury, et. al., Phys. Rev. Special Topics AB **16** (2013) 052001.
[16] S. Dechoudhury, et. al., Phys. Rev. Special Topics AB **17** (2014) 074201.
[17] D. Bhowmick, et.al., Mod. Phys. Lett. A **13** (1998) 266.
[18] Vaishali Naik, et. al., Proc. of Linear Accelerator Conference LINAC10 (2010)

ISBN 978-3-95450-131-1

ISBN 978-3-95450-131-1

List of Authors

Bold papercodes indicate primary authors

ISBN 978-3-95450-131-1

ISBN 978-3-95450-131-1

ISBN 978-3-95450-131-1

— N —

— O —

— P —

ISBN 978-3-95450-131-1

ISBN 978-3-95450-131-1

ISBN 978-3-95450-131-1

ISBN 978-3-95450-131-1

Institutes List

AEC
Chiba, Japan
- Arai, H.
- Fujimoto, T.

ANL
Argonne, Illinois, USA
- Barcikowski, A.
- Cherry, G.L.
- Conway, Z.A.
- Dickerson, C.
- DiGiovine, B.
- Gerbick, S.M.
- Guilfoyle, B.M.
- Hendricks, M.R.
- Hoffman, C.R.
- Hopper, C.S.
- Kedzie, M.
- Kelly, M.P.
- Kim, S.H.
- Krupa, T.
- Lin, L.Y.
- Luo, Y.
- MacDonald, S.W.T.
- Momozaki, Y.
- Mustapha, B.
- Nolen, J.A.
- Ostroumov, P.N.
- Pardo, R.C.
- Perry, A.
- Peters, C.E.
- Power, M.A.
- Reed, C.B.
- Rehm, E.
- Reid, T.
- Savard, G.
- Scott, R.H.
- Sharamentov, S.I.
- Vondrasek, R.C.
- Zinkann, G.P.

BINP SB RAS
Novosibirsk, Russia
- Parkhomchuk, V.V.

BNL
Upton, Long Island, New York, USA
- Alessi, J.G.
- Beebe, E.N.
- Costanzo, M.R.
- DeSanto, L.
- Hseuh, H.-C.
- Jamilkowski, J.P.
- Kanesue, T.
- Lambiase, R.F.
- Lehn, D.
- Liaw, C.J.
- McCafferty, D.R.
- Morris, J.
- Okamura, M.
- Olsen, R.H.
- Pikin, A.I.
- Raparia, D.
- Steszyn, A.N.

CERN
Geneva, Switzerland
- Angoletta, M.E.
- Axensalva, J.
- Bodendorfer, M.A.
- Delruelle, N.
- Ferreira Somoza, J.A.
- Garcia Borge, M.J.
- Gayde, J.
- Kadi, Y.
- Kautzmann, G.
- Manglunki, D.
- Martino, M.
- Pasinelli, S.
- Rodriguez, J.A.
- Siesling, E.
- Valdarno, L.
- Venturini Delsolaro, W.

CIAE
Beijing, People's Republic of China
- Yang, J.J.

CNS
Saitama, Japan
- Imai, N.
- Kotaka, Y.
- Kubono, S.
- Muto, H.
- Ohshiro, Y.
- Shimoura, S.
- Watanabe, S.-I.
- Yamaguchi, H.
- Yamaka, S.

Cockcroft Institute
Warrington, Cheshire, United Kingdom
- Tzoganis, V.
- Welsch, C.P.

Colorado School of Mines
Golden, USA
- Greife, U.

Department of Energy Sciences, Tokyo Institute of Technology

ISBN 978-3-95450-131-1

Yokohama, Japan
- Liu, X.
- Munemoto, N.

FRIB
East Lansing, Michigan, USA
- Ao, H.
- Bultman, N.K.
- Casagrande, F.
- Compton, C.
- Dalesio, L.R.
- Davidson, K.D.
- Durickovic, B.
- Facco, A.
- Feyzi, F.
- Ganshin, A.
- Gibson, P.E.
- Glasmacher, T.
- Guetschow, P.
- Hartung, W.
- Hodges, L.
- Hoff, L.T.
- Holland, K.
- Hseuh, H.-C.
- Hussain, A.
- Ikegami, M.
- Jones, S.
- Kranz, K.
- Laxdal, R.E.
- Lidia, S.M.
- Lund, S.M.
- Machicoane, G.
- Marti, F.
- Miller, S.J.
- Morris, D.
- Nolen, J.A.
- Peng, S.
- Popielarski, J.
- Popielarski, L.
- Pozdeyev, G.
- Russo, T.
- Saito, K.
- Shen, G.
- Stanley, S.
- Wei, J.
- Xu, T.
- Yamazaki, Y.

GANIL
Caen, France
- Anger, P.
- Bajeat, O.
- Bisson, P.
- Chautard, F.
- Danna, O.
- Delahaye, P.
- Dubois, M.
- Hulin, X.
- Kamalou, O.
- Lagniel, J.-M.
- Maunoury, L.
- Normand, G.
- Perocheau, F.
- Petit, E.
- Roupsard, L.
- Savalle, A.

GSI
Darmstadt, Germany
- Adonin, A.
- Barth, W.A.
- Bevcic, M.
- Du, X.
- Düllmann, Ch.E.
- Gerhard, P.
- Groening, L.
- Hartmann, W.
- Hollinger, R.
- Horn, K.P.
- Jäger, E.
- Kaiser, M.
- Khuyagbaatar, J.
- Krier, J.
- Litvinov, S.A.
- Litvinov, Yu.A.
- Mickat, S.
- Nolden, F.
- Rubin, A.
- Scharrer, P.
- Schlitt, B.
- Schreiber, G.
- Steck, M.
- Tinschert, K.
- Vormann, H.
- Voss, K.-O.
- Xiao, C.
- Yakushev, A.
- Zhang, C.

Gunma University, Heavy-Ion Medical Research Center
Maebashi-Gunma, Japan
- Ohno, T.

GYCOM Ltd
Nizhny Novgorod, Russia
- Bakulin, M.I.

HIL
Warsaw, Poland
- Gmaj, P.

HIM
Mainz, Germany
- Barth, W.A.
- Düllmann, Ch.E.
- Khuyagbaatar, J.
- Scharrer, P.

ISBN 978-3-95450-131-1

IAP/RAS
Nizhny Novgorod, Russia
- Eremeev, A.G.
- Izotov, I.
- Movshevich, B.Z.
- Skalyga, V.

IAP
Frankfurt am Main, Germany
- Hähnel, H.
- Ratzinger, U.
- Seibel, A.
- Tiede, R.

IBS
Daejeon, Republic of Korea
- Jeong, S.C.
- Joung, M.J.
- Jung, Y.
- Kim, H.J.
- Kim, J.-W.
- Park, Y.H.
- Son, H.J.

IMP/CAS
Lanzhou, People's Republic of China
- Chen, W.L.
- Feng, C.
- Gao, D.Q.
- Ge, Z.
- Guo, J.W.
- He, Y.
- Jia, H.
- Jiang, P.
- Li, C.X.
- Li, P.
- Liu, S.H.
- Lu, W.
- Ma, L.Z.
- Ma, X.
- Mao, L.J.
- Mao, R.S.
- Meng, J.
- Sun, L.T.
- Tao, Y.
- Wang, W.S.
- Wang, Z.J.
- Wu, J.X.
- Wu, Q.
- Wu, W.
- Xia, J.W.
- Xu, Z.
- Yang, J.C.
- Yang, Y.
- Yin, X.
- Yuan, Y.J.
- Zhang, W.
- Zhang, X.H.
- Zhao, H.W.

Indian Institute of Technology
New Delhi, India
- Malik, H.K.

INFN- Sez. di Padova
Padova, Italy
- Ferrari, L.

INFN-Bologna
Bologna, Italy
- Margotti, A.

INFN/LNL
Legnaro (PD), Italy
- Andrighetto, A.
- Ballan, M.
- Bellan, L.
- Bisoffi, G.
- Boratto, E.
- Borgna, F.
- Campo, D.
- Comunian, M.
- Corradetti, S.
- Facco, A.
- Ferrari, L.
- Guerzoni, M.
- Manzolaro, M.
- Monetti, A.
- Mozzi, A.
- Palmieri, A.
- Pisent, A.
- Prete, G.P.
- Rossignoli, M.
- Scarpa, D.
- Silingardi, R.
- Vivian, G.

INFN/LNS
Catania, Italy
- Calabretta, L.
- Calanna, A.
- Cuttone, G.
- Dagostino, G.
- Rifuggiato, D.
- Russo, A.D.

ITEP
Moscow, Russia
- Chalykh, B.B.

ITT-Group
Moscow, Russia
- Konev, N.N.

ISBN 978-3-95450-131-1

IUAC
New Delhi, India
- Hariwal, R.V.
- Kedia, S.
- Mehta, R.

JAEA/J-PARC
Tokai-Mura, Naka-Gun, Ibaraki-Ken, Japan
- Harada, H.
- Kinsho, M.
- Saha, P.K.
- Sako, H.
- Tamura, J.
- Yamamoto, M.

JAEA/TARRI
Gunma-ken, Japan
- Kashiwagi, H.
- Kurashima, S.
- Miyawaki, N.
- Okumura, S.

JINR/FLNR
Moscow region, Russia
- Fomichev, A.S.
- Grigorenko, L.V.
- Kazacha, V.I.
- Krupko, S.A.
- Stepantsov, S.V.
- Ter-Akopian, G.M.

JINR/VBLHEP
Moscow, Russia
- Brovko, O.I.

JINR
Dubna, Moscow Region, Russia
- Agapov, N.N.
- Bekhterev, V.
- Bogomolov, S.L.
- Butenko, A.V.
- Donets, E.D.
- Donets, E.E.
- Efremov, A.A.
- Eliseev, A.V.
- Fimushkin, V.V.
- Govorov, A.
- Gulbekyan, G.G.
- Ivanenko, I.A.
- Ivanov, E.V.
- Karpinsky, V.
- Kazarinov, N.Yu.
- Kekelidze, V.D.
- Khodzhibagiyan, H.G.
- Kovalenko, A.D.
- Mikhailov, V.A.
- Monchinsky, V.
- Morozov, N.A.
- Romanov, S.
- Samsonov, E.V.
- Sidorin, A.O.
- Slepnev, V.
- Smirnov, A.V.
- Smirnov, V.L.
- Syresin, E.
- Trubnikov, G.V.
- Tuzikov, A.
- Volkov, V.
- Vorozhtsov, S.B.

JLab
Newport News, Virginia, USA
- Dixon, K.
- Ganni, V.
- Guo, J.
- Wiseman, M.
- Zhang, Y.

Justus-Liebig-University Giessen, I. Physics Institute, Atomic and Molecular Physics
Giessen, Germany
- Schippers, S.
- Spruck, K.

Kanagawa Cancer Center, Ion-beam Radiation Oncology Center in Kanagawa
Kanagawa, Japan
- Kusano, Y.
- Minohara, S.
- Takeshita, E.
- Yamada, S.

KEK
Ibaraki, Japan
- Adachi, T.
- Kadokura, E.
- Kako, E.
- Kawakubo, T.
- Liu, X.
- Monma, T.
- Nakai, H.
- Ogitsu, T.
- Okamura, K.
- Oyaizu, M.
- Takano, S.
- Takayama, K.
- Umemori, K.
- Wake, M.
- Yamane, I.
- Yoshimoto, T.

Korea Basic Science Institute
Busan, Republic of Korea
- Choi, S.

ISBN 978-3-95450-131-1

- Hong, J.G.
- Kim, H.G.
- Kim, S.J.
- Lee, B.S.
- Ok, J.W.
- Park, J.Y.
- Shin, C.S.
- Won, M.
- Yoon, J.H.

Kyoto ICR
Uji, Kyoto, Japan
- Fuwa, Y.

Kyoto University
Kyoto, Japan
- Amemiya, N.

Kyungpook National University
Daegu, Republic of Korea
- Bahng, J.

LNCMI
Grenoble Cedex, France
- Debray, F.
- Dumas, J.M.
- Grandclement, C.
- Sala, P.
- Trophime, C.

LPSC
Grenoble Cedex, France
- Angot, J.
- Jacob, J.
- Lamy, T.
- Sole, P.
- Thuillier, T.

LSU
Baton Rouge, Louisiana, USA
- Deibel, C.
- Lai, J.
- Santiago-Gonzalez, D.

Mainz University
Mainz, Germany
- Düllmann, Ch.E.
- Scharrer, P.

Malaysian Nuclear Agency
Kajang, Malaysia
- Leo, K.W.

MHI
Hiroshima, Japan
- Hara, H.
- Miyamoto, A.
- Sennyu, K.
- Yanagisawa, T.

MIT/PSFC
Cambridge, Massachusetts, USA
- Radovinsky, A.

Mitsubishi Heavy Industries Ltd. (MHI)
Takasago, Japan
- Matsuda, R.

MIT
Cambridge, Massachusetts, USA
- Alonso, J.R.

MPI-K
Heidelberg, Germany
- Becker, A.
- Blaum, K.
- Breitenfeldt, C.
- Fellenberger, F.
- George, S.
- Grieser, M.
- Grussie, F.
- Göck, J.
- Herwig, P.
- Karthein, J.
- Krantz, C.
- Kreckel, H.
- Lion, J.
- Lohmann, S.
- Meyer, C.
- Mishra, P. M.
- Novotny, O.
- O'Connor, A.
- Repnow, R.
- Saurabh, S.
- Schröter, C.D.
- Schwalm, D.
- Sudhakaran, S.K.
- Vogel, S.
- von Hahn, R.
- Wolf, A.

Nagaoka University of Technology
Nagaoka, Niigata, Japan
- Toba, R.

National Institute of Radiological Sciences
Chiba, Japan
- Fujita, T.F.
- Mizushima, K.
- Muramatsu, M.

ISBN 978-3-95450-131-1

- Nagatsu, K.
- Saraya, Y.
- Suzuki, H.

NIRS
Chiba-shi, Japan
- Drentje, A.G.
- Furukawa, T.
- Hara, Y.
- Hattori, T.
- Hojo, S.
- Iwata, Y.
- Katagiri, K.
- Kitagawa, A.
- Matsuba, S.
- Mizushima, K.
- Mori, S.
- Muramatsu, M.
- Nakao, M.
- Noda, A.
- Noda, E.
- Noda, K.
- Saotome, N. S.
- Saraya, Y.
- Sato, S.
- Shirai, T.
- Shoda, K.
- Sugiura, A.
- Suzuki, K.
- Tansho, R.
- Wakui, T.

Notre Dame University
Notre Dame, Iowa, USA
- Couder, M.
- Wiescher, M.

Osaka University, Graduate School of Engineering
Osaka, Japan
- Iida, T.
- Kato, Y.
- Sato, F.

PKU
Beijing, People's Republic of China
- Liu, G.
- Lu, Y.R.
- Zhu, K.

PSI
Villigen PSI, Switzerland
- Adelmann, A.

RCNP
Osaka, Japan
- Fukuda, M.
- Hatanaka, K.
- Kamakura, K.
- Morinobu, S.
- Nagayama, K.
- Saito, T.
- Shimada, K.
- Tamura, H.
- Ueda, H.
- Yasuda, Y.
- Yorita, T.

Research School of Physics and Engineering, Australian National University
Canberra, Australian Capitol Territory, Australia
- Linardakis, P.
- Lobanov, N.R.
- Tsifakis, D.
- Tunningley, T.

RIKEN Nishina Center
Saitama, Japan
- Abe, T.
- Dantsuka, T.
- Fujimaki, M.
- Fujinawa, T.
- Fukunishi, N.
- Hara, M.
- Hasebe, H.
- Higurashi, Y.
- Hirano, T.
- Ichikawa, S.
- Ikezawa, E.
- Imao, H.
- Kageyama, T.
- Kamigaito, O.
- Kase, M.
- Kidera, M.
- Komiyama, M.
- Kuboki, H.
- Kubono, S.
- Kumagai, K.
- Maie, T.
- Nagae, D.
- Nagase, M.
- Nagatomo, T.
- Naimi, S.
- Nakagawa, T.
- Nakamura, M.
- Ohnishi, J.
- Ohnishi, T.
- Okuno, H.
- Ozeki, K.
- Sakamoto, N.
- Suda, K.
- Suzaki, F.
- Tzoganis, V.
- Uchiyama, A.
- Uesaka, T.
- Wakasugi, M.
- Watanabe, S.
- Watanabe, T.

ISBN 978-3-95450-131-1

- Watanabe, Y.
- Yamada, K.
- Yamasawa, H.
- Yano, Y.
- Zenihiro, J.

RIKEN/RARF/CC
Saitama, Japan
- Nakagawa, T.

RIKEN
Saitama, Japan
- Abe, Y.
- Ikeda, S.
- Yamaguchi, Y.

Rikkyo University
Tokyo, Japan
- Kurita, K.
- Togasaki, M.
- Yamada, K.

RLNR
Tokyo, Japan
- Hayashizaki, N.

Saitama University
Saitama, Japan
- Kato, I.
- Miura, H.
- Nishimura, T.
- Omika, S.
- Suzuki, T.
- Tadano, N.
- Takeuchi, Y.
- Yamaguchi, T.

SAMEER
Mumbai, India
- Dixit, T.S.

SHI Accelerator Service Ltd.
Tokyo, Japan
- Fukuzawa, S.
- Hamanaka, M.
- Ishikawa, S.
- Kaneko, K.
- Kobayashi, K.
- Koyama, R.
- Nakamura, T.
- Nishida, M.
- Nishimura, M.
- Ohki, T.O.
- Oyamada, K.
- Shibata, J.
- Tamura, M.
- Tsukiori, N.
- Yadomi, K.
- Yamauchi, H.
- Yusa, Y.A.

Sigmaphi Electronics
Haguenau, France
- Kreiss, A.

SIGMAPHI S.A.
Vannes, France
- Tasset, O.

Sigmaphi
Vannes, France
- Antoine, S.
- Beeckman, W.
- Bocher, P.
- Cavellier, M.
- Cosson, O.
- Forest, F.
- Huttin, N.
- Jehanno, P.
- Jivkov, P.
- Lancelot, J.L.
- Leray, M.J.
- Milpied, X.

Sokendai
Ibaraki, Japan
- Adachi, T.
- Takayama, K.

South Dakota School of Mines and Technology
Rapid City, USA
- Strieder, F.

The University of Liverpool
Liverpool, United Kingdom
- Tzoganis, V.
- Welsch, C.P.

TIFR
Mumbai, India
- Karande, J.N.
- Nanal, V.
- Pal, S.
- Pillay, R.G.
- Rozario, C.

TIT
Tokyo, Japan
- Ikeda, S.
- Liu, X.
- Shibuya, T.
- Takayama, K.
- Yoshimoto, T.

ISBN 978-3-95450-131-1

Tokyo City University
Tokyo, Japan
- Hirose, M.
- Kobayashi, H.

Toshiba
Tokyo, Japan
- Nagamoto, Y.
- Orikasa, T.
- Takayama, S.

TRIUMF, Canada's National Laboratory for Particle and Nuclear Physics
Vancouver, Canada
- Crawford, J.
- Kiy, S.
- Kunz, P.
- Laxdal, R.E.
- Ma, Y.
- Marchetto, M.
- Ramogida, C.
- Ruth, T..J.
- Schaffer, P.
- Shelbaya, O.
- Verzilov, V.A.
- Yao, Z.Y.
- Zvyagintsev, V.

UNIST
Ulsan, Republic of Korea
- Chung, M.

Univ. degli Studi di Padova
Padova, Italy
- Bellan, L.
- Meneghetti, G.
- Oboe, R.

University of Brescia
Brescia, Italy
- Ferrari, M.
- Zenoni, A.

University of Notre Dame
Indiana, USA
- Robertson, D.

University of Tsukuba, Graduate School of Pure and Applied Sciences,
Tsukuba, Ibaraki, Japan
- Hiraishi, K.
- Ichikawa, Y.
- Ozawa, A.
- Suzuki, S.
- Tajiri, Y.

UTTAC
Tsukuba, Ibaraki, Japan
- Ishii, S.
- Kita, K.
- Moriguchi, T.
- Oshima, H.
- Sasa, K.
- Sekiba, D.
- Tajima, Y.
- Takahashi, T.
- Yamato, Y.

VECC
Kolkata, India
- Chakrabarti, A.

Warsaw University
Warsaw, Poland
- Choinski, J.

Weizmann Institute of Science, Physics
Rehovot, Israel
- Zajfman, D.

Yamagata University
Yamagata, Japan
- Goto, A.

ISBN 978-3-95450-131-1

Participants List

— A —

Abdelhakim, Said
CNRS, Orsay
France

Amirikas, Ramila
IMP/CAS, Lanzhou
Germany

Andrighetto, Alberto
INFN/LNL, Legnaro
Italy

Anger, Pascal
GANIL, Caen
France

— B —

Beeckman, William
SIGMAPHI
France

Bisoffi, Giovanni
INFN/LNL, Legnaro
Italy

Bodendorfer, Michael
CERN, Geneva
Switzerland

— C —

Calanna, Alessandra
INFN/LNS, Catania
Italy

Chakrabarti, Alok
VECC, Kolkata
India

Chen, Weilong
IMP/CAS, Lanzhou
China

Choinski, Jaroslaw
HIL, Warsaw
Poland

Comunian, Michele
INFN/LNL, Legnaro
Italy

Conway, Zachary
ANL, Argonne
U.S.A.

— D —

Dehnel, Morgan
D-Pace, Inc, Nelson
Canada

Dickerson, Clayton
ANL, Argonne
U.S.A.

Donzel, Xavier
Pantechnik, Bayeux
France

— E —

Efremov, Andrey
FLNR/JINR, Dubna
Russian Federation

E'nyo, Hideto
RIKEN Nishina Center, Wako
Japan

Etoh, Haruhiko
Sumitomo Heavy Industries, Ltd.
Japan

— F —

Fukuda, Mitsuhiro
RCNP, Osaka University
Japan

Fukunishi, Nobuhisa
RIKEN Nishina Center, Wako
Japan

— G —

Gerhard, Peter
GSI, Darmstadt
Germany

Gmaj, Przemyslaw
HIL, Warsaw
Poland

Grieser, Manfred
MPI-K, Heidelberg
Germany

Groening, Lars
GSI, Darmstadt
Germany

Guo, Jiquan
JLab, Newport News
U.S.A.

— H —

Harada, Hiroyuki
J-PARC/JAEA, Tokai-Mura
Japan

Hariwal, Rajesh
IUAC, New Delhi
India

Hasebe, Hiroo
RIKEN Nishina Center, Wako
Japan

Hatanaka, Kichiji
RCNP, Osaka University
Japan

Hendricks, Matthew
ANL, Argonne
U.S.A.

Higurashi, Yoshihide
RIKEN Nishina Center, Wako
Japan

Hirose, Masatake
Tokyo City University
Japan

Hojo, Satoru
NIRS, Chiba-shi
Japan

— I —

Ikeda, Shota
Tokyo Institute of Technology
Japan

Ikeda, Shunsuke
RIKEN Nishina Center, Wako
Japan

Ikeda, Naoaki
Mitsubishi Heavy Industries, Ltd.
Japan

Ikezawa, Eiji
RIKEN Nishina Center, Wako
Japan

Imao, Hiroshi
RIKEN Nishina Center, Wako
Japan

Ivanenko, Ivan
JINR, Dubna
Russian Federation

Iwata, Yoshiyuki
NIRS, Chiba-shi
Japan

ISBN 978-3-95450-131-1

— J —

Joung, Mijoung
IBS, Daejeon
Korea

— K —

Kadi, Yacine
CERN, Geneva
Switzerland

Kamakura, Keita
Osaka University
Japan

Kamalou, Omar
GANIL, Caen
France

Kamigaito, Osamu
RIKEN Nishina Center, Wako
Japan

Kase, Masayuki
RIKEN Nishina Center, Wako
Japan

Katagiri, Ken
NIRS, Chiba-shi
Japan

Kato, Yushi
Osaka Univ.
Japan

Keens, Simon
Ampegon AG, Turgi
Switzerland

Kester, Oliver
GSI, Darmstadt
Germany

Kim, Hyung Jin
IBS, Daejeon
Korea

Kobayshi, Hiroshi
Tokyo City University
Japan

Koji, Noda
NIRS, Chiba-shi
Japan

Komiyama, Misaki
RIKEN Nishina Center, Wako
Japan

Kotaka, Yasuteru
CNS, Tokyo
Japan

Kurashima, Satoshi
JAEA/TARRI, Gunma-ken
Japan

Kurokawa, Shin-Ichi
Cosylab
Japan

— L —

Lagniel, Jean-Michel
GANIL, Caen
France

Lamy, Thierry
LPSC/CNRS/IN2P3, Grenoble
France

Li, Chenxing
IMP/CAS, Lanzhou
China

Liu, Xingguang
Tokyo Institute of Technology
Japan

Lobanov, Nikolai
ANU, Canberra
Australia

— M —

Mahner, Edgar
FAIR, Darmstadt
Germany

Marchetto, Marco
TRIUMF, Vancouver
Canada

Marti, Felix
FRIB/MSU, East Lansing
U.S.A.

Miura, Hiroshi
Saitama University
Japan

Miyawaki, Nobumasa
JAEA, Gunma-ken
Japan

Monma, Takumi
Tokyo Tech
Japan

Munemoto, Naoya
Tokyo Institute of Technology
Japan

Muramatsu, Masayuki
NIRS, Chiba-shi
Japan

Muto, Hideshi
Tokyo University of Science
Suwa

— N —

Nagatomo, Takashi
RIKEN Nishina Center, Wako
Japan

Nakagawa, Takahide
RIKEN Nishina Center, Wako
Japan

Nakao, Masao
NIRS, Chiba-shi
Japan

Noda, Akira
NIRS, Chiba-shi
Japan

— O —

Ohnishi, Jun-ichi
RIKEN Nishina Center, Wako
Japan

Ohnishi, Tetsuya
RIKEN Nishina Center, Wako
Japan

Ohno, Tatsuya
Gunma University Heavy Ion Medical Center
Japan

Okamura, Masahiro
BNL, Upton
U.S.A.

Okubo, Koichi
Mitsubishi Heavy Industries Ltd.
Japan

Okuno, Hiroki
RIKEN Nishina Center, Wako
Japan

Osswald, Francis
CNRS, Orsay
France

Ozeki, Kazutaka
RIKEN Nishina Center, Wako
Japan

ISBN 978-3-95450-131-1

— P —

Pal, Sanjoy
TIFR, Mumbai
India

Palmieri, Antonio
INFN/LNL, Legnaro
Italy

Pardo, Richard
ANL, Argonne
U.S.A.

Park, Jin Yong
Korea Basic Science Institute, Busan
Korea

Paul, Schaffer
TRIUMF, Vancouver
Canada

— R —

Robertson, Daniel
University of Notre Dame
U.S.A.

— S —

Saha, Pranab
JAEA/J-PARC, Tokai-Mura
Japan

Sakamoto, Naruhiko
RIKEN Nishina Center, Wako
Japan

Saraya, Yuichi
National Institute of Radiological Science, Chiba
Japan

Sasa, Kimikazu
University of Tsukuba
Japan

Scharrer, Paul
HIM, Mainz
Germany

Sennyu, Katsuya
Mitsubishi Heavy Industries, Ltd.
Japan

Son, Hyock-Jun
IBS, Daejeon
Korea

Suda, Kenji
RIKEN Nishina Center, Wako
Japan

Sun, Liangting
IMP/CAS, Lanzhou
China

Suzaki, Fumi
RIKEN Nishina Center, Wako
Japan

Syresin, Evgeny
JINR, Dubna
Russian Federation

— T —

Takayama, Ken
High Energy Accelerator Research Organization
Japan

Takeshita, Eri
Kanagawa Cancer Center
Japan

Tamaki, Watanabe
RIKEN Nishina Center, Wako
Japan

Tamura, Jun
JAEA
Japan

Tao, Yue
IMP/CAS, Lanzhou
China

Tatami, Atsushi
TASC Graphene Division
Japan

Togasaki, Mamoru
Rikkyo University, Tokyo
Japan

Tzoganis, Vasilis
RIKEN Nishina Center, Cockcroft Institute, University of Liverpool
Japan

— U —

Uchiyama, Akito
RIKEN Nishina Center, Wako
Japan

— V —

Vondrasek, Richard
ANL, Argonne
U.S.A.

— W —

Wah, Leo
Malaysian Nuclear Agency
Malaysia

Wakui, Takashi
NIRS, Chiba-shi
Japan

Watanabe, Yutaka
RIKEN Nishina Center, Wako
Japan

Wei, Jie
FRIB, East Lansing
U.S.A.

Won, Mi-Sook
Korea Basic Science Institute, Busan
Korea

— Y —

Yamada, Kazunari
RIKEN Nishina Center, Wako
Japan

Yamada, Michiaki
Mitsubishi Heavy Industries, Ltd.
Japan

Yamaguchi, Yoshitaka
RIKEN Nishina Center, Wako
Japan

Yanagisawa, Takeshi
Mitsubishi Heavy Industries, Ltd.
Japan

Yorita, Tetsuhiko
RCNP, Osaka University
Japan

Yoshimoto, Takashi
Tokyo Institute of Technology
Japan

Yuri, Yosuke
JAEA
Japan

— Z —

Zhijun, Wang
IMP/CAS, Lanzhou
China

ISBN 978-3-95450-131-1